

Photoactive Materials Enabled by and for Emerging Synthetic Technologies

Emmanouil Broumidis

Submitted for the degree of Doctor of Philosophy

Heriot-Watt University

School of Engineering and Physical Sciences

Institute of Chemical Sciences

September 2022

The copyright in this thesis is owned by the author. Any quotation from the thesis or use of any of the information contained in it must acknowledge this thesis as the source of the quotation or information.

Abstract

In recent years there has been a significant increase in the development and commercialisation of new synthetic tools and technologies, which offer significant advantages compared to traditional round-bottomed flask chemistry. This work explores the use of some of these emerging technologies with the goal of developing new photocatalytic processes, which would not otherwise be easily feasible with batch techniques. Specifically, we have used continuous flow chemistry, mechanochemistry, and 3D printing in four distinct research projects. This thesis is split into five chapters in total.

Chapter 1 aims to act as a global introduction to the different synthetic technologies that were used and compare their utility and drawbacks against traditional batch synthetic methodologies. The remaining chapters 2-5 each represent a separate research project that utilises these new technologies. Each chapter contains its own introduction to the topic of research along with conclusions and proposed future work.

Specifically, in **Chapter 2**, a rapid, high yielding, and work-up free synthesis of an unusual organic luminophore is developed. Its twisted, propeller-like geometry gives rise to much sought aggregation induced emission properties. Moreover, we were able to use this material as a reusable heterogeneous photosensitiser to produce singlet oxygen under continuous flow conditions.

In **Chapter 3**, we report the unprecedented ring contraction of 1,2,6-thiadiazines to 1,2,5-thiadiazole 1-oxides. The transformation is fast, work-up free, offers quantitative yields, and is mediated by auto-photosensitised singlet oxygen. We exploited continuous flow processes to further improve the reaction scope and efficiency.

Then, in **Chapter 4** we describe the batch and mechanochemical syntheses of optically active dihydroxamic acids ligands, and their subsequent use for the synthesis of metallo-organic assemblies.

Finally, **Chapter 5** demonstrates how mechanochemical and 3D printing technologies were used to access a series of *N*-aryl amides from *O*-protected hydroxamic acids.

The broad scope of this work aims to demonstrate the usefulness of alternative reactor designs in chemical synthesis and encourage their implementation by others.

Acknowledgements

First and foremost, I owe my supervisor, Dr Filipe Vilela my gratitude for accepting me into his group, continuous guidance, troubleshooting efforts, and commitment to this project over the past four years. I am especially grateful to Filipe for not only granting me freedom to explore new ideas, but also for his constant encouragement, which taught me to be ambitious, seize opportunities, and not be afraid to pursue my dreams. Thank you Filipe, you have been an exceptional supervisor.

A big thank you is also owed to my external supervisor, Dr Gareth Lloyd, who introduced me to the wonderful fields of mechanochemistry and supramolecular chemistry. He gave me ample support throughout the duration of the project, and his invigorating and optimistic attitude helped me overcome several ‘turbulent’ phases of my studies.

I also want to recognise the contributions of Prof. Panayiotis Koutentis to this work and thank him for his willingness to collaborate with us, and also for introducing me to the world of research, when back in 2016, he accepted me for an Erasmus traineeship in his research group. My experience during that period cemented my love for chemistry and motivated me to pursue this PhD.

Due to the collaborative and multidisciplinary nature of this work, there are many (too many to list!) other people who supported me along the way, to whom I am indebted. However, I would like to especially thank Dr Georgina Rosair, for her crystallographic expertise, Dr Dave Ellis, for helping me with NMR spectroscopy, and Prof. Stuart Macgregor, for providing computational support.

Special mention is also warranted to past and present member of the VilelaLab, including Chris, Dominic, Cathryn, Mary, and Sam. I want to thank them for their support and for being great lab mates in general!

Of course, I want to thank my childhood friends, George and Dennis, for sticking with me all those years and all the fun memories we made.

And finally, this work could not have been done without the constant support of my parents, and all their sacrifices over the years, which gave me a chance for a better future. For this I am grateful.

Impact Statement

Work for this thesis started in March of 2018 under the supervision of Dr Gareth Lloyd. The project was aiming to develop new hydroxamate-based coordination cages and explore their application in catalysis and was sponsored by the CRITICAT centre for doctoral training.

During the first year (March 2018-2019), significant progress was made towards understanding how to synthesise the hydroxamate ligands and their coordination assemblies. Moreover, mechanochemistry was found to be a key technology that provided easier access to key intermediates, and the conversion of *O*-protected hydroxamic acids to *N*-aryl amides. The results of this work can be found in chapters 4 and 5.

However, in April of 2019, Dr Lloyd moved to a new position at the University of Lincoln, and his role as my primary supervisor was taken by Dr Filipe Vilela, who is conducting research in the areas of photoactive polymeric and molecular materials. This presented a challenge for me, as I had to spend a considerable amount of time learning new techniques and operate new instrumentation as well as the necessary theoretical background. However, this was also an opportunity, which allowed me to expand the scope of my research from supramolecular catalysis, to the use of enabling technologies such as mechanochemistry, flow chemistry and 3D printing to enhance and enable new chemical processes.

Another hurdle came in March of 2020, where the COVID-19 pandemic and subsequent quarantines led to the closure of our laboratory until late July, when it was reopened on a limited occupation capacity. From that time and for the following three months I was able to resume working on a part-time basis. Between January and September of 2021, the practical work of the project was completed.

Then, at that time, I obtained a six-month temporary suspension of studies as I was accepted into InnovateUK's Innovation to Commercialisation of University Research (ICURe) programme. The goal of this programme is to provide business development training and enable the participants to conduct market research activities to evaluate the commercial feasibility of university research. In our case we had developed a novel

planetary ball mill device made specifically to improve the efficacy of mechanochemical reactions. In April of 2022, when the programme concluded, our proposal won a ca. £300,000 grant for the creation of a spinout company.

Finally, from April and for the next three months, I completed the writing of this thesis, and it was submitted to the university in July of 2022. That three-month period was funded by CRITICAT CDT to compensate for time lost during the initial COVID-19 outbreak. The timeline described above is also summarised in the following figure.

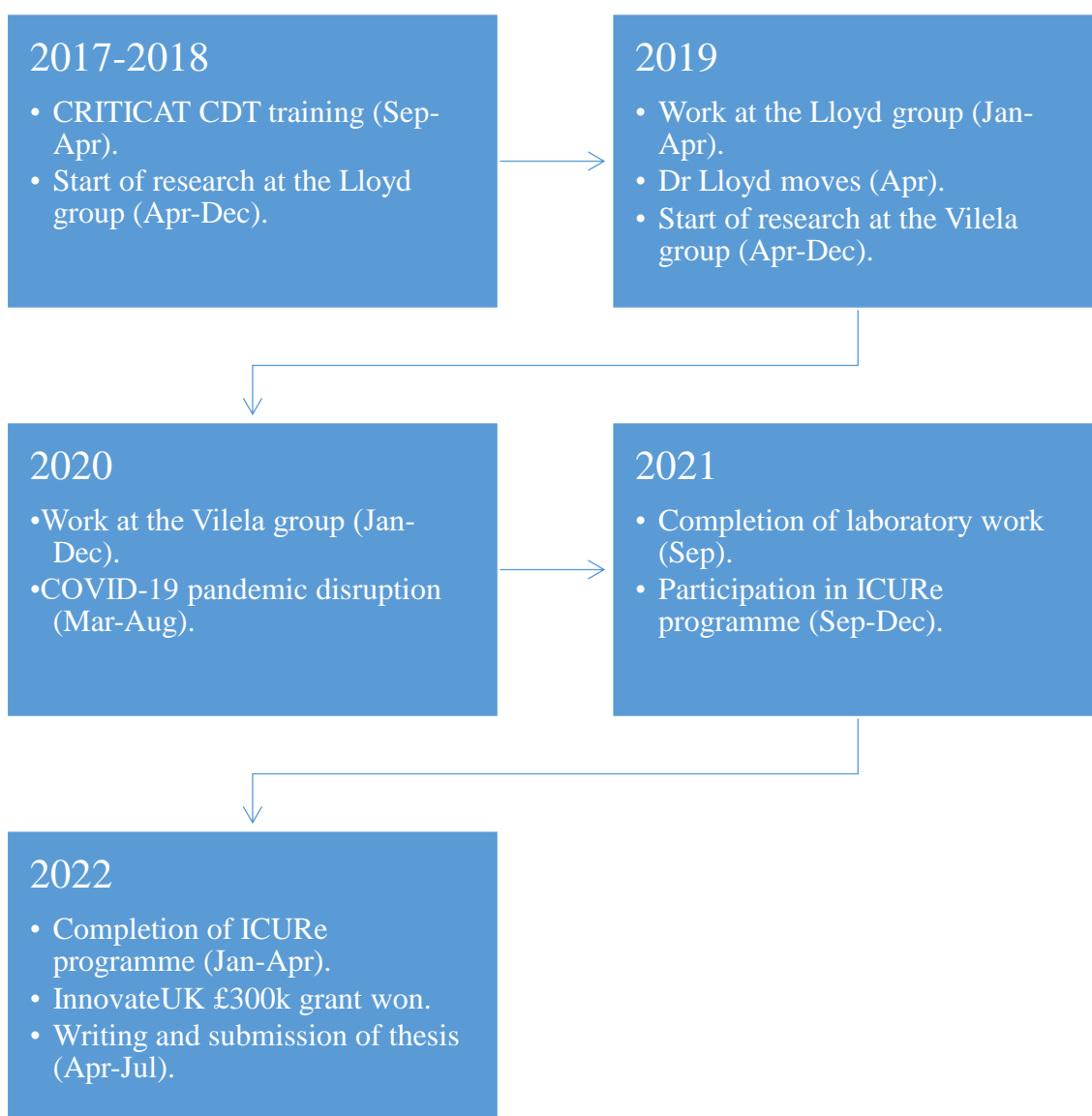


Figure 1. Graphical timeline of research work progression.

Research Thesis Submission

Name:	Emmanouil Broumidis		
School:	School of Engineering and Physical Sciences		
Version: (<i>i.e.</i> <i>First,</i> <i>Resubmission,</i> <i>Final</i>)	Final	Degree Sought:	PhD

Declaration

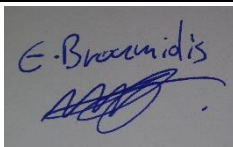
In accordance with the appropriate regulations, I hereby submit my thesis and I declare that:

1. The thesis embodies the results of my own work and has been composed by myself
2. Where appropriate, I have made acknowledgement of the work of others
3. The thesis is the correct version for submission and is the same version as any electronic versions submitted*.
4. My thesis for the award referred to, deposited in the Heriot-Watt University Library, should be made available for loan or photocopying and be available via the Institutional Repository, subject to such conditions as the Librarian may require
5. I understand that as a student of the University I am required to abide by the Regulations of the University and to conform to its discipline.
6. I confirm that the thesis has been verified against plagiarism via an approved plagiarism detection application e.g. Turnitin.
7. Where the thesis contains published outputs under Regulation 6 (9.1.2) or Regulation 43 (9) these are accompanied by a critical review which accurately describes my contribution to the research and, for multi-author outputs, a signed declaration indicating the contribution of each author (complete)
8. Inclusion of published outputs under Regulation 6 (9.1.2) or Regulation 43 (9) shall not constitute plagiarism.

* *Please note that it is the responsibility of the candidate to ensure that the correct version of the thesis is submitted.*

Signature of Candidate:		Date:	28/09/2022
-------------------------	---	-------	------------

Submission

Submitted By (<i>name in capitals</i>):	EMMANOUIL BROUMIDIS
Signature of Individual Submitting:	
Date Submitted:	28/09/2022

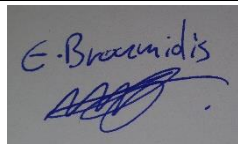
For Completion in the Student Service Centre (SSC)

Limited Access	Requested	Yes	No	Approved	Yes	No
E-thesis Submitted (mandatory for final theses)						
Received in the SSC by (<i>name in capitals</i>):				Date:		

Inclusion of Published Works

Declaration

This thesis contains one or more multi-author published works. In accordance with Regulation 6 (9.1.2) I hereby declare that the contributions of each author to these publications is as follows:

Citation details	E. Broumidis, M. C. Jones, F. Vilela, G. O. Lloyd, <i>ChemPlusChem</i> 2020 , 85, 1754
E. Broumidis	Discovery of the transformation, reaction optimisations, reaction scope, mechanistic experiments, data analysis, CAD design of milling jars, 3D printing, writing of the published manuscript
M. C. Jones	Batch photosensitisation experiment, collection of UV-Vis absorption spectrum of compound 2I, manuscript revision
F. Vilela	Project supervision
G. O. Lloyd	Project supervision
Signature:	
Date:	28/09/2022

Citation details	E. Broumidis, C. M. S. Jones, M. Koyioni, A. Kourtellaris, G. O. Lloyd, J. Marques-Hueso, P. A. Koutentis, F. Vilela, <i>RSC Adv.</i> 2021 , 11, 29102–29107
E. Broumidis	Synthesis of photocatalyst, photocatalytic performance evaluation, experiment design, photophysical and photochemical data interpretation, writing of the published manuscript
C. M. S. Jones	Photophysical experiments
M. Koyioni	Computational experiments, crystallisations, TGA experiments
A. Kourtellaris	SC-XRD data collection

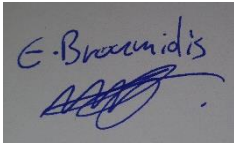
G. O. Lloyd	Project supervision, SC-XRD data interpretation
J. Marques-Hueso	Access to fluorescence spectroscopy instrumentation
P. A. Koutentis	Project supervision
F. Vilela	Project supervision
Signature	
Date:	28/09/2022

Table of Contents

Abstract.....	ii
Acknowledgements.....	iii
Impact Statement.....	iv
Research Thesis Submission.....	vi
Inclusion of Published Works.....	vii
Table of Contents.....	ix
List of Abbreviations.....	xiv
Chapter 1: Introduction to Synthetic Technologies.....	1
1.1 Declaration.....	1
1.2 Background and Aims.....	1
1.3 Traditional Synthetic Technologies.....	2
1.4 Emerging Synthetic Technologies.....	5
1.4.1 Flow Chemistry.....	5
1.4.2 Mechanochemistry.....	9
1.4.3 3D Printing.....	14
1.5 Concluding Remarks and Research Aims.....	18
1.6 References.....	20
Chapter 2: Development of a Novel Molecular Heterogeneous Photocatalyst with Aggregated-Induced Emission Properties.....	31
2.1 Declaration.....	31
2.2 Background and Aims.....	32
2.3 Abstract.....	34
2.4 Introduction.....	34
2.5 Results and Discussion.....	35
2.5.1 Synthesis and Characterisation of Compounds 5 and 5H ₂ ²⁺	35
2.5.2 Photochemical Studies.....	38
2.5.3 Photophysical Studies.....	41
2.6 Conclusions.....	45
2.7 Future Work.....	46
2.8 Supporting Information.....	52
2.8.1 TGA Curves of 5 and 5H ₂ ²⁺	52
2.8.2 Crystallographic Data ^s	53
2.8.3 Computational Data ^s	56
2.8.4 Additional Photophysical Data.....	61
2.8.5 Continuous Flow Set-Up and Cycle Data.....	64
2.8.6 X-Ray Powder Diffraction of 5.....	69

2.8.7 Solubility of 5 in Various Organic Solvents	69
2.8.8 ¹ O ₂ Generation Efficiencies of 5 and 5H ₂ ²⁺ Under Identical Conditions	70
2.8.9 Aerobic Oxidative Hydroxylation of Phenylboronic Acid (HPLC Data)	71
2.9 Experimental Section	72
2.9.1 General Methods and Materials	72
2.9.2 Preparation of Compounds 1, 2, 5 and 5H ₂ ²⁺	73
2.9.3 Heterogeneous Flow Mediated Photocatalytic Generation of ¹ O ₂ With In-Line NMR Analysis.....	76
2.9.4 Photoluminescence Quantum Yield (PLQY) Calculations ^s	77
2.10 References.....	78
Chapter 3: Photochemical Ring Editing: Selective Carbon Excision from Thiadiazines ..	89
3.1 Declaration.....	89
3.2 Background and Aims.....	90
3.3 Introduction.....	91
3.4 Results and Discussion	94
3.4.1 Reaction Discovery	94
3.4.2 Reaction Optimisation.....	96
3.4.3 Reaction Scope.....	98
3.4.4 Crystallographic Data ^s	107
3.4.5 Mechanistic Studies	107
3.4.6 Computational Studies ^s	110
3.4.7 Proposed Reaction Mechanism.....	111
3.5 Conclusions.....	113
3.6 Future Work.....	114
3.7 Supporting Information.....	119
3.7.1 Comparison Between 1a and 1b As Seen by NMR, FT-IR and UV-Vis	119
3.7.2 Reaction Optimisation Under Continuous Flow Conditions (Method B).....	121
3.7.3 Photographs of Experimental Setup (Method A and Method B).....	124
3.7.4 Stability Profile of 2-Benzoyl-4-phenyl-1,2,5-thiadiazol-3(2 <i>H</i>)-one 1-oxide (1b)..	125
3.7.5 Additional Mechanistic Experiments.....	128
3.7.5.1 Control Experiments	128
3.7.5.2 Reaction Between 1a and <i>m</i> -CPBA to Form Sulfone 1c	132
3.7.5.3 Concurrent Ring Contraction of Two Symmetrical 1,2,6-Thiadiazines	133
3.7.5.4 Equivalents of O ₂ Needed for the Complete Transformation of 1a to 1b.....	134
3.7.5.6 Irradiation of Isolated 1,2,6-Thiadiazine Sulfones 50d and 51d.....	135
3.7.6 Comments on the Role of Superoxide ^s	138

3.7.7 Single Crystal X-Ray Diffraction Data Collection and Refinement Details [§]	139
3.8 Experimental Section	163
3.8.1 General Methods and Materials	163
3.8.2 Preparation of 4 <i>H</i> -1,2,6-Thiadiazine Starting Materials [§]	164
3.8.2.1 Preparation of Symmetrical 3,5-Diaryl-4 <i>H</i> -1,2,6-thiadiazines	165
3.8.2.2 Preparation of Asymmetrical 3,5-Diaryl-4 <i>H</i> -1,2,6-thiadiazines.....	168
3.8.3 Preparation of 1,2,5-Thiadiazole 1-oxides from 4 <i>H</i> -1,2,6-Thiadiazines	173
3.8.3.1 Preparation of Symmetric 1,2,5-Thiadiazole 1-oxides	173
3.8.3.2 Preparation of Asymmetric 1,2,5-Thiadiazole 1-oxides	185
3.8.4 Characterisation of Isolated Side-Products and Reference Compounds	191
3.9 References.....	196
Chapter 4: Development of Photoactive Hydroxamate-Based Coordination Cages	210
4.1 Declaration.....	210
4.2 Background and Aims.....	211
4.3 Introduction.....	212
4.3.1 Introduction to Supramolecular Cages and Their Applications	212
4.3.2 Hydroxamic Acids and Their Use in Supramolecular Assemblies	214
4.3.2.1 Properties and Structure of Hydroxamic Acids	214
4.3.2.2 Supramolecular Cages based on Hydroxamic Acid Ligands	217
4.3.2.3 Previous Work on M ₄ L ₆ Tetrahedral Cages.....	219
4.4 Results and Discussion	221
4.4.1 Terephthaloyl Dihydroxamic Acid-Based Complexes [§]	221
4.4.1.1 Synthesis of Ligands H ₂ A-H ₂ D.....	221
4.4.1.2 Synthesis and Characterisation of Ga ³⁺ /Fe ³⁺ Complexes with Ligands H ₂ A-H ₂ D	223
4.4.2 Naphthaloyl Dihydroxamic Acid-Based Complexes	226
4.4.2.1 Synthesis and Characterisation of Ligands AlaHA, ValHA, LeuHA and PheHA	226
4.4.2.2 Synthesis and Characterisation Ga ³⁺ Complexes with Ligands AlaHA, ValHA, LeuHA and PheHA.....	231
4.5 Conclusions.....	237
4.6 Future Work.....	237
4.6.1 Work Involving 2,6-Naphthalene-Based Ligands.....	237
4.6.2 Work Involving Ligands with Other Spacer Units	241

4.7 Supporting Information.....	247
4.7.1 D ₂ O Effect on AlaHA, ValHA, LeuHA and PheHA ¹ H NMR Spectra	247
4.7.2 D ₂ O Effect on AlaHA-Ga Complex.....	248
4.7.3 Gel Formation After TEA addition to AlaHA-Fe Complex	249
4.7.4 ¹ H NMR Titration Experiment Using ValHA.....	250
4.7.5 ¹ H NMR Titration Experiment Using LeuHA.....	251
4.7.6 DOSY Spectra of PheHA and PheHA-Ga Complexes	252
4.8 Experimental Section	252
4.8.1 General Methods and Materials	252
4.8.2 Preparation of New Compounds.....	253
4.9 References.....	261
Chapter 5: Mechanochemically Mediated Synthesis of <i>N</i>-Aryl Benzamides from <i>O</i>-protected Hydroxamic Acids.....	274
5.1 Declaration.....	274
5.2 Background and Aims.....	274
5.3 Abstract.....	277
5.4 Introduction.....	278
5.5 Results and Discussion	279
5.5.1 Mechanochemical SM Synthesis and Iron Leaching Problem.....	279
5.5.2 Reaction Optimisation.....	283
5.5.3 Reaction Scope.....	286
5.5.4 Custom 3D Printed Jars for Reaction Scale-Up.....	289
5.6 Conclusions.....	290
5.7 Future Work.....	292
5.8 Supporting Information.....	294
5.8.1 Optimisation of protocols A and B	294
5.8.2 Aryl Halide Scope.....	299
5.8.3 Iron Leaching During Milling.....	300
5.8.4 Effect of Various Catalysts and Additives	300
5.8.5 Comparison of Jar Materials (Protocol A)	302
5.8.6 Efficacy of Solution Chemistry Versus Mechanochemistry (Protocols A and B) ...	302
5.8.7 3D Printing of Large Volume Milling Jars	304
5.8.8 Generation of ¹ O ₂ Under Batch Conditions ^s	306
5.8.9 Generation of ¹ O ₂ Under Mechanochemically-Assisted Solid-State Photocatalysed (MASSPC) Conditions.....	308
5.9 Experimental Section	311
5.9.1 General Methods and Materials	311
5.9.2 Preparation of 4,7-Diiodobenzo[c][1,2,5]thiadiazole	312

5.9.3 Preparation of <i>O</i> -Protected Hydroxamic Acids	313
5.9.4 Preparation of <i>N</i> -Aryl Benzamides (Protocols A and B)	317
5.9.5 Gram-Scale Mechanochemical Preparations (Protocol A and B)	323
5.10 References	324

List of Abbreviations

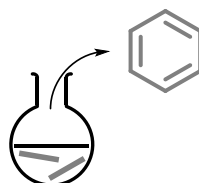
3D	Three dimensional
A	Absorbance
ASAP	Atmospheric solids analysis probe
AIE	Aggregation induced emission
Ar	Aryl group
AU	Arbitrary units
BTZ	2,1,3-Benzothiadiazole
BODIPY	4,4-Difluoro-4-bora-3a,4a-diaza-s-indacene
Bpin	Pinacol boronic ester
Bn	Benzyl
Bz	Benzoyl
BQ	1,4-Benzoquinone
calc.	Calculated
ca.	Circa
°C	Degrees Celsius
C	Concentration
CAD	Computer-aided design
cat.	Catalytic amount
CDI	1,1'-Carbonyldiimidazole
COSY	Correlated Spectroscopy
CHCl ₃	Chloroform
DCM	Dichloromethane
d.r.	Diastereomeric ratio
DIPEA	Diisopropylethylamine
DMF	<i>N,N</i> -Dimethylformamide
DMN	1,4-Dimethylnaphthalene
DOSY	Diffusion-ordered spectroscopy
DMSO	Dimethyl sulfoxide
DSC	Differential scanning calorimetry
DABCO	1,4-Diazabicyclo[2,2,2]-octane

eq./equiv.	Equivalent
ESI	Electrospray ionisation
EI	Electron ionisation
Et	Ethyl
Et ₂ O	Diethyl ether
EtOH	Ethanol
EtOAc	Ethyl acetate
EPO	Endoperoxide
EWG	Electron withdrawing group
EDG	Electron donating group
EDX	Energy dispersive X-ray analysis
FT-IR	Fourier transform infrared
G	Gauss
h	Hours
HA	Hydroxamic acid
HRMS	High resolution mass spectroscopy
Hz	Hertz
Het	Heteroarene
HOMO	Highest occupied molecular orbital
ISC	Inter-system crossing
LUMO	Lowest unoccupied molecular orbital
LC-MS	Liquid chromatography-mass spectrometry
lit.	Literature value
LED	Light emitting diode
Mp	Melting point
min	Minutes
M	Molarity
mol	Mole
Me	Methyl
MeOH	Methanol
m/z	Mass-over-charge-ratio
MS	Mass spectrometry

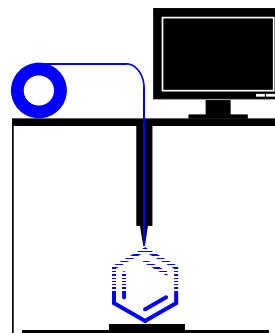
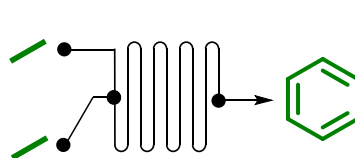
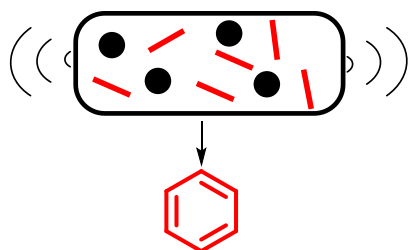
MB	Methylene blue
NMR	Nuclear magnetic resonance
NOESY	Nuclear Overhauser effect spectroscopy
n.r.	No reaction
$^1\text{O}_2$	Singlet oxygen
$^3\text{O}_2$	Triplet oxygen
$\text{O}_2^{\cdot-}$	Superoxide radical
PDT	Photodynamic therapy
PLQY	Photoluminescence quantum yield
PS	Photosensitiser
Ph	Phenyl
quant.	Quantitative
R	Alkyl/Aryl
R_f	Retention factor
ROS	Reactive oxygen species
SET	Single electron transfer
s	Second
SI	Supporting information
SM	Starting material
SC-XRD	Single crystal X-ray diffraction
SEM	Scanning electron microscope
TFA	Trifluoroacetic acid
TLC	Thin layer chromatography
TTA	Triplet-triplet annihilation
THF	Tetrahydrofuran
TGA	Thermogravimetric analysis
UV	Ultraviolet
Vis	Visible
*	Excited state
§	Indicates work that has been carried out by a collaborator

Chapter 1: Introduction to Synthetic Technologies

Past - Batch reactors



Future - Mechanochemical, continuous flow, 3D printed reactors



1.1 Declaration

The following people have contributed to this work:

Emmanouil Broumidis: Main author of the current chapter.

Gareth O. Lloyd and Filipe Vilela: General supervision and manuscript review.

Unless otherwise stated, all the photographs that are shown in this chapter were taken by current and past members of the Vilela group. Permission was acquired by the owner of each photograph before use.

1.2 Background and Aims

The work presented in this thesis consists of four distinct projects each of which contains an introduction, aiming to familiarise the reader with the topic of study. Despite this, all these four projects have a common underlying theme, namely the utilisation of new synthetic technologies to enable a process, or the synthesis of new materials with photoactive properties and related applications. This chapter aims to act as a general introduction, informing the reader about these technologies and their importance in contemporary chemical research and manufacturing.

1.3 Traditional Synthetic Technologies

When it comes to the way scientists conduct their experiments, it is a well-known fact that amongst the natural sciences, chemistry is one of the most ‘change-resistant’ disciplines, as chemists usually prefer to work using established techniques and equipment and are not as open to adopting new methodologies.¹ This can be demonstrated by comparing a contemporary synthetic laboratory with one from one century ago (Figure 1). As it can be seen, in both cases the main features are the same,



Figure 1. Photographs showing a chemical laboratory at: a) Heriot-Watt University, Scotland, 2022 and b) ETH Zurich, Switzerland, ca. 1920s. Credit: Wellcome Collection, London.

consisting of a series of workbenches, equipped with racks for storing bottles with chemicals, storage drawers and washbasins, as well as appropriate ventilation and fume hoods along the walls (not pictured). In fact, what we consider as a ‘modern’ laboratory today has been in existence since around 1860, when the first ones were built in a few select German universities,² and if a person from that era was shown what a chemistry

laboratory looks like today, they would be able to recognise most of the glassware and equipment (except perhaps from a few ‘mystery’ electrical boxes!).³

When it comes to reaction vessels, glass containers of various shapes and sizes have been the ‘gold-standard’ since the dawn of modern chemistry, as glass possesses unique properties such as chemical inertness, resistance to high temperatures, and high malleability, making it possible to construct intricate shapes, depending on the intended use.⁴ Even though it is seen as a ubiquitous material today, it took several millennia from its initial discovery by the Phoenicians (*ca.* 5000 BC) until glassmaking technology made it a suitable material for reaction containers, as, for most of its history, glass was known to break easily, especially when subjected to high temperatures.⁵ This trend started to shift after the 13th century, as incremental changes in its composition by glassmakers in central and northern Europe transformed it into a versatile material suitable for use in chemical applications. Perhaps one of the biggest improvements in glassmaking came in 1915, when the American company Corning Glass Works developed borosilicate glass, (marketed as ‘Pyrex’), known for its durability and resistance to temperature-shock.⁶ Consequently, this type of glass remains the material out of which most chemistry glassware is made, even to this day.⁷ This also includes reaction vessels, such as the round bottom flask (Figure 2), one of the most ubiquitous and widely used reactors.⁸

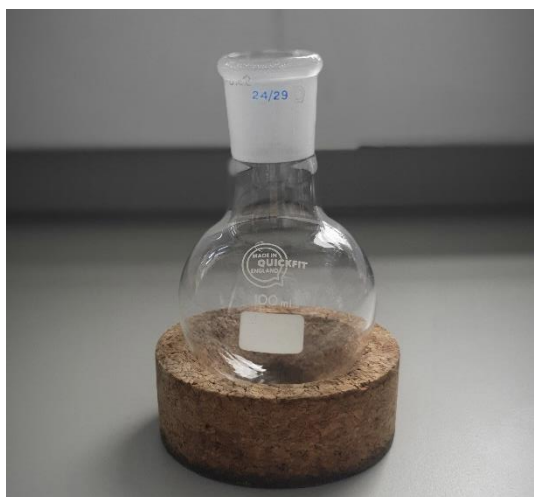


Figure 2. A 100 mL borosilicate round bottom flask, made possible by thousands of years of innovation, and one of the most common reaction vessels in the world today.

These vessels, which are also known as batch reactors, are inexpensive, versatile and owing to their borosilicate glass construction have many positive attributes that

contributed to their popularity, but their use comes with several downsides notwithstanding, many of which will become evident in the following pages.

In the past few decades, it has become clear that if humanity wants to continue living on this planet in the long term, then fundamental changes on all levels of society must occur, most of which pertain to the way we produce and consume commodities. As the chemical industry (including research activities⁹) is notorious for both consuming vast amounts of energy¹⁰ (*ca.* 20% of industrial energy consumption in the US¹¹), and generating substantial waste, there are many changes that chemists can implement to help accelerate the transition to a more sustainable future, and is something that has been the main focus of research for many groups around the world. This shift formally started with the introduction of the field of Green Chemistry, nearly 30 years ago, which aims to exploit chemical innovation to produce more sustainable and environmentally friendly practices.¹² At the same period, the now infamous 12 principles of Green Chemistry were introduced by Paul Anastas and John Warner¹³ (Figure 3), in an effort to make clear what

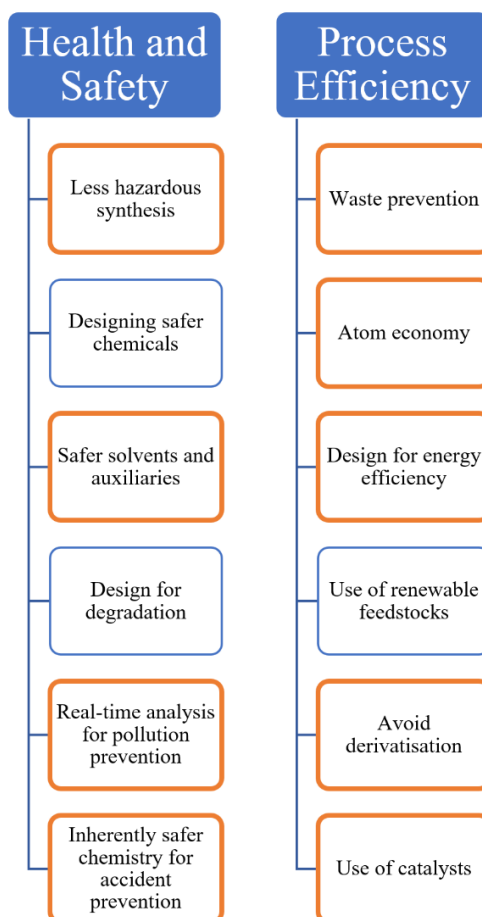


Figure 3. 12 principles of Green Chemistry, split in two categories. Principles within orange boxes signify that reactor design can be used to aid in their implementation.

steps should be taken into consideration when designing new research methodologies so that they are in line with the framework of Green Chemistry. As it will become evident in the next sections, many of the principles outlined below can be realised by moving away from traditional, batch-type reactors.

1.4 Emerging Synthetic Technologies

Over the past 20 years, advances in computer technology, networks, and artificial intelligence (AI) have transformed society on many levels, which is evident by the infiltration of chip-laden devices in our daily lives, from smartphones to AI voice assistants and self-driving cars, machines are now ubiquitous.¹⁴ This ‘digital revolution’ has also manifested into several new synthetic technologies, which aim to alleviate issues associated with conventional batch chemistry while helping chemists increase their productivity in a safe and sustainable manner.¹⁵ More specifically, this thesis has focused on the use of flow chemistry, mechanochemistry and additive manufacturing for chemically active objects, each of which is briefly introduced below. More in-depth reviews for each technology can be found in the literature.¹⁶⁻¹⁸

1.4.1 Flow Chemistry

Flow chemistry, also known as continuous flow chemistry, works by replacing the conventional flask with pumps and small diameter (<5 mm in most cases) tubing, which has a large surface to volume ratio resulting in superior mixing, heat/mass transfer, light penetration, scalability and safety profiles.¹⁹ Early instances of flow chemistry utilised custom-made electronics and pumps,²⁰ used to control the flow rate, however, over the years several private companies²¹⁻²⁴ started offering integrated systems, known as flow machines, which are commonly used today in industrial and academic research laboratories (Figure 4). In general, flow chemistry offers several advantages compared to batch reactors, the main of which are:

Superior mixing. Efficient mixing of liquid media enables the frequent collision of the reactants in solution, thus rendering it a vital factor in synthetic chemistry and has a direct

impact on heat transfer, reaction kinetics, and yield.²⁵ Batch chemistry employs mechanical stirring 95% of the time,²⁶ which is usually achieved by magnetically rotated stir bars, providing adequate, albeit suboptimal mixing. In addition, since rotation speed and stirrer bar size are most of the time not reported in published synthetic protocols, reliability issues may arise, which inadvertently contribute to the current ‘reproducibility crisis’ in chemistry.^{27,28} Furthermore, it has been shown that routinely-used Teflon-coated stir bars are prone to micro-structural damage and contamination with trace metal impurities that can catalyse subsequent reactions.²⁹ Moreover, it has also been shown that the presence of external magnetic fields can dictate the outcome of certain chemical reactions, a fact that has been historically overlooked but gained attention in more recent years.^{30,31} On the other hand, flow chemistry offers substantially more effective mixing mechanisms. Examples include the use of different ‘mixers’ which are junction points where two or more solutions pumped from different tubes meet,³² and the type of reactor that is used, which can range from a simple coil to more intricate chip-type reactors with μm wide channels and multiple recombination junctions.³³



Figure 4. Photograph showing a contemporary flow machine, manufactured by Vapourtec Ltd.

Heat Transfer. As a result of the small diameter tubing that is used in flow chemistry, heat gradients are generally smaller than those in batch reactors, however this also depends on the reactor wall material. For example, it is expected that a coil reactor made from copper metal to provide more efficient heat transfer than one which uses PTFE (Figure 5). In contrast, borosilicate flasks used in batch chemistry offer poor heat transfer,

making flow chemistry the ideal choice for temperature sensitive reactions, as well as exothermic reactions, since the tubing acts as a heatsink, preventing temperature spikes.¹⁹



Figure 5. Photographs of copper, stainless steel, and PTFE coil reactors (from left to right).

Light Penetration. As it is known, light gets absorbed when traversing through a liquid medium and the rate of absorption is directly related to the distance it has to travel through that medium, as described by the Beer-Lambert law (Figure 6).³⁴ This makes flow chemistry the ideal synthetic methodology for photochemical reactions since the light path between entering and exiting the solution is only a few mm's (or even μm 's in the case of micro-reactors). Coupled with advances in LED technology and the development of commercial flow photoreactors, the field of flow photochemistry has received a lot of attention in the past decade,³⁵ leading to better reaction times, improved yields and synthesis of photosensitive materials. As we will demonstrate in chapters 2 and 3, its use was instrumental in the successful development of our chemistry.

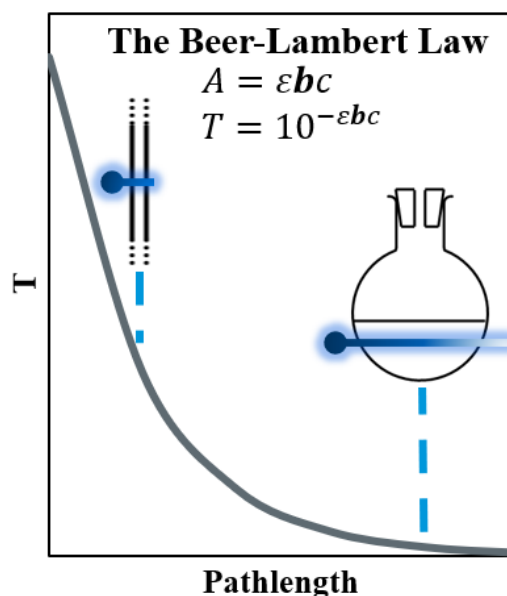


Figure 6. Graphical and mathematical representation of the Beer-Lambert Law. A = Absorbance, T = Transmittance, ϵ = molar absorptivity, b = length of light path, c = concentration of solution. It is evident that a round bottom flask with a much larger b value compared to that of a thin tube used in flow chemistry will absorb an incoming light beam to a much greater degree, leading to a decreased photon flux at the opposite end of the reactor wall.

Scalability. This is another area where flow chemistry is usually superior to its batch counterpart. Generally scaling up a reaction that was developed at laboratory scale (mg to a few g) using batch reactors is a challenging task, mainly due to heat and mass transport limitations, and it requires costly and time-consuming efforts to successfully transition to an industrially relevant scale.³⁶ Conversely, when flow reactors are utilised scaling up is achieved more easily, due to its continuous mode of operation. In principle, if there are starting materials fed to the pumps, product(s) will keep being produced at the other side. It has to be stressed that this is possible not only for homogeneous systems but heterogeneous ones as well, perfectly demonstrated by Merck Inc., which developed a scale-up protocol for the synthesis of a potential active pharmaceutical ingredient (API) with a productivity of 250 Kg/h.³⁷ The ability of flow chemistry systems to facilitate process intensification is one of the reasons that has increased its popularity within the pharmaceutical sector.³⁸ In fact, it was one of the key technologies that enabled the rapid development of antiviral compounds used to alleviate the severity of COVID-19 symptoms during the 2020 coronavirus pandemic. In April of 2020, Gilead Sciences Inc., reported how they used flow chemistry to synthesise 500 Kg of a key precursor of the antiviral Remdesivir, just one month after the virus started to spread globally.³⁹

Safety. Most flow chemistry processes are inherently safer compared to those performed in batch, which again stems from the fine channels that are used to carry the solvents, as this translates to only a small amount of material reacting at a time, reducing exposure to toxic or explosive substances.⁴⁰ Furthermore, during the process of reaction optimisation, microreactors can be used for rapid screening of conditions, allowing researchers to identify the ones producing the least amount of waste material.⁴¹

In addition to the factors outlined thus far, flow chemistry also provides numerous other advantages, some of which are the ability to control and regulate the internal temperature and pressure,¹⁶ compatibility with in-line reaction monitoring techniques,⁴² and suitability to be coupled with other green processes, such as electrochemistry⁴³ and biocatalysis.⁴⁴ Recent advances in AI and robotics are also making it possible to create automated flow machines,⁴⁵ further enhancing their utility. Ultimately, those factors enable flow chemistry to precisely control the reaction conditions, making it a great platform for developing green processes.

1.4.2 Mechanochemistry

Mechanochemistry can be defined as the promotion of chemical reactions by introducing energy in the form of a mechanical force, without the need of using a solvent. This is usually achieved by grinding the materials together in a ball-mill mixer, by utilising ultrasound irradiation using special sonication equipment, or by extrusion methods⁴⁶ (Figure 7).

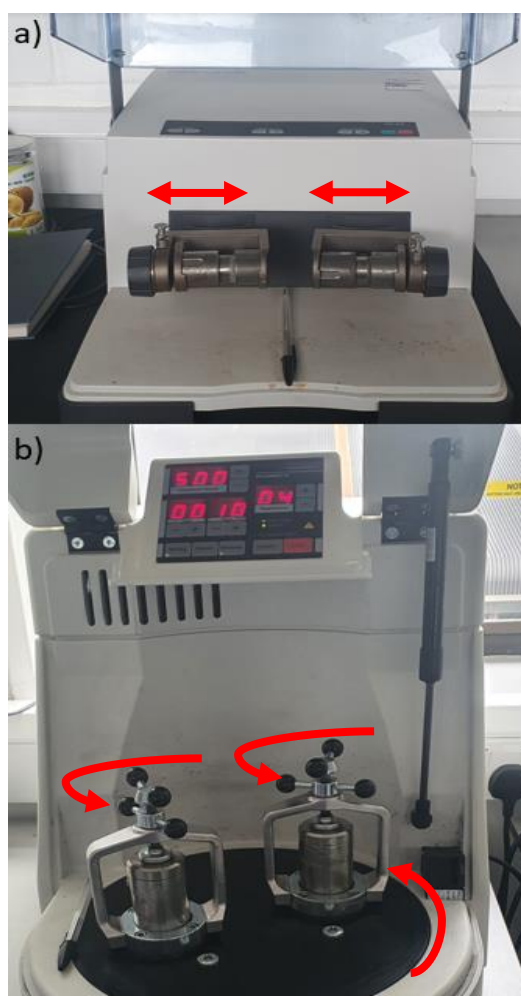


Figure 7. Photographs of a) Mixer and b) planetary type ball mills frequently used for mechanochemical reactions. In case of the mixer mill, grinding is achieved by the back-and-forth oscillation of each arm which holds a milling jar. Planetary mills work differently; the main platform (black) rotates in one direction (e.g. clockwise), while each jar holder rotates on the opposite direction (counter clockwise). Red arrows show the motions involved in each ball mill. In all cases, each jar contains a number of small diameter balls, usually made of the same material as the jar. The impacts between the balls, jar and material of choice, facilitate the grinding process.

Traditionally, mechanochemistry has been considered as a technique of lesser importance by chemists, and as a result, it has not been widely accepted by the synthetic community

as a plausible method of inducing chemical reactions. However, this is rapidly changing in recent years (Figure 8). There are two main reasons for this sudden spark of interest regarding the use of mechanochemistry,⁴⁷ the first one being the advent of Green Chemistry and the need to find more environmentally friendly and sustainable methods of producing chemicals, both on preparative and industrial scales. The second one is that during the past two decades there have been hundreds of new examples within the literature of this method successfully being applied to access previously elusive compounds and as such, it has become apparent to many scientists that this is now a viable and robust method that could be applied to most areas of chemistry.

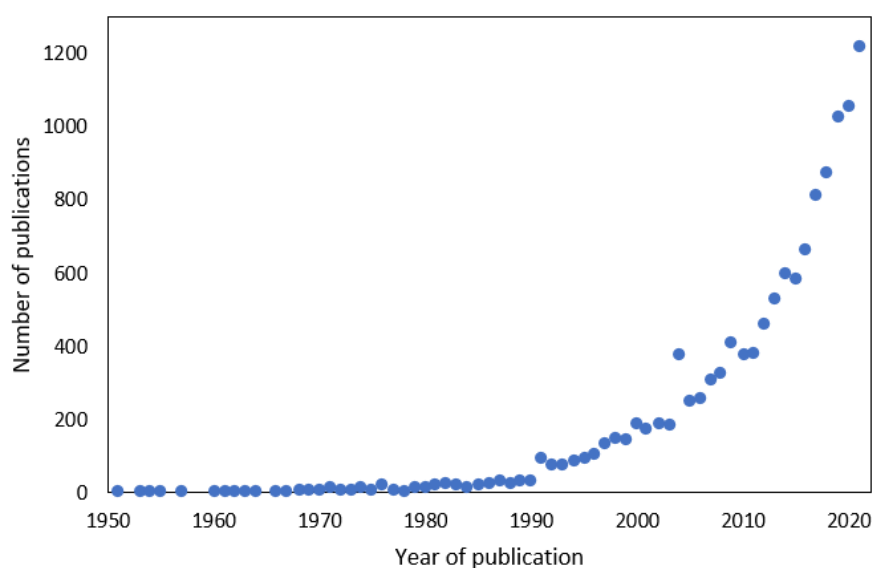


Figure 8. Plot showing the number of publications per year for the period 1950-2021. Data was obtained from the Web of Science database on 17/06/2022 using the search terms (Mechanochemistry OR Mechanochemical).

A notable example of those compounds includes a dimerization of fullerene (C_{60}) achieved by Komatsu *et al.*,⁴⁸ that occurred in the presence of KCN while ball-milling the mixture (solvent-free). This resulted in a dumbbell shaped C_{120} dimer, which was unexpected since a hydrocyanation product should form based on previous results in solution-based chemistry (Figure 9a). Another example of ‘impossible’ molecules made by mechanochemical means includes the synthesis of a tris(allyl)aluminium complex based on the sterically hindered bis(trimethylsilyl)allyl ligand (Figure 9b), reported by Rightmire *et al.* in 2014.⁴⁹ The solvent synthesis of the same product proved to be extremely challenging, usually yielding solvates or other adducts instead of the target compound. The solid-state synthesis was achieved by milling $AlCl_3$ with a potassium salt of bis(trimethylsilyl)allyl anion that gave the product as a white powder. Dissolving this

product in a solvent, produced an oil and formed mixtures of other compounds, something that was consistent with solution synthesis attempts. Another interesting example includes the isolation of a reaction intermediate known as aryl *N*-thiocarbamoyltriazole that was not stable in solution (Figure 9c). This solid-state method accelerated by liquid-assisted grinding (LAG) provided access to the intermediate which was found to be bench stable for long periods of time (>1 year) but dissociated immediately upon dissolving in a solvent.

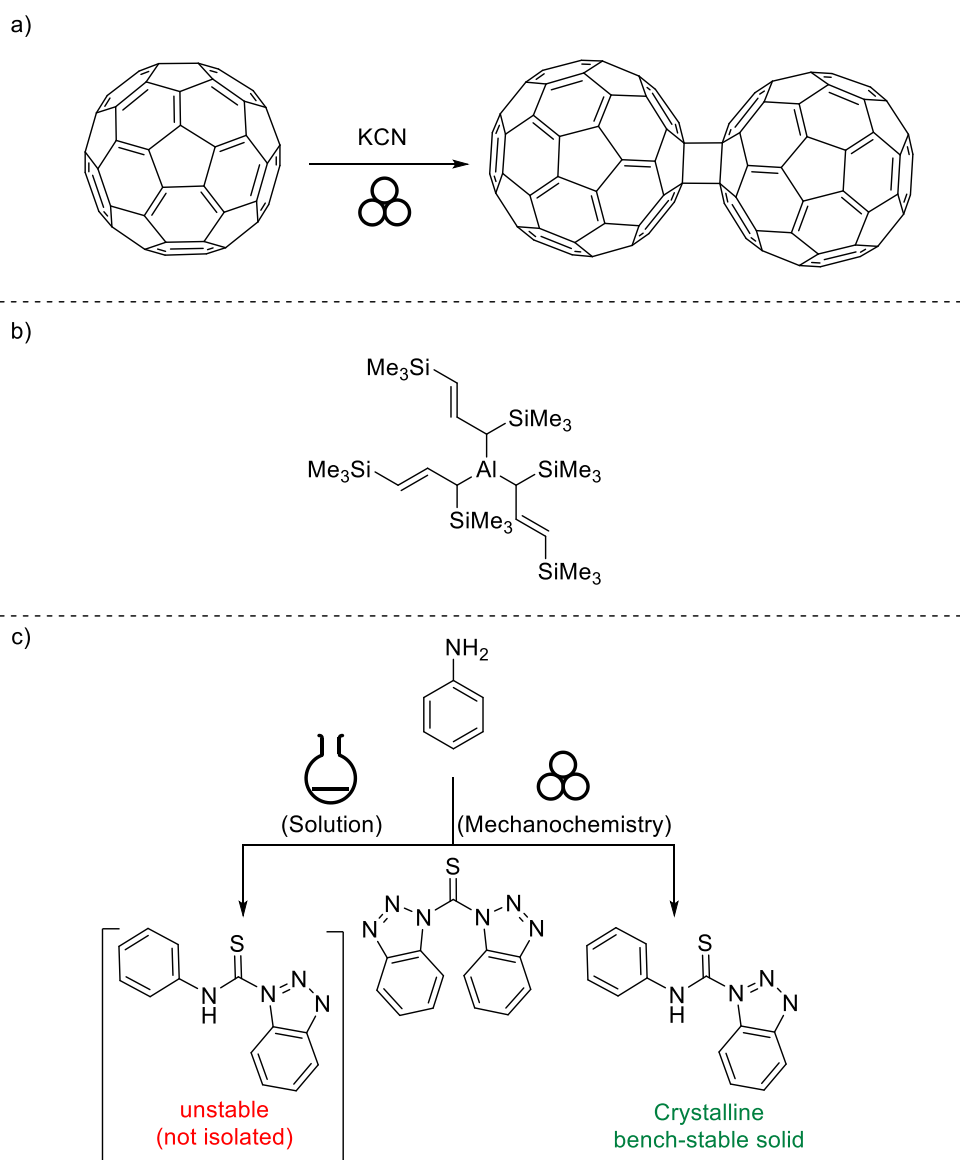


Figure 9. Examples of previously elusive compounds made accessible via solvent-free mechanochemical methods.⁴⁷

Moreover, the fact that most syntheses use a solvent ‘by default’ both at the lab and industrial scales, means that a tremendous amount of waste solvents are being produced

every year. The vast majority of these are using energy-demanding methods and are also being derived from fossil fuels and hence are contributing to climate change. Furthermore, it has been reported that in the pharmaceutical industry, about 85% of the chemicals that are being used are solvents,⁵⁰ and a large percentage of them are never recycled, ending up in the environment as pollutants. It is thus now becoming increasingly important for chemists to seriously consider implementing alternative, greener methods for synthesising compounds and mechanochemistry is a great means to achieve that.

Regarding the mechanistic aspects of mechanochemistry, several different theories have been proposed to explain the increased reactivity of those systems. The most common physical effects that are taking place during the mechanical milling of two reactants are as follows:⁵¹

- i) The breaking up of large solids into fine particles, something which dramatically increases their surface area and consequently, their reactivity. This process also removes any protective surface coatings such as oxides that can inhibit reactivity.
- ii) The thorough mixing of the fine reactant particles ensures maximum reactivity.
- iii) In case there are any crystals present in the reactants, the milling process can introduce several defects, promoting the formation of amorphous materials that are in turn are more prone to react.
- iv) Intense milling can cause increased friction between the particles, something that raises the temperature, both locally and in bulk. This is crucial for accelerating reaction rates. In fact, it has been observed that frictional processes can cause local temperatures to rise to thousands of degrees for very small time periods (0.1-1 μ s). This is known as the ‘hot-spot theory’ and may partially explain increased reactivity during the milling process.

Although previous research in this field mainly emphasised the advantage of totally solvent-free conditions during the reaction, it has since been found that, in many cases, introducing small amounts of liquid in the reaction mixture can accelerate the reaction rate hundreds or thousands of times. This has therefore attracted the interest of many

researchers, as well as shown its potential in chemo/regio-selectivity control and yield improvement. This technique is now known as liquid-assisted grinding (LAG), and although the exact mechanism of the role of the introduced liquid is unknown in most cases,⁵² its use is widespread. A modification of this method was introduced by Frišćić *et al.* where, in addition to a liquid, they introduced various salts for metal organic framework (MOF) synthesis, known as ion- and liquid-assisted grinding (ILAG) mediated mechanochemistry.⁵³

Like flow chemistry, mechanochemical reactors can be used in synergy with other green methodologies, to further enhance their potential. Examples of this include the use of transparent milling jars to conduct solvent-free photochemical reactions⁵⁴ (also known as photomechanochemistry), using mechanically activated enzymes as potent biocatalysts⁵⁵ (mechanoenzymology), and utilising piezoelectric materials to facilitate redox transformations^{56,57} (mechanoredox or electro-mechanochemistry). Another interesting area of active research encompasses the development of ‘mechanophores’, compounds which undergo a structural or conformational change when subjected to mechanical forces. These mechano-responsive materials can be incorporated in polymeric substrates and have many potential uses in engineering applications⁵⁸ (e.g. damage sensors, mechanochromic materials). A particularly relevant application of mechanophores was reported in 2020 by Akkaya *et al.*,⁵⁹ where a bench-stable, cross-linked elastomer containing an endoperoxide bridge was used as a ‘dark’ reactive oxygen species generator, releasing $^1\text{O}_2$ under mechanical strain.

Perhaps one area in which the use of mechanochemical reactors is problematic is that of reaction scale-up, as most laboratory-scale ball mills can only accommodate small quantities of materials (up to 10s of grams). Simply using larger ball mills is not an effective way of circumventing this problem, as many of the same issues encountered in the scaling-up of batch processes arise, such as large temperature gradients, and uneven mixing. In an effort to overcome this, a technique known as ‘continuous flow mechanochemistry’ was brought into existence in 2017, by James and co-workers.⁶⁰ Instead of using a ball-mill, the researchers showed that a twin-screw extruder can be used to facilitate a Knoevenagel reaction between vanillin and barbituric acid. The extruder works in an analogous manner to a flow machine; if the starting materials are fed in the machine, product(s) will emerge from the other side, and in the aforementioned case, a production rate of 0.52 Kg/h was reported. Since that first report many other

research groups have developed continuous flow mechanochemical processes⁶¹ and in 2019 IUPAC listed the technology in the top 10 most impactful chemical innovations that could accelerate our transition to a sustainable world.⁶² It has to be mentioned that the technique does not aim to replace the more traditional used ball mills, and in fact, their use (particularly that of planetary ball mills) is a necessary part of the small-scale reaction optimisation process since extruders can only process relatively large amounts of material at a time.⁶¹ Despite this, it is a valuable addition to the mechanochemical reactor toolbox available to the synthetic community.

Gaining access to mechanistic insights of mechanochemical reactions also poses a major challenge at the moment, due to the fact that the milling session has to be stopped in order for a sample to be taken out for analysis (*ex situ*), which inadvertently disrupts any mechanochemical steady-state equilibrium process.⁶³ Nonetheless, in recent years various time-resolved *in situ* (TRIS) methods have been developed for uninterrupted monitoring of mechanochemical reactions. Examples include using X-ray diffraction,⁶⁴ Raman spectroscopy,⁶⁵ temperature monitoring,⁶⁶ pressure monitoring,⁶⁷ solid-state NMR,⁶⁸ and *operando* acoustic analysis.⁶⁹ Additional work is currently underway to develop integrated and more efficient monitoring techniques, with the help of AI and data science.^{70,71}

In summary, mechanochemistry can help reduce the quantity of solvents used overall in a synthetic process, help avoid the use of particularly toxic solvents, reduce the energy requirements for the reaction and provide access to previously elusive products that may otherwise not form or decompose in solution. The past decade has seen tremendous developments in the field, and it appears that more and more researchers are starting to adopt this reaction technology, in an attempt to create more sustainable chemistries.^{72,73}

1.4.3 3D Printing

The final synthetic technology that we cover in this thesis is 3D printing, also known as additive manufacturing. The concept behind the operation of this method is quite simple; as the name suggests, the desired object is built sequentially, by adding layers of material on top of previously added layers. To achieve this, a 3D object is first designed in a CAD program, which is then transferred to a ‘slicing’ program which

separates the object in small sections, or slices. The data is then downloaded to a 3D printer, which builds the object, slice by slice. The width of each layer can usually be set by the user, most commonly ranging between 25 – 100 μm . It may sound surprising, but modern 3D printing as we know it today was developed in the 1980s, however, the broad-scale adoption of the technology only started in the 2010s. This is attributed to the convergence of several changes in the technical and commercial landscape that occurred around that period. For instance, the expiration of key patents, maturation of computer hardware, high penetration rate of broadband networks, and the emergence of the ‘tech economy’ made the manufacturing of 3D printers an attractive value proposition which led to the formation of several new start-up companies, such as Prusa⁷⁴ (est. 2009) and crowdfunding-backed FormLabs⁷⁵ (est. 2011), which transformed 3D fabrication from a mere engineering curiosity to an invaluable prototyping platform, used by a vast number of businesses and research institutions (Figure 10).⁷⁶

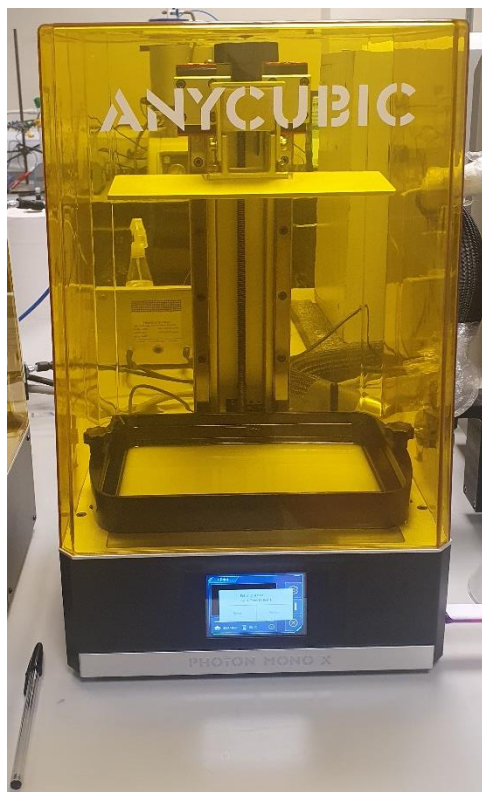


Figure 10. An example of a contemporary SLA 3D printer used by the Vilela group.

There are many mechanisms by which a 3D solid object can be fabricated, however, most commercially available devices today are centred around three main technologies:

Selective Laser Sintering (SLS).⁷⁷ In this technique, each layer is created by using lasers to fuse together fine particles, usually made out of a polymer or even metal.

Selective Solidification.⁷⁸ This mode of operation uses a vat containing a photopolymerisable liquid resin comprised of a mixture of monomers, a photoinitiator and auxiliary additives. Each layer is exposed to light, forming a solid cross-linked polymer. Depending on the light-source, this technique is further split into stereolithography (SLA) and digital light projection (DLP).

Selective Deposition.⁷⁹ This is by far the most widely used technique, mostly due to its relative cost-effectiveness and simple mode of operation. A filament, which is usually made from different polymeric materials is melted by an extruder, located on a moving platform. The molten polymer is deposited on a platform and solidifies. The process is then repeated for each layer. This method is usually known as filament fused fabrication (FFF) or fused deposition modelling (FDM).

When it comes to its use in chemistry, 3D printing has proven to be an extremely valuable tool, and its popularity is reflected by the number of published works in the last decade (Figure 11). Out of the 6087 reports, 1710 were reported in 2021 (28%!). It is no coincidence that the exponential spread of this technology in the chemical sciences started in 2011, the same year that consumer-grade 3D printers started to appear on the market.

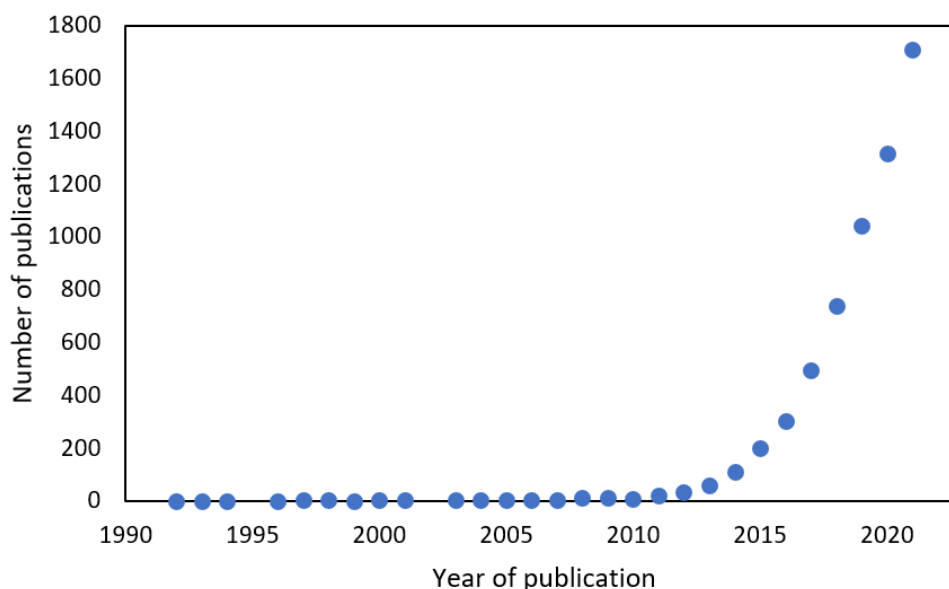


Figure 11. Plot showing the number of publications per year for the period 1992-2021. Data was obtained from the Web of Science database on 17/06/2022 using the search terms ((3D printing AND Chemistry) OR (3D printing AND Reactionware)).

Many interesting applications have emerged over the years, using additive manufacturing methods, and most of them are focused around new reactor designs, catalytic materials

and bespoke laboratory equipment.⁸⁰ The freedom of design, paired with high fidelity, intricate geometries offered by 3D printing makes it possible to create reaction vessels that would be impossible to manufacture using traditional glassblowing techniques, or any other methods for this matter. In 2012, a seminal report published by Cronin and co-workers⁸¹ perfectly demonstrated this, by designing and 3D printing a series of bespoke, inexpensive, and reusable reactors with unique geometry tailored for a specific application. They showed that it was possible to alter the reaction outcome based on the reactor architecture. Moreover, by embedding an inorganic catalyst (Pd/C) in the printing filament, they illustrated that it is possible to print catalytically active reactors, which are now widely known as ‘reactionware’. This work initiated a paradigm shift in the broader area of reactor design, leading to a plethora of interesting reactionware being reported. Within the last five years, the Vilela group has actively worked in this area and has used 3D printing to produce a large variety of new reactor designs (Figure 12).

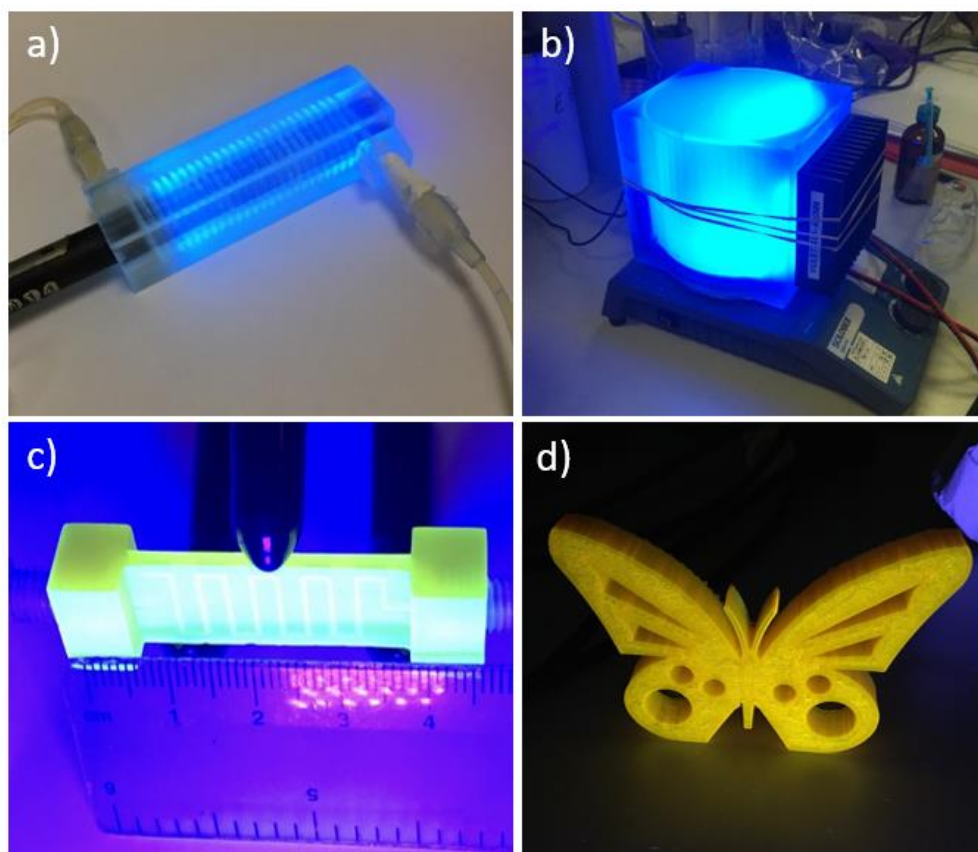


Figure 12. Photographs of 3D printed objects fabricated by the Vilela group: a) Microfluidic reactor, b) batch photoreactor, c) microfluidic reactor impregnated with a photosensitiser and, d) butterfly-shaped object made by a custom photoactive FDM filament.

Noteworthy examples of the use of 3D printing in reactor design include the production of: Photoactive microfluidic devices for ROS production in flow,⁸² catalytically active cases for common magnetic stir bars able to catalyse Mannich and Suzuki reactions,^{83,84} an inexpensive and modular flow machine,⁸⁵ photoactive monolithic reactors for heterogeneous ROS production in flow,⁸⁶ photoreactors for batch applications,⁸⁷ pressure tight NMR tubes for in situ monitoring of Sonogashira reactions,⁸⁸ and bioactive monoliths for enzymatic transformations in flow.^{89,90}

It is expected that the role of this emerging technology in the design and fabrication of increasingly more complex and robust reactors will only intensify in the coming years, especially with the advent of automation,⁹¹ and the development of new high-performance resins and filament materials.⁹² The advent of new print materials is of paramount importance, as existing 3D printed reactionware are not compatible with most organic solvents, as they are prone to swelling and cracking.^{83,93} These changes will enable chemists to tailor their reactor design around each reaction type, resulting in safer and reproducible protocols, offering higher yields whilst minimising waste.

1.5 Concluding Remarks and Research Aims

Hopefully, by this point, the reader will have a clear understanding of the drawbacks presented using conventional batch reactors and how recent technological advancements have given rise to new synthetic technologies which can be used as an ideal platform for developing green synthetic methodologies.

The main objectives of this work were to explore how these technologies can be exploited to promote and enable various photochemical processes and use the results to illustrate their potential and practicality, whilst encouraging their implementation by others. We chose to focus on organic photochemistry as it constitutes one of the greenest approaches in contemporary synthetic chemistry, utilising photons as clean and evanescent reagents to induce chemical transformations.⁹⁴ The use of visible light photons, in particular, is seen as the ultimate green approach, allowing us to harvest the seemingly inexhaustible supply of energy provided by our sun, something that natural systems such as photosynthetic organisms have already evolved to exploit.⁹⁵ Therefore, we focused on the use of visible-light photosensitisers (PS), for the production of singlet oxygen (¹O₂),

a potent and highly reactive species able to oxygenate a wide range of organic substrates.⁹⁶ There are two accessible singlet excited states of molecular oxygen, $^1\Delta_g$ and $^1\Sigma_g^+$ and are typically produced *via* type II energy transfer process known as triplet-triplet annihilation, in which 1O_2 is formed after ground state molecular oxygen (3O_2) collides with the photoexcited sensitizer ($^3PS^*$), although in practice only the $^1\Delta_g$ form is long-lived enough to be used as a reactant since $^1\Sigma_g^+$ transitions (spin-allowed process) to the energetically lower $^1\Delta_g$ form (Figure 13).⁹⁷

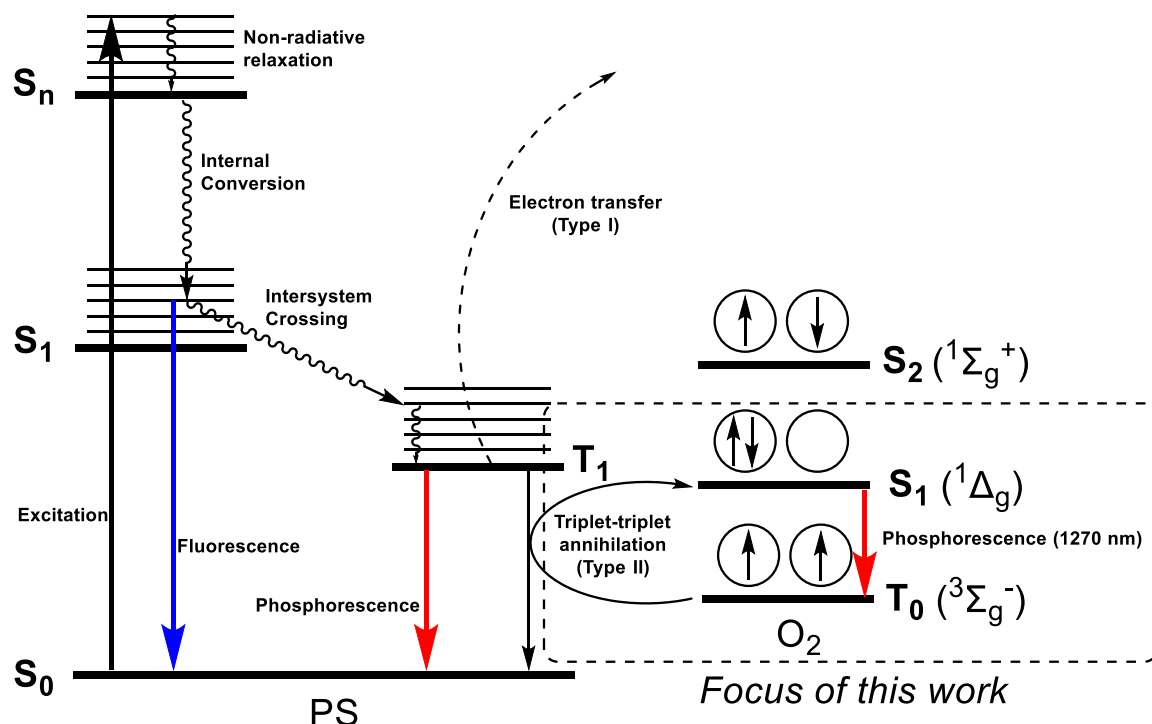


Figure 13. Jablonski diagram depicting a series of common photophysical processes encountered in a PS-O₂ system. The relative energy levels between the PS and O₂ are not in scale and depend on the PS that is used. The two circles on T_0 , S_1 and S_2 states of O₂ represent the electronic configuration of the π_x and π_y antibonding molecular orbitals.

In **Chapter 2**, we describe the development of a helically-shaped organic chromophore which was obtained in excellent yield and was able to be used as an effective molecular heterogeneous photosensitizer under continuous flow conditions. Real-time 1O_2 production monitoring was achieved by connecting a benchtop NMR instrument to the flow machine. Moreover, due to its unusual geometry, the compound was found to exhibit the relatively rare aggregation-induced emission (AIE) property, which was thoroughly investigated.

Next, in **Chapter 3**, we present an unprecedented molecular ring editing methodology whereby a carbon atom is removed from the six-membered S,N heterocycle 1,2,6-

thiadiazine to afford the corresponding 5-membered 1,2,5-thiadiazole 1-oxide. The transformation is mediated by $^1\text{O}_2$, produced by the thiadiazine SM, which acts as its own photosensitiser. Moreover, the products are obtained in quantitative yields, by simply removing the solvent and the reaction tolerates a wide range of functionalities. Flow chemistry played a crucial role in this project by enabling us to access several derivatives which were unable to be synthesised in classical batch reactors.

Chapter 4 describes our efforts to synthesise and characterise a series of hydroxamic acid-based supramolecular metallocages with the aim to use their internal cavity as ‘nanocontainers’ and test how they can affect various photosensitisation processes. In this work, mechanochemistry gave us access to a key ligand compound which was not easily accessible *via* conventional flask reactors.

Finally, in **Chapter 5**, we develop a new amicable mechanochemical methodology for synthesising a series of substituted *N*-benzamides, one of which was successfully used for the photosensitised $^1\text{O}_2$ production under solvent-free, mechanochemical conditions. Moreover, by using SLA 3D printing we were able to fabricate large, custom milling jars which enabled the multi-gram scale-up of the reaction. The same technique was also utilised to fabricate reactionware; photoactive milling jars and balls for the solid-state production of $^1\text{O}_2$.

1.6 References

- (1) Fitzpatrick, D. E.; Battilocchio, C.; Ley, S. V. Enabling Technologies for the Future of Chemical Synthesis. *ACS Cent. Sci.* **2016**, *2* (3), 131–138. <https://doi.org/10.1021/acscentsci.6b00015>.
- (2) Morris, P. J. T. The History of Chemical Laboratories: A Thematic Approach. *ChemTexts* **2021**, *7* (3), 21. <https://doi.org/10.1007/s40828-021-00146-x>.
- (3) Lowe, D. Laboratory History: The Chemistry Chronicles. *Nature* **2015**, *521* (7553), 422. <https://doi.org/10.1038/521422a>.
- (4) Donnelly, A. F. The Romantic History of Laboratory Glassware. *Lab. Med.* **1970**, *1* (3), 28–33. <https://doi.org/10.1093/labmed/1.3.28>.

- (5) Rasmussen, S. C. Advances in 13th Century Glass Manufacturing and Their Effect on Chemical Sciences. *Bull. Hist. Chem.* **2008**, *33* (1), 28–34.
- (6) Kurkjian, C. R.; Prindle, W. R. Perspectives on the History of Glass Composition. *J. Am. Ceram. Soc.* **1998**, *81* (4), 795–813. <https://doi.org/10.1111/j.1151-2916.1998.tb02415.x>.
- (7) Kolb, D.; Kolb, K. E. The Chemistry of Glass. *J. Chem. Educ.* **1979**, *56* (9), 604. <https://doi.org/10.1021/ed056p604>.
- (8) Geyer, K.; Codée, J. D. C.; Seeberger, P. H. Microreactors as Tools for Synthetic Chemists—The Chemists’ Round-Bottomed Flask of the 21st Century? *Chem. Eur. J.* **2006**, *12* (33), 8434–8442. <https://doi.org/10.1002/chem.200600596>.
- (9) Goh, H. Y.; Wong, W. W. C.; Ong, Y. Y. A Study To Reduce Chemical Waste Generated in Chemistry Teaching Laboratories. *J. Chem. Educ.* **2020**, *97* (1), 87–96. <https://doi.org/10.1021/acs.jchemed.9b00632>.
- (10) Vooradi, R.; Anne, S. B.; Tula, A. K.; Eden, M. R.; Gani, R. Energy and CO₂ Management for Chemical and Related Industries: Issues, Opportunities and Challenges. *BMC Chem. Eng.* **2019**, *1* (1), 7. <https://doi.org/10.1186/s42480-019-0008-6>.
- (11) Worrell, E.; Phylipsen, D.; Einstein, D.; Martin, N. *Energy Use and Energy Intensity of the U.S. Chemical Industry*; United States, 2000. <https://doi.org/10.2172/773773>.
- (12) Anastas, P.; Eghbali, N. Green Chemistry: Principles and Practice. *Chem. Soc. Rev.* **2010**, *39* (1), 301–312. <https://doi.org/10.1039/b918763b>.
- (13) Anastas, P. T.; Warner, J. C. *Green Chemistry: Theory and Practice*; Oxford University Press, 1998.
- (14) Romero Dexeus, C. The Deepening Effects of the Digital Revolution - The Future of Tourism: Innovation and Sustainability. In *The Future of Tourism*; Springer International Publishing: Cham, 2019; pp 43–69. https://doi.org/10.1007/978-3-319-89941-1_3.
- (15) Ley, S. V; Fitzpatrick, D. E.; Ingham, R. J.; Myers, R. M. Organic Synthesis: March of the Machines. *Angew. Chem. Int. Ed.* **2015**, *54* (11), 3449–3464.

<https://doi.org/10.1002/anie.201410744>.

- (16) Plutschack, M. B.; Pieber, B.; Gilmore, K.; Seeberger, P. H. The Hitchhiker's Guide to Flow Chemistry. *Chem. Rev.* **2017**, *117* (18), 11796–11893. <https://doi.org/10.1021/acs.chemrev.7b00183>.
- (17) Friščić, T.; Mottillo, C.; Titi, H. M. Mechanochemistry for Synthesis. *Angew. Chem. Int. Ed.* **2020**, *59* (3), 1018–1029. <https://doi.org/10.1002/anie.201906755>.
- (18) Hartings, M. R.; Ahmed, Z. Chemistry from 3D Printed Objects. *Nat. Rev. Chem.* **2019**, *3* (5), 305–314. <https://doi.org/10.1038/s41570-019-0097-z>.
- (19) Hartman, R. L.; McMullen, J. P.; Jensen, K. F. Deciding Whether To Go with the Flow: Evaluating the Merits of Flow Reactors for Synthesis. *Angew. Chem. Int. Ed.* **2011**, *50* (33), 7502–7519. <https://doi.org/10.1002/anie.201004637>.
- (20) Bannock, J. H.; Krishnadasan, S. H.; Heeney, M.; de Mello, J. C. A Gentle Introduction to the Noble Art of Flow Chemistry. *Mater. Horizons* **2014**, *1* (4), 373–378. <https://doi.org/10.1039/C4MH00054D>.
- (21) <https://www.vapourtec.com/> (accessed Jun 21, 2022).
- (22) <https://www.ika.com/en/Products-Lab-Eq/FLOW-System-csp-919/> (accessed Jun 21, 2022).
- (23) <https://www.syrris.com/families/asia-lab-scale-flow-chemistry/> (accessed Jun 21, 2022).
- (24) <https://kilolabs.com/uniqsis/> (accessed Jun 21, 2022).
- (25) Shah, S. I. A.; Kostjuk, L. W.; Kresta, S. M. The Effects of Mixing, Reaction Rates, and Stoichiometry on Yield for Mixing Sensitive Reactions—Part I: Model Development. *Int. J. Chem. Eng.* **2012**, *2012*, 750162. <https://doi.org/10.1155/2012/750162>.
- (26) Barabash, V. M.; Abiev, R. S.; Kulov, N. N. Theory and Practice of Mixing: A Review. *Theor. Found. Chem. Eng.* **2018**, *52* (4), 473–487. <https://doi.org/10.1134/S004057951804036X>.
- (27) Cooper, M. M. The Replication Crisis and Chemistry Education Research. *J. Chem. Educ.* **2018**, *95* (1), 1–2. <https://doi.org/10.1021/acs.jchemed.7b00907>.

- (28) Ioannidis, J. P. A. Why Most Published Research Findings Are False. *PLOS Med.* **2005**, 2 (8), 696–701.
- (29) Pentsak, E. O.; Eremin, D. B.; Gordeev, E. G.; Ananikov, V. P. Phantom Reactivity in Organic and Catalytic Reactions as a Consequence of Microscale Destruction and Contamination-Trapping Effects of Magnetic Stir Bars. *ACS Catal.* **2019**, 9 (4), 3070–3081. <https://doi.org/10.1021/acscatal.9b00294>.
- (30) McLauchlan, K. A. The Effects of Magnetic Fields on Chemical Reactions. *Sci. Prog.* **1981**, 67 (268), 509–529.
- (31) Buchachenko, A.; Lawler, R. G. New Possibilities for Magnetic Control of Chemical and Biochemical Reactions. *Acc. Chem. Res.* **2017**, 50 (4), 877–884. <https://doi.org/10.1021/acs.accounts.6b00608>.
- (32) Schwolow, S.; Hollmann, J.; Schenkel, B.; Röder, T. Application-Oriented Analysis of Mixing Performance in Microreactors. *Org. Process Res. Dev.* **2012**, 16 (9), 1513–1522. <https://doi.org/10.1021/op300107z>.
- (33) Bojang, A. A.; Wu, H.-S. Design, Fundamental Principles of Fabrication and Applications of Microreactors. *Processes.* **2020**, 8(8), 891. <https://doi.org/10.3390/pr8080891>.
- (34) Swinehart, D. F. The Beer-Lambert Law. *J. Chem. Educ.* **1962**, 39 (7), 333. <https://doi.org/10.1021/ed039p333>.
- (35) Donnelly, K.; Baumann, M. Scalability of Photochemical Reactions in Continuous Flow Mode. *J. Flow Chem.* **2021**, 11 (3), 223–241. <https://doi.org/10.1007/s41981-021-00168-z>.
- (36) Rossetti, I.; Compagnoni, M. Chemical Reaction Engineering, Process Design and Scale-up Issues at the Frontier of Synthesis: Flow Chemistry. *Chem. Eng. J.* **2016**, 296, 56–70. <https://doi.org/10.1016/j.cej.2016.02.119>.
- (37) Thaisrivongs, D. A.; Naber, J. R.; Rogus, N. J.; Spencer, G. Development of an Organometallic Flow Chemistry Reaction at Pilot-Plant Scale for the Manufacture of Verubecestat. *Org. Process Res. Dev.* **2018**, 22 (3), 403–408. <https://doi.org/10.1021/acs.oprd.7b00385>.
- (38) Jolliffe, H. G.; Gerogiorgis, D. I. Process Modelling and Simulation for

- Continuous Pharmaceutical Manufacturing of Ibuprofen. *Chem. Eng. Res. Des.* **2015**, *97*, 175–191. <https://doi.org/10.1016/j.cherd.2014.12.005>.
- (39) Vieira, T.; Stevens, A. C.; Chtchemelinine, A.; Gao, D.; Badalov, P.; Heumann, L. Development of a Large-Scale Cyanation Process Using Continuous Flow Chemistry En Route to the Synthesis of Remdesivir. *Org. Process Res. Dev.* **2020**, *24* (10), 2113–2121. <https://doi.org/10.1021/acs.oprd.0c00172>.
- (40) Hessel, V. Novel Process Windows – Gate to Maximizing Process Intensification via Flow Chemistry. *Chem. Eng. Technol.* **2009**, *32* (11), 1655–1681. <https://doi.org/10.1002/ceat.200900474>.
- (41) Wegner, J.; Ceylan, S.; Kirschning, A. Ten Key Issues in Modern Flow Chemistry. *Chem. Commun.* **2011**, *47* (16), 4583–4592. <https://doi.org/10.1039/C0CC05060A>.
- (42) Thomson, C. G.; Jones, C. M. S.; Rosair, G.; Ellis, D.; Marques-Hueso, J.; Lee, A. L.; Vilela, F. Continuous-Flow Synthesis and Application of Polymer-Supported BODIPY Photosensitisers for the Generation of Singlet Oxygen; Process Optimised by in-Line NMR Spectroscopy. *J. Flow Chem.* **2020**, *10* (1), 327–345. <https://doi.org/10.1007/s41981-019-00067-4>.
- (43) Noël, T.; Cao, Y.; Laudadio, G. The Fundamentals Behind the Use of Flow Reactors in Electrochemistry. *Acc. Chem. Res.* **2019**, *52* (10), 2858–2869. <https://doi.org/10.1021/acs.accounts.9b00412>.
- (44) Benítez-Mateos, A. I.; Contente, M. L.; Roura Padrosa, D.; Paradisi, F. Flow Biocatalysis 101: Design, Development and Applications. *React. Chem. Eng.* **2021**, *6* (4), 599–611. <https://doi.org/10.1039/D0RE00483A>.
- (45) Li, Y.; Xia, L.; Fan, Y.; Wang, Q.; Hu, M. Recent Advances in Autonomous Synthesis of Materials. *ChemPhysMater* **2022**, *1* (2), 77–85. <https://doi.org/10.1016/j.chphma.2021.10.002>.
- (46) Métro, T. X.; Martinez, J.; Lamaty, F. 1,1'-Carbonyldiimidazole and Mechanochemistry: A Shining Green Combination. *ACS Sustain. Chem. Eng.* **2017**, *5* (11), 9599–9602. <https://doi.org/10.1021/acssuschemeng.7b03260>.
- (47) James, S. L.; Adams, C. J.; Bolm, C.; Braga, D.; Collier, P.; Frišćic, T.; Grepioni,

- F.; Harris, K. D. M.; Hyett, G.; Jones, W.; et al. Playing with Organic Radicals as Building Blocks for Functional Molecular Materials. *Chem. Soc. Rev.* **2012**, *41* (1), 413–447. <https://doi.org/10.1039/c1cs15171a>.
- (48) Wang, G.-W.; Tanaka, T.; Komatsu, K.; Murata, Y.; Yamamoto, K.; Saunders, M.; Fujiwara, K. Mechanochemical Synthesis and Characterization of the Fullerene Dimer C₁₂₀. *J. Org. Chem.* **2002**, *63* (25), 9358–9366. <https://doi.org/10.1021/jo981319t>.
- (49) Rightmire, N. R.; Hanusa, T. P. Advances in Organometallic Synthesis with Mechanochemical Methods. *Dalt. Trans.* **2016**, *45* (6), 2352–2362. <https://doi.org/10.1039/c5dt03866a>.
- (50) Sabatini, M. T.; Boulton, L. T.; Sneddon, H. F.; Sheppard, T. D. A Green Chemistry Perspective on Catalytic Amide Bond Formation. *Nat. Catal.* **2019**, *2* (1), 10–17. <https://doi.org/10.1038/s41929-018-0211-5>.
- (51) Howard, J. L.; Brand, M. C.; Browne, D. L. Switching Chemoselectivity: Using Mechanochemistry to Alter Reaction Kinetics. *Angew. Chem. Int. Ed.* **2018**, 16104–16108. <https://doi.org/10.1002/anie.201810141>.
- (52) Belenguer, A. M.; Lampronti, G. I.; Cruz-Cabeza, A. J.; Hunter, C. A.; Sanders, J. K. M. Solvation and Surface Effects on Polymorph Stabilities at the Nanoscale. *Chem. Sci.* **2016**, *7* (11), 6617–6627. <https://doi.org/10.1039/C6SC03457H>.
- (53) Do, J. L.; Friščić, T. Mechanochemistry: A Force of Synthesis. *ACS Cent. Sci.* **2017**, *3* (1), 13–19. <https://doi.org/10.1021/acscentsci.6b00277>.
- (54) Hernández, J. G. Mechanochemical Borylation of Aryldiazonium Salts; Merging Light and Ball Milling. *Beilstein J. Org. Chem.* **2017**, *13*, 1463–1469. <https://doi.org/10.3762/bjoc.13.144>.
- (55) Pérez-Venegas, M.; Juaristi, E. Mechanoenzymology: State of the Art and Challenges towards Highly Sustainable Biocatalysis. *ChemSusChem* **2021**, *14* (13), 2682–2688. <https://doi.org/10.1002/cssc.202100624>.
- (56) Leitch, J. A.; Browne, D. L. Mechanoredox Chemistry as an Emerging Strategy in Synthesis. *Chem. Eur. J.* **2021**, *27* (38), 9721–9726. <https://doi.org/10.1002/chem.202100348>.

- (57) Schumacher, C.; Hernández, J. G.; Bolm, C. Electro-Mechanochemical Atom Transfer Radical Cyclizations Using Piezoelectric BaTiO₃. *Angew. Chem. Int. Ed.* **2020**, *59* (38), 16357–16360. <https://doi.org/10.1002/anie.202003565>.
- (58) Deneke, N.; Rencheck, M. L.; Davis, C. S. An Engineer's Introduction to Mechanophores. *Soft Matter* **2020**, *16* (27), 6230–6252. <https://doi.org/10.1039/D0SM00465K>.
- (59) Turksoy, A.; Yildiz, D.; Aydonat, S.; Beduk, T.; Canyurt, M.; Baytekin, B.; Akkaya, E. U. Mechanochemical Generation of Singlet Oxygen. *RSC Adv.* **2020**, *10* (16), 9182–9186. <https://doi.org/10.1039/d0ra00831a>.
- (60) Crawford, D. E.; Miskimmin, C. K. G.; Albadarin, A. B.; Walker, G.; James, S. L. Organic Synthesis by Twin Screw Extrusion (TSE): Continuous, Scalable and Solvent-Free. *Green Chem.* **2017**, *19* (6), 1507–1518. <https://doi.org/10.1039/C6GC03413F>.
- (61) Bolt, R. R. A.; Leitch, J. A.; Jones, A. C.; Nicholson, W. I.; Browne, D. L. Continuous Flow Mechanochemistry: Reactive Extrusion as an Enabling Technology in Organic Synthesis. *Chem. Soc. Rev.* **2022**, *51* (11), 4243–4260. <https://doi.org/10.1039/D1CS00657F>.
- (62) Gomollón-Bel, F. Ten Chemical Innovations That Will Change Our World: IUPAC Identifies Emerging Technologies in Chemistry with Potential to Make Our Planet More Sustainable. *Chem. Int.* **2019**, *41* (2), 12–17. <https://doi.org/10.1515/ci-2019-0203>.
- (63) Descamps, M.; Willart, J. F.; Dudognon, E.; Lefort, R.; Desprez, S.; Caron, V. Phase Transformations Induced by Grinding: What Is Revealed by Molecular Materials. *MRS Online Proc. Libr.* **2011**, *979* (1), 606. <https://doi.org/10.1557/PROC-979-0979-HH06-06>.
- (64) Halasz, I.; Kimber, S. A. J.; Beldon, P. J.; Belenguer, A. M.; Adams, F.; Honkimäki, V.; Nightingale, R. C.; Dinnebier, R. E.; Friščić, T. in situ and Real-Time Monitoring of Mechanochemical Milling Reactions Using Synchrotron X-Ray Diffraction. *Nat. Protoc.* **2013**, *8* (9), 1718–1729. <https://doi.org/10.1038/nprot.2013.100>.

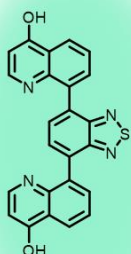
- (65) Gracin, D.; Štrukil, V.; Friščić, T.; Halasz, I.; Užarević, K. Laboratory Real-Time and *In Situ* Monitoring of Mechanochemical Milling Reactions by Raman Spectroscopy. *Angew. Chem. Int. Ed.* **2014**, *53* (24), 6193–6197. <https://doi.org/10.1002/anie.201402334>.
- (66) Atzmon, M. *In Situ* Thermal Observation of Explosive Compound-Formation Reaction during Mechanical Alloying. *Phys. Rev. Lett.* **1990**, *64* (4), 487–490. <https://doi.org/10.1103/PhysRevLett.64.487>.
- (67) Doppiu, S.; Schultz, L.; Gutfleisch, O. *In Situ* Pressure and Temperature Monitoring during the Conversion of Mg into MgH₂ by High-Pressure Reactive Ball Milling. *J. Alloys Compd.* **2007**, *427* (1), 204–208. <https://doi.org/10.1016/j.jallcom.2006.02.045>.
- (68) Schiffmann, J. G.; Emmerling, F.; Martins, I. C. B.; Van Wüllen, L. *In-Situ* Reaction Monitoring of a Mechanochemical Ball Mill Reaction with Solid State NMR. *Solid State Nucl. Magn. Reson.* **2020**, *109*, 101687. <https://doi.org/10.1016/j.ssnmr.2020.101687>.
- (69) Leroy, C.; Mittelelte, S.; Félix, G.; Fabregue, N.; Špačková, J.; Gaveau, P.; Métro, T.-X.; Laurencin, D. Operando Acoustic Analysis: A Valuable Method for Investigating Reaction Mechanisms in Mechanochemistry. *Chem. Sci.* **2022**, *13* (21), 6328–6334. <https://doi.org/10.1039/D2SC01496C>.
- (70) Michalchuk, A. A. L.; Emmerling, F. Time-Resolved *In Situ* Monitoring of Mechanochemical Reactions. *Angew. Chem. Int. Ed.* **2022**, *61* (21). <https://doi.org/10.1002/anie.202117270>.
- (71) Lukin, S.; Germann, L. S.; Friščić, T.; Halasz, I. Toward Mechanistic Understanding of Mechanochemical Reactions Using Real-Time *In Situ* Monitoring. *Acc. Chem. Res.* **2022**, *55* (9), 1262–1277. <https://doi.org/10.1021/acs.accounts.2c00062>.
- (72) Ardila-Fierro, K. J.; Hernández, J. G. Sustainability Assessment of Mechanochemistry by Using the Twelve Principles of Green Chemistry. *ChemSusChem* **2021**, *14* (10), 2145–2162. <https://doi.org/10.1002/cssc.202100478>.

- (73) Espro, C.; Rodríguez-Padrón, D. Re-Thinking Organic Synthesis: Mechanochemistry as a Greener Approach. *Curr. Opin. Green Sustain. Chem.* **2021**, *30*, 100478. <https://doi.org/10.1016/j.cogsc.2021.100478>.
- (74) https://www.prusa3d.com/page/about-us_77/ (accessed Jun 22, 2022).
- (75) <https://formlabs.com/uk/company/> (accessed Jun 22, 2022).
- (76) Horvath, J. A Brief History of 3D Printing. In *Mastering 3D printing*; Apress; Berkeley, CA, 2014; pp 3–10. https://doi.org/10.1007/978-1-4842-0025-4_1.
- (77) Charoo, N. A.; Barakh Ali, S. F.; Mohamed, E. M.; Kuttolamadom, M. A.; Ozkan, T.; Khan, M. A.; Rahman, Z. Selective Laser Sintering 3D Printing – an Overview of the Technology and Pharmaceutical Applications. *Drug Dev. Ind. Pharm.* **2020**, *46* (6), 869–877. <https://doi.org/10.1080/03639045.2020.1764027>.
- (78) Voet, V. S. D.; Strating, T.; Schnelting, G. H. M.; Dijkstra, P.; Tietema, M.; Xu, J.; Woortman, A. J. J.; Loos, K.; Jager, J.; Folkersma, R. Biobased Acrylate Photocurable Resin Formulation for Stereolithography 3D Printing. *ACS Omega* **2018**, *3* (2), 1403–1408. <https://doi.org/10.1021/acsomega.7b01648>.
- (79) Mazzanti, V.; Malagutti, L.; Mollica, F. FDM 3D Printing of Polymers Containing Natural Fillers: A Review of Their Mechanical Properties. *Polymers* . **2019**, *11*(7), 1094. <https://doi.org/10.3390/polym11071094>.
- (80) Alimi, O. A.; Meijboom, R. Current and Future Trends of Additive Manufacturing for Chemistry Applications: A Review. *J. Mater. Sci.* **2021**, *56* (30), 16824–16850. <https://doi.org/10.1007/s10853-021-06362-7>.
- (81) Symes, M. D.; Kitson, P. J.; Yan, J.; Richmond, C. J.; Cooper, G. J. T.; Bowman, R. W.; Vilbrandt, T.; Cronin, L. Integrated 3D-Printed Reactionware for Chemical Synthesis and Analysis. *Nat. Chem.* **2012**, *4* (5), 349–354. <https://doi.org/10.1038/nchem.1313>.
- (82) Zhakeyev, A.; Tobin, J.; Wang, H.; Vilela, F.; Xuan, J. Additive Manufacturing of Photoactive Polymers for Visible Light Harvesting. *Energy Procedia* **2019**, *158*, 5608–5614. <https://doi.org/10.1016/j.egypro.2019.01.579>.
- (83) Penny, M. R.; Rao, Z. X.; Thavarajah, R.; Ishaq, A.; Bowles, B. J.; Hilton, S. T. 3D Printed Tetrakis(Triphenylphosphine)Palladium (0) Impregnated Stirrer

- Devices for Suzuki–Miyaura Cross-Coupling Reactions. *React. Chem. Eng.* **2022**.
<https://doi.org/10.1039/D2RE00218C>.
- (84) Penny, M. R.; Hilton, S. T. Design and Development of 3D Printed Catalytically-Active Stirrers for Chemical Synthesis. *React. Chem. Eng.* **2020**, *5* (5), 853–858.
<https://doi.org/10.1039/C9RE00492K>.
- (85) Penny, M. R.; Rao, Z. X.; Peniche, B. F.; Hilton, S. T. Modular 3D Printed Compressed Air Driven Continuous-Flow Systems for Chemical Synthesis. *Eur. J. Org. Chem.* **2019**, (23), 3783–3787. <https://doi.org/10.1002/ejoc.201900423>.
- (86) Zhakeyev, A.; Jones, M. C.; Thomson, C. G.; Tobin, J. M.; Wang, H.; Vilela, F.; Xuan, J. Additive Manufacturing of Intricate and Inherently Photocatalytic Flow Reactor Components. *Addit. Manuf.* **2021**, *38*, 101828.
<https://doi.org/10.1016/j.addma.2020.101828>.
- (87) Schiel, F.; Peinsipp, C.; Kornigg, S.; Böse, D. A 3D-Printed Open Access Photoreactor Designed for Versatile Applications in Photoredox- and Photoelectrochemical Synthesis. *ChemPhotoChem* **2021**, *5* (5), 431–437.
<https://doi.org/10.1002/cptc.202000291>.
- (88) Lederle, F.; Meyer, F.; Kaldun, C.; Namyslo, J. C.; Hübner, E. G. Sonogashira Coupling in 3D-Printed NMR Cuvettes: Synthesis and Properties of Arylnaphthylalkynes. *New J. Chem.* **2017**, *41* (5), 1925–1932.
<https://doi.org/10.1039/C6NJ03614G>.
- (89) Mandon, C. A.; Blum, L. J.; Marquette, C. A. Adding Biomolecular Recognition Capability to 3D Printed Objects. *Anal. Chem.* **2016**, *88* (21), 10767–10772.
<https://doi.org/10.1021/acs.analchem.6b03426>.
- (90) Maier, M.; Radtke, C. P.; Hubbuch, J.; Niemeyer, C. M.; Rabe, K. S. On-Demand Production of Flow-Reactor Cartridges by 3D Printing of Thermostable Enzymes. *Angew. Chem. Int. Ed.* **2018**, *57* (19), 5539–5543.
<https://doi.org/10.1002/anie.201711072>.
- (91) Hou, W.; Bubliauskas, A.; Kitson, P. J.; Francoia, J.-P.; Powell-Davies, H.; Gutierrez, J. M. P.; Frei, P.; Manzano, J. S.; Cronin, L. Automatic Generation of 3D-Printed Reactionware for Chemical Synthesis Digitization Using ChemSCAD.

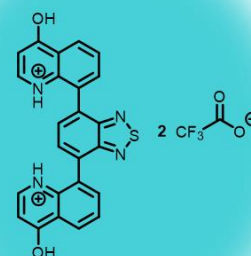
- ACS Cent. Sci.* **2021**, 7 (2), 212–218. <https://doi.org/10.1021/acscentsci.0c01354>.
- (92) Kotz, F.; Risch, P.; Helmer, D.; Rapp, B. E. High-Performance Materials for 3D Printing in Chemical Synthesis Applications. *Adv. Mater.* **2019**, 31 (26), 1805982. <https://doi.org/10.1002/adma.201805982>
- (93) Capel, A. J.; Edmondson, S.; Christie, S. D. R.; Goodridge, R. D.; Bibb, R. J.; Thurstans, M. Design and Additive Manufacture for Flow Chemistry. *Lab Chip* **2013**, 13 (23), 4583–4590. <https://doi.org/10.1039/C3LC50844G>.
- (94) Oelgemöller, M.; Jung, C.; Mattay, J. Green Photochemistry: Production of Fine Chemicals with Sunlight. *Pure Appl. Chem.* **2007**, 79 (11), 1939–1947. <https://doi.org/10.1351/pac200779111939>.
- (95) Albini, A.; Fagnoni, M. Green Chemistry and Photochemistry Were Born at the Same Time. *Green Chem.* **2004**, 6 (1), 1–6. <https://doi.org/10.1039/B309592D>.
- (96) Pibiri, I.; Buscemi, S.; Palumbo Piccionello, A.; Pace, A. Photochemically Produced Singlet Oxygen: Applications and Perspectives. *ChemPhotoChem* **2018**, 2 (7), 535–547. <https://doi.org/10.1002/cptc.201800076>.
- (97) DeRosa, M. C.; Crutchley, R. J. Photosensitized Singlet Oxygen and Its Applications. *Coord. Chem. Rev.* **2002**, 233–234, 351–371. [https://doi.org/10.1016/S0010-8545\(02\)00034-6](https://doi.org/10.1016/S0010-8545(02)00034-6).

Chapter 2: Development of a Novel Molecular Heterogeneous Photocatalyst with Aggregated-Induced Emission Properties



- ❖ Facile Synthesis (5 min, 97% yield)
- ❖ Thermally Stable & Photo Stable
- ❖ Efficient Molecular $^1\text{O}_2$ Heterogeneous Photosensitiser in Flow
- ❖ Tuneable AIE Properties

$\lambda_{\text{em}} = 512 \text{ nm}$
(Neutral)



$\lambda_{\text{em}} = 485 \text{ nm}$
(TFA Salt)

2.1 Declaration

This chapter contains sections of work that have been published:

E. Broumidis, C. M. S. Jones, M. Koyioni, A. Kourtellaris, G. O. Lloyd, J. Marques-Hueso, P. A. Koutentis, F. Vilela, *RSC Adv.* **2021**, *11*, 29102–29107.

As the primary author of this publication, I can confirm that most of the work is my own. The contributions of each collaborator are outlined below:

Emmanouil Broumidis (EB): Synthesis of photocatalyst, photocatalytic performance evaluation, experiment design, photophysical and photochemical data interpretation, writing of the published manuscript (main text and supporting information).

Callum M. C. Jones: Photophysical experiments.

Maria Koyioni: Computational experiments, crystallisation of compound 5H_2^{2+} , TGA.

Andreas Kourtellaris: SC-XRD data collection.

Jose Marques-Hueso: Access to fluorescence spectroscopy equipment.

Panayiotis Koutentis, Gareth O. Lloyd and Filipe Vilela: Overall project supervision, experiment design, manuscript review.

2.2 Background and Aims

This work is the result of our group's efforts of developing new molecular and polymeric 2,1,3-benzothiadiazole (BTZ) containing photocatalytic materials that can facilitate enhanced singlet oxygen ($^1\text{O}_2$) production. The BTZ motif is a frequently used chromophore owing to its excellent light-absorption properties, and has been incorporated in materials used in various applications including photodynamic therapy (PDT),¹ H_2 production,² dye-sensitised solar cells (DSSC),³ water purification,⁴ and reduction of heavy metals in solution.⁵ In most cases, these materials contain at least one pair comprising of an electron donor (D) and electron acceptor (A) subunits, and for $^1\text{O}_2$ production it has been found that materials containing D-A-D or A-D-A sequences are the most efficacious, as it they help facilitate ISC to generate triplet state photosensitisers.¹ In addition, in recent years aggregated-induced emission (AIE) luminophores have been shown to be effective and versatile $^1\text{O}_2$ generators.⁶ It was thus decided that a new AIE molecular D-A-D chromophore would be constructed with A being a 6,9-substituted BTZ unit. In order to create an AIE compound the D unit would need to be relatively bulky, yet planar, in order to induce the propeller-like geometry seen in AIE compounds.⁷ Since EB was familiar with the chemistry of quinolines (Figure 1a),

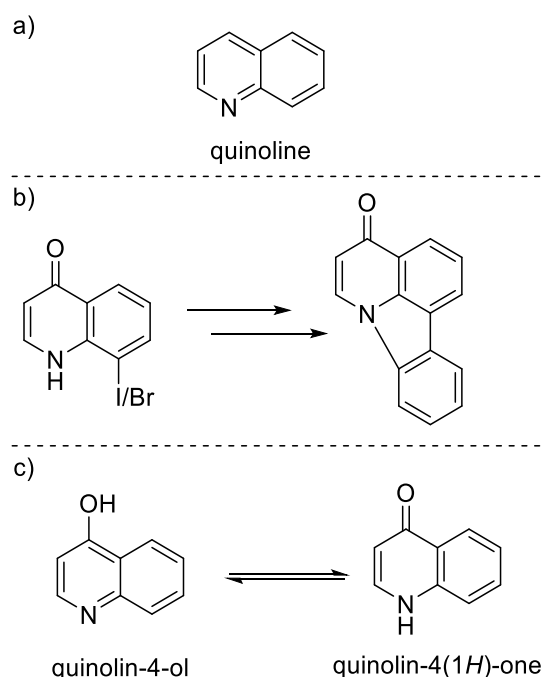


Figure 1. a) Quinoline scaffold, b) previous work involving quinolines, c) quinolin-4-ol and its tautomer, quinoline-4(1H)-one.

which were used in a past project as starting materials for the synthesis of a series of canthin-4-one alkaloid compounds⁸ (Figure 1b), we considered using the substituted quinoline-4-ol scaffold as a D (Figure 1c).

Even though the quinoline family is mostly known for its potent biological activity and medicinal applications,^{9,10} it has also found use as a chromophore.^{11–15} One of its unique characteristics that makes it an attractive choice is its ability to be protonated by acids. This property has been exploited to create tuneable smart fluorescent materials such as inks, sensors, and optical switches.¹⁶ Generally, as the heterocyclic N atom is protonated, the electron withdrawing capacity of the quinoline moiety is increased; this in-turn leads to increased ICT and a bathochromic shift in absorption, while the emission is usually quenched.^{17,18} At a first glance using a quinoline as an electron donating moiety might seem odd, as they are considered electron deficient, and more appropriate to be used as A, however, this also depends on their substituents. In 2016, Krompiec *et al.*, showed that in a series of quinoline-fluorene dyads, the role of quinoline as A shifted to that of a D when an electron donating -NH₂ group was installed (Figure 2a).¹⁹ It is therefore reasonable to assume that by using the -OH substituted quinoline-4-ol, it might be capable of acting as an D, when paired with the BTZ A subunit (Figure 2b).

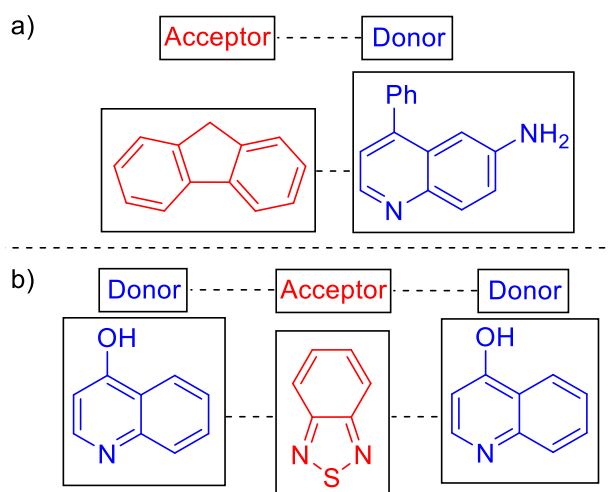


Figure 2. a) A -NH₂ substituted quinoline acts as an electron donor, b) proposed plan for the new AIE D-A-D photosensitiser.

Despite our relevant certainty that the proposed plan would perform as expected, engineering new photoactive compounds remains a trial-and-error process, and as such, the only way to determine if our system would work in practice was to proceed and make

the compound. The following pages discuss the results of this project and our future plans for furthering its impact.

2.3 Abstract

A new benzothiadiazole (BTZ) luminogen is prepared *via* the Suzuki-Miyaura Pd-catalysed C-C cross-coupling of 8-iodoquinolin-4(1H)-one and a BTZ bispinacol boronic ester. The rapid reaction (5 min) affords the air-, thermo-, and photostable product in 97% yield as a yellow precipitate that can be isolated by filtration. The luminogen exhibits AIE properties, which are attributed to its photoactive BTZ core and nonplanar geometry. It also behaves as a molecular heterogeneous photosensitiser to produce $^1\text{O}_2$ under continuous flow conditions.

2.4 Introduction

Photoluminescent materials such as organic dyes and fluorescent polymers have multiple applications in areas such as chemical sensing,²⁰ organic electronics²¹ and bioimaging.^{22,23} Up until the dawn of the 21st century, most organic luminescent materials were typically large, planar and highly conjugated systems. Unsurprisingly, these materials suffer from aggregation-caused quenching (ACQ) effects, owing to solid state face-to-face π stacking interactions, that fully or partially suppress the photoluminescent (PL) properties and thus, the intended functionality of these materials.²⁴

In 2001, Tang and coworkers²⁵ introduced a silole-based organic material which exhibited the opposite behaviour of known ACQ luminogens. Specifically, it was weakly emitting in solution but a strong emitter in the solid state. This unusual photophysical phenomenon is known as AIE, and there have been extensive efforts to uncover its underlying mechanism of action, as well as develop new photoactive materials with AIE properties.²⁶ Most AIE active materials (AIEgens) have rigid, nonplanar geometries in contrast to the planar ACQ based materials. In solution, an AIEgen is subject to intramolecular rotation, vibration or stretching and, as such, any emissions occur mostly *via* non-radiative processes. In contrast, when in an aggregated or solid state, owing to

their rigid nonplanar geometry, π - π stacking and intramolecular motions are limited. This leads to a significant enhancement of the corresponding photoluminescence quantum yield (PLQY), as radiative processes become more prevalent.²⁷ While other mechanistic pathways exist, such as the twisted intramolecular charge transfer process (TICT)²⁸ or crystallization-induced emission enhancement (CIEE),²⁹ the aforementioned restriction of intramolecular motion (RIM) process is dominant for most AIEgen materials.²⁶ Even though in recent years there have been significant advancements in the development of new AIEgen materials, particularly in the organic light-emitting diode (OLED) industry,³⁰ some of the challenges that remain include the need for tuneable and multifunctional AIEgens with properties such as broad excitation wavelength range, increased biocompatibility, and ability of generating reactive oxygen species (ROS).²⁷ These characteristics are especially useful for synthesising AIEgens which can be used as probes for the elucidation of antibiotic mechanisms of action,³¹ or as potent agents for photodynamic therapy (PDT).⁷

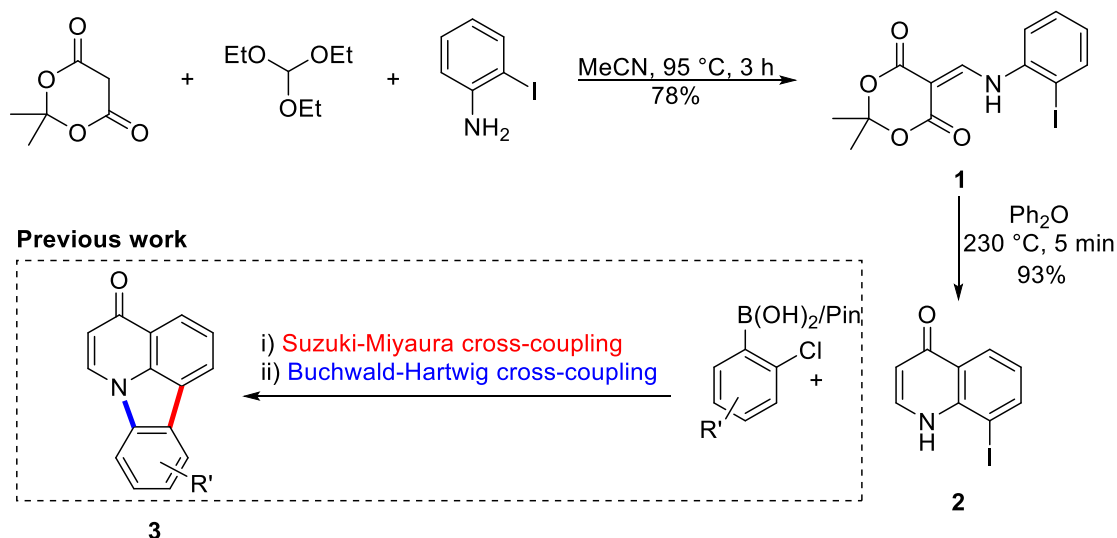
One of the luminophores that has attracted the attention of researchers in recent years is the *S,N*-heterocycle 2,1,3-benzothiadiazole (BTZ). BTZ and its derivatives have an appealing set of properties which can make them useful building blocks for developing new photoactive materials.³²⁻³⁴ These include their biocompatibility, and their strong electron-withdrawing character that makes them useful partners in electron donor (D) – acceptor (A) or D-A-D photoactive systems as well as in organic semiconductor materials such as photovoltaics and OLEDs.³⁵ As part of our work on new molecular and polymeric BTZ containing photoactive materials,³⁶⁻³⁹ we have developed a high yielding, scalable and rapid synthesis of a new quinolin-4-ol incorporating a central BTZ unit. Gratifyingly, this material has a helical, nonplanar geometry, and exhibits AIE and ROS generation properties.

2.5 Results and Discussion

2.5.1 Synthesis and Characterisation of Compounds **5 and **5H₂²⁺****

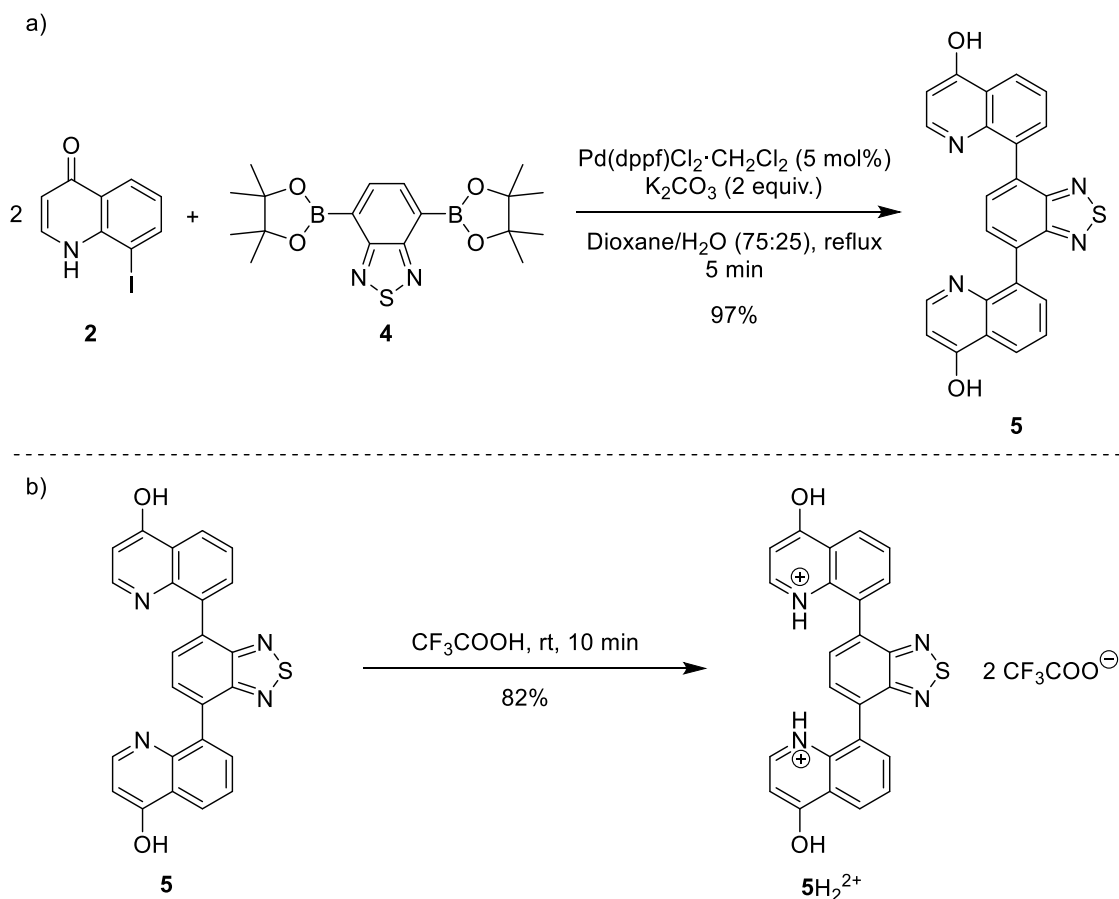
The chemistry used to access the starting material, the antimicrobial core⁴⁰ 8-iodoquinolin-4(1*H*)-one (**2**), was previously developed by Koutentis and co-workers to

gain access to the natural product derivative deazacanthin-4-one **3** (Scheme 1).^{8,41} Heating an equimolar mixture of triethyl orthoformate, Meldrum's acid and 2-iodoaniline in acetonitrile (MeCN) under reflux conditions for 3 h, gives 5-[(2-iodophenyl)amino]methylene}-2,2-dimethyl-1,3-dioxane-4,6-dione (**1**), thermolysis of which affords 8-iodoquinolin-4(1*H*)-one (**2**).¹⁷



Scheme 1. Synthetic pathway for and use of 8-iodoquinolin-4(1*H*)-one **2** to prepare deazacanthin-4-one **3**.

In our prior work, quinolone **2** was reacted with 2-chloroarylboronic acids or pinacol esters in a two-step, C-C and C-N bond forming process to afford the desired deazacanthin-4-ones **3**.⁸ Herein, quinolone **2** was reacted with 4,7-bis(4,4,5,5-tetramethyl-1,3,2-dioxaborolan-2-yl)benzo[*c*][1,2,5]thiadiazole [BTZ(Bpin)₂] (**4**) to give the desired 8,8'-(benzo[*c*][1,2,5]thiadiazole-4,7-diyl)bis(quinolin-4-ol) (**5**) in up to 97% yield (Scheme 2). Product **5** precipitated from the reaction mixture and, following a simple filtration and subsequent washes with THF and EtOH, was collected as a yellow semi-crystalline powder without the need for further purification, as determined by LC-MS (SI, 2.8.5, 2.8.6). Compound **5** exhibited very poor solubility in both polar and non-polar solvents (SI, 2.8.7); hot dimethyl sulfoxide (DMSO) only sparingly dissolved the compound and was not suitable for obtaining satisfactory ¹³C NMR data. Fortunately, compound **5** dissolved in trifluoroacetic acid (TFA), forming the salt **5**H₂²⁺ 2TFA⁻ (referred to as **5**H₂²⁺). X-ray quality single crystals were obtained from a hot PhCl/TFA solution that was left to slowly cool at room temperature over several days. The asymmetric unit cell was *P*2₁/*n* monoclinic and revealed the formation of [**5**H₂²⁺ 2TFA⁻]₂·2TFA.



Scheme 2. a) Suzuki-Miyaura reaction of 8-iodoquinolin-4(1*H*)-one (**2**) with BTZ(Bpin)₂ **4** to afford 8,8'-(benzo[*c*][1,2,5]thiadiazole-4,7-diyl)bis(quinolin-4-ol) (**5**). b) Synthesis of 5H₂²⁺ from **5**.

This structure represents the pyridinium dication 5H₂²⁺ co-crystallised with two molecules of TFA and two TFA anions (Figure. 3).

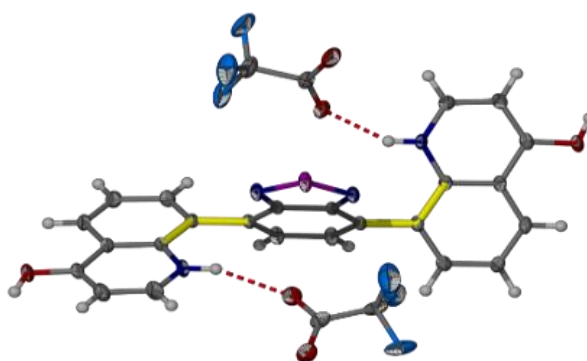


Figure 3. Structure of 5H₂²⁺ shown as 50% probability ellipsoids. Hydrogen bonding of the TFA molecules to 5H₂²⁺ highlights the protonation and enol tautomer of **5**. Disorder of one of the triflate and both TFA molecules in the asymmetric unit are not shown for clarity. Yellow and thicker bonds indicate the torsion angle of 126.11(17)°, which represents the rotation of the two quinolinol groups to opposite sides of the BTZ.

In addition, the C-O bond lengths ($d_{\text{C-O}} = \text{C24-O2 } 1.319(3) \text{ \AA}$ and $\text{C9-O1 } 1.326(3) \text{ \AA}$) suggest that, in this protonated form, compound **5** exists in the enol tautomer instead as the keto tautomer, which was the case with product **3**. TD-DFT calculations at the B3LYP/6-311G(d,p) level of theory confirmed this (SI, 2.8.3), as the calculated UV-Vis absorption of the enol tautomer of the neutral molecule and the pyridinium form in the presence of coordinated anionic and neutral TFA molecules is in good agreement with the experimental UV-Vis absorption in TFA as solvent (SI, 2.8.3). The crystal structure showed that the quinolinols deviate from the plane of the BTZ and the torsion angle between the planes defined by each quinolinol and the BTZ is $126.11(17)^\circ$. Support for this propeller-type geometry in solution came from the NOE 2D NMR spectrum of product $\mathbf{5H}_2^{2+}$, which suggested a nonplanar geometry, as there was no interaction between the BTZ and quinolinol protons, showing that the two quinolinol moieties must be nearly orthogonal with respect to each other, from a top-bottom perspective. Both neutral and protonated compounds were thermally stable up to at least 400°C as revealed by TGA analysis (SI, 2.8.1).

2.5.2 Photochemical Studies

As mentioned above, the presence of the chromophore BTZ core in compound **5**, prompted an investigation of its ability to act as a photosensitizer for ROS generation. More specifically, we decided to focus on the production of $^1\text{O}_2$, as it has a high synthetic utility⁴² and it is believed to be the main damaging agent in PDT applications.⁴³ The formation of ascaridole *via* a Diels-Alder reaction between singlet oxygen ($^1\text{O}_2$) and α -terpinene was undertaken to evaluate the ability of compound **5** to act as a photosensitizer for the generation of $^1\text{O}_2$.³⁶ Owing to the low solubility of compound **5** (SI, 2.8.7), we carried out the reaction heterogeneously by using continuous-flow technology. This alternative enabling technology is an effective method for use with heterogeneous photosensitizers, and can offer better results compared to batch experiments, as it was recently demonstrated by our group.⁴⁴ For this work, 1 mol% of compound **5** (0.0025 mmol) was mixed with 500 mg of silica (solid support). The mixture was then added into a short column reactor and was ready for use. To take full advantage of the flow

instrumentation capabilities, we connected an O₂ gas line to the set-up and the operating overall system pressure was set at 2 bar, allowing more O₂ to be dissolved in solution.

Moreover, a 60 MHz Nanalysis-60e benchtop ¹H NMR instrument was connected to the set-up, which allowed us to monitor the reaction progress in real time (Figure. 4b). To make the ¹H NMR data acquisition possible, CDCl₃ was used as the solvent, which also offers significantly increased lifetime of ¹O₂ in solution compared to non-deuterated and non-chlorinated solvents.⁴⁵ While compound **5** absorbs mostly in the long UV region of the spectrum (SI, 2.8.3), we used an LED emitting at 390-440 nm to test whether its absorbance at 400-420 nm was enough to produce its excited state. Gratifyingly, when the reaction was tested using the aforementioned parameters, in-line ¹H NMR spectroscopy indicated that after 1500 seconds (25 min) the reaction was complete.

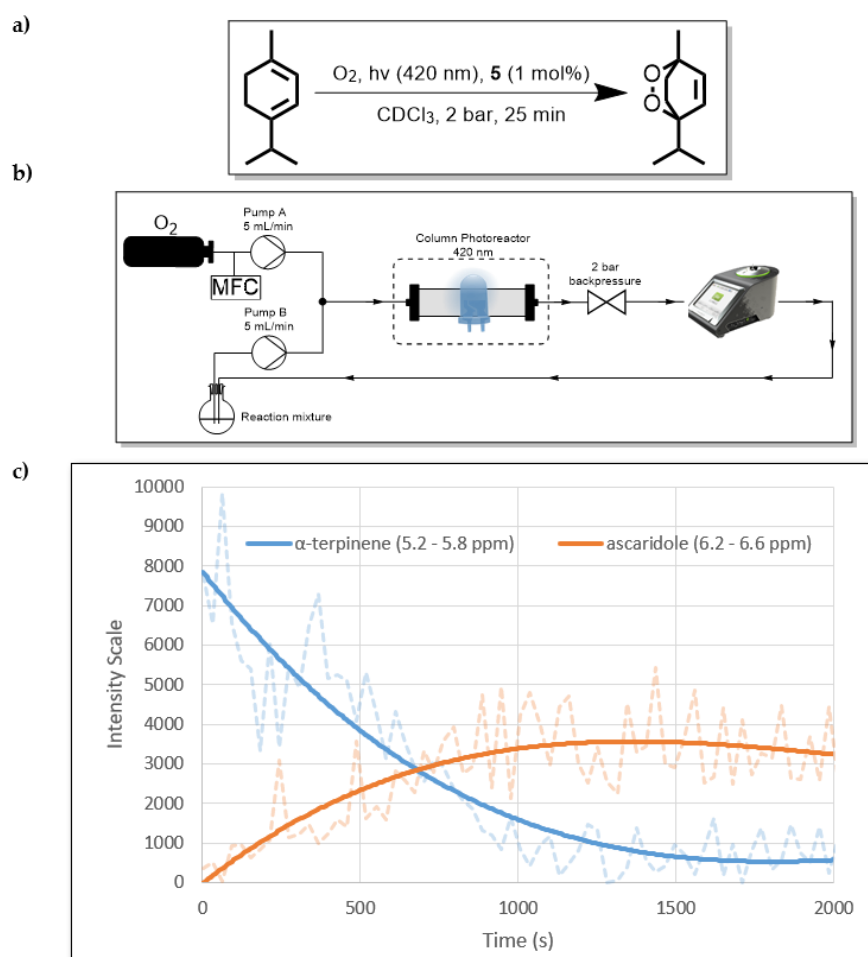


Figure 4. a) The overall reaction from α -terpinene to ascaridole. b) Schematic diagram of the flow set-up. MFC= mass flow controller. c) In-line ¹H NMR data for the first run of the reaction.

Since α -terpinene reacts selectively with ¹O₂,³⁹ by calculating its conversion to ascaridole, the amount of generated ¹O₂ can be estimated. For the optimised reaction conditions

above, this was found to be 0.54 mmol h⁻¹ per mg of **5**. This performance is comparable with previously described BTZ-based heterogeneous photosensitisers that were used under continuous flow conditions (Table 1).

Table 1. ¹O₂ generation efficiencies of various BTZ-based heterogeneous photosensitisers under continuous flow conditions and visible light (420nm) illumination.

Entry	Photosensitiser characteristics	Reactor type	¹ O ₂ Productivity (mmol h ⁻¹) ^a
1 ³⁷	Conjugated microporous BTZ polymer	Coil	1.44
2 ³⁹	High internal phase emulsion BTZ polymer	Column	0.15
3 ³⁶	High internal phase emulsion BTZ polymer	Column	0.05
4 ³⁶	Polymer supported BTZ (microbeads)	Coil	4.04
5-current work	Molecular BTZ, SiO ₂ supported	Column	0.54

^a Per mg of photosensitiser

Even though its performance is not particularly outstanding, what makes compound **5** stand out is that it is the first example of a molecular based BTZ heterogeneous photosensitiser that has been used for ¹O₂ production. A comparison between the ¹O₂ productivities of compounds **5** and **5H₂²⁺** was also made, to test if they behave differently under identical conditions, however there was negligible difference in their performance (SI, 2.8.8).

To test the durability of compound **5** as a photosensitiser, we repeated the same reaction four more times without replacing the original packed column. By ¹H NMR analysis, we observed that even after five cycles, there was quantitative consumption of α -terpinene (0.25 mmol per cycle) without any apparent photo-bleaching of **5**, judging by its consistent performance. This behaviour highlights the excellent stability of **5** against ¹O₂. The graph (Figure. 4c) follows signal intensity for two specific spectral regions which

correspond to α -terpinene and ascaridole. The actual real time data are represented by the faded dashed lines, which were used to generate a moving average trend line. The noise in the raw data is partly attributed to the flow of O₂ bubbles through the bench-top ¹H NMR instrument, which lowered the signal quality. Nonetheless, the signal was accurate enough to provide real-time qualitative information about the reaction progression. To confirm reaction completion, after each run the content of the collection flask was isolated by removing the solvent under reduced pressure and ¹H NMR spectra using a 300 MHz instrument were obtained (SI, 2.8.5). It was also observed that when alumina was used instead of silica as a solid support, poor adsorption of compound **5** resulted in gradual leaching of solid photosensitiser into the reaction mixture (SI, 2.8.5).

To prove that the reaction was catalysed heterogeneously and not due to low concentrations of soluble **5**, a hot suspension of compound **5** (1 mol%) in CDCl₃ was stirred for 30 min, and the solids were then removed by filtration. To the resulting solution was added α -terpinene (0.25 mmol). After irradiating the solution, no ascaridole was detected, proving that luminogen **5** acts as a true molecular heterogeneous photosensitiser (SI, 2.8.5). Finally, as we have shown that **5** can produce a stable excited triplet state for the subsequent type II energy transfer to occur, we wanted to assess whether it can also participate in type I photosensitised reactions, to produce other types of ROS, such as superoxide (O₂^{•-}). As such, we used compound **5** as a photoredox catalyst for the aerobic hydroxylation of phenylboronic acid to phenol. This single electron-transfer reaction has been shown to be mediated by O₂^{•-},⁴⁶ and when 1 mol% of **5** was used, there was 36% conversion to phenol, as measured by HPLC (SI, 2.8.9).

2.5.3 Photophysical Studies

Due to the insolubility of compound **5** in organic solvents, its photoluminescence behaviour was only studied in the solid (semi-crystalline) state. A broad green emission at 512 nm was observed (SI, 2.8.4). The protonated TFA salt **5**H₂²⁺ was slightly more soluble in polar organic solvents such as DMSO and thus, it was used to make dilute solutions in different ratios of DMSO/water and TFA/water (water fraction, f_w ranged from 0 to 90%) and their fluorescence spectra were recorded (Figure 5, 7). At 100% DMSO (Figure 8), the emission spectrum was weak, containing two peaks, a sharp one

at 428 nm which can be attributed to the singlet excited state and a broad one at 446 nm. The rotatable, D-A bond between the quinolinol and BTZ moieties indicated that this broad peak may be the result of ICT or possibly twisted intramolecular charge transfer (TICT).⁴⁷ TD-DFT calculations showed that in the molecular orbitals associated with the vertical excitations responsible for the absorption profile of $5H_2^{2+}$ the HOMO to LUMO transition has significant charge transfer character from the quinolinol moieties to the BTZ core (SI, 2.8.3), which further strengthens the case of ICT emission. A third, redshifted broad peak at 574 nm is believed to originate from an excimer, which forms a broad UV-Vis absorption band at 460 nm with increasing concentrations (SI, S2.8.4). When f_w was increased to 10% a fine precipitate started to appear with concomitant disappearance of the excimer peak, bathochromic and hyperchromic transformation of the ICT peak, and appearance of a new, broad peak, which continued to increase in intensity until f_w reached 40% (Figure 5).

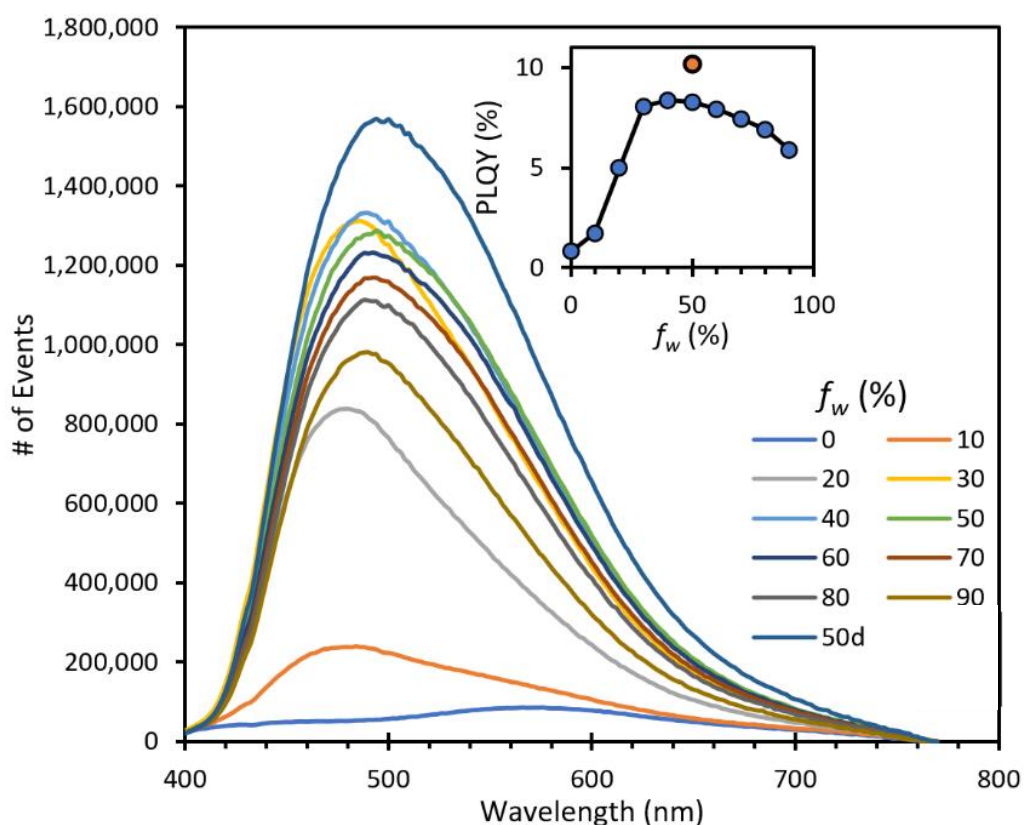


Figure 5. DMSO/H₂O series emission spectra. Inset shows relation between f_w and PLQY (%). $C = 2.05 \times 10^{-4}$ M. Excitation wavelength was 320 nm.

At this point, there was a 24-fold increase in emission intensity and 10-fold increase in photoluminescence quantum yield (PLQY), which reached 8.4%. The peak continued to redshift until 490 nm when f_w reached 50%. This can be attributed to ICT

solvatochromism⁴⁸ and shows that both AIE and ICT effects are active initially. Between f_w 50-90% the emission decreased, a rarely observed behaviour seen in other AIE systems which has been ascribed to changes in the crystallisation processes and available surface area of the nanoaggregates, as more water is added.⁴⁹

The UV-Vis absorption spectra of the DMSO/water series show two new shoulders appearing at 371 and 410 nm (Figure 6). The latter follows the same behaviour as the emission spectra, showing a maximum absorbance when f_w is 40% and decreasing thereafter.

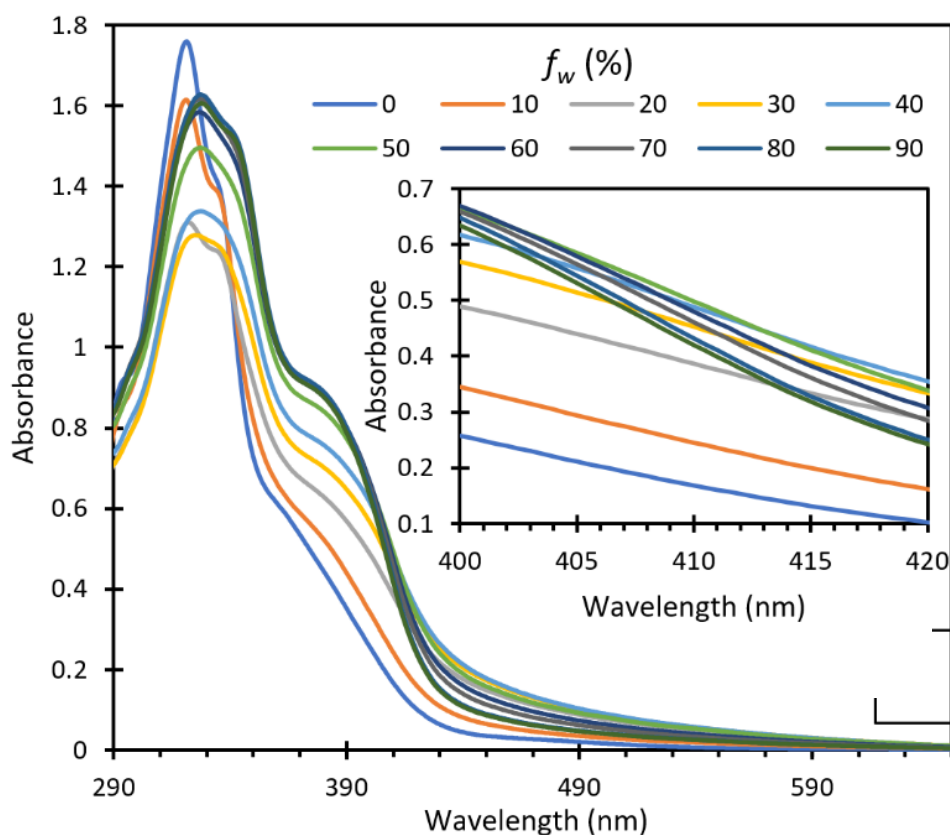


Figure 6. DMSO/H₂O series absorption spectrum of $5H_2^{2+}$. Inset shows an enlarged section between 400 nm and 420 nm.

To verify the relationship of this absorption shoulder with the formation of nanoaggregates, we used varying excitation wavelengths spanning from 320 nm ($\lambda_{\text{abs,max}}$ of $5H_2^{2+}$) to 430 nm to monitor the AIE emission peak at 478 nm. When λ_{exc} was 410 nm, the λ_{em} intensity was maximised (SI, 2.8.4).

When TFA was used instead of DMSO (Figure 7), no aggregation was observed until f_w reached 70%, confirmed by the corresponding UV-Vis absorption spectra (SI, 2.8.4), showing a significant level-off tail above 400 nm, which is due to the light scattering

caused by the nanoaggregate suspension.²⁵ In spite of this, no AIE peak emerged, which can be explained by TFAs ability to form strong intermolecular H-bonds between the phenolic and pyridinium moieties of compound $5H_2^{2+}$, as seen by the crystal structure (SI, 2.8.2). These H-bonds can in turn induce non-radiative pathways, by competing with the radiative ICT processes between the BTZ and quinolinol moieties.⁵⁰ To further demonstrate this point, when D_2O was used instead of H_2O for the solutions with f_w of 50%, their fluorescence was enhanced, increasing their PLQYs for the DMSO and TFA solutions by 22 and 29%, respectively. A striking difference was seen in the TFA spectra, where the weaker ICT/AIE peak became more intense than the monomeric peak while also getting broader and bathochromically shifted to 462 nm (Figure 7).

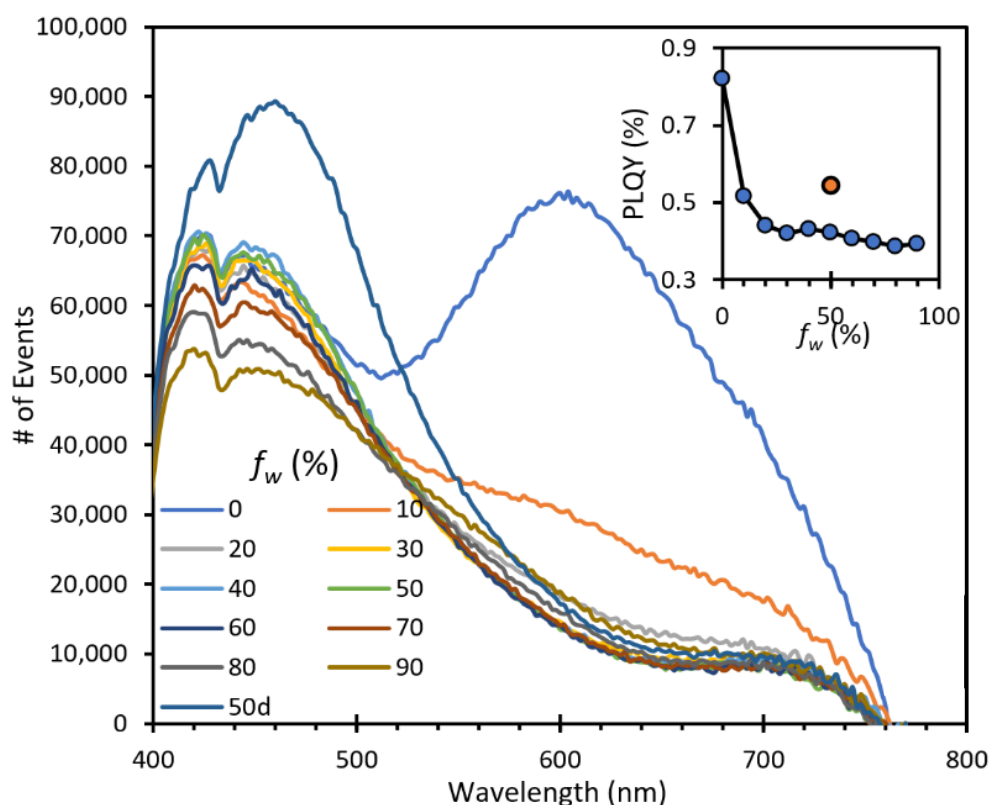


Figure 7. TFA/ H_2O series emission spectrum of $5H_2^{2+}$. Inset shows relation between f_w and PLQY (%). $C = 2.05 \times 10^{-4}$ M. Excitation wavelength was 320 nm.

This effect is associated to the inferior quenching abilities of deuterium,⁵¹ and strengthens the case of H-bonding having an important role in the quenching of the AIE peak in the TFA solution.

Finally, an aerated TFA/ D_2O ($f_w = 50\%$) solution exhibited a weak emission at 1274 nm (SI, 2.8.4), caused by 1O_2 phosphorescence, which directly supported its ability to generate 1O_2 , even in solution.⁵²

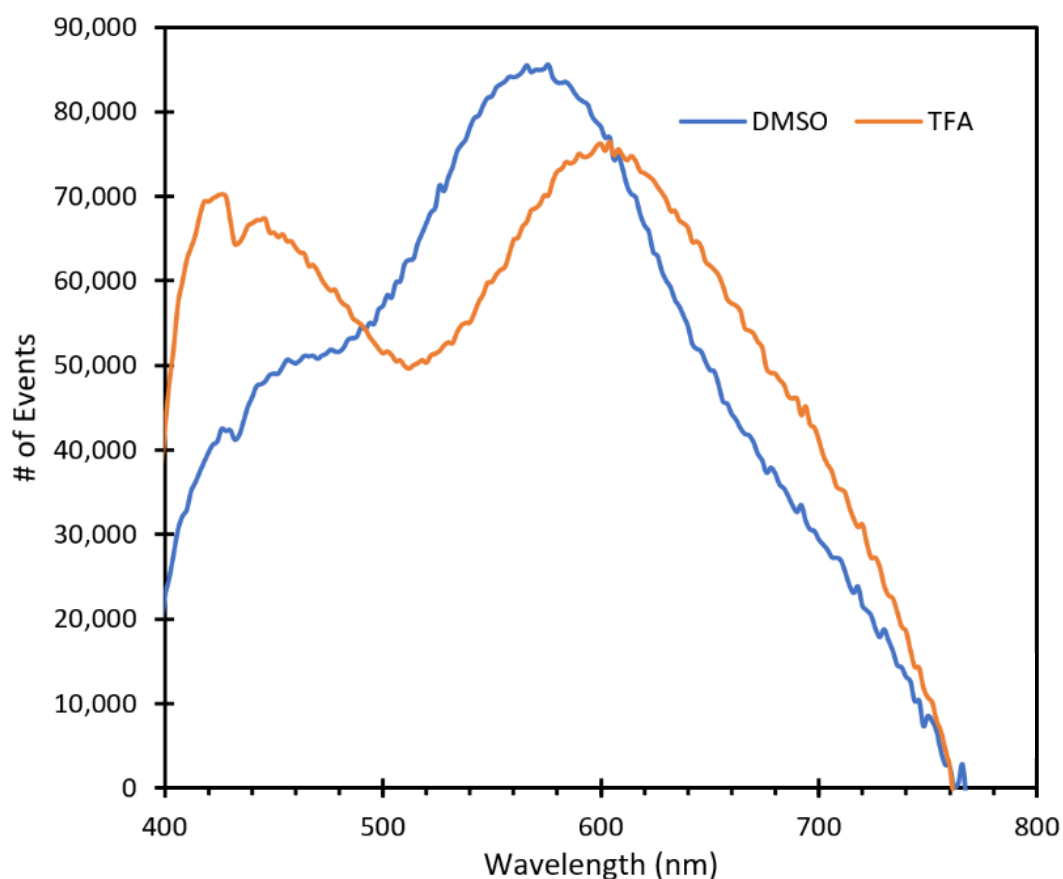


Figure 8. Comparison of emission spectra of $5H_2^{2+}$ dissolved in DMSO and TFA, while f_w was 0. $C = 2.05 \times 10^{-4}$ M. Excitation wavelength was 320 nm.

2.6 Conclusions

In summary, we have discovered a robust and easily accessible D-A-D chromophore with a twisted geometry. Its high insolubility allowed us to use it as a very effective molecular heterogeneous photosensitizer for 1O_2 production in continuous flow. In addition, we explored the photophysical properties of its TFA salt, which revealed a tuneable dual emission between a redshifted excimer and a combination of ICT/AIE which was controlled by adjusting the water fraction. When TFA was used as a solvent the AIE emission was turned off due to increased H-bonding. This study acts as a gateway for further investigation of this unique class of quinolinol-BTZ AIEgen triads, and we think the combination of their facile synthesis, tunability, heterogeneous 1O_2 generating capabilities and potential antimicrobial properties make them attractive targets for future research.

2.7 Future Work

There are many avenues of exploration to further develop this new class of AIEgens. Both compounds **5** and $5H_2^{2+}$ displayed physicochemical characteristics resembling that of other quinoline-based AIE compounds, namely quenching, or ‘turning-off’ of the fluorescence after protonation with TFA, with a concomitant redshift of the emission wavelength.^{16,18,19} As such, we can use these known compounds as a reference for future experiments.

As discussed in section 2.4, one contemporary area of interest is the use of AIEgen systems for fluorescent thermometry applications. This is considered to be a relatively challenging area of research, as most fluorophores, including AIEgens suffer from thermally induced fluorescence quenching;⁵³ this is caused by non-radiative energy loss *via* thermally induced vibrations.⁵⁴ One way to reduce these vibrations is to use a carrier matrix, which can act as a shell and protect the fluorophore from external vibrations. A prime example of this, came from Zhu *et al.* in 2019.⁵⁵ The team developed a co-polymer that consisted of a quinoline-malononitrile AIEgen unit and a Poly(*N*-isopropylacrylamide) thermo-responsive carrier (Figure 9). When heated, the carrier forms a globular aggregate which in turn helps rigidify the AIEgen, resulting in a positive temperature coefficient of fluorescence.

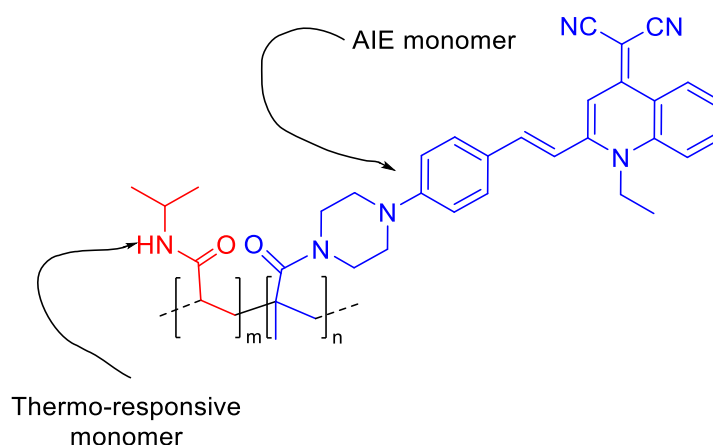


Figure 9. AIE-grafted co-polymer developed by Zhu *et al.*

By modifying our fluorescence spectrometer, we were able to measure the emission spectra of $5H_2^{2+}$ in TFA solution, at a set of different temperatures, as seen in Figure 10. Unsurprisingly, by increasing the temperature the emission intensity decreased.

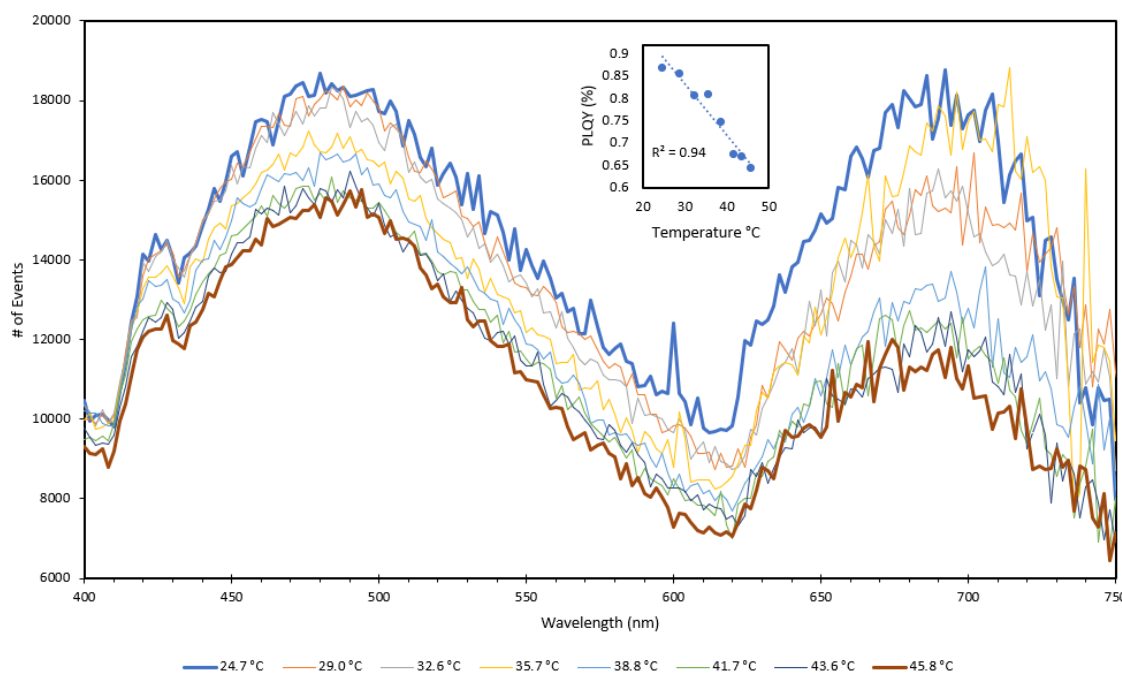


Figure 10. Emission spectra of $5H_2^{2+}$ dissolved in 100% TFA at different temperatures. Inlet shows the PLQY with relation to the temperature. $C = 2.05 \times 10^{-4}$ M. Excitation wavelength was 270 nm using a Xe lamp.

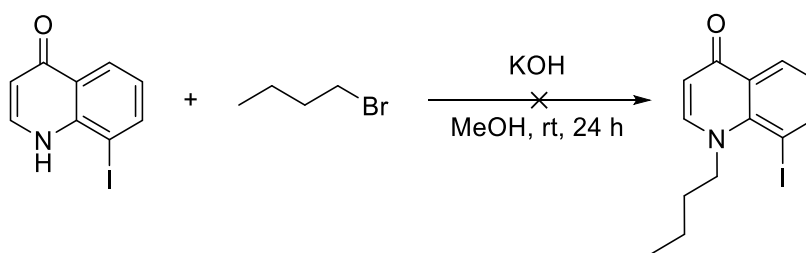
When heated to 45.8 °C, the PLQY dropped to 0.64%, from 0.87% at 24.7 °C. Interestingly, it appeared that the third peak at *ca.* 686 nm was affected by temperature effects more than the 1st (monomeric) and 2nd (CT) peaks, as its intensity was reduced by 36%, compared to 17% for the other two. This effect corroborates with the hypothesis that the third peak is the result of excimeric emission, as it has been shown that at higher temperatures excimer dissociation can occur, resulting in a pair of triplet and ground state monomers.⁵⁶ It is also noted, that due to experimental constraints at the time of spectral measurements, the excitation wavelength was set at 270 nm, compared to 320 nm that was used in the initial experiments. As the absorbance of $5H_2^{2+}$ at 270 nm is lower (SI, 2.8.3), this resulted in emission of lower intensity, leading to high noise in the acquired data. Therefore, and to better understand how temperature affects the photophysics of compound **5** and $5H_2^{2+}$, additional experiments are needed.

Firstly, the thermometry experiment should be repeated using an excitation wavelength of 320 nm, so that the data are consistent with the initial results. Secondly, samples with different f_w values should also be tested, to gain insights about how the different aggregation levels respond to changing temperature. Thirdly, a series of different concentrations should also be measured at different temperatures. This will provide clues

to help determine the origin of each emission peak, and the type of aggregation that is occurring.⁵⁷

It can be envisaged that future work may also include efforts to improve the optoelectronic properties of compounds **5** and **5H₂²⁺** by modifying their structure. This is important, as it will allow us to design materials tailored for more targeted applications. For instance, lowering the HOMO-LUMO gap of the sensitizers could in principle lead to more effective absorption of visible light photons, and the emergence of near-infrared (NIR) luminescence,⁵⁸ which is a much sought after, albeit rare, property that is especially useful for bioimaging and biosensing applications.⁵⁹

Preliminary work towards that goal has already started, and it involved attempts to perform a N-alkylation on the quinoline SM with the aim to increase the solubility of the final AIEgen, so it can be used in its freebase form, in multiple solvents (Scheme 3).

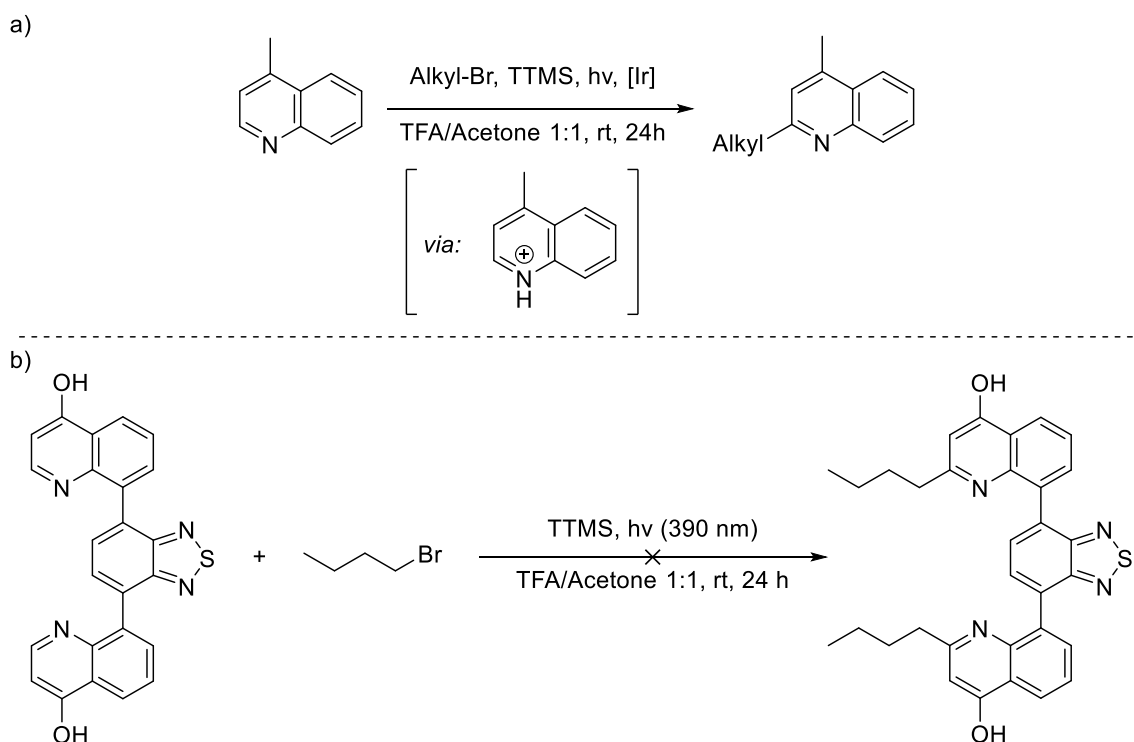


Scheme 3. N-butylation attempt of the 4-quinolone **2**.

However, after employing literature conditions,⁶⁰ including ones developed specifically for the N-alkylation of substituted 4-quinolones,⁶¹ the desired product could not be obtained, as the SM remained unreactive after 24h (based on TLC).

A more ambitious strategy to achieve alkylation was also pursued; the quinoline moiety present in AIEgen **5** is an electron deficient heterocycle that has been used to participate in photoredox Minisci-type, α C-H alkylations.⁶² More specifically, a 2018 report from Wang *et al.*,⁶³ showed that quinolines can be α -alkylated by using inactivated alkyl bromides, visible light, an Ir-based catalyst that was used to produce $O_2^{\cdot -}$ *in situ*, and a halogen abstraction agent, tris(trimethylsilyl)silane (TTMS). Interestingly, the reaction was carried out using TFA/Acetone (1:1) as the solvent, as protonation of the quinoline was necessary (Scheme 4a) for the reaction to proceed. This immediately drew our attention, as due to its limited solubility, compound **5** could not participate in most alkylating reactions, however since we knew that TFA is a good solvent, and produces the necessary protonated intermediate **5H₂²⁺**, we thought that it would be a good candidate

for the reaction (Scheme 4b). Additionally, since we proved (section 2.5.2) that under the right conditions compound **5** can be used to produce O_2^- in principle we could omit the use of the Ir-photocatalyst and utilise **5** in an autocatalytic fashion. After confirming that the reported TFA/Acetone (1:1) solvent system could dissolve our SM, we proceeded to test our hypothesis. Unfortunately, however, even after modifying several reaction parameters such as irradiation wavelength, temperature, time, and equivalents of TTMS/Alkyl-Br, the desired product could not be detected (nor its monomer).

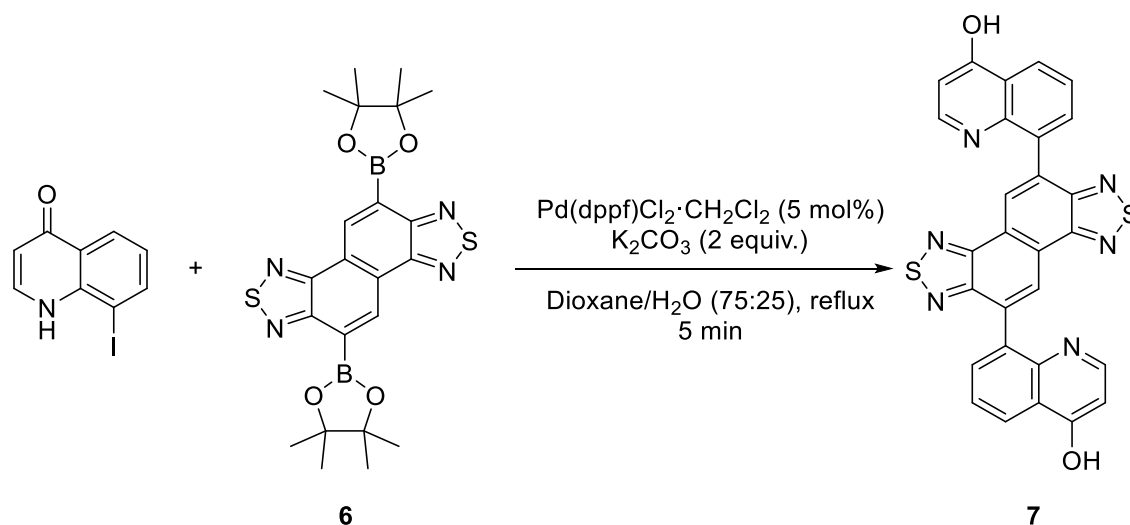


Scheme 4. a) Published light-mediated Minisci alkylation of quinolines, and the protonated intermediate involved in the reaction. b) Adapted reaction conditions using **5** as the SM and the photocatalyst.

Despite failing to obtain the desired product, we believe that Minisci conditions might still present a viable way to proceed forward; perhaps by using an external photocatalyst the reaction could work as intended. As mentioned, the low solubility of **5** is one of the main reasons that prohibits us to test other known alkylation conditions. A different way to combat this issue could be by transferring existing protocols from batch to the mechanochemical domain, as it is conceivable that several of them could work in a solvent-free manner, as there is already precedent for dark mechanochemical Minisci reactions.⁶⁴

Another exploratory modification that was attempted, included replacing the central BTZ core of the AIEgen. Naphtho[1,2-*c*:5,6-*c'*]bis[1,2,5]thiadiazole (NTZ) is a benzo-fused

heteroaromatic containing two BTZ subunits. In recent years its use has gained substantial popularity, as it has been shown to be a versatile acceptor group in D- π -A organic semiconductors⁶⁵ and is effective in lowering the HOMO-LUMO gap, as its rigid π -conjugated system results in reduced LUMO energy levels.⁶⁶ As a result it has been used to produce organic solar cells with superior performance characteristics to those of the analogous BTZ-based molecules.⁶⁷ Moreover due to its extended π -system, and electron accepting capabilities we anticipated that a quinoline-NTZ-quinoline triad, might have better overall solubility, and exhibit TICT emission, since its planar configuration would be more accessible while in solution.⁶⁸ In addition, its synthesis would be relatively trivial, as the pinacol ester of this NTZ, *5,10-bis(4,4,5,5-tetramethyl-1,3,2-dioxaborolan-2-yl)naphtho[1,2-c:5,6-c']bis([1,2,5]thiadiazole)* (**6**) is commercially available, albeit expensive (£230/100 mg).⁶⁹ As we only had a limited supply of boronic ester **6** at the time (*ca.* 1 mg) the test reaction was performed at a very small scale. Overall, the reaction conditions were identical to the ones developed for the BTZ analogue **5** (Scheme 5).



Scheme 5. Attempt to synthesise an NTZ-analogue of AIEgen 5.

After reacting for 5 minutes, the SM was consumed (by TLC), and a yellow precipitate was seen to be suspended in solution. After filtration, the precipitate was washed with dioxane and dried. Unfortunately, a yield could not be obtained, as the precipitate was stuck to the filter paper. To identify the structure of the precipitate it was subjected to ¹H-NMR analysis. First, we tried to dissolve it in CDCl₃ or (CD₃)₂CO to recover it after analysing, however it appeared that only DMSO-d₆ could dissolve it completely. Due to the small amount of material that we were working with, the resulting ¹H NMR spectrum

appeared to have a very high signal-to-noise ratio, and as a result, it was not possible to draw any definitive conclusions regarding its structure (Figure 11a). Despite this, by integrating the visible peaks, a total of 14 protons could be counted. The most downfield signal was at 10.8 ppm and could tentatively correspond to the labile -OH protons. Furthermore, by comparing the spectrum with that of compound **5** (Figure 11b), it was evident that the two appeared to be very similar. Based on this similarity, the correct number of protons, the physical appearance, and reaction behaviour, it is not unreasonable to assume that the reaction did indeed work, to produce the desired NTZ analogue, 8,8'-(naphtho[1,2-c:5,6-c']bis([1,2,5]thiadiazole)-5,10-diyl)bis(quinolin-4-ol) (**7**). More conclusive evidence about its identity could be obtained by LC-MS analysis, however at the time we did not yet have access to that instrumentation.

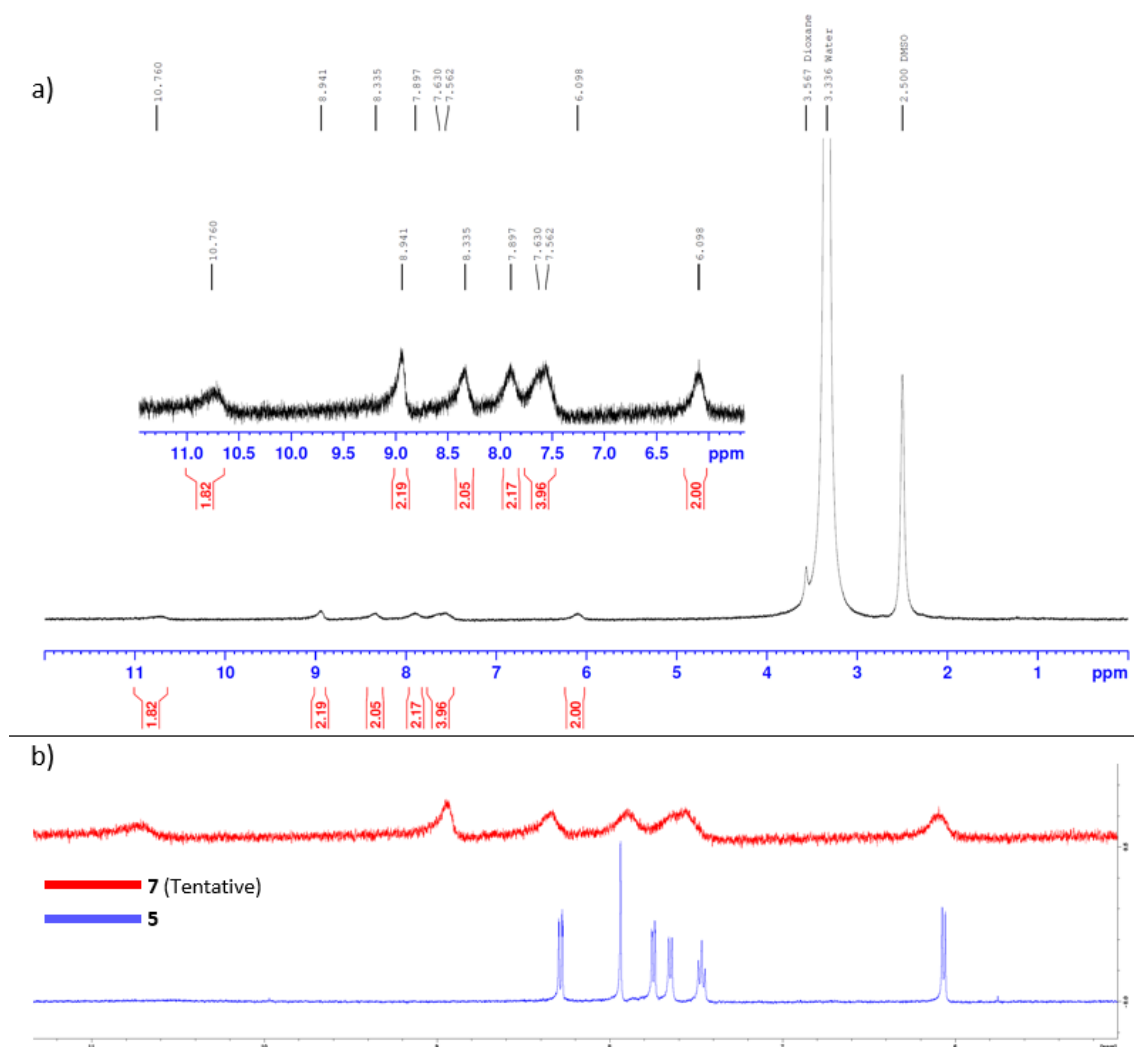
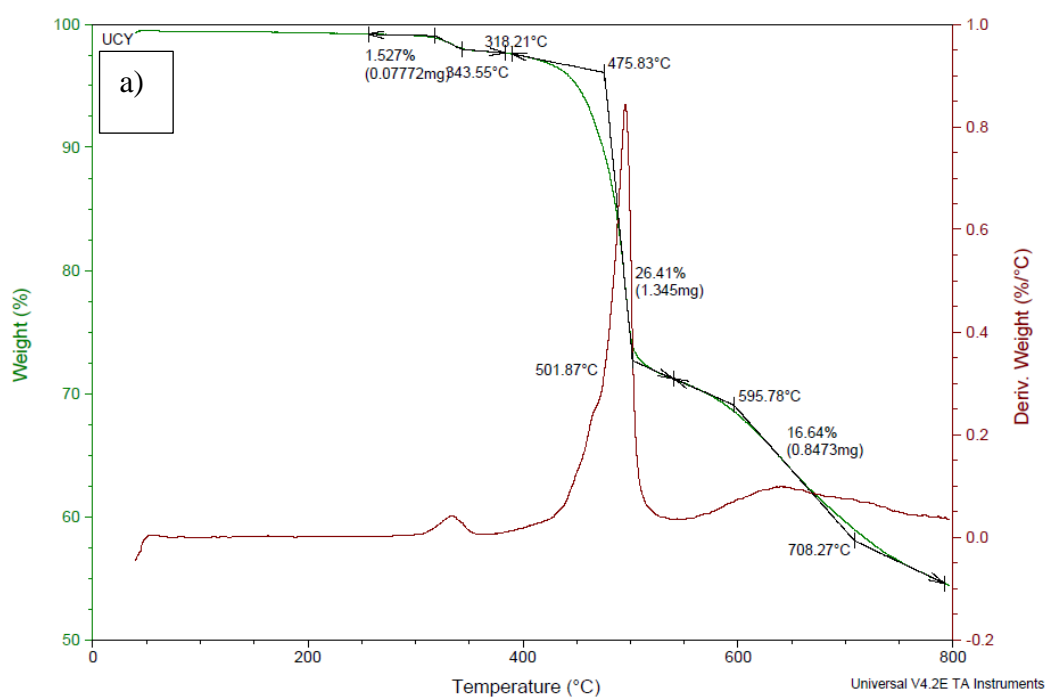


Figure 11. a) ¹H NMR spectrum of tentative compound **7** dissolved in DMSO-d₆. b) Comparison between the ¹H NMR spectra of the newly formed compound and AIEgen **5**.

With satisfactory evidence that NTZ analogues could be obtained with relative ease, other structural changes that could be implemented include the addition of halogen atoms within the BTZ/NTZ/quinoline subunits, as their presence is able to facilitate ISC ($S_1 \rightarrow T_n$),⁷⁰ although they can also induce cytotoxicity, which could limit their use as PDT agents.⁷¹ Finally, substituting the chalcogen atom of the BTZ/NTZ subunits with Se, or Te atoms is also a worthy endeavour, as their presence in luminophores can ‘turn-on’ the heavy-atom effect (HAE). As the atomic weight of the chalcogen increases, fluorescence quenching is observed by the simultaneous emergence of phosphorescence. This happens due to the enhanced spin-orbit coupling constants of heavier atoms, which lead to the enhancement of ICS.⁷² In recent years, the HAE has successfully been exploited to synthesise a large variety of heterocyclic triplet sensitisers.^{73–75}

2.8 Supporting Information

2.8.1 TGA Curves of 5 and 5H₂²⁺⁸



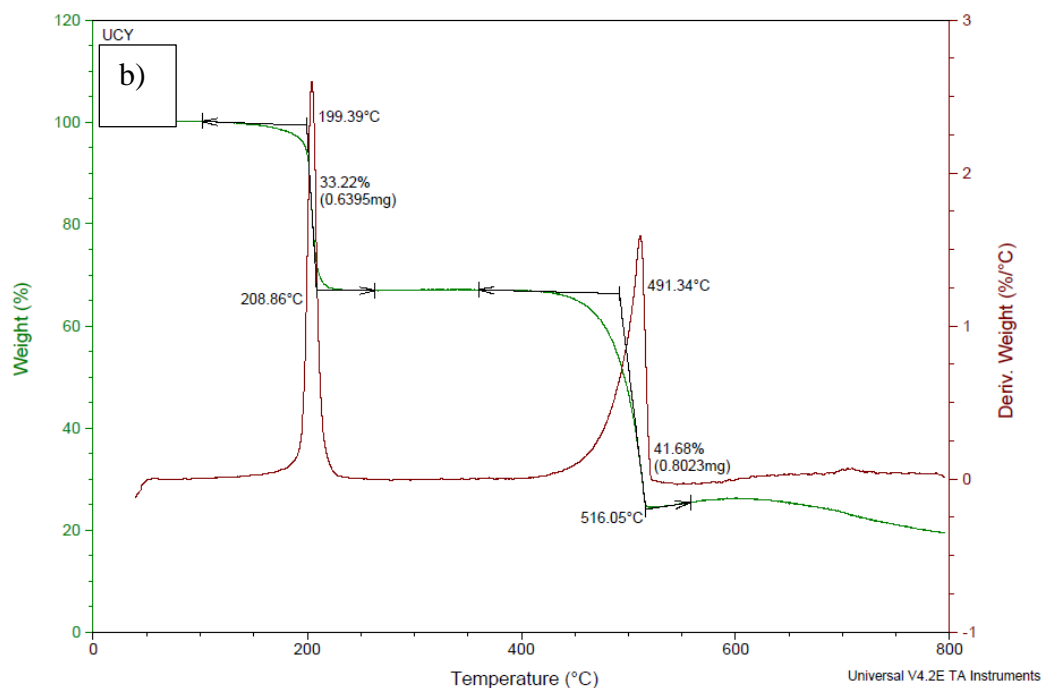


Figure S1. a) TGA thermogram of freebase compound **5** has a very small % mass loss at around 320 °C which may be associated with a small impurity that is present in the sample. b) TGA thermogram of $5H_2^{2+}$ in which the first % mass loss corresponds to the loss of the two TFA molecules.

2.8.2 Crystallographic Data^s

The structure has been deposited with the CCDC with a Deposition Number 2086024.

Crystal data for $[5H_2^{2+} \cdot 2TFA^-] \cdot 2TFA$: $[C_{24}H_{16}N_4O_2S^{2+} \cdot 2(C_2F_3O_2^-)] \cdot 2C_2F_3O_2H$, $M = 878.56$, yellow plates, $0.18 \times 0.04 \times 0.03 \text{ mm}^3$, monoclinic, space group $P2_1/n$ (No. 14), $a = 8.14670(10)$, $b = 21.3962(3)$, $c = 20.1733(3) \text{ \AA}$, $\beta = 90.509(2)^\circ$, $V = 3516.24(8) \text{ \AA}^3$, $Z = 4$, $D_c = 1.660 \text{ g cm}^{-3}$, $F_{000} = 1768$, SuperNova, Dual, Cu at home/near, Atlas, MoK α radiation, $\lambda = 0.71065 \text{ \AA}$, $T = 100(2) \text{ K}$, $2\theta_{\text{max}} = 51.9^\circ$, 12906 reflections collected, 6738 unique ($R_{\text{int}} = 0.0269$). Final $Goof = 1.035$, $R_1 = 0.0513$, $wR_2 = 0.1380$, R indices based on 5767 reflections with $I > 2\sigma(I)$ (refinement on F^2), 660 parameters, 0 restraints. Lp and absorption corrections applied, $\mu = 0.220 \text{ mm}^{-1}$.

Comparison of the calculated structures with the structure determined from the TFA-crystal of **5** indicates that the match in conformation and geometry is high. It appears structurally there is little difference in the protonation of **5** on distances or angles. This

is highlighted by the low RMSD and maximum deviation numbers when comparing the molecular geometries (Table S1 and Figure S2).

Table S1. Comparison of the geometry parameters from the X-ray structure and the optimised structures in the gas phase at the RB3LYP/6-311G(d,p) level of theory.

Structures compared	RMSD (Å)	Maximum deviation (Å)
Crystal:[5H ₂ ²⁺ 2TFA ⁻]-2TFA	0.1947	0.3532
Crystal:[5H ₂ ²⁺ 4TFA ⁻]-4TFA	0.1775	0.3247
Crystal: 5	0.0605	0.1507
[5H ₂ ²⁺ 4TFA ⁻]-4TFA: 5	0.1876	0.3668

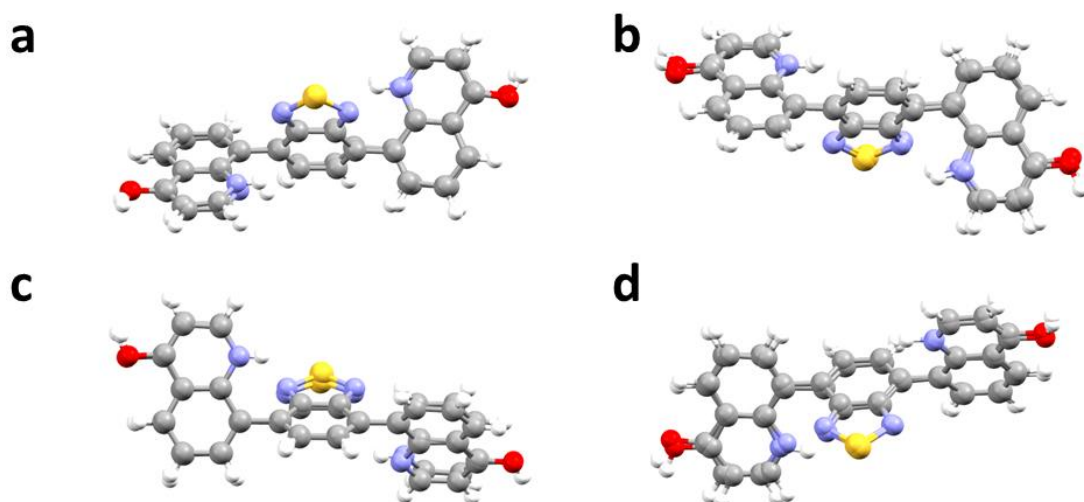


Figure S2. Overlay of the crystal structure with the computed structures **5**, [5H₂²⁺ 4TFA⁻]-4TFA and [5H₂²⁺ 2TFA⁻]-2TFA. a) Crystal:[5H₂²⁺ 2TFA⁻]-2TFA, b) Crystal:[5H₂²⁺ 4TFA⁻]-4TFA, c) Crystal:**5**, d) [5H₂²⁺ 4TFA⁻]-4TFA:**5**. Molecules in ball-and-stick representation and only molecules of **5** shown for clarity.

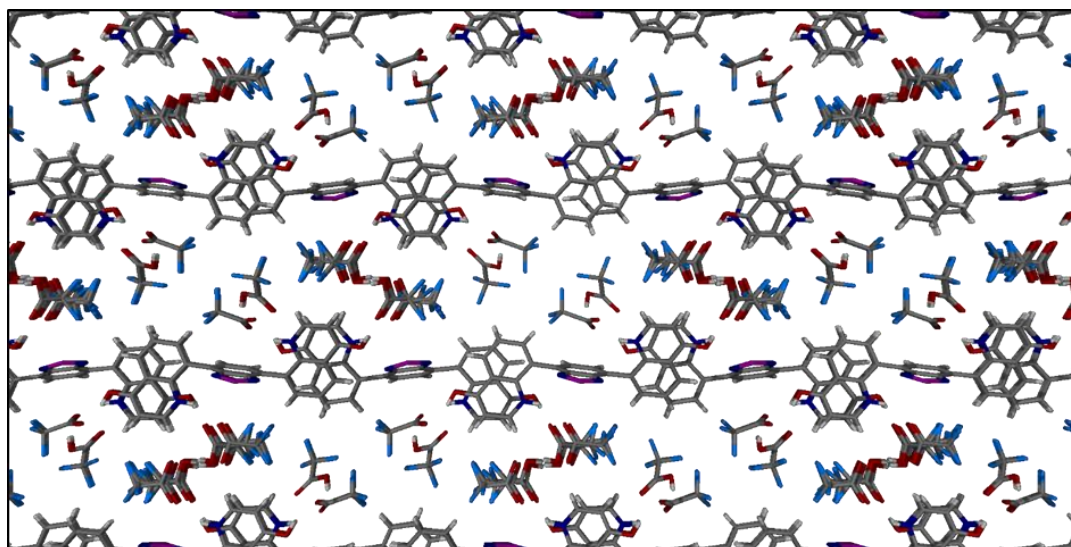


Figure S3. Crystal packing structure of $5H_2^{2+}$ with the molecules shown as capped stick representations and viewed down the a axis. Disorder of one of the hydrogen bonded CF_3COO^- CF_3COOH pairs shown. π - π stacking of **5** results in layers of **5** and layers of CF_3COO^- CF_3COOH . There is extensive hydrogen bonding between the O-H and N-H groups of **5** and the donors and acceptors of the CF_3COO^- and CF_3COOH .

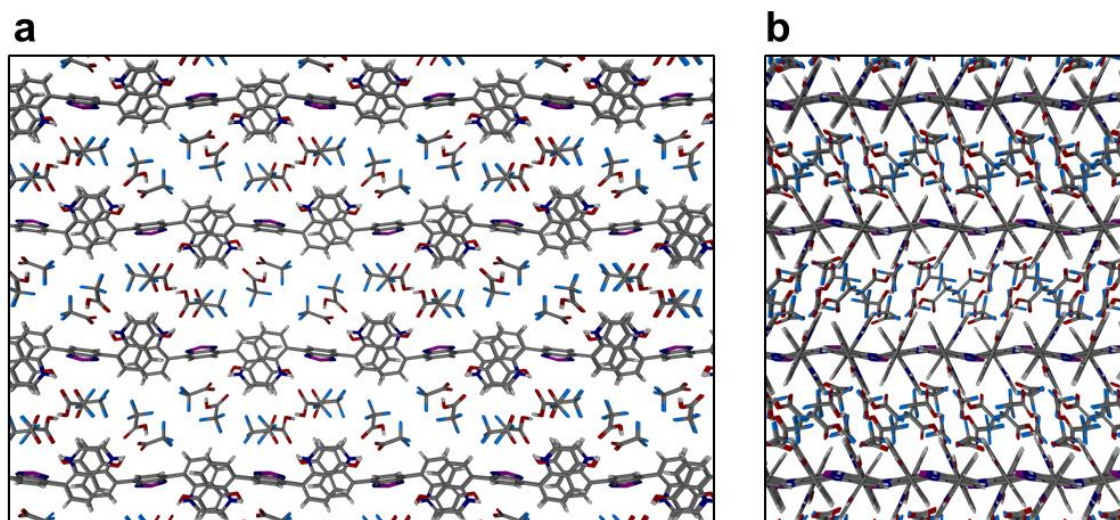


Figure S4. Crystal packing structure of $5H_2^{2+}$ with the molecules shown as capped stick representation. a) Structure as viewed down the a axis. b) Structure as viewed down the c axis. Disorder not shown for clarity.

2.8.3 Computational Data⁸

The geometries of the molecule **5** in neutral and protonated form were fully optimized at the DFT RB3LYP/6-311G(d,p) level of theory and analytical second derivatives were computed using vibrational analysis to confirm each stationary point to be a minimum by yielding zero imaginary frequencies. TD-DFT calculations were performed also at the RB3LYP/6-311G(d,p) level of theory to obtain the vertical excitation energies. All the above computations were performed using the Gaussian 03 suite of programs.⁷⁶

X-ray crystallography showed that molecule **5** exists in the solid state as the phenolic prototautomeric form **5''** cocrystallised with molecules of TFA that participate *via* various H-bonding interactions (Figure S5). In the absence of TFA or in the gas or solution phase the structure of compound **5** can differ. As two possible symmetrical prototautomers **5'** and **5''** exist, and one unsymmetrical, **5'''**, all were optimised at the RB3LYP/6-311G(d,p) level of theory in gas phase. The quinolone tautomer **5'** was computed to be 42.3 kJ·mol⁻¹ more stable than prototautomer **5''** and 14.6 kJ·mol⁻¹ more stable than **5'''**.

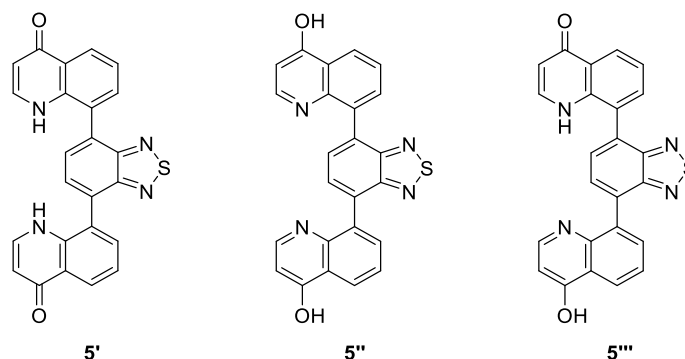


Figure S5. Structures of the three possible prototautomers of compound **5**.

TD-DFT calculations on the optimized structures of tautomers **5'**, **5''** and **5'''**, revealed a significant blue shift for the longest wavelength absorption of tautomer **5''** compared to **5'** and **5'''**, *ca.* 140 and 132 nm, respectively, with the absorption of the former being in best agreement with the experimental absorption spectra (Figure S6).

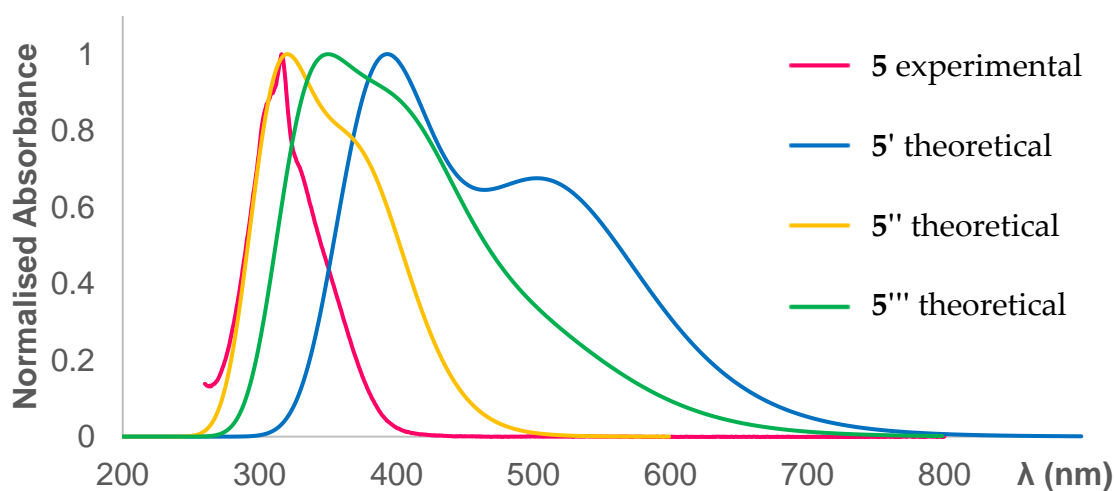


Figure S6. Comparison of the experimental absorption spectrum for compound **5** and the theoretical absorption spectra for the prototautomers **5'**, **5''** and **5'''**.

The main vertical excitations for molecule **5''** were calculated using TD-DFT at the B3LYP/6-311G(d,p) level of theory (Table S2), which indicated that the longest wavelength absorption corresponds to a HOMO \rightarrow LUMO transition; observed as a shoulder in the theoretical and the experimental spectrum, blue shifted in the latter by *ca.* 51 nm). The two other absorptions observed theoretically at 322 and 312 nm, have a main contribution from a HOMO-2 \rightarrow LUMO and a HOMO \rightarrow LUMO+1 transition, respectively.

Table S2. Singlet excited states for **5''** from TD-DFT data at the B3LYP/6-311G(d,p) level of theory

Excited state	transition (contribution)	energy (eV)	λ (nm)	osc. strength
S1	HOMO-2 \rightarrow LUMO (2%)	3.2951	376	0.1525
	HOMO \rightarrow LUMO (91%)			
S2	HOMO-1 \rightarrow LUMO (98%)	3.5507	349	0.0007
S3	HOMO-2 \rightarrow LUMO (84%)	3.8447	322	0.0955
	HOMO \rightarrow LUMO+1 (4%)			
S4	HOMO-2 \rightarrow LUMO (3%)	3.9741	312	0.1171
	HOMO-2 \rightarrow LUMO+1 (6%)			
	HOMO \rightarrow LUMO+1 (85%)			

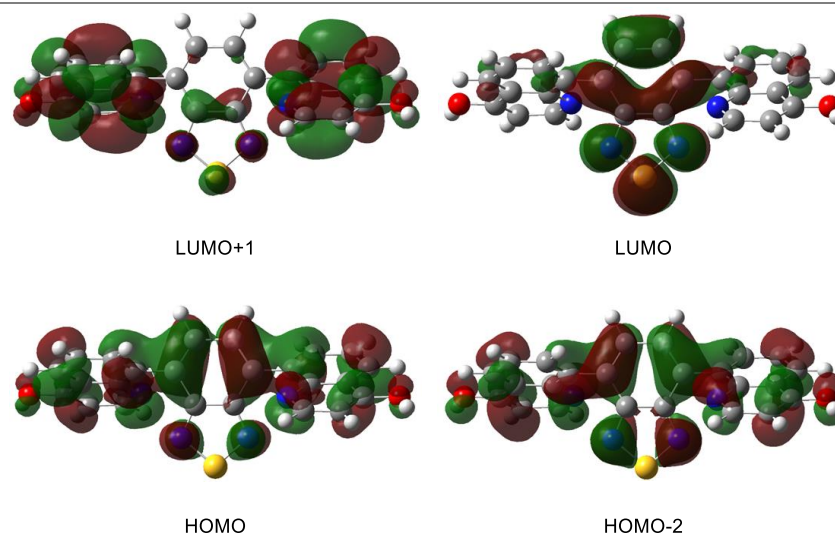


Figure S7. The molecular orbitals associated with the vertical excitations responsible for the absorption profile of tautomer **5''** revealed that the HOMO \rightarrow LUMO transition has significant charge transfer character from the quinolinol moieties to the benzothiadiazole core.

As supported by X-ray crystallography, in TFA we expect the quinolinols to be in the protonated form, and as such the dication in the presence and absence of coordinated TFA

molecules were studied computationally. In the absence of explicitly added TFA molecules in the cationic form the absorption is significantly red shifted owing to an intramolecular hydrogen bond between the NH of the protonated quinolinol and the nitrogen of the thiadiazole ring. This leads to increased planarity of the system, and, as such, the absorption was shifted to longer wavelengths presumably owing to greater conjugation (Figure S8).

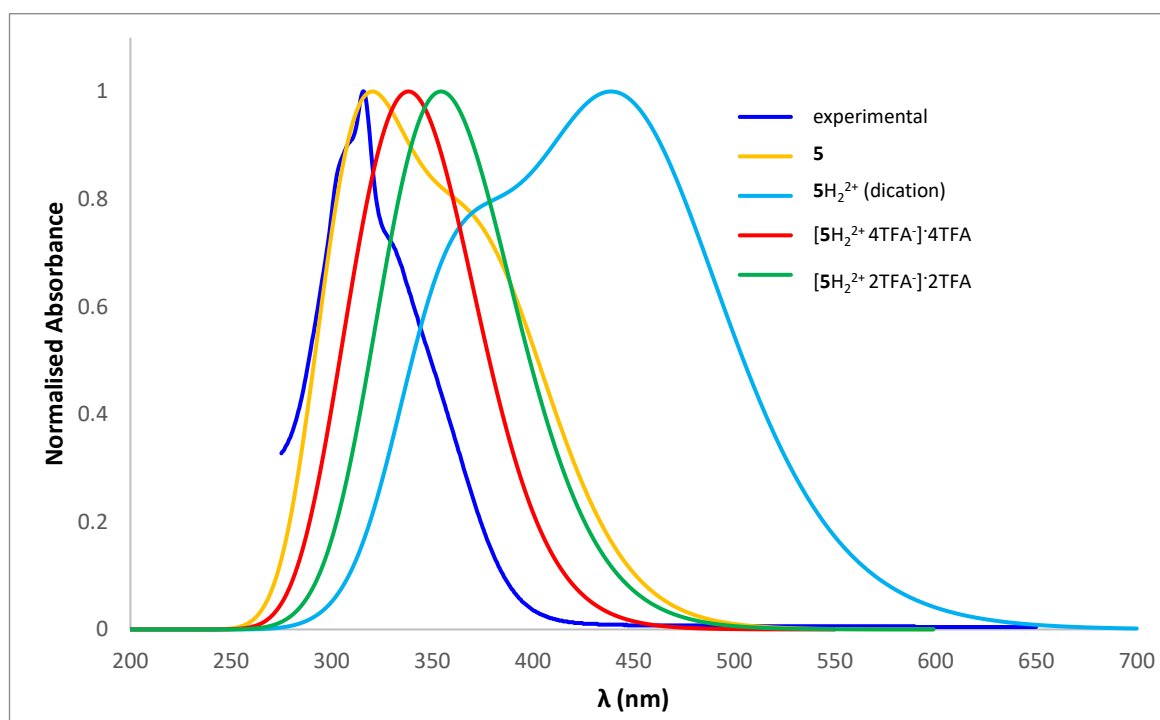


Figure S8. Comparison of the experimental absorption spectrum for compound **5** and the theoretical absorption spectra for the neutral and dication species of **5**.

The UV-vis absorption of the neutral molecule and the pyridinium form in the presence of coordinated anionic and neutral TFA molecules, however, is in good agreement with the experimental UV-vis absorption in TFA as solvent. The more TFA molecules incorporated into the calculation, the closer is the absorption to the experimental data in TFA.

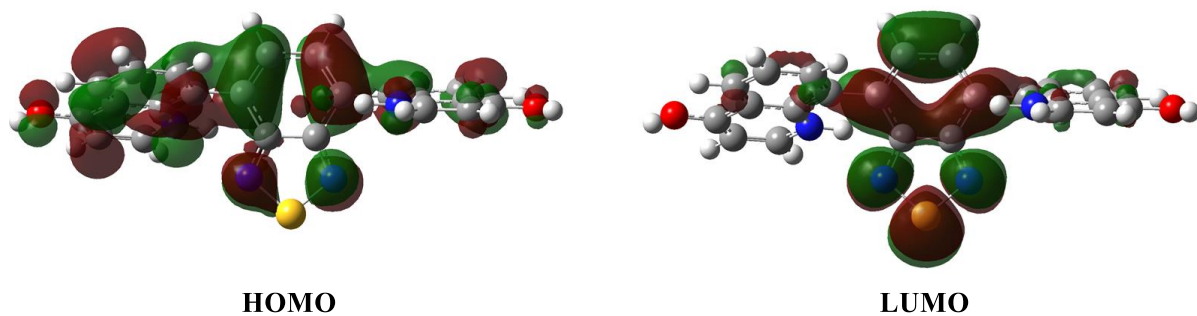


Figure S9. HOMO and LUMO representations of the optimized structure of molecule **5** in the presence of eight TFA molecules (4 neutral and 4 anions, total charge -2). TFA molecules are omitted for clarity.

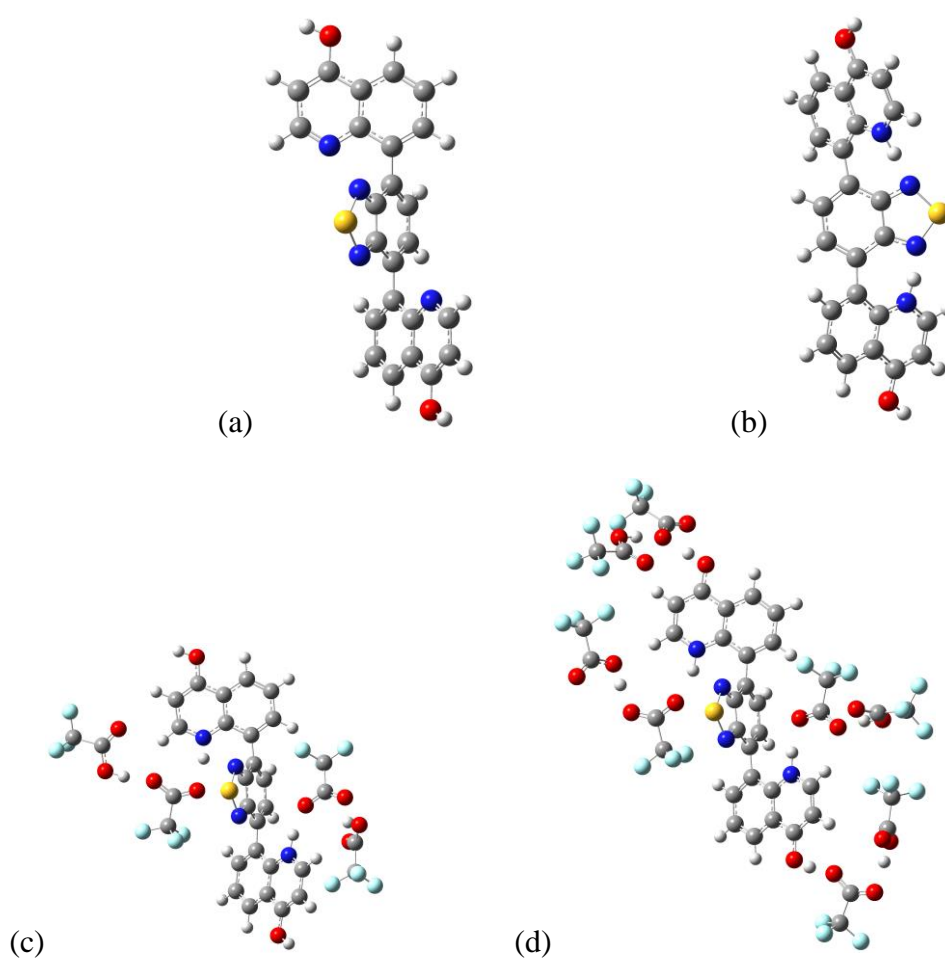


Figure S10. Optimized structures of molecule **5** in (a) neutral form; (b) pyridinium form without counterion; (c) pyridinium form with two trifluoroacetates and two TFA; (d) pyridinium form with four trifluoroacetates and four TFA molecules.

2.8.4 Additional Photophysical Data

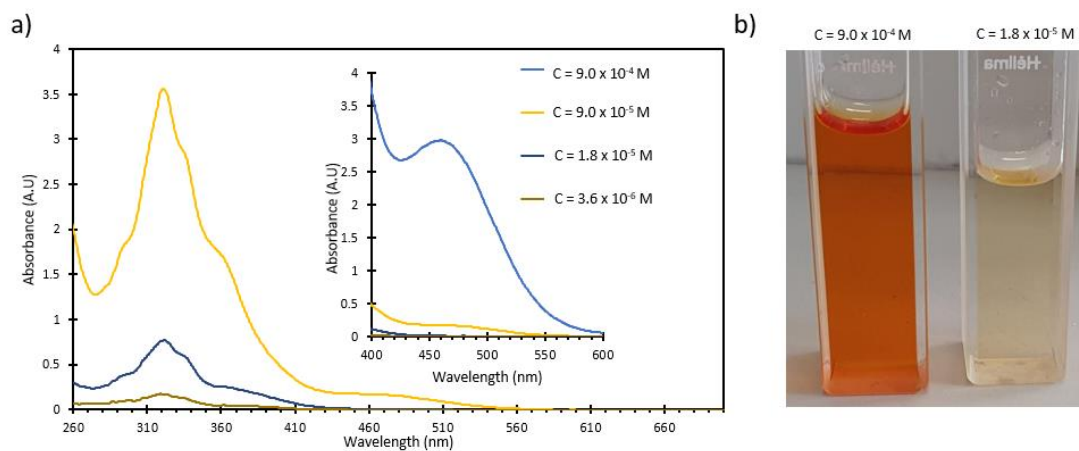


Figure S11. a) UV-Vis absorption spectra of 5H_2^{2+} dissolved in DMSO in various concentrations. Insert shows that a new peak appears at 460 nm consistent with excimer formation. b) Photograph of a concentrated (left) and dilute (right) solution of 5H_2^{2+} reveals a stark colour difference between the two. The deep orange colour on the left is caused by the appearance of the new absorption peak at 460 nm.

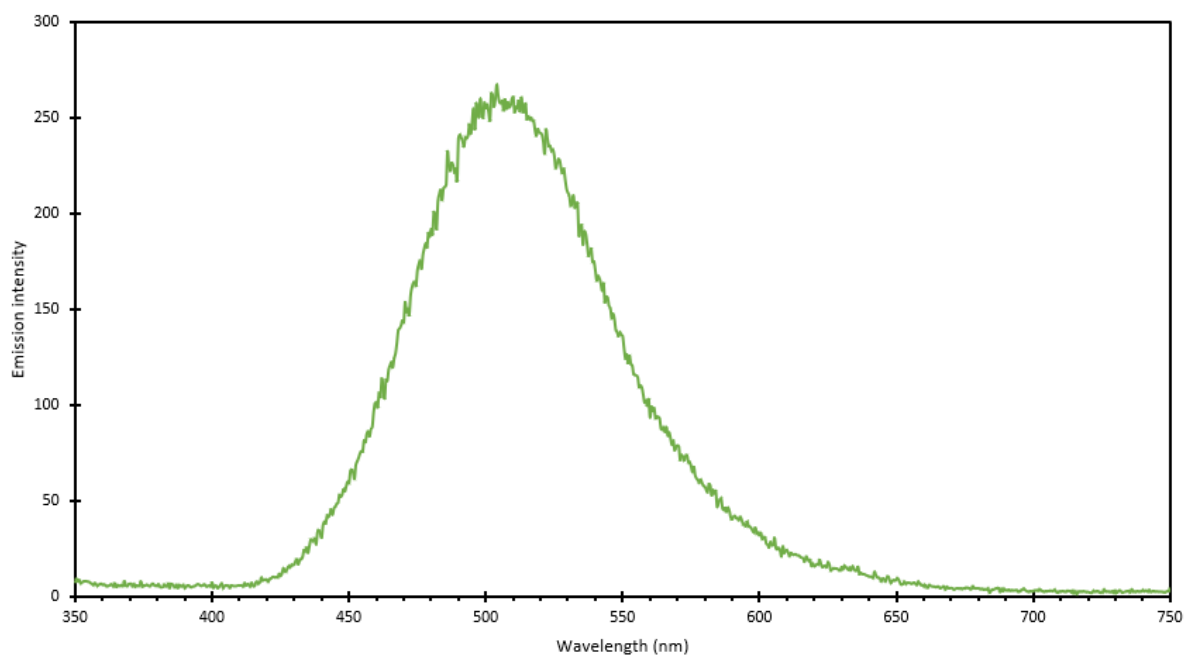


Figure S12. Solid state fluorescence of **5**. Maximum emission was recorded at $\lambda_{\text{em}} = 512 \text{ nm}$.

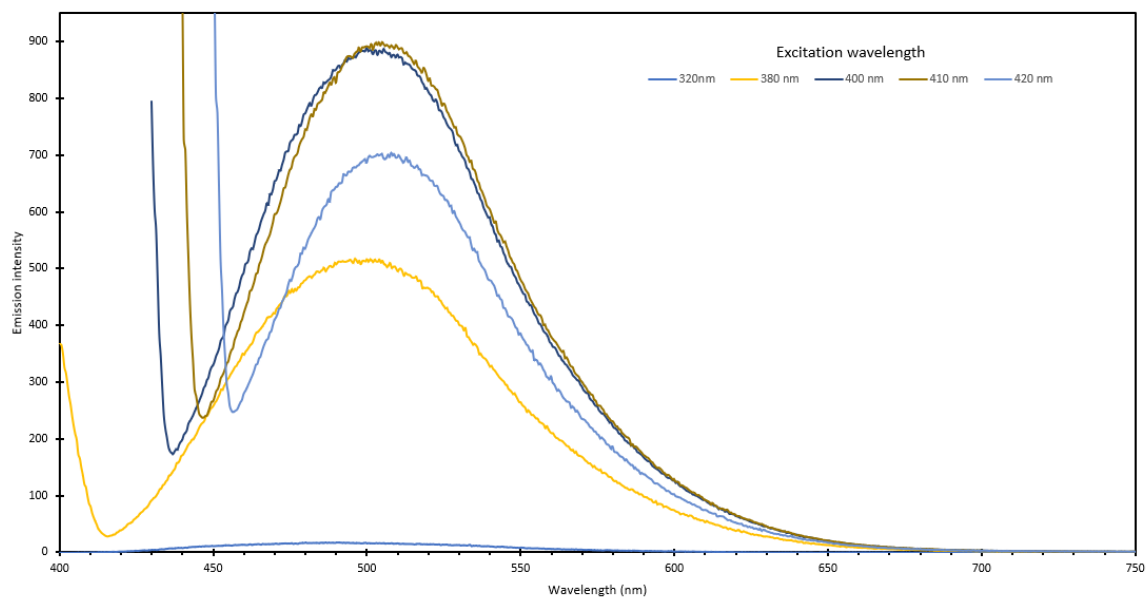


Figure S13. Fluorescence spectra of $5H_2^{2+}$ in DMSO with varying excitation wavelengths. Maximum emission intensity is observed when $\lambda_{ex} = 410$ nm.

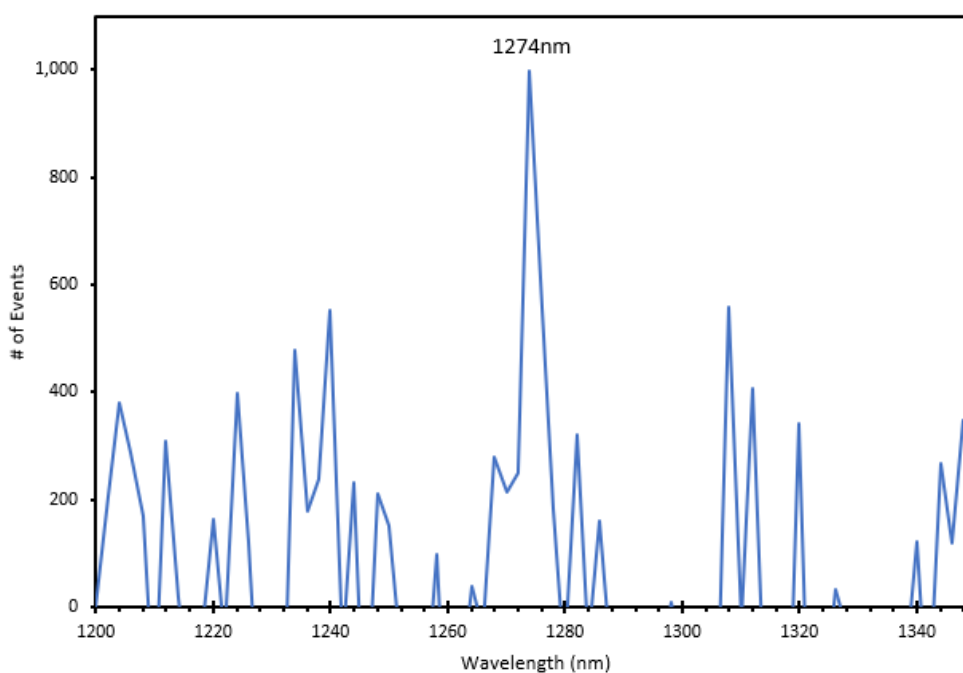


Figure S14. IR emission spectrum of $5H_2^{2+}$ in TFA/D₂O (1:1) solution shows a weak peak at 1274 nm which is attributed to 1O_2 phosphorescence.

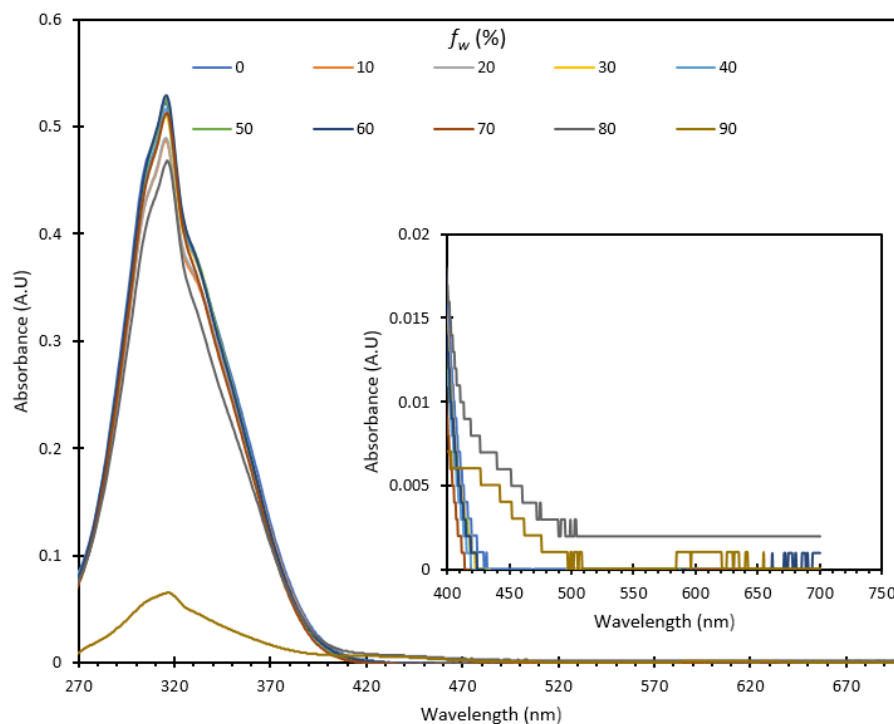


Figure S15. UV-Vis spectra corresponding to the TFA solution series. Insert highlights the tailing-off effect caused by the production of nanoaggregates. It can be seen that at 80% water, tailing occurs. At 90% the effect is not as pronounced, possibly due to sedimentation of the nanoaggregates.

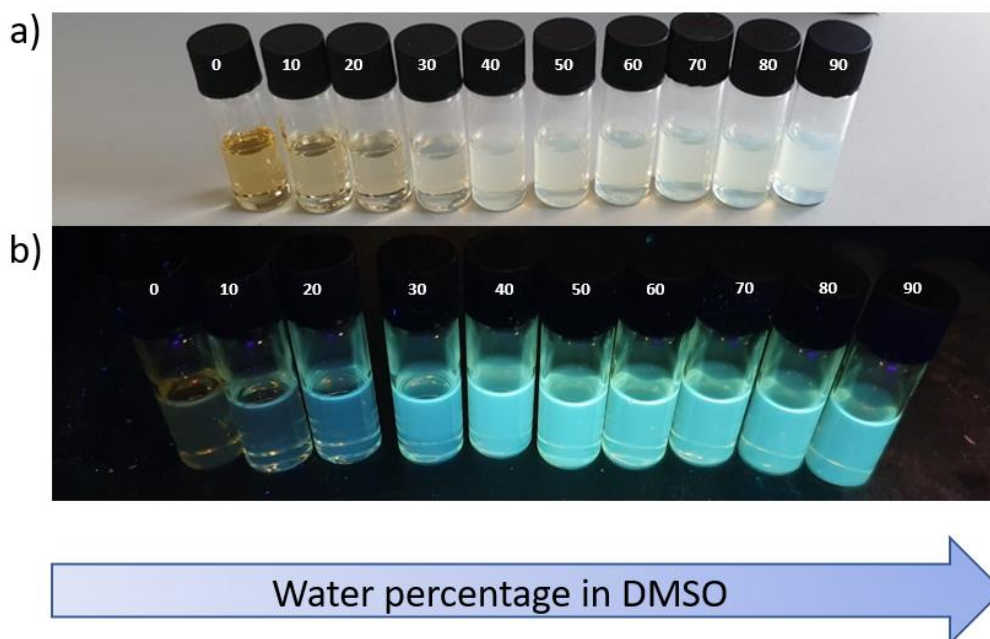


Figure S16. Picture of series in increasing water percentage compared to DMSO. Concentration was kept constant at 2.05×10^{-4} M. a) Illumination with visible light shows that visible cloudiness occurs when water reaches 20%. b) Illumination with far UV light shows the AIE effect in action; when $5H_2^{2+}$ is fully dissolved in DMSO (0% vial), no emission is visible, but as the water percentage increases, a green-blue emission appears, originating from the solid that is precipitating out of solution.

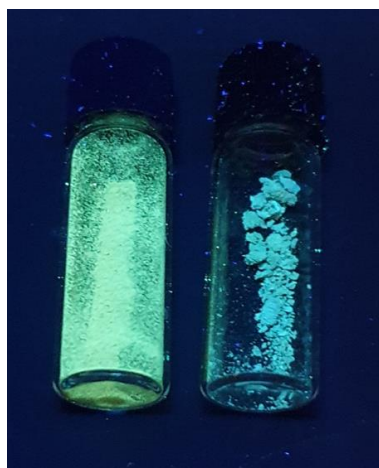


Figure S17. Left: Solid **5** under far UV illumination. $\lambda_{em} = 512$ nm. Right: Solid **5H₂²⁺** under far UV illumination. $\lambda_{em} = 485$ nm.

2.8.5 Continuous Flow Set-Up and Cycle Data

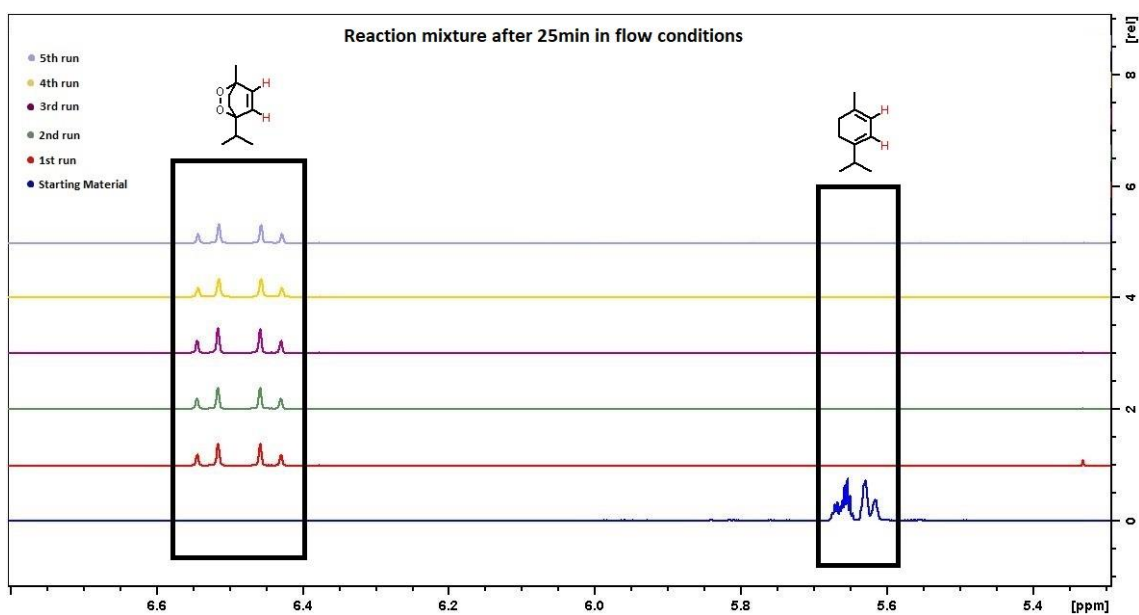
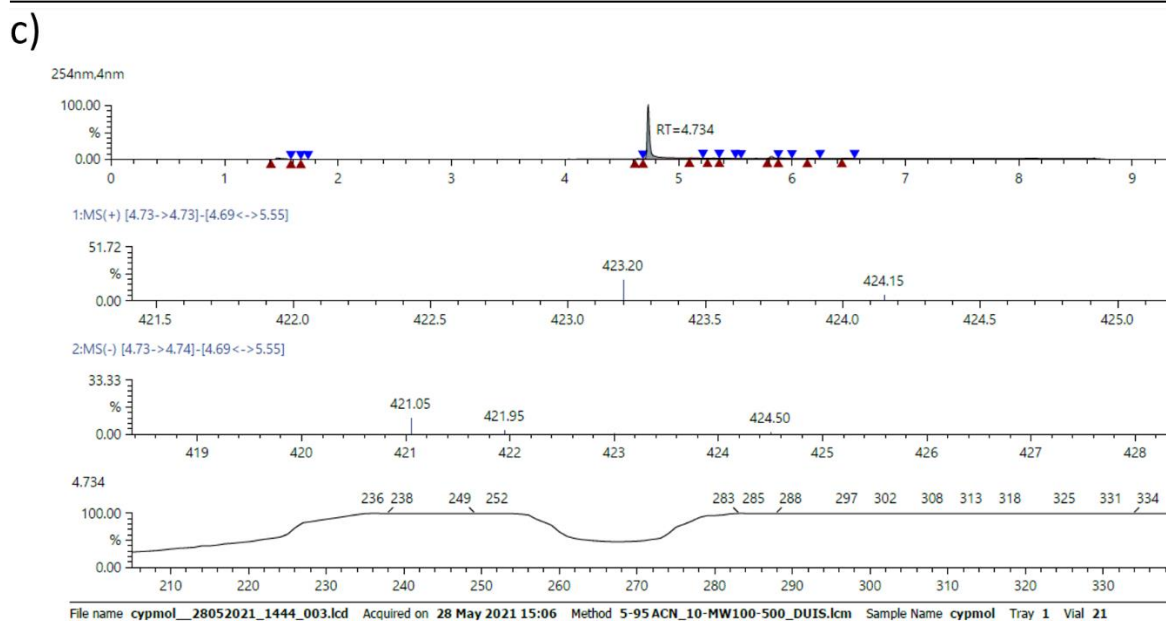
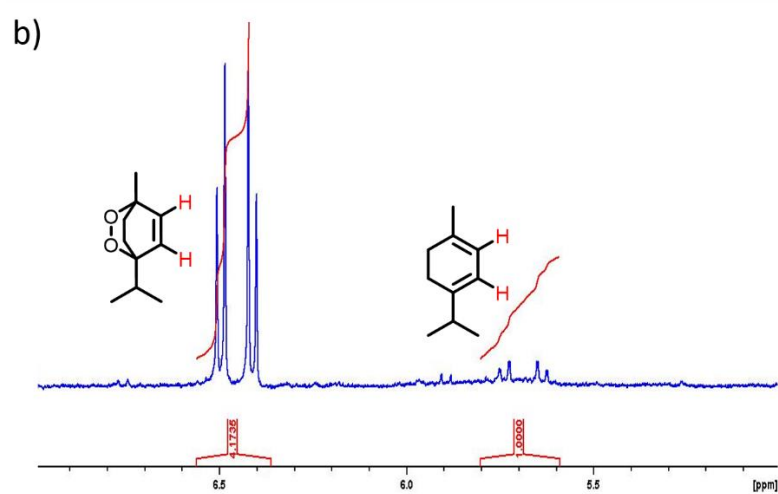
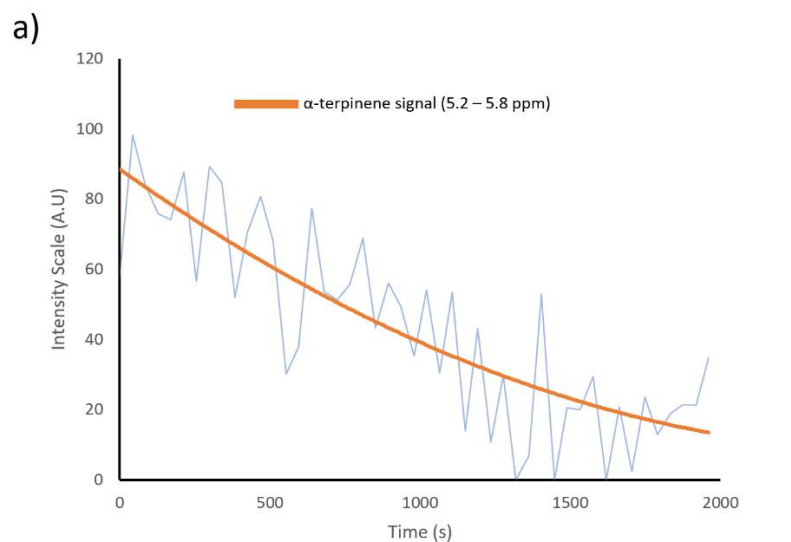


Figure S18. Stacked 300 MHz ¹H NMR spectra illustrating the conversion to ascaridole after each run. The conversion was monitored by the disappearance of the alkene protons of the α -terpinene starting material (5.6 – 5.7 ppm range) and the subsequent appearance of the alkene protons of the product (6.4 – 6.6 ppm range).



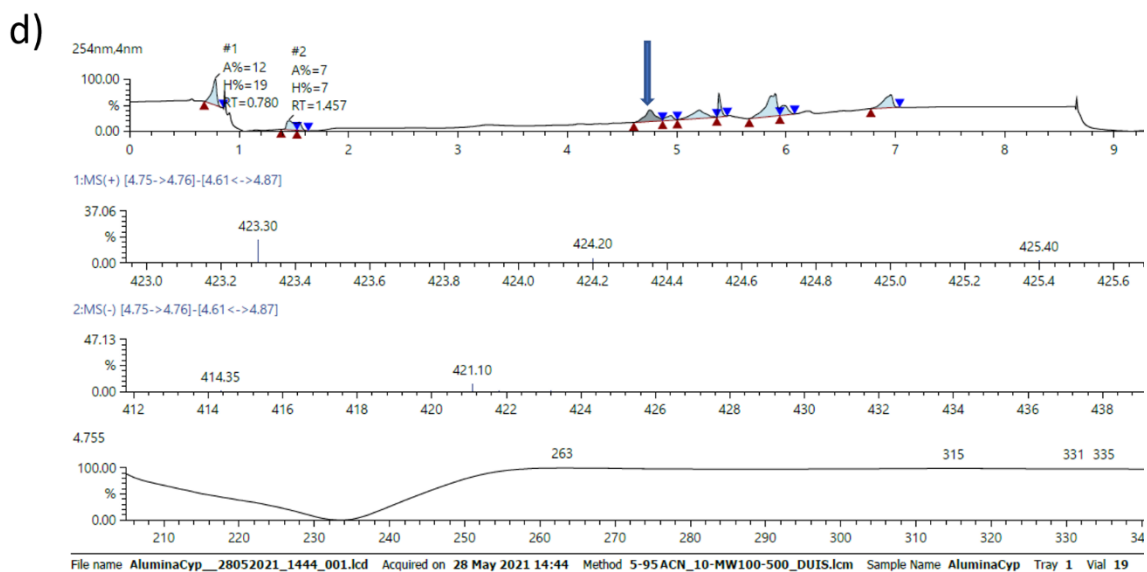
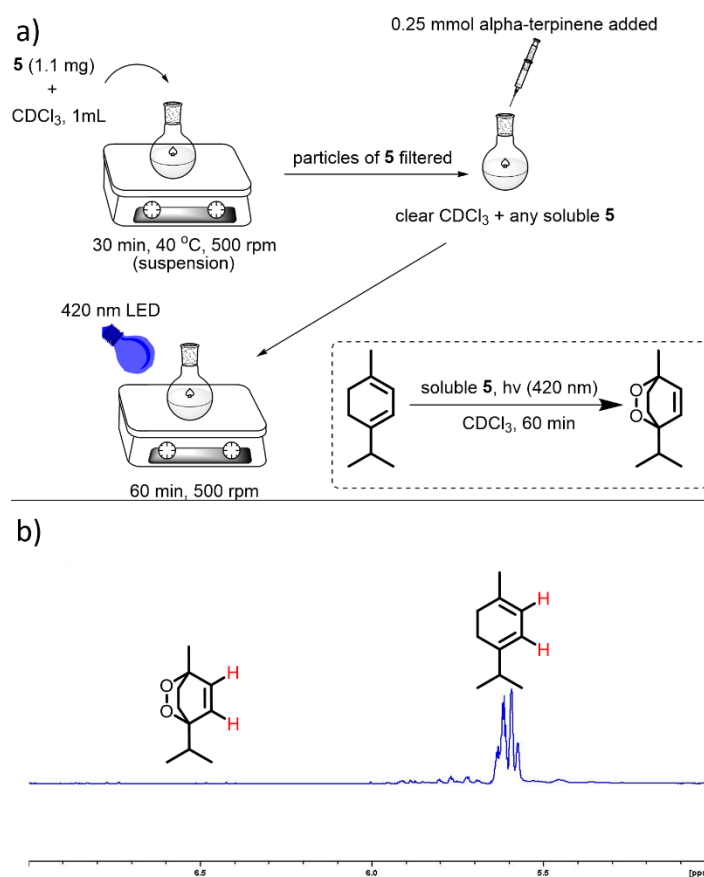


Figure S19. a) Photosensitisation of **5** (1 mol%) for $^1\text{O}_2$ production under flow conditions. The graph shows benchtop ^1H NMR monitoring of α -terpinene disappearance over time, when an alumina column support is used instead of silica. b) 400 MHz ^1H NMR spectrum of the reaction mixture after 2000 s shows 80.7% conversion to ascaridole. c) LC-MS trace of pristine **5** (sample was dissolved in DMSO and filtered prior to injection). Retention time (RT) was 4.734 min. d) LC-MS trace of alumina supported **5** reaction mixture after 2000 s of irradiation shows the presence of leached **5**. The sample was obtained by removing the reaction solvent under vacuum and dissolving the resulting residue in DMSO.



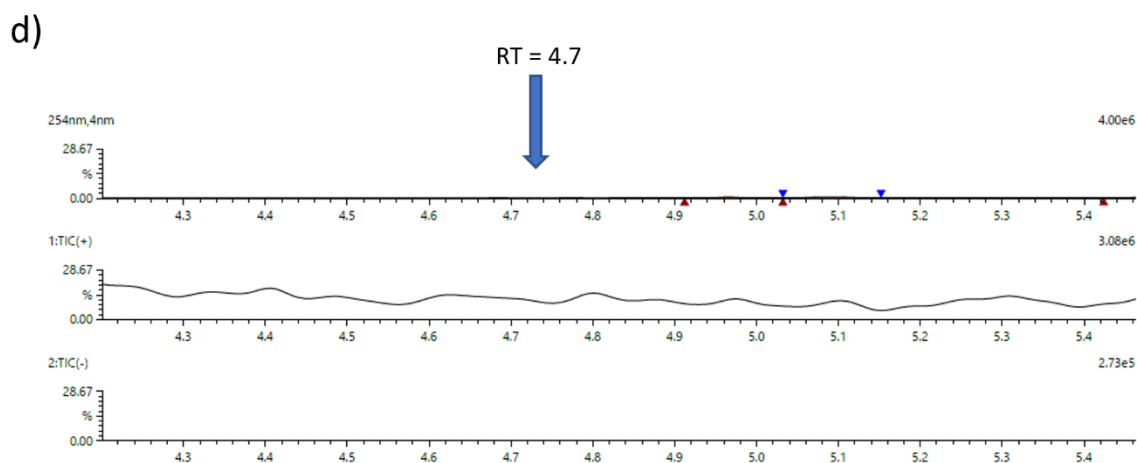
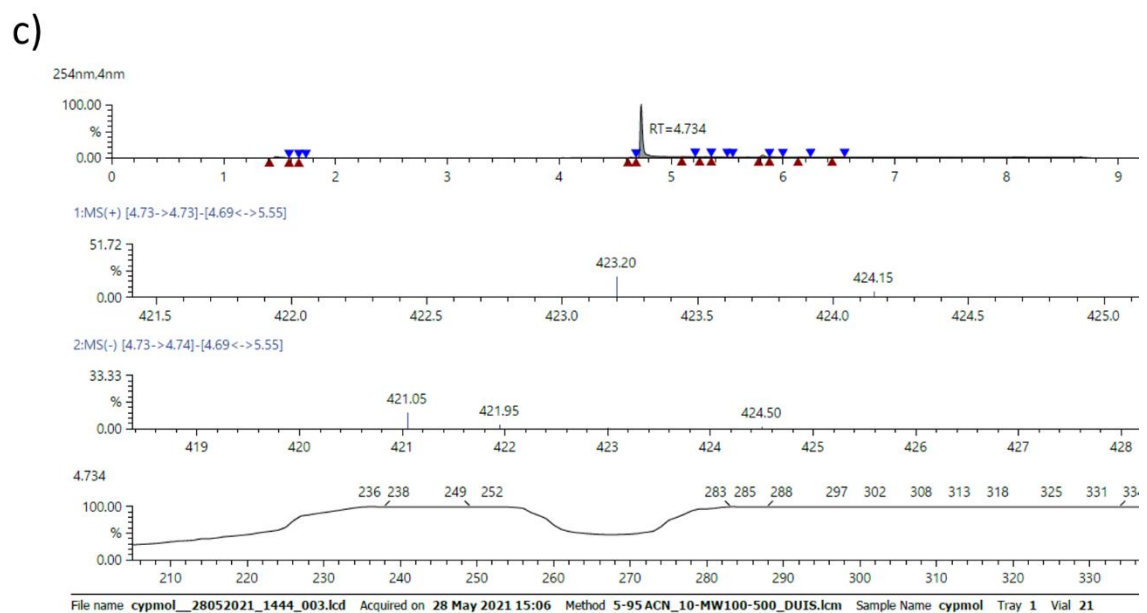


Figure S20. a) Schematic of procedure that was conducted to test whether trace quantities of soluble **5** can photocatalyse the production of ascaridole from α -terpinene. b) 300 MHz ^1H NMR spectrum of the reaction mixture after 60 min shows no conversion to ascaridole, confirming that the original flow reaction is indeed heterogeneously mediated. c) LC-MS trace of pristine **5** (sample was dissolved in DMSO and filtered prior to injection). Retention time (RT) was 4.734 min. d) LC-MS trace of filtered CDCl_3 solution that was stirred with solid **5** (a). No compound **5** was detected.

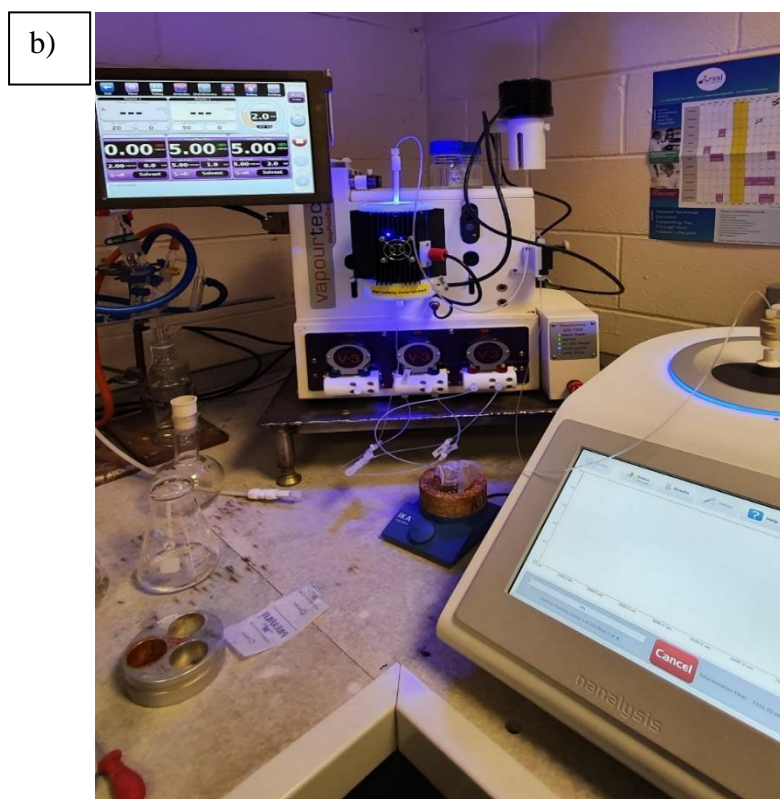
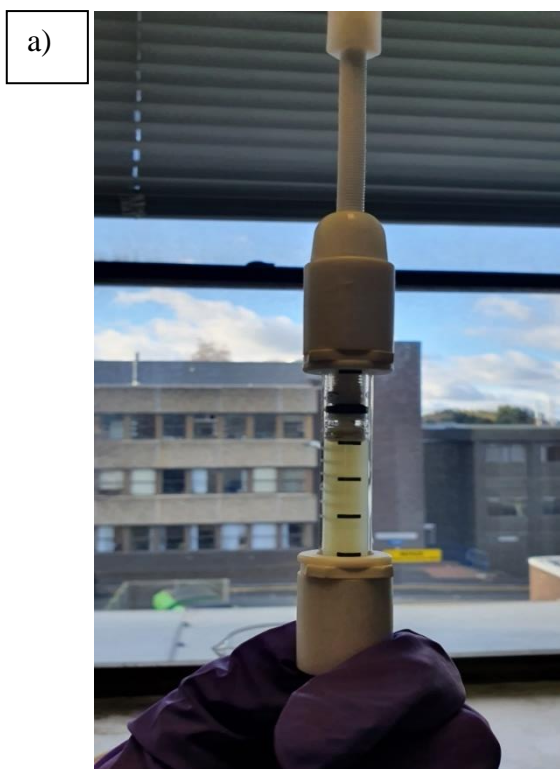


Figure S21. a) A loaded borosilicate glass column fixed bed reactor with silica and **5**. The column is primed with CDCl_3 . b) Picture depicting the flow reactor set-up that was used during the photosensitisation experiments.

2.8.6 X-Ray Powder Diffraction of 5

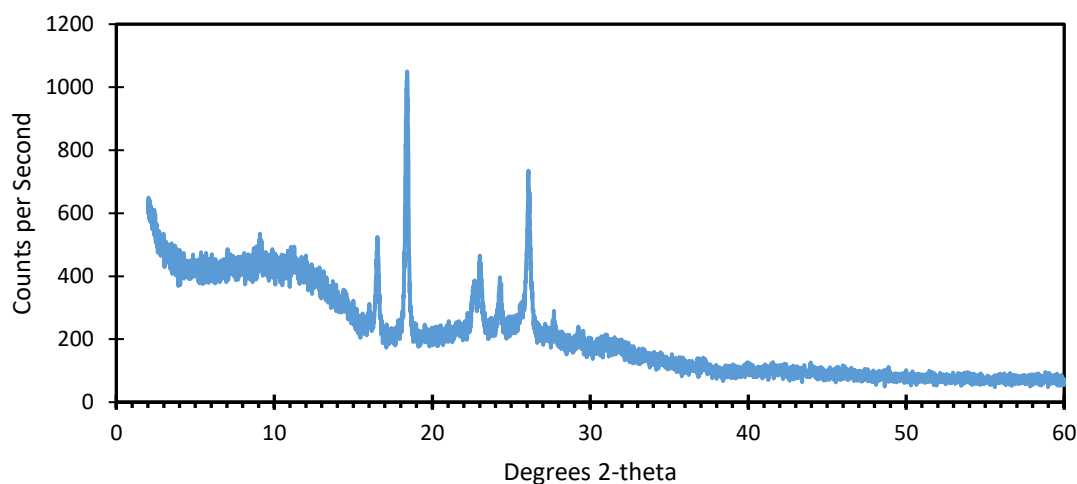


Figure S22. XRD diffractogram of compound **5** directly after its synthesis shows the presence of a semi-crystalline solid.

2.8.7 Solubility of 5 in Various Organic Solvents

Table S3. Solubility of **5** in various organic solvents

Entry	Solvent	Solvent Relative Polarity ⁷⁷	Solubility ^a
1	Water	1.000	Negligible
2	Trifluoroacetic acid	N/A	Soluble
3	Methanol	0.762	Negligible
4	Acetonitrile	0.460	Negligible
5	Dimethylsulfoxide	0.444	Partially soluble
6	Acetone	0.355	Negligible
7	Methylene Chloride	0.309	Negligible

Entry	Solvent	Solvent Relative Polarity ⁷⁶	Solubility ^a
8	Chloroform	0.259	Negligible
9	Ethyl Acetate	0.228	Negligible
10	Tetrahydrofuran	0.207	Negligible
11	Diethyl Ether	0.117	Negligible
12	Toluene	0.099	Negligible
13	n-Hexane	0.009	Negligible

^a As determined by HPLC analysis of a filtered solution resulting from stirring 1.1 mg of **5** in 1 mL of solvent.

2.8.8 ¹O₂ Generation Efficiencies of **5** and **5H₂²⁺** Under Identical Conditions

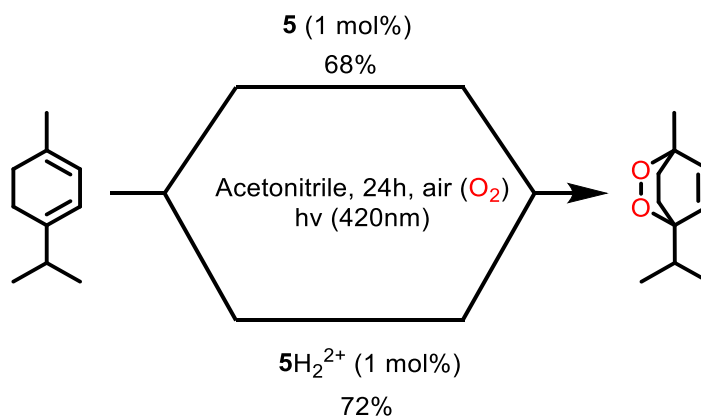


Figure S23. α -terpinene (0.25 mmol) conversion to ascaridole under batch conditions. Photosensitisers **5** and **5H₂²⁺** exhibited similar performance under identical conditions.

2.8.9 Aerobic Oxidative Hydroxylation of Phenylboronic Acid (HPLC Data)

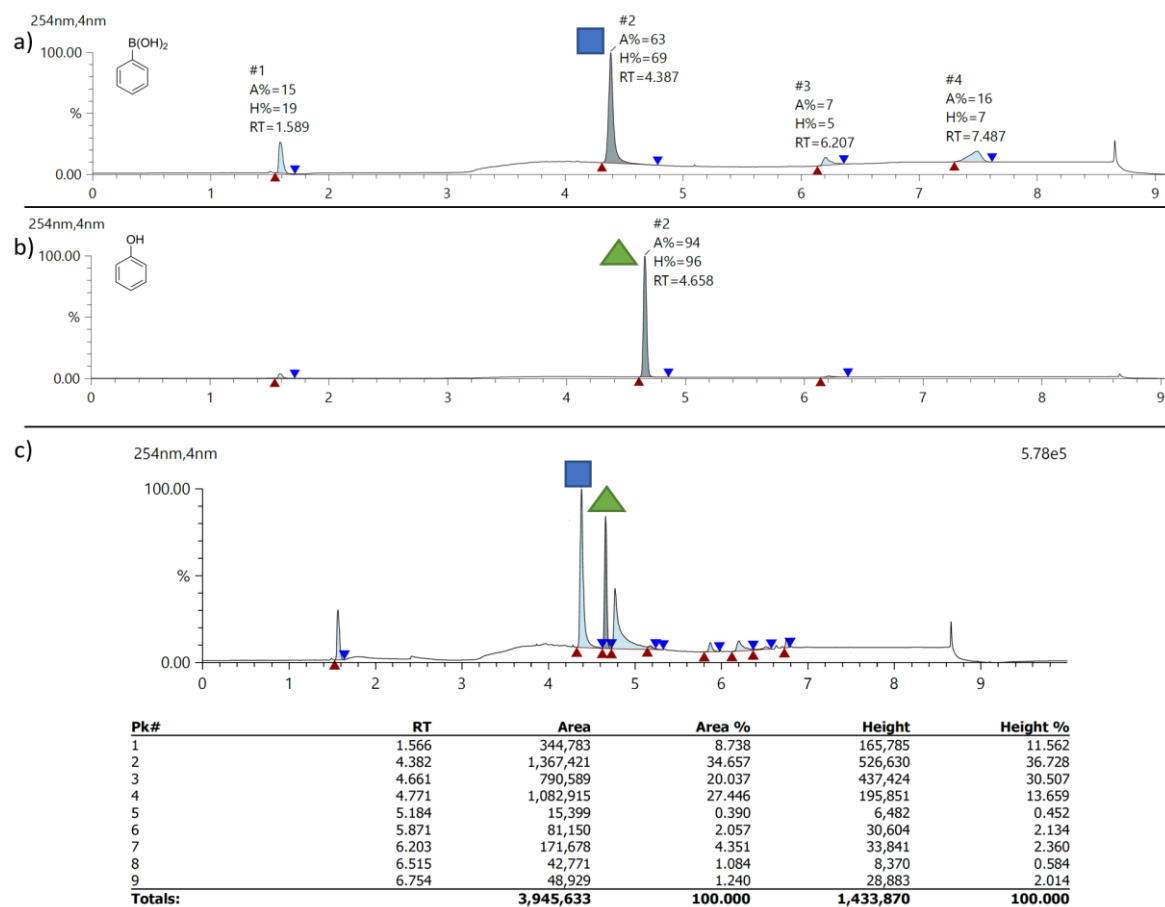


Figure S24. HPLC chromatograms of a) Neat phenylboronic acid. b) Neat phenol. c) Reaction mixture when **5** was used as a photoredox catalyst for the hydroxylation of phenylboronic acid to phenol.

2.9 Experimental Section

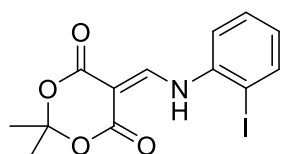
2.9.1 General Methods and Materials

All chemicals were commercially available except those whose syntheses are herein described. Anhydrous MgSO₄ was used for drying organic extracts and all volatiles were removed under reduced pressure. All reaction mixtures and column eluents were monitored by TLC using commercial aluminium backed thin layer chromatography (TLC) plates (Merck Kieselgel 60 F₂₅₄). The plates were observed under UV light at 254 and 365 nm. The technique of flash chromatography was used throughout for all non-TLC scale chromatographic separations using Merck Silica Gel 60 (less than 0.063 mm). Melting points were determined using a Stuart SMP10 digital melting point apparatus. Small scale (μ L) liquid handling measurements were made using variable volume (1.00–5000.00 μ L) single channel Gilson PIPETMAN precision micropipettes. Solvents used for recrystallisation are indicated after the melting point. IR spectra were recorded on a Thermo Scientific Nicolet iS5 FTIR spectrometer with iD5 ATR accessory and broad, strong, medium and weak peaks are represented by b, s, m and w, respectively. ¹H and ¹³C NMR spectra were recorded on a Bruker AVANCE III HD machine (at 400 and 100 MHz, respectively). An AVANCE III 300 MHz NMR Spectrometer was also used for reaction monitoring. The benchtop NMR that was used for flow reaction monitoring was a NANALYSIS corp. NMRReady 60 Benchtop ¹H NMR. Chemical shifts (δ) are expressed in ppm and coupling constants *J* are given in Hz. Data are represented as follows: chemical shift, multiplicity (s = singlet, d = doublet, t = triplet, q = quartet, m = multiplet and/or multiple resonances, br s = broad singlet). Deuterated solvents were used for homonuclear lock, and the signals are referenced to the deuterated solvent peaks. For the acquisition of mass spectra, the samples were prepared as detailed below and analysed by positive ion nanoelectrospray (nES) using a Thermo Scientific™ LTQ Orbitrap XL™ ETD Hybrid Ion Trap-Orbitrap Mass Spectrometer. The absolute PLQY of each sample was measured using a calibrated spectrofluorometer (Edinburgh Instruments, FLS920), equipped with an integrating sphere (Jobin-Yvon). Flow reactions were carried out with a commercial E-series Photochem reactor by Vapourtec Ltd, with two V-3 peristaltic pumps and using an LED module emitting at 390-440 nm with 7.44 W light output

(EPILED, Future Eden Ltd.). For the collection of LC-MS data a Shimadzu LC-2040C 3D Plus instrument was used.

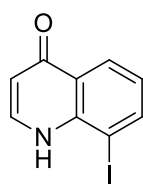
2.9.2 Preparation of Compounds **1**, **2**, **5** and **5H₂²⁺**

Preparation of 5-[[2-Iodophenyl]amino]methylene]-2,2-dimethyl-1,3-dioxane-4,6-dione **1**



To a stirred solution of 2-iodoaniline (3.00 g, 13.6 mmol), in anhydrous acetonitrile (50 mL) at *ca.* 20 °C was added in one portion Meldrum's acid (2.15 g, 15.0 mmol), followed by triethyl orthoformate (2.41 g, 16.3 mmol). The resulting mixture was then heated to *ca.* 95 °C (reflux) for 2 h until the 2-iodoaniline was consumed (by TLC). The resulting mixture was then allowed to cool to *ca.* 20 °C, evaporated to dryness under vacuum, and the residue recrystallised by hot ethanol (EtOH) to afford the title compound **1** (4.01 g, 78%) as orange cubes, mp (hot-stage) 177-178 °C (EtOH) [literature value: 176.1-177.9 °C (EtOH)]⁸; *R_f* 0.44 (*n*-hexane/EtOAc, 60:40); $\nu_{\max}/\text{cm}^{-1}$ 3163w (aryl C-H), 2995w (alkyl C-H), 1726m and 1680s (C=O), 1601w, 1582m, 1568m, 1493w, 1433w, 1389m, 1377m, 1319s, 1300m, 1269s, 1227w, 1200s, 1144w, 1119w, 1016m, 993w, 984m, 930m, 889w, 845w, 806m, 779m, 746s, 723m; δ_{H} (400 MHz, DMSO-*d*₆) 11.37 (1H, d, *J* = 14.0 Hz, NH), 8.65 (1H, d, *J* = 14.0 Hz, =CH), 7.93 (1H, dd, *J* = 7.6 Hz, 1.2 Hz, Ar *H*), 7.73 (1H, dd, *J* = 8.0 Hz, 0.8 Hz, Ar *H*), 7.46-7.50 (1H, m, Ar *H*), 7.05 (1H, ddd, *J* = 7.8 Hz, 7.8 Hz, 1.6 Hz, Ar *H*), 1.69 (6H, s, CH₃); δ_{C} (100 MHz, DMSO-*d*₆) 164.6, 162.3, 153.5, 139.6, 139.2, 129.9, 128.0, 118.6, 104.6, 90.7 87.7, 26.6; identical to an authentic sample.⁸

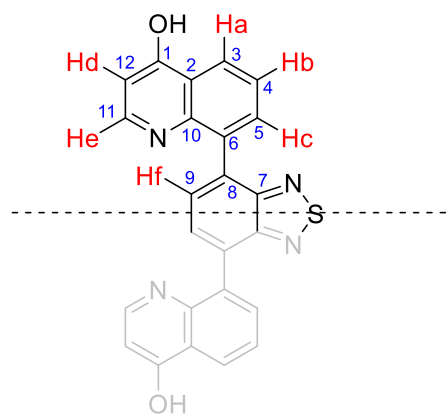
Preparation of 8-Iodoquinolin-4(1*H*)-one **2**



To stirred diphenyl ether (5 mL) preheated to *ca.* 220 °C (Wood's metal bath), was added portion wise over a 4 min period 5-[[2-iodophenyl]amino]methylene]-2,2-dimethyl-1,3-dioxane-4,6-dione **1** (1.00 g, 2.7 mmol) and the mixture was heated at *ca.* 220 °C for another 5 min until the starting material was consumed (by TLC). The resulting mixture was then

allowed to cool to *ca.* 20 °C, diluted (*n*-hexane, 15 mL) and the insoluble precipitate was isolated by filtration and recrystallised by hot toluene (PhMe) to afford the title compound **2** (679 mg, 93%) as beige-coloured cubes, mp (hot-stage) 76-77 °C (PhMe) [literature value: 75.3-76.3 °C (PhMe)]⁸; R_f 0.41 (THF/EtOAc, 50:50); $\nu_{\max}/\text{cm}^{-1}$ 3090 brw (N-H), 1618s (C=O), 1585s, 1543s, 1504s, 1431m, 1325m, 1300w, 1240m, 1215w, 1188s, 1099w, 1074w, 1051m, 889w, 866w, 835w, 793s, 775m, 746s; δ_H (400 MHz, DMSO- d_6) 10.72 (1H, br s, NH), 8.18 (1H, dd, $J = 7.6$ Hz, 1.2 Hz, Ar H), 8.11 (1H, dd, $J = 8.0$ Hz, 1.2 Hz, Ar H), 7.88 (1H, d, $J = 6.8$ Hz, Ar H) 7.11 (1H, dd, $J = 8.0$ Hz, 8.0 Hz, Ar H), 6.13 (1H, d, $J = 6.0$ Hz, Ar H); δ_C (100 MHz, DMSO- d_6) 176.7, 142.2, 140.7, 140.4, 126.6, 125.6, 124.7, 109.0, 87.4; identical to an authentic sample.⁸

Preparation of 8,8'-(Benzo[*c*][1,2,5]thiadiazole-4,7-diyl)bis(quinolin-4-ol) **5**

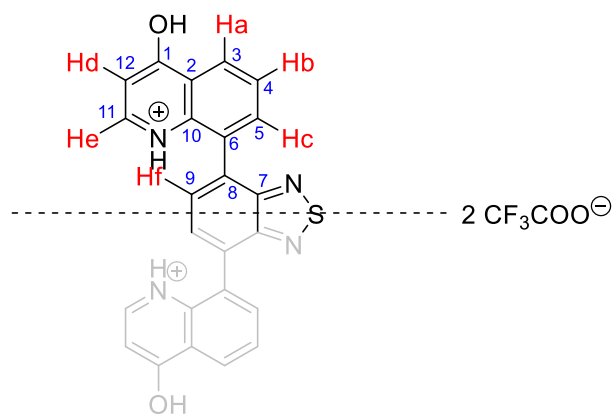


To a stirred solution of 8-iodoquinolin-4(1*H*)-one **2** (100.0 mg, 0.368 mmol) in dioxane/H₂O (75:25) (1 mL) at *ca.* 20 °C was added in sequence powdered K₂CO₃ (101.6 mg, 0.720 mmol), followed by 4,7-bis(4,4,5,5-tetramethyl-1,3,2-dioxaborolan-2-yl)benzo[*c*][1,2,5]thiadiazole **4** (71.4 mg, 0.184 mmol), and then Pd(dppf)Cl₂·CH₂Cl₂ (15.0 mg, 5 mol %). The reaction mixture was then immersed

into a preheated oil bath and heated at *ca.* 89 °C (reflux) for 5 min until the iodoquinolinone **2** was consumed (by TLC, THF/EtOAc, 50:50). The reaction mixture was then allowed to cool to *ca.* 20 °C leading to the formation of a powdery yellow precipitate, which was isolated by filtration, washed thoroughly using THF (2 × 5 mL), CHCl₃ (2 × 5 mL) and EtOH (2 × 5 mL), and then dried under a stream of air, to afford the title compound **5** (75.2 mg, 97%) as a fine yellow powder, mp (TGA) > 400 °C (decomp.); $\lambda_{\max}(\text{DMSO})/\text{nm}$ 306 inf (log ϵ 3.42), 317 (3.48), 325 (3.35); $\nu_{\max}/\text{cm}^{-1}$ 3166brw (C-H), 1619s, 1617s, 1567s, 1506s, 1433m, 1403w, 1335m, 1310w, 1284w, 1247w, 1191s, 1146w, 1122m, 1066m, 979w, 975m, 901w, 880m, 860w, 849m, 810m, 795m, 756s; δ_H (400 MHz, DMSO- d_6) 8.28 (2H, dd, $J = 8.0$ Hz, 1.2 Hz, Ar H_a), 7.94 (2H, s, Ar H_f), 7.75 (2H, dd, $J = 7.2$ Hz, 1.2 Hz, Ar H_e), 7.65 (2H, d, $J = 7.2$ Hz, Ar H_c), 7.47

(2H, dd, $J = 7.6$ Hz, 7.6 Hz, Ar H_b), 6.07 (2H, d, $J = 7.2$ Hz, Ar H_d); m/z (ESI+): calculated for $[M+H]^+$ 423.0910, found 423.0905.

Preparation of $5H_2^{2+}$ from **5**



To a 5 mL glass vial was added compound **5** (20.0 mg, 0.047 mmol) in 1 mL of TFA. The reaction mixture was then allowed to stir at *ca.* 20 °C for 10 minutes at which point all the solid was dissolved. The contents of the vial were then transferred into a 50 mL conical flask containing 10 mL of

distilled water, leading to the formation of a powdery dark yellow precipitate, which was isolated by filtration, washed thoroughly using cold distilled water (2×5 mL) and acetone (2×5 mL), and then dried under a stream of air, to afford the title compound $5H_2^{2+}$ (25.0 mg, 82%) as a fine yellow powder. Crystals of $5H_2^{2+}$ were grown by dissolving a small amount (~ 5 mg) in a 1:1 mixture (1 mL) of hot chlorobenzene (PhCl) and TFA. Mp (TGA) > 400 °C (decomp.) (TFA/PhCl); found: C, 51.30; H, 2.42; N, 8.43. $C_{28}H_{16}F_6N_4O_6S$ requires: C, 51.70; H, 2.48; N, 8.61%; λ_{max} (TFA)/nm 306 inf (log ϵ 3.42), 317 (3.48), 325 (3.35); ν_{max}/cm^{-1} 3166brw (C-H), 1619s, 1617s, 1567s, 1506s, 1433m, 1403w, 1335m, 1310w, 1284w, 1247w, 1191s, 1146w, 1122m, 1066m, 979w, 975m, 901w, 880m, 860w, 849m, 810m, 795m, 756s; δ_H (400 MHz, TFA- d) 8.73 (2H, dd, $J = 8.4$ Hz, 1.2 Hz, Ar H_a), 8.57 (2H, d, $J = 6.8$ Hz, Ar H_e), 8.25 (2H, dd, $J = 7.2$ Hz, 1.2 Hz, Ar H_c) 8.15 (2H, s, Ar H_f), 7.04 (2H, dd, $J = 7.2$ Hz, 1.2 Hz, Ar H_b), 7.39 (2H, d, $J = 6.8$ Hz, Ar H_d); δ_C (100 MHz, TFA- d) 172.8 (1), 155.6 (7), 146.7 (11), 140.0 (10), 139.3 (6), 134.8 (9), 131.3 (8), 130.8 (4), 129.7 (5), 127.4 (3), 123.0 (2), 107.7 (12); δ_F (376 MHz, DMSO- d_6) -74.49.; m/z (ESI-): calculated for $[M-TFA-H]^-$ 535.0693, found 535.0665.

2.9.3 Heterogeneous Flow Mediated Photocatalytic Generation of $^1\text{O}_2$ With In-Line NMR Analysis

The procedure for the heterogeneous flow photosensitisation of **5** to produce $^1\text{O}_2$ was adapted from Thomson *et al.*,⁴⁴ and was carried out as follows:

To a transparent borosilicate glass column fixed bed reactor (6.6 mm ID, 100 mm length) was added a mixture of photocatalyst **5** (1.1 mg, 0.0025 mmol, 1 mol%) and 500 mg chromatography grade (60Å, 40 – 63 µm particle size) SiO_2 . The dry-packed mixture was then attached to the Vapourtec flow instrument, and it was primed with CDCl_3 (10 mL) for 5 min by flowing solvent through the column at 5 mL/min. To a dry 20 mL round bottom flask loaded with a magnetic stirrer bar, was added α -terpinene (34.1 mg, 40.1 µL, 0.25 mmol) and CDCl_3 (5 mL) before sealing with a septum. The flask was connected to the Vapourtec flow machine and then covered to prevent photosensitisation events from ambient light. The reaction solution was pumped at 5 mL/min using peristaltic pumps (Vapourtec V-3) to a T-junction where it was mixed with O_2 gas from a cylinder which was being pumped concurrently at 5 mL/min by a second peristaltic pump. The heterogeneous liquid-gas mixture formed a slug flow at the T-junction and was pumped through the fixed bed column reactor placed in a reflective housing, irradiated by an LED array (390 - 440 nm, 7.44 W). After exiting the photoreactor, the slug flow was then passed through a back pressure regulator which kept the pressure at 2 bar before passing through a 60 MHz Nanalysis-60e benchtop ^1H NMR instrument which monitored the reaction progression in real time. Following that, the slug flow was returned to the initial reaction flask to be continuously cycled for 25 min. The catalyst bed was permitted to form a ‘mixed bed’ regime (hybrid between a packed bed and fluidised bed) to prevent pressure build up.

After the reaction was complete, as indicated by the bench-top NMR, the resulting solution was evaporated under reduced pressure to afford an oily residue. ^1H NMR (300 MHz) analysis of the residue revealed the complete disappearance of the α -terpinene alkene protons (δ_{H} 5.6–5.7 ppm) and the appearance of the corresponding ascaridole alkene protons (δ_{H} 6.4–6.6 ppm), confirming the bench-top NMR data and the complete transformation of the starting material.

For the cycling experiments, the loaded packed bed reactor was left in place, 15 mL of fresh CDCl_3 was flowed through the aforementioned set-up and it was then discarded. A new cycle could then be initiated by following the protocol above.

Safety statement for flow chemistry manipulations

The flow machine that was used for the experiments in this chapter was placed inside a fume hood equipped with an extraction fan. The sash window of the fume hood was lowered when the flow machine was in operation to minimise the risk of accidental solvent/chemical vapour release into the surrounding area. When the flow machine was used to perform reactions under high pressure, a test run was initiated first, where only solvent was circulated under pressure for a period of 15 min. This was done to ensure that the pressurised section of the line (between the peristaltic pump and the back pressure regulator) was stable and did not leak, thus minimising the risk of an uncontained loss of pressure and/or spillage during the experiment. In addition to the pressure checks, the reactor tubing was visually checked for blocks or cracks before each experiment was performed. If any anomaly was detected, appropriate steps were taken to mitigate the issue (e.g., by replacing damaged parts). When a gaseous reagent was used (e.g., oxygen), the gas flow to the flow machine's peristaltic pump was regulated by a mass flow controller device (MFC). At the end of each session, all of the lines were depressurised, and flushed several times with clean solvent.

2.9.4 Photoluminescence Quantum Yield (PLQY) Calculations⁸

The FLS920 spectrofluorometer was equipped with an extended red-sensitive single-photon counting photon multiplier (Hamamatsu, R2658P, 200-1010 nm), which was used to measure all spectra. A Xenon lamp, centered to 320 nm, was used as the excitation source.

The PLQY is defined by equation 1.⁷⁸ It is determined by dividing the number of photons emitted (L_{sample}), by the number of photons absorbed. The latter is calculated by measuring the intensity of excitation light ($E_{\text{reference}}$) and subtracting it from the intensity of excitation light not absorbed by the sample (E_{sample}).

$$\text{PLQY} = \frac{\# \text{ photons emitted}}{\# \text{ photons absorbed}} = \frac{L_{\text{sample}}}{E_{\text{reference}} - E_{\text{sample}}}$$

Eq. 1

L_{sample} = emission intensity

$E_{\text{reference}}$ = intensity of excitation light

E_{sample} = intensity of excitation light not absorbed by the sample

2.10 References

- (1) Liu, S.; Zhang, H.; Li, Y.; Liu, J.; Du, L.; Chen, M.; Kwok, R. T. K.; Lam, J. W. Y.; Phillips, D. L.; Tang, B. Z. Strategies to Enhance the Photosensitization: Polymerization and the Donor–Acceptor Even–Odd Effect. *Angew. Chem. Int. Ed.* **2018**, *57* (46), 15189–15193. <https://doi.org/10.1002/anie.201810326>.
- (2) Bartolini, M.; Gombac, V.; Sinicropi, A.; Reginato, G.; Dessì, A.; Mordini, A.; Filippi, J.; Montini, T.; Calamante, M.; Fornasiero, P.; et al. Tuning the Properties of Benzothiadiazole Dyes for Efficient Visible Light-Driven Photocatalytic H₂ Production under Different Conditions. *ACS Appl. Energy Mater.* **2020**, *3* (9), 8912–8928. <https://doi.org/10.1021/acsaem.0c01391>.
- (3) Ji, J.-M.; Zhou, H.; Kim, H. K. Rational Design Criteria for D– π –A Structured Organic and Porphyrin Sensitizers for Highly Efficient Dye-Sensitized Solar Cells. *J. Mater. Chem. A* **2018**, *6* (30), 14518–14545. <https://doi.org/10.1039/C8TA02281J>.
- (4) Tobin, J. M.; McCabe, T. J. D.; Prentice, A. W.; Holzer, S.; Lloyd, G. O.; Paterson, M. J.; Arrighi, V.; Cormack, P. A. G.; Vilela, F. Polymer-Supported Photosensitizers for Oxidative Organic Transformations in Flow and under Visible Light Irradiation. *ACS Catal.* **2017**, *7* (7), 4602–4612. <https://doi.org/10.1021/acscatal.7b00888>.
- (5) Chen, W.; Yang, Z.; Xie, Z.; Li, Y.; Yu, X.; Lu, F.; Chen, L. Benzothiadiazole Functionalized D–A Type Covalent Organic Frameworks for Effective

- Photocatalytic Reduction of Aqueous Chromium(VI). *J. Mater. Chem. A* **2019**, *7* (3), 998–1004. <https://doi.org/10.1039/C8TA10046B>.
- (6) Zhao, Z.; Zhang, H.; Lam, J. W. Y.; Tang, B. Z. Aggregation-Induced Emission: New Vistas at the Aggregate Level. *Angew. Chem. Int. Ed.* **2020**, *59* (25), 9888–9907. <https://doi.org/10.1002/anie.201916729>.
- (7) Alifu, N.; Dong, X.; Li, D.; Sun, X.; Zebibula, A.; Zhang, D.; Zhang, G.; Qian, J. Aggregation-Induced Emission Nanoparticles as Photosensitizer for Two-Photon Photodynamic Therapy. *Mater. Chem. Front.* **2017**, *1* (9), 1746–1753. <https://doi.org/10.1039/c7qm00092h>.
- (8) Broumidis, E.; Koutentis, P. A. A One-Pot, Two-Step Synthesis of 3-Deazacanthin-4-Ones *via* Sequential Pd-Catalyzed Suzuki-Miyaura and Cu-Catalyzed Buchwald-Hartwig Reactions. *Tetrahedron Lett.* **2017**, *58* (27), 2661–2664. <https://doi.org/10.1016/J.TETLET.2017.05.076>.
- (9) Patel, A.; Patel, S.; Mehta, M.; Patel, Y.; Patel, R.; Shah, D.; Patel, D.; Shah, U.; Patel, M.; Patel, S.; et al. A Review on Synthetic Investigation for Quinoline-Recent Green Approaches. *Green Chem. Lett. Rev.* **2022**, *15* (2), 336–371. <https://doi.org/10.1080/17518253.2022.2064194>.
- (10) Weyesa, A.; Mulugeta, E. Recent Advances in the Synthesis of Biologically and Pharmaceutically Active Quinoline and Its Analogues: A Review. *RSC Adv.* **2020**, *10* (35), 20784–20793. <https://doi.org/10.1039/D0RA03763J>.
- (11) Mao, M.; Zhang, X.; Zhu, B.; Wang, J.; Wu, G.; Yin, Y.; Song, Q. Comparative Studies of Organic Dyes with a Quinazoline or Quinoline Chromophore as π -Conjugated Bridges for Dye-Sensitized Solar Cells. *Dye. Pigment.* **2016**, *124*, 72–81. <https://doi.org/10.1016/j.dyepig.2015.09.002>.
- (12) Chakraborty, G.; Das, P.; Mandal, S. K. Quinoline-Tagged Fluorescent Organic Probes for Sensing of Nitro-Phenolic Compounds and Zn^{2+} Ions at the Ppb Level. *Mater. Adv.* **2021**, *2* (7), 2334–2346. <https://doi.org/10.1039/D1MA00025J>.
- (13) Jänsch, D.; Li, C.; Chen, L.; Wagner, M.; Müllen, K. Versatile Colorant Syntheses by Multiple Condensations of Acetyl Anilines with Perylene Anhydrides. *Angew. Chem. Int. Ed.* **2015**, *54* (7), 2285–2289. <https://doi.org/10.1002/anie.201409634>.

- (14) Zhang, P.; Meng, L.-H.; Mándi, A.; Kurtán, T.; Li, X.-M.; Liu, Y.; Li, X.; Li, C.-S.; Wang, B.-G. Brocaeloids A–C, 4-Oxoquinoline and Indole Alkaloids with C-2 Reversed Prenylation from the Mangrove-Derived Endophytic Fungus *Penicillium Brocae*. *Eur. J. Org. Chem.* **2014**, 2014 (19), 4029–4036. <https://doi.org/10.1002/ejoc.201400067>.
- (15) Bilici, A.; Doğan, F.; Yıldırım, M.; Kaya, İ. Tunable Multicolor Emission in Oligo(4-Hydroxyquinoline). *J. Phys. Chem. C* **2012**, 116 (37), 19934–19940. <https://doi.org/10.1021/jp304432k>.
- (16) Ibrahim Mohamed Allaoui, Z.; le Gall, E.; Fihey, A.; Plaza-Pedroche, R.; Katan, C.; Robin-le Guen, F.; Rodríguez-López, J.; Achelle, S. Push–Pull (Iso)Quinoline Chromophores: Synthesis, Photophysical Properties, and Use for White-Light Emission. *Chem. Eur. J.* **2020**, 26 (36), 8153–8161. <https://doi.org/10.1002/chem.202000817>.
- (17) Hariharan, P. S.; Mothi, E. M.; Moon, D.; Anthony, S. P. Halochromic Isoquinoline with Mechanochromic Triphenylamine: Smart Fluorescent Material for Rewritable and Self-Erasable Fluorescent Platform. *ACS Appl. Mater. Interfaces* **2016**, 8 (48), 33034–33042. <https://doi.org/10.1021/acsami.6b11939>.
- (18) Achelle, S.; Rodríguez-López, J.; Cabon, N.; Guen, F. R. Protonable Pyrimidine Derivative for White Light Emission. *RSC Adv.* **2015**, 5 (130), 107396–107399. <https://doi.org/10.1039/C5RA21514E>.
- (19) Slodek, A.; Matussek, M.; Filapek, M.; Szafraniec-Gorol, G.; Szlapa, A.; Grudzka-Flak, I.; Szczurek, M.; Malecki, J. G.; Maron, A.; Schab-Balcerzak, E.; et al. Small Donor–Acceptor Molecules Based on a Quinoline–Fluorene System with Promising Photovoltaic Properties. *Eur. J. Org. Chem.* **2016**, 2016 (14), 2500–2508. <https://doi.org/10.1002/ejoc.201600318>.
- (20) Ma, X.-Q.; Wang, Y.; Wei, T.-B.; Qi, L.-H.; Jiang, X.-M.; Ding, J.-D.; Zhu, W.-B.; Yao, H.; Zhang, Y.-M.; Lin, Q. A Novel AIE Chemosensor Based on Quinoline Functionalized Pillar[5]Arene for Highly Selective and Sensitive Sequential Detection of Toxic Hg^{2+} and CN^- . *Dye. Pigment.* **2019**, 164, 279–286. <https://doi.org/10.1016/j.dyepig.2019.01.049>.
- (21) Bossi, A.; Arnaboldi, S.; Castellano, C.; Martinazzo, R.; Cauteruccio, S.

- Benzodithienyl Silanes for Organic Electronics: AIE Solid-State Blue Emitters and High Triplet Energy Charge-Transport Materials. *Adv. Opt. Mater.* **2020**, *8* (22), 2001018. <https://doi.org/10.1002/adom.202001018>.
- (22) Pu, L. Fluorescence of Organic Molecules in Chiral Recognition. *Chem. Rev.* **2004**, *104* (3), 1687–1716. <https://doi.org/10.1021/cr030052h>.
- (23) Zhuang, W.; Yang, L.; Ma, B.; Kong, Q.; Li, G.; Wang, Y.; Tang, B. Z. Multifunctional Two-Photon AIE Luminogens for Highly Mitochondria-Specific Bioimaging and Efficient Photodynamic Therapy. *ACS Appl. Mater. Interfaces* **2019**, *11* (23), 20715–20724. <https://doi.org/10.1021/acsami.9b04813>.
- (24) Ma, X.; Sun, R.; Cheng, J.; Liu, J.; Gou, F.; Xiang, H.; Zhou, X. Fluorescence Aggregation-Caused Quenching versus Aggregation-Induced Emission: A Visual Teaching Technology for Undergraduate Chemistry Students. *J. Chem. Educ.* **2016**, *93* (2), 345–350. <https://doi.org/10.1021/acs.jchemed.5b00483>.
- (25) Luo, J.; Xie, Z.; Xie, Z.; Lam, J. W. Y.; Cheng, L.; Chen, H.; Qiu, C.; Kwok, H. S.; Zhan, X.; Liu, Y.; et al. Aggregation-Induced Emission of 1-Methyl-1,2,3,4,5-Pentaphenylsilole. *Chem. Commun.* **2001**, *18*, 1740–1741. <https://doi.org/10.1039/b105159h>.
- (26) Mei, J.; Hong, Y.; Lam, J. W. Y.; Qin, A.; Tang, Y.; Tang, B. Z. Aggregation-Induced Emission: The Whole Is More Brilliant than the Parts. *Adv. Mater.* **2014**, *26* (31), 5429–5479. <https://doi.org/10.1002/adma.201401356>.
- (27) Chen, Y.; Lam, J. W. Y.; Kwok, R. T. K.; Liu, B.; Tang, B. Z. Aggregation-Induced Emission: Fundamental Understanding and Future Developments. *Mater. Horizons* **2019**, *6* (3), 428–433. <https://doi.org/10.1039/c8mh01331d>.
- (28) Hu, R.; Lager, E.; Aguilar-Aguilar, A.; Liu, J.; Lam, J. W. Y.; Sung, H. H. Y.; Williams, I. D.; Zhong, Y.; Wong, K. S.; Peña-Cabrera, E.; et al. Twisted Intramolecular Charge Transfer and Aggregation-Induced Emission of BODIPY Derivatives. *J. Phys. Chem. C* **2009**, *113* (36), 15845–15853. <https://doi.org/10.1021/jp902962h>.
- (29) Dong, Y.; Lam, J. W. Y.; Qin, A.; Li, Z.; Sun, J.; Sung, H. H. Y.; Williams, I. D.; Tang, B. Z. Switching the Light Emission of (4-Biphenyl)Phenyldibenzofulvene

- by Morphological Modulation: Crystallization-Induced Emission Enhancement. *Chem. Commun.* **2007**, *1* (1), 40–42. <https://doi.org/10.1039/b613157c>.
- (30) Zhao, Z.; Nie, H.; Ge, C.; Cai, Y.; Xiong, Y.; Qi, J.; Wu, W.; Kwok, R. T. K.; Gao, X.; Qin, A.; et al. Furan Is Superior to Thiophene: A Furan-Cored AIEgen with Remarkable Chromism and OLED Performance. *Adv. Sci.* **2017**, *4* (8), 1–8. <https://doi.org/10.1002/advs.201700005>.
- (31) Li, N. N.; Li, J. Z.; Liu, P.; Pranantyo, D.; Luo, L.; Chen, J. C.; Kang, E. T.; Hu, X. F.; Li, C. M.; Xu, L. Q. An Antimicrobial Peptide with an Aggregation-Induced Emission (AIE) Luminogen for Studying Bacterial Membrane Interactions and Antibacterial Actions. *Chem. Commun.* **2017**, *53* (23), 3315–3318. <https://doi.org/10.1039/c6cc09408b>.
- (32) Westrup, J. L.; Oenning, L. W.; Da Silva Paula, M. M.; Da Costa Duarte, R.; Rodembusch, F. S.; Frizon, T. E. A.; Da Silva, L.; Dal-Bó, A. G. New Photoactive D- π -A- π -D Benzothiadiazole Derivative: Synthesis, Thermal and Photophysical Properties. *Dye. Pigment.* **2016**, *126*, 209–217. <https://doi.org/10.1016/j.dyepig.2015.12.003>.
- (33) Wang, Y.; Michinobu, T. Benzothiadiazole and Its π -Extended, Heteroannulated Derivatives: Useful Acceptor Building Blocks for High-Performance Donor-Acceptor Polymers in Organic Electronics. *J. Mater. Chem. C* **2016**, *4* (26), 6200–6214. <https://doi.org/10.1039/c6tc01860b>.
- (34) Rakitin, O. A. Recent Developments in the Synthesis of 1,2,5-Thiadiazoles and 2,1,3-Benzothiadiazoles. *Synthesis* **2019**, *51* (23), 4338–4347. <https://doi.org/10.1055/s-0039-1690679>.
- (35) Neto, B. A. D.; Lapis, A. A. M.; Da Silva Júnior, E. N.; Dupont, J. 2,1,3-Benzothiadiazole and Derivatives: Synthesis, Properties, Reactions, and Applications in Light Technology of Small Molecules. *Eur. J. Org. Chem.* **2013**, *2*, 228–255. <https://doi.org/10.1002/ejoc.201201161>.
- (36) Tobin, J. M.; McCabe, T. J. D.; Prentice, A. W.; Holzer, S.; Lloyd, G. O.; Paterson, M. J.; Arrighi, V.; Cormack, P. A. G.; Vilela, F. Polymer-Supported Photosensitizers for Oxidative Organic Transformations in Flow and under Visible Light Irradiation. *ACS Catal.* **2017**, *7* (7), 4602–4612.

<https://doi.org/10.1021/acscatal.7b00888>.

- (37) Zhang, K.; Kopetzki, D.; Seeberger, P. H.; Antonietti, M.; Vilela, F. Surface Area Control and Photocatalytic Activity of Conjugated Microporous Poly(Benzothiadiazole) Networks. *Angew. Chem. Int. Ed.* **2013**, *52* (5), 1432–1436. <https://doi.org/10.1002/anie.201207163>.
- (38) Urakami, H.; Zhang, K.; Vilela, F. Modification of Conjugated Microporous Poly-Benzothiadiazole for Photosensitized Singlet Oxygen Generation in Water. *Chem. Commun.* **2013**, *49* (23), 2353–2355. <https://doi.org/10.1039/c3cc38956a>.
- (39) Zhang, K.; Vobecka, Z.; Tauer, K.; Antonietti, M.; Vilela, F. π -Conjugated PolyHIPEs as Highly Efficient and Reusable Heterogeneous Photosensitizers. *Chem. Commun.* **2013**, *49* (95), 11158–11160. <https://doi.org/10.1039/c3cc45597a>.
- (40) Pham, T. D. M.; Ziora, Z. M.; Blaskovich, M. A. T. Quinolone Antibiotics. *Medchemcomm* **2019**, *10* (10), 1719–1739. <https://doi.org/10.1039/c9md00120d>.
- (41) Ioannidou, H. A.; Martin, A.; Gollner, A.; Koutentis, P. A. Three-Step Synthesis of Ethyl Canthinone-3-Carboxylates from Ethyl 4-Bromo-6-Methoxy-1,5-Naphthyridine-3-Carboxylate *via* a Pd-Catalyzed Suzuki-Miyaura Coupling and a Cu-Catalyzed Amidation Reaction. *J. Org. Chem.* **2011**, *76* (12), 5113–5122. <https://doi.org/10.1021/jo200824b>.
- (42) Ghogare, A. A.; Greer, A. Using Singlet Oxygen to Synthesize Natural Products and Drugs. *Chem. Rev.* **2016**, *116* (17), 9994–10034. <https://doi.org/10.1021/acs.chemrev.5b00726>.
- (43) Benov, L. Photodynamic Therapy: Current Status and Future Directions. *Med. Princ. Pract.* **2015**, *24*, 14–28. <https://doi.org/10.1159/000362416>.
- (44) Thomson, C. G.; Jones, C. M. S.; Rosair, G.; Ellis, D.; Marques-Hueso, J.; Lee, A. L.; Vilela, F. Continuous-Flow Synthesis and Application of Polymer-Supported BODIPY Photosensitisers for the Generation of Singlet Oxygen; Process Optimised by in-Line NMR Spectroscopy. *J. Flow Chem.* **2020**, *10* (1), 327–345. <https://doi.org/10.1007/s41981-019-00067-4>.
- (45) Schweitzer, C.; Schmidt, R. Physical Mechanisms of Generation and Deactivation

- of Singlet Oxygen. *Chem. Rev.* **2003**, *103* (5), 1685–1757. <https://doi.org/10.1021/cr010371d>.
- (46) Zou, Y. Q.; Chen, J. R.; Liu, X. P.; Lu, L. Q.; Davis, R. L.; Jørgensen, K. A.; Xiao, W. J. Highly Efficient Aerobic Oxidative Hydroxylation of Arylboronic Acids: Photoredox Catalysis Using Visible Light. *Angew. Chem. Int. Ed.* **2012**, *51* (3), 784–788. <https://doi.org/10.1002/anie.201107028>.
- (47) Li, K.; Liu, Y.; Li, Y.; Feng, Q.; Hou, H.; Tang, B. Z. 2,5-Bis(4-Alkoxy-carbonylphenyl)-1,4-Diaryl-1,4-Dihydropyrrolo[3,2-b]Pyrrole (AAPP) AIEgens: Tunable RIR and TICT Characteristics and Their Multifunctional Applications. *Chem. Sci.* **2017**, *8* (10), 7258–7267. <https://doi.org/10.1039/c7sc03076b>.
- (48) Zhang, M.; Li, J.; Yu, L.; Wang, X.; Bai, M. Tuning the Fluorescence Based on the Combination of TICT and AIE Emission of a Tetraphenylethylene with D- π -A Structure. *RSC Adv.* **2020**, *10* (25), 14520–14524. <https://doi.org/10.1039/d0ra00107d>.
- (49) Cai, M.; Gao, Z.; Zhou, X.; Wang, X.; Chen, S.; Zhao, Y.; Qian, Y.; Shi, N.; Mi, B.; Xie, L.; et al. A Small Change in Molecular Structure, a Big Difference in the AIEE Mechanism. *Phys. Chem. Chem. Phys.* **2012**, *14* (15), 5289–5296. <https://doi.org/10.1039/c2cp23040b>.
- (50) Xie, S.; Manuguri, S.; Ramström, O.; Yan, M. Impact of Hydrogen Bonding on the Fluorescence of N-Amidinated Fluoroquinolones. *Chem. Asian J.* **2019**, *14* (6), 910–916. <https://doi.org/10.1002/asia.201801916>.
- (51) Maillard, J.; Klehs, K.; Rumble, C.; Vauthey, E.; Heilemann, M.; Fürstenberg, A. Universal Quenching of Common Fluorescent Probes by Water and Alcohols. *Chem. Sci.* **2021**, *12* (4), 1352–1362. <https://doi.org/10.1039/d0sc05431c>.
- (52) Baier, J.; Fuß, T.; Pöllmann, C.; Wiesmann, C.; Pindl, K.; Engl, R.; Baumer, D.; Maier, M.; Landthaler, M.; Bäuml, W. Theoretical and Experimental Analysis of the Luminescence Signal of Singlet Oxygen for Different Photosensitizers. *J. Photochem. Photobiol. B Biol.* **2007**, *87* (3), 163–173. <https://doi.org/10.1016/j.jphotobiol.2007.02.006>.

- (53) Feng, J.; Tian, K.; Hu, D.; Wang, S.; Li, S.; Zeng, Y.; Li, Y.; Yang, G. A Triarylboron-Based Fluorescent Thermometer: Sensitive Over a Wide Temperature Range. *Angew. Chem. Int. Ed.* **2011**, *50* (35), 8072–8076. <https://doi.org/10.1002/anie.201102390>.
- (54) v. Bünau, G. J. B. Birks: Photophysics of Aromatic Molecules. *Berichte der Bunsengesellschaft für Phys. Chemie* **1970**, *74* (12), 1294–1295. <https://doi.org/10.1002/bbpc.19700741223>.
- (55) Yang, J.; Gu, K.; Shi, C.; Li, M.; Zhao, P.; Zhu, W.-H. Fluorescent Thermometer Based on a Quinolinemalononitrile Copolymer with Aggregation-Induced Emission Characteristics. *Mater. Chem. Front.* **2019**, *3* (8), 1503–1509. <https://doi.org/10.1039/C9QM00147F>.
- (56) Martinho, J. M. G.; Reis e Sousa, A. T.; Oliveira Torres, M. E.; Fedorov, A. Fluorescence Quenching of Pyrene Monomer and Excimer by CH₃I. *Chem. Phys.* **2001**, *264* (1), 111–121. [https://doi.org/10.1016/S0301-0104\(00\)00385-2](https://doi.org/10.1016/S0301-0104(00)00385-2).
- (57) Dimitriev, O. P.; Piryatinski, Y. P.; Slominskii, Y. L. Excimer Emission in J-Aggregates. *J. Phys. Chem. Lett.* **2018**, *9* (9), 2138–2143. <https://doi.org/10.1021/acs.jpcllett.8b00481>.
- (58) Yang, Q.; Ma, H.; Liang, Y.; Dai, H. Rational Design of High Brightness NIR-II Organic Dyes with S-D-A-D-S Structure. *Accounts Mater. Res.* **2021**, *2* (3), 170–183. <https://doi.org/10.1021/accountsmr.0c00114>.
- (59) Zhang, F.; Tang, B. Z. Near-Infrared Luminescent Probes for Bioimaging and Biosensing. *Chem. Sci.* **2021**, *12* (10), 3377–3378. <https://doi.org/10.1039/D1SC90046C>.
- (60) Dobscha, J. R.; Debnath, S.; Fadler, R. E.; Fatila, E. M.; Pink, M.; Raghavachari, K.; Flood, A. H. Host–Host Interactions Control Self-Assembly and Switching of Triple and Double Decker Stacks of Tricarbazole Macrocycles Co-Assembled with Anti-Electrostatic Bisulfate Dimers. *Chem. Eur. J.* **2018**, *24* (39), 9841–9852. <https://doi.org/10.1002/chem.201800827>.
- (61) Bichovski, P.; Haas, T. M.; Kratzert, D.; Streuff, J. Synthesis of Bridged Benzazocines and Benzoxocines by a Titanium-Catalyzed Double-Reductive

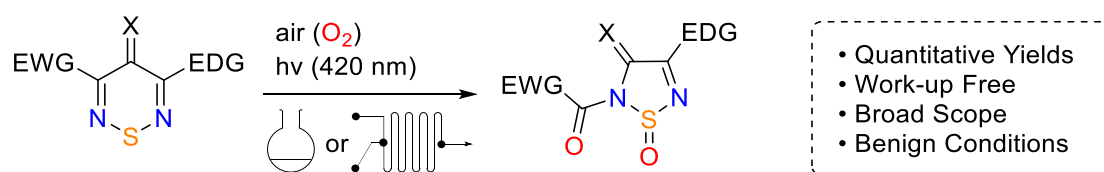
- Umpolung Strategy. *Chem. Eur. J.* **2015**, *21* (6), 2339–2342. <https://doi.org/10.1002/chem.201405852>.
- (62) Proctor, R. S. J.; Phipps, R. J. Recent Advances in Minisci-Type Reactions. *Angew. Chem. Int. Ed.* **2019**, *58* (39), 13666–13699. <https://doi.org/10.1002/anie.201900977>.
- (63) Dong, J.; Lyu, X.; Wang, Z.; Wang, X.; Song, H.; Liu, Y.; Wang, Q. Visible-Light-Mediated Minisci C–H Alkylation of Heteroarenes with Unactivated Alkyl Halides Using O₂ as an Oxidant. *Chem. Sci.* **2019**, *10* (4), 976–982. <https://doi.org/10.1039/C8SC04892D>.
- (64) Wu, C.; Ying, T.; Yang, X.; Su, W.; Dushkin, A. V.; Yu, J. Mechanochemical Magnesium-Mediated Minisci C–H Alkylation of Pyrimidines with Alkyl Bromides and Chlorides. *Org. Lett.* **2021**, *23* (16), 6423–6428. <https://doi.org/10.1021/acs.orglett.1c02241>.
- (65) Chatterjee, S.; Ie, Y.; Seo, T.; Moriyama, T.; Wetzelaer, G.-J. A. H.; Blom, P. W. M.; Aso, Y. Fluorinated Naphtho[1,2-c:5,6-c']Bis[1,2,5]Thiadiazole-Containing π -Conjugated Compound: Synthesis, Properties, and Acceptor Applications in Organic Solar Cells. *NPG Asia Mater.* **2018**, *10* (10), 1016–1028. <https://doi.org/10.1038/s41427-018-0088-4>.
- (66) Chatterjee, S.; Ie, Y.; Karakawa, M.; Aso, Y. Naphtho[1,2-c:5,6-c']Bis[1,2,5]Thiadiazole-Containing π -Conjugated Compound: Nonfullerene Electron Acceptor for Organic Photovoltaics. *Adv. Funct. Mater.* **2016**, *26* (8), 1161–1168. <https://doi.org/10.1002/adfm.201504153>.
- (67) Wang, M.; Hu, X.; Liu, P.; Li, W.; Gong, X.; Huang, F.; Cao, Y. Donor–Acceptor Conjugated Polymer Based on Naphtho[1,2-c:5,6-c]Bis[1,2,5]Thiadiazole for High-Performance Polymer Solar Cells. *J. Am. Chem. Soc.* **2011**, *133* (25), 9638–9641. <https://doi.org/10.1021/ja201131h>.
- (68) Osaka, I.; Takimiya, K. Naphthobischalcogenadiazole Conjugated Polymers: Emerging Materials for Organic Electronics. *Adv. Mater.* **2017**, *29* (25), 1605218. <https://doi.org/10.1002/adma.201605218>.
- (69) <https://www.sigmaaldrich.com/GB/en/product/aldrich/795518> (accessed June 6,

- 2022).
- (70) Zhang, X.; Hu, H.; Liu, W.; Wang, Y.; Liu, J.; Wu, P. Selective Heavy Atom Effect Forming Photosensitizing Hot Spots in Double-Stranded DNA Matrix. *J. Phys. Chem. Lett.* **2021**, *12* (38), 9205–9212. <https://doi.org/10.1021/acs.jpcclett.1c02809>.
- (71) Lim, S. H.; Thivierge, C.; Nowak-Sliwinska, P.; Han, J.; van den Bergh, H.; Wagnières, G.; Burgess, K.; Lee, H. B. In Vitro and In Vivo Photocytotoxicity of Boron Dipyrromethene Derivatives for Photodynamic Therapy. *J. Med. Chem.* **2010**, *53* (7), 2865–2874. <https://doi.org/10.1021/jm901823u>.
- (72) Koziar, J. C.; Cowan, D. O. Photochemical Heavy-Atom Effects. *Acc. Chem. Res.* **1978**, *11* (9), 334–341. <https://doi.org/10.1021/ar50129a003>.
- (73) Acharya, R.; Cekli, S.; Zeman, C. J.; Altamimi, R. M.; Schanze, K. S. Effect of Selenium Substitution on Intersystem Crossing in π -Conjugated Donor–Acceptor–Donor Chromophores: The LUMO Matters the Most. *J. Phys. Chem. Lett.* **2016**, *7* (4), 693–697. <https://doi.org/10.1021/acs.jpcclett.5b02902>.
- (74) Fernández-Lodeiro, J.; Pinatto-Botelho, M. F.; Soares-Paulino, A. A.; Gonçalves, A. C.; Sousa, B. A.; Princival, C.; Dos Santos, A. A. Synthesis and Biological Properties of Selenium- and Tellurium-Containing Dyes. *Dye. Pigment.* **2014**, *110*, 28–48. <https://doi.org/10.1016/j.dyepig.2014.04.044>.
- (75) Lee, D. R.; Lee, K. H.; Shao, W.; Kim, C. L.; Kim, J.; Lee, J. Y. Heavy Atom Effect of Selenium for Metal-Free Phosphorescent Light-Emitting Diodes. *Chem. Mater.* **2020**, *32* (6), 2583–2592. <https://doi.org/10.1021/acs.chemmater.0c00078>.
- (76) Gaussian 03, Revision C.02, Frisch, M. J.; Trucks, G. W.; Schlegel, H. B.; Scuseria, G. E.; Robb, M. A.; Cheeseman, J. R.; Montgomery, Jr., J. A.; Vreven, T.; Kudin, K. N.; Burant, J. C.; Millam, J. M.; Iyengar, S. S.; Tomasi, J.; Barone, V.; Mennucci, B.; Cossi, M.; Scalmani, G.; Rega, N.; Petersson, G. A.; Nakatsuji, H.; Hada, M.; Ehara, M.; Toyota, K.; Fukuda, R.; Hasegawa, J.; Ishida, M.; Nakajima, T.; Honda, Y.; Kitao, O.; Nakai, H.; Klene, M.; Li, X.; Knox, J. E.; Hratchian, H. P.; Cross, J. B.; Bakken, V.; Adamo, C.; Jaramillo, J.; Gomperts, R.; Stratmann, R. E.; Yazyev, O.; Austin, A. J.; Cammi, R.; Pomelli, C.; Ochterski, J. W.; Ayala, P. Y.; Morokuma, K.; Voth, G. A.; Salvador, P.; Dannenberg, J. J.;

Zakrzewski, V. G.; Dapprich, S.; Daniels, A. D.; Strain, M. C.; Farkas, O.; Malick, D. K.; Rabuck, A. D.; Raghavachari, K.; Foresman, J. B.; Ortiz, J. V.; Cui, Q.; Baboul, A. G.; Clifford, S.; Cioslowski, J.; Stefanov, B. B.; Liu, G.; Liashenko, A.; Piskorz, P.; Komaromi, I.; Martin, R. L.; Fox, D. J.; Keith, T.; Al-Laham, M. A.; Peng, C. Y.; Nanayakkara, A.; Challacombe, M.; Gill, P. M. W.; Johnson, B.; Chen, W.; Wong, M. W.; Gonzalez, C.; and Pople, J. A., Gaussian, Inc., Wallingford CT, 2004

- (77) Reichardt, P. D. C. Empirical Parameters of Solvent Polarity. In *Solvents and Solvent Effects in Organic Chemistry*; John Wiley & Sons, Ltd, 2002; pp 389–469. <https://doi.org/10.1002/3527601791.ch7>.
- (78) Jones, C. M. S.; Panov, N.; Skripka, A.; Gibbons, J.; Hesse, F.; Bos, J.-W. G.; Wang, X.; Vetrone, F.; Chen, G.; Hemmer, E.; et al. Effect of Light Scattering on Upconversion Photoluminescence Quantum Yield in Microscale-to-Nanoscale Materials. *Opt. Express* **2020**, 28 (15), 22803. <https://doi.org/10.1364/oe.398353>.

Chapter 3: Photochemical Ring Editing: Selective Carbon Excision from Thiadiazines



3.1 Declaration

This work was made possible by the collaborative effort of 13 scientists spanning 2 countries, and 5 universities and was completed after 3 years of continuous effort. The contribution of each person is detailed below:

Emmanouil Broumidis: Discovery of the transformation, reaction optimisations, majority of reaction scope, mechanistic experiments, data analysis, main author of the current chapter.

Christopher G. Thomson: Mechanistic experiments, data analysis.

Brendan Ghallagher: Reaction scope (compounds **22b**, **33b**, **41a**, **41b**).

Lia Sottoríos: Computational experiments, data analysis, author of the relevant section.

Georgina M. Rosair: SC-XRD data analysis, author of the relevant section.

Gareth O. Lloyd: SC-XRD data analysis.

Andreas S. Kalogirou: Synthesis of starting materials **Xa**.

Janet E. Lovett: Access to EPR spectroscopy instrumentation.

Kenneth G McKendrick: Supervision of kinetic experiments.

Stuart A. Macgregor and Martin J. Paterson: Supervision of computational experiments.

Panayiotis. A. Koutentis and Filipe Vilela: Overall project supervision, experiment design, manuscript review.

3.2 Background and Aims

As part of our efforts to discover new photoactive materials that can be used for the production of singlet oxygen ($^1\text{O}_2$) and other reactive oxygen species (ROS) under continuous flow conditions, we obtained a relatively underutilised S,N heterocycle, the non-S oxidised 3,5-diphenyl-4H-1,2,6-thiadiazin-4-one (**1a**), as shown in Figure 1.

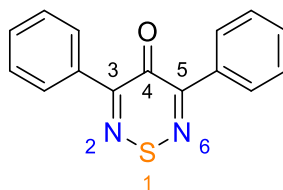


Figure 1. Structure of the parent 1,2,6-thiadiazine **1a** that was used during the initial studies.

To our knowledge this family of compounds has never been evaluated for their photosensitisation potential, and since they are structurally similar to the very widely used class of 1,2,5-thiadiazoles¹ we thought that it was likely that thiadiazine **1a** would exhibit interesting photocatalytic properties. In addition, due to the presence of an electron withdrawing carbonyl group at C4 (see Figure 1), its absorption spectrum is broadened by the increased HOMO \rightarrow LUMO transitions ($\pi\rightarrow\pi^*$, $n\rightarrow\pi^*$), caused by the growing electron delocalisation. As a result, virtually all known thiadiazines bearing an electron withdrawing substituent at the C4 position can absorb light >400 nm,² making them suitable candidates for visible light photocatalytic applications. Despite the initial plan as briefly outlined above, when compound **1a** was used in flow under illumination at 420 nm, its behaviour was different than anticipated. After further investigation, it was found that thiadiazine **1a** had ring contracted to form 2-benzoyl-4-phenyl-1,2,5-thiadiazol-3(2H)-one 1-oxide (**1b**), as seen in Figure 2.

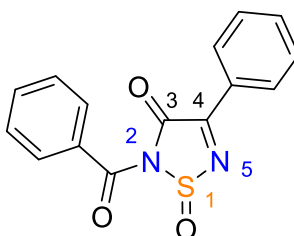


Figure 2. Structure of the novel 1,2,5-thiadiazole 1-oxide **1b** that was formed.

Following this unexpected result, the goal of the project shifted, and we focused our efforts to uncover the underlying mechanism, scope, and limits of this transformation. The results of this work are the focus of this chapter.

3.3 Introduction

Monocyclic non-S-oxidised 1,2,5-thiadiazoles^{3,4} have a wide range of uses such as pesticides,⁵ fungicides,⁶ corrosion inhibitors,⁷ cell staining agents⁸ and pharmaceuticals.⁹ Important monocyclic 1,2,5-thiadiazole-based pharmaceuticals currently on the market include Timolol (β -blocker),¹⁰ and Xanomeline (antipsychotic).¹¹ Fused 1,2,5-thiadiazole based pharmaceuticals include Tizanidine (antispasmodic)¹² (Figure 3).

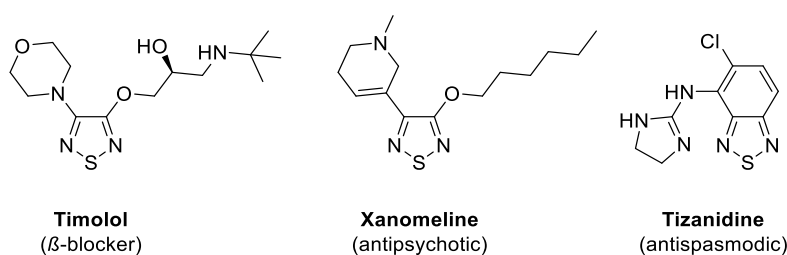


Figure 3. Series of pharmaceutically relevant 1,2,5-Thiadiazoles.

In the 1980s, Evans coined the term ‘privileged scaffold’, which refers to chemical structures that frequently appear in pharmaceutically active compounds.¹³ Thiadiazoles are ‘privileged scaffolds’, owing to their electronic properties, which provide favourable pharmacokinetics to enable drug delivery in the body.¹⁴ More specifically, the mesoionic character of the heterocycle leads to areas of positive and negative charge which enables the ring to easily cross the cell membranes and interact with a biological target.¹⁵ Another key factor attributing to the effectiveness of thiadiazoles is the presence of the sulfur atom that gives rise to high liposolubility, which improves the pharmacokinetic properties and enhances their biological activity.¹⁶

Whilst Timolol was patented as early as 1969,¹⁷ literature precedent on the rarer 1,2,5-thiadiazole 1-oxides are surprisingly less common. Nevertheless, in 1982 a patent appeared describing 1,2,5-thiadiazole 1-oxides as elastase inhibitors for the treatments of diseases such as pancreatitis, emphysema and rheumatoid arthritis.¹⁸ In the same year, Lumma Jr and co-workers investigated 1,2,5-thiadiazole 1-oxides for the inhibition of gastric acid secretion.¹⁹ Despite their promising utility, there are relatively few reliable pathways to access 1,2,5-thiadiazole 1-oxides.^{3,20–22} This is true for all sulfoxide-bearing scaffolds, as they are prone to overoxidation, and many chemoselective methods for their synthesis from sulfides requires the use of oxidants such as 2-iodobenzoic acid (IBX)²³

or Oxone,²⁴ often in over stoichiometric quantities and high temperatures.²⁵ The most accessible synthetic pathways towards S-oxidised 1,2,5-thiadiazoles involve reacting thionyl chloride with *vic*-1,2-bisimines²⁶ or bis(trimethylsilyl) derivatives,²⁷ but these reactions offer low to moderate yields and use harsh reagents. Weinstock *et al.* showcased that the lack of aromaticity of S-oxidised 1,2,5-thiadiazoles renders them highly electrophilic and thermally unstable.²⁸ Therefore, the development of new mild and practical methods will allow researchers to explore this previously difficult to access chemical space. Figure 4 illustrates the disparity between the number of published papers and chemical substructures between non-, mono- and di-S-oxidised 1,2,5-thiadiazoles.

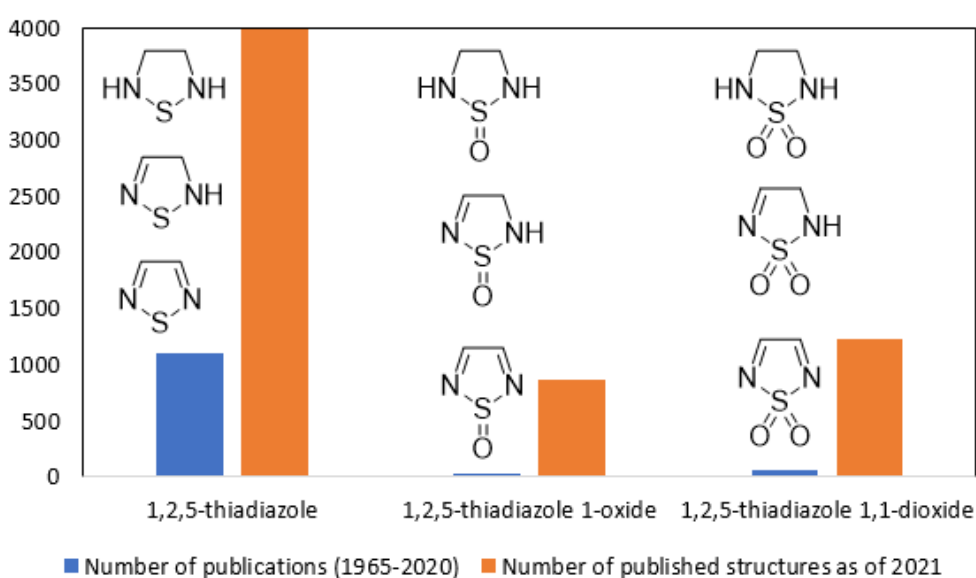


Figure 4. Plot of number of publications (1965-2020) and published chemical structures (as of 2021) for search terms ‘1,2,5-thiadiazole(s)’, ‘1,2,5-thiadiazole 1-oxide(s)’ and ‘1,2,5-thiadiazole 1,1-dioxide(s)’. Generated on 13/09/2021 using the Web of Science database.

Light-driven ring contractions leading to selective atom removal from the core structure, represent a persuasive alternative to traditional synthetic approaches and offer new routes which can lead to early- and late-stage diversification of valuable compounds.²⁹ Surprisingly, only two such photo-mediated single-step skeletal transformations have been reported as of 2022. These transformations were effectively used to access indolic³⁰ and amino-cyclopentane³¹ scaffolds, *via* selective carbon and nitrogen atom deletion, respectively, and substantial efforts are underway to further expand the collective molecular editing armamentarium. 4*H*-1,2,6-Thiadiazines^{32,33} are six-membered heterocycles that are structurally similar to 1,2,5-thiadiazoles, the only difference being the presence of an additional carbon atom in the ring (Figure 5).

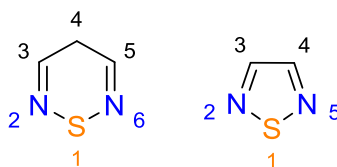
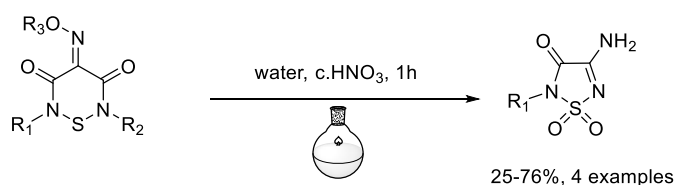


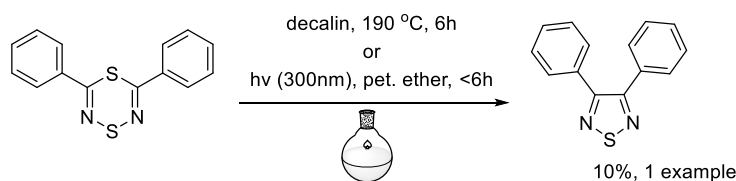
Figure 5. Structure comparison between non-S-oxidised 4H-1,2,6-thiadiazine (left) and 1,2,5-thiadiazole cores (right).

To the best of our knowledge, there are five examples where a six-membered heterocycle has been used to access 1,2,5-thiadiazoles, and in three of those, the heterocycle was a 4H-1,2,6-thiadiazine (Scheme 1). Vicente and co-workers reported the first of these in 1986,³⁴ whereby this contraction converted 2-substituted 1,2,6-thiadiazine 1,1-dioxides to 1,2,5-thiadiazole 1,1-dioxides under harsh acidic conditions.

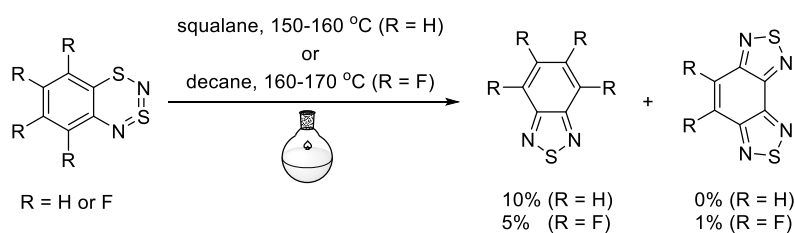
1. *J. Chem. Soc., Perkin Trans. 1*, **1986**, 643-645



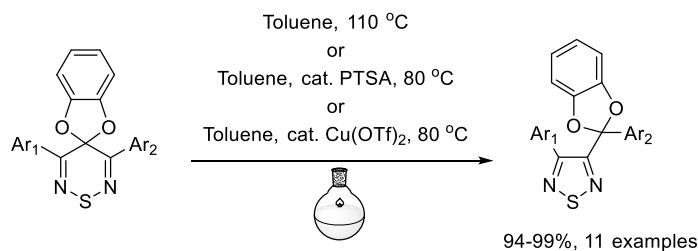
2. *J. Chem. Soc., Perkin Trans. 1*, **1987**, 207-210

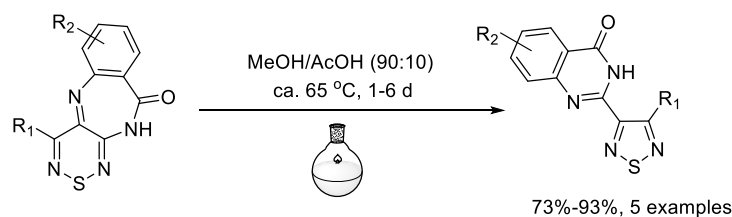


3. *Eur. J. Inorg. Chem.*, **2005**, 4099-4108

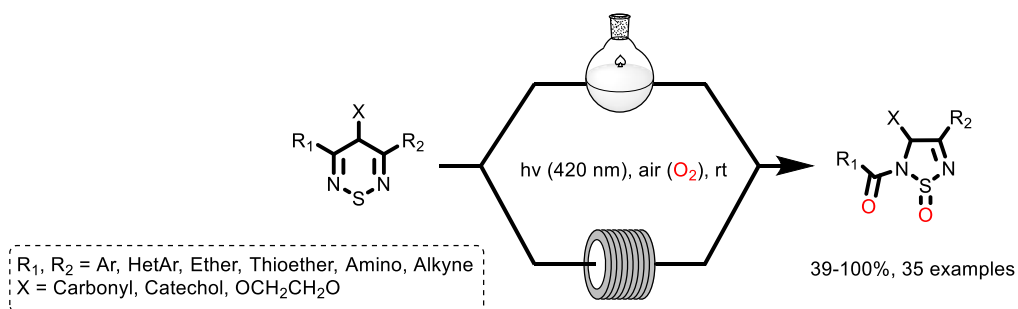


4. *Org. Lett.*, **2016**, 18, 16, 4056-4059



5. *J. Org. Chem.*, **2021**, 86, 5702-5713

6. This work



Scheme 1. Comparison between previous examples of ring contractions to afford 1,2,5-thiadiazoles and current work.

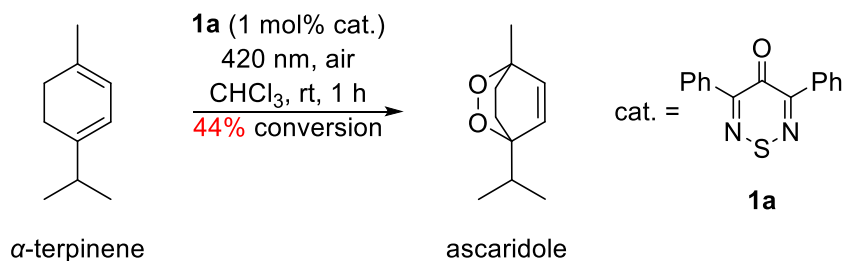
The second³⁵ and third³⁶ reports, only isolated 1,2,5-thiadiazoles as minor side-products and thus do not offer synthetic utility. In 2016 Koutentis and co-workers reported the acid and/or thermal ring contractions of readily prepared 3',5'-diarylspiro(benzo[*d*][1,3]dioxole-2,4'-[1,2,6]thiadiazines) to afford non-S-oxidised 1,2,5-thiadiazoles in high yields,³⁷ and in 2021 the same group developed the thermal transformation of benzo[*e*][1,2,6]thiadiazino[3,4-*b*][1,4]diazepin-10(11*H*)-ones to 2-(4-substituted-1,2,5-thiadiazol-3-yl)quinazolin-4(3*H*)-ones.³⁸ Surprisingly, these and the other ring contractions of thiadiazine to thiadiazole involve cleavage of the 'stronger' C-C bond but not the N-S bond. Herein, we report the unprecedented oxidation and ring contraction of 4*H*-1,2,6-thiadiazines to 1,2,5-thiadiazole 1-oxides under visible light irradiation under aerobic conditions.

3.4 Results and Discussion

3.4.1 Reaction Discovery

As part of our past work in the development of new 1,2,5-benzothiadiazole (BTZ) derivatives for use as singlet oxygen (¹O₂) photosensitisers,³⁹⁻⁴³ we postulated, that 4*H*-

1,2,6-thiadiazines might be effective triplet sensitizers since they share many structural and electronic properties with the 1,2,5-thiadiazole family.⁴⁴ As such, we used 1 mol% (1.0 mg, 0.00375 mmol) of 3,5-diphenyl-4*H*-1,2,6-thiadiazin-4-one (**1a**) as a ¹O₂ photosensitizer for the conversion of α -terpinene to ascaridole (Scheme 2). The former reacts selectively with ¹O₂ and is commonly used to assess the performance of triplet photosensitisers.³⁹ To our satisfaction, after 1 hour of irradiation using a blue LED light source, there was a 44% conversion to ascaridole, as assessed by ¹H NMR.

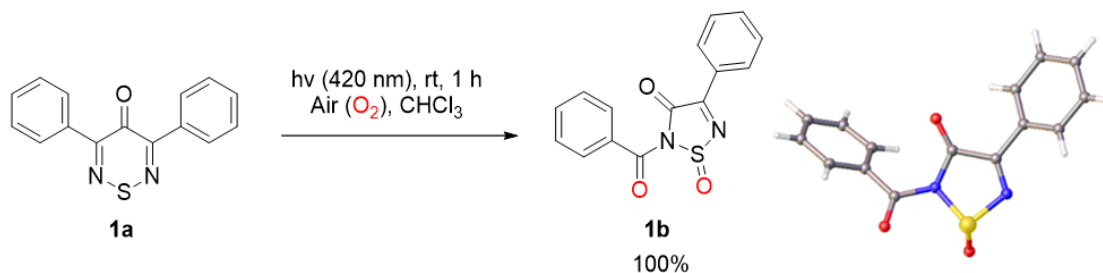


Scheme 2. Conversion of α -terpinene to ascaridole using diphenylthiadiazine **1a** as the photosensitizer.

Interestingly, after irradiation, we noticed decolouration of the initially yellow reaction mixture. As the yellow colour originated from the diphenylthiadiazine **1a**, we hypothesised that this change was attributed to photobleaching of the thiadiazine **1a** and/or its decomposition as photosensitisers exposed to reactive oxygen species (ROS), such as ¹O₂, or superoxide radicals (O₂⁻), can readily decompose.⁴⁵

To investigate the fate of the photosensitizer, a solution containing solely diphenylthiadiazine **1a** (10.0 mg, 0.0375 mmol) in chloroform was irradiated using the same 420 nm LED lamp. After one hour, we were surprised to see that the solution had again turned colourless and based on TLC (*n*-Hex/CHCl₃, 50:50) thiadiazine **1a** had been fully consumed and a new intractable spot appeared on the baseline. Removal of the solvent under vacuum gave a colourless solid (11.2 mg). Elemental analysis together with mass spectrometry (HRMS, ESI+), gave a formula of C₁₅H₁₀N₂O₃S, indicating that compared to the starting material, the product had gained two oxygen atoms, presumably, *via* the addition of molecular oxygen. Tentatively, based on the mass recovery, the reaction yield was quantitative, indicating a remarkable 100% atom economy.⁴⁶ In addition, the IR spectrum of the product clearly showed two carbonyl stretches at $\nu(\text{C}=\text{O})$ 1733 and 1699 cm⁻¹, which was also supported by ¹³C NMR spectroscopy with resonances at δ_{C} 167.9 and 166.4. The UV-vis profile ($\lambda_{\text{max}} = 296$ nm) shifted hypsochromically compared to **1a** ($\lambda_{\text{max}} = 350$ nm) pointing to a less conjugated, less

aromatic system than the starting thiadiazine. ^1H NMR spectroscopy indicated that the ten protons of the two phenyl groups were present but unlike thiadiazine **1a**, the product was no longer symmetrical. Worthy of note, ^1H NMR spectroscopy of the crude non-recrystallised material indicated that the sample was remarkably clean. In spite of the above data, we were unable to conclusively assign a structure, and resorted to single crystal x-ray crystallography which revealed the identity of this unknown product to be 2-benzoyl-4-phenyl-1,2,5-thiadiazol-3(2*H*)-one 1-oxide (**1b**) (Scheme 3).



Scheme 3. Ring contraction of thiadiazine **1a** to thiazole **1b**, and its crystal structure.

3.4.2 Reaction Optimisation

Our next step was to further optimise the reaction parameters to maximize its efficiency. We started by measuring the reaction time in different organic solvents with a large range of polarities (Figure 6).

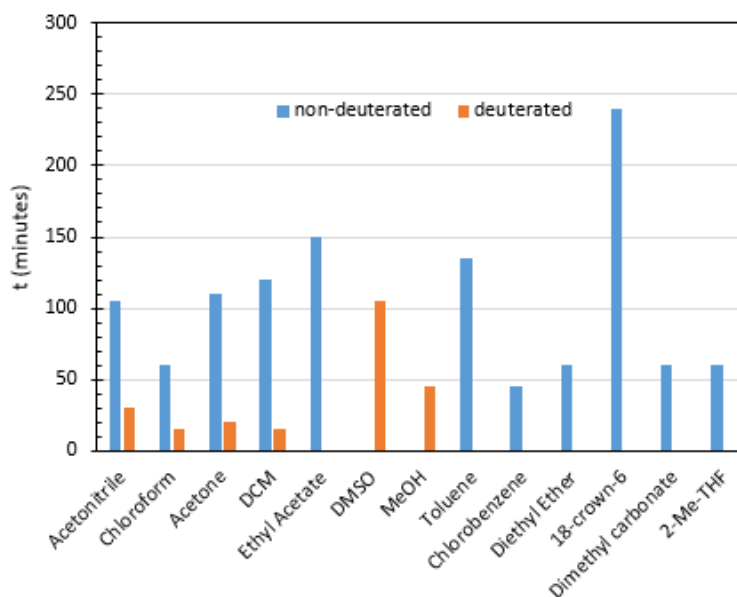
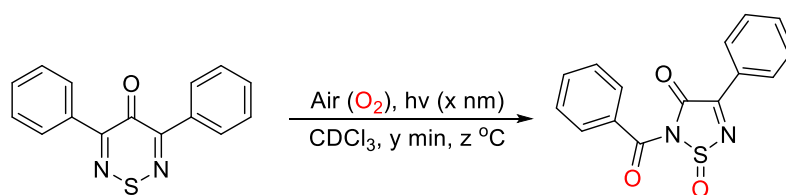


Figure 6. Comparison of the effect of different solvents on the reaction time (based on the disappearance of thiadiazine **1a** on TLC).

The reaction times in deuterated solvents were markedly shorter compared to their non-deuterated counterparts. This suggested that the reaction was mediated by $^1\text{O}_2$; in the presence of deuterated solvents, intermolecular vibronic coupling between the $^1\text{O}_2$ and the solvent leads to deactivation of the $^1\text{O}_2$; vibronic coupling is less effective in deuterated solvents.⁴⁷ Moreover, we observed that deuterated DMSO, performed poorly compared to the other deuterated solvents; DMSO is a known $^1\text{O}_2$ scavenger.⁴⁸ Another notable result, was that when deuterated MeOH was used, the product decomposed upon formation. In the case of diethyl ether (Et_2O), the product **1b** on forming precipitated out of the solution, as its solubility in Et_2O was very low. Green solvents, such as dimethyl carbonate (DMC) and 2-methyltetrahydrofuran (2-MeTHF)⁴⁹ were also tested, however, in the case of DMC, a sticky residue was left after the completion of the reaction, and when 2-MeTHF was used, the ^1H NMR spectrum of the crude mixture contained impurities, possibly by the interaction between the solvent and $^1\text{O}_2$.⁵⁰ Based on the above results, we selected deuterated chloroform (CDCl_3), as the primary solvent, as it offered the fastest reaction time (15 min), and ease of reaction monitoring *via* ^1H NMR.

External parameters, such as atmosphere, temperature, and irradiation wavelength, were also examined (Table 1). Revealingly, when the reaction was attempted in the absence of a light source or under an inert atmosphere (Table 1, entries 1 & 9), thiadiazine **1a** was not consumed. Unsurprisingly, the use of a light source > 420 nm, also stalled the reaction (Table 1, entries 3 & 4), as the UV-Vis spectrum of thiadiazine **1a** shows no absorption at wavelengths > 430 nm (SI, 3.7.1). When low temperatures were employed (Table 1, entries 5 & 6), the reaction time was markedly reduced. This was attributed to the increased solubility of gases in low temperature solvents.⁵¹ Based on these observations, the optimised conditions for the batch ring contraction of thiadiazine **1a** to thiadiazole **1b** were identified (Method A: air, hv (420 nm), CDCl_3 , rt).

The stability of the product was also investigated: thiadiazole **1b** decomposed on prolonged exposure to light (long UV (320-400 nm), and blue (420 nm)), protic solvents (MeOH), bases (KOH), and silica. This made it incompatible with TLC and column chromatography purification techniques. Several decomposition products were isolated and characterised (SI, 3.7.4). Simple recrystallisation from CHCl_3 or trituration using Et_2O were suitable methods for obtaining analytically pure product (as judged by elemental analysis).

Table 1. Parameter optimisation for the ring contraction of thiadiazine **1a** to thiadiazole **2a**.^a

Entry	Temp. (°C)	Light (nm)	Time (min)	Conversion (%) ^b
1	20	dark	60	0
1	20	390	30	100
2	20	420	15	100
3	20	520	60	0
4	20	620	60	0
5	-12	420	5	81
6	0	420	5	73
7	20	420	5	56
8	65	420	5	8
9^c	20	420	60	0

^a Conditions: **1a** (0.0375 mmol) dissolved in CDCl₃ (1 mL); ^b Determined by ¹H NMR; ^c Under N₂ atmosphere.

The light-sensitive nature of thiadiazole **1b** was a cause for concern, as while the other deleterious agents could be avoided, limiting the light exposure was more challenging, as it was necessary for the reaction to occur. We posited that by performing the reaction under continuous flow conditions, we could reduce the total irradiation time, as the technique offers better mass transfer and photon penetration when compared to traditional batch processes.⁵² Indeed, after some optimisation, we developed an analogous continuous flow protocol to Method A, where the total residence time of the solution in the flow photoreactor for full conversion to product **1b** was as little as 60 seconds (SI, 3.7.2). With these optimised conditions in hand, we then explored the reaction scope.

3.4.3 Reaction Scope

We started by examining the significance of thiadiazine's **1a** C4 carbonyl group in the reaction, by substituting it with thioketone **2a**, phenylimine **3a** and

ylidenemalononitrile **4a** groups. Thione **2a** was consumed under both Methods A and B, however, ^1H NMR spectroscopy indicated decomposition. Conversely, the imine **3a** and ylidene **4a** failed to react and were recovered after 24 h of irradiation. By using either thiadiazines **3a** or **4a** as photosensitisers for the conversion of α -terpinene to ascaridole, no $^1\text{O}_2$ was produced as indicated by the absence of ascaridole at the end of the experiment. This further strengthened the hypothesis that the reaction was mediated by $^1\text{O}_2$ and explained the lack of reactivity of analogues **3a** and **4a**. We then tested ketal groups (-OCH₂CH₂O- and -OC₆H₄O-, **5a** and **9a**, respectively) and the corresponding products **5b** and **9b** were obtained in excellent yields, albeit only when Method B was used (Figure 7A).

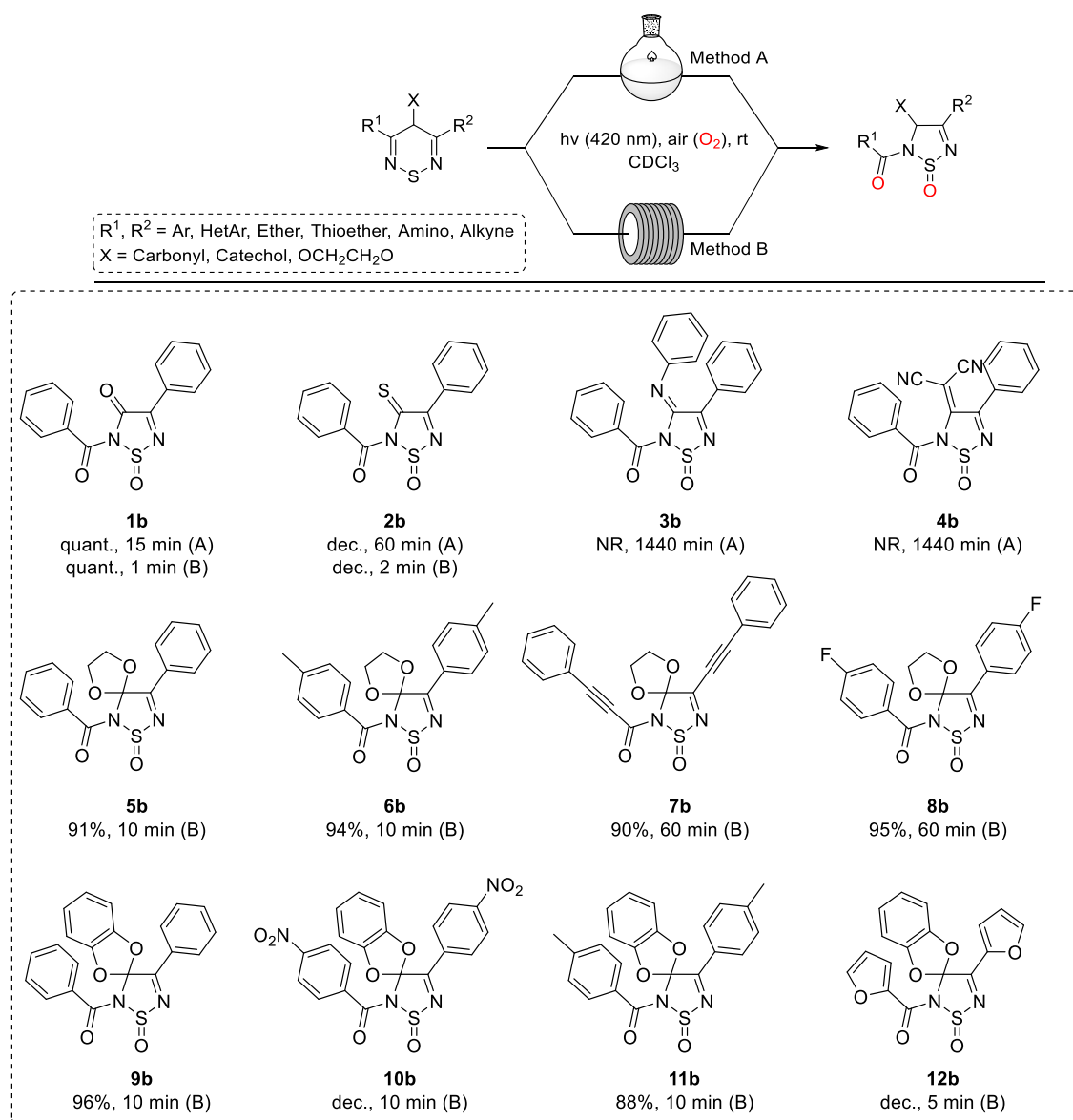


Figure 7A. Overall reaction (Methods A & B) and 4-Substituted 1,2,5-thiadiazole 1-oxides (**1b** – **12b**).

These ketals were highly prone to photodecomposition and, as such, by using the continuous flow (Method B), the exposure time was minimised, and the products had time to exit the reactor before degrading. When Method A was used, most of the product decomposed before the starting material (SM) was consumed. This highlighted the utility and importance of continuous flow techniques when dealing with delicate molecules.

The reaction of other ketal thiadiazine analogues with varying R groups (**6b-8b** & **11b**) was then studied. Unfortunately, while product **11b** was obtained in 88% yield, compounds **10b** and **12b** bearing p-nitrophenyl and 2-furyl groups were not obtained, even under flow conditions due to degradation. However, the fact that we were able to use SMs bearing ketal groups showcased two things: *i*) we were able to differentiate between the two carbonylic O atoms present in **1b**, as by looking at **5b** and **9b** it becomes clear that C4 does not migrate during the contraction; and, *ii*) the use of SMs without carbonyl groups supported that they were not essential in the reaction mechanism; carbonyls are chromophores known to participate in a plethora of photochemical reactions,⁴⁷ and its lack of involvement in this reaction will simplify the mechanistic elucidation process. It is worth mentioning, that an alternative approach for the differentiation of the O atoms in **1b**, would be to employ isotopically enriched ¹⁷O₂ gas, instead of the naturally abundant ¹⁶O₂ source. We could then use a combination of ¹⁷O NMR and MS techniques to determine where the new O atoms are located.⁵³ Luckily, we were able to avoid this, by obtaining the indirect evidence as discussed above.

Next, a set of *ortho*-, *meta*- and *para*-substituted phenylthiadiazines were used to assess how steric and electronic effects affect the reaction (Figure 7B). As expected, in all cases (**13b** – **21b**), the bulkier *ortho* substituents required more time to react. Interestingly, *m*-Me thiadiazole **14b** was particularly unstable, and could only be obtained *via* Method B.

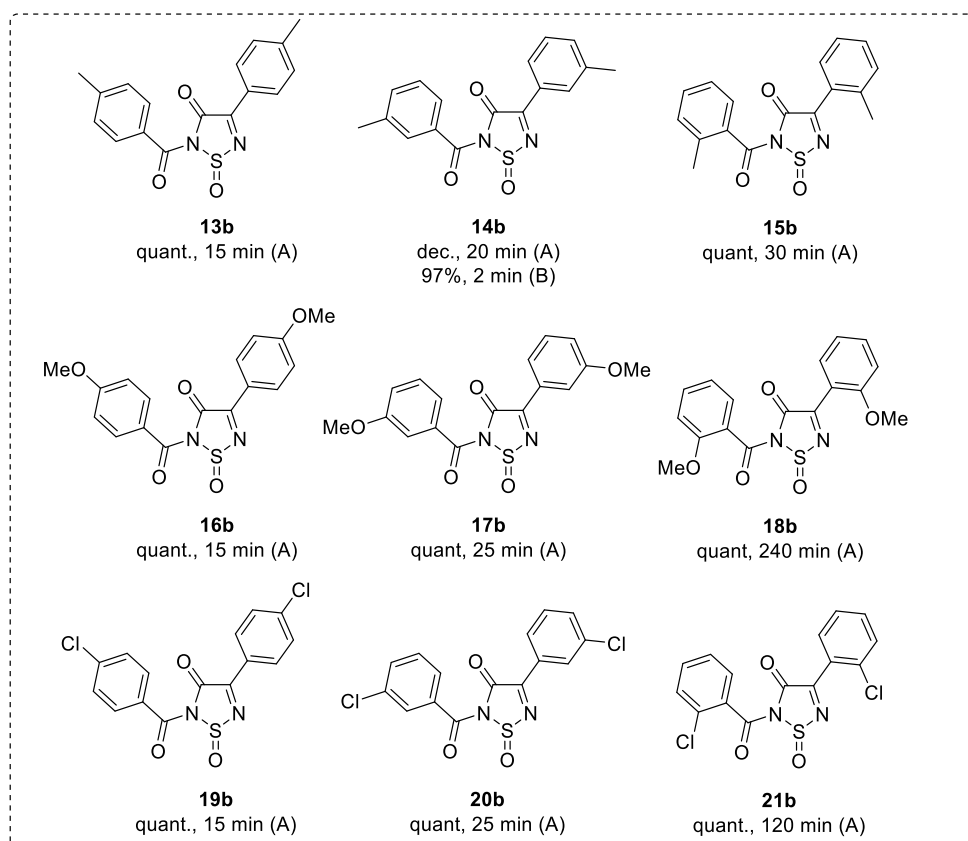


Figure 7B. *O*-, *m*-, and *p*-substituted 1,2,5-thiadiazole 1-oxides (19b - 21b).

A series of products containing ether and thioether groups was synthesised, except for product 26b, bearing benzylthioether groups (Figure 7C).

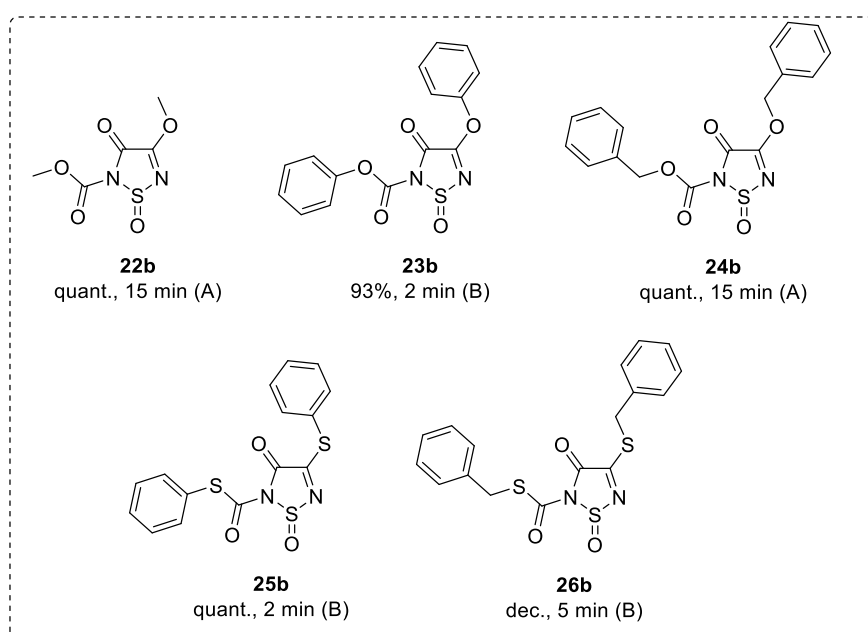


Figure 7C. RO- and RS-substituted 1,2,5-thiadiazole 1-oxides (22b - 26b).

We then moved our attention to a set of hetaryl-substituted analogues (Figure 7D). While compounds bearing thien-2-yl (**27b**), thien-3-yl (**28b**) and 1-methyl-1*H*-pyrrol-2-yl (**29b**) groups were effortlessly obtained, fur-2-yl-bearing **30b** was not, as it decomposed rapidly upon formation, similarly, with the analogous ketal protected compound **12b**. The instability of the fur-2-yl group was not surprising, as furans are known to react with $^1\text{O}_2$ to form endoperoxide intermediates.⁵⁴

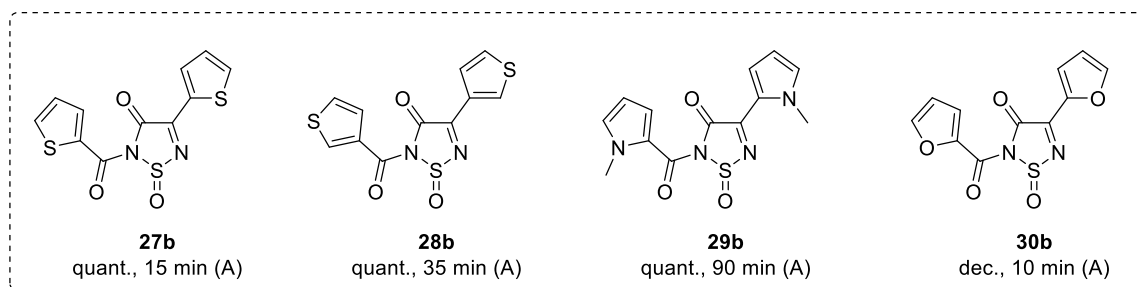


Figure 7D. Heterocyclic-substituted 1,2,5-thiadiazole 1-oxides (**27b** - **30b**).

Other symmetric derivatives were also synthesised (**31b** – **34b**) (Figure 7E). In the case of substrate **31b**, bearing two -Cl groups, the reaction failed, giving a complex mixture. Curiously, crystals of a degradation product were obtained after slow evaporation of the crude solution, which upon analysis were identified to be parabanic acid,⁵⁵ a compound that is known to form in the presence of ROS.⁵⁶ Electronic effects attributed to different R groups do not appear to have a significant effect on the reaction time. A comparison between electron donating **16b** (4-MeO), and electron withdrawing **32b** (4-MeO₂C) products demonstrated this, as both required only 15 minutes for completion of the reaction. In general, for this reaction, it was not easy to generalise or establish reactivity trends based on ‘classical’ parameters such as sterics or electronics since the reaction performance also depended upon various photophysical parameters which determine the ability of each thiadiazine SM to access the triplet excited state and produce $^1\text{O}_2$.

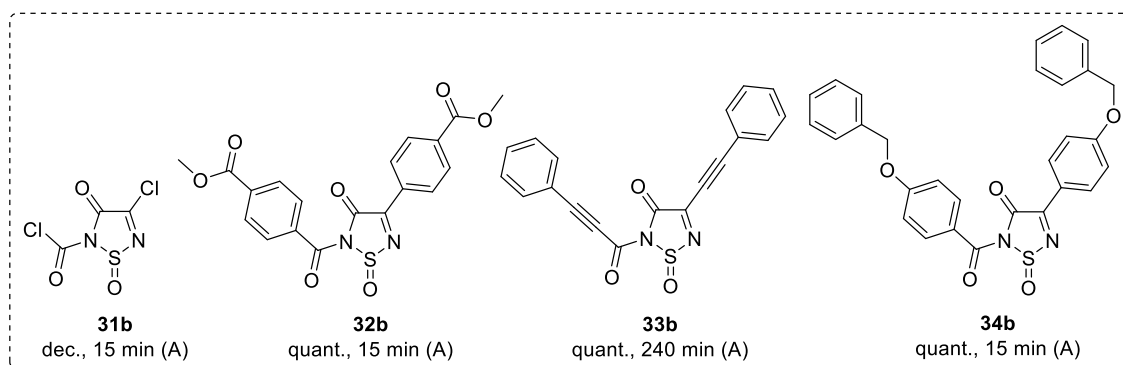


Figure 7E. Other substituted 1,2,5-thiadiazole 1-oxides (**31b** - **34b**).

The reactions of several asymmetric thiadiazine SMs were also studied (**35a** – **45a**, **47a**, **50a** - **54a**) (Figure 7F). It quickly became evident that the reaction was highly regioselective, and during the ring contraction, the most electron withdrawing R group preferentially migrated, while the more electron donating remained in its original position. This was very informative, as it provided mechanistic clues. Since the distinction between the two possible regioisomers based solely on spectroscopic evidence was not trivial, we obtained crystal structures for several of the asymmetric products (SI, 3.7.7). Where crystal structures could not be acquired, the structure of the regioisomers was determined by comparing the ^1H NMR data between the asymmetric analogue and its symmetric counterparts (SI, 3.8.3).

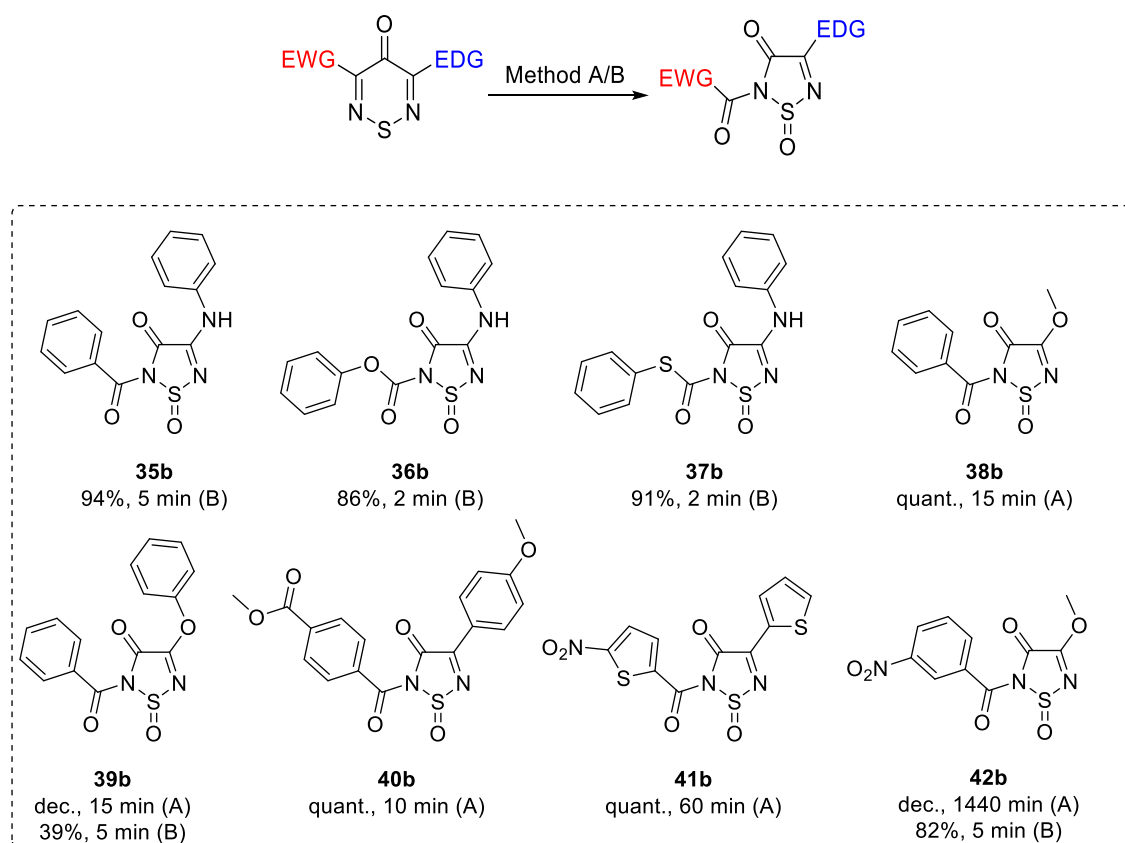


Figure 7F. Asymmetric 1,2,5-thiadiazole 1-oxides with one regioisomer (**35b** - **42b**).

The next step was to test the limits of this selectivity by using SMs with R groups of similar electronegativity (Figure 7G). This was achieved with thiadiazine **43a** ($\text{R}^1 = 4\text{-MeOC}_6\text{H}_4$, $\text{R}^2 = 4\text{-Tol}$) that gave two regioisomers **43b** and **43c**, in a ratio of 69:31 (as determined by ^1H NMR). The major product **43b** was the one where the relatively less electron donating -Me group migrated. Asymmetric thiadiazines **44a** ($\text{R}^1 = 4\text{-MeOC}_6\text{H}_4$, $\text{R}^2 = 3\text{-MeOC}_6\text{H}_4$) and **45a** ($\text{R}^1 = 4\text{-MeOC}_6\text{H}_4$, $\text{R}^2 = 2\text{-MeOC}_6\text{H}_4$) were used to measure

how the regioisomeric ratio was affected by steric effects. *Ortho*-substituted aryl thiadiazines migrated preferentially, as opposed to *meta*- or *para*-ones. Interestingly, the ratio between the two sets of regioisomers **44b,c** and **45b,c** was the same (60:40 in both cases). Unfortunately, in all cases where the regioselectivity was not 100% and both isomers formed, separation of the two was not possible. As mentioned earlier, these compounds were unstable on silica, and while the products appeared more stable on reverse phase media, the use of an HPLC system equipped with a C18 reverse phase column failed to separate the mixture.

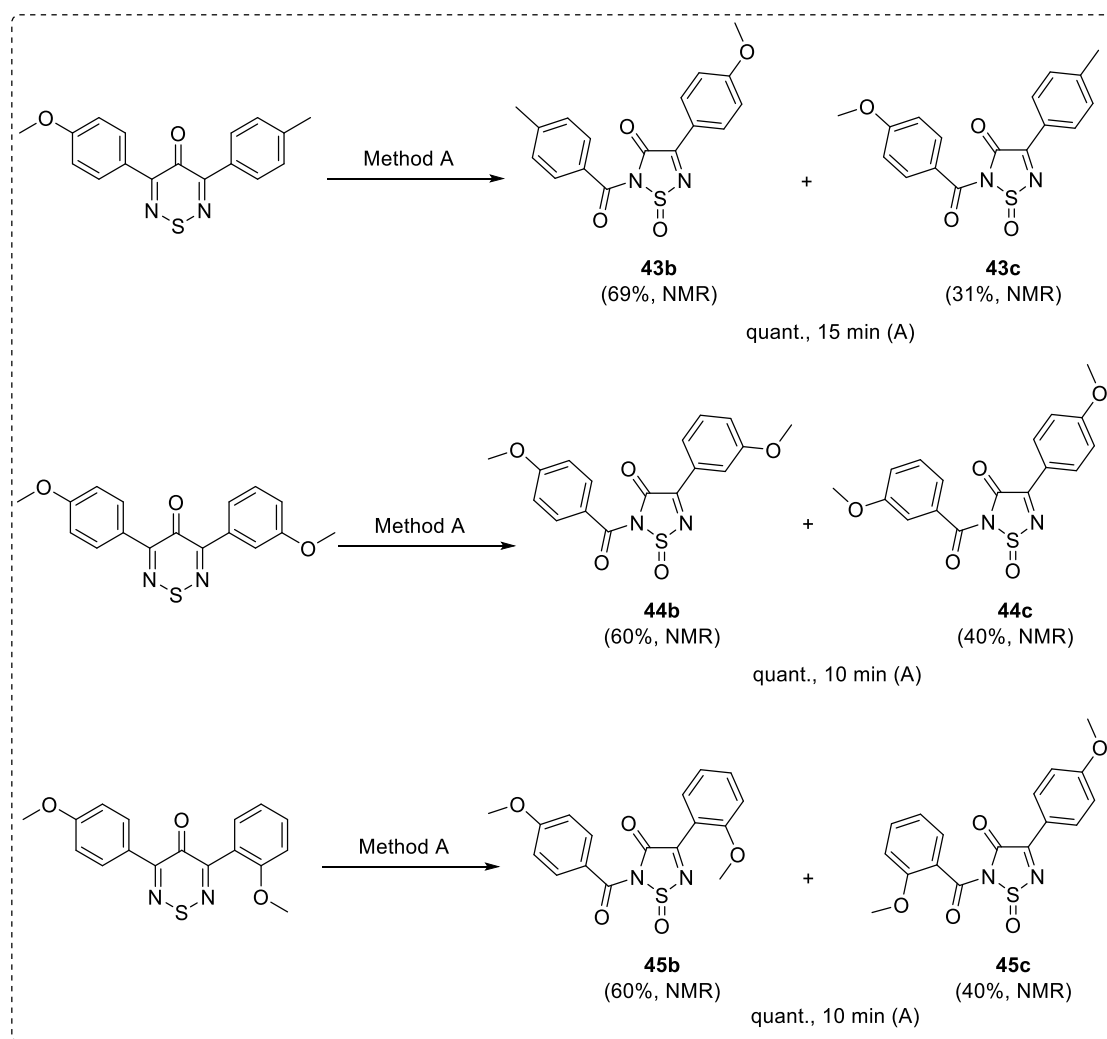


Figure 7G. Asymmetric 1,2,5-thiadiazole 1-oxides with two regioisomers (**43b** - **45c**).

Diamino-substituted thiadiazines **46a** – **51a** behaved poorly (Figure 7H). Starting materials **46a** and **47a** were unreactive, and as with thiadiazines **3a** and **4a** they did not produce any $^1\text{O}_2$ upon irradiation. Thiadiazines **48a** and **49a** were consumed, but the anticipated products did not form. Similar to the case of the dichloro- **31a**, the reaction

mixture of diamino **49a** formed crystals after slow evaporation, which were identified as the sulfate salt of 1,3-diaminopropane-2,2-diol (SI, 3.7.7).

The most unusual reactivity came from tertiary amino-thiadiazines (**50a**, **51a**), where instead of forming the expected ring-contracted 1,2,5-thiadiazole 1-oxide products, they instead formed mixtures of the corresponding 1,2,6-thiadiazine 1-oxides. Sulfones **50d** and **51d** were the major products (73 and 55%, respectively), and we were able to isolate and fully characterise them. Unfortunately, the isolation of minor products, sulfoxides **50c** and **51c** proved to be more challenging. However, elucidation of their chemical structures was made possible, as crystals suitable for SC-XRD were grown after slow evaporation of their respective crude solutions after chromatography (SI, 3.7.7). The structure of the ring contracted **51b**, is tentative and based on LC-MS data. It is not yet clear why these two thiadiazines exhibit this behaviour. Even though the oxidation of sulfides by $^1\text{O}_2$ to afford sulfoxides and sulfones is a well-known reaction,⁵⁷ this did not explain why the rest of the thiadiazines have a preference to ring-contract *via* a carbon excision mechanism instead.

The isolated 1,2,6-thiadiazine sulfones **50d** and **51d** were individually subjected to 420 nm irradiation under the optimised batch conditions (Method A). To our surprise, subsequent LC-MS analysis after 48 h revealed the formation of new products, one of which was tentatively the ring contracted 2,4-bis[methyl(phenyl)amino]-1,2,5-thiadiazol-3(2*H*)-one 1,1-dioxide (**51e**) (SI, 3.7.5.6). This indicated that the ring contraction was not limited to only non-S oxidised 1,2,6-Thiadiazine SMs, and potentially can be applied to a broader family of heterocycles.

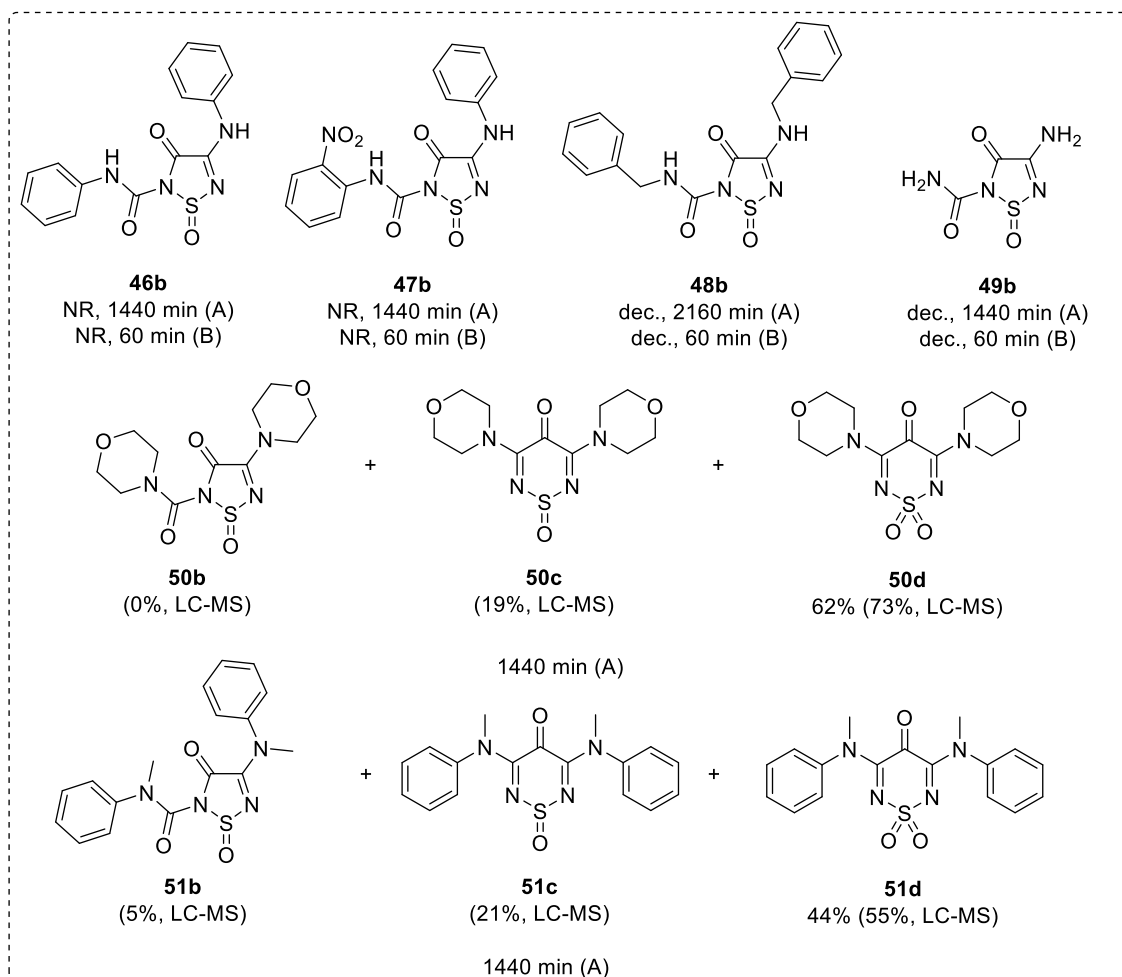


Figure 7H. Diamino-substituted 1,2,5-thiadiazole 1-oxides (46b - 51d).

We concluded the reaction scope studies by testing the asymmetric monochloro-thiadiazines **52a**, **53a**, and **54a**, and as seen with the previous chloro-substituted derivative **31a**, no product was formed (Figure 7I).

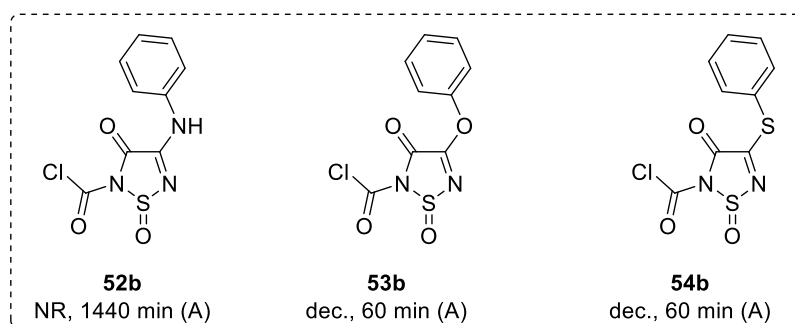


Figure 7I. Asymmetric Cl-substituted 1,2,5-thiadiazole-1-oxides (52b - 54b).

Finally, since the S atom of the 1,2,5-thiadiazole 1-oxides constitutes a stereogenic centre,⁵⁸ the question of whether the resulting products were chiral was answered by polarimetry measurements, which showed that the specific rotation $[\alpha]$ was 0, thus

proving that racemic mixtures were formed. This is logical, as the thiadiazine core is planar, making an attack from an ROS equally likely on both sides.

3.4.4 Crystallographic Data⁸

The crystal structure of thiadiazole **1b** contains notably short intermolecular S \cdots O contacts [2.888(3) Å] where the S-O bonds stack on top of each other parallel to the *b*-axis. This may have implications for the reactivity of **1b**. The structures of compounds **1b**, **3b**, **8b**, **13b**, **20b** and **27b** were confirmed by single crystal XRD as racemates. All crystallised in centrosymmetric space groups despite the chiral sulfur atom. However, compound **5b** crystallised in the chiral space group $P2_12_12_1$, albeit as a two-component twin and compound **28b** crystallised in the polar space group $Pna2_1$ where the S lone pair faces in one direction parallel to the *c* axis. Close intermolecular S \cdots O contacts were observed in sulfoxide **20b** [2.782(3) Å], running parallel to the *a*-axis. These close contacts were also observed in the structure of sulfoxide **1b** (*vide supra*) which differs only in the phenyl *meta* substituents (H *cf.* Cl). The structure of compound **32b** was supported by X-ray diffraction and crystallised in the polar space group Cc with molecules packing in such a way that the S lone pair faces in one direction along the *a*-axis. The structures of compounds **35b**, **37b** and **40b** were supported by single crystal XRD as racemates in $P2_1/c$ while compound **39b** crystallised in the chiral space group $P2_12_12_1$, albeit as a two-component twin. All crystal structures can be found in the SI, 3.7.7

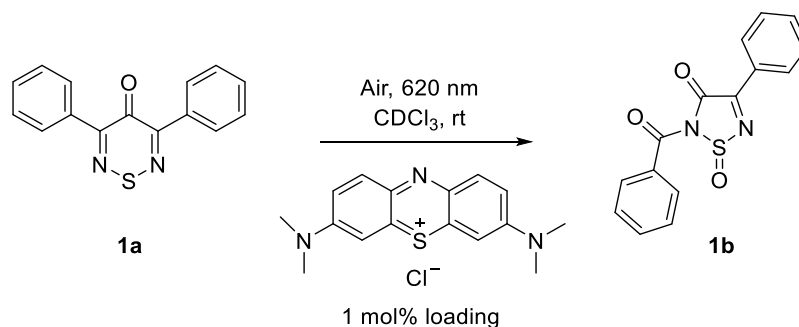
3.4.5 Mechanistic Studies

To better understand the underlying mechanism that drives the ring contraction, a series of experimental control studies were conducted (SI, 3.7.5.1). The use of various selective traps for reactive oxygen species (ROS) provided definitive proof that 1O_2 is involved in the ring contraction, and compelling evidence that superoxide radicals ($O_2^{\cdot-}$) are also generated during the irradiation of the SMs. Conversely, hydroxyl radicals (OH \cdot) are neither generated nor participate in the reaction mechanism. The existence of

persulfoxide anion intermediates, known to occasionally form during aerobic photochemical sulfide oxidations²⁵ was also excluded, whilst tentative proof of electron transfer processes was obtained.

At this point, we wanted to establish whether the excited state of the thiadiazine **1a** reacted with the photogenerated ROS ($^1\text{O}_2$, O_2^-), however, Stern-Volmer quenching experiments⁵⁹ could not be conducted, as thiadiazine **1a** was both the reactant and the photosensitiser, thus differentiating between a fluorescence reduction caused by TTA ($^3\mathbf{1a}^* + ^3\text{O}_2 \rightarrow \mathbf{1a} + ^1\text{O}_2$) and a reaction of thiadiazine **1a*** with a ROS to produce thiadiazole **1b** was not possible. For this reason, we decided to use a known ROS photosensitiser, methylene blue (MB), as an orthogonal light absorbing species since it has a strong absorption at 620 nm where the thiadiazine **1a** does not absorb light.

To our surprise, when MB (1 mol%) was used there was 100% conversion of **1a** to thiadiazole **1b** after 1 hour (Scheme 4). This showed that the ROS generated by MB reacts with the ground state of thiadiazine **1a** and that the excited state **1a*** does not participate in the reaction. This method however, has some limitations as MB can produce multiple ROS, including $^1\text{O}_2$ and O_2^- .⁶⁰ In addition, even though thiadiazine **1a** does not absorb 620 nm light, it was not possible to exclude energy transfer between the excited MB and thiadiazine **1a** to produce **1a***.



Scheme 4. Photosensitisation of thiadiazine **1a** using methylene blue.

To circumvent these limitations, we employed known ‘dark’ $^1\text{O}_2$ generators.⁶¹ To our satisfaction, in the absence of light irradiation, thiadiazole **1b** was obtained quantitatively, agreeing with the results obtained when MB was used. Furthermore, we demonstrated that exactly 1 equivalent of O_2 was required to facilitate the ring contraction of thiadiazine **1a** (SI, 3.7.5.4). An experiment looking at whether exchange between different R groups took place during the ring contraction and carbon excision was performed, by reacting two symmetric thiadiazines **32a** ($\text{R}^1 = 4\text{-MeO}_2\text{CC}_6\text{H}_4$) and **34a** ($\text{R}^2 = 4\text{-BnOC}_6\text{H}_4$) in a

single pot (SI, 3.7.5.3). If the R groups were labile and detached from the main ring during the contraction, then we would expect to see asymmetric products containing both R¹ and R² groups. However, after the completion of the reaction, only the symmetric products **32b** and **34b** formed, as confirmed by ¹H NMR and DOSY spectroscopic analysis, indicating that the R groups stay attached to the ring during the transformation. Finally, when the O₂^{•-} spin trap 5,5-dimethyl-1-pyrroline N-oxide (DMPO)⁶² was irradiated in the presence of thiadiazine **1a**, electron paramagnetic resonance (EPR) spectroscopy produced a distinct signal that corresponds to the transient [DMPO-O₂^{•-}] adduct,⁶³ cementing the evidence that compound **1a** produces O₂^{•-} under the optimised reaction conditions (Figure 8).

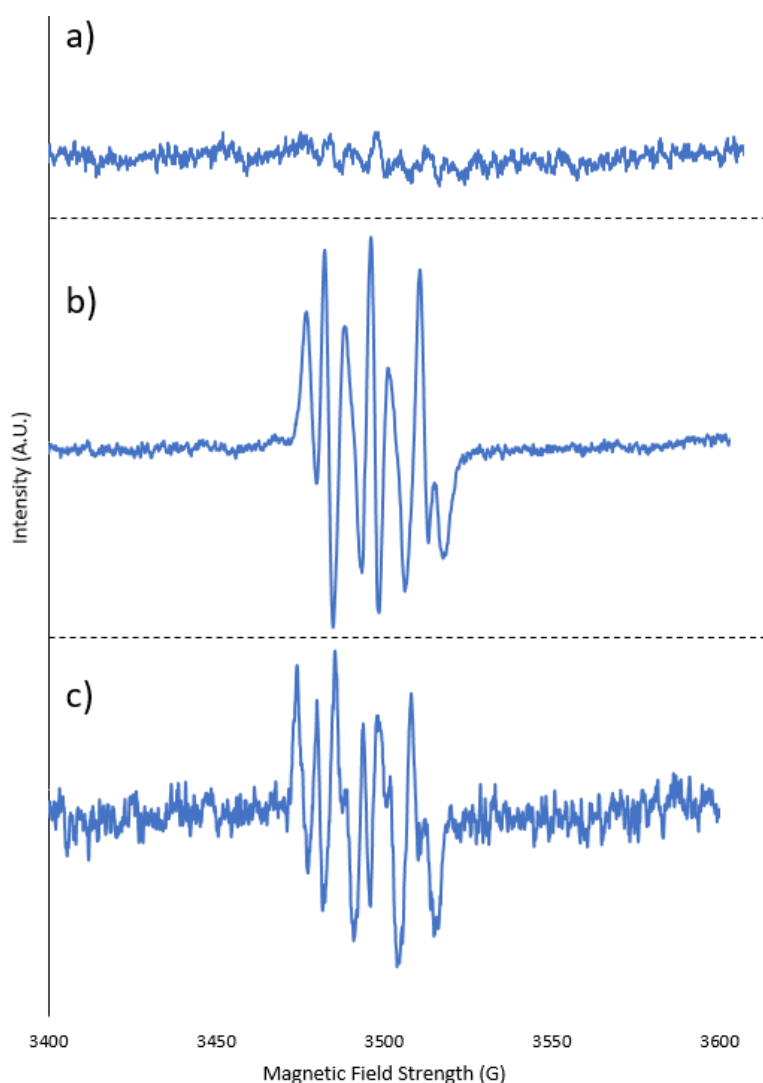


Figure 8. a) EPR signal of equimolar mixture of thiadiazine **1a** and DMPO in chlorobenzene (CB) without irradiation. b) EPR signal when the aforementioned solution was irradiated using a long-UV LED lamp for 15 min. c) Reference signal using TiO₂ (rutile) in CB as the photosensitiser.

3.4.6 Computational Studies⁸

The mechanism of the reaction of thiadiazine **1a** with singlet oxygen was investigated computationally. Geometries were optimised with UB3LYP using 6-31G** basis sets and included the effects of chloroform solvent (PCM approach). Electronic energies were then recomputed using CASPT2(16,13) and these were combined with thermodynamic corrections from the UB3LYP frequency calculations to give the free energies reported in Figure 9.

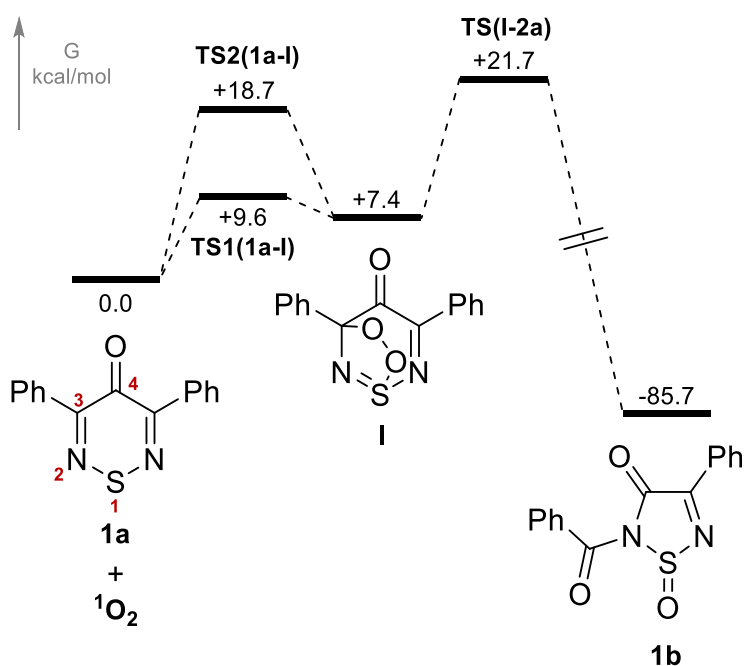


Figure 9. Computed free energy profiles (CASPT2(16,13)/6-31G**//UB3LYP(CHCl₃)/6-31G**); kcal/mol) for the reaction of $^1\text{O}_2$ with thiadiazine **1a** to form thiadiazole **1b**.

Figure 9 shows the initial addition of $^1\text{O}_2$ to thiadiazine **1a** can occur in two ways to give a common endoperoxide intermediate **I** at 7.4 kcal/mol: i) a concerted [3+2] addition across the C(Ph)-N=S moiety, *via* **TS1(1a-I)** at 9.6 kcal/mol; or ii) an end-on addition of $^1\text{O}_2$ onto C3 *via* **TS2(1a-I)** at 18.7 kcal/mol followed by barrierless S-O bond formation. From **I**, O-O bond cleavage occurs with concomitant ring contraction in a single step *via* **TS(I-2a)** at 21.7 kcal/mol. This process entails the simultaneous cleavage of the O-O and C3-C4 bonds as well as the formation of a new amide bond between N2 and C4 (Figure 10). The formation of the thiadiazole ring in **1b** is very exergonic ($\Delta G = -85.7$ kcal/mol) and proceeds with an overall barrier of 21.7 kcal/mol, consistent with the room

temperature reactivity observed experimentally. **TS(I-2a)** will be both the rate-determining and selectivity-determining transition state.

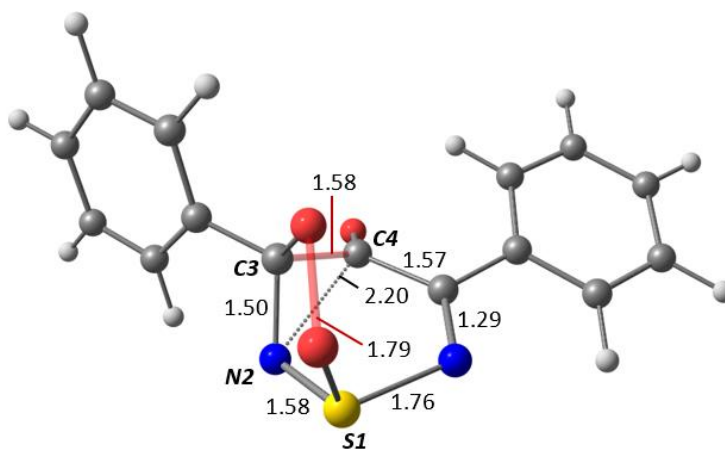


Figure 10. Geometry of **TS(I-2a)**. Breaking bonds in red, forming bond as a fragmented line. Key distances in Å.

The possible participation of O_2^- in the reaction mechanism was also assessed, but the results were not definitive. More details regarding on the role of superoxide can be found in the SI, 3.7.6.

3.4.7 Proposed Reaction Mechanism

Based on the insights gained from the aforementioned control experiments, as well as the computational calculations, the following conclusions can be drawn: i) the thiadiazine SM is in the ground state when it participates in the ring contraction; ii) the reaction can be mediated solely by 1O_2 , but residual O_2^- produced by single electron transfer (SET)⁶⁴ between the 1O_2 and SM might also mediate the reaction by reacting with a S-centred radical cation; iii) the addition of the ROS to the thiadiazine appears to be concerted, as implied by the absence of a persulfoxide anion; iv) in asymmetric SMs, the electron withdrawing group (EWG) migrates preferentially, whereas the electron donating group (EDG) remains in the same position during the ring contraction, and; v) no exchange between R groups occurs during the ring contraction and/or carbon excision step. According to these observations, and literature precedents^{65,66} a plausible mechanism is proposed (Figure 11).

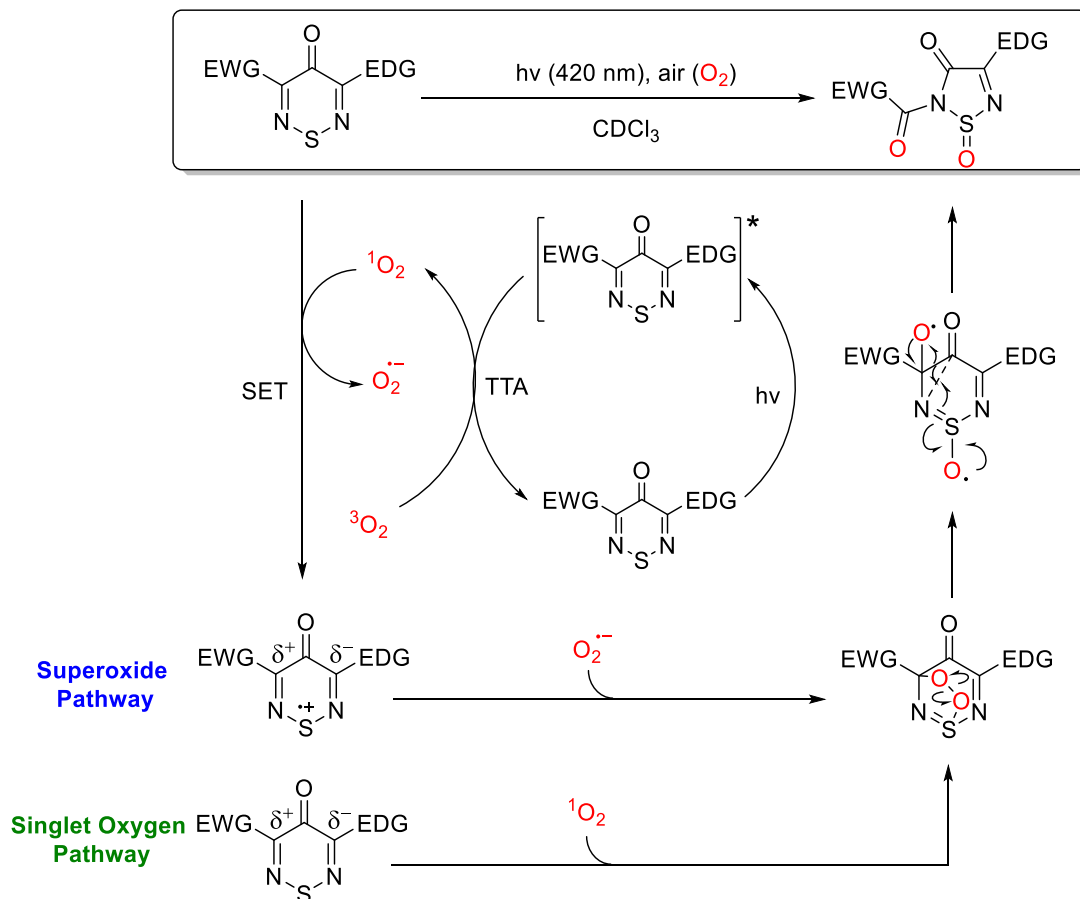


Figure 11. Proposed mechanism for the light mediated ring contraction of 1,2,6-thiadiazines to 1,2,5-thiadiazole 1-oxides.

Here, the thiadiazine SM, absorbs a photon producing its triplet excited state *via* intersystem crossing which can undergo triplet-triplet annihilation (TTA) with atmospheric oxygen ($^3\text{O}_2$) to produce $^1\text{O}_2$ and ground state SM, which can react in a [3+2] concerted fashion to form an endoperoxide bridge between the sulfur and the most electron deficient C=N carbon of the thiadiazine. To our knowledge, this is only the second known instance where $^1\text{O}_2$ participates in a [3+2] cycloaddition. The first one was reported in 2012 by Hilmey *et al.*, where $^1\text{O}_2$ reacted with pyridoxine to form a ring contracted lactam.⁶⁷ This is quite surprising as, $^1\text{O}_2$ in most cases undergoes either [4+2] or [2+2] cycloadditions.^{68,69}

Alternatively, the $^1\text{O}_2$ can receive an electron *via* SET from the ground state SM, to produce O_2^- and a radical cation of the SM, which can in turn react to form the same endoperoxide intermediate.⁷⁰ It has to be stressed, however, that the plausibility of this pathway is tenuous, as it is not supported by our theoretical calculations, and is based entirely on the use of various ROS trapping agents. While these can provide useful

mechanistic clues, their reliability is questionable, as their selectivity towards a specific ROS is not guaranteed.⁷¹ For instance, spin trap DMPO has been shown to form the EPR active 5,5-dimethyl-2-oxopyrroline-1-oxyl (DMPOX) when oxidised by $^1\text{O}_2$ under certain conditions.⁷² Another example is the ability of 1,4-benzoquinone (BQ), a commonly used $\text{O}_2^{\cdot-}$ scavenger,^{25,73} to also act as $^1\text{O}_2$ quencher, by forming exciplexes which can decay either chemically or physically.⁷⁴

Nevertheless, both proposed pathways lead to the formation of the same endoperoxide, which can then rapidly rearrange to form the ring contracted 1,2,5-thiadiazole 1-oxide.

3.5 Conclusions

In conclusion, the reported ring contraction of 1,2,6-thiadiazines mediated by visible light and air, provides an environmentally friendly, sustainable, and atom economic ring editing route to afford elusive 1,2,5-thiadiazole 1-oxides in quantitative or near quantitative yields with minimal workup, while tolerating a wide range of functional groups. We showed how flow photochemistry enabled us to access delicate substrates, unable to be obtained using conventional batch photochemistry. Additionally, asymmetric 1,2,6-thiadiazines bearing R groups with moderate or high difference in electronegativity produce 1,2,5-thiadiazole 1-oxides with 100% regioselectivity. Mechanistic studies revealed that the ring contraction is most likely driven by the rare [3+2] cycloaddition of $^1\text{O}_2$ to the ground state 1,2,6-thiadiazine, which gives rise to the aforementioned regioselectivity. An alternative process might be mediated by $\text{O}_2^{\cdot-}$, albeit its involvement at this point is inconclusive. Finally, we believe this ring contraction can be utilised to provide access to high value compounds that can be used in the pharmaceutical, agrochemical, or material science industries. Moreover, this transformation has the potential to be used on other heterocyclic scaffolds, which can greatly expand its future applicability.

3.6 Future Work

Additional work is needed to fully understand the mechanistic basis of the reaction, as it is still not clear why certain derivatives do not work (no reaction or decomposition), even with the addition of external ROS agents. Furthermore, the unexpected behaviour of the amino-substituted SMs needs to be investigated. Having a complete understanding of the reaction mechanism is imperative, as it will not only allow us to make predictions about the reactivity of SMs but also to design functionalised scaffolds that can participate in late-stage modifications. Computational calculations may provide valuable insights to achieve these goals.

It is conceivable that a compound containing two or more λ -orthogonal chromophores can be designed, in a way that separate transformations can occur depending on the irradiation wavelength that is used.

The results of this work on 4*H*-1,2,6-thiadiazine precursors can be used to test its applicability on the broader 1,2,6-thiadiazine family of compounds, as seen in Figure 12. It is reasonable to assume that if the attack by $^1\text{O}_2$ or O_2^- can occur, the intermediate endoperoxide can be accessed, and the ring contracted product will form. This infers that the thiadiazine SM only needs to have one double bond for the transformation to work. This substantially increases the available 1,2,6-thiadiazine SMs that can be tested, as there are more than 4000 reported compounds in that family.

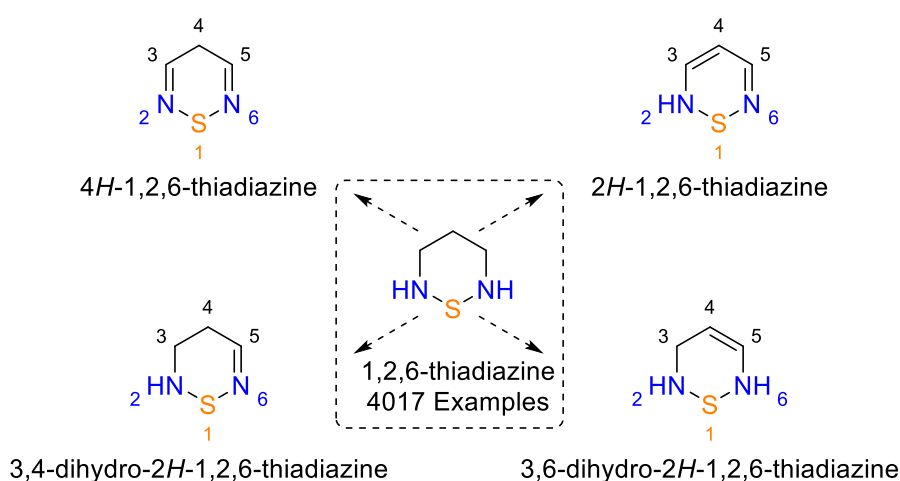
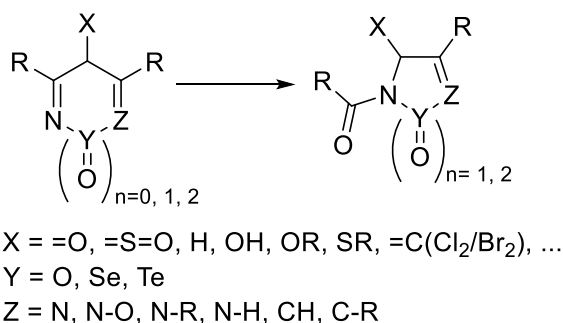


Figure 12. Different 1,2,6-thiadiazine scaffolds. Number of examples is based on data from the SciFinder[®] database (accessed on 21/5/2022).

Additional experiments are needed to fully gauge the importance of certain atoms on the transformation. As seen in Scheme 5, these include the substituent X attached on C4, the chalcogen atom Y and its oxidation state, and the heteroatom Z. Access to these precursors is not a trivial matter, and the development of new synthetic procedures for their synthesis is thus required.



Scheme 5. Possible modifications in the thiadiazine scaffold.

An additional proposal would be to test the effect of the heteroatom's position on the six-membered ring (Figure 13). For instance, there are several 1,2,5-, 1,2,3- and 1,3,5-thiadiazine scaffolds that are synthetically available and could be used for C or N atom excision purposes. Furthermore, the number of atoms on the thiadiazine core could also be altered. Seven-membered ring thiadiazines have been made before and could theoretically be used to form the corresponding 6-membered ring contracted 1-oxide products.

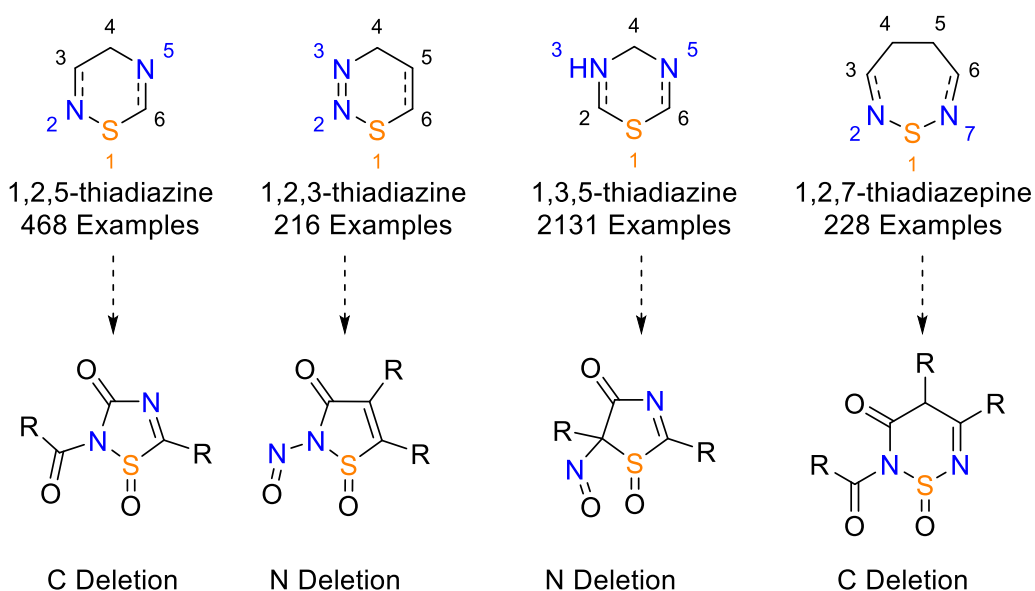
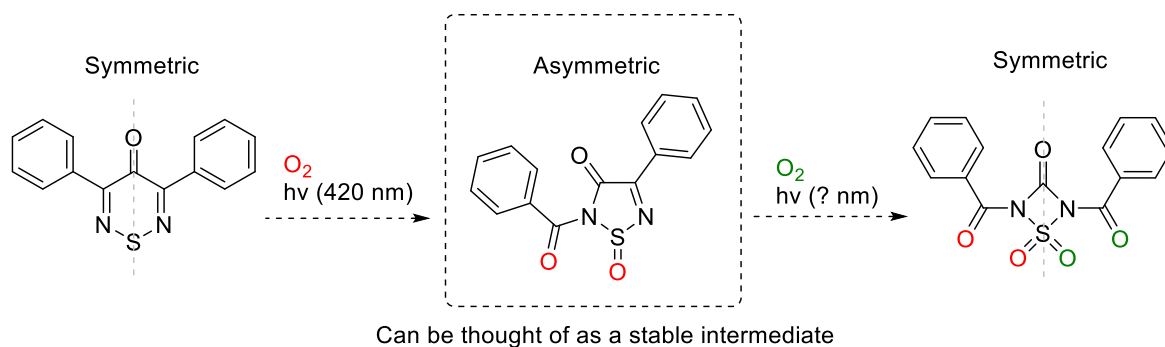


Figure 13. Different thiadiazine-based scaffolds that can be used in the future (with various degrees of unsaturation). The number of reported examples for each category was obtained by the SciFinder[®] database (accessed on 21/05/2022).

Another intriguing possibility lies in the ability of the reported 1,2,5-thiadiazole 1-oxides to be used as SMs to be further ring contracted to form the symmetric 1,2,4-thiadiazetidone 1,1-dioxides, as seen in Scheme 6. This 4-membered core has been reported before, meaning that the proposed compound could be stable.



Scheme 6. Proposed ring contraction of 1,2,5-thiadiazole 1-oxides to form 1,2,4-thiadiazetidone 1,1-dioxides.

It is possible that under the right conditions (UV light, increased O_2 pressure) this transformation could be achieved. In fact, when looking at the LC-MS chromatogram of **1b**'s (long) UV decomposition mixture, at least two minor peaks (<1%) with a mass identical to the expected 4-ringed sulfone were detected.

Additionally, this proposed compound closely resembles the broader family of β -sultams (1,2-thiadiazetidone 1,1-dioxides) which themselves are the sulfonyl analogues of the widely-known β -lactam based antibiotics (Figure 14a).⁷⁵ Compounds such as the 3-oxo- β -sultam and N-acyl- β -sultam shown in Figure 14b, have been shown to be 10^2 – 10^3 times more reactive than β -lactams toward alkaline hydrolysis, which represents one of the main mechanisms for their deactivation, making them useful surrogates for mechanistic elucidation.⁷⁶ Furthermore, they are potent inhibitors of various serine-based enzymes,⁷⁷ such as the Human Neutrophil Elastase (HNE),⁷⁸ a destructive protease that is involved in diseases such as cystic fibrosis, emphysema and rheumatoid arthritis. Thus, the proposed 3-oxo- β -sultam analogues, could prove to possess similar or even better biological utility.

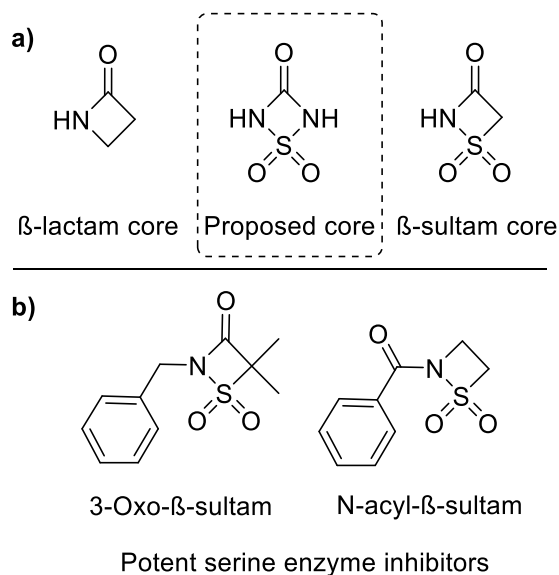
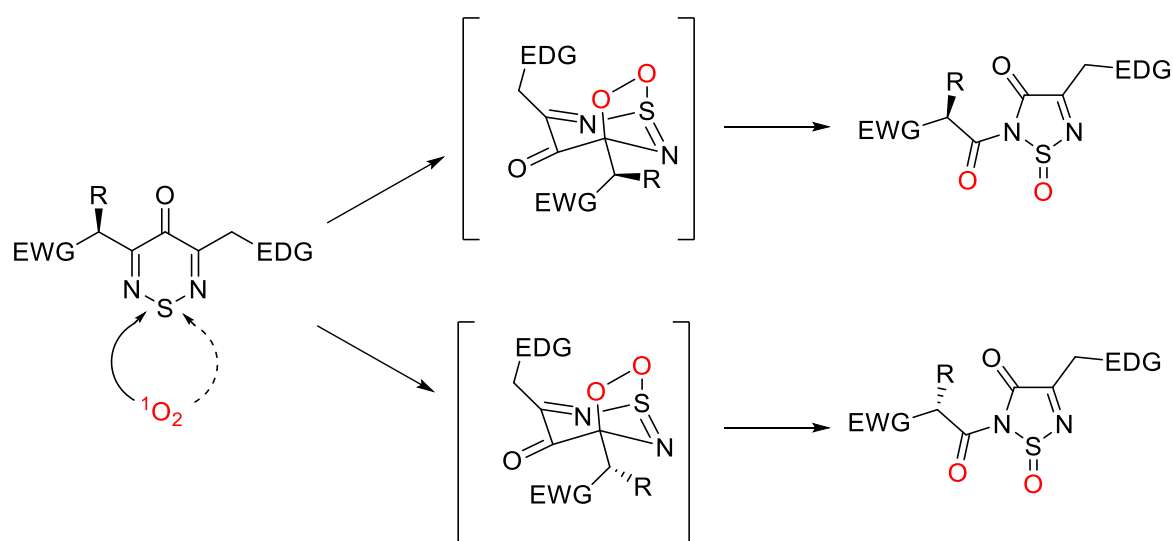


Figure 14. a) Comparison between proposed compound, and β -lactam, β -sultam cores. b) Known bioactive β -sultam compounds that highly resemble the proposed structure in Figure 13.

Another intriguing aspect of this ring contraction that is ought to be explored is how the presence of one or more stereogenic centres in the thiadiazine SM, affects the outcome of the reaction (Scheme 7). One might expect that the ROS will approach the SM at the least sterically hindered side, however whether the optical purity is retained, remains to be seen. Since we have already established that the regioselectivity in asymmetric derivatives depends on the relative electronegativities of the C3- and C5 substituents, by introducing one or more chiral centres it is expected that the result will be quite challenging to predict.



Scheme 7. A hypothetical ring contraction where a chiral thiadiazine is used as the SM. The endoperoxide intermediates are shown in brackets.

Finally, inspired by the M_2L_4 coordination cages bearing 2,6-bis(pyridin-3-ylethynyl)pyridine ligands developed by Lusby *et al.*,^{79,80} we believe that using substituted 1,2,6-thiadiazines as ligands to form photoactive metal-organic cages is worth investigating. As seen in Figure 15b, the proposed thiadiazine-based ligands are structurally very similar to Lusby's pyridine ligands and could thus form cages that can change shape when irradiated.

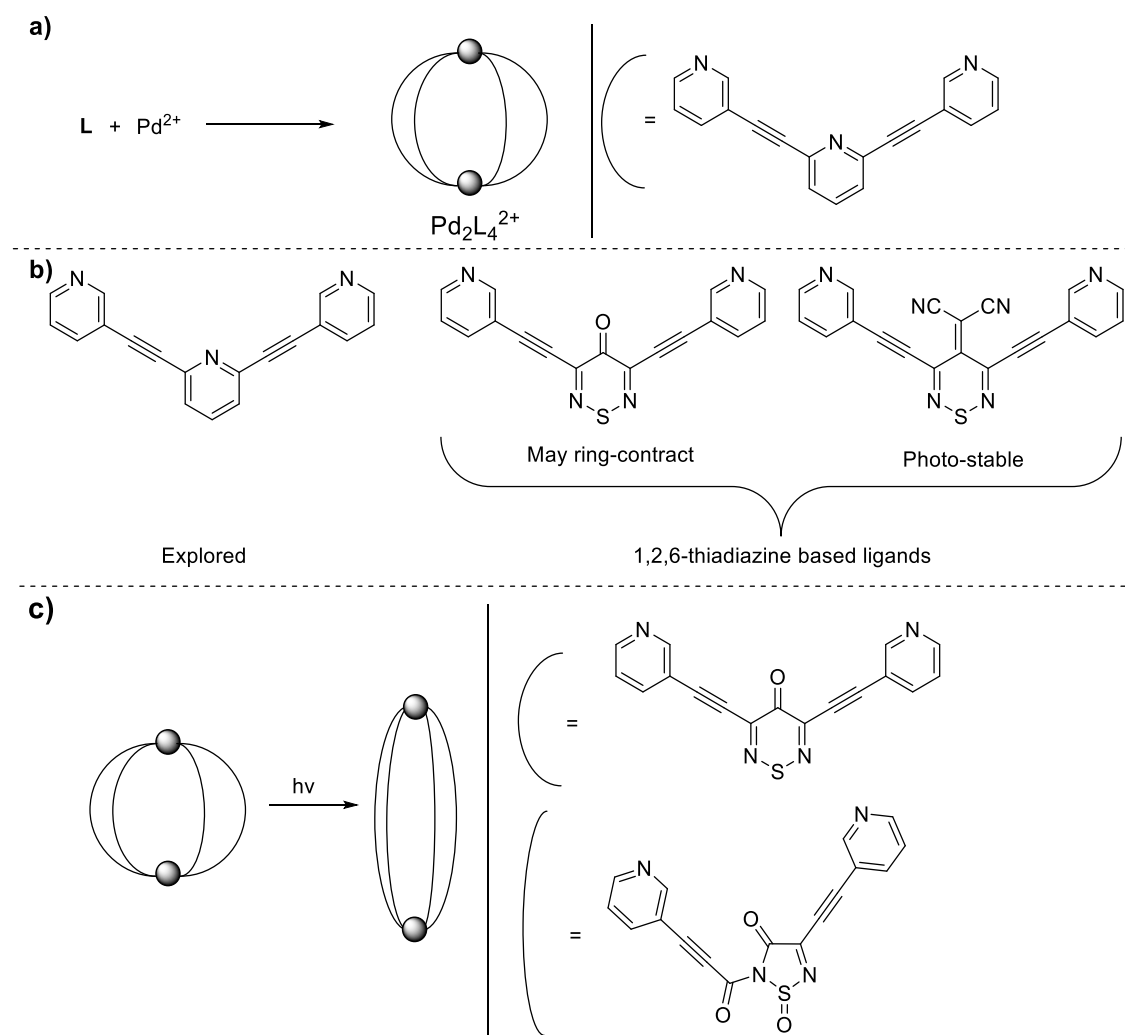


Figure 15. a) M_2L_4 coordination cage using Pd^{2+} and an organic ligand. b) Comparison between Lusby's pyridine based ligand and closely-related 1,2,6-thiadiazine analogues. c) Graphical representation of a thiadiazine-based cage ring contracting under light exposure.

The suitability of the proposed C4-carboxy thiadiazine-based ligand was tested by using the CGbind computational platform.⁸¹ Interestingly, if the ring contraction will occur in the metal cage in the same manner that it does with the free ligand the shape of the cage changed from a 'sphere' (120 \AA^3 enclosed sphere) to a 'tube' (1.41 \AA^3 enclosed sphere), as depicted in Figure 15c. This could be used to eject potential hosts when

the cage/host system is irradiated with light. The host affinity algorithm predicted that Quinone (guest used by Lusby⁸⁰) binds better in the proposed cage than the original one (confidence 0.952 vs 0.747 respectively). The thiadiazine cage also has the 4 carbonyl O atoms pointed towards the inside of the cavity, which means they can be used to trap guests *via* H-bonding interactions. Photo-stable thiadiazine cages may also be synthesised, by using a ligand that is unreactive under the conditions developed in this work. For instance, C4-ylidenemalonitrile thiadiazine (Figure 15b) should in principle form a photo-stable cage. By using two different ligands (reactive and unreactive), it should also be possible to form heteroleptic cages, which can partially ring-contract under irradiation.⁸²

So far, in chapters 2 and 3 we have demonstrated how flow chemistry can be used to enable the usage of new photoactive materials and expand the reaction scope of batch methodologies. Next, in chapters 4 and 5, we will focus on the benefits of mechanochemistry and 3D printed reactionware.

3.7 Supporting Information

3.7.1 Comparison Between 1a and 1b As Seen by NMR, FT-IR and UV-Vis

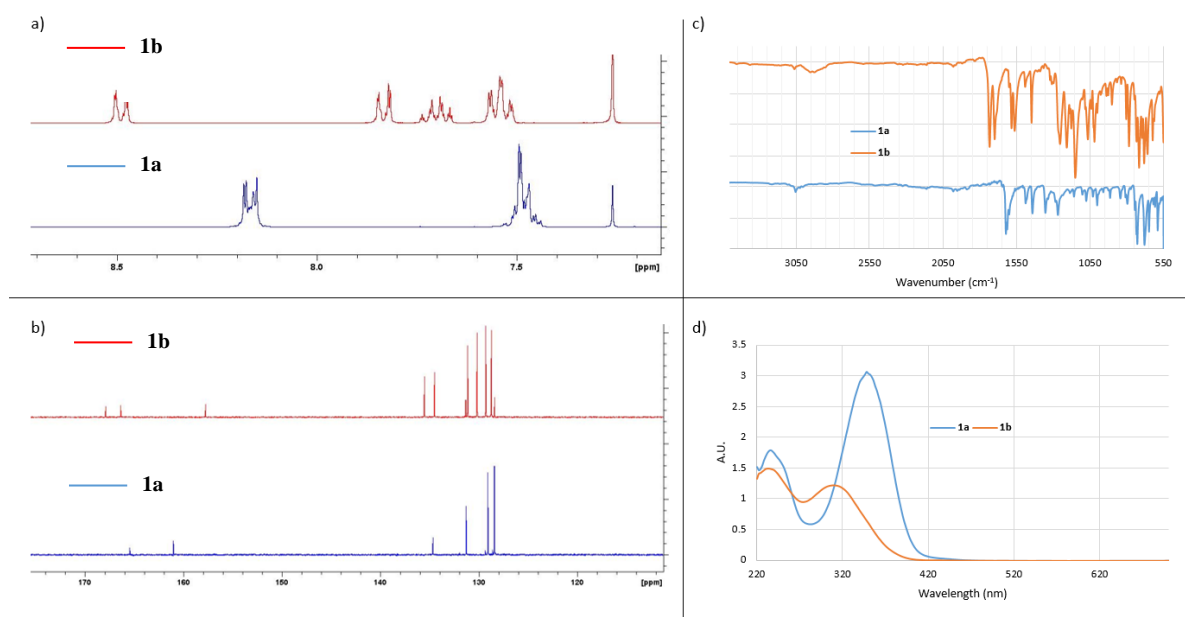


Figure S1. Spectroscopic comparison between the starting material **1a** and product **1b**. a) ¹H NMR, b) ¹³C NMR, c) FT-IR, d) UV-Vis, C = 6.8×10^{-5} M.

When looking at the ^1H NMR spectra of compounds **1a** and **1b** (Figure S1, a), the most striking difference stems from the number of peaks in the aromatic region. While the two Ph- groups of **1a** are represented by 2 multiplets at 8.17 (4H), and 7.47 (6H) ppm, the same Ph- protons of product **1b** are split into 4 multiplets, at 8.49 (2H), 7.83 (2H), 7.74 (2H), and 7.54 (4H) ppm. Consequently, as both compounds have the same number of protons, this increase in the number of signals signifies that in product **1b**, the Ph- groups are not equivalent, meaning that the compound has lost its original symmetry. Furthermore, the downfield shift of 2 protons (peak at 8.49 ppm), suggests that they reside next to an electron withdrawing moiety or are deshielded.

A substantial increase in complexity was also observed at the corresponding ^{13}C NMR spectrum of product **1b**, when compared with that of thiadiazine **1a** (Figure S1, b). The formation of a new carbonyl group can be inferred, judging by the presence of 2 peaks in the 165-170 ppm region of the spectrum (as opposed to 1 peak in **1a**). This was further confirmed when the FT-IR spectra of the two compounds were compared (Figure S1, c), as compound **1b** appears to have two strong C=O stretches at 1733 and 1699 cm^{-1} , whereas **1a** has only one, at 1622 cm^{-1} . The product also has a medium/strong absorption at 1066 cm^{-1} which can be tentatively ascribed to an S=O stretch (sulfoxide) and is absent from the IR spectrum of the starting material.

Finally, the UV-Vis absorption spectra of compounds **1a** and **1b** were collected (Figure S1, d). The starting material **1a**, has a planar geometry (SI, 3.7.7), is conjugated and mildly aromatic leading to an absorption profile that extends into the visible wavelengths (up to 450 nm), making its solutions yellow in colour. Conversely, solutions of the product **1b** appear colourless, and its UV-Vis spectrum shows a substantial blue-shifting of its peaks has taken place.

3.7.2 Reaction Optimisation Under Continuous Flow Conditions (Method B)

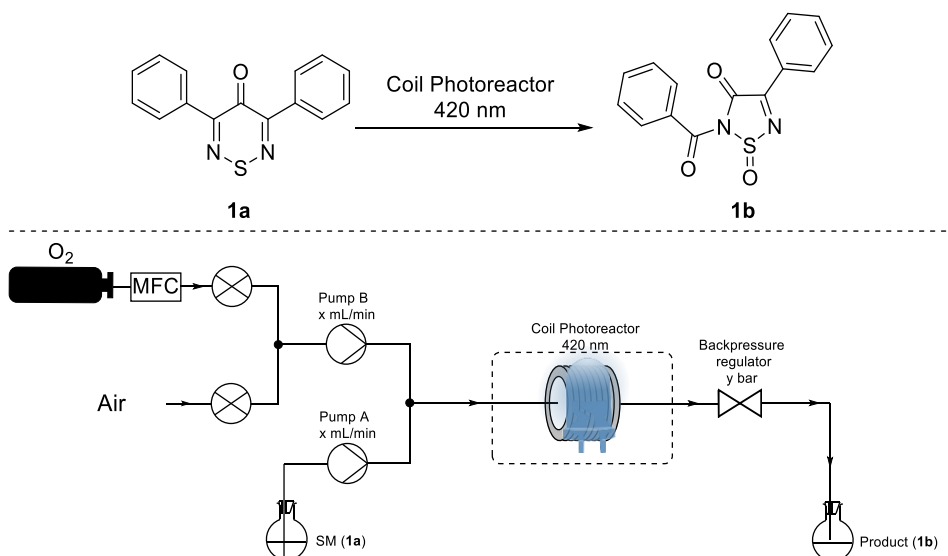


Figure S2. Diagram showing the experimental set-up that was used for the optimisation of the ring contraction under continuous flow conditions.

To determine the optimal reaction conditions under continuous flow conditions, we used the commercial E-series Photochem UV-150 reactor (420 nm LED module) by Vapourtec Ltd. The coil reactor consisted of commercially available, clear PTFE tubing (internal diameter 1 mm). The total internal volume of the coil reactor was 3.33 mL. As seen in Figure S2, two peristaltic pumps were used. The first one (pump A) pumped a solution of **1a** ($C = 37.5$ mM) in 100 mL of dimethyl carbonate (DMC). DMC was selected for the optimisation runs as it is a green solvent and performed comparable to $CHCl_3$ in batch conditions. The second pump, (pump B), was used to introduce either air from the atmosphere, or pure O_2 . The two fluids were then mixed at a T-junction, creating a plug-flow regime, which entered the coil reactor. The contents of the reactor were illuminated by the Photochem module. It is noted that the heat generated by the LEDs, raised the temperature inside the coil reactor to 29 °C (steady state). The residence time of the fluid was regulated by changing the flow rates of pumps A + B accordingly. Upon exiting the reactor, the fluid was then passed through a backpressure regulator (BPR, 0-10 bar). It was observed that when the pressure was raised above 2 bar, the flow regime changed from plug to continuous. Finally, the fluid was collected in a 10 mL round bottom flask. Both flasks (SM + product) were covered in aluminium foil for the duration of the experiments to protect the compounds from external ambient light sources. The performance of each run was evaluated by subjecting the contents of the collection flask to HPLC analysis and measuring the percentage of unreacted **1a** (Figure S3, a).

The parameters that were tested during the optimisation runs included the gaseous source (air/O₂) and the effect of pressure (0, 1, 3, 5, and 7 bar), at four different residence times (0.5, 1, 5, and 10 min). As expected, in all cases it was observed that by increasing the residence time, more SM **1a** was consumed. By using the data generated for the four residence times, the average performance was calculated to reveal the central tendency for each parameter group. The percentages on the y axis were normalised to 100 (with respect to the 'air' group), creating a performance score, between 0 and 100 (100 being the worst). (Figure S3, b). Substantial lowering of the score was seen when air was replaced by O₂ and by increasing the external pressure. However, after 1 bar, the effect of increased pressure on the lowering of the score was not as pronounced. Overall, the lowest score was obtained when O₂ was used at 7 bar (85.6), however, the difference from 3 bar (87.2) was not substantial. Moreover, above 5 bar, it became more difficult to maintain a constant pressure throughout the experiment, and continuous input was required by the operator to ensure the pressure did not deviate. For those reasons, the optimal conditions that were adopted for use during the reaction scope experiments, were external O₂, at 3 bar.

Safety statement for flow chemistry manipulations

The flow machine that was used for the experiments in this chapter was placed inside a fume hood equipped with an extraction fan. The sash window of the fume hood was lowered when the flow machine was in operation to minimise the risk of accidental solvent/chemical vapour release into the surrounding area. When the flow machine was used to perform reactions under high pressure, a test run was initiated first, where only solvent was circulated under pressure for a period of 15 min. This was done to ensure that the pressurised section of the line (between the peristaltic pump and the back pressure regulator) was stable and did not leak, thus minimising the risk of an uncontained loss of pressure and/or spillage during the experiment. In addition to the pressure checks, the reactor tubing was visually checked for blocks or cracks before each experiment was performed. If any anomaly was detected, appropriate steps were taken to mitigate the issue (e.g., by replacing damaged parts). When a gaseous reagent was used (e.g., oxygen), the gas flow to the flow machine's peristaltic pump was regulated by a mass flow controller device (MFC). At the end of each session, all of the lines were depressurised, and flushed several times with clean solvent.

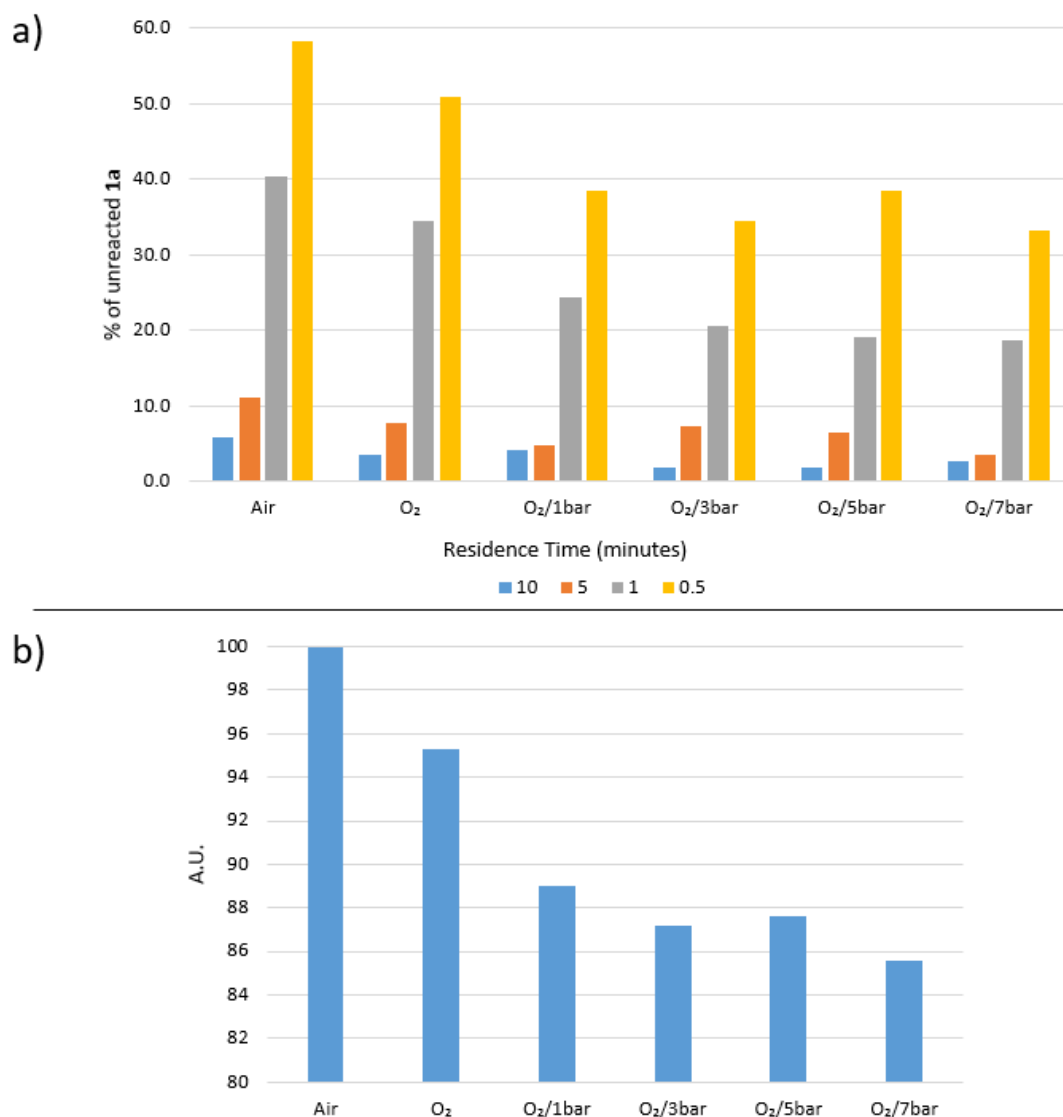


Figure S3. Results of the flow optimisation studies. a) Percentage of unreacted SM for six (gas/pressure) groups for four different residence times. b) Averaged and normalised data for each group.

After having these optimal conditions in hand, we switched the solvent from DMC to CDCl_3 , to ensure that the overall residence time needed for complete consumption of SM **1a** was minimised, protecting the newly formed 1,2,5-thiadiazole S-oxide **1b** from photodecomposition. To our surprise, when the residence time was set at 30 seconds, only 0.8% of thiadiazine **1a** remained unreacted. When the contents of the collection flask were passed a second time through the system, no SM **1a** was detected, and product **1b** was obtained with a quantitative yield.

3.7.3 Photographs of Experimental Setup (Method A and Method B)

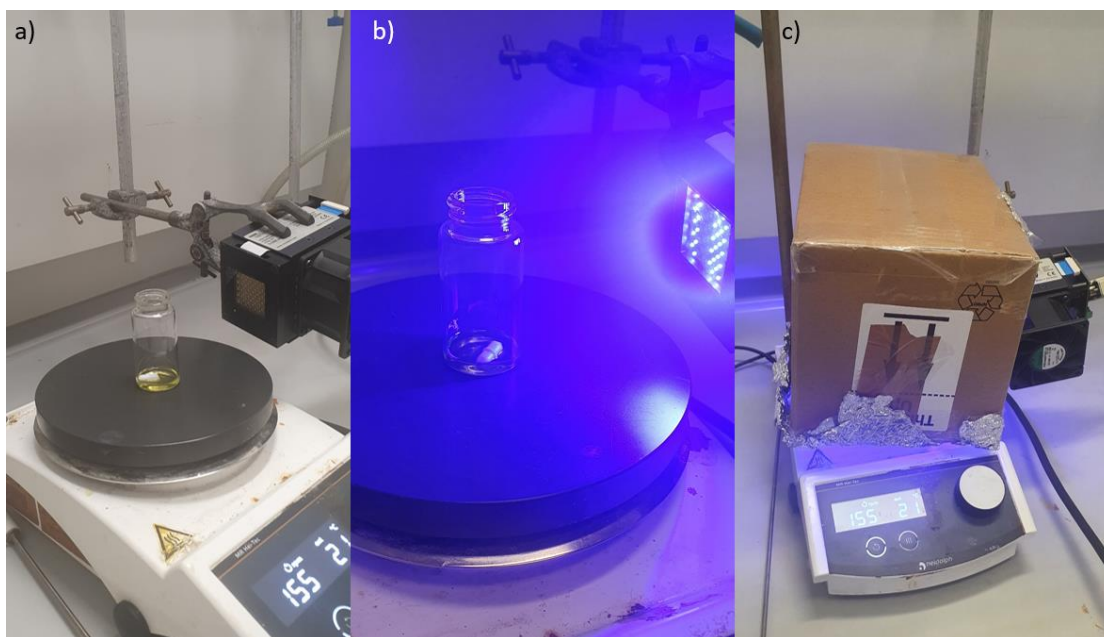
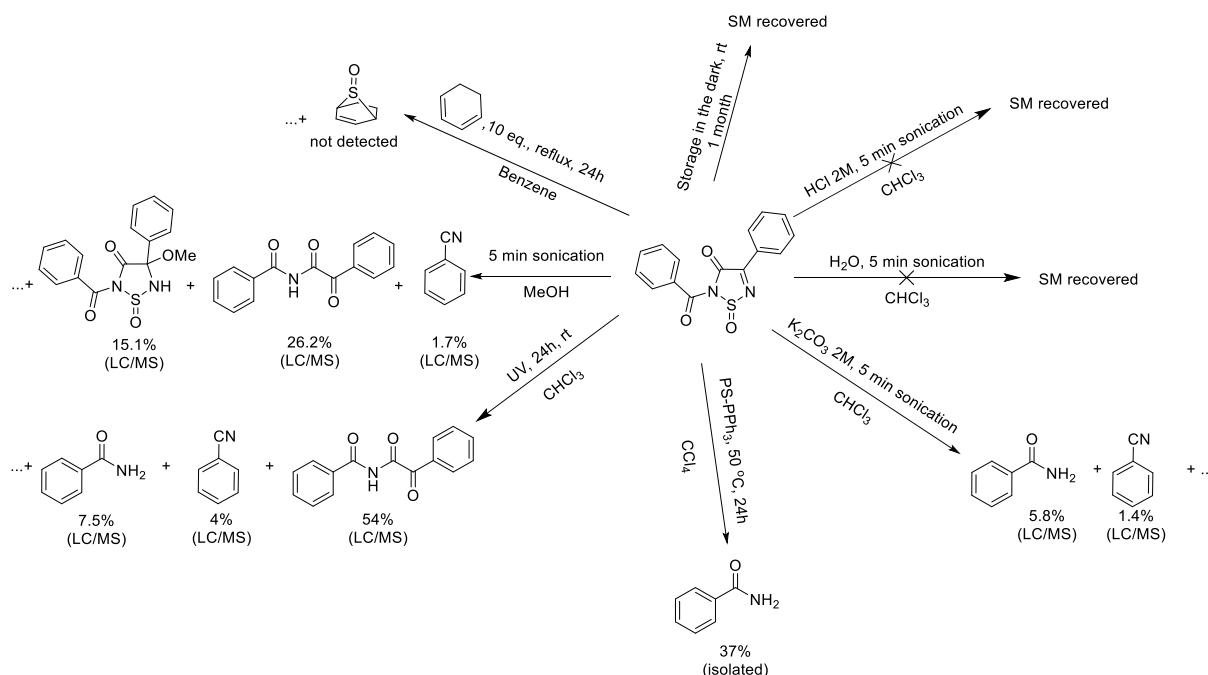


Figure S4. Photographs of batch setup (Method A). a) A 5 mL vial charged with 1,2,6-thiadiazine SM dissolved in 1 mL of CDCl_3 . The lid is not used to allow atmospheric O_2 in the vial. b) Reaction underway. c) A cardboard box lined with aluminium foil is placed on top of the hotplate to limit photon leakage and ensure the safety of the operator.



Figure S5. Photographs of the flow reaction setup (Method B). a) Vapourtec E-series equipped with the Photochem UV-150 module. b) Close-up photograph of the UV-150 reactor during operation. The tube on the left containing the yellow-coloured solution is flowing towards the reactor. The tube of the right is the outlet of the reactor, and as it can be seen, the fluid is colourless, indicating that the reaction is complete.

3.7.4 Stability Profile of 2-Benzoyl-4-phenyl-1,2,5-thiadiazol-3(2H)-one 1-oxide (**1b**)

Scheme S1. Various decomposition pathways for **1b**. For each experiment, a stock solution (10 mg (0.0375 mmol) of **1b** (SM) dissolved in 1 mL of CHCl_3) was used.

To better understand the overall stability of compound **1b**, a series of experiments were conducted, as shown in Scheme S1. Initially, 1 mL of H_2O was added in the stock solution and the biphasic mixture was sonicated for 5 min. After the aqueous layer was removed, the organic solvent was evaporated, and the resulting residue was analysed by ^1H NMR, which indicated the residue was clean **1b** and no decomposition had taken place. Similarly, the same experiment was performed by adding aqueous HCl (2M) and K_2CO_3 (2M): Under the acidic conditions, the SM was isolated intact, however under basic conditions and after work-up a brown tar was obtained with a sharp odour resembling burning rubber. Subsequent analysis of the residue by LC-MS revealed a complex mixture of decomposition by-products. Whilst most of those products could not be recognised, benzamide (5.8%) and benzonitrile (1.4%) were conclusively identified, by comparison with pristine samples in conjunction with their respective MS and UV-Vis traces. An attempt was made to deoxygenate the sulfoxide **1b**, by employing known deoxygenation procedures^{83,84} that use free or polymer-bound Ph_3P in the presence of CCl_4 , however, after the reaction mixture was worked-up benzamide was isolated (37%) instead of the desired sulfide. The photostability of sulfoxide **1b** was then assessed by

employing a far UV LED lamp, which overlaps with its absorption UV-Vis spectrum. After 24 hours of irradiation, and removal of the solvent, a residue was isolated with a distinct smell of bitter almonds. After subsequent LC-MS analysis, the source of the smell was attributed to benzonitrile (4%). In addition, benzamide was also present (7.5%), however, the majority of the mixture consisted of *N*-(2-oxo-2-phenylacetyl)benzamide (54%), an α -ketoimide, which was confirmed by comparison with an independently synthesised sample.⁸⁵ Interestingly, α -ketoimides are useful bioactive compounds that are traditionally made using transition metal catalysts, or under harsh conditions.^{86,87} The isolation of this elusive compound by the photodecomposition of sulfoxide **1b** represents a new and benign avenue for obtaining these compounds and will be explored further. To our surprise, when CHCl₃ was substituted by MeOH, sulfoxide **1b** was partially decomposed within 5 min. After removal of the solvent a clear oily residue was obtained which contained multiple decomposition by-products, as seen by its LC-MS chromatogram (Figure S6, a). Those included benzonitrile (1.7%) and *N*-(2-oxo-2-phenylacetyl)benzamide (26.2%), which could be assigned with certainty, as they were compared with clean, reference compounds.

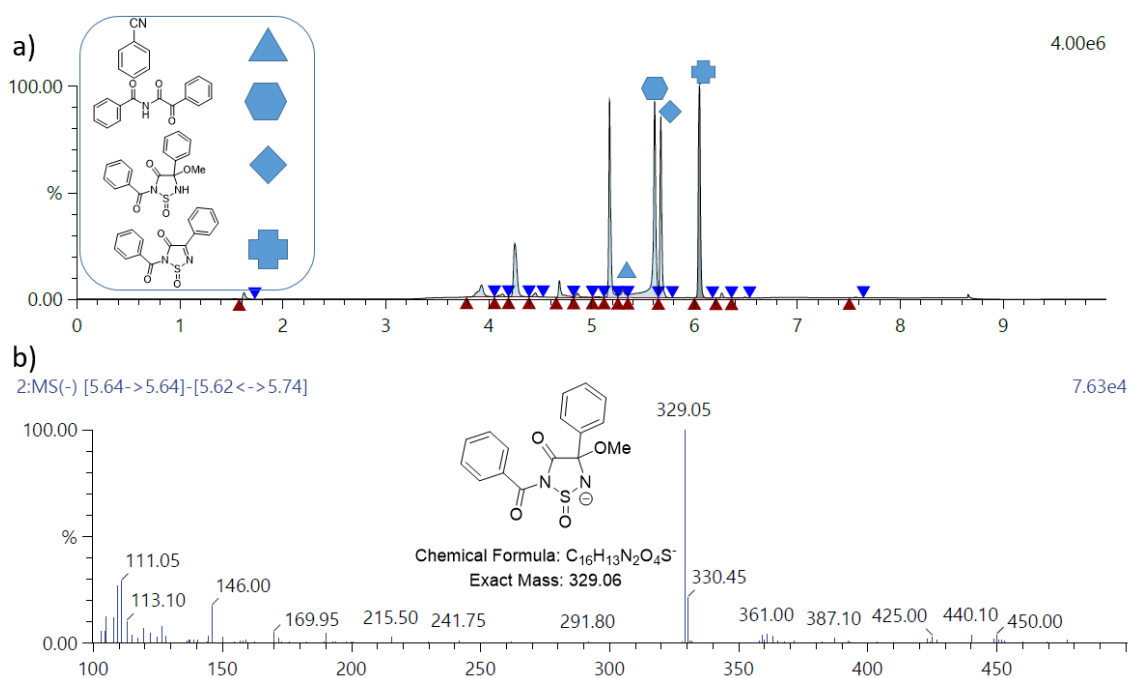


Figure S6. a) LC trace of the partial decomposition of **1b** when it was treated with MeOH. b) MS(EI-) spectrum of the putative by-product 2-benzoyl-4-methoxy-4-phenyl-1,2,5-thiadiazolidin-3-one 1-oxide.

The nucleophilic nature of MeOH, allows it to attack *S,N*-heterocyclic compounds, as it has been demonstrated before.³⁸ As such, and based on the corresponding MS data, we

were able to identify 2-benzoyl-4-methoxy-4-phenyl-1,2,5-thiadiazolidin-3-one 1-oxide as a possible by-product (15.1%) (Figure S6, b).

We then wanted to evaluate the potential of sulfoxide **1b** to act as a sulfur monoxide (SO) source. It has been shown that certain compounds containing the SO moiety can be used as SO generators by means of thermal decomposition.^{88,89} Treatment of compound **1b** with known SO trap 1,3-cyclohexadiene in benzene heated at reflux over a period of 24 hours led to its decomposition without producing any of the expected SO transfer product, indicating that SO is likely not one of the decomposition by-products. Furthermore, we illustrated that sulfoxide **1b** is shelf-stable for at least 1 month, when stored at room temperature in darkness. Finally, compound **1b** was found to be unstable in silica (SiO₂), making traditional TLC and chromatographic manipulations incompatible with this compound. Changing the acidic properties of silica by adding small amounts of trimethylamine (TEA, 1%), did not alter the behaviour of the compound.

The thermal stability profile of compound **1b** was examined by thermogravimetric analysis (TGA) as shown in Figure S7.

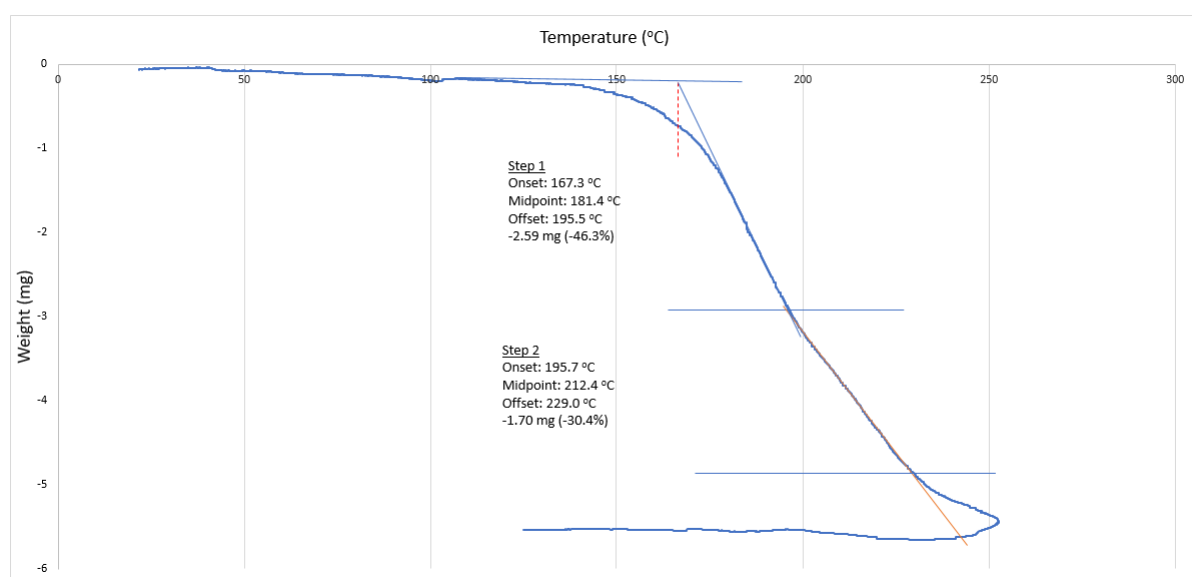


Figure S7. TGA thermogram of 2-benzoyl-4-phenyl-1,2,5-thiadiazol-3(2H)-one 1-oxide (**1b**). Initial sample weight was 5.6 mg. The sample was placed into an aluminium pan and heated to 252 °C, under a stream of N₂ at a rate of 1 °C/min.

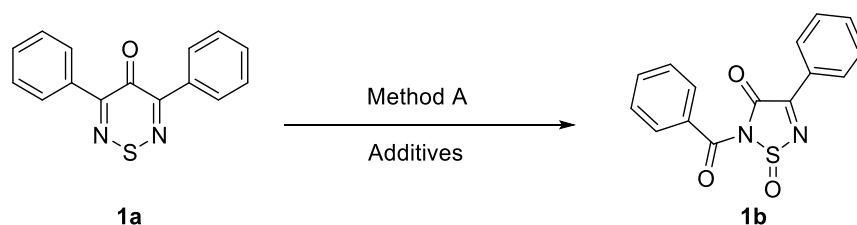
The thermogram showed a small (4.46%) weight loss between 22.9–141.7 °C which can be attributed to residual moisture within the sample and its potential sublimation. Following that, the thermogram shows a substantial 46.3% weight loss with an onset

temperature of 167.3 °C, which closely matches the observed hot-stage melting point of sulfoxide **1b** at 171-172 °C. This indicates that the product rapidly decomposes when it reaches its melting point. A subsequent weight loss of 30.4% was observed, with an onset temperature of 195.7 °C. Notably, a 34.6% loss is equivalent to the loss of benzonitrile, a common decomposition fragment based on the studies above (Figure S7).

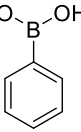
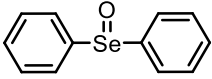
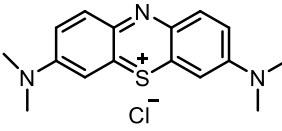
3.7.5 Additional Mechanistic Experiments

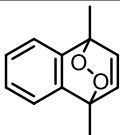
3.7.5.1 Control Experiments

Table S1. Control experiments for the ring contraction of **1a** to **1b** (Method A).



Entry	Additive	Function	Solvent	Light wavelength h (nm)	Reaction time (min)	Conversion to 1b (%)
1	TEMPO, 2 equiv.	Radical trap ⁶⁶	CDCl ₃	420	45	100
2	DABCO, 2 equiv.	¹ O ₂ trap ⁹⁰	CDCl ₃	420	1440	trace
3	Ph ₃ P, 2 equiv.	¹ O ₂ trap ⁹¹	CDCl ₃	420	120	100
4	<i>t</i> -BuOH, 2 equiv.	OH ⁻ trap ⁹²	CDCl ₃	420	15	100
5	1,4-benzoquinone, 2 equiv.	O ₂ ⁻ trap ⁹³	CDCl ₃	420	45	100
6	DMPO, 5 equiv.	O ₂ ⁻ trap ⁹³	CDCl ₃	420	1440	0, 33% of 1a left

Entry	Additive	Function	Solvent	Light wavelengt h (nm)	Reaction time (min)	Conversion to 1b (%)
7^a	 + 2 eq. DIPEA	O ₂ ⁻ trap ⁹⁴	DMF	390	120	Complete consumption of 1a , 1b not detected.
8	CuCl ₂ , 2 equiv.	SET trap ⁶⁶	Aceton e -d ₆	420	1440	trace
9	1,4-dimethoxybenzene	R ₂ S ⁺ trap ²⁵	CDCl ₃	420	120	100
10	 2 equiv.	Persulfoxide trap ⁹⁵	CDCl ₃	420	15	100
11	 1 mol%	ROS sensitizer ⁴⁸	CDCl ₃	620	60	100
12	CaO ₂ ·2H ₂ O ₂ , 5 equiv.	dark ¹ O ₂ generator ⁹⁶	CDCl ₃	-	120	0
13	CaO ₂ ·2H ₂ O ₂ , 5 equiv.	dark ¹ O ₂ generator	THF- <i>d</i> ₈	-	120	48
14	CaO ₂ ·2H ₂ O ₂ , 5 equiv. + 1,4-benzoquinone, 5 equiv.	dark ¹ O ₂ generator + O ₂ ⁻ trap	THF- <i>d</i> ₈	-	1440	0, 55% of 1a recovered

Entry	Additive	Function	Solvent	Light wavelength (nm)	Reaction time (min)	Conversion to 1b (%)
15	 5 equiv.	dark $^1\text{O}_2$ generator ⁹⁷	CDCl_3	-	60	57
16	KO_2 in 18-crown-6 (50:50), 5 equiv.	$\text{O}_2^{\cdot-}$ source ⁹³	DMSO- d_6	-	1440	0
17	KO_2 in 18-crown-6 (50:50), 5 equiv., N_2	$\text{O}_2^{\cdot-}$ source	DMSO- d_6	420	1440	0

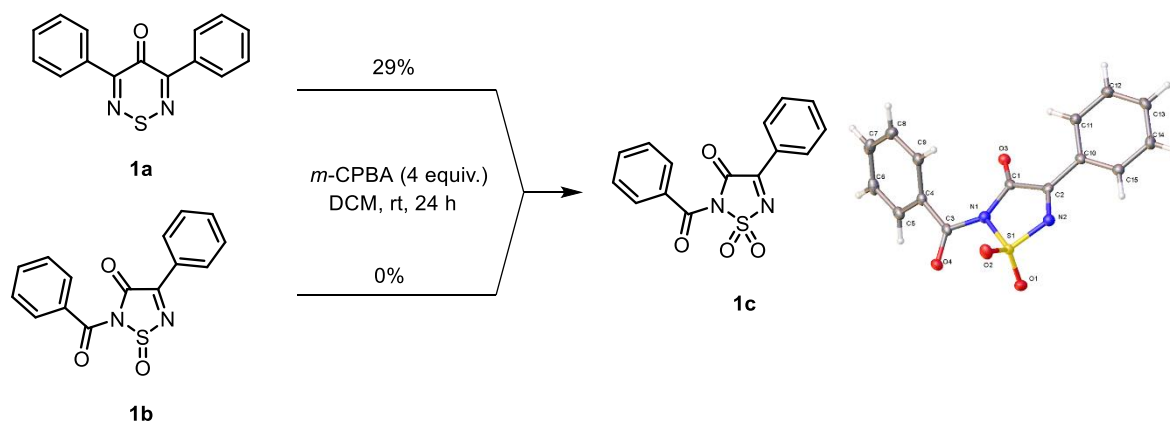
^a **1a** was used as a catalyst (1 mol%). After the reaction was complete, phenol was detected (65% ^1H NMR yield).

To gain insight into the underlying mechanism that drives the ring contraction, a series of control studies were conducted (Table S1). When TEMPO was added (Table S1, entry 1) the reaction required 45 min for completion instead of 15, which implies the involvement of radical species. DABCO and Ph_3P (Table S1, entries 2,3) were used as selective $^1\text{O}_2$ traps and both stalled the reaction; the former completely inhibited the formation of sulfoxide **1b**, while the latter increased the reaction time to 120 min with concomitant production of $\text{Ph}_3\text{P}=\text{O}$, which was detected by ^{31}P NMR. These results, along with the impact of deuterated solvents on the reaction times offer compelling evidence that $^1\text{O}_2$ is involved in the ring contraction.

The addition of *t*-BuOH (Table S1, entry 4), a hydroxyl radical (OH^{\cdot}) trap, did not affect the reaction time or the conversion percentage, and thus hydroxyl radical participation was excluded from the mechanism. We then used 1,4-benzoquinone (BQ), a well-known $\text{O}_2^{\cdot-}$ trap (Table S1, entry 5), which slowed the reaction time to 45 min, indicating the potential involvement of $\text{O}_2^{\cdot-}$ radicals. The participation of $\text{O}_2^{\cdot-}$ was further supported by using the trap 5,5-dimethyl-1-pyrroline-*N*-oxide (DMPO) as additive (Table S1, entry 6) and **1a** as a catalyst for the aerobic hydroxylation of phenylboronic acid to phenol, which is mediated by $\text{O}_2^{\cdot-}$ (Table S1, entry 7). Furthermore, when CuCl_2 was used (Table S1, entry 8), the reaction failed completely, implying that single electron transfer (SET)

processes were needed for the ring contraction to occur. When 1,4-dimethoxybenzene, a sulphide radical trap was added (Table S1, entry 9), formation of sulfoxide **1b** was suppressed, taking 2 hours for full consumption of SM. In addition, we also employed diphenylselenoxide (Table S1, entry 10), which selectively reacts with persulfoxide anions ($R-S^+OO^-$) to form diphenylselenone, however in our case, LC-MS analysis showed the absence of the selenone and the reaction time was unaffected, which makes the involvement of persulfoxide anion intermediates unlikely.

A series of known dark 1O_2 sources were also investigated to assess the role of light on the reaction mechanism. These included an orthogonal photosensitiser, methylene blue (Table S1, entry 11), and two dark 1O_2 generators, which slowly release 1O_2 in solution at room temperatures (Table S1, entries 12–15). In all cases, the sulfoxide **1b** was formed, albeit not quantitatively. Interestingly, when an excess of BQ was used together with the generator $CaO_2 \cdot 2H_2O_2$ (Table S1, entry 14), the SM **1a** was not fully consumed, providing further evidence that O_2^- participates in the reaction mechanism. Furthermore, since the reaction was performed under dark conditions, there was no source of O_2^- , meaning that it may be generated by the interaction between 1O_2 and **1a**. We then employed a dark source of O_2^- (table S1, entries 16 & 17), and no conversion was observed.

3.7.5.2 Reaction Between **1a** and *m*-CPBA to Form Sulfone **1c**

Scheme S2. Oxidation of **1a** by *m*-CPBA to form sulfone **1c**, and its SC-XRD crystal structure.

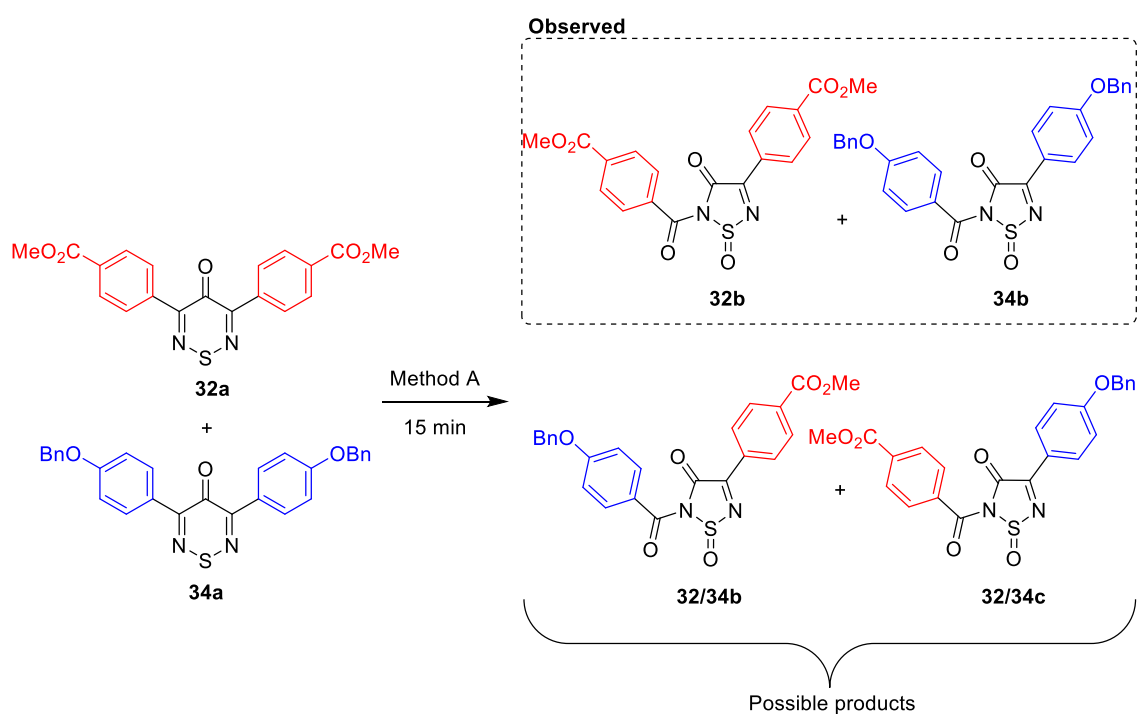
In an attempt to explore the reactivity of thiadiazine **1a** towards alternative oxidants, an unexpected discovery was made; when *m*-CPBA (4 equiv. in total) was added in a DCM solution ($c = 37.5$ mM) of **1a**, a gradual colour change was observed over 24 h (Scheme S2). Upon working up the reaction mixture, a colourless solid was isolated in 29% yield. It was believed that the solid could be the sulfoxide of the SM **1a**, as it has been shown previously that treatment of electron rich 1,2,6-thiadiazines with *m*-CPBA or N_2O_4 can yield the corresponding sulfoxides.⁹⁸ If that had occurred with **1a**, we would expect that its sulfoxide would indeed be a colourless compound, as the presence of the sulfoxide group would lead to less delocalisation of the electron density, and a widening of the HOMO-LUMO gap, resulting in blueshift of its absorption spectrum.⁹⁹

Conversely, the product's asymmetric 1H NMR spectrum (SI, 3.8.4) meant that the opposite had happened. Surprisingly, the IR spectrum of this unknown solid revealed the presence of a sulfone, based on the strong band at 1300 cm^{-1} , along with two $C=O$ stretching bands. NMR spectroscopic analysis also showed a marked similarity to the spectra of 1,2,5-thiadiazole *S*-oxide **1b**. Furthermore, the compound appeared to have the same behaviour when interacting with silica (decomposition).

Finally, the structure was fully elucidated by SC-XRD, revealing it to be 2-benzoyl-4-phenyl-1,2,5-thiadiazol-3(2*H*)-one 1,1-dioxide (**1c**). Interestingly, when the same treatment with *m*-CPBA was enacted on **1b**, no reaction occurred, and the sulfoxide **1b** was recovered. Tentatively, this suggested that the reaction mechanism for the formation of sulfone **1c**, did not involve the formation of sulfoxide **1b**, and that the transformation

follows a different mechanism. Studies are currently underway to further investigate this alternative ring-contraction pathway.

3.7.5.3 Concurrent Ring Contraction of Two Symmetrical 1,2,6-thiadiazines



Scheme S3. Anticipated outcomes when two symmetrical 1,2,6-thiadiazines are irradiated in one-pot, under the optimised batch conditions (Method A).

To help us obtain more mechanistic clues about the light-driven ring contraction, we conducted a crossover experiment to test the outcome of the reaction when two different symmetrical 1,2,6-thiadiazines were irradiated together. If any of the substituted aryl moieties detach from the thiadiazine core during the contraction, then in principle we should observe asymmetrical 1,2,5-thiadiazine 1-oxides being formed (Scheme S3).

However, subsequent spectroscopic evidence (Figure S8) proved that only the expected symmetric products are formed, indicating that the rearrangement that takes place during the ring contraction is intramolecular in nature.

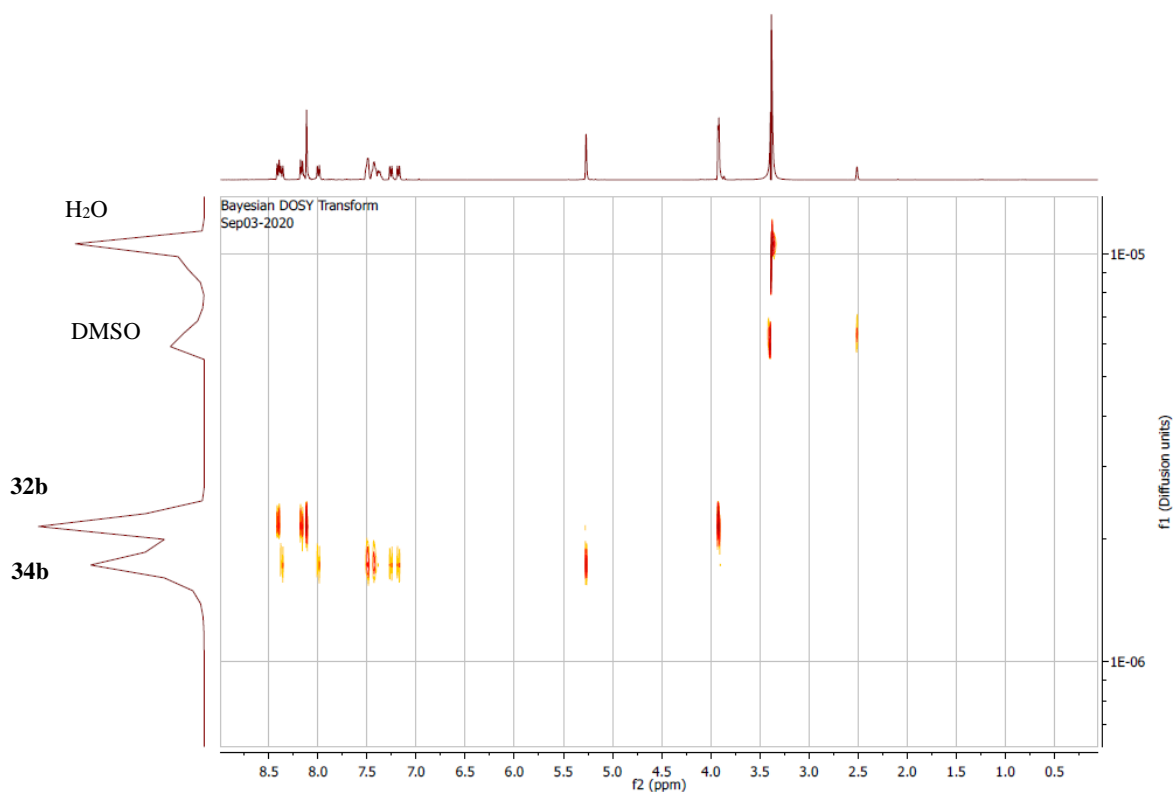


Figure S8. DOSY spectrum after irradiating (1 h) a mixture of **32a** and **34a** in DMSO-*d*₆. The presence of two distinct diffusion coefficients for each of the products **32b** and **34b** support that these are the only species present in the solution.

3.7.5.4 Equivalents of O₂ Needed for the Complete Transformation of **1a** to **1b**

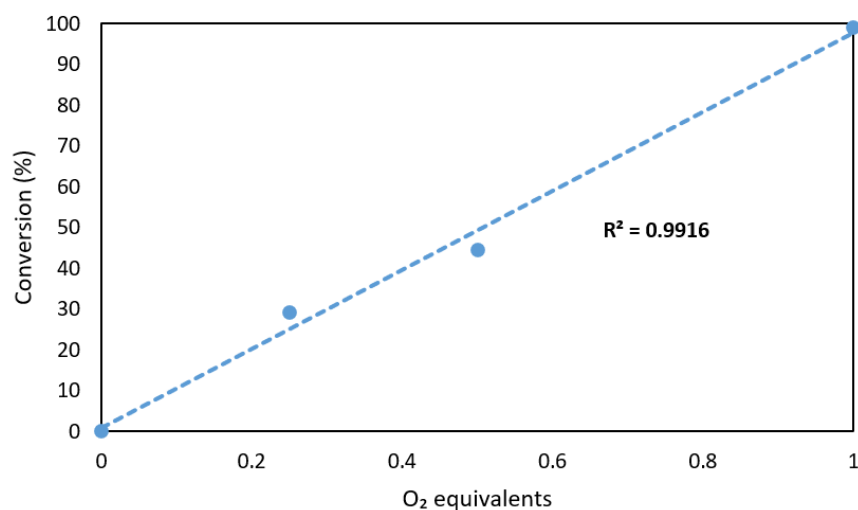


Figure S9. Chart showing the relationship between O₂ equivalents and the conversion of **1a** to **1b**. The almost perfect linear relationship between conversion to **1b** and O₂ equivalents supports the observed quantitative yields. The experiment was conducted using 100 mg (0.375 mmol) of **1a**, dissolved in 10 mL of CDCl₃, and 8.14 mL of O₂ (d=1.428 g/L at STP¹⁰⁰).

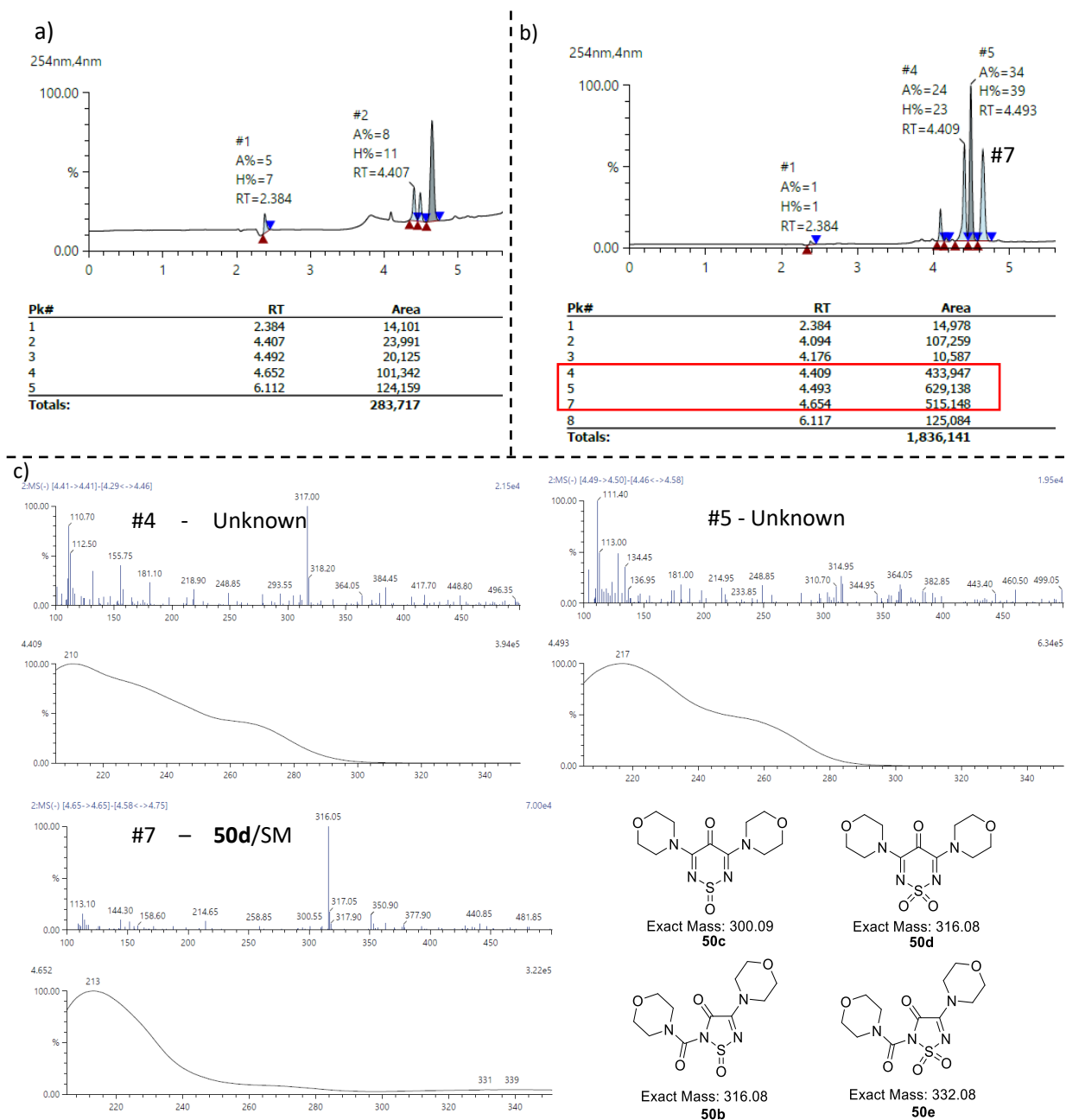
3.7.5.6 Irradiation of Isolated 1,2,6-Thiadiazine Sulfones **50d** and **51d**

Figure S10. LC-MS analysis sulfone SM **50d** before (a) and after (b) irradiation (Method A) for 48 h. Panel c) shows the MS (ESI-)/UV-Vis spectra for the most prominent LC traces (b) post irradiation.

With the aim to determine whether the isolated 1,2,6-thiadiazine sulfones **50d** and **51d**, would behave in a similar manner with the starting non-S-oxidised thiadiazines, we subjected them to the same conditions that were developed previously (Method A), albeit for a substantially longer time period. Aliquots of the reaction mixture were taken before and after the compounds were exposed to the 420 nm light. For the morpholino sulfone **50d**, the results were inconclusive (Figure S10, a), and it was noted that even before the

reaction was started, there were at least 3 species present in the reaction mixture. After 48 h of irradiation, the same 3 peaks were present, however it seemed that peak #7 which belonged to the SM had a reduced area compared to the ‘products’ (peaks #4, #5 as seen in Figure S10, b). Based on the corresponding MS and UV-Vis traces of these new peaks, it was not possible to identify the new compounds (Figure S10,c). Notwithstanding, the results of this experiment clearly show that the sulfone **50d** does indeed participate in a light-driven reaction.

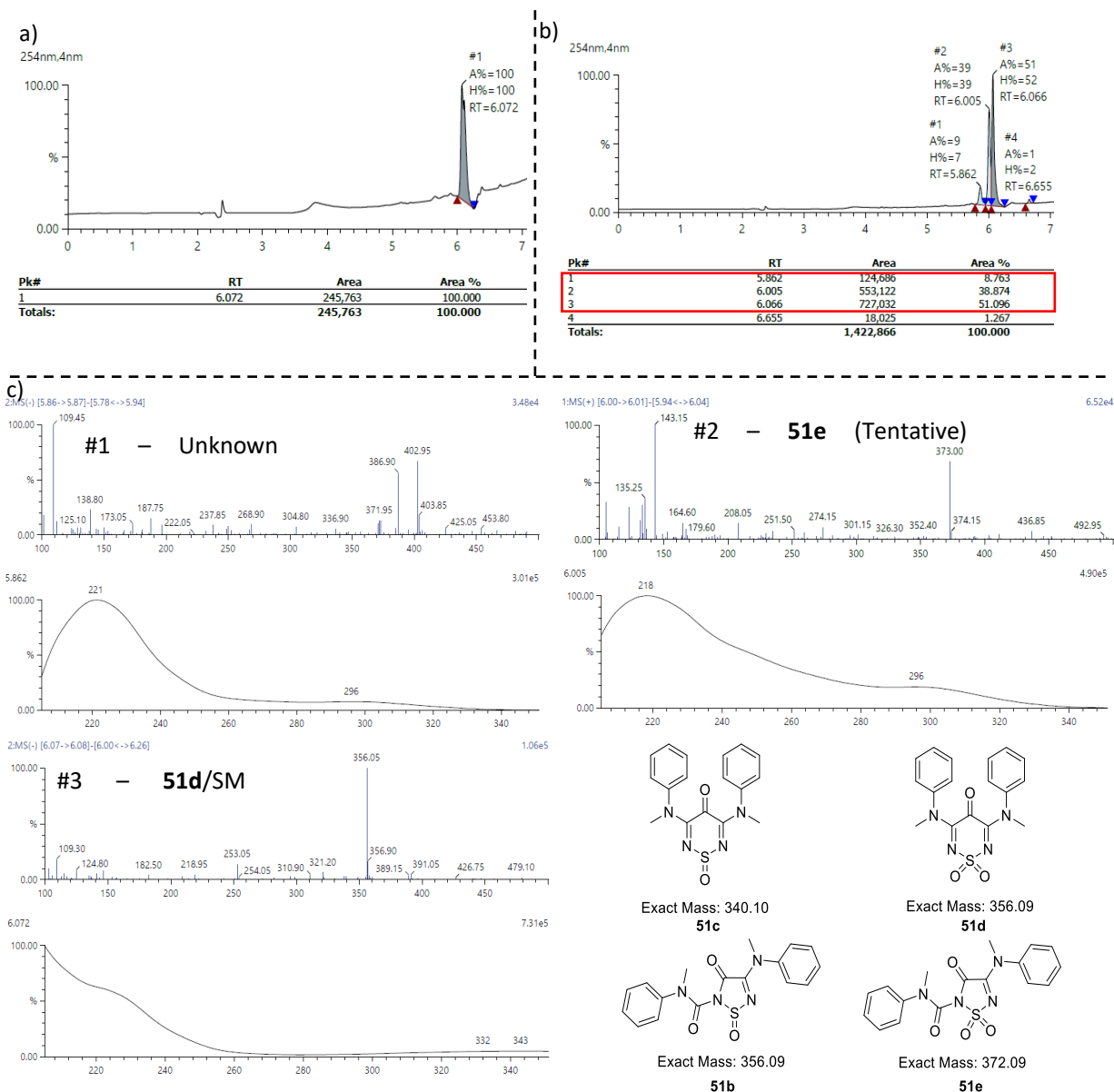


Figure S11. LC-MS analysis sulfone SM **51d** before (a) and after (b) irradiation (Method A) for 48 h. Panel c) shows the MS/UV-Vis spectra for the most prominent LC traces (b) post irradiation.

A similar experiment was then conducted using the N-Me sulfone derivative **51d**. As seen in Figure S11, a), the SM was clean before the reaction was commenced. Post irradiation, two new peaks appeared (Figure S11, b).

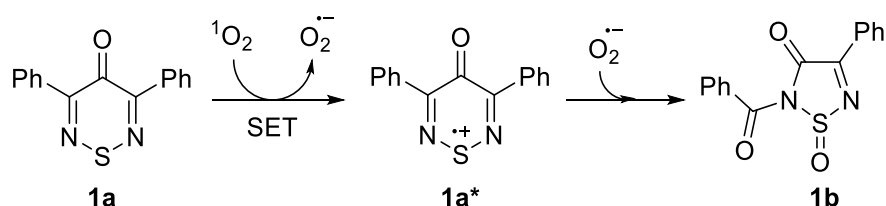
A minor (peak #1, 17% w.r.t the SM) and a major (peak #2, 76% w.r.t SM). Both compounds were more polar than the SM, based on their decreased retention time. In addition, based on their respective UV-Vis spectra (Figure S11, c), they appeared to be less conjugated, with maximum absorption wavelengths of *ca.* 330 nm. Intriguingly, the MS (ESI+) spectrum of the major peak #2, showed a large signal at 373 *m/z*, which closely matches with the expected mass of the ring contracted *N*-methyl-4-[methyl(phenyl)amino]-3-oxo-*N*-phenyl-1,2,5-thiadiazole-2(3*H*)-carboxamide 1,1-dioxide (**51e**) ($[M+H]^+ = 373.10$). Paired with the expected hypsochromic shift (vs. SM) on its UV-Vis spectrum, and increased polarity it is reasonable to assume that the corresponding 1,2,5-thiadiazole S,S-dioxide was formed.

As for the minor peak #1, its MS (ESI-) spectrum showed strong signals at 386.90 and 402.95 *m/z*, however a tentative structural assignment was not possible at this time. As with SM **50d**, it is evident that **51d** is also photoactive and may be able to produce the ring contracted thiadiazole S,S-dioxide. Further research is needed to reveal the mechanism of this transformation and identify the structure of these products.

It is noted that, performing the above experiments using the corresponding sulfoxides **50c** and **51c** was not possible at this time, as the compounds were isolated along with multiple contaminants, rendering them inappropriate for further use.

3.7.6 Comments on the Role of Superoxide⁸

According to the computational results presented in section 3.4.7, the reaction can proceed without superoxide. However, experimental evidence for the presence of superoxide in the reaction was found, where this is believed to form by SET from substrate **1a** (Scheme S4). The possible role of superoxide was therefore assessed, but the results were not conclusive:



Scheme S4. Possible implication of superoxide in the formation of **1a**.

(i) Test calculations showed the energy of superoxide and **1b*** (i.e. R = H) computed separately is over 200 kcal/mol higher in energy than that of singlet oxygen and **1b** (also computed separately).

(ii) attempts to simulate the attack of superoxide at **1a*** in the open-shell singlet state led immediately to a closed-shell configuration of the system.

(iii) attempts to simulate the attack of superoxide at **1a*** in the triplet spin state resulted in electron transfer to provide substrate **1a** and triplet oxygen.

Based on the charges and spin density distributions (Figure S12) we would propose that the attack of superoxide at **1a*** would most likely occur at the S atom and attempts to locate an end-on S-O-O adduct led directly to endoperoxide intermediate.

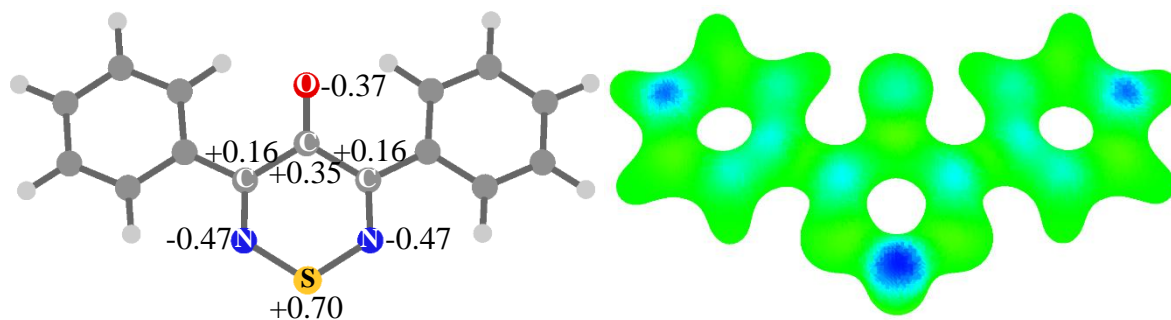


Figure S12. Computed Mulliken charges and spin densities in **1a***.

3.7.7 Single Crystal X-Ray Diffraction Data Collection and Refinement Details⁸

X-ray structures were determined for **1a**, **27a**, **1b**, **5b**, **8b**, **13b**, **20b**, **27b**, **28b**, **32b**, **35b**, **37b**, **39b**, **40b**, **1c**, **9c**, **49c**, **1d**, **50c**, **51c**, **50d**, and **51d**. **1a**, **5b**, **39b** and **9c**, were refined as two component twins with hklf 4 data with the twin law (-1 0 0, 0 -1 0, 0 0 -1) (ie hkl data from one domain only) .

In **27a**, **27b** and **28b** there was substitutional disorder in the five-membered rings between carbon and sulphur atoms. The coordinates and displacement parameters were constrained to be the same at the disordered positions with the commands EXYZ and EADP and the relative occupancies tied so that the occupancies of the positions and constituent elements summed to 100%.

In **13b** there is 2-fold rotational disorder in the phenyl ring along the Cipso-Me axis. The occupancies were fixed at 50:50 and the displacement parameters in the two conformations are the same.

The structure of **1d** only solved in *P1*. A Flack parameter was obtained 0.3(2). There are warnings that this could be *P1* however, all the largest correlation matrix elements are between atoms within the same molecule. There are 8 molecules on the asymmetric unit. The data were refined against hklf 5 data which were compiled from the OLEX2 twinning processing procedure. There is a mixture of isotropic and anisotropic refinement chosen on the basis of atomic parameter refinement stability and standard deviation on the Flack parameter. RIGU (rigid bond restraint) and isotropic restraints were applied.

CCDC deposition numbers and structure codes

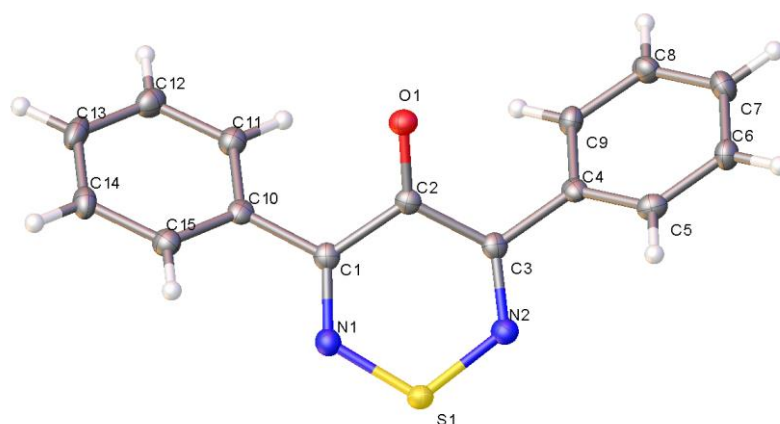
Deposition Number	2168267	2167996	2168265	2168225	2167997
Compound code	1a	1b	1c	1d	5b

Deposition Number	2167999	2168226	2168000	2168157	2168266
Compound code	8b	9c	13b	20b	27a

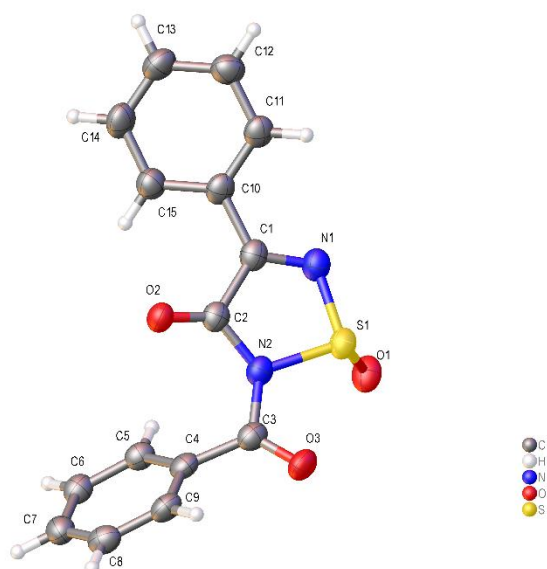
Deposition Number	2168187	2168217	2168147	2168218	2168219
Compound code	27b	28b	32b	35b	37b

Deposition Number	2168220	2168224	2168213	2168263	2168264
Compound code	39b	40b	49c	50d	51d

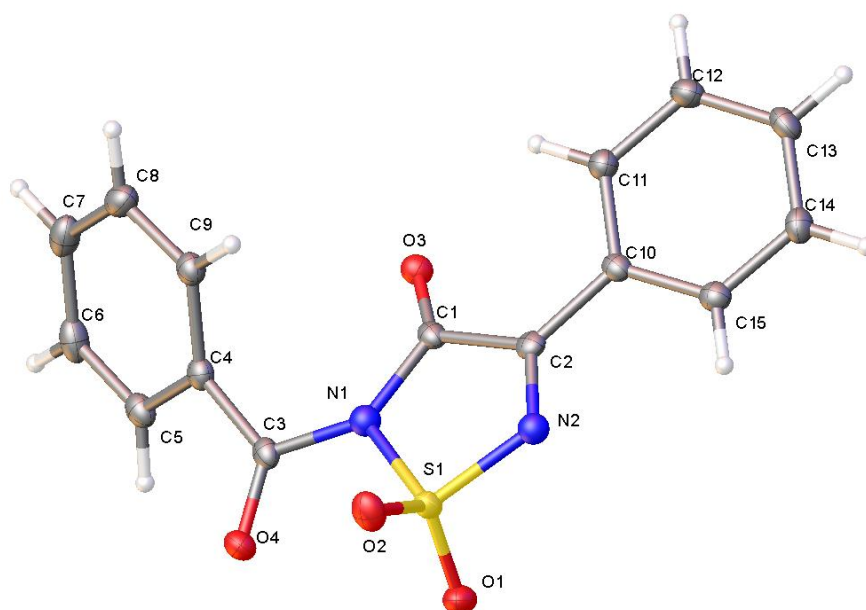
Deposition Number	2173994	2173995
Compound code	50c	51c

**Table S2.** Crystal data and structure refinement for **1a**.

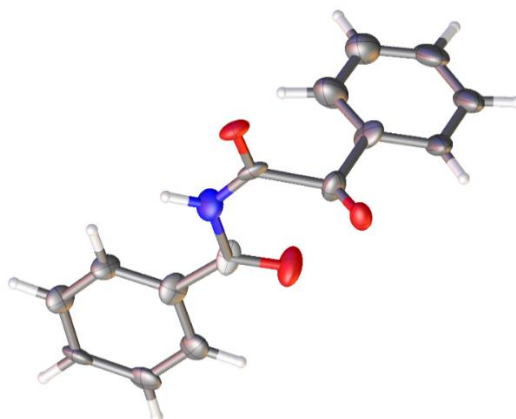
Identification code	1a
Empirical formula	C ₁₅ H ₁₀ N ₂ OS
Formula weight	266.31
Temperature/K	100.0
Crystal system	trigonal
Space group	P3 ₁
a/Å	16.6569(10)
b/Å	16.6569(10)
c/Å	3.7166(3)
α/°	90
β/°	90
γ/°	120
Volume/Å³	893.03(13)
Z	3
ρ_{calc}/cm³	1.486
μ/mm⁻¹	2.343
F(000)	414.0
Crystal size/mm³	0.24 × 0.04 × 0.03
Radiation	CuKα (λ = 1.54178)
2θ range for data collection/°	6.126 to 148.926
Index ranges	-20 ≤ h ≤ 17, -20 ≤ k ≤ 20, -4 ≤ l ≤ 4
Reflections collected	13130
Independent reflections	2410 [R _{int} = 0.0621, R _{sigma} = 0.0380]
Data/restraints/parameters	2410/148/173
Goodness-of-fit on F²	1.059
Final R indexes [I ≥ 2σ(I)]	R ₁ = 0.0279, wR ₂ = 0.0684
Final R indexes [all data]	R ₁ = 0.0294, wR ₂ = 0.0691
Largest diff. peak/hole / e Å⁻³	0.20/-0.21
Flack parameter	0.046(12)

**Table S3.** Crystal data and structure refinement for **1b**.

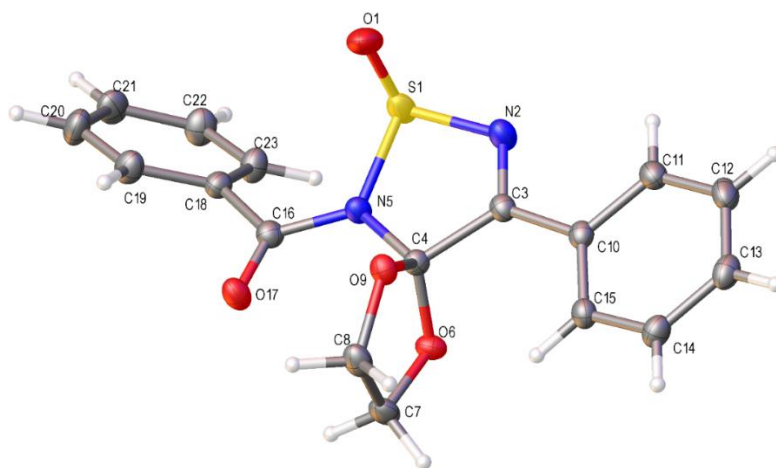
Identification code	1b
Empirical formula	C ₁₅ H ₁₀ N ₂ O ₃ S
Formula weight	298.31
Temperature/K	100.0
Crystal system	monoclinic
Space group	P2 ₁ /c
a/Å	9.7612(5)
b/Å	4.3248(2)
c/Å	31.9875(17)
α/°	90
β/°	93.392(3)
γ/°	90
Volume/Å³	1347.99(12)
Z	4
ρ_{calc}/cm³	1.470
μ/mm⁻¹	2.250
F(000)	616.0
Crystal size/mm³	0.22 × 0.06 × 0.03
Radiation	CuKα (λ = 1.54178)
2θ range for data collection/°	5.536 to 149.262
Index ranges	-12 ≤ h ≤ 12, -5 ≤ k ≤ 5, -40 ≤ l ≤ 40
Reflections collected	35241
Independent reflections	2747 [R _{int} = 0.0790, R _{sigma} = 0.0303]
Data/restraints/parameters	2747/0/190
Goodness-of-fit on F²	1.139
Final R indexes [I ≥ 2σ(I)]	R ₁ = 0.0670, wR ₂ = 0.1749
Final R indexes [all data]	R ₁ = 0.0746, wR ₂ = 0.1788
Largest diff. peak/hole / e Å⁻³	0.83/-0.40

**Table S4.** Crystal data and structure refinement for **1c**.

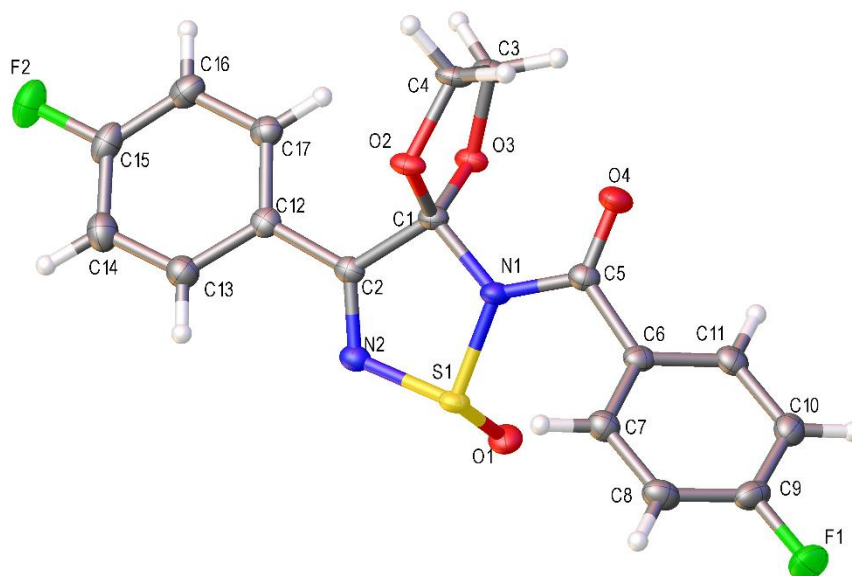
Identification code	1c
Empirical formula	C ₁₅ H ₁₀ N ₂ O ₄ S
Formula weight	314.31
Temperature/K	100
Crystal system	monoclinic
Space group	P2 ₁ /n
a/Å	9.143(5)
b/Å	9.617(8)
c/Å	15.379(7)
α/°	90
β/°	103.96(3)
γ/°	90
Volume/Å³	1312.4(14)
Z	4
ρ_{calc}/cm³	1.591
μ/mm⁻¹	2.404
F(000)	648.0
Crystal size/mm³	0.18 × 0.08 × 0.04
Radiation	CuKα (λ = 1.54178)
2θ range for data collection/°	10.296 to 140.458
Index ranges	-11 ≤ h ≤ 11, -11 ≤ k ≤ 11, -18 ≤ l ≤ 18
Reflections collected	18102
Independent reflections	2493 [R _{int} = 0.0676, R _{sigma} = 0.0332]
Data/restraints/parameters	2493/0/199
Goodness-of-fit on F²	1.044
Final R indexes [I ≥ 2σ(I)]	R ₁ = 0.0308, wR ₂ = 0.0745
Final R indexes [all data]	R ₁ = 0.0390, wR ₂ = 0.0780
Largest diff. peak/hole / e Å⁻³	0.29/-0.44

**Table S5.** Crystal data and structure refinement for **1d**.

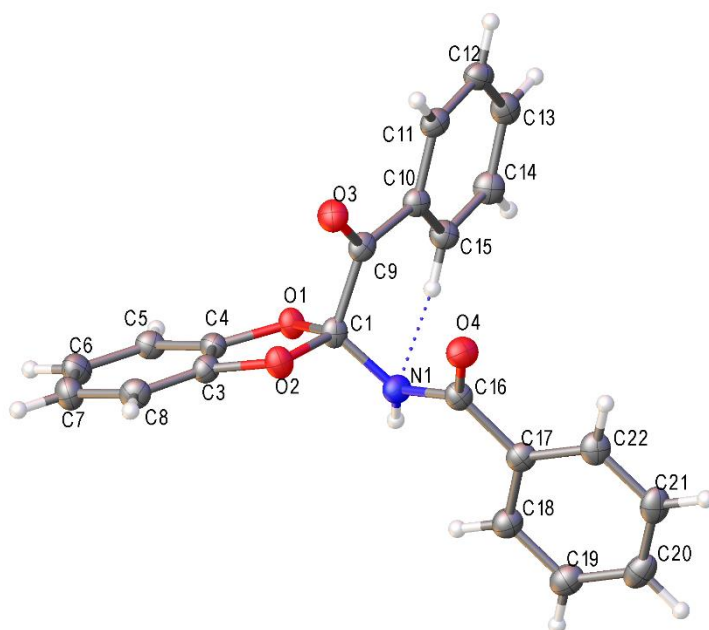
Identification code	1d
Empirical formula	C ₁₅ H ₁₁ NO ₃
Formula weight	253.25
Temperature/K	100.0
Crystal system	triclinic
Space group	P1
a/Å	5.449(3)
b/Å	21.007(9)
c/Å	21.065(9)
α/°	88.01(2)
β/°	82.915(15)
γ/°	84.80(3)
Volume/Å³	2382.2(18)
Z	8
ρ_{calc}/cm³	1.412
μ/mm⁻¹	0.820
F(000)	1056.0
Crystal size/mm³	0.54 × 0.04 × 0.02
Radiation	CuKα (λ = 1.54178)
2θ range for data collection/°	4.224 to 158.088
Index ranges	-6 ≤ h ≤ 6, -26 ≤ k ≤ 26, -26 ≤ l ≤ 26
Reflections collected	105763
Independent reflections	17524 [R _{int} 0.0731, R _{sigma} = 0.0575]
Data/restraints/parameters	17524/1230/1333
Goodness-of-fit on F²	1.068
Final R indexes [I ≥ 2σ(I)]	R ₁ = 0.1327, wR ₂ = 0.3894
Final R indexes [all data]	R ₁ = 0.1444, wR ₂ = 0.3971
Largest diff. peak/hole / e Å⁻³	1.06/-0.97
Flack parameter	0.28(19)

**Table S6.** Crystal data and structure refinement for **5b**.

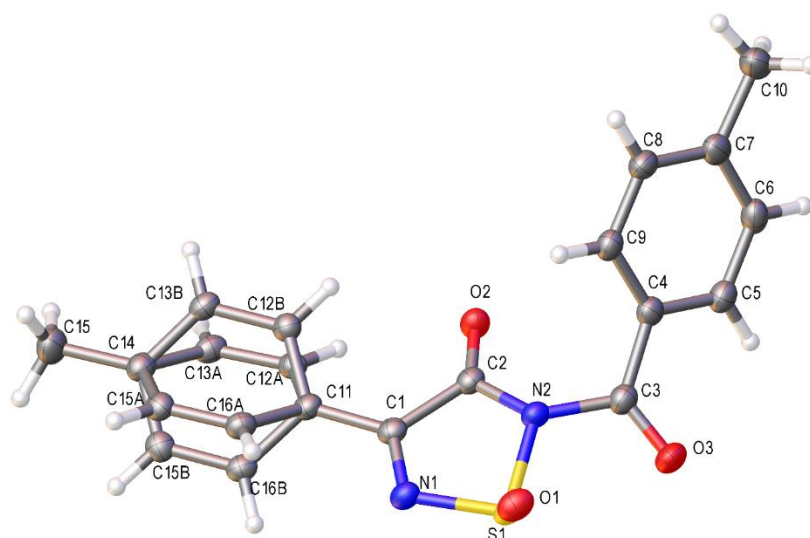
Identification code	5b
Empirical formula	C ₁₇ H ₁₄ N ₂ O ₄ S
Formula weight	342.36
Temperature/K	100.0
Crystal system	orthorhombic
Space group	P2 ₁ 2 ₁ 2 ₁
a/Å	8.4196(7)
b/Å	13.2151(12)
c/Å	14.0737(10)
α/°	90
β/°	90
γ/°	90
Volume/Å³	1565.9(2)
Z	4
ρ_{calc}/cm³	1.452
μ/mm⁻¹	2.061
F(000)	712.0
Crystal size/mm³	0.2 × 0.2 × 0.1
Radiation	CuKα (λ = 1.54178)
2θ range for data collection/°	12.464 to 159.958
Index ranges	-10 ≤ h ≤ 10, -16 ≤ k ≤ 16, -17 ≤ l ≤ 17
Reflections collected	53271
Independent reflections	3362 [R _{int} = 0.0259, R _{sigma} = 0.0103]
Data/restraints/parameters	3362/0/218
Goodness-of-fit on F²	1.034
Final R indexes [I ≥ 2σ(I)]	R ₁ = 0.0226, wR ₂ = 0.0616
Final R indexes [all data]	R ₁ = 0.0226, wR ₂ = 0.0616
Largest diff. peak/hole / e Å⁻³	0.23/-0.24
Flack parameter	0.483(14)

Table S7. Crystal data and structure refinement for **8b**.

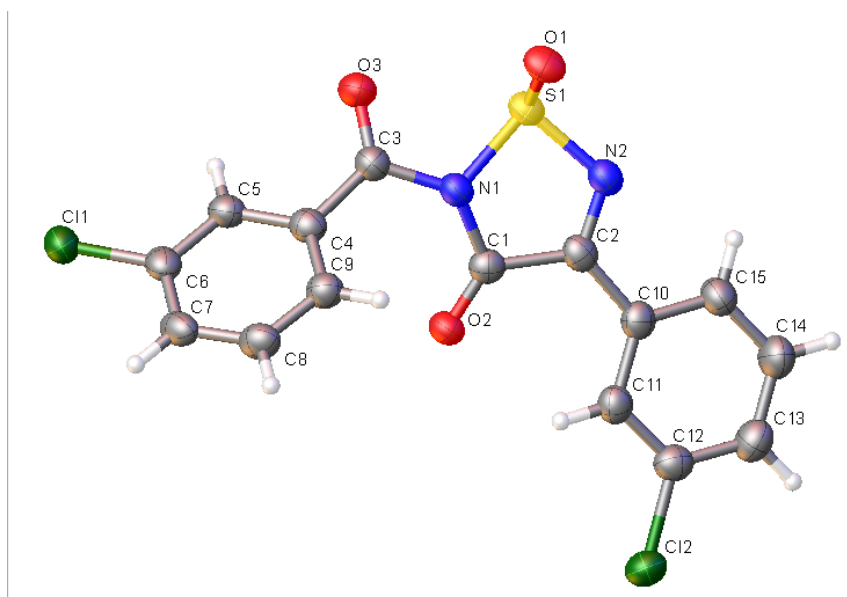
Identification code	8b
Empirical formula	C ₁₇ H ₁₂ F ₂ N ₂ O ₄ S
Formula weight	378.35
Temperature/K	100.0
Crystal system	monoclinic
Space group	P2 ₁ /c
a/Å	13.153(3)
b/Å	15.142(4)
c/Å	8.3150(15)
α/°	90
β/°	104.933(6)
γ/°	90
Volume/Å³	1600.1(6)
Z	4
ρ_{calc}/cm³	1.571
μ/mm⁻¹	2.266
F(000)	776.0
Crystal size/mm³	0.42 × 0.18 × 0.08
Radiation	CuKα (λ = 1.54178)
2θ range for data collection/°	6.956 to 144.32
Index ranges	-16 ≤ h ≤ 16, -18 ≤ k ≤ 16, -9 ≤ l ≤ 10
Reflections collected	21101
Independent reflections	3156 [R _{int} = 0.0536, R _{sigma} = 0.0319]
Data/restraints/parameters	3156/0/235
Goodness-of-fit on F²	1.070
Final R indexes [I ≥ 2σ(I)]	R ₁ = 0.0321, wR ₂ = 0.0873
Final R indexes [all data]	R ₁ = 0.0353, wR ₂ = 0.0894
Largest diff. peak/hole / e Å⁻³	0.32/-0.33

**Table S8.** Crystal data and structure refinement for **9c**.

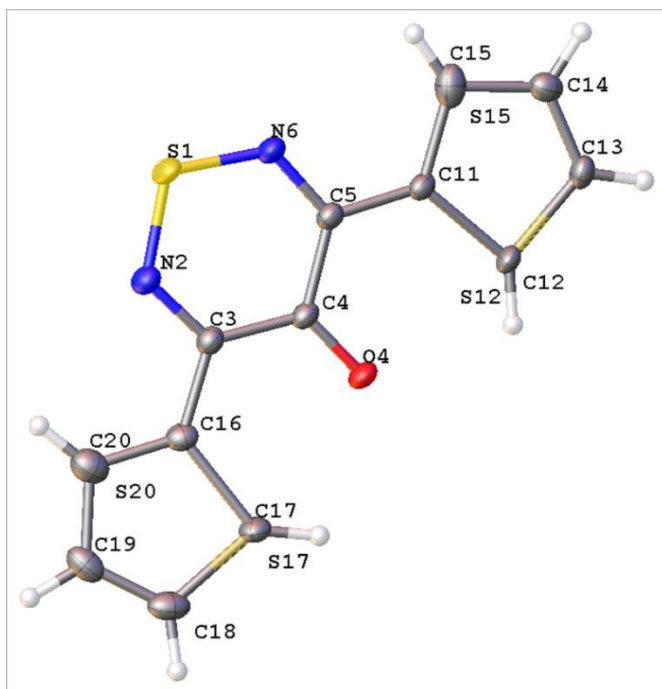
Identification code	9c
Empirical formula	C ₂₁ H ₁₅ NO ₄
Formula weight	345.34
Temperature/K	100.0
Crystal system	monoclinic
Space group	Pn
a/Å	9.237(4)
b/Å	9.516(4)
c/Å	9.930(5)
α/°	90
β/°	113.65(3)
γ/°	90
Volume/Å³	799.5(6)
Z	2
ρ_{calc}/cm³	1.435
μ/mm⁻¹	0.822
F(000)	360.0
Crystal size/mm³	0.28 × 0.2 × 0.04
Radiation	CuKα (λ = 1.54178)
2θ range for data collection/°	9.294 to 150.82
Index ranges	-11 ≤ h ≤ 11, -11 ≤ k ≤ 11, -12 ≤ l ≤ 12
Reflections collected	26084
Independent reflections	3244 [R _{int} = 0.0697, R _{sigma} = 0.0339]
Data/restraints/parameters	3244/2/237
Goodness-of-fit on F²	1.074
Final R indexes [I ≥ 2σ(I)]	R ₁ = 0.0350, wR ₂ = 0.0875
Final R indexes [all data]	R ₁ = 0.0375, wR ₂ = 0.0895
Largest diff. peak/hole / e Å⁻³	0.19/-0.20
Flack parameter	0.1(2)

**Table S9.** Crystal data and structure refinement for **13b**.

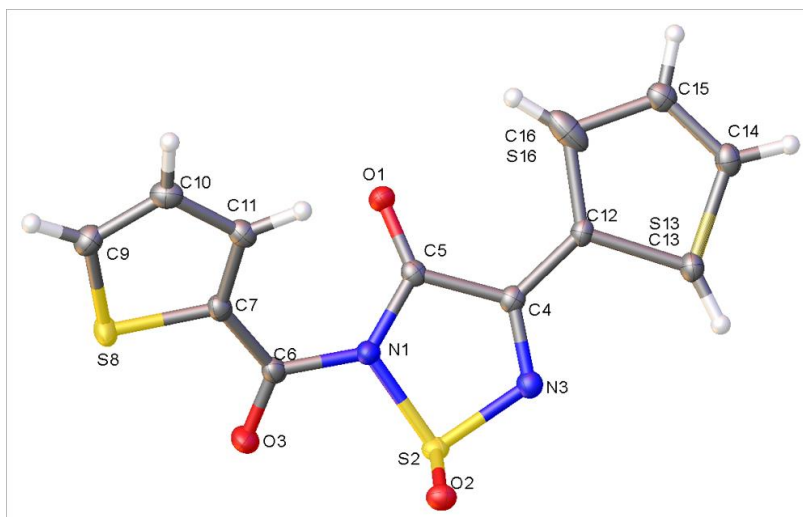
Identification code	13b
Empirical formula	C ₁₇ H ₁₄ N ₂ O ₃ S
Formula weight	326.36
Temperature/K	100.0
Crystal system	monoclinic
Space group	C2/c
a/Å	18.1894(8)
b/Å	4.4604(2)
c/Å	37.7102(17)
α/°	90
β/°	91.048(2)
γ/°	90
Volume/Å³	3059.0(2)
Z	8
ρ_{calc}/cm³	1.417
μ/mm⁻¹	2.031
F(000)	1360.0
Crystal size/mm³	0.46 × 0.1 × 0.04
Radiation	CuKα (λ = 1.54178)
2θ range for data collection/°	4.688 to 149.22
Index ranges	-22 ≤ h ≤ 22, -5 ≤ k ≤ 5, -47 ≤ l ≤ 46
Reflections collected	33296
Independent reflections	3139 [R _{int} = 0.0617, R _{sigma} = 0.0297]
Data/restraints/parameters	3139/0/246
Goodness-of-fit on F²	1.037
Final R indexes [I ≥ 2σ(I)]	R ₁ = 0.0389, wR ₂ = 0.1020
Final R indexes [all data]	R ₁ = 0.0435, wR ₂ = 0.1082
Largest diff. peak/hole / e Å⁻³	0.36/-0.40

Table S10. Crystal data and structure refinement for **20b**.

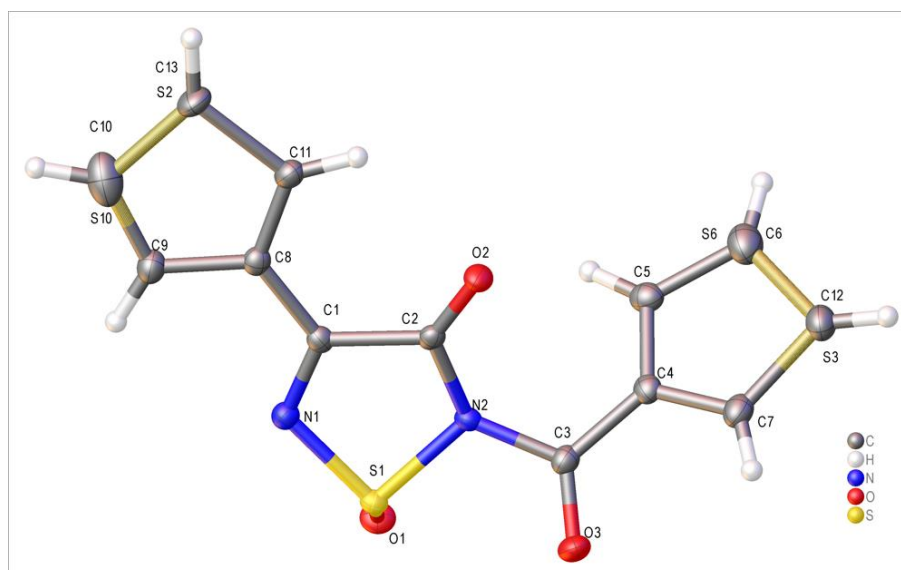
Identification code	20b
Empirical formula	C ₁₅ H ₈ Cl ₂ N ₂ O ₃ S
Formula weight	367.19
Temperature/K	100.0
Crystal system	monoclinic
Space group	P2 ₁ /c
a/Å	4.228(2)
b/Å	18.934(10)
c/Å	18.988(10)
α/°	90
β/°	95.597(18)
γ/°	90
Volume/Å³	1512.8(14)
Z	4
ρ_{calc}/cm³	1.612
μ/mm⁻¹	5.305
F(000)	744.0
Crystal size/mm³	0.26 × 0.04 × 0.04
Radiation	CuKα (λ = 1.54178)
2θ range for data collection/°	6.608 to 117.892
Index ranges	-4 ≤ h ≤ 4, -20 ≤ k ≤ 20, -20 ≤ l ≤ 20
Reflections collected	16161
Independent reflections	2162 [R _{int} = 0.0662, R _{sigma} = 0.0339]
Data/restraints/parameters	2162/0/208
Goodness-of-fit on F²	1.070
Final R indexes [I ≥ 2σ(I)]	R ₁ = 0.0488, wR ₂ = 0.1293
Final R indexes [all data]	R ₁ = 0.0547, wR ₂ = 0.1341
Largest diff. peak/hole / e Å⁻³	0.35/-0.54

Table S11. Crystal data and structure refinement for **27a**.

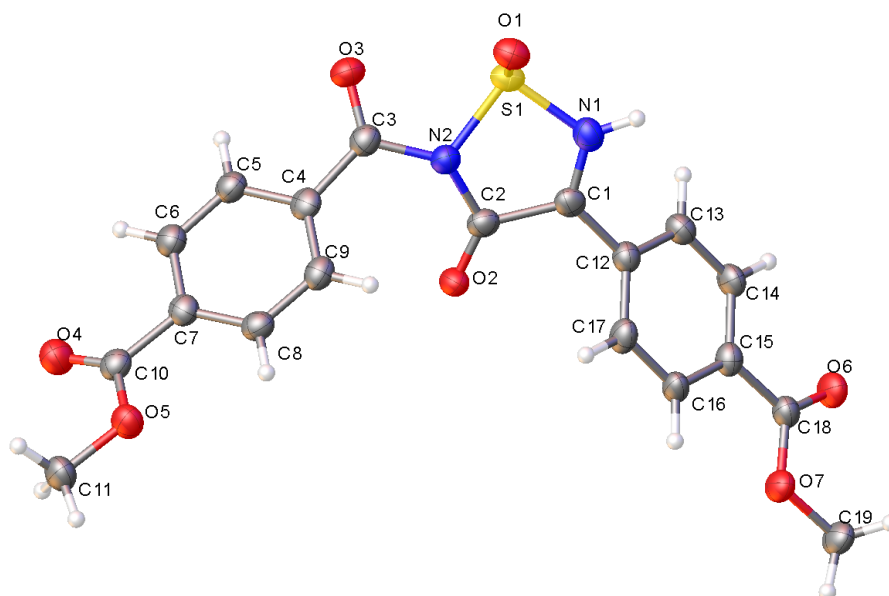
Identification code	27a
Empirical formula	C ₁₁ H ₆ N ₂ OS ₃
Formula weight	278.36
Temperature/K	100.0
Crystal system	monoclinic
Space group	P2 ₁ /n
a/Å	14.0787(8)
b/Å	4.9634(3)
c/Å	16.2584(10)
α/°	90
β/°	104.691(2)
γ/°	90
Volume/Å³	1098.97(11)
Z	4
ρ_{calc}/cm³	1.682
μ/mm⁻¹	0.654
F(000)	568.0
Crystal size/mm³	0.46 × 0.08 × 0.04
Radiation	MoKα (λ = 0.71073)
2θ range for data collection/°	5.984 to 57.548
Index ranges	-19 ≤ h ≤ 19, -6 ≤ k ≤ 6, -21 ≤ l ≤ 22
Reflections collected	45729
Independent reflections	2855 [R _{int} = 0.0841, R _{sigma} = 0.0295]
Data/restraints/parameters	2855/0/156
Goodness-of-fit on F²	1.067
Final R indexes [I ≥ 2σ(I)]	R ₁ = 0.0478, wR ₂ = 0.1043
Final R indexes [all data]	R ₁ = 0.0663, wR ₂ = 0.1144
Largest diff. peak/hole / e Å⁻³	0.41/-0.48

Table S12. Crystal data and structure refinement for **27b**.

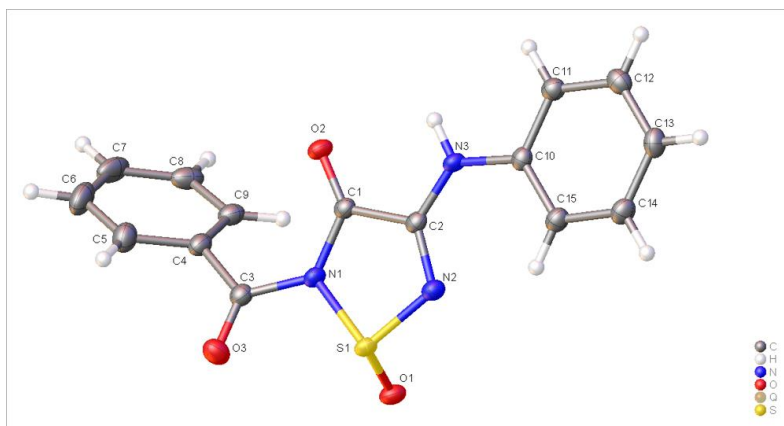
Identification code	27b
Empirical formula	C ₁₁ H ₆ N ₂ O ₃ S ₃
Formula weight	310.36
Temperature/K	100.0
Crystal system	monoclinic
Space group	P2 ₁ /c
a/Å	6.79830(10)
b/Å	19.5591(4)
c/Å	8.9836(2)
α/°	90
β/°	95.2280(10)
γ/°	90
Volume/Å³	1189.57(4)
Z	4
ρ_{calc}/cm³	1.733
μ/mm⁻¹	5.770
F(000)	632.0
Crystal size/mm³	0.24 × 0.04 × 0.02
Radiation	CuKα (λ = 1.54178)
2θ range for data collection/°	9.042 to 148.836
Index ranges	-8 ≤ h ≤ 8, -24 ≤ k ≤ 24, -11 ≤ l ≤ 11
Reflections collected	43523
Independent reflections	2437 [R _{int} = 0.0422, R _{sigma} = 0.0154]
Data/restraints/parameters	2437/0/173
Goodness-of-fit on F²	1.080
Final R indexes [I ≥ 2σ(I)]	R ₁ = 0.0259, wR ₂ = 0.0691
Final R indexes [all data]	R ₁ = 0.0272, wR ₂ = 0.0700
Largest diff. peak/hole / e Å⁻³	0.52/-0.33

**Table S13.** Crystal data and structure refinement for **28b**.

Identification code	28b
Empirical formula	C ₁₁ H ₆ N ₂ O ₃ S ₃
Formula weight	310.36
Temperature/K	100.0
Crystal system	orthorhombic
Space group	Pna2 ₁
a/Å	16.2994(7)
b/Å	17.9235(8)
c/Å	4.3228(2)
α/°	90
β/°	90
γ/°	90
Volume/Å³	1262.87(10)
Z	4
ρ_{calc}/cm³	1.632
μ/mm⁻¹	5.435
F(000)	632.0
Crystal size/mm³	0.44 × 0.1 × 0.04
Radiation	CuKα (λ = 1.54178)
2θ range for data collection/°	7.33 to 144.636
Index ranges	-20 ≤ h ≤ 20, -21 ≤ k ≤ 22, -5 ≤ l ≤ 5
Reflections collected	14359
Independent reflections	2438 [R _{int} = 0.0369, R _{sigma} = 0.0263]
Data/restraints/parameters	2438/1/174
Goodness-of-fit on F²	1.053
Final R indexes [I ≥ 2σ (I)]	R ₁ = 0.0239, wR ₂ = 0.0628
Final R indexes [all data]	R ₁ = 0.0242, wR ₂ = 0.0631
Largest diff. peak/hole / e Å⁻³	0.23/-0.23
Flack parameter	-0.005(11)

**Table S14.** Crystal data and structure refinement for **32b**.

Identification code	32b
Empirical formula	C ₁₉ H ₁₄ N ₂ O ₇ S
Formula weight	414.38
Temperature/K	100.0
Crystal system	monoclinic
Space group	Cc
a/Å	8.9745(3)
b/Å	32.8200(11)
c/Å	6.9065(2)
α/°	90
β/°	119.452(2)
γ/°	90
Volume/Å³	1771.37(10)
Z	4
ρ_{calc}/cm³	1.554
μ/mm⁻¹	2.069
F(000)	856.0
Crystal size/mm³	0.22 × 0.18 × 0.04
Radiation	CuKα (λ = 1.54178)
2θ range for data collection/°	5.386 to 149.056
Index ranges	-11 ≤ h ≤ 11, -40 ≤ k ≤ 40, -8 ≤ l ≤ 8
Reflections collected	22913
Independent reflections	3591 [R _{int} = 0.0625, R _{sigma} = 0.0388]
Data/restraints/parameters	3591/2/265
Goodness-of-fit on F²	1.049
Final R indexes [I ≥ 2σ(I)]	R ₁ = 0.0404, wR ₂ = 0.0999
Final R indexes [all data]	R ₁ = 0.0437, wR ₂ = 0.1031
Largest diff. peak/hole / e Å⁻³	0.36/-0.25
Flack parameter	0.11(3)

**Table S15.** Crystal data and structure refinement for **35b**.

Identification code	35b
Empirical formula	C ₁₅ H ₁₁ N ₃ O ₃ S
Formula weight	313.33
Temperature/K	100.0
Crystal system	monoclinic
Space group	P2 ₁ /c
a/Å	14.7665(5)
b/Å	13.0019(5)
c/Å	7.1500(3)
α/°	90
β/°	90.591(2)
γ/°	90
Volume/Å³	1372.67(9)
Z	4
ρ_{calc}/cm³	1.516
μ/mm⁻¹	2.260
F(000)	648.0
Crystal size/mm³	0.42 × 0.28 × 0.04
Radiation	CuKα (λ = 1.54178)
2θ range for data collection/°	5.986 to 140.424
Index ranges	-18 ≤ h ≤ 16, -15 ≤ k ≤ 15, -8 ≤ l ≤ 8
Reflections collected	17655
Independent reflections	2613 [R _{int} = 0.1543, R _{sigma} = 0.0821]
Data/restraints/parameters	2613/0/199
Goodness-of-fit on F²	1.054
Final R indexes [I >= 2σ(I)]	R ₁ = 0.0411, wR ₂ = 0.1053
Final R indexes [all data]	R ₁ = 0.0658, wR ₂ = 0.1129
Largest diff. peak/hole / e Å⁻³	0.49/-0.38

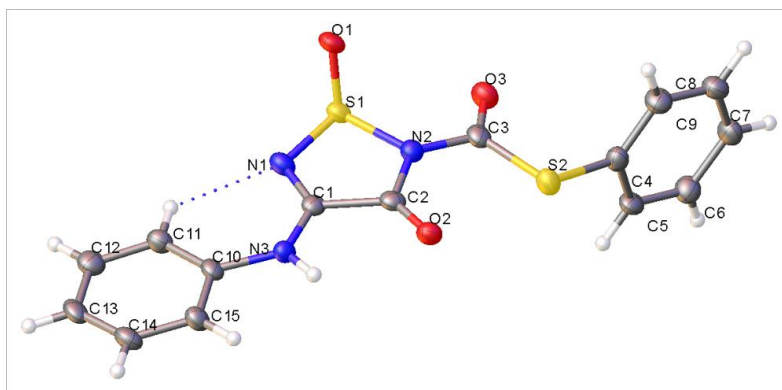
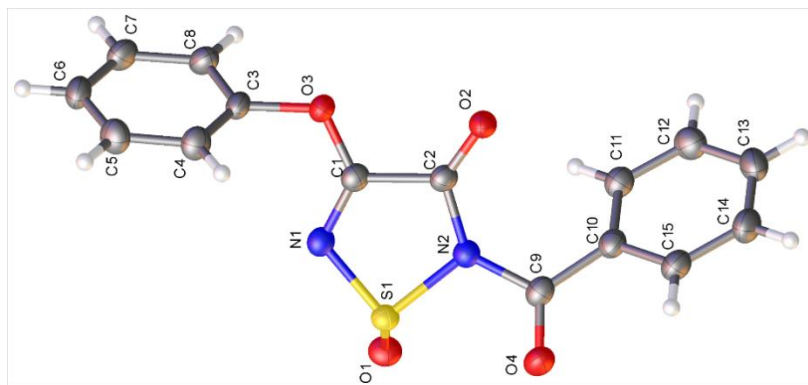
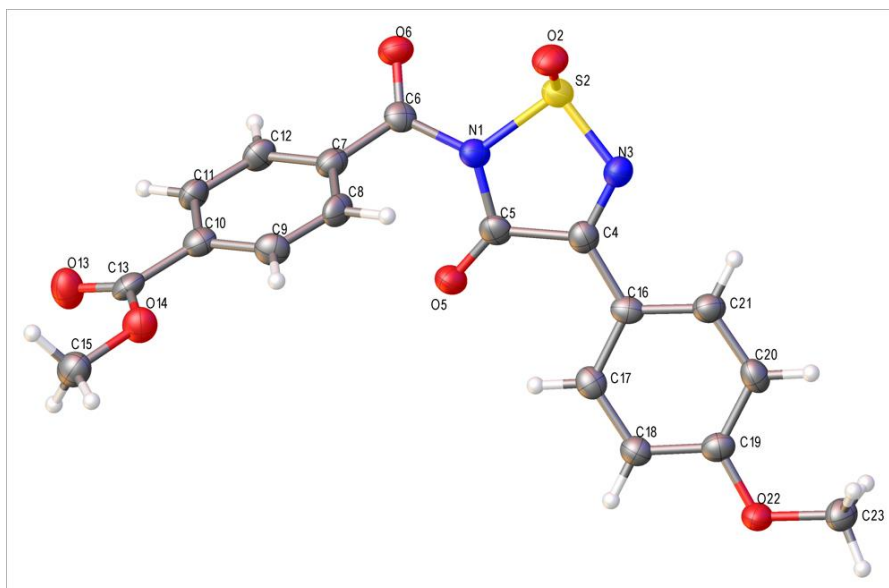


Table S16. Crystal data and structure refinement for 37b.

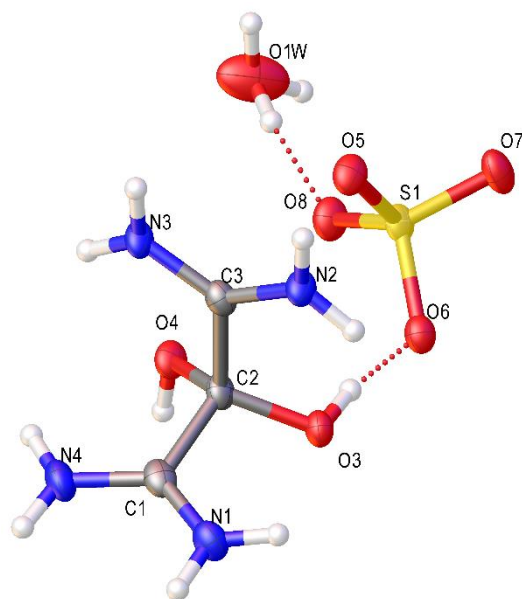
Identification code	37b
Empirical formula	C ₁₅ H ₁₁ N ₃ O ₃ S ₂
Formula weight	345.39
Temperature/K	100.0
Crystal system	triclinic
Space group	P-1
a/Å	6.9681(4)
b/Å	7.5359(4)
c/Å	15.4390(9)
α/°	79.625(4)
β/°	88.507(4)
γ/°	67.320(4)
Volume/Å ³	734.96(7)
Z	2
ρ _{calc} /cm ³	1.561
μ/mm ⁻¹	3.463
F(000)	356.0
Crystal size/mm ³	0.12 × 0.04 × 0.02
Radiation	CuKα (λ = 1.54178)
2θ range for data collection/°	5.826 to 127.45
Index ranges	-8 ≤ h ≤ 8, -8 ≤ k ≤ 8, 0 ≤ l ≤ 17
Reflections collected	21852
Independent reflections	2350 [R _{int} = 0.1070, R _{sigma} = 0.0645]
Data/restraints/parameters	2350/0/209
Goodness-of-fit on F ²	1.110
Final R indexes [I >= 2σ(I)]	R ₁ = 0.0715, wR ₂ = 0.1827
Final R indexes [all data]	R ₁ = 0.0861, wR ₂ = 0.1942
Largest diff. peak/hole / e Å ⁻³	0.45/-0.49

**Table S17.** Crystal data and structure refinement for **39b**.

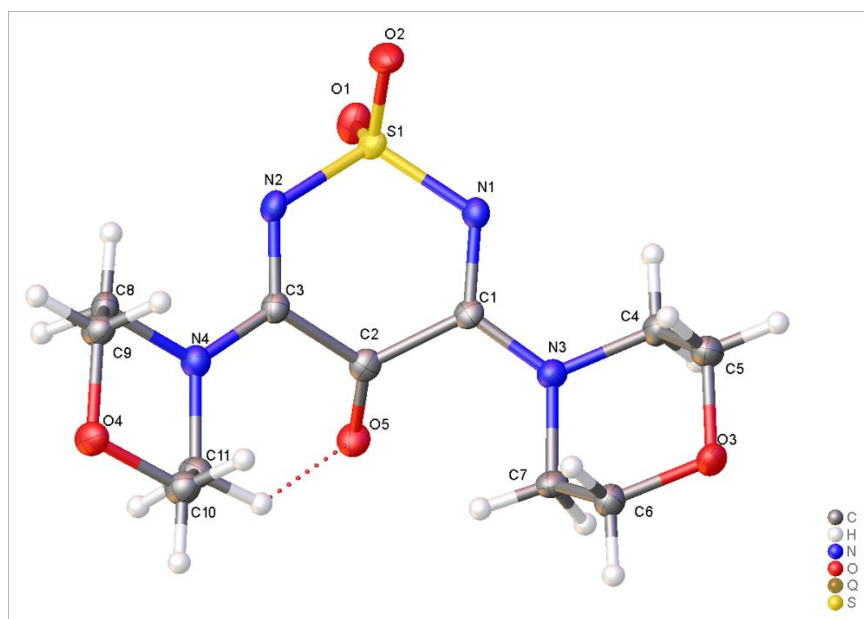
Identification code	39b
Empirical formula	C ₁₅ H ₁₀ N ₂ O ₄ S
Formula weight	314.31
Temperature/K	100.0
Crystal system	orthorhombic
Space group	P2 ₁ 2 ₁ 2 ₁
a/Å	4.34330(10)
b/Å	17.9288(6)
c/Å	18.4384(6)
α/°	90
β/°	90
γ/°	90
Volume/Å³	1435.80(7)
Z	4
ρ_{calc}/cm³	1.454
μ/mm⁻¹	2.197
F(000)	648.0
Crystal size/mm³	0.22 × 0.08 × 0.04
Radiation	CuKα (λ = 1.54178)
2θ range for data collection/°	6.876 to 149.246
Index ranges	-5 ≤ h ≤ 5, -21 ≤ k ≤ 22, -22 ≤ l ≤ 23
Reflections collected	17077
Independent reflections	2932 [R _{int} = 0.0585, R _{sigma} = 0.0358]
Data/restraints/parameters	2932/0/200
Goodness-of-fit on F²	1.058
Final R indexes [I ≥ 2σ(I)]	R ₁ = 0.0332, wR ₂ = 0.0807
Final R indexes [all data]	R ₁ = 0.0364, wR ₂ = 0.0827
Largest diff. peak/hole / e Å⁻³	0.28/-0.18
Flack parameter	0.44(2)

**Table S18.** Crystal data and structure refinement for **40b**.

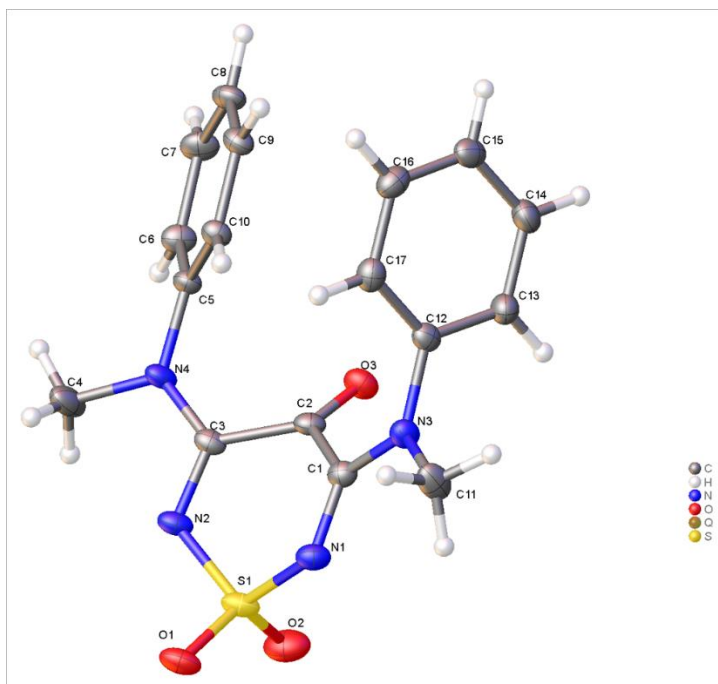
Identification code	40b
Empirical formula	C ₁₈ H ₁₄ N ₂ O ₆ S
Formula weight	386.37
Temperature/K	100.0
Crystal system	monoclinic
Space group	P2 ₁ /n
a/Å	15.333(7)
b/Å	5.838(2)
c/Å	18.736(8)
α/°	90
β/°	91.048(18)
γ/°	90
Volume/Å³	1676.8(12)
Z	4
ρ_{calc}/cm³	1.531
μ/mm⁻¹	2.091
F(000)	800.0
Crystal size/mm³	0.36 × 0.04 × 0.02
Radiation	CuKα (λ = 1.54178)
2θ range for data collection/°	7.384 to 150.274
Index ranges	-13 ≤ h ≤ 19, -7 ≤ k ≤ 7, -23 ≤ l ≤ 23
Reflections collected	21525
Independent reflections	3427 [R _{int} = 0.0983, R _{sigma} = 0.0616]
Data/restraints/parameters	3427/0/246
Goodness-of-fit on F²	1.023
Final R indexes [I ≥ 2σ (I)]	R ₁ = 0.0625, wR ₂ = 0.1625
Final R indexes [all data]	R ₁ = 0.0799, wR ₂ = 0.1773
Largest diff. peak/hole / e Å⁻³	0.38/-0.60

Table S19. Crystal data and structure refinement for **49c**.

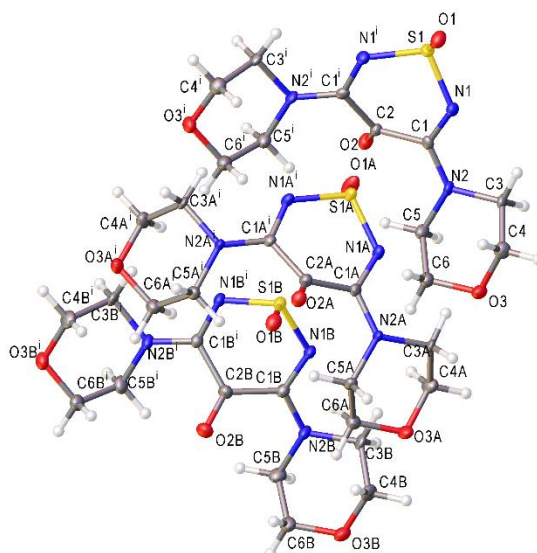
Identification code	49c
Empirical formula	C ₃ H ₁₂ N ₄ O ₇ S
Formula weight	248.23
Temperature/K	100.0
Crystal system	monoclinic
Space group	P2 ₁ /n
a/Å	11.8880(6)
b/Å	6.9467(3)
c/Å	11.8972(6)
α/°	90
β/°	113.475(2)
γ/°	90
Volume/Å³	901.18(8)
Z	4
ρ_{calc}/cm³	1.830
μ/mm⁻¹	3.581
F(000)	520.0
Crystal size/mm³	0.18 × 0.06 × 0.03
Radiation	CuKα (λ = 1.54178)
2θ range for data collection/°	8.892 to 133.474
Index ranges	-14 ≤ h ≤ 13, -8 ≤ k ≤ 8, -14 ≤ l ≤ 14
Reflections collected	10073
Independent reflections	1592 [R _{int} = 0.0665, R _{sigma} = 0.0393]
Data/restraints/parameters	1592/4/147
Goodness-of-fit on F²	1.049
Final R indexes [I ≥ 2σ(I)]	R ₁ = 0.0434, wR ₂ = 0.1164
Final R indexes [all data]	R ₁ = 0.0524, wR ₂ = 0.1240
Largest diff. peak/hole / e Å⁻³	0.68/-0.56

Table S20. Crystal data and structure refinement for **50d**.

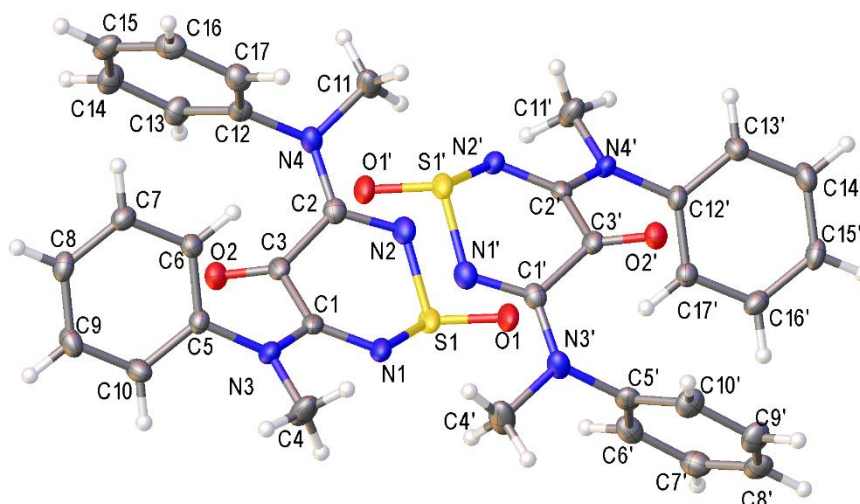
Identification code	50d
Empirical formula	C ₁₁ H ₁₆ N ₄ O ₅ S
Formula weight	316.34
Temperature/K	103.0
Crystal system	monoclinic
Space group	P2 ₁ /n
a/Å	9.2026(18)
b/Å	7.6788(16)
c/Å	19.314(5)
α/°	90
β/°	100.157(9)
γ/°	90
Volume/Å³	1343.4(5)
Z	4
ρ_{calc}/cm³	1.564
μ/mm⁻¹	2.436
F(000)	664.0
Crystal size/mm³	0.36 × 0.03 × 0.02
Radiation	CuKα (λ = 1.54178)
2θ range for data collection/°	9.304 to 137.09
Index ranges	-11 ≤ h ≤ 11, -9 ≤ k ≤ 9, -22 ≤ l ≤ 23
Reflections collected	20332
Independent reflections	2472 [R _{int} = 0.0773, R _{sigma} = 0.0372]
Data/restraints/parameters	2472/0/190
Goodness-of-fit on F²	1.054
Final R indexes [I ≥ 2σ(I)]	R ₁ = 0.0477, wR ₂ = 0.1227
Final R indexes [all data]	R ₁ = 0.0630, wR ₂ = 0.1329
Largest diff. peak/hole / e Å⁻³	0.83/-0.57

Table S21. Crystal data and structure refinement for **51d**.

Identification code	51d
Empirical formula	C ₁₇ H ₁₆ N ₄ O _{2.75} S
Formula weight	352.40
Temperature/K	100
Crystal system	triclinic
Space group	P-1
a/Å	9.7663(3)
b/Å	9.9019(3)
c/Å	10.1948(3)
α/°	88.9643(11)
β/°	65.4274(11)
γ/°	68.8774(10)
Volume/Å³	826.21(4)
Z	2
ρ_{calc}/cm³	1.417
μ/mm⁻¹	0.219
F(000)	368.0
Crystal size/mm³	0.24 × 0.2 × 0.12
Radiation	MoKα (λ = 0.71073)
2θ range for data collection/°	5.012 to 56.574
Index ranges	-13 ≤ h ≤ 13, -13 ≤ k ≤ 13, -13 ≤ l ≤ 13
Reflections collected	25337
Independent reflections	4080 [R _{int} = 0.0382, R _{sigma} = 0.0244]
Data/restraints/parameters	4080/0/228
Goodness-of-fit on F²	1.038
Final R indexes [I ≥ 2σ (I)]	R ₁ = 0.0378, wR ₂ = 0.0895
Final R indexes [all data]	R ₁ = 0.0475, wR ₂ = 0.0951
Largest diff. peak/hole / e Å⁻³	0.33/-0.49

**Table S22.** Crystal data and structure refinement for **50c**.

Identification code	50c
Empirical formula	C ₁₁ H ₁₆ N ₄ O ₄ S
Formula weight	300.34
Temperature/K	100.0
Crystal system	monoclinic
Space group	Cm
a/Å	7.98980(10)
b/Å	21.7995(3)
c/Å	11.6915(2)
α/°	90
β/°	109.9253(8)
γ/°	90
Volume/Å³	1914.45(5)
Z	6
ρ_{calc}/cm³	1.563
μ/mm⁻¹	2.469
F(000)	948.0
Crystal size/mm³	0.2 × 0.14 × 0.03
Radiation	CuKα (λ = 1.54178)
2θ range for data collection/°	8.044 to 144.458
Index ranges	-9 ≤ h ≤ 9, -26 ≤ k ≤ 26, -14 ≤ l ≤ 14
Reflections collected	24106
Independent reflections	3705 [R _{int} = 0.0495, R _{sigma} = 0.0301]
Data/restraints/parameters	3705/2/290
Goodness-of-fit on F²	1.069
Final R indexes [I ≥ 2σ(I)]	R1 = 0.0373, wR2 = 0.0990
Final R indexes [all data]	R1 = 0.0380, wR2 = 0.1001
Largest diff. peak/hole / e Å⁻³	0.64/-0.23
Flack parameter	-0.059(15)

**Table S23.** Crystal data and structure refinement for **51c**.

Identification code	51c
Empirical formula	C ₁₇ H ₁₆ N ₄ O ₂ S
Formula weight	340.40
Temperature/K	100.0
Crystal system	triclinic
Space group	P-1
a/Å	10.7889(3)
b/Å	11.1624(3)
c/Å	14.1533(3)
α/°	81.1030(10)
β/°	78.8280(10)
γ/°	79.6240(10)
Volume/Å³	1632.12(7)
Z	4
ρ_{calc}/cm³	1.385
μ/mm⁻¹	1.914
F(000)	712.0
Crystal size/mm³	0.55 × 0.4 × 0.25
Radiation	CuKα (λ = 1.54178)
2θ range for data collection/°	6.414 to 149.53
Index ranges	-13 ≤ h ≤ 13, -13 ≤ k ≤ 13, -17 ≤ l ≤ 17
Reflections collected	36321
Independent reflections	6612 [R _{int} = 0.0413, R _{sigma} = 0.0287]
Data/restraints/parameters	6612/0/438
Goodness-of-fit on F²	1.133
Final R indexes [I ≥ 2σ(I)]	R ₁ = 0.0504, wR ₂ = 0.1317
Final R indexes [all data]	R ₁ = 0.0513, wR ₂ = 0.1322
Largest diff. peak/hole / e Å⁻³	1.16/-0.55

3.8 Experimental Section

3.8.1 General Methods and Materials

Chemicals used were commercially available except those whose synthesis is described herein. Anhydrous MgSO₄ was used for drying organic extracts and all volatiles were removed under reduced pressure. Reaction mixtures and column eluents were monitored by TLC using commercial aluminium backed thin layer chromatography (TLC) plates (Merck Kieselgel 60 F₂₅₄); the plates were observed under UV light at 254 and 365 nm. The technique of flash chromatography was used throughout for all non-TLC scale chromatographic separations using Merck Silica Gel 60 (< 0.063 mm). Melting points were determined using a Stuart SMP10 digital melting point apparatus. Small scale (μ L) liquid handling measurements were made using variable volume (10–100 μ L) single channel Gilson PIPETMAN precision micropipettes. Solvents used for recrystallisation are indicated after the melting point. UV-vis spectra were obtained using a Perkin-Elmer Lambda-25 UV/vis spectrophotometer and inflections are identified by the abbreviation “inf”. IR spectra were recorded on a Thermo Scientific Nicolet iS5 FTIR spectrometer with iD5 ATR accessory or a Shimadzu FTIR-NIR Prestige-21 spectrometer with Pike Miracle Ge ATR accessory and broad, strong, medium, and weak peaks are represented by br, s, m and w, respectively. ¹H and ¹³C NMR spectra were recorded on either a Bruker AVANCE III HD machine (at 400 and 100 MHz, respectively), a Bruker Avance 300 (at 300 and 75 MHz, respectively), or a 500 machine (at 500 and 125 MHz, respectively). Chemical shifts (δ) are expressed in ppm and coupling constants *J* are given in Hz. Data are represented as follows: chemical shift, multiplicity (s singlet, d doublet, t triplet, q quartet, m multiplet and/or multiple resonances, br s broad singlet). Deuterated solvents were used for homonuclear lock, and the signals are referenced to the deuterated solvent peaks. For the acquisition of mass spectra, the samples were prepared as detailed below and analysed by positive ion nanoelectrospray (nES) using a Thermo Scientific™ LTQ Orbitrap XL™ ETD Hybrid Ion Trap-Orbitrap Mass Spectrometer. Matrix-Assisted Laser Desorption/Ionization-Time Of Flight (MALDI-TOF) mass spectra (+ve mode) were recorded on a Bruker Autoflex III Smartbeam instrument (Bruker), ESI-APCI+ mass spectra were recorded on a Model 6110 Quadrupole MSD, Agilent Technologies and ES-API spectra on a Model 1260 Infinity II Quadrupole MSD,

Agilent Technologies. Flow reactions were carried out with a commercial E-series Photochem UV-150 reactor by Vapourtec Ltd, with two V-3 peristaltic pumps and using an LED module emitting at 420 nm with 61 W light output and a light intensity of 10.2 W.cm⁻². For light driven batch reactions, a commercially available LED module was used, emitting at 420 nm/620 nm with 28 W light output and a light intensity of 3.5 W.cm⁻² (OSA Opto lights, OLM-018 series, Berlin, Germany), placed at a distance of 5 cm from the reaction vessel. For the collection of LC-MS data a Shimadzu LC-2040C 3D Plus instrument was used. EPR studies were carried out using a Bruker microESR instrument, operating at X-band (9.8 GHz) frequency. Sample tubes were Blaubrand micropipettes. Cristaseal putty was used for sealing. Acquisition parameters were the following: Microwave power, 10 mW; Sweep field range, 3333 – 3657 G; Sweep time, 14.9 s; Number of points, 2592; Number of sweeps, 5; Temperature, 26.7 °C. Elemental analysis was carried out at London Metropolitan University, with a Thermo Scientific™ FLASH 2000 CHNS Analyser. For structure determination using single crystal X-ray diffraction samples were mounted on a Molecular Dimensions Litholoop in mineral oil. Data was collected on a Bruker D8 Venture diffractometer using either a copper or molybdenum microsource sealed tube with triumph monochromator and the Apex3 suite of programs. The crystal was kept at 100.0 K during data collection. Using Olex2,¹⁰¹ the structure was solved with the SHELXT structure solution program using Intrinsic Phasing and refined with the SHELXL refinement package using Least Squares minimisation.¹⁰²

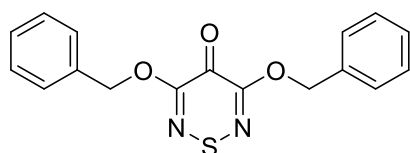
3.8.2 Preparation of 4*H*-1,2,6-thiadiazine Starting Materials[§]

3,5-Dichloro-4*H*-1,2,6-thiadiazin-4-one (**31a**),¹⁰³ 3,5-bis(phenylamino)-4*H*-1,2,6-thiadiazin-4-one (**46a**),¹⁰³ 3,5-dimethoxy-4*H*-1,2,6-thiadiazin-4-one (**22a**),¹⁰³ 3,5-diphenoxy-4*H*-1,2,6-thiadiazin-4-one (**23a**),¹⁰³ 3,5-bis(phenylthio)-4*H*-1,2,6-thiadiazin-4-one (**25a**),¹⁰³ 3-chloro-5-(phenylthio)-4*H*-1,2,6-thiadiazin-4-one (**54a**),¹⁰³ 3-chloro-5-phenoxy-4*H*-1,2,6-thiadiazin-4-one (**53a**),¹⁰³ 3-chloro-5-(phenylamino)-4*H*-1,2,6-thiadiazin-4-one (**52a**),¹⁰³ 3-methoxy-5-phenyl-4*H*-1,2,6-thiadiazin-4-one (**38a**),¹⁰⁴ 3',5'-diphenylspiro[benzo[*d*][1,3]dioxole-2,4'-[1,2,6]thiadiazine] (**9a**),¹⁰⁵ 6,10-diphenyl-1,4-dioxa-8-thia-7,9-diazaspiro[4.5]deca-6,9-diene (**5a**),¹⁰⁵ *N*,3,5-triphenyl-4*H*-1,2,6-thiadiazin-4-imine (**3a**),¹⁰⁶ 3,5-diphenyl-4*H*-1,2,6-thiadiazine-4-thione (**2a**),¹⁰⁴ 2-(3,5-

diphenyl-4*H*-1,2,6-thiadiazin-4-ylidene)malononitrile (**4a**),¹⁰⁴ 3,5-bis(phenylethynyl)-4*H*-1,2,6-thiadiazin-4-one (**7a**)¹⁰⁷ and all symmetrical 3,5-diarylthiadiazinones were prepared according to the reported procedures.

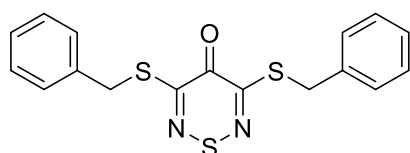
It is stated for clarity that the compounds in this section (3.8.2) were synthesised by our collaborators at the university of Cyprus, and their characterisation data and synthetic procedures are included in this thesis to present a complete storyline.

3.8.2.1 Preparation of Symmetrical 3,5-Diaryl-4*H*-1,2,6-thiadiazines



3,5-Bis(benzyloxy)-4*H*-1,2,6-thiadiazin-4-one (24a).

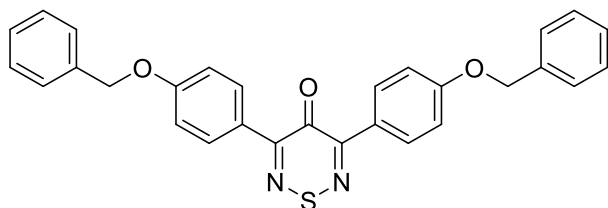
To a stirred solution of 3,5-dichloro-4*H*-1,2,6-thiadiazin-4-one (**31a**) (183 mg, 1.00 mmol) in THF (5 mL), at *ca.* 20 °C, was added, in one portion, benzyl alcohol (227 μ L, 2.00 mmol) and the mixture was cooled to *ca.* 0 °C. To this cooled mixture was added NaH 60% in paraffin oil (80 mg, 2.00 mmol) and the mixture was stirred at this temperature for 1 h, then allowed to warm to *ca.* 20 °C and stirred until complete consumption of the starting material (TLC, 24 h). The mixture was then adsorbed onto silica and chromatographed (*n*-hexane/DCM, 50:50) to give the *title compound* **24a** (301 mg, 92%) as colourless needles, mp 152-153 °C (from *c*-hexane); R_f 0.16 (*n*-hexane/DCM, 50:50); (found: C, 62.71; H, 4.36; N, 8.77. $C_{17}H_{14}N_2O_3S$ requires C, 62.56; H, 4.32; N, 8.58%); λ_{max} (DCM)/nm 271 (log ϵ 4.07), 359 (4.18); ν_{max}/cm^{-1} 3069w (aryl C-H), 2961 (alkyl C-H), 1639s, 1522m, 1454m, 1395w, 1319s, 1281m, 1221w, 1082s, 986s, 924w, 847w, 764m, 750m, 735s; δ_H (500 MHz; $CDCl_3$) 7.45-7.43 (4H, m, Ar *H*), 7.38-7.31 (6H, m, Ar *H*), 5.36 (4H, s, CH_2); δ_C (125 MHz; $CDCl_3$) 157.4 (Cq), 155.7 (Cq), 135.1 (Cq), 128.54 (CH), 128.47 (CH), 128.43 (CH), 69.2 (CH_2); m/z (ES-API+) 326 (M^+ , 15), 270 (M^+-H , 100%), 118 (38).



3,5-Bis(benzylthio)-4*H*-1,2,6-thiadiazin-4-one (26a).

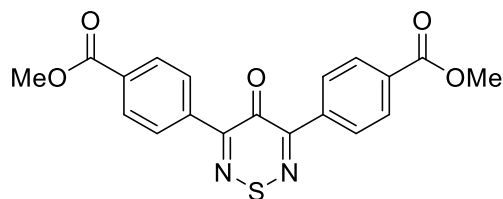
To a stirred solution of 3,5-dichloro-4*H*-1,2,6-thiadiazin-4-one (**31a**) (183 mg, 1.00 mmol) in EtOH (5 mL), at *ca.* 20 °C, was added, in one portion, phenylmethanethiol (235 μ L, 2.00 mmol)

and the mixture was cooled to *ca.* 0 °C. To this cooled mixture was added NaH 60% in paraffin oil (80 mg, 2.00 mmol) and the mixture was stirred at this temperature for 1 h, then allowed to warm to *ca.* 20 °C and stirred until complete consumption of the starting material (TLC, 24 h). The mixture was then poured onto H₂O (10 mL), filtered and washed with *n*-hexane (5 mL) to give the *title compound* **26a** (253 mg, 71%) as yellow needles, mp 91-92 °C (from *c*-hexane); *R_f* 0.19 (*n*-hexane/DCM, 70:30); (found: C, 56.80; H, 3.81; N, 7.73. C₁₇H₁₄N₂OS₃ requires C, 56.96; H, 3.94; N, 7.81%); λ_{\max} (DCM)/nm 250 inf (log ϵ 4.30), 340 (4.01), 396 (4.07); ν_{\max} /cm⁻¹ 3055w and 3024w (aryl C-H), 2922w and 2853w (alkyl C-H), 1618s, 1493m, 1477w, 1452m, 1425w, 1391w, 1302m, 1242m, 1202w, 1074m, 1028w, 868w, 835w, 781m, 745s; δ_{H} (500 MHz; CDCl₃) 7.37 (4H, d, *J* 7.1, Ar *H*), 7.31 (4H, dd, *J* 7.0, 7.0, Ar *H*), 7.26 (2H, dd, *J* 6.4, 6.4, Ar *H*), 4.20 (4H, s, CH₂); δ_{C} (125 MHz; CDCl₃) 160.7 (Cq), 158.0 (Cq), 136.0 (Cq), 129.1 (CH), 128.6 (CH), 127.6 (CH), 33.8 (CH₂); *m/z* (MALDI-TOF) 359 (MH⁺, 29%), 358 (M⁺, 42), 357 (M⁺-H, 100), 180 (66), 153 (62), 90 (99).



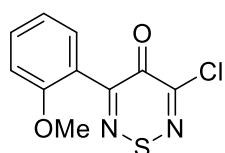
3,5-Bis[4-(benzyloxy)phenyl]-4H-1,2,6-thiadiazin-4-one (34a). A stirred solution of 3,5-dichloro-4H-1,2,6-thiadiazin-4-one (**31a**) (91.5 mg, 0.500

mmol), [4-(benzyloxy)-phenyl]tributylstannane (520 mg, 1.10 mmol) and Pd(Ph₃P)₂Cl₂ (17.5 mg, 5 mol %) in PhMe (1 mL) was deaerated by bubbling of Ar through it for 5 min and then heated at *ca.* 110 °C under Ar until complete consumption of the starting thiadiazine (TLC, 1.5 h). The mixture was then allowed to cool to *ca.* 20 °C and the precipitate filtered to give the *title compound* **34a** (189 mg, 79%) as yellow plates, mp 214-215 °C (from PhMe); *R_f* 0.59 (*n*-hexane/DCM, 50:50); (found: C, 73.00; H, 4.37; N, 5.63. C₂₉H₂₂N₂O₃S requires C, 72.78; H, 4.63; N, 5.85%); λ_{\max} (DCM)/nm 255 (log ϵ 4.20), 270 inf (4.16), 382 (4.46); ν_{\max} /cm⁻¹ 3065w and 3051w (aryl C-H), 2947 (alkyl C-H), 1620s, 1597m, 1570w, 1558w, 1504m, 1468m, 1456m, 1412m, 1379m, 1337m, 1304m, 1240s, 1179s, 1138m, 1121w, 1084w, 1016m, 1005m, 991m, 928m, 866m, 839s, 785m, 756m, 743s; δ_{H} (500 MHz; CDCl₃) 8.08 (4H, d, *J* 8.1, Ar *H*), 7.49 (4H, d, *J* 7.5, Ar *H*), 7.42 (4H, dd, *J* 7.4, 7.4, Ar *H*), 7.36 (2H, d, *J* 9.0, Ar *H*), 7.13 (4H, d, *J* 7.1, Ar *H*), 5.21 (4H, s, CH₂); ¹³C NMR could not be recorded due to insolubility; *m/z* (MALDI-TOF) 479 (MH⁺, 27), 386 (32), 91 (100).



Dimethyl 4,4'-(4-oxo-4H-1,2,6-thiadiazine-3,5-diyl)dibenzoate (32a).

To an intimate mixture of 3,5-dichloro-4H-1,2,6-thiadiazin-4-one (**31a**) (100 mg, 0.546 mmol), [4-(methoxycarbonyl)phenyl]boronic acid (216 mg, 1.20 mmol), Pd(Ph₃P)₄ (31.5 mg, 5 mol %), and Na₂CO₃ (115.7 mg, 1.092 mmol) was added dioxane (1 mL) and H₂O (0.6 mL) and the mixture heated to *ca.* 100 °C until complete consumption of the starting thiadiazine (TLC, 30 min). The mixture was then allowed to cool to *ca.* 20 °C, the precipitate filtered and washed with H₂O (5 mL), then EtOH (5 mL) and dried under vacuum to give the *title compound* **32a** (187 mg, 90%) as yellow needles, mp 234-235 °C (from DCE/*c*-hexane); R_f 0.76 (DCM); (found: C, 59.82; H, 3.67; N, 7.55. C₁₉H₁₄N₂O₅S requires C, 59.68; H, 3.69; N, 7.33%); λ_{max}(DCM)/nm 258 (log ε 4.22), 356 (4.40); ν_{max}/cm⁻¹ 1724s (C=O), 1616s, 1433m, 1400m, 1331w, 1307w, 1281s, 1259s, 1234m, 1188m, 1177m, 1107s, 1013m, 997w, 953m, 856m, 837w, 779m, 764m, 750s; δ_H(500 MHz; CD₂Cl₂) 8.23 (4H, d, *J* 8.6, Ar *H*), 8.12 (4H, d, *J* 8.6, Ar *H*), 3.93 (6H, s, CH₃); δ_C(125 MHz; CD₂Cl₂) 166.7 (Cq), 165.4 (Cq), 160.7 (Cq), 138.6 (Cq), 132.8 (Cq), 129.7 (CH), 129.3 (CH), 52.6 (CH₃); *m/z* (MALDI-TOF) 383 (MH⁺, 86%), 381 (M⁺-H, 100), 353 (61), 341 (36).

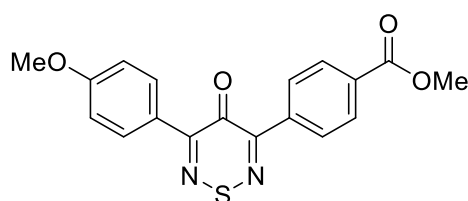


3-Chloro-5-(2-methoxyphenyl)-4H-1,2,6-thiadiazin-4-one (Int1).

To an intimate mixture of 3,5-dichloro-4H-1,2,6-thiadiazin-4-one (**31a**) (100 mg, 0.546 mmol), (2-methoxyphenyl)boronic acid (83 mg, 0.546 mmol), Pd(Ph₃P)₄ (15.8 mg, 2.5 mol %), and Na₂CO₃ (57.9 mg, 0.546 mmol) was added dioxane (1 mL) and H₂O (0.6 mL) and the mixture heated to *ca.* 60 °C until complete consumption of the boronic acid (TLC, 30 min). The mixture was then allowed to cool to *ca.* 20 °C, adsorbed onto silica and chromatographed (*n*-hexane/DCM, 50:50) to give the *title compound* **Int1** (88.9 mg, 64%) as a yellow oil; R_f 0.18 (*n*-hexane/DCM, 50:50); (found: C, 47.28; H, 2.68; N, 10.97. C₁₀H₇ClN₂O₂S requires C, 47.16; H, 2.77; N, 11.00%); λ_{max}(DCM)/nm 314 (log ε 4.16); ν_{max}/cm⁻¹ 1655s, 1599m, 1497m, 1481m, 1437m, 1321m, 1300m, 1275m, 1250s, 1192m, 1182m, 1165m, 1117m, 1051m, 1022m, 1016s, 866m, 841m, 799s, 783m, 766s, 756s, 719s; δ_H(500 MHz; CDCl₃) 7.47 (1H, ddd, *J* 7.5, 7.5, 1.7, Ar *H*), 7.35 (1H, dd, *J* 7.6, 1.8, Ar *H*), 7.05 (1H, ddd, *J* 7.5, 7.5, 0.9, Ar *H*), 7.00 (1H, d, *J* 8.4, Ar *H*), 3.83 (3H, s, CH₃); δ_C(125 MHz; CDCl₃) 161.5 (Cq), 159.9

(Cq), 157.3 (Cq), 151.8 (Cq), 132.3 (CH), 130.0 (CH), 123.8 (Cq), 120.8 (CH), 111.6 (CH), 55.9 (CH₃); *m/z* (MALDI-TOF) 257 (MH⁺+2, 69%), 255 (MH⁺, 100), 193 (40), 177 (34). A final elution (*n*-hexane/DCM, 50:50) gave 3,5-bis(2-methoxyphenyl)-4*H*-1,2,6-thiadiazin-4-one (**18a**) (25.5 mg, 14%) as yellow needles, mp 128-129 °C (from *c*-hexane) [lit. mp 128.5-129 °C],¹⁰⁷ *R_f* 0.47 (*n*-hexane/DCM, 50:50); δ_H(500 MHz; CDCl₃) 7.45-7.40 (4H, m, Ar *H*), 7.05 (2H, dd, *J* 7.5, 7.5, Ar *H*), 6.99 (2H, d, *J* 8.0, Ar *H*), 3.84 (6H, s, OCH₃), identical to an authentic sample.¹⁰⁷

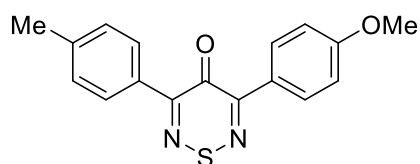
3.8.2.2 Preparation of Asymmetrical 3,5-Diaryl-4*H*-1,2,6-Thiadiazinones



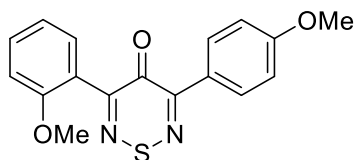
Methyl 4-[5-(4-methoxyphenyl)-4-oxo-4*H*-1,2,6-thiadiazin-3-yl]benzoate (40a): (Typical procedure A, one pot). To an intimate mixture of

3,5-dichloro-4*H*-1,2,6-thiadiazin-4-one (**31a**) (100 mg, 0.546 mmol), [4-(methoxycarbonyl)phenyl]boronic acid (98.3 mg, 0.546 mmol), Pd(Ph₃P)₄ (15.8 mg, 2.5 mol %), and Na₂CO₃ (57.9 mg, 0.546 mmol) was added dioxane (1 mL) and water (0.6 mL) and the mixture heated at *ca.* 60 °C for 1 h. Then (4-methoxyphenyl)boronic acid (91.3 mg, 0.601 mmol), Pd(Ph₃P)₄ (15.8 mg, 2.5 mol %), and Na₂CO₃ (57.9 mg, 0.546 mmol) were added and the mixture heated at *ca.* 100 °C until complete consumption of the intermediate mono-arylthiadiazinone (TLC, 1 h). The mixture was allowed to cool to *ca.* 20 °C, adsorbed onto silica and chromatographed (*n*-hexane/DCM, 50:50) to give 3,5-bis(4-methoxyphenyl)-4*H*-1,2,6-thiadiazin-4-one (**16a**) (19.5 mg, 11%) as yellow needles, mp 169-171 °C (from *c*-hexane) [lit. mp 169-171 °C],¹⁰⁷ *R_f* 0.55 (*n*-hexane/DCM, 50:50); 8.22 (4H, d, *J* 9.0, Ar *H*), 6.97 (4H, d, *J* 8.5, Ar *H*), 3.87 (6H, s, OCH₃), identical to an authentic sample.¹⁰⁷ Further elution (*n*-hexane/DCM, 30:70) gave the *title compound* **40a** (103.5 mg, 54%) as yellow plates, mp 186-187 °C (from DCE/*c*-hexane); *R_f* 0.28 (*n*-hexane/DCM, 30:70); (found: C, 61.14; H, 3.83; N, 7.73. C₁₈H₁₄N₂O₄S requires C, 61.01; H, 3.98; N, 7.91%); λ_{max}(DCM)/nm 251 (log ε 4.39), 376 (4.54); ν_{max}/cm⁻¹ 2951w (alkyl C-H), 1715s, 1624s, 1601m, 1572w, 1564w, 1504m, 1452w, 1431m, 1412m, 1402m, 1331m, 1310m, 1283s, 1256s, 1177m, 1138w, 1109m, 1026m, 1016m, 997w, 961m, 870m, 843m, 808m, 766m, 743m; δ_H(500 MHz; CDCl₃) 8.26 (2H, d, *J* 8.9, Ar *H*), 8.22 (2H, d, *J* 8.6, Ar *H*), 8.12 (2H, dd, *J* 8.6, Ar

H), 6.98 (2H, d, *J* 9.0, Ar *H*), 3.95 (3H, s, CH₃), 3.89 (3H, s, CH₃); δ_C(125 MHz; CDCl₃) 166.5 (Cq), 165.3 (Cq), 162.2 (Cq), 160.3 (Cq), 159.2 (Cq), 138.6 (Cq), 131.8 (Cq), 131.1 (CH), 129.4 (CH), 128.9 (CH), 127.0 (Cq), 113.7 (CH), 55.4 (CH₃), 55.3 (CH₃); *m/z* (MALDI-TOF) 355 (MH⁺, 100%), 239 (65). A final elution (DCM) gave dimethyl 4,4'-(4-oxo-4*H*-1,2,6-thiadiazine-3,5-diyl)dibenzoate (**32a**) (37.1 mg, 18%), R_f 0.76 (DCM); δ_H(500 MHz; CD₂Cl₂) 8.23 (4H, d, *J* 8.6, Ar *H*), 8.12 (4H, d, *J* 8.6, Ar *H*), 3.93 (6H, s, CH₃), identical to that described above.

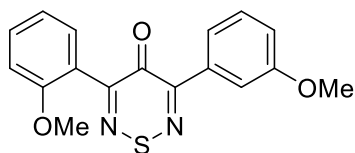


3-(4-Methoxyphenyl)-5-(p-tolyl)-4*H*-1,2,6-thiadiazin-4-one (43a). Similar treatment (typical procedure A) of 3,5-dichloro-4*H*-1,2,6-thiadiazin-4-one (**31a**) (100 mg, 0.546 mmol) with *p*-tolylboronic acid (74.2 mg, 0.546 mmol) for 1 h, followed by (4-methoxyphenyl)boronic acid (91.3 mg, 0.601 mmol) for 1 h, gave after chromatography (*n*-hexane/DCM, 60:40) 3,5-di-*p*-tolyl-4*H*-1,2,6-thiadiazin-4-one (**13a**) (21.6 mg, 13%) as yellow needles, mp 201-203 °C (from *c*-hexane) [lit. mp 202-204 °C],¹⁰⁷ R_f 0.35 (*n*-hexane/DCM, 70:30); δ_H(500 MHz; CDCl₃) 8.11 (2H, d, *J* 8.0, Ar *H*), 7.29 (2H, d, *J* 8.5, Ar *H*), 2.44 (6H, s, CH₃), identical to an authentic sample.¹⁰⁷ Further elution (*n*-hexane/DCM, 60:40) gave the *title compound* **43a** (92.3 mg, 55%) as yellow needles, mp 144-145 °C (from *c*-hexane/EtOH); R_f 0.30 (*n*-hexane/DCM, 60:40); (found: C, 65.90; H, 4.65; N, 9.17. C₁₇H₁₄N₂O₂S requires C, 65.79; H, 4.55; N, 9.03%); λ_{max}(DCM)/nm 248 (log ε 4.16), 374 (4.40); ν_{max}/cm⁻¹ 1628m, 1601s, 1571w, 1506m, 1460m, 1441w, 1410m, 1333m, 1304m, 1258s, 1177s, 1140m, 1117w, 1036m, 837s, 785m, 741m; δ_H(500 MHz; CDCl₃) 8.24 (2H, d, *J* 9.0, Ar *H*), 8.07 (2H, d, *J* 8.3, Ar *H*), 7.27 (2H, d, *J* 9.2, Ar *H*), 6.97 (2H, d, *J* 9.0, Ar *H*), 3.88 (3H, s, CH₃), 2.42 (3H, s, CH₃); δ_C(125 MHz; CDCl₃) 165.6 (Cq), 161.9 (Cq), 160.2 (Cq), 159.7 (Cq), 141.4 (Cq), 132.1 (Cq), 130.9 (CH), 129.0 (CH), 128.9 (CH), 127.4 (Cq), 113.6 (CH), 55.4 (OCH₃), 21.5 (CH₃); *m/z* (MALDI-TOF) 311 (MH⁺, 95%), 310 (M⁺, 100), 290 (99), 279 (96), 214 (94), 165 (78), 135 (93), 119 (95). A final elution (*n*-hexane/DCM, 50:50) gave 3,5-bis(4-methoxyphenyl)-4*H*-1,2,6-thiadiazin-4-one (**16a**) (15.3 mg, 9%) as yellow needles, mp 169-171 °C (from *c*-hexane) [lit. mp 169-171 °C],¹⁰⁷ R_f 0.55 (*n*-hexane/DCM, 50:50); 8.22 (4H, d, *J* 9.0, Ar *H*), 6.97 (4H, d, *J* 8.5, Ar *H*), 3.87 (6H, s, OCH₃), identical to an authentic sample.¹⁰⁷



3-(2-Methoxyphenyl)-5-(4-methoxyphenyl)-4H-1,2,6-thiadiazin-4-one (45a): (Typical procedure B, two-pot).

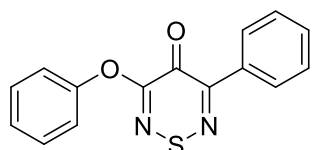
To an intimate mixture of 3-chloro-5-(2-methoxyphenyl)-4H-1,2,6-thiadiazin-4-one (**Int1**) (50.9 mg, 0.200 mol), (4-methoxy-phenyl)boronic acid (33.4 mg, 0.220 mol), Pd(Ph₃P)₄ (5.8 mg, 2.5 mol %), and Na₂CO₃ (21.2 mg, 0.200 mmol) was added dioxane (0.5 mL) and H₂O (0.3 mL) and the mixture heated to *ca.* 100 °C until complete consumption of the starting thiadiazine (TLC, 1 h). The mixture was allowed to cool to *ca.* 20 °C, adsorbed onto silica and chromatographed (*n*-hexane/DCM, 50:50) to give the *title compound* **45a** (64.6 mg, 99%) as yellow plates, mp 134-135 °C (from EtOH); R_f 0.26 (*n*-hexane/DCM, 50:50); (found: C, 62.78; H, 4.25; N, 8.31. C₁₇H₁₄N₂O₃S requires C, 62.56; H, 4.32; N, 8.58%); λ_{max}(DCM)/nm 246 (log ε 4.11), 272 inf (3.96), 365 (4.33); ν_{max}/cm⁻¹ 3011w (aryl C-H), 2928w, 2930w and 2831w (alkyl C-H), 1616m, 1599s, 1572w, 1508m, 1497m, 1466m, 1456m, 1431m, 1414m, 1342m, 1314m, 1288m, 1258s, 1180s, 1165w, 1150m, 1113m, 1051m, 1030m, 1011w, 997m, 878w, 864w, 851m, 814m, 758s, 735m; δ_H(500 MHz; Acetone-*d*₆) 8.22 (2H, d, *J* 9.1, Ar *H*), 7.48 (1H, ddd, *J* 7.5, 7.5, 1.8, Ar *H*), 7.46 (1H, dd, *J* 7.3, 1.8, Ar *H*), 7.13 (1H, d, *J* 8.2, Ar *H*), 7.08 (1H, ddd, *J* 7.5, 7.5, 0.9, Ar *H*), 7.05 (2H, d, *J* 9.1, Ar *H*), 3.89 (3H, s, CH₃), 3.83 (3H, s, CH₃); δ_C(125 MHz; Acetone-*d*₆) 165.8 (Cq), 164.1 (Cq), 163.1 (Cq), 159.1 (Cq), 157.9 (Cq), 132.3 (CH), 131.4 (CH), 130.9 (CH), 128.1 (Cq), 126.7 (Cq), 121.5 (CH), 114.5 (CH), 112.3 (CH), 56.2 (CH₃), 55.0 (CH₃); *m/z* (MALDI-TOF) 327 (MH⁺, 54%), 326 (M⁺, 92), 304 (86), 295 (68), 256 (100), 228 (95), 192 (63), 135 (89).



3-(2-Methoxyphenyl)-5-(3-methoxyphenyl)-4H-1,2,6-thiadiazin-4-one (44a). Similar treatment (typical procedure B) of 3-chloro-5-(2-methoxyphenyl)-4H-1,2,6-

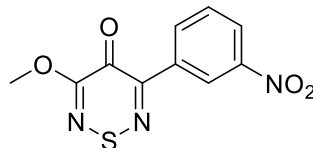
thiadiazin-4-one (**Int1**) (50.9 mg, 0.200 mol) with (3-methoxyphenyl)boronic acid (33.4 mg, 0.220 mol) for 30 min gave after chromatography (*n*-hexane/DCM, 50:50) the *title compound* **44a** (55.6 mg, 85%) as yellow needles, mp 91-92 °C (from *c*-hexane); R_f 0.33 (*n*-hexane/DCM, 50:50); (found: C, 62.26; H, 4.10; N, 8.69. C₁₇H₁₄N₂O₃S requires C, 62.56; H, 4.32; N, 8.58%); λ_{max}(DCM)/nm 239 (log ε 4.06), 342 (4.11); ν_{max}/cm⁻¹ 2940w and 2837w (alkyl C-H), 1643m, 1599m, 1574m, 1491m, 1464m, 1427m, 1341m, 1292m, 1287m, 1269s, 1250m, 1227m, 1179w, 1159w, 1134w, 1047s, 1024m, 1011m, 881m,

758s, 723m; δ_{H} (500 MHz; Acetone- d_6) 7.74 (1H, ddd, J 7.7, 1.5, 1.0, Ar H), 7.72 (1H, dd, J 2.6, 1.6, Ar H), 7.51-7.46 (2H, m, Ar H), 7.42 (1H, dd, J 8.1, 8.1, Ar H), 7.14 (1H, d, J 8.3, Ar H), 7.12-7.07 (2H, m, Ar H), 3.86 (3H, s, CH_3), 3.85 (3H, s, CH_3); δ_{C} (125 MHz; Acetone- d_6) 165.6 (Cq), 164.7 (Cq), 160.4 (Cq), 159.5 (Cq), 157.9 (Cq), 136.8 (Cq), 132.4 (CH), 130.9 (CH), 130.2 (CH), 126.5 (Cq), 121.8 (CH), 121.5 (CH), 117.7 (CH), 114.6 (CH), 112.4 (CH), 56.3 (CH_3), 55.7 (CH_3); m/z (MALDI-TOF) 327 (MH^+ , 54%), 285 (100), 151 (81), 135 (47).



3-Phenoxy-5-phenyl-4H-1,2,6-thiadiazin-4-one (39a).

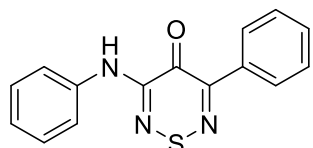
Similar treatment (typical procedure B) of 3-chloro-5-phenoxy-4H-1,2,6-thiadiazin-4-one (**53a**) (120 mg, 0.500 mol) with phenylboronic acid (67.0 mg, 0.550 mmol) for 2 h gave after chromatography (*n*-hexane/DCM, 60:40) the *title compound* **39a** (78 mg, 55%) as yellow plates, mp 152-153 °C (from *c*-hexane); R_f 0.17 (*n*-hexane/DCM, 60:40); (found: C, 63.75; H, 3.50; N, 9.95. $\text{C}_{15}\text{H}_{10}\text{N}_2\text{O}_2\text{S}$ requires C, 63.82; H, 3.57; N, 9.92%); λ_{max} (DCM)/nm 243 inf (log ϵ 3.77), 316 (4.16), 354 (4.17); ν_{max} /cm $^{-1}$ 3092w and 3065w (aryl C-H), 1632m, 1589w, 1524m, 1487m, 1454w, 1441m, 1342s, 1314m, 1279s, 1194s, 1180m, 1165m, 1121m, 1078w, 1022m, 1003w, 974w, 876m, 754s, 733s; δ_{H} (500 MHz; CDCl_3) 8.20-8.18 (2H, m, Ar H), 7.50-7.45 (5H, m, Ar H), 7.33 (1H, ddt, J 7.4, 7.4, 1.0, Ar H), 7.22-7.20 (2H, m, Ar H); δ_{C} (125 MHz; CDCl_3) 161.1 (Cq), 158.9 (Cq), 157.9 (Cq), 151.5 (Cq), 134.2 (Cq), 130.9 (CH), 129.8 (CH), 128.8 (CH), 128.3 (CH), 126.4 (CH), 121.8 (CH); m/z (MALDI-TOF) 283 (MH^+ , 64%), 281 (M^+ , 81), 279 (100), 272 (60), 256 (35), 180 (39).



3-Methoxy-5-(3-nitrophenyl)-4H-1,2,6-thiadiazin-4-one (42a).

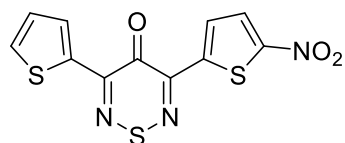
Similar treatment (typical procedure B) of 3-chloro-5-methoxy-4H-1,2,6-thiadiazin-4-one (**53a**) (89.3 mg, 0.500 mol) with (3-nitrophenyl)boronic acid (91.8 mg, 0.550 mol) for 15 min gave after chromatography (*n*-hexane/DCM, 40:60) the *title compound* **42a** (72.5 mg, 55%) as yellow needles, mp 175-176 °C (from DCE/*c*-hexane); R_f 0.29 (*n*-hexane/DCM, 40:60); (found: C, 45.00; H, 2.34; N, 15.76. $\text{C}_{10}\text{H}_7\text{N}_3\text{O}_4\text{S}$ requires C, 45.28; H, 2.66; N, 15.84%); λ_{max} (DCM)/nm 281 (log ϵ 3.99), 314 (4.00), 356 (4.12); ν_{max} /cm $^{-1}$ 3123w, 3098w, 2945w (C-H), 1632s, 1535s, 1518s, 1477w, 1449w, 1427w, 1342s, 1281m, 1192m, 1179w,

1146m, 1092m, 1001m, 955m, 907m, 866m, 812m, 745m, 735m; δ_{H} (500 MHz; CDCl_3) 9.03 (1H, dd, J 2.0, 2.0, Ar H), 8.59 (1H, ddd, J 7.9, 1.1, 1.1, Ar H), 8.31 (1H, ddd, J 8.2, 2.2, 1.4, Ar H), 7.65 (1H, dd, J 8.0, 8.0, Ar H), 4.04 (3H, s, CH_3); δ_{C} (125 MHz; CDCl_3) 161.0 (Cq), 159.2 (Cq), 154.6 (Cq), 148.2 (Cq), 135.6 (Cq), 134.4 (CH), 129.3 (CH), 124.9 (CH), 123.7 (CH), 55.1 (CH_3); m/z (MALDI-TOF) 266 (MH^+ , 100%).



3-Phenyl-5-(phenylamino)-4H-1,2,6-thiadiazin-4-one (35a).

Similar treatment (general procedure B) of 3-chloro-5-(phenylamino)-4H-1,2,6-thiadiazin-4-one (**52a**) (120 mg, 0.500 mol) with phenylboronic acid (67.0 mg, 0.550 mmol) for 2 h gave after chromatography (*n*-hexane/DCM, 70:30) the *title compound* **35a** (128.3 mg, 91%) as orange needles, mp 158-159 °C (from *c*-hexane); R_f 0.30 (*n*-hexane/DCM, 70:30); (found: C, 64.28; H, 3.64; N, 14.89. $\text{C}_{15}\text{H}_{11}\text{N}_3\text{OS}$ requires C, 64.04; H, 3.94; N, 14.94%); λ_{max} (DCM)/nm 253 inf (log ϵ 3.89), 346 (4.34), 411 (3.87); ν_{max} /cm $^{-1}$ 3300w (N-H), 1605m, 1584s, 1551s, 1510w, 1497m, 1447m, 1342m, 1310w, 1229m, 1186w, 1030w, 893m, 872m, 750s; δ_{H} (500 MHz; CDCl_3) 9.02 (1H, br. s, NH), 8.18 (2H, dd, J 8.2, 1.9, Ar H), 7.69 (2H, d, J 7.8, Ar H), 7.49-7.45 (3H, m, Ar H), 7.40 (2H, dd, J 7.8, 7.8, Ar H), 7.17 (1H, dd, J 7.4, 7.4, Ar H); δ_{C} (125 MHz; CDCl_3) 159.1 (Cq), 152.2 (Cq), 151.9 (Cq), 137.4 (Cq), 135.2 (Cq), 130.0 (CH), 129.2 (CH), 128.4 (CH), 128.2 (CH), 124.5 (CH), 119.7 (CH); m/z (APCI+) 282 (MH^+ , 100%), 153 (16), 130 (45), 124 (22).



3-(5-Nitrothien-2-yl)-5-(thien-2-yl)-4H-1,2,6-thiadiazin-4-one (41a).

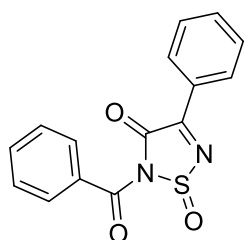
To a beaker cooled at -15 °C using a salt/ice water bath, 15 mL of Ac_2O was added and allowed to cool. Then, concd HNO_3 (3.5 mL) was slowly added and mixed thoroughly. The resulting solution was then added to a 50 mL round bottom flask containing 3,5-di(thien-2-yl)-4H-1,2,6-thiadiazin-4-one (**27a**) (100 mg, 0.359 mmol) in DCM (10 mL) and the solution stirred until complete consumption of **27a** as monitored by TLC (*n*-hexane/DCM, 50:50). The solution was then placed in a separation funnel, and the organic phase was collected and washed with brine. The organic phase was then dried with Na_2SO_4 , and the solvent was evaporated under vacuum. The resulting residue was then separated using column chromatography using an eluent mixture of *n*-hexane/DCM (50:50) to afford the *title*

compound **41a** (97.4 mg, 84%) as orange needles. mp (hot-stage) 206-207 °C (CHCl₃); R_f 0.43 (*n*-hexane/DCM, 50:50); λ_{max}(DCM)/nm 287 (log ε 3.88), 436.5 (3.91); ν_{max}/cm⁻¹ 3102m, 2922m, 1598s (C=O), 1522w, 1492s, 1408m, 1391m, 1325s, 1260m, 1221w, 1200w, 1150w, 1125w, 1056m, 1037m, 1000m, 873m, 844w, 820w, 844w, 820s, 789m, 731m, 713s; δ_H(400 MHz, CDCl₃) 8.37 (1H, dd, *J* 4.0, 1.2, Ar *H*), 8.04 (1H, d, *J* 4.4, Ar *H*), 7.96 (1H, d, *J* 4.8, Ar *H*), 7.74 (1H, dd, *J* 5.2, 1.2, Ar *H*), 7.24 (1H, dd, *J* 5.2, 4.0, Ar *H*); δ_C(100 MHz, CDCl₃) 161.2, 155.1, 152.0, 139.8, 136.1, 135.0, 133.7, 129.4, 128.4, 127.7, one C resonance missing; *m/z* (ESI-) Calculated for [M+Cl]⁻ 357.9187, found: 357.9173.

3.8.3 Preparation of 1,2,5-Thiadiazole 1-oxides from 4*H*-1,2,6-Thiadiazines

It is noted that no R_f values are reported for the 1,2,5-thiadiazole 1-oxide products as those decomposed on silica, as explained in section 3.7.4. Moreover, it was observed that some of the derivatives, exhibited substantial fragmentation upon MS analysis, making the identification of their molecular peaks challenging. Since this scaffold has not been reported previously, a known fragmentation pattern is not available.

3.8.3.1 Preparation of Symmetric 1,2,5-Thiadiazole 1-oxides

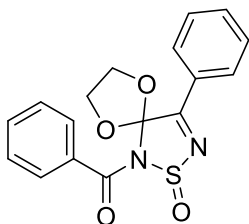


2-Benzoyl-4-phenyl-1,2,5-thiadiazol-3(2*H*)-one 1-oxide (1b).

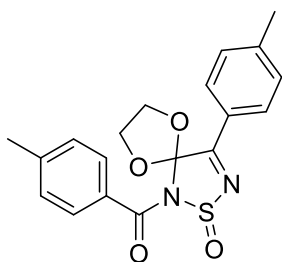
Method A (batch): In a screw capped 5 mL glass vial, a stirred solution of 3,5-diphenyl-4*H*-1,2,6-thiadiazin-4-one (**1a**) (10.0 mg, 0.0375 mmol) in CDCl₃ (1 mL) at *ca.* 20 °C was irradiated with 420 nm light until it was consumed (monitored by TLC, CHCl₃/*n*-hexane, 50:50) over a period of 15 min. The resulting solution was then evaporated giving the *title compound* **1b** (11.2 mg, 100%) as colourless needles, mp (hot-stage) 171-172 °C (CHCl₃); (found: C, 60.04; H, 3.38; N, 9.45; S, 10.77. C₁₅H₁₀N₂O₃S requires C, 60.39; H, 3.38; N, 9.39; S, 10.75%); λ_{max}(DCM)/nm 244.5 (log ε 4.32), 296 (4.26); ν_{max}/cm⁻¹ 1733s (C=O), 1699s (C=O), 1600w, 1584m, 1563m, 1491w, 1447m, 1322w, 1309w, 1254m, 1208m, 1186s, 1177w, 1150s, 1066m (S=O), 1041m, 1019m, 1000w, 977w, 938w, 926w, 900w, 866w, 837w,

803m, 784w, 747m, 715m; δ_{H} (300 MHz, CDCl_3) 8.47-8.51 (2H, m, Ar H), 7.81-7.85 (2H, m, Ar H), 7.66-7.74 (2H, m, Ar H), 7.50-7.57 (4H, m, Ar H); δ_{C} (100 MHz, CDCl_3) 167.9, 166.4, 157.8, 135.5, 134.5, 131.3, 131.1, 130.2, 129.3, 128.7, 128.4; m/z (ESI+): Calculated for $[\text{M}+\text{H}]^+$ 299.0490, found: 299.0468.

Method B (flow): The contents of a 25 mL round bottom flask containing a solution of 3,5-diphenyl-4H-1,2,6-thiadiazin-4-one (**1a**) (10.0 mg, 0.0375 mmol) in CDCl_3 (5 mL) were pumped through a Vapourtec UV-150 photochemical reactor, equipped with a 420 nm LED lamp at 3.30 mL min^{-1} (1 min residence time). After exiting the photoreactor, the solution was then passed through a back pressure regulator which kept the pressure at 3 bar before exiting the flow machine and collected in a 25 mL round bottom flask. The resulting solution was then evaporated giving the *title compound* **1b** (11.2 mg, 100%) as colourless needles, mp (hot-stage) 171-172 °C (CHCl_3); identical to that described above.

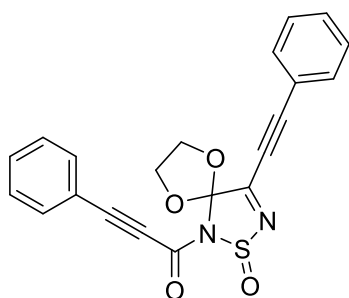


(2-Oxido-4-phenyl-6,9-dioxo-2-thia-1,3-diazaspiro[4.4]non-3-en-1-yl)(phenyl)methanone (5b). Similar treatment (**Method B**) of 6,10-diphenyl-1,4-dioxo-8-thia-7,9-diazaspiro[4.5]deca-6,9-diene (**5a**) (11.6 mg, 0.0375 mmol) under 420 nm light for 10 min gave the *title compound* **5b** (11.7 mg, 91%) as colourless needles, mp (hot-stage) 100-101 °C (CHCl_3) decomp.; λ_{max} (DCM)/nm 268.5 (log ϵ 5.02); ν_{max} / cm^{-1} 2916m (alkyl C-H), 1681s (C=O), 1596m, 1570m, 1489w, 1446m, 1361w, 1289s, 1206m, 1125m, 1051s, 977w, 948w, 896m, 849w, 794m, 746m 722m; δ_{H} (400 MHz, CDCl_3) 7.95-7.98 (2H, m, Ar H), 7.66-7.71 (2H, m, Ar H), 7.63 (1H, tt, J 6.2, 1.3, Ar H), 7.57 (1H, tt, J 7.5, 1.4, Ar H), 7.48-7.53 (4H, m, Ar H), 4.74-4.79 (1H, m, CH_2), 4.62-4.67 (1H, m, CH_2), 4.28-4.38 (2H, m, CH_2); δ_{C} (100 MHz, CDCl_3) 176.7, 168.6, 135.0, 133.7, 132.2, 129.9, 129.5, 129.0, 128.9, 128.4, 119.6, 69.0; m/z (ESI+): Calculated for $[\text{M}+\text{H}]^+$ 343.0753, found: 343.0770.



[2-Oxido-4-(p-tolyl)-6,9-dioxo-2-thia-1,3-diazaspiro[4.4]non-3-en-1-yl](p-tolyl)methanone (6b). Similar treatment (**Method B**) of 6,10-di-p-tolyl-1,4-dioxo-8-thia-7,9-diazaspiro[4.5]deca-6,9-diene (**6a**) (12.7 mg, 0.0375 mmol) under 420 nm light for 14 min gave the *title compound* **6b** (13.1 mg, 94%) as colourless

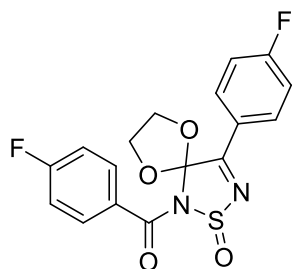
needles, mp (hot-stage) 169-170 °C (Et₂O); λ_{\max} (DCM)/nm 287 (log ϵ 4.12); $\nu_{\max}/\text{cm}^{-1}$ 1677s (C=O), 1588s, 1557m, 1510w, 1485w, 1297s, 1183m, 1158m, 1127m, 1051s, 1017m, 977w, 947m, 900m, 858m, 823m, 790m, 752s, 702m; δ_{H} (400 MHz, CDCl₃) 7.87 (2H, d, J 8.4, Ar H), 7.60 (2H, d, J 8.4, Ar H), 7.30 (4H, dd, J 8.0, 0.4, Ar H), 4.65-4.83 (2H, m, CH₂), 4.30-4.40 (2H, m, CH₂), 2.45 (3H, s, CH₃), 2.42 (3H, s, CH₃); δ_{C} (100 MHz, CDCl₃) 176.5, 168.7, 144.9, 142.8, 132.2, 129.8, 129.6, 129.5, 128.5, 127.0, 119.6, 69.03, 68.97, 21.9, 21.8; m/z (ESI⁺): Calculated for [M+H]⁺ 371.1066, found: 371.1071.



[2-Oxido-4-(phenylethynyl)-6,9-dioxo-2-thia-1,3-diazaspiro[4.4]non-3-en-1-yl]-3-phenylprop-2-yn-1-one (22b). Similar treatment (**Method B**) of 6,10-

bis(phenylethynyl)-1,4-dioxo-8-thia-7,9-diazaspiro[4.5]deca-6,9-diene (**7a**) (13.4 mg, 0.0375 mmol) under 420 nm light for 60 min gave the *title compound 7b*

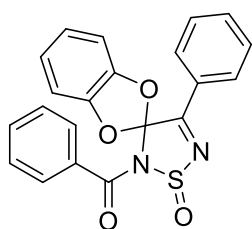
(13.1 mg, 90%) as beige plates, mp (hot-stage) 115-117 °C (Et₂O); λ_{\max} (DCM)/nm 277 (log ϵ 4.10), 286 (4.09), 320 inf (3.92); $\nu_{\max}/\text{cm}^{-1}$ 2203s (C≡C), 1676s (C=O), 1601w, 1580s, 1490w, 1443w, 1393w, 1306s, 1231m, 1190s, 1150s, 1045s, 929m, 887m, 820m, 783w, 757s, 722m; δ_{H} (400 MHz, CDCl₃) 7.67 (2H, d, J 7.2, Ar H), 7.60-7.63 (2H, m, Ar H), 7.46-7.54 (2H, m, Ar H), 7.40-7.45 (4H, m, Ar H), 4.63-4.70 (2H, m, CH₂), 4.40-4.47 (2H, m, CH₂); δ_{C} (100 MHz, CDCl₃) 133.3, 133.2, 131.9, 131.5, 129.1, 128.9, 119.5, 119.0, 80.6, 69.4, 68.8. Five of the C resonances belonging to alkyne and phenyl groups are overlapping; m/z (ESI⁺): Calculated for [M+H]⁺ 391.0753, found: 391.0753.



(4-Fluorophenyl)[4-(4-fluorophenyl)-2-oxido-6,9-dioxo-2-thia-1,3-diazaspiro[4.4]non-3-en-1-yl]methanone (8b).

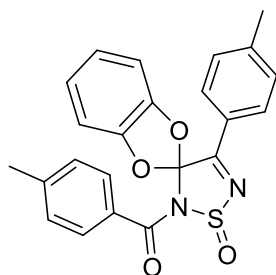
Similar treatment (**Method B**) of 6,10-bis(4-fluorophenyl)-1,4-dioxo-8-thia-7,9-diazaspiro[4.5]deca-6,9-diene (**8a**) (13.0 mg, 0.0375 mmol) under 420 nm light for 60 min gave the *title compound 8b* (13.5 mg, 95%) as colourless needles, mp (hot-stage) 160-161 °C (Et₂O); λ_{\max} (DCM)/nm 276 (log ϵ 4.13); $\nu_{\max}/\text{cm}^{-1}$ 2986w and 2908w (alkyl C-H), 1688s (C=O), 1600s, 1580s, 1507m, 1484w, 1408w, 1303s, 1240m, 1230m, 1208m, 1165w, 1157m, 1139s, 1123s, 1104w, 1052s, 1005s, 981m, 959m, 945s, 900s, 852m, 844s, 822w, 799w,

758s, 749s, 719w, 701w; δ_{H} (400 MHz, CDCl_3) 7.99-8.03 (2H, m, Ar H), 7.71-7.75 (2H, m, Ar H), 7.17-7.23 (4H, m, Ar H), 4.69-4.82 (2H, m, CH_2), 4.31-4.40 (2H, m, CH_2); δ_{C} (100 MHz, CDCl_3) 174.5, 167.5, 166.3 (d, $^1J_{\text{CF}}$ 255.0), 165.0 (d, $^1J_{\text{CF}}$ 252.0), 132.2 (d, $^3J_{\text{CF}}$ 9.0), 131.1 (d, $^3J_{\text{CF}}$ 9.0), 125.9 (d, $^4J_{\text{CF}}$ 3.0), 119.5, 116.5 (d, $^2J_{\text{CF}}$ 22.0), 116.2 (d, $^2J_{\text{CF}}$ 22.0), 69.1. One C resonance is missing; m/z (ESI+): Calculated for $[\text{M}+\text{H}]^+$ 379.0564, found: 379.0564.



(1'-oxido-4'-phenyl-2'H-spiro[benzo[*d*][1,3]dioxole-2,3'-[1,2,5]thiadiazol]-2'-yl)(phenyl)methanone (**9b**). Similar

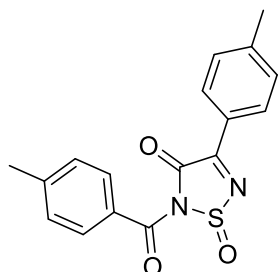
treatment (**Method B**) of 3',5'-diphenylspiro[benzo[*d*][1,3]dioxole-2,4'-[1,2,6]thiadiazine (**9a**) (13.4 mg, 0.0375 mmol) under 420 nm light for 10 min gave the *title compound 9b* (14.0 mg, 96%) as a colourless needles, mp (hot-stage) 155-160 °C (Et_2O) decomp.; λ_{max} (DCM)/nm 277 (log ϵ 3.81); $\nu_{\text{max}}/\text{cm}^{-1}$ 1698s (C=O), 1605m, 1595m, 1572w, 1482s, 1445m, 1362w, 1279s, 1261m, 1228s, 1197w, 1180w, 1129s, 1098m, 1063s, 1024m, 1001m, 980w, 961m, 918w, 796s, 739s, 717s; δ_{H} (300 MHz, CDCl_3) 7.86-7.90 (2H, m, Ar H), 7.66-7.69 (2H, m, Ar H), 7.59 (1H, tt, J 7.5, 1.2, Ar H), 7.52 (1H, tt, J 7.5, 1.5, Ar H), 7.36-7.45 (4H, m, Ar H), 6.98-7.06 (3H, m, Ar H), 6.89-6.91 (1H, m, Ar H); δ_{C} (100 MHz, CDCl_3) 172.3, 168.3, 146.1, 146.0, 134.7, 134.0, 132.5, 129.9, 129.3, 128.8, 128.5, 128.3, 123.4, 123.2, 121.0, 109.1, 108.7; m/z (ESI+): Calculated for $[\text{M}+\text{H}]^+$ 391.0753, found: 391.0752.



[1'-Oxido-4'-(p-tolyl)-2'H-spiro(benzo[*d*][1,3]dioxole-2,3'-[1,2,5]thiadiazol)-2'-yl](p-tolyl)methanone (**11b**). Similar

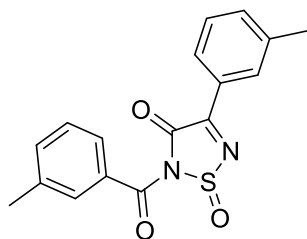
treatment (**Method B**) of 3',5'-di-*p*-tolylspiro(benzo[*d*][1,3]dioxole-2,4'-[1,2,6]thiadiazine) (**11a**) (14.5 mg, 0.0375 mmol) under 420 nm light for 10 min gave the *title compound 11b* (13.8 mg, 88%) as colourless needles, mp (hot-stage) 166-167 °C (Et_2O) decomp.; λ_{max} (DCM)/nm 284 (log ϵ 4.17), 297 inf (4.13); $\nu_{\text{max}}/\text{cm}^{-1}$ 1696m (C=O), 1591m, 1560w, 1481s, 1278s, 1229w, 1183w, 1136m, 1063w, 1018w, 961w, 910w, 826w, 804w, 780w, 749s; δ_{H} (400 MHz, CDCl_3) 7.77 (2H, d, J 8.4, Ar H), 7.58 (2H, d, J 8.4, Ar H), 7.21 (4H, dd, J 12.8, 7.6, Ar H), 6.98-7.05 (3H, m, Ar H), 6.89-6.91 (1H, m, Ar H), 2.38 (6H, s, CH_3); δ_{C} (100 MHz, CDCl_3) 172.2, 168.2,

146.22, 146.15, 143.2, 131.3, 130.1, 130.0, 129.5, 129.4, 128.7, 125.6, 123.3, 123.0, 121.0, 109.0, 108.6, 22.0, 21.8; m/z (ESI+): Calculated for $[M+H]^+$ 419.1066, found: 419.1063.



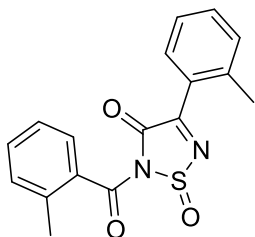
2-(4-Methylbenzoyl)-4-(p-tolyl)-1,2,5-thiadiazol-3(2H)-one 1-oxide (13b). Similar treatment (**Method A**) of 3,5-di-*p*-tolyl-4*H*-1,2,6-thiadiazin-4-one (**13a**) (11.0 mg, 0.0375 mmol) under 420 nm light for 15 min gave the *title compound* **13b** (12.2 mg, 100%) as colourless needles, mp (hot-stage) 169-170 °C (CHCl₃) decomp.; λ_{\max} (DCM)/nm 250 (log ϵ 4.17), 326 (4.13); $\nu_{\max}/\text{cm}^{-1}$

2920w (alkyl C-H), 1728m (C=O), 1700m (C=O), 1606m, 1585m, 1551m, 1509w, 1447w, 1401w, 1364w, 1309w, 1254m, 1207m, 1171m, 1149s, 1063m, 1033w, 1017s, 968w, 906w, 833m, 826m, 796w, 777w, 758m, 740s; δ_{H} (400 MHz, CDCl₃) 8.40 (2H, dd, J 6.8, 1.6, Ar H), 7.74 (2H, dd, J 6.8, 1.6, Ar H), 7.31-7.34 (4H, m, Ar H), 2.46 (6H, s, CH₃); δ_{C} (100 MHz, CDCl₃) 167.7, 166.0, 158.1, 147.2, 145.8, 131.2, 130.4, 130.1, 129.5, 128.6, 125.8, 22.2, 22.1; m/z (ESI+): Calculated for $[M+H]^+$ 327.0803, found: 327.0790.



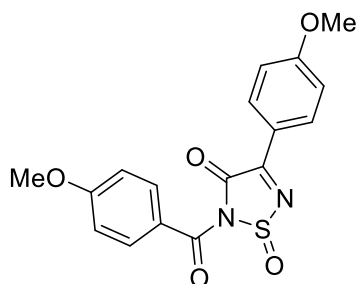
2-(3-Methylbenzoyl)-4-(m-tolyl)-1,2,5-thiadiazol-3(2H)-one 1-oxide (14b). Similar treatment (**Method B**) of 3,5-di-*m*-tolyl-4*H*-1,2,6-thiadiazin-4-one (**14a**) (11.0 mg, 0.0375 mmol) under 420 nm light for 2 min gave the *title compound* **14b** (11.8 mg, 97%) as colourless needles, mp (hot-stage) 143-144 °C

(CHCl₃); λ_{\max} (DCM)/nm 253 (log ϵ 4.91), 314 (4.86); $\nu_{\max}/\text{cm}^{-1}$ 2923w (alkyl C-H), 1728s (C=O), 1695m (C=O), 1606w, 1581m, 1554m, 1479w, 1456w, 1425w, 1385w, 1276m, 1225m, 1193m, 1161s, 1085m, 1054m, 1000w, 939m, 932w, 890m, 826m, 797m, 760s, 739s, 716m; δ_{H} (400 MHz, CDCl₃) 8.29 (2H, dd, J 5.6, 0.4, Ar H), 7.59-7.62 (2H, m, Ar H), 7.49 (2H, dd, J 8.0, 8.0, Ar H), 7.38-7.43 (2H, m, Ar H), 2.43 (3H, s, CH₃), 2.42 (3H, s, CH₃); δ_{C} (100 MHz, CDCl₃) 168.1, 166.4, 157.9, 139.2, 138.8, 136.4, 135.3, 131.4, 130.5, 129.2, 128.6, 128.41, 128.37, 127.3, 21.5, 21.4. One C resonance missing; m/z (ESI+): Calculated for $[M+H]^+$ 327.0803, found: 327.0809.



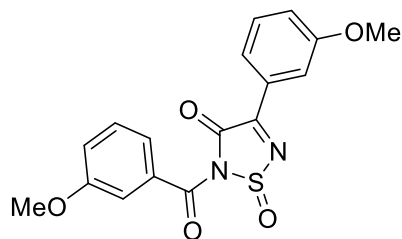
2-(2-Methylbenzoyl)-4-(o-tolyl)-1,2,5-thiadiazol-3(2H)-one 1-oxide (15b). Similar treatment (**Method A**) of 3,5-di-*o*-tolyl-4*H*-1,2,6-thiadiazin-4-one (**15a**) (11.0 mg, 0.0375 mmol) under 420 nm light for 30 min gave the *title compound* **15b** (12.2 mg, 100%) as colourless needles, mp (hot-stage) 175-176 °C (CHCl₃)

decomp.; $\lambda_{\max}(\text{DCM})/\text{nm}$ 247 (log ϵ 3.94), 308 (3.92); $\nu_{\max}/\text{cm}^{-1}$ 2927w (alkyl C-H), 1735m (C=O), 1692m (C=O), 1586m, 1573m, 1487w, 1457m, 1381w, 1300w, 1242s, 1213s, 1197m, 1147s, 1056m, 1044m, 1021m, 905w, 868w, 824w, 777m, 762m, 747m, 734s, 700m; $\delta_{\text{H}}(400 \text{ MHz, CDCl}_3)$ 8.00 (1H, dd, J 8.4, 1.6, Ar H), 7.44-7.52 (3H, m, Ar H), 7.29-7.38 (4H, m, Ar H), 2.63 (3H, s, CH₃), 2.47 (3H, s, CH₃); $\delta_{\text{C}}(100 \text{ MHz, CDCl}_3)$ 168.4, 168.3, 157.6, 141.3, 137.7, 133.7, 132.44, 132.38, 132.3, 131.9, 131.4, 128.6, 126.9, 126.2, 126.0, 22.0, 19.8; m/z (ESI⁺): Calculated for [M+H]⁺ 327.0803, found: 327.0783.



2-(4-Methoxybenzoyl)-4-(4-methoxyphenyl)-1,2,5-thiadiazol-3(2H)-one 1-oxide (16b). Similar treatment (**Method A**) of 3,5-bis(4-methoxyphenyl)-4*H*-1,2,6-thiadiazin-4-one (**16a**) (12.2 mg, 0.0375 mmol) under 420 nm light for 15 min gave the *title compound* **16b** (13.4 mg, 100%) as yellow needles, mp (hot-stage) 192-193 °C

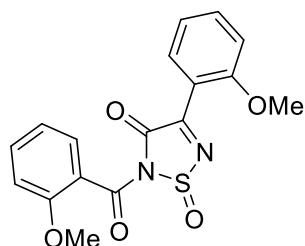
(CHCl₃) decomp. ; $\lambda_{\max}(\text{DCM})/\text{nm}$ 257 (log ϵ 3.99), 281 (3.97), 359 (4.05); $\nu_{\max}/\text{cm}^{-1}$ 2941w and 2846w (alkyl C-H), 1728m (C=O), 1692m (C=O), 1601s, 1577m, 1548m, 1511m, 1459w, 1445w, 1424w, 1317m, 1258s, 1182w, 1166m, 1152s, 1064m, 1018m, 907m 841m, 817w, 784w, 762m, 753m, 727w, 717w, 702m; $\delta_{\text{H}}(400 \text{ MHz, CDCl}_3)$ 8.53-8.57 (2H, m, Ar H), 7.83-7.87 (2H, m, Ar H), 6.98-7.03 (4H, m, Ar H), 3.92 (3H, s, CH₃), 3.91 (3H, s, CH₃); $\delta_{\text{C}}(100 \text{ MHz, CDCl}_3)$ 166.9, 165.8, 164.9, 164.8, 158.6, 133.8, 133.1, 123.6, 121.1, 114.9, 114.1, 55.9, 55.8; m/z (ESI⁺): Calculated for [M+H]⁺ 359.0702, found: 359.0683.



2-(3-Methoxybenzoyl)-4-(3-methoxyphenyl)-1,2,5-thiadiazol-3(2H)-one 1-oxide (17b).

Similar treatment (**Method A**) of 3,5-bis(3-methoxyphenyl)-4H-1,2,6-thiadiazin-4-one (**17a**) (12.2 mg, 0.0375 mmol) under 420 nm light for 25 min gave the *title compound 17b*

(13.4 mg, 100%) as yellow needles, mp (hot-stage) 119-120 °C (CHCl₃) decomp.; λ_{\max} (DCM)/nm 260 (log ϵ 4.07), 310 (4.00), 379 inf (3.44); ν_{\max} /cm⁻¹ 3080w (aryl C-H) and 3003w (C-H), 2940w and 2830w (alkyl C-H), 1732s (C=O), 1688m (C=O), 1597m, 1557m, 1487m, 1425m, 1335w, 1291w, 1275m, 1247m, 1227m, 1197w, 1152s, 1083w, 1056w, 1029s, 994m, 943m, 890w, 857m, 822m, 790m, 756m, 740m; δ_{H} (400 MHz, CDCl₃) 8.14 (1H, dt, *J* 7.6, 1.2, Ar *H*), 7.97 (1H, dd, *J* 2.4, 1.6, Ar *H*), 7.38-7.46 (3H, m, Ar *H*), 7.33 (1H, dd, *J* 2.4, 1.2, Ar *H*), 7.22-7.26 (2H, m, Ar *H*), 3.88 (3H, s, CH₃), 3.87 (3H, s, CH₃); δ_{C} (100 MHz, CDCl₃) 167.7, 166.1, 160.1, 159.8, 157.8, 132.6, 130.3, 129.8, 129.5, 124.0, 122.7, 122.5, 120.9, 114.6, 55.74, 55.72. One C resonance missing; *m/z* (ESI⁺): Calculated for [M+H]⁺ 359.0702, found: 359.0714.

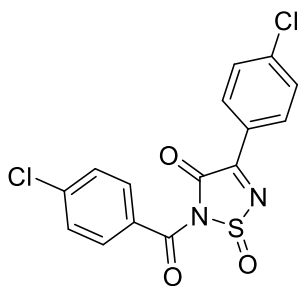


2-(2-Methoxybenzoyl)-4-(2-methoxyphenyl)-1,2,5-thiadiazol-3(2H)-one 1-oxide (18b).

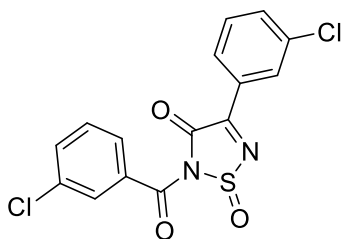
Similar treatment (**Method A**) of 3,5-bis(2-methoxyphenyl)-4H-1,2,6-thiadiazin-4-one (**18a**) (12.2 mg, 0.0375 mmol) under 420 nm light for 4 h gave the

title compound 18b (13.4 mg, 100%) as yellow needles, mp

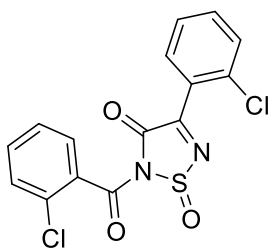
(hot-stage) 139-140 °C (CHCl₃) decomp.; λ_{\max} (DCM)/nm 262 (log ϵ 4.15), 297 (3.14), 370 inf (3.60); ν_{\max} /cm⁻¹ 2931w and 2836w (alkyl C-H), 1762m (C=O), 1664m (C=O), 1664m, 1598s, 1490m, 1455m, 1432m, 1297m, 1276m, 1243s, 1196w, 1162w, 1143s, 1124m, 1073w, 1052w, 1041w, 1019s, 936w, 907m, 851w, 816w, 747s, 708m; δ_{H} (400 MHz, CDCl₃) 7.74 (1H, dd, *J* 8.0, 1.6, Ar *H*), 7.50-7.57 (3H, m, Ar *H*), 7.03-7.08 (3H, m, Ar *H*), 6.96 (1H, d, *J* 8.4, Ar *H*), 3.88 (3H, s, CH₃), 3.83 (3H, s, CH₃); δ_{C} (100 MHz, CDCl₃) 169.1, 166.5, 159.9, 157.7, 156.5, 135.2, 134.2, 132.2, 130.3, 122.3, 121.0, 120.9, 117.9, 112.3, 111.4, 56.3, 56.0; *m/z* (ESI⁺): Calculated for [M+H]⁺ 359.0702, found: 359.0711.



2-(4-Chlorobenzoyl)-4-(4-chlorophenyl)-1,2,5-thiadiazol-3(2H)-one 1-oxide (19b). Similar treatment (**Method A**) of 3,5-bis(4-chlorophenyl)-4*H*-1,2,6-thiadiazin-4-one (**19a**) (12.6 mg, 0.0375 mmol) under 420 nm light for 15 min gave the *title compound 19b* (13.8 mg, 100%) as colourless needles, mp (hot-stage) 179-181 °C (CHCl₃) decomp.; λ_{\max} (DCM)/nm 250 (log ϵ 4.18), 325 (4.10); ν_{\max} /cm⁻¹ 3100w (aryl C-H), 1728m (C=O), 1673m (C=O), 1586s, 1488m, 1402m, 1304w, 1270m, 1210m, 1185w, 1151s, 1117w, 1090s, 1032w, 1011m, 958w, 901m, 840s, 790m, 763m, 743s, 715m; δ_{H} (400 MHz, CDCl₃) 8.45 (2H, dd, *J* 8.8, 2.4, Ar *H*), 7.77 (2H, dd, *J* 8.8, 2.4, Ar *H*), 7.50-7.55 (4H, m, Ar *H*); δ_{C} (100 MHz, CDCl₃) 166.9, 165.4, 157.6, 142.8, 141.4, 132.4, 131.6, 129.9, 129.5, 129.2, 126.7; *m/z* (ESI⁺): Calculated for [M+Na]⁺ 388.9530, found: 388.9530.

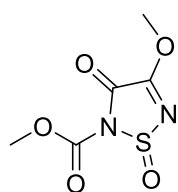


2-(3-Chlorobenzoyl)-4-(3-chlorophenyl)-1,2,5-thiadiazol-3(2H)-one 1-oxide (20b). Similar treatment (**Method A**) of 3,5-bis(3-chlorophenyl)-4*H*-1,2,6-thiadiazin-4-one (**20a**) (12.6 mg, 0.0375 mmol) under 420 nm light for 25 min gave the *title compound 20b* (13.8 mg, 100%) as colourless needles, mp (hot-stage) 167-169 °C (CHCl₃) decomp.; λ_{\max} (DCM)/nm 244 (log ϵ 3.57), 300 (3.49); ν_{\max} /cm⁻¹ 3069w (aryl C-H), 1736m (C=O), 1692s (C=O), 1576m, 1551s, 1472w, 1423m, 1408m, 1284m, 1252s, 1197m, 1153s, 1089w, 1072m, 1032w, 998w, 928m, 914w, 889m, 830w, 800m, 792m, 769w, 740s, 712m; δ_{H} (400 MHz, CDCl₃) 8.47 (1H, dd, *J* 2.0, 2.0, Ar *H*), 8.38 (1H, dt, *J* 8.4, 1.2, Ar *H*), 7.78 (1H, dd, *J* 2.0, 2.0, Ar *H*) 7.65-7.70 (3H, m, Ar *H*), 7.49 (2H, dd, *J* 15.2, 7.6, Ar *H*); δ_{C} (100 MHz, CDCl₃) 166.7, 165.4, 157.3, 135.7, 135.6, 135.1, 134.5, 132.8, 130.8, 130.6, 130.1, 130.0, 129.8, 129.2, 128.1; *m/z* (ESI⁺): Calculated for [M+Na]⁺ 388.9530, found: 388.9549.



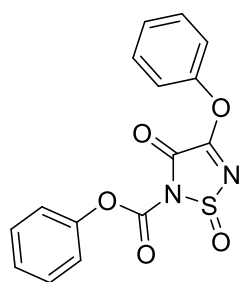
2-(2-Chlorobenzoyl)-4-(2-chlorophenyl)-1,2,5-thiadiazol-3(2H)-one 1-oxide (21b). Similar treatment (**Method A**) of 3,5-bis(2-chloro-phenyl)-4*H*-1,2,6-thiadiazin-4-one (**21a**) (12.6 mg, 0.0375 mmol) under 420 nm light for 2 h gave the *title compound 21b* (13.8 mg, 100%) as colourless plates, mp (hot-stage) 173-175

°C (CHCl₃) decomp.; $\lambda_{\max}(\text{DCM})/\text{nm}$ 241 (log ϵ 3.90), 296 (3.76); $\nu_{\max}/\text{cm}^{-1}$ 3098w (C-H), 1743s (C=O), 1703s (C=O), 1589m, 1566w, 1473w, 1436m, 1291w, 1249s, 1210s, 1151s, 1094m, 1072w, 1031m, 1020m, 958w, 909w, 875w, 803m, 777m, 744s, 715w; $\delta_{\text{H}}(400 \text{ MHz, CDCl}_3)$ 7.69-7.71 (1H, m, Ar *H*), 7.53-7.55 (2H, m, Ar *H*), 7.48-7.51 (3H, m, Ar *H*) 7.39-7.43 (2H, m, Ar *H*); $\delta_{\text{C}}(100 \text{ MHz, CDCl}_3)$ 169.0, 165.6, 156.1, 134.5, 134.1, 133.1, 132.29, 132.25, 131.5, 131.2, 130.2, 129.4, 127.4, 127.13, 127.08; m/z (ESI+): Calculated for [M+H]⁺ 366.9711, found: 366.9743.



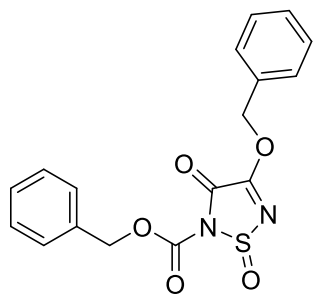
Methyl 4-methoxy-3-oxo-1,2,5-thiadiazole-2(3H)-carboxylate 1-oxide (15b). Similar treatment (**Method A**) of 3,5-dimethoxy-4*H*-1,2,6-thiadiazin-4-one (**22a**) (6.5 mg, 0.0375 mmol) under 420 nm light for 15 min gave the *title compound 22b* (7.7 mg, 100%) as colourless plates, mp

(hot-stage) 98-100 °C (CHCl₃); $\lambda_{\max}(\text{DCM})/\text{nm}$ no absorption above 235 nm; $\nu_{\max}/\text{cm}^{-1}$ 2961w (alkyl C-H), 1790s (C=O), 1729m (C=O), 1612s, 1441m, 1370w, 1265s, 1228s, 1157s, 1033s, 1011s, 945m, 894s, 846w, 894s, 846w, 787w, 760m, 741m; $\delta_{\text{H}}(300 \text{ MHz, CDCl}_3)$ 4.21 (3H, s, CH₃), 4.03 (3H, s, CH₃); $\delta_{\text{C}}(100 \text{ MHz, CDCl}_3)$ 164.8, 151.6, 148.7, 59.1, 55.2; m/z (ESI-): Calculated for [M+Na-2H]⁻ 226.9739, found: 226.9780.



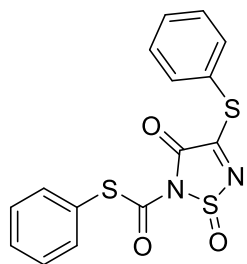
Phenyl 3-oxo-4-phenoxy-1,2,5-thiadiazole-2(3H)-carboxylate 1-oxide (23b). Similar treatment (**Method B**) of 3,5-diphenoxy-4*H*-1,2,6-thiadiazin-4-one (**23a**) (11.2 mg, 0.0375 mmol) under 420 nm light for 2 min gave the *title compound 23b* (11.5 mg, 93%) as colourless plates, mp (hot-stage) 163-164 °C (Et₂O) decomp.;

$\lambda_{\max}(\text{DCM})/\text{nm}$ 258 (log ϵ 3.99); $\nu_{\max}/\text{cm}^{-1}$ 1784m (C=O), 1732s (C=O), 1622m, 1583m, 1487s, 1457w, 1373m, 1277s, 1217m, 1187m, 1168s, 1157s, 1068w, 1026w, 1005m, 974w, 931m, 915w, 894m, 838m, 757s, 726s; $\delta_{\text{H}}(400 \text{ MHz, Acetone-}d_6)$ 7.46-7.60 (6H, m, Ar *H*), 7.42-7.46 (1H, m, Ar *H*), 7.39 (1H, tt, *J* 7.6, 1.2, Ar *H*), 7.32-7.34 (2H, m, Ar *H*); $\delta_{\text{C}}(100 \text{ MHz, Acetone-}d_6)$ 165.0, 153.1, 153.0, 150.8, 148.2, 131.0, 130.8, 128.3, 127.9, 122.2, 121.5; m/z (ESI+): Calculated for [M+H]⁺ 331.0389, found: 331.0388.



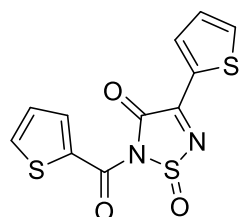
Benzyl **4-(benzyloxy)-3-oxo-1,2,5-thiadiazole-2(3H)-carboxylate 1-oxide (24b).**

Similar treatment (**Method A**) of 3,5-bis(benzyloxy)-4*H*-1,2,6-thiadiazin-4-one (**24a**) (12.6 mg, 0.0375 mmol) under 420 nm light for 15 min gave the *title compound* **24b** (13.4 mg, 100%) as colourless plates, mp (hot-stage) 79-81 °C (CHCl₃); λ_{\max} (MeOH)/nm 232 (log ϵ 3.72); ν_{\max} /cm⁻¹ 3186 w, 3061w and 3033w (aryl C-H), 1775m (C=O), 1745s (C=O), 1704w, 1683w, 1535w, 1495m, 1454m, 1405w, 1301s, 1227m, 1186s, 1079w, 1047s, 1018m, 943m, 906m, 770m, 744w, 728s; δ_{H} (400 MHz, CDCl₃) 7.37-7.48 (10H, m, Ar *H*), 5.53 (2H, s, CH₂), 5.42 (2H, q, *J* 12.0, CH₂); δ_{C} (100 MHz, CDCl₃) 163.9, 151.8, 148.2, 133.9, 132.6, 129.8, 129.5, 129.2, 129.1, 129.0, 128.7, 74.6, 70.1; *m/z* (ESI⁺): Calculated for [M+CH₃OH+H]⁺ 391.0964, found: 391.0948.



S-Phenyl **3-oxo-4-(phenylthio)-1,2,5-thiadiazole-2(3H)-carbothioate 1-oxide (25b).**

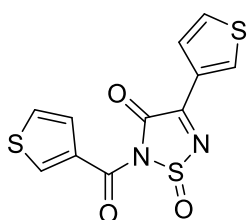
Similar treatment (**Method A**) of 3,5-bis(phenylthio)-4*H*-1,2,6-thiadiazin-4-one (**25a**) (12.4 mg, 0.0375 mmol) under 420 nm light for 15 min gave the *title compound* **25b** (13.6 mg, 100%) as beige-yellow plates, mp (hot-stage) 131-133 °C (CHCl₃) decomp.; λ_{\max} (DCM)/nm 234 (log ϵ 4.23), 245 inf (4.15), 309 inf (3.95), 335 (4.02), 352 inf (3.70), 393 (3.53); ν_{\max} /cm⁻¹ 3060w (aryl C-H), 1737s (C=O), 1674s (C=O), 1618m, 1577w, 1538s, 1475m, 1441m, 1271s, 1159w, 1138m, 1059s, 1022m, 1000w, 899m, 846w, 733s, 704w; δ_{H} (400 MHz, CDCl₃) 7.61 (1H, dd, *J* 7.6, 1.6, Ar *H*), 7.43-7.55 (9H, m, Ar *H*); δ_{C} (100 MHz, CDCl₃) 177.3, 166.8, 160.2, 159.1, 156.4, 135.8, 135.5, 134.4, 131.4, 130.8, 130.2, 130.1, 129.7, 129.6, 129.2, 127.7, 126.9; *m/z* (ESI⁻): Calculated for [M-H]⁻ 360.9781, found: 360.9751.



4-(Thien-2-yl)-2-(thiophene-2-carbonyl)-1,2,5-thiadiazol-3(2H)-one 1-oxide (27b).

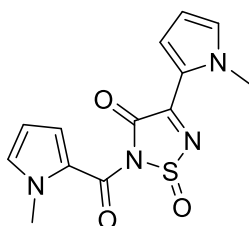
Similar treatment (**Method A**) of 3,5-di(thien-2-yl)-4*H*-1,2,6-thiadiazin-4-one (**27a**) (10.4 mg, 0.0375 mmol) under 420 nm light for 15 min gave the *title compound* **27b** (11.6 mg, 100%) as beige-yellow needles, mp (hot-stage) 180-181 °C (CHCl₃) decomp.; λ_{\max} (DCM)/nm 264 (log ϵ 4.03), 353.5 (4.03); ν_{\max} /cm⁻¹ 3105m and 3087m

(aryl C-H), 1723s (C=O), 1648s (C=O), 1558s, 1515m, 1421m, 1406s, 1353m, 1262s, 1238s, 1160s, 1053s, 995m, 850m, 829w, 728s; δ_{H} (300 MHz, CDCl_3) 8.61 (1H, dd, J 4.2, 1.2, Ar H), 8.01 (1H, dd, J 3.9, 1.2, Ar H), 7.97 (1H, dd, J 5.1, 1.2, Ar H), 7.85 (1H, dd, J 4.8, 1.2, Ar H), 7.32 (1H, dd, J 5.1, 3.9, Ar H), 7.23 (1H, dd, J 5.1, 4.2, Ar H); δ_{C} (100 MHz, CDCl_3) 160.9, 160.3, 157.2, 139.4, 138.6, 137.07, 137.06, 134.8, 131.1, 129.7, 128.5; m/z (ESI+): Calculated for $[\text{M}+\text{H}]^+$ 310.9619, found: 310.9613.



4-(Thien-3-yl)-2-(thiophene-3-carbonyl)-1,2,5-thiadiazol-3(2H)-one 1-oxide (28b). Similar treatment (**Method A**) of 3,5-di(thien-3-yl)-4*H*-1,2,6-thiadiazin-4-one (**28a**) (10.4 mg, 0.0375 mmol) under 420 nm light for 35 min gave the *title compound 28b* (11.6 mg, 100%) as beige needles, mp (hot-stage) 138-140 °C (CHCl_3)

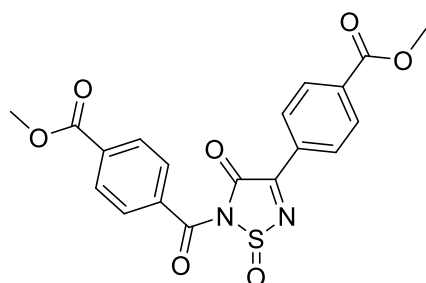
decomp.; λ_{max} (DCM)/nm 259 (log ϵ 4.11), 319 (4.09); $\nu_{\text{max}}/\text{cm}^{-1}$ 3108m (aryl C-H), 1731s (C=O), 1664s (C=O), 1562s, 1511m, 1408w, 1385m, 1299m, 1255m, 1226m, 1200w, 1151s, 1069m, 1040m, 943m, 911m, 877m, 854m, 815s, 803s, 774w, 732s; δ_{H} (400 MHz, CDCl_3) 9.09 (1H, dd, J 3.2, 1.2, Ar H), 8.30 (1H, dd, J 3.2, 1.2, Ar H), 7.91 (1H, dd, J 5.2, 1.6, Ar H), 7.57 (1H, dd, J 5.2, 1.2, Ar H), 7.48 (1H, dd, J 5.2, 3.2, Ar H), 7.40 (1H, dd, J 5.2, 2.8, Ar H); δ_{C} (100 MHz, CDCl_3) 161.4, 161.0, 157.8, 138.8, 136.7, 133.6, 130.7, 128.6, 128.2, 127.5, 126.5; m/z (ESI+): Calculated for $[\text{M}+\text{H}]^+$ 310.9619, found: 310.9608.



4-(1-Methyl-1H-pyrrol-2-yl)-2-(1-methyl-1H-pyrrole-2-carbonyl)-1,2,5-thiadiazol-3(2H)-one 1-oxide (29b). Similar treatment (**Method A**) of 3,5-bis(1-methyl-1*H*-pyrrol-2-yl)-4*H*-1,2,6-thiadiazin-4-one (**29a**) (10.2 mg, 0.0375 mmol) under 420 nm light for 90 min gave the *title compound 29b* (11.4 mg, 100%) as

brown plates, mp (hot-stage) 170-180 °C (Et_2O) decomp.; λ_{max} (DCM)/nm 296 (log ϵ 3.94), 376 (4.10); $\nu_{\text{max}}/\text{cm}^{-1}$ 3121w (aryl C-H), 1729m (C=O), 1664m (C=O), 1561m, 1512w, 1406m, 1389m, 1330m, 1246m, 1144m, 1064s, 1007m, 758s; δ_{H} (400 MHz, CDCl_3) 8.09 (1H, dd, J 4.4, 1.6, Ar H), 7.17 (1H, dd, J 2.0, 2.0, Ar H), 7.05 (1H, dd, J 4.4, 1.6, Ar H), 7.00 (1H, dd, J 2.0, 2.0, Ar H), 6.35 (1H, dd, J 4.4, 2.4, Ar H), 6.24 (1H, dd, J 4.4, 2.8, Ar H), 4.01 (3H, s, CH_3), 3.98 (3H, s, CH_3); δ_{C} (100 MHz, CDCl_3) 159.2,

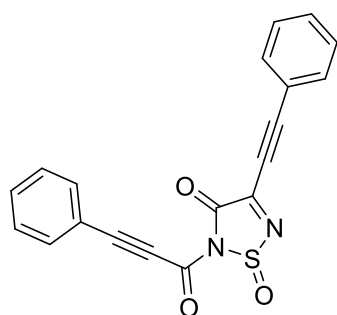
157.8, 155.6, 136.8, 134.0, 126.7, 124.4, 124.1, 122.7, 111.7, 109.6, 39.0, 37.4; m/z (ESI+): Calculated for $[M+H]^+$ 305.0708, found: 305.0711.



Methyl 4-{5-[4-(methoxycarbonyl)benzoyl]-1-oxido-4-oxo-4,5-dihydro-1,2,5-thiadiazol-3-yl}benzoate (32b).

Similar treatment (**Method A**) of dimethyl 4,4'-(4-oxo-4*H*-1,2,6-thiadiazine-3,5-diyl)dibenzoate (**32a**) (14.2 mg, 0.0375 mmol) under 420 nm light for 15 min gave the *title compound 32b* (15.5 mg, 100%)

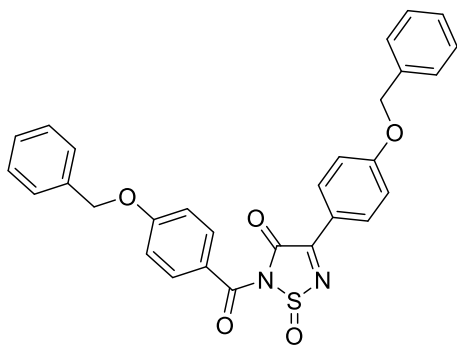
as off-yellow plates, mp (hot-stage) 182-183 °C (CHCl₃); λ_{\max} (DCM)/nm 244 (log ϵ 4.35), 300 (4.24); $\nu_{\max}/\text{cm}^{-1}$ 2964w (alkyl C-H), 1727s (C=O), 1698m (C=O), 1579m, 1555m, 1503w, 1433m, 1407m, 1394w, 1317w, 1266s, 1260s, 1206m, 1158s, 1107s, 1069m, 1031w, 1014m, 955m, 908m, 866m, 826m, 796w, 781m, 779m, 727s, 701m; δ_{H} (400 MHz, CD₂Cl₂) 8.50-8.53 (2H, m, Ar *H*), 8.16-8.19 (4H, m, Ar *H*), 7.86-7.88 (2H, m, Ar *H*), 3.952 (3H, s, CH₃), 3.946 (3H, s, CH₃); δ_{C} (100 MHz, CD₂Cl₂) 167.9, 166.6, 166.2, 157.8, 136.4, 135.6, 135.4, 132.2, 131.4, 130.5, 130.3, 130.1, 53.12, 53.08. One C resonance missing; m/z (ESI+): Calculated for $[M+H]^+$ 415.0594, found: 415.0595.



4-(Phenylethynyl)-2-(3-phenylpropioloyl)-1,2,5-thiadiazol-3(2H)-one 1-oxide (33b).

Similar treatment (**Method A**) of 3,5-bis(phenylethynyl)-4*H*-1,2,6-thiadiazin-4-one (**33a**) (11.8 mg, 0.0375 mmol) under 420 nm light for 4 h gave the *title compound 33b* (13.0 mg, 100%) as orange plates, mp (hot-stage) 126-127 °C (CHCl₃); λ_{\max} (DCM)/nm 345 (log ϵ

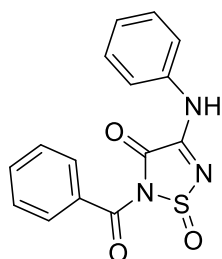
4.20); $\nu_{\max}/\text{cm}^{-1}$ 2197s (C \equiv C), 1756m (C=O), 1669m (C=O), 1595w, 1563m, 1489m, 1443m, 1290m, 1232m, 1158s, 1111s, 1069m, 1025m, 998m 959w, 900m, 812m, 755s; δ_{H} (300 MHz, CDCl₃) 7.74-7.78 (3H, m, Ar *H*), 7.37-7.62 (7H, m, Ar *H*); δ_{C} (100 MHz, CDCl₃) 157.4, 154.8, 148.9, 134.1, 134.0, 132.7, 132.2, 129.1, 129.0, 119.1, 118.7, 110.2, 97.6, 81.0, 80.8; m/z (ESI+): Calculated for $[M+H]^+$ 347.0485, found: 347.0465.



2-[4-(Benzyloxy)benzoyl]-4-[4-(benzyloxy)phenyl]-1,2,5-thiadiazol-3(2H)-one 1-oxide (34b). Similar treatment (**Method A**) of 3,5-bis[4-(benzyloxy)phenyl]-4H-1,2,6-thiadiazin-4-one (**34a**) (17.9 mg, 0.0375 mmol) under 420 nm light for 15 min gave the *title compound 34b* (19.1 mg, 100%) as yellow plates, mp (hot-stage) 163-164 °C (CHCl₃);

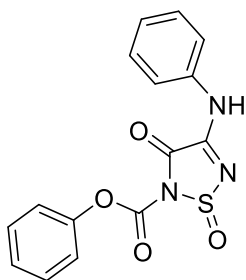
λ_{\max} (DCM)/nm 259 (log ϵ 4.08), 283 (4.09), 361 (4.13); ν_{\max} /cm⁻¹ 3064w and 3037w (aryl C-H), 2873w (alkyl C-H), 1730m (C=O), 1690w (C=O), 1674m (C=O), 1602s, 1569m, 1542s, 1509s, 1466w, 1455m, 1423m, 1384m 1307m, 1274m, 1255s, 1210m, 1153s, 1123m, 1069m, 1033m, 988s, 917w, 905m, 835m, 812w, 776m, 750s, 742m; δ_{H} (400 MHz, CD₂Cl₂) 8.53 (2H, dt, *J* 9.2, 3.2, Ar *H*), 7.84 (2H, dt, *J* 9.2, 2.8, Ar *H*), 7.37-7.48 (10H, m, Ar *H*), 7.08-7.13 (4H, m, Ar *H*), 5.19 (4H, d, *J* 5.2, CH₂); δ_{C} (100 MHz, CD₂Cl₂) 167.4, 165.44, 165.41, 164.5, 158.8, 136.6, 136.4, 134.1, 133.4, 129.3, 129.2, 129.0, 128.9, 128.2, 124.3, 121.8, 116.1, 115.3, 71.03, 70.97. One C resonance missing; *m/z* (ESI⁺): Calculated for [M+H]⁺ 511.1322, found: 511.1317.

3.8.3.2 Preparation of Asymmetric 1,2,5-Thiadiazole 1-oxides

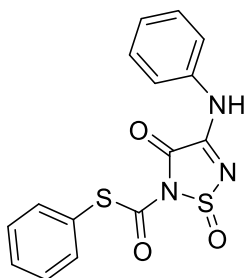


2-Benzoyl-4-(phenylamino)-1,2,5-thiadiazol-3(2H)-one 1-oxide (35b). Similar treatment (**Method B**) of 3-phenyl-5-(phenylamino)-4H-1,2,6-thiadiazin-4-one (**35a**) (10.5 mg, 0.0375 mmol) under 420 nm light for 5 min gave the *title compound 35b* (11.0 mg, 94%) as off white needles, mp (hot-stage) 86-90 °C (CHCl₃) decomp.;

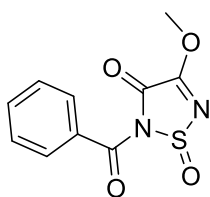
λ_{\max} (DCM)/nm 258 inf (log ϵ 3.95), 326 (3.76); ν_{\max} /cm⁻¹ 3297m (N-H), 3249br (N-H), 3140m and 3089m (aryl C-H), 1751s (C=O), 1721w, 1683s (C=O), 1624s, 1582s, 1495s, 1450s, 1267s, 1202m, 1178m, 1137s, 1084w, 1055m, 1020m, 1006m, 969w, 926w, 898s, 843m, 779m, 757s, 715m; δ_{H} (400 MHz, CDCl₃) 8.14 (1H, s, NH), 7.80-7.85 (2H, m, Ar *H*), 7.74-7.80 (2H, m, Ar *H*), 7.63-7.72 (1H, m, Ar *H*), 7.50-7.56 (2H, m, Ar *H*), 7.42-7.49 (2H, m, Ar *H*), 7.27-7.32 (1H, m, Ar *H*); δ_{C} (100 MHz, CDCl₃) 167.2, 156.4, 152.8, 135.5, 134.5, 131.5, 130.2, 129.8, 128.8, 126.8, 120.5; *m/z* (ESI⁺): Calculated for [M+H]⁺ 314.0599, found: 314.0582.



Phenyl 3-oxo-4-(phenylamino)-1,2,5-thiadiazole-2(3H)-carboxylate 1-oxide (36b). Similar treatment (**Method B**) of 3-phenoxy-5-(phenylamino)-4*H*-1,2,6-thiadiazin-4-one (**36a**) (11.2 mg, 0.0375 mmol) under 420 nm light for 2 min gave the *title compound 36b* (10.7 mg, 86%) as beige needles, mp (hot-stage) 155-165 °C (Et₂O) decomp.; $\lambda_{\max}(\text{DCM})/\text{nm}$ 272 (log ϵ 3.48), 277 inf (3.46), 313 (3.36), 410 inf (2.02); $\nu_{\max}/\text{cm}^{-1}$ 3262m (N-H), 3145w, 3078w (aryl C-H), 1801s (C=O), 1734m (C=O), 1629s, 1584s, 1492s, 1451m, 1331w, 1293s, 1263w, 1230m, 1186s, 1137s, 1073w, 1019s, 901s, 836w, 757s, 743s, 730s; $\delta_{\text{H}}(400 \text{ MHz, CDCl}_3)$ 8.31 (1H, s, NH), 7.80-7.82 (2H, m, Ar *H*), 7.43-7.49 (4H, m, Ar *H*), 7.28-7.34 (4H, m, Ar *H*); $\delta_{\text{C}}(100 \text{ MHz, CDCl}_3)$ 156.2, 152.6, 149.8, 147.0, 135.4, 129.9, 129.8, 127.2, 126.9, 121.3, 120.7; m/z (ESI⁺): Calculated for [M+H]⁺ 330.0549, found: 330.0568.

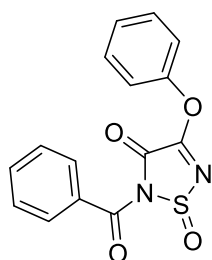


S-Phenyl 3-oxo-4-(phenylamino)-1,2,5-thiadiazole-2(3H)-carbothioate 1-oxide (37b). Similar treatment (**Method B**) of 3-(phenylamino)-5-(phenylthio)-4*H*-1,2,6-thiadiazin-4-one (**37a**) (11.8 mg, 0.0375 mmol) under 420 nm light for 2 min gave the *title compound 37b* (11.8 mg, 91%) as beige needles, mp (hot-stage) 155-165 °C (Et₂O) decomp.; $\lambda_{\max}(\text{DCM})/\text{nm}$ 330 (log ϵ 3.94); $\nu_{\max}/\text{cm}^{-1}$ 3275m (N-H), 3075w (aryl C-H), 1742s (C=O), 1678s (C=O), 1630s, 1589s, 1494m, 1475m, 1452m, 1441m, 1342w, 1328w, 1284s, 1256m, 1208m, 1153s, 1096m, 1073s, 1023m, 1009m, 967m, 896s, 838m, 775w, 758s, 747s; $\delta_{\text{H}}(400 \text{ MHz, CDCl}_3)$ 8.20 (1H, s, NH), 7.77-7.79 (2H, m, Ar *H*), 7.55-7.57 (2H, m, Ar *H*), 7.45-7.52 (4H, m, Ar *H*), 7.28-7.44 (2H, m, Ar *H*); $\delta_{\text{C}}(100 \text{ MHz, CDCl}_3)$ 171.0, 166.4, 156.4, 152.6, 135.5, 135.4, 130.7, 129.8, 129.7, 129.2, 127.7, 126.9, 120.6; m/z (ESI⁺): Calculated for [M+H]⁺ 346.0320, found: 346.0326.



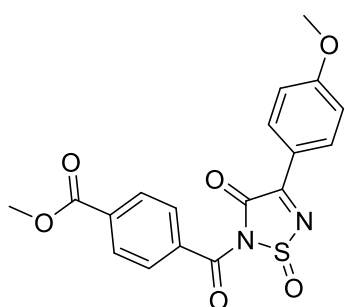
2-Benzoyl-4-methoxy-1,2,5-thiadiazol-3(2H)-one 1-oxide (38b). Similar treatment (**Method A**) of 3-methoxy-5-phenyl-4*H*-1,2,6-thiadiazin-4-one (**38a**) (8.1 mg, 0.0375 mmol) under 420 nm light for 15 min gave the *title compound 38b* (9.3 mg, 100%) as off white

plates, mp (hot-stage) 79-81 °C (CHCl₃); λ_{\max} (MeOH)/nm 268 inf (log ϵ 3.45), 339 (3.07); $\nu_{\max}/\text{cm}^{-1}$ 3062w (alkyl C-H), 1747m (C=O), 1686 (C=O), 1600w, 1574w, 1502w, 1478m, 1438m, 1352w, 1305w, 1202s, 1155s, 1053m, 1025w, 1000w, 971w, 907m, 800m, 705s; δ_{H} (400 MHz, CDCl₃) 7.78 (2H, d, J 7.2, Ar H), 7.67 (1H, dd, J 8.0, 8.0, Ar H), 7.51 (2H, dd, J 7.6, 7.6, Ar H), 4.24 (3H, s, CH₃); δ_{C} (100 MHz, CDCl₃) 167.3, 164.6, 152.2, 134.7, 130.8, 130.3, 128.7, 59.1; m/z (ESI⁺): Calculated for [M+H]⁺ 315.04, found: 315.02.



2-Benzoyl-4-phenoxy-1,2,5-thiadiazol-3(2H)-one 1-oxide (39b).

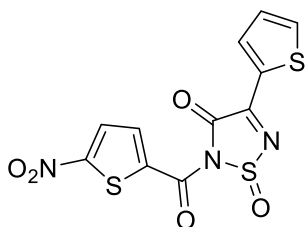
Similar treatment (**Method B**) of 3-phenoxy-5-phenyl-4H-1,2,6-thiadiazin-4-one (**39a**) (10.6 mg, 0.0375 mmol) under 420 nm light for 5 min gave the *title compound 39b* (4.6 mg, 39%) as colourless needles, mp (hot-stage) >129 °C (Et₂O) decomp.; λ_{\max} (DCM)/nm 256 (log ϵ 4.18), 283 inf (3.95); $\nu_{\max}/\text{cm}^{-1}$ 2971w (aryl C-H), 1766s (C=O), 1691m (C=O), 1620s, 1581s, 1486s, 1364m, 1259s, 1253s, 1166m, 1050m, 1021m, 918w, 881m, 832w, 756m, 713m; δ_{H} (400 MHz, Acetone-*d*₆) 7.94-7.96 (2H, m, Ar H), 7.73-7.77 (1H, m, Ar H), 7.54-7.61 (4H, m, Ar H), 7.40-7.46 (3H, m, Ar H); δ_{C} (100 MHz, Acetone-*d*₆) 153.2, 136.0, 135.1, 131.0, 130.9, 129.4, 128.2, 121.5. Three quaternary C peaks are missing; m/z (ESI⁺): Calculated for [M+Na]⁺ 337.0259, found: 337.0248.



Methyl 4-[4-(4-methoxyphenyl)-1-oxido-3-oxo-2,3-dihydro-1,2,5-thiadiazole-2-carbonyl]benzoate (40b).

Similar treatment (**Method A**) of methyl 4-[5-(4-methoxyphenyl)-4-oxo-4H-1,2,6-thiadiazin-3-yl]benzoate (**40a**) (13.3 mg, 0.0375 mmol) under 420 nm light for 10 min gave the *title compound 40b* (14.5 mg, 100%) as pale yellow needles, mp (hot-stage) 159-160 °C (CHCl₃) decomp.; λ_{\max} (DCM)/nm 247 (log ϵ 4.58), 365 (4.40); $\nu_{\max}/\text{cm}^{-1}$ 2958w, 2925w and 2844w (alkyl C-H), 1732m (C=O), 1719s (C=O), 1690s (C=O), 1603s, 1568s, 1529s, 1504s, 1487w, 1464m, 1437m, 1424m, 1405m, 1339w, 1312m, 1268s, 1254s, 1247m, 1212m, 1188w, 1166s, 1104s, 1069m, 1031m, 1007s, 959m, 910m, 844s, 791s, 776s, 736m, 715s; δ_{H} (400 MHz, CDCl₃) 8.51-8.54 (2H, m, Ar H), 8.17-8.20 (2H, m, Ar H), 7.84-7.87 (2H, m, Ar H), 6.99-7.03 (2H,

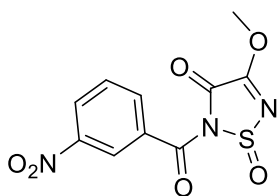
m, Ar H), 3.97 (3H, s, CH₃), 3.93 (3H, s, CH₃); δ_{C} (100 MHz, CDCl₃) 167.5, 166.1, 166.0, 164.8, 158.4, 135.4, 134.9, 133.8, 129.8, 121.0, 115.0, 55.9, 52.7. One C resonance missing; m/z (ESI+): Calculated for [M+H]⁺ 387.0645, found: 387.0628.



2-(5-Nitrothiophene-2-carbonyl)-4-(thien-2-yl)-1,2,5-thiadiazol-3(2H)-one 1-oxide (41b). Similar treatment

(**Method A**) of 3-(5-nitrothien-2-yl)-5-(thien-2-yl)-4H-1,2,6-thiadiazin-4-one (**41a**) (12.1 mg, 0.0375 mmol) under 420 nm light for 60 min gave the *title compound 41b* (13.3 mg 100%)

as orange needles, mp (hot-stage) 184-185 °C (CHCl₃); λ_{max} (DCM)/nm 322.5 (log ϵ 3.81), 370 inf (log ϵ 3.64); ν_{max} /cm⁻¹ 3112m (aryl C-H), 2923m (aryl C-H), 1743m (C=O), 1662m (C=O), 1638w, 1553m, 1537m, 1508s, 1435m, 1354w, 1260m, 1193m, 1159s, 1122m, 1081m, 1046m, 992w, 863m, 815w, 767m, 729s; δ_{H} (300 MHz, CDCl₃) 8.61 (1H, d, J 3.6, Ar H), 8.01 (1H, d, J 4.8, Ar H), 7.93 (2H, s, Ar H), 7.34 (1H, t, J 4.2, 4.2, Ar H); δ_{C} (100 MHz, DMSO-*d*₆) 163.2, 157.6, 152.1, 150.4, 134.1, 133.6, 131.6, 129.8, 128.8, 124.9, 99.2; m/z (ESI+): Calculated for [M+H]⁺ 355.9464, found: 355.9453.

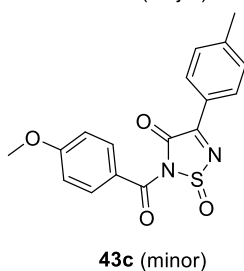
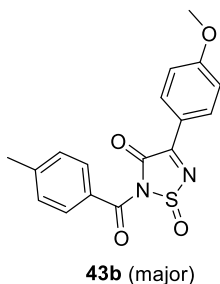


4-Methoxy-2-(3-nitrobenzoyl)-1,2,5-thiadiazol-3(2H)-one (42b). Similar treatment (**Method B**) of 3-methoxy-5-(3-nitrophenyl)-4H-1,2,6-thiadiazin-4-one (**42a**) (9.9 mg, 0.0375

mmol) under 420 nm light for 5 min gave the *title compound 42b*

(9.1 mg, 82%) as off white plates, mp (hot-stage) >86 °C (CHCl₃) decomp.; λ_{max} (DCM)/nm 243 inf (log ϵ 3.70); ν_{max} /cm⁻¹ 3088w (aryl C-H), 2954w (alkyl C-H), 1761s (C=O), 1694s (C=O), 1604s, 1583w, 1532s, 1478m, 1441m, 1351s, 1296m, 1259s, 1227m, 1180s, 1168s, 1103m, 1056m, 1010m, 930w, 913w, 889m, 868m, 817w, 799m, 784w, 758m, 718s, 706s; δ_{H} (400 MHz, CDCl₃) 8.57-8.62 (1H, m, Ar H), 8.51 (1H, ddd, J 8.3, 2.3, 1.1, Ar H), 8.07 (1H, ddd, J 7.8, 1.7, 1.1, Ar H), 7.73 (1H, ddd, J 8.3, 7.9, 0.5, Ar H), 4.27 (3H, s, CH₃); δ_{C} (100 MHz, CDCl₃) 165.5, 164.4, 152.2, 148.2, 135.5, 132.4, 130.0, 128.6, 125.1, 59.4; m/z (ESI+): Calculated for [M+H]⁺ 298.01, found: 298.01. HRMS analysis did not show peaks corresponding to any of the anticipated molecular adducts. However, it has been reported that other nitro-thiadiazole 1-oxide compounds

can produce specific signals for loss of oxygen and nitro groups.¹⁰⁸ After further analysis, the following adduct was found: Calculated for $[M-NO_2-O]^+$ 235.0177, found: 235.0182.



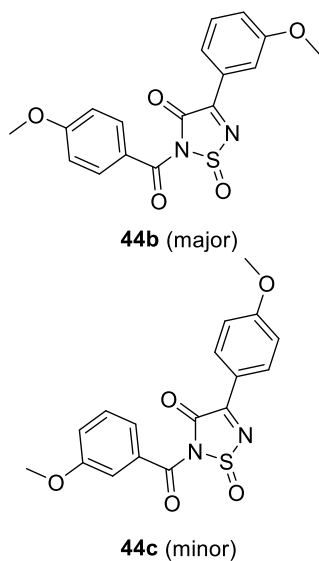
4-(4-Methoxyphenyl)-2-(4-methylbenzoyl)-1,2,5-thiadiazol-3(2H)-one 1-oxide (43b) and **2-(4-methoxybenzoyl)-4-(p-tolyl)-1,2,5-thiadiazol-3(2H)-one 1-oxide (43c)**. Similar treatment

(**Method A**) of 3-(4-methoxyphenyl)-5-(p-tolyl)-4H-1,2,6-thiadiazin-4-one (**43a**) (11.6 mg, 0.0375 mmol) under 420 nm light for 15 min gave the *title compounds* **43b** and **43c** as an

inseparable mixture (molar ratio **43b/43c** 69:31 as judged by the integrations of the peaks at δ_H 8.53-8.56 and 8.41 in the 1H NMR spectrum) (12.8 mg, 100%) as beige needles, mp (hot-stage) 159-

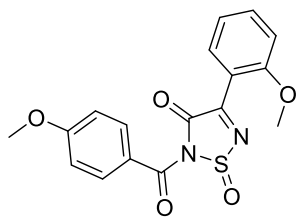
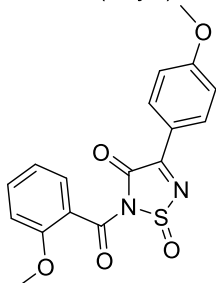
166 °C (CHCl₃) decomp.; λ_{max} (DCM)/nm 255 (log ϵ 3.94), 357 (3.86); ν_{max}/cm^{-1} 2940w (alkyl C-H), 1732s (C=O), 1698s

(C=O), 1604s, 1577m, 1547s, 1511s, 1456w, 1425m, 1383w, 1321w, 1259s, 1210m, 1183w, 1168s, 1150s, 1062s, 1015s, 906m, 846m, 826m, 798w, 763s, 742s, 717w; δ_H (400 MHz, CDCl₃) crude after completion of the reaction containing **43b** and **43c**: 8.53-8.56 (2.04H, m, Ar H), 8.41 (0.90H, d, J 8.4, Ar H), 7.83-7.87 (0.94H, m, Ar H), 7.74 (2.06H, dd, J 6.4, 1.6, Ar H), 7.31-7.35 (3.03H, m, Ar H), 6.99-7.01 (3.06H, m, Ar H), 3.92 (3H, s, CH₃O), 3.91 (1.40H, s, CH₃O), 2.47 (1.35H, s, CH₃), 2.46 (3.03H, s, CH₃); δ_C (100 MHz, CDCl₃) crude after completion of the reaction containing **43b** and **43c**: 167.8, 166.9, 166.0, 165.9, 165.0, 164.8, 158.5, 158.2, 147.1, 145.8, 133.8, 133.2, 131.2, 130.4, 130.1, 129.5, 128.8, 125.9, 123.5, 121.1, 114.9, 114.2, 55.9, 55.8, 22.2, 22.1; m/z (ESI⁺): Calculated for $[M+H]^+$ 343.0753, found: 346.0736. The assignment of the structures for **43b** and **43c** is tentative and was based on comparison of the 1H and ^{13}C NMR spectra of the mixture of the two compounds (focusing on the peaks of the CH₃O and CH₃ groups) with that of **13b** and **16b**.



2-(4-Methoxybenzoyl)-4-(3-methoxyphenyl)-1,2,5-thiadiazol-3(2H)-one 1-oxide (44b) and 2-(3-methoxybenzoyl)-4-(4-methoxyphenyl)-1,2,5-thiadiazol-3(2H)-one 1-oxide (44c).

Similar treatment (**Method A**) of 3-(3-methoxyphenyl)-5-(4-methoxyphenyl)-4*H*-1,2,6-thiadiazin-4-one (**44a**) (12.2 mg, 0.0375 mmol) under 420 nm light for 10 min gave the *title compounds* **44b** and **44c** as an inseparable mixture (molar ratio **44b/44c** 60:40 as judged by the integrations of the peaks at δ_{H} 3.91 and 3.80 in the ^1H NMR spectrum) (13.4 mg, 100%) as yellow needles, mp (hot-stage) 115-127 °C (CHCl_3) decomp.; $\lambda_{\text{max}}(\text{DCM})/\text{nm}$ 262 (log ϵ 3.73), 306 (3.58), 381 inf (3.12); $\nu_{\text{max}}/\text{cm}^{-1}$ 2942w and 2837w (alkyl C-H), 1746s (C=O), 1700s (C=O), 1599s, 1585s, 1489s, 1463s, 1427m, 1333m, 1299w, 1276m, 1230s, 1196w, 1149s, 1121w, 1067m, 1033s, 1019s, 984w, 924m, 897w, 882m, 842w, 809w, 798w, 788w, 753s, 740s, 715s; δ_{H} (400 MHz, CDCl_3) crude after completion of the reaction containing **44b** and **44c**: 8.11 (0.67H, ddd, J 8.0, 1.6, 1.2, Ar H), 7.93 (0.65H, dd, J 2.4, 1.6, Ar H), 7.76 (1H, ddd, J 7.6, 1.6, 0.4, Ar H), 7.53-7.61 (2.42H, m, Ar H), 7.40-7.44 (2.81H, m, Ar H), 7.33-7.34 (1H, m, Ar H), 7.19-7.21 (1.77H, m, Ar H), 7.01-7.11 (2.80H, m, Ar H), 6.99 (0.80H, d, J 8.4, Ar H), 3.91 (3H, s, CH_3O), 3.86 (5.04H, s, CH_3O), 3.80 (1.98H, s, CH_3O); δ_{C} (100 MHz, CDCl_3) crude after completion of the reaction containing **44b** and **44c**: 169.5, 167.8, 166.2, 160.0, 159.7, 157.7, 157.2, 157.0, 135.5, 134.4, 132.6, 132.0, 130.5, 130.3, 129.73, 129.68, 123.8, 122.6, 122.4, 122.2, 121.1, 120.7, 117.8, 114.9, 114.5, 112.4, 111.5, 56.3, 56.0, 55.72, 55.70; m/z (ESI $^{+}$): Calculated for $[\text{M}+\text{H}]^{+}$ 359.0702, found: 359.0696. The assignment of the structures for **44b** and **44c** is tentative and was based on comparison of the ^1H and ^{13}C NMR spectra of the mixture of the two compounds (focusing on the peaks of the CH_3O groups) with that of **16b** and **17b**.

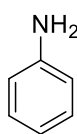
**45b** (major)**45c** (minor)

2-(4-Methoxybenzoyl)-4-(2-methoxyphenyl)-1,2,5-thiadiazol-3(2H)-one 1-oxide (45b) and 2-(2-methoxybenzoyl)-4-(4-methoxyphenyl)-1,2,5-thiadiazol-3(2H)-one 1-oxide (45c). Similar treatment (**Method A**) of 3-

(2-methoxyphenyl)-5-(4-methoxyphenyl)-4*H*-1,2,6-thiadiazin-4-one (**45a**) (12.2 mg, 0.0375 mmol) under 420 nm light for 10 min gave the *title compounds* **45b** and **45c** as an inseparable mixture (molar ratio **45b/45c** 60:40 as judged by the integrations of the peaks at δ_H 3.90 and 3.80 in the 1H NMR spectrum) (13.4 mg, 100%) as yellow needles, mp (hot-stage) 159-176 °C (CHCl₃) decomp.; λ_{max} (DCM)/nm 257 (log ϵ

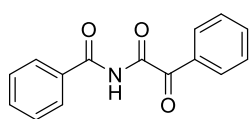
3.51), 283 inf (3.36), 362 (3.43); ν_{max}/cm^{-1} 2941w and 2841w (alkyl C-H), 1749s (C=O), 1687s (C=O), 1601s, 1532w, 1513m, 1489s, 1461m, 1437m, 1332w, 1308w, 1260s, 1201m, 1173s, 1165s, 1153s, 1120m, 1069m, 1046m, 1020s, 935w, 906m, 847s, 815m, 788w, 776w, 759s, 746s, 730m, 712s; δ_H (400 MHz, CDCl₃) crude after completion of the reaction containing **45b** and **45c**: 8.49-8.52 (1.99H, m, Ar *H*), 7.84-7.86 (1.32H, m, Ar *H*), 7.77 (0.66H, ddd, *J* 7.6, 2.0, 0.4, Ar *H*), 7.54-7.62 (1.73H, m, Ar *H*), 7.52 (0.98H, ddd, *J* 7.6, 1.6, 0.4, Ar *H*), 7.06-7.11 (2.38H, m, Ar *H*), 6.97-7.00 (4.45H, m, Ar *H*), 3.913 (2.10H, s, CH₃O), 3.910 (2.91H, s, CH₃O), 3.90 (1.98H, s, CH₃O), 3.80 (3H, s, CH₃O); δ_C (100 MHz, CDCl₃) crude after completion of the reaction containing **45b** and **45c**: 169.6, 166.9, 166.3, 165.8, 165.1, 165.0, 160.1, 157.80, 157.76, 157.4, 135.3, 134.2, 133.6, 133.2, 132.0, 130.4, 121.4, 121.1, 114.9, 114.1, 112.5, 111.6, 56.4, 56.1, 55.84, 55.77; *m/z* (ESI⁺): Calculated for [M+H]⁺ 359.0702, found: 359.0699. The assignment of the structures for **45b** and **45c** is tentative and was based on comparison of the 1H and ^{13}C NMR spectra of the mixture of the two compounds (focusing on the peaks of the CH₃O groups) with that of **16b** and **18b**.

3.8.4 Characterisation of Isolated Side-Products and Reference Compounds

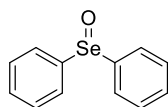


Benzamide. To a stirred solution of 2-benzoyl-4-phenyl-1,2,5-thiadiazol-3(2H)-one 1-oxide (**1b**) (10.0 mg, 0.034 mmol) in dry DCM (5 mL) was added Ph₃P (0.068 mmol, 2equiv.) and CCl₄ (10 equiv.). The resulting solution was heated

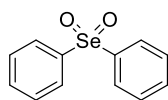
to 40 °C (reflux) and stirred for 24 h, after which the sulfoxide **1b** was consumed (monitored by ¹H NMR). The resulting solution was then concentrated under reduced pressure, and the title compound was isolated after column chromatography (CHCl₃/n-hexane, 50:50) as a white solid (1.5 mg, 37%); δ_H(400 MHz, CDCl₃) 7.81-7.83 (2H, m, Ar H), 7.54 (1H, tt, *J* 7.2, 1.6, Ar H), 7.43-7.47 (2H, m, Ar H), 6.11 (1H, s, NH₂), 5.82 (1H, s, NH₂); δ_C(100 MHz, CDCl₃) 169.5, 133.5, 132.2, 128.8, 127.5; LC (ret. time): 4.040 min; *m/z* (ESI+): Calculated for [2M+H]⁺ 243.11, found: 243.15. Identical to spectra obtained from commercially available sample.



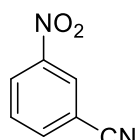
***N*-(2-oxo-2-phenylacetyl)benzamide.** The title compound was synthesised according to known procedures⁸⁵ and was obtained as a yellow solid (0.88 g, 59%); δ_H(300 MHz, CDCl₃) 9.78 (1H, s, NH), 8.12 (2H, dd, *J* 8.7, 1.5, Ar H), 7.88-7.93 (2H, m, Ar H), 7.61-7.69 (2H, m, Ar H), 7.51-7.55 (4H, m, Ar H); δ_C(75 MHz, CDCl₃) 186.7, 165.4, 161.0, 134.9, 134.1, 132.5, 131.2, 130.4, 129.30, 129.1, 128.2; LC (ret. time): 5.581 min; *m/z* (ESI+): Calculated for [M+H]⁺ 254.08, found: 254.00. Identical to published spectra.^{85,86}



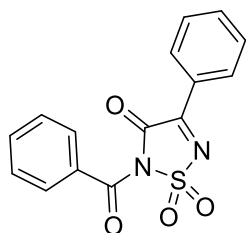
Seleninyldibenzene. The title compound was synthesised according to known procedures¹⁰⁹ and was obtained as a colourless solid (0.20 g, 10%); δ_H(400 MHz, CDCl₃) 7.69-7.71 (4H, m, Ar H), 7.46-7.48 (6H, m, Ar H); δ_C(100 MHz, CDCl₃) 142.7, 131.5, 129.9, 126.4; LC (ret. time): 4.737 min; *m/z* (ESI+): Calculated for [M+H]⁺ 251.00, found: 251.05. Identical to published spectra.¹⁰⁹



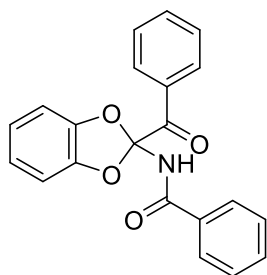
Selenonyldibenzene. The title compound was synthesised according to known procedures¹¹⁰ and was obtained as a colourless solid (0.19 g, 72%); δ_H(400 MHz, CD₂Cl₂) 7.96-7.98 (4H, m, Ar H), 7.67-7.69 (2H, m, Ar H), 7.61-7.65 (4H, m, Ar H); δ_C(100 MHz, CD₂Cl₂) 142.9, 134.1, 130.3, 126.9; LC (ret. time): 4.740 min; *m/z* (ESI+): Calculated for [M+H]⁺ 266.99, found: 267.05. Identical to published spectra.¹¹⁰



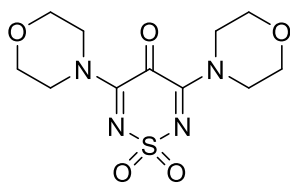
3-Nitrobenzonitrile. Similar treatment (**Method A**) of 3-methoxy-5-(3-nitrophenyl)-4*H*-1,2,6-thiadiazin-4-one (**42a**) (9.9 mg, 0.0375 mmol) under 420 nm light for 24 h led to its consumption (by ¹H NMR) and the concomitant appearance of multiple new spots on TLC (CHCl₃/EtOAc, 90:10). The reaction mixture was subjected to column chromatography (CHCl₃/EtOAc, 90:10), and the major band was isolated. After the solvent was removed, the title compound was isolated (0.5 mg, 9%) as colourless needles, mp (hot-stage) 115-116 °C (CHCl₃), lit. mp¹¹¹ 115-117 °C (EtOH); $\nu_{\max}/\text{cm}^{-1}$ 3080m (aryl C-H), 2237m (C≡N), 1618m, 1535s, 1474m, 1434w, 1335s, 1202w, 1102m, 1080w, 921m, 904m, 817m, 789m, 735m; δ_{H} (400 MHz, CDCl₃) 8.47 (1H, t, *J* 1.7, Ar *H*), 8.41 (1H, ddd, *J* 8.4, 2.3, 1.1, Ar *H*), 7.89-7.96 (1H, m, Ar *H*), 7.61-7.71 (1H, m, Ar *H*); δ_{C} (100 MHz, CDCl₃) 148.4, 137.7, 130.8, 127.7, 127.4, 116.7, 114.3. Identical to published spectra.¹¹¹



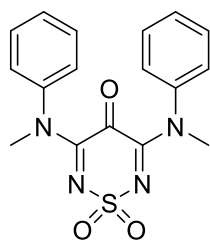
2-Benzoyl-4-phenyl-1,2,5-thiadiazol-3(2H)-one 1,1-dioxide (1c). To a stirred solution of 3,5-diphenyl-4*H*-1,2,6-thiadiazin-4-one (**1a**) (20 mg, 0.075 mmol) in DCM (5 mL) at 20 °C, mCPBA (2 equiv.) was added in one portion. After 30 min the mixture still contained starting material (by ¹H NMR); however, the introduction of a further portion of mCPBA (2 equiv.) resulted in the complete consumption of the starting material within 30 min. After the reaction was complete, the mixture was transferred to a separation funnel, the organic layer was separated, and the aqueous layer was extracted with DCM (3 × 5 mL). The combined organic fractions were washed with brine, dried with MgSO₄, filtered and evaporated under reduced pressure. The resulting residue was washed with cold Et₂O (3 × 1 mL) and dried under reduced pressure to afford the *title compound 1c* (6.8 mg, 29%) as colourless needles, mp (hot-stage) 172-173 °C (Et₂O); $\lambda_{\max}(\text{DCM})/\text{nm}$ 295 (log ϵ 3.72); $\nu_{\max}/\text{cm}^{-1}$ 1772m (C=O), 1681s (C=O), 1597w, 1507w, 1576w, 1560s, 1491w, 1449m, 1416m, 1389s, 1300m, 1258s, 1207s, 1193s, 1177s, 1067m, 1021m, 923m, 898w, 820s, 793m, 785m, 749m, 740w, 715s; δ_{H} (400 MHz, Acetone-*d*₆) 8.45-8.50 (2H, m, Ar *H*), 7.99-8.02 (2H, m, Ar *H*), 7.83-7.87 (1H, m, Ar *H*), 7.74-7.78 (1H, m, Ar *H*), 7.65-7.70 (2H, m, Ar *H*), 7.58-7.62 (2H, m, Ar *H*); δ_{C} (100 MHz, Acetone-*d*₆) 165.8, 165.1, 155.4, 136.7, 134.9, 132.7, 132.6, 130.1, 129.4, 128.1. One C resonance missing; *m/z* (ESI⁺): Calculated for [M+H]⁺ 315.0440, found: 315.0425.



N-(2-Benzoylbenzo[d][1,3]dioxol-2-yl)benzamide (9c). Similar treatment (**Method A**) of 3',5'-diphenylspiro[benzo[d][1,3]dioxole-2,4'-[1,2,6]thiadiazine] (**9a**) (13.4 mg, 0.0375 mmol) under 420 nm light in CDCl₃ (1 mL) at *ca.* 20 °C was irradiated with 420 nm light until it was consumed (TLC, CHCl₃/*n*-hexane, 50:50) over a period of 3 days. The resulting solution turned cloudy, and TLC analysis revealed the formation of multiple spots, indicative of decomposition by-products. After removal of the solvent under reduced pressure, the crude mixture was subjected to a preparative TLC separation (DCM/*n*-hexane, 50:50). The major band was isolated, extracted with CHCl₃, and was then dried under reduced pressure to afford the *title compound* **9c** (2.5 mg, 19%) as colourless needles, mp (hot-stage) 120-123 °C (CHCl₃); R_f 0.66 (CHCl₃/EtOAc, 95:5); λ_{max}(DCM)/nm 254 inf (log ε 4.05), 273 inf (3.86); ν_{max}/cm⁻¹ 3258br (N-H), 1708m (C=O), 1666s (C=O), 1600w, 1580w, 1516m, 1478s, 1464w, 1359m, 1314w, 1260w, 1233s, 1179w, 1099s, 1026w, 1003m, 909s, 901m, 801w, 729s, 709s; δ_H(400 MHz, CDCl₃) 8.32 (1H, s, NH), 8.00-8.02 (2H, m, Ar H), 7.82-7.84 (2H, m, Ar H), 7.52-7.59 (2H, m, Ar H), 7.38-7.47 (4H, m, Ar H), 6.97-7.02 (4H, m, Ar H); δ_C(100 MHz, Acetone-d₆) 185.6, 167.4, 146.7, 134.6, 133.9, 133.5, 133.3, 130.0, 129.5, 129.2, 128.6, 123.2. Two C resonances missing; *m/z* (ESI⁺): Calculated for [M]⁺ 345.09, found: 345.09.



3,5-dimorpholino-4H-1,2,6-thiadiazin-4-one 1,1-dioxide (50d). Similar treatment (**Method A**) of 3,5-dimorpholino-4H-1,2,6-thiadiazin-4-one (**50a**) (10.7 mg, 0.0375 mmol) under 420 nm light for 24 h led to its consumption (by TLC) and the concomitant appearance of multiple new spots on TLC (EtOAc). The reaction mixture was subjected to column chromatography (EtOAc), and the major band was isolated. After the solvent was removed, the *title compound* **50d** was isolated (7.4 mg, 62%) as yellow needles, mp (hot-stage) 252-254 °C (CHCl₃); R_f 0.19 (EtOAc); λ_{max}(DCM)/nm 358 (log ε 3.54); ν_{max}/cm⁻¹ 2924 (alkyl C-H), 1713m (C=O), 1607s, 1550s, 1445m, 1491w, 1352w, 1304s, 1269m, 1223w, 1186m, 1132s, 1121m, 1109s, 1069m, 1044m, 1020w, 997w, 936s, 912w, 870s, 858s, 845w, 831m, 797w; δ_H(400 MHz, Acetone-d₆) 3.70-3.75 (8H, m, CH₂), 3.63-3.65 (8H, m, CH₂); δ_C(100 MHz, Acetone-d₆) 177.0, 157.1, 67.1, 66.6, 49.1, 45.2; *m/z* (ESI⁻): Calculated for [M]⁻ 316.08, found: 316.10



3,5-bis(methyl(phenyl)amino)-4H-1,2,6-thiadiazin-4-one 1,1-dioxide (51d). Similar treatment (**Method A**) of 3,5-bis(methyl(phenyl)amino)-4H-1,2,6-thiadiazin-4-one (**51a**) (12.2 mg, 0.0375 mmol) under 420 nm light for 24 h led to its consumption (by ^1H NMR) and the concomitant appearance of multiple new spots on TLC ($\text{CHCl}_3/\text{EtOAc}$, 90:10). The reaction mixture was subjected to column chromatography ($\text{CHCl}_3/\text{EtOAc}$, 90:10), and the major band was isolated. After the solvent was removed, the *title compound* **50d** was isolated (5.9 mg, 44%) as orange needles, R_f 0.80 (EtOAc); mp (hot-stage) 260-262 °C (CHCl_3); $\lambda_{\text{max}}(\text{DCM})/\text{nm}$ 347 (log ϵ 3.74); $\nu_{\text{max}}/\text{cm}^{-1}$ 2936w (aryl C-H), 1719m (C=O), 1603m, 1582s, 1530s, 1499m, 1406, 1310s, 1163s, 1148s, 1099m, 1053w, 1028w, 933m, 878s, 808s, 791w, 774m, 754m; δ_{H} (500 MHz, DMSO-d_6) 7.20-7.42 (10H, m, Ar *H*), 3.32 (6H, s, CH_3); δ_{C} (125 MHz, DMSO-d_6) 155.4, 142.3, 129.4, 127.8, 126.0, 40.5; m/z (ESI-): Calculated for $[\text{M-H}]^-$ 355.08, found: 355.05

3.9 References

- (1) Bartolini, M.; Gombac, V.; Sinicropi, A.; Reginato, G.; Dessì, A.; Mordini, A.; Filippi, J.; Montini, T.; Calamante, M.; Fornasiero, P.; et al. Tuning the Properties of Benzothiadiazole Dyes for Efficient Visible Light-Driven Photocatalytic H₂ Production under Different Conditions. *ACS Appl. Energy Mater.* **2020**, *3* (9), 8912–8928. <https://doi.org/10.1021/acsaem.0c01391>.
- (2) Theodorou, E.; Ioannidou, H. A.; Ioannou, T. A.; Kalogirou, A. S.; Constantinides, C. P.; Manoli, M.; Koutentis, P. A.; Hayes, S. C. Spectroscopic Characterization of C-4 Substituted 3,5-Dichloro-4*H*-1,2,6-Thiadiazines. *RSC Adv.* **2015**, *5* (24), 18471–18481. <https://doi.org/10.1039/C4RA16144K>.
- (3) Rakitin, O. A. 1,2,5-Thiadiazoles. In *Comprehensive Heterocyclic Chemistry IV*; Black, D. S., Cossy, J., Stevens; Elsevier: Oxford, 2022; pp 371–406. <https://doi.org/10.1016/B978-0-12-409547-2.14813-9>.
- (4) Koutentis, P. A. 1,2,5-Thiadiazoles. In *Comprehensive Heterocyclic Chemistry III*; Katritzky, A. R., Ramsden, C. A., Scriven, E. F. V, Taylor; Elsevier: Oxford, 2008; pp 515–565. <https://doi.org/10.1016/B978-008044992-0.00509-5>.
- (5) Dungan, L. B.; Rowley, E. G.; Dixon, J. A.; Ali, S. F.; Crawford, S. D.; Sehgel, S.; Whiteside, M. P.; Zydowsky, T. M.; Yeager, W. H. Pesticidal Substituted 1,2,5,-Thiadiazole Derivatives. WO2005006858A2, 2005.
- (6) Hanasaki, Yasuaki; Watanabe, Hiroyuki; Katsuura, Kimio; Fujiwara, Masatoshi; Ide, T. 3,4-Dioxy-1,2,5-Thiadiazoles Partly Useful as Fungicides. EP0621272A1, 1994.
- (7) Banera, M. J.; Caram, J. A.; Gervasi, C. A.; Mirífico, M. V. Corrosion Inhibition of Mild Steel in Sulphuric Acid Using a Bicyclic Thiadiazolidine. *J. Appl. Electrochem.* **2014**, *44* (12), 1337–1344. <https://doi.org/10.1007/s10800-014-0729-4>.
- (8) Ji Ram, V.; Sethi, A.; Nath, M.; Pratap, R. Chapter 5 - Five-Membered Heterocycles. In *The Chemistry of Heterocycles*; Elsevier, 2019; pp 149–478. <https://doi.org/10.1016/B978-0-08-101033-4.00005-X>.

- (9) Sabb, A. L.; Vogel, R. L.; Kelly, M. G.; Palmer, Y.; Smith, D. L.; Andree, T. H.; Schechter, L. E. 1,2,5-Thiadiazole Derivatives Are Potent and Selective Ligands at Human 5-HT_{1A} Receptors. *Bioorg. Med. Chem. Lett.* **2001**, *11* (8), 1069–1071. [https://doi.org/10.1016/S0960-894X\(01\)00151-2](https://doi.org/10.1016/S0960-894X(01)00151-2).
- (10) Zimmerman, T. J.; Kaufman, H. E. Timolol: A β -Adrenergic Blocking Agent for the Treatment of Glaucoma. *Arch. Ophthalmol.* **1977**, *95* (4), 601–604. <https://doi.org/10.1001/archopht.1977.04450040067008>.
- (11) Serban, G. Future Prospects in the Treatment of Parasitic Diseases: 2-Amino-1,3,4-Thiadiazoles in Leishmaniasis. *Molecules* **2019**, *24* (8). <https://doi.org/10.3390/molecules24081557>.
- (12) Nance, P. W.; Bugaresti, J.; Shellenberger, K.; Sheremata, W.; Martinez-Arizala, A. Efficacy and Safety of Tizanidine in the Treatment of Spasticity in Patients with Spinal Cord Injury. North American Tizanidine Study Group. *Neurology* **1994**, *44*.
- (13) Evans, B. E.; Rittle, K. E.; Bock, M. G.; DiPardo, R. M.; Freidinger, R. M.; Whitter, W. L.; Lundell, G. F.; Veber, D. F.; Anderson, P. S.; Chang, R. S. L.; et al. Methods for Drug Discovery: Development of Potent, Selective, Orally Effective Cholecystokinin Antagonists. *J. Med. Chem.* **1988**, *31* (12), 2235–2246. <https://doi.org/10.1021/jm00120a002>.
- (14) Coppola, B. P.; Noe, M. C.; Schwartz, D. J.; L. Abdon, R.; Trost, B. M. Intermolecular 1,3-Dipolar Cycloadditions of M \ddot{u} chnones with Acetylenic Dipolarophiles: Sorting out the Regioselectivity. *Tetrahedron* **1994**, *50* (1), 93–116. [https://doi.org/10.1016/S0040-4020\(01\)80739-0](https://doi.org/10.1016/S0040-4020(01)80739-0).
- (15) Li, Y.; Geng, J.; Liu, Y.; Yu, S.; Zhao, G. Thiadiazole—a Promising Structure in Medicinal Chemistry. *ChemMedChem* **2013**, *8* (1), 27–41. <https://doi.org/10.1002/cmdc.201200355>.
- (16) Kumar, D.; Kumar, N. M.; Noel, B.; Shah, K. A Series of 2-Arylamino-5-(Indolyl)-1,3,4-Thiadiazoles as Potent Cytotoxic Agents. *Eur. J. Med. Chem.* **2012**, *55*, 432–438. <https://doi.org/10.1016/j.ejmech.2012.06.047>.
- (17) Wasson, B. K. 4-(3-Secondary Amino-2-Hydroxy-Proxy) 1,2,5-Thiadiazoles. US3655663A, 1969.

- (18) Karady, S.; Leonard, M.; Mead, B. Substituted 1,2,5-thiadiazole-1-oxide Compounds, Compositions and Use. US4362726, 1982.
- (19) Lumma, W. C.; Anderson, P. S.; Baldwin, J. J.; Bolhofer, W. A.; Britcher, S. F.; Clineschmidt, B. V.; Denny, G. H.; Habecker, C. N.; Hirshfield, J. M. Inhibitors of Gastric Acid Secretion: 3,4-Diamino-1,2,5-Thiadiazole 1-Oxides and 1,1-Dioxides as Urea Equivalents in a Series of Histamine H₂ Receptor Antagonists. *J. Med. Chem.* **1982**, 25 (3), 207–210. <https://doi.org/10.1021/jm00345a002>.
- (20) Katritzky, A. R.; Ramsden, C. A.; Scriven, E. F. V.; Taylor, R. J. K. *Comprehensive Heterocyclic Chemistry III*; Elsevier Amsterdam, 2008; Vol. 1. <https://doi.org/10.1016/C2009-1-28335-3>.
- (21) Koutentis, P. A. *Science of Synthesis, 13: Category 2, Hetarenes and Related Ring Systems*; Thieme Chemistry: Stuttgart, Germany, 2004; Vol. 13, pp 297–348.
- (22) Clerici, F. B. T.-A. in H. C. Thiazole and Thiadiazole S-Oxides. In *Advances in Heterocyclic Chemistry*; Academic Press, 2002; Vol. 83, pp 71–115. [https://doi.org/10.1016/S0065-2725\(02\)83004-5](https://doi.org/10.1016/S0065-2725(02)83004-5).
- (23) Moorthy, J. N.; Senapati, K.; Parida, K. N. 6-Membered Pseudocyclic IBX Acids: Syntheses, X-Ray Structural Characterizations, and Oxidation Reactivities in Common Organic Solvents. *J. Org. Chem.* **2010**, 75 (24), 8416–8421. <https://doi.org/10.1021/jo101639j>.
- (24) Yu, B.; Liu, A.-H.; He, L.-N.; Li, B.; Diao, Z.-F.; Li, Y.-N. Catalyst-Free Approach for Solvent-Dependent Selective Oxidation of Organic Sulfides with Oxone. *Green Chem.* **2012**, 14 (4), 957–962. <https://doi.org/10.1039/C2GC00027J>.
- (25) Skolia, E.; Gkizis, P. L.; Kokotos, C. G. Aerobic Photocatalysis: Oxidation of Sulfides to Sulfoxides. *Chempluschem* **2022**, 87 (4). <https://doi.org/10.1002/cplu.202200008>.
- (26) Joseph S. Amato, Sandor Karady, L. M. W. Substituted-1,2,5-Thiadiazole-1-Oxide Compounds, Compositions and Use. US4362726A, 1981.
- (27) Linder, T.; Badiola, E.; Baumgartner, T.; Sutherland, T. C. Synthesis of π -Extended Thiadiazole (Oxides) and Their Electronic Properties. *Org. Lett.* **2010**, 12 (20), 4520–4523. <https://doi.org/10.1021/ol1018213>.

- (28) Amato, J. S.; Karady, S.; Reamer, R. A.; Schlegel, H. B.; Springer, J. P.; Weinstock, L. M. Theoretical Investigation of the Inversion Barrier. *J. Am. Chem. Soc.* **1982**, *9* (2), 1375–1380.
- (29) Jurczyk, J.; Woo, J.; Kim, S. F.; Dherange, B. D.; Sarpong, R.; Levin, M. D. Single-Atom Logic for Heterocycle Editing. *Nat. Synth.* **2022**, *1* (5), 352–364. <https://doi.org/10.1038/s44160-022-00052-1>.
- (30) Woo, J.; Christian, A. H.; Burgess, S. A.; Jiang, Y.; Mansoor, U. F.; Levin, M. D. Scaffold Hopping by Net Photochemical Carbon Deletion of Azaarenes. *Science* **2022**, *532*, 527–532.
- (31) Jurczyk, J.; Lux, M. C.; Adpressa, D.; Kim, S. F.; Lam, Y. H.; Yeung, C. S.; Sarpong, R. Photomediated Ring Contraction of Saturated Heterocycles. *Science* **2021**, *373* (6558), 1004–1012. <https://doi.org/10.1126/science.abi7183>.
- (32) Kalogirou, A. S.; Koutentis, P. A. The Chemistry of Non-S-Oxidised 4*H*-1, 2, 6-Thiadiazines. *Targets Heterocycl. Syst* **2018**, *22*, 82–118.
- (33) Kalogirou, A. S. 1,2,6-Oxadiazines and 1,2,6-Thiadiazines. In *Comprehensive Heterocyclic Chemistry IV*; Elsevier: Oxford, 2022; pp 363–401. <https://doi.org/10.1016/B978-0-12-818655-8.00063-9>.
- (34) Arán, V. J.; Bielsa, A. G.; Ruiz, J. R.; Stud, M. Ring Contraction of 1,2,6-Thiadiazines to 1,2,5-Thiadiazoles: Synthesis of 2-Substituted 4-Amino-2,3-Dihydro-3-Oxo-1,2,5-Thiadiazole 1,1-Dioxides. *J. Chem. Soc. Perkin Trans. 1* **1986**, 643–645. <https://doi.org/10.1039/P19860000643>.
- (35) Daley, S. T. A. K.; Rees, C. W. Organic Heterocyclothiazenes. Part 2. Reaction of Tetrasulphur Tetranitride with Phenylacetylene and Diphenylacetylene. *J. Chem. Soc. Perkin Trans. 1* **1987**, 207–210. <https://doi.org/10.1039/P19870000207>.
- (36) Zhivonitko, V. V.; Makarov, A. Y.; Bagryanskaya, I. Y.; Gatilov, Y. V.; Shakirov, M. M.; Zibarev, A. V. New Polysulfur-Nitrogen Heterocycles by Thermolysis of 1, 3λ⁴δ²,2,4-Benzodithiadiazines in the Hydrocarbon and Fluorocarbon Series. *Eur. J. Inorg. Chem.* **2005**, No. 20, 4099–4108. <https://doi.org/10.1002/ejic.200500383>.
- (37) Kalogirou, A. S.; Kourtellaris, A.; Koutentis, P. A. The Acid and/or Thermal

- Mediated Ring Contraction of 4*H*-1,2,6-Thiadiazines to Afford 1,2,5-Thiadiazoles. *Org. Lett.* **2016**, *18* (16), 4056–4059. <https://doi.org/10.1021/acs.orglett.6b01929>.
- (38) Kalogirou, A. S.; Kourtellaris, A.; Koutentis, P. A. Synthesis and Chemistry of Benzo[e][1,2,6]Thiadiazino[3,4-b][1,4]Diazepin-10(1*H*)-Ones and Related Ring Transformations. *J. Org. Chem.* **2021**, *86* (8), 5702–5713. <https://doi.org/10.1021/acs.joc.1c00206>.
- (39) Broumidis, E.; Jones, C. M. S.; Koyioni, M.; Kourtellaris, A.; Lloyd, G. O.; Marques-Hueso, J.; Koutentis, P. A.; Vilela, F. 8,8'-(Benzo[c][1,2,5]Thiadiazole-4,7-Diyl)Bis(Quinolin-4(1*H*)-One): A Twisted Photosensitizer with AIE Properties. *RSC Adv.* **2021**, *11* (47), 29102–29107. <https://doi.org/10.1039/d1ra06263h>.
- (40) Zhakeyev, A.; Jones, M. C.; Thomson, C. G.; Tobin, J. M.; Wang, H.; Vilela, F.; Xuan, J. Additive Manufacturing of Intricate and Inherently Photocatalytic Flow Reactor Components. *Addit. Manuf.* **2021**, *38*, 101828. <https://doi.org/10.1016/j.addma.2020.101828>.
- (41) Tobin, J. M.; McCabe, T. J. D.; Prentice, A. W.; Holzer, S.; Lloyd, G. O.; Paterson, M. J.; Arrighi, V.; Cormack, P. A. G.; Vilela, F. Polymer-Supported Photosensitizers for Oxidative Organic Transformations in Flow and under Visible Light Irradiation. *ACS Catal.* **2017**, *7* (7), 4602–4612. <https://doi.org/10.1021/acscatal.7b00888>.
- (42) Urakami, H.; Zhang, K.; Vilela, F. Modification of Conjugated Microporous Poly-Benzothiadiazole for Photosensitized Singlet Oxygen Generation in Water. *Chem. Commun.* **2013**, *49* (23), 2353–2355. <https://doi.org/10.1039/c3cc38956a>.
- (43) Zhang, K.; Vobecka, Z.; Tauer, K.; Antonietti, M.; Vilela, F. π -Conjugated PolyHIPEs as Highly Efficient and Reusable Heterogeneous Photosensitizers. *Chem. Commun.* **2013**, *49* (95), 11158–11160. <https://doi.org/10.1039/c3cc45597a>.
- (44) Chochos, C. L.; Kalogirou, A. S.; Ye, T.; Tatsi, E.; Katsouras, A.; Zissimou, G. A.; Gregoriou, V. G.; Avgeropoulos, A.; Koutentis, P. A. 4*H*-1,2,6-Thiadiazine-Containing Donor–Acceptor Conjugated Polymers: Synthesis, Optoelectronic

- Characterization and Their Use in Organic Solar Cells. *J. Mater. Chem. C* **2018**, *6* (14), 3658–3667. <https://doi.org/10.1039/C7TC03889E>.
- (45) Zheng, Q.; Jockusch, S.; Zhou, Z.; Blanchard, S. C. The Contribution of Reactive Oxygen Species to the Photobleaching of Organic Fluorophores. *Photochem. Photobiol.* **2014**, *90* (2), 448–454. <https://doi.org/10.1111/php.12204>.
- (46) Sheldon, R. A. Metrics of Green Chemistry and Sustainability: Past, Present, and Future. *ACS Sustain. Chem. Eng.* **2018**, *6* (1), 32–48. <https://doi.org/10.1021/acssuschemeng.7b03505>.
- (47) Nicholas J. Turro, V. R. and J. C. S. *Modern Molecular Photochemistry of Organic Molecules*; John Wiley & Sons, Ltd, 2010. <https://doi.org/10.1002/anie.201003826>.
- (48) Lutkus, L. V.; Rickenbach, S. S.; McCormick, T. M. Singlet Oxygen Quantum Yields Determined by Oxygen Consumption. *J. Photochem. Photobiol. A: Chem.* **2019**, *378*, 131–135. <https://doi.org/10.1016/j.jphotochem.2019.04.029>.
- (49) Byrne, F. P.; Jin, S.; Paggiola, G.; Petchey, T. H. M.; Clark, J. H.; Farmer, T. J.; Hunt, A. J.; Robert McElroy, C.; Sherwood, J. Tools and Techniques for Solvent Selection: Green Solvent Selection Guides. *Sustain. Chem. Process.* **2016**, *4* (1), 1–24. <https://doi.org/10.1186/s40508-016-0051-z>.
- (50) Sagadevan, A.; Hwang, K. C.; Su, M.-D. Singlet Oxygen-Mediated Selective C–H Bond Hydroperoxidation of Ethereal Hydrocarbons. *Nat. Commun.* **2017**, *8* (1), 1812. <https://doi.org/10.1038/s41467-017-01906-5>.
- (51) Fischer, K.; Wilken, M. Experimental Determination of Oxygen and Nitrogen Solubility in Organic Solvents up to 10 MPa at Temperatures between 298 K and 398 K. *J. Chem. Thermodyn.* **2001**, *33* (10), 1285–1308. <https://doi.org/10.1006/jcht.2001.0837>.
- (52) Sambiagio, C.; Noël, T. Flow Photochemistry: Shine Some Light on Those Tubes! *Trends Chem.* **2020**, *2* (2), 92–106. <https://doi.org/10.1016/j.trechm.2019.09.003>.
- (53) Theodorou, V.; Skobridis, K.; Alivertis, D.; Gerothanassis, I. P. Synthetic Methodologies in Organic Chemistry Involving Incorporation of [¹⁷O] and [¹⁸O] Isotopes. *J. Label. Compd. Radiopharm.* **2014**, *57* (8), 481–508.

<https://doi.org/10.1002/jlcr.3212>.

- (54) Montagnon, T.; Kalaitzakis, D.; Triantafyllakis, M.; Stratakis, M.; Vassilikogiannakis, G. Furans and Singlet Oxygen – Why There Is More to Come from This Powerful Partnership. *Chem. Commun.* **2014**, 50 (98), 15480–15498. <https://doi.org/10.1039/C4CC02083A>.
- (55) Craven, B. M.; McMullan, R. K. Charge Density in Parabanic Acid from X-Ray and Neutron Diffraction. *Acta Crystallogr. Sect. B* **1979**, 35 (4), 934–945. <https://doi.org/10.1107/S0567740879005203>.
- (56) Hillered, L.; Persson, L. Parabanic Acid for Monitoring of Oxygen Radical Activity in the Injured Human Brain. *Neuroreport* **1995**, 6 (13).
- (57) Ye, C.; Zhang, Y.; Ding, A.; Hu, Y.; Guo, H. Visible Light Sensitizer-Catalyzed Highly Selective Photo Oxidation from Thioethers into Sulfoxides under Aerobic Condition. *Sci. Rep.* **2018**, 8 (1), 2205. <https://doi.org/10.1038/s41598-018-20631-7>.
- (58) Han, J.; Soloshonok, V. A.; Klika, K. D.; Drabowicz, J.; Wzorek, A. Chiral Sulfoxides: Advances in Asymmetric Synthesis and Problems with the Accurate Determination of the Stereochemical Outcome. *Chem. Soc. Rev.* **2018**, 47 (4), 1307–1350. <https://doi.org/10.1039/c6cs00703a>.
- (59) Boaz, H.; Rollefson, G. K. The Quenching of Fluorescence. Deviations from the Stern-Volmer Law. *J. Am. Chem. Soc.* **1950**, 72 (8), 3435–3443. <https://doi.org/10.1021/ja01164a032>.
- (60) Ye, Y.; Bruning, H.; Yntema, D.; Mayer, M.; Rijnaarts, H. Homogeneous Photosensitized Degradation of Pharmaceuticals by Using Red Light LED as Light Source and Methylene Blue as Photosensitizer. *Chem. Eng. J.* **2017**, 316, 872–881. <https://doi.org/10.1016/j.cej.2017.02.053>.
- (61) Elsherbini, M.; Allemann, R. K.; Wirth, T. “Dark” Singlet Oxygen Made Easy. *Chem. Eur. J.* **2019**, 25 (54), 12486–12490. <https://doi.org/10.1002/chem.201903505>.
- (62) Reszka, K.; Bilski, P.; Chignell, C. F. Epr Spectra of DMPO Spin Adducts of Superoxide and Hydroxyl Radicals in Pyridine. *Free Radic. Res.* **1992**, 17 (6),

377–385. <https://doi.org/10.3109/10715769209083142>.

- (63) Chen, L.; Mizukado, J.; Suzuki, Y.; Kutsuna, S.; Aoyama, Y.; Yoshida, Y.; Suda, H. An ESR Study on Superoxide Radical Anion Generation and Its Involvement in the Photooxidative Degradation of Poly-3-Hexylthiophene in Chlorobenzene Solution. *Chem. Phys. Lett.* **2014**, *605–606*, 98–102. <https://doi.org/10.1016/j.cplett.2014.05.030>.
- (64) Bonesi, S. M.; Manet, I.; Freccero, M.; Fagnoni, M.; Albini, A. Photosensitized Oxidation of Sulfides: Discriminating between the Singlet-Oxygen Mechanism and Electron Transfer Involving Superoxide Anion or Molecular Oxygen. *Chem. Eur. J.* **2006**, *12* (18), 4844–4857. <https://doi.org/10.1002/chem.200501144>.
- (65) Yang, M. Q.; Zhang, Y.; Zhang, N.; Tang, Z. R.; Xu, Y. J. Visible-Light-Driven Oxidation of Primary C-H Bonds over CdS with Dual Co-Catalysts Graphene and TiO₂. *Sci. Rep.* **2013**, *3*, 1–7. <https://doi.org/10.1038/srep03314>.
- (66) Kollmann, J.; Zhang, Y.; Schilling, W.; Zhang, T.; Riemer, D.; Das, S. A Simple Ketone as an Efficient Metal-Free Catalyst for Visible-Light-Mediated Diels-Alder and Aza-Diels-Alder Reactions. *Green Chem.* **2019**, *21* (8), 1916–1920. <https://doi.org/10.1039/c9gc00485h>.
- (67) Samuel, D.; Norrell, K.; Hilmey, D. G. Novel Ring Chemistry of Vitamin B₆ with Singlet Oxygen and an Activated Ene: Isolated Products and Identified Intermediates Suggesting an Operable [3 + 2] Cycloaddition. *Org. Biomol. Chem.* **2012**, *10* (36), 7278–7281. <https://doi.org/10.1039/C2OB26067K>.
- (68) Gollnick, K.; Griesbeck, A. Solvent Dependence of Singlet Oxygen / Substrate Interactions in Ene-Reactions, [4+2]- and [2+2]-Cycloaddition Reactions. *Tetrahedron Lett.* **1984**, *25* (7), 725–728. [https://doi.org/10.1016/S0040-4039\(01\)80010-1](https://doi.org/10.1016/S0040-4039(01)80010-1).
- (69) Montagnon, T.; Tofi, M.; Vassilikogiannakis, G. Using Singlet Oxygen to Synthesize Polyoxygenated Natural Products from Furans. *Acc. Chem. Res.* **2008**, *41* (8), 1001–1011. <https://doi.org/10.1021/ar800023v>.
- (70) Ferroud, C.; Rool, P.; Santamaria, J. Singlet Oxygen Mediated Alkaloid Tertiary Amines Oxidation by Single Electron Transfer. *Tetrahedron Lett.* **1998**, *39* (51),

9423–9426. [https://doi.org/10.1016/S0040-4039\(98\)02184-4](https://doi.org/10.1016/S0040-4039(98)02184-4).

- (71) Albéniz, A. C.; Espinet, P.; López-Fernández, R.; Sen, A. A Warning on the Use of Radical Traps as a Test for Radical Mechanisms: They React with Palladium Hydrido Complexes. *J. Am. Chem. Soc.* **2002**, *124* (38), 11278–11279. <https://doi.org/10.1021/ja0271126>.
- (72) Bilski, P.; Reszka, K.; Bilska, M.; Chignell, C. F. Oxidation of the Spin Trap 5,5-Dimethyl-1-Pyrroline *N*-Oxide by Singlet Oxygen in Aqueous Solution. *J. Am. Chem. Soc.* **1996**, *118* (6), 1330–1338. <https://doi.org/10.1021/ja952140s>.
- (73) Ayed, C.; Caire Da Silva, L.; Wang, D.; Zhang, K. A. I. Designing Conjugated Microporous Polymers for Visible Light-Promoted Photocatalytic Carbon-Carbon Double Bond Cleavage in Aqueous Medium. *J. Mater. Chem. A* **2018**, *6* (44), 22145–22151. <https://doi.org/10.1039/c8ta05772a>.
- (74) Gutiérrez, M. I. Solvent Effect on the Physical Quenching of Singlet Molecular Oxygen by *p*-Quinones. *Photochem. Photobiol. Sci.* **2008**, *7* (4), 480–484. <https://doi.org/10.1039/B713929B>.
- (75) Carvalho, L. A. R.; Almeida, V. T.; Brito, J. A.; Lum, K. M.; Oliveira, T. F.; Guedes, R. C.; Gonçalves, L. M.; Lucas, S. D.; Cravatt, B. F.; Archer, M.; et al. 3-Oxo- β -Sultam as a Sulfonylating Chemotype for Inhibition of Serine Hydrolases and Activity-Based Protein Profiling. *ACS Chem. Biol.* **2020**, *15* (4), 878–883. <https://doi.org/10.1021/acscchembio.0c00090>.
- (76) Page, M. I.; Tsang, W. Y.; Ahmed, N. Comparison of the Mechanisms of Reactions of β -Lactams and β -Sultams, Including Their Reactions with Some Serine Enzymes. *J. Phys. Org. Chem.* **2006**, *19* (8–9), 446–451. <https://doi.org/https://doi.org/10.1002/poc.1016>.
- (77) Meinzer, A.; Breckel, A.; Thaher, B. A.; Manicone, N.; Otto, H.-H. Properties and Reactions of Substituted 1,2-Thiazetidone 1,1-Dioxides: Chiral Mono- and Bicyclic 1,2-Thiazetidone 1,1-Dioxides from α -Amino Acids. *Helv. Chim. Acta* **2004**, *87* (1), 90–105. <https://doi.org/10.1002/hlca.200490021>.
- (78) Beardsell, M.; Hinchliffe, P. S.; Wood, J. M.; Wilmouth, R. C.; Schofield, C. J.; Page, M. I. β -Sultams—A Novel Class of Serine Protease Inhibitors. *Chem.*

- Commun.* **2001**, *5*, 497–498. <https://doi.org/10.1039/B100294P>.
- (79) August, D. P.; Nichol, G. S.; Lusby, P. J. Maximizing Coordination Capsule–Guest Polar Interactions in Apolar Solvents Reveals Significant Binding. *Angew. Chem. Int. Ed.* **2016**, *55* (48), 15022–15026. <https://doi.org/10.1002/anie.201608229>.
- (80) Young, T. A.; Martí-Centelles, V.; Wang, J.; Lusby, P. J.; Duarte, F. Rationalizing the Activity of an “Artificial Diels-Alderase”: Establishing Efficient and Accurate Protocols for Calculating Supramolecular Catalysis. *J. Am. Chem. Soc.* **2020**, *142* (3), 1300–1310. <https://doi.org/10.1021/jacs.9b10302>.
- (81) Young, T. A.; Gheorghe, R.; Duarte, F. Cgbind: A Python Module and Web App for Automated Metallocage Construction and Host–Guest Characterization. *J. Chem. Inf. Model.* **2020**, *60* (7), 3546–3557. <https://doi.org/10.1021/acs.jcim.0c00519>.
- (82) Li, R.-J.; Tessarolo, J.; Lee, H.; Clever, G. H. Multi-Stimuli Control over Assembly and Guest Binding in Metallo-Supramolecular Hosts Based on Dithienylethene Photoswitches. *J. Am. Chem. Soc.* **2021**, *143* (10), 3865–3873. <https://doi.org/10.1021/jacs.0c12188>.
- (83) Koutentis, P. A.; Rees, C. W. Chemistry of 4-Dicyanomethylene-1,2,6-Thiadiazines. *J. Chem. Soc. Perkin Trans. 1* **2000**, *7*, 1081–1088. <https://doi.org/10.1039/b000964o>.
- (84) Jang, Y.; Kim, K. T.; Jeon, H. B. Deoxygenation of Sulfoxides to Sulfides with Thionyl Chloride and Triphenylphosphine: Competition with the Pummerer Reaction. *J. Org. Chem.* **2013**, *78* (12), 6328–6331. <https://doi.org/10.1021/jo4008157>.
- (85) Kalmode, H. P.; Vadagaonkar, K. S.; Chaskar, A. C. The Oxidative Cross-Coupling of Benzonitriles with Multifunctional Substrates: A Domino Strategy Inspired Easy Access to α -Keto-Imides. *Synthesis* **2015**, *47* (3), 429–438. <https://doi.org/10.1055/s-0034-1379955>.
- (86) Kalmode, H. P.; Vadagaonkar, K. S.; Chaskar, A. C. Metal-Free in Situ sp^3 , sp^2 , and sp C-H Functionalization and Oxidative Cross Coupling with Benzamidine Hydrochloride: A Promising Approach for the Synthesis of α -Ketoimides. *RSC*

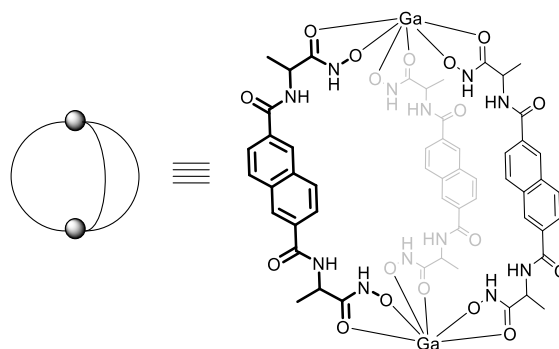
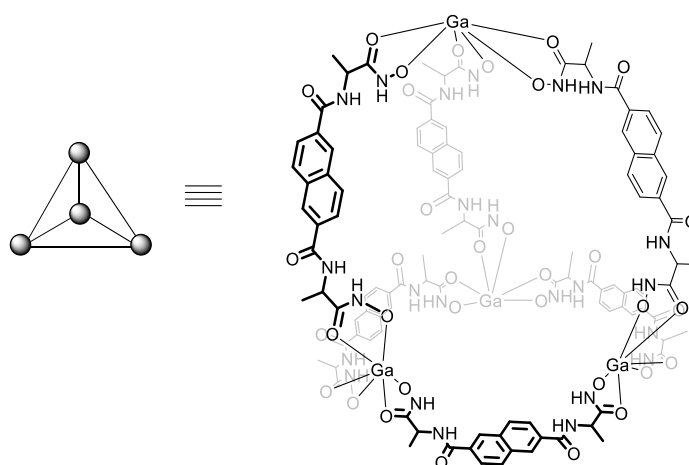
- Adv.* **2014**, *4* (104), 60316–60326. <https://doi.org/10.1039/c4ra07556k>.
- (87) Wu, X.; Gao, Q.; Liu, S.; Wu, A. I₂-Catalyzed Oxidative Cross-Coupling of Methyl Ketones and Benzamidines Hydrochloride: A Facile Access to α -Ketoimides. *Org. Lett.* **2014**, *16* (11), 2888–2891. <https://doi.org/10.1021/ol501029w>.
- (88) Chow, Y. L.; Tam, J. N. S.; Blier, J. E.; Szmant, H. H. Mechanism of Sulphur Monoxide Extrusion. *J. Chem. Soc. D Chem. Commun.* **1970**, *23*, 1604–1605. <https://doi.org/10.1039/C29700001604>.
- (89) Joost, M.; Nava, M.; Transue, W. J.; Martin-Drumel, M. A.; McCarthy, M. C.; Patterson, D.; Cummins, C. C. Sulfur Monoxide Thermal Release from an Anthracene-Based Precursor, Spectroscopic Identification, and Transfer Reactivity. *Proc. Natl. Acad. Sci. U. S. A.* **2018**, *115* (23), 5866–5871. <https://doi.org/10.1073/pnas.1804035115>.
- (90) Fatima, K.; Masood, N.; Luqman, S. Quenching of Singlet Oxygen by Natural and Synthetic Antioxidants and Assessment of Electronic UV/Visible Absorption Spectra for Alleviating or Enhancing the Efficacy of Photodynamic Therapy. *Biomed. Res. Ther.* **2016**, *3* (2), 8. <https://doi.org/10.7603/s40730-016-0008-6>.
- (91) Mendoza, C.; Emmanuel, N.; Páez, C. A.; Dreesen, L.; Monbaliu, J.-C. M.; Heinrichs, B. Improving Continuous Flow Singlet Oxygen Photooxygenation Reactions with Functionalized Mesoporous Silica Nanoparticles. *ChemPhotoChem* **2018**, *2* (10), 890–897. <https://doi.org/10.1002/cptc.201800148>.
- (92) Li, X.; Li, J.; Bai, J.; Dong, Y.; Li, L.; Zhou, B. The Inhibition Effect of Tert-Butyl Alcohol on the TiO₂ Nano Assays Photoelectrocatalytic Degradation of Different Organics and Its Mechanism. *Nano-Micro Lett.* **2016**, *8* (3), 221–231. <https://doi.org/10.1007/s40820-015-0080-2>.
- (93) Hayyan, M.; Hashim, M. A.; AlNashef, I. M. Superoxide Ion: Generation and Chemical Implications. *Chem. Rev.* **2016**, *116* (5), 3029–3085. <https://doi.org/10.1021/acs.chemrev.5b00407>.
- (94) Tobin, J. M.; McCabe, T. J. D.; Prentice, A. W.; Holzer, S.; Lloyd, G. O.; Paterson, M. J.; Arrighi, V.; Cormack, P. A. G.; Vilela, F. Polymer-Supported Photosensitizers for Oxidative Organic Transformations in Flow and under Visible

- Light Irradiation. *ACS Catal.* **2017**, *7* (7), 4602–4612. <https://doi.org/10.1021/acscatal.7b00888>.
- (95) Sofikiti, N.; Rabalakos, C.; Stratakis, M. Efficient Trapping of the Intermediates in the Photooxygenation of Sulfides by Aryl Selenides and Selenoxides. *Tetrahedron Lett.* **2004**, *45* (7), 1335–1337. <https://doi.org/10.1016/j.tetlet.2003.12.065>.
- (96) Pierlot, C.; Nardello, V.; Schrive, J.; Mabile, C.; Barbillat, J.; Sombret, B.; Aubry, J. M. Calcium Peroxide Diperoxohydrate as a Storable Chemical Generator of Singlet Oxygen for Organic Synthesis. *J. Org. Chem.* **2002**, *67* (8), 2418–2423. <https://doi.org/10.1021/jo010766x>.
- (97) You, Y. Chemical Tools for the Generation and Detection of Singlet Oxygen. *Org. Biomol. Chem.* **2018**, *16* (22), 4044–4060. <https://doi.org/10.1039/C8OB00504D>.
- (98) Koutentis, P. A.; Rees, C. W. Chemistry of 4-Dicyanomethylene-1,2,6-Thiadiazines. *J. Chem. Soc. Perkin Trans. 1* **2000**, 1081–1088. <https://doi.org/10.1039/B000964O>.
- (99) Hanson, K.; Roskop, L.; Djurovich, P. I.; Zahariev, F.; Gordon, M. S.; Thompson, M. E. A Paradigm for Blue- or Red-Shifted Absorption of Small Molecules Depending on the Site of π -Extension. *J. Am. Chem. Soc.* **2010**, *132* (45), 16247–16255. <https://doi.org/10.1021/ja1075162>.
- (100) Rauh, A.; Kletting, M.; Aschemann, H.; Hofer, E. P. Reduction of Overestimation in Interval Arithmetic Simulation of Biological Wastewater Treatment Processes. *J. Comput. Appl. Math.* **2007**, *199* (2), 207–212. <https://doi.org/10.1016/j.cam.2005.07.029>.
- (101) Dolomanov, O. V.; Bourhis, L. J.; Gildea, R. J.; Howard, J. A. K.; Puschmann, H. OLEX2: A Complete Structure Solution, Refinement and Analysis Program. *J. Appl. Crystallogr.* **2009**, *42* (2), 339–341. <https://doi.org/10.1107/S0021889808042726>.
- (102) Sheldrick, G. M. SHELXT: Integrated Space-Group and Crystal-Structure Determination. *Acta Crystallogr. Sect. A* **2015**, *71* (1), 3–8. <https://doi.org/10.1107/S2053273314026370>.

- (103) Geever, J.; Trompen, W. P. Synthesis and Reactions of 3,5-Dichloro-4*H*-1,2,6-Thiadiazin-4-One. *Recl. des Trav. Chim. des Pays-Bas* **1974**, *93* (9–10), 270–272. <https://doi.org/10.1002/recl.19740930911>.
- (104) Ioannidou, H. A.; Koutentis, P. A. Synthesis of Asymmetric 3,5-Diaryl-4*H*-1,2,6-Thiadiazin-4-Ones via Suzuki–Miyaura and Stille Coupling Reactions. *Tetrahedron* **2012**, *68* (36), 7380–7385. <https://doi.org/10.1016/j.tet.2012.06.079>.
- (105) Kalogirou, A. S.; Koutentis, P. A. Regioselective Geminal Dichloride Reactivity of 3,4,4,5-Tetrachloro-4*H*-1,2,6-Thiadiazine: Access to 4,4-Dioxo- and Dithio-Ketals. *Tetrahedron Lett.* **2016**, *57* (2), 203–205. <https://doi.org/10.1016/j.tetlet.2015.11.100>.
- (106) Kalogirou, A. S.; Manoli, M.; Koutentis, P. A. Synthesis of *N*-Aryl-3,5-Dichloro-4*H*-1,2,6-Thiadiazin-4-Imines from 3,4,4,5-Tetrachloro-4*H*-1,2,6-Thiadiazine. *Org. Lett.* **2015**, *17* (16), 4118–4121. <https://doi.org/10.1021/acs.orglett.5b02237>.
- (107) Ioannidou, H. A.; Kizas, C.; Koutentis, P. A. Palladium Catalyzed C-C Coupling Reactions of 3,5-Dichloro-4*H*-1,2,6-Thiadiazin-4-One. *Org. Lett.* **2011**, *13* (13), 3466–3469. <https://doi.org/10.1021/ol201212b>.
- (108) Konstantinova, L. S.; Knyazeva, E. A.; Gatilov, Y. V.; Zlotin, S. G.; Rakitin, O. A. Nitro Derivatives of 2,1,3-Benzothiadiazole 1-Oxides: Synthesis, Structural Study, and NO Release. *Russ. Chem. Bull.* **2018**, *67* (1), 95–101. <https://doi.org/10.1007/s11172-018-2042-6>.
- (109) McCulla, R. D.; Jenks, W. S. Deoxygenation and Other Photochemical Reactions of Aromatic Selenoxides. *J. Am. Chem. Soc.* **2004**, *126* (49), 16058–16065. <https://doi.org/10.1021/ja045935k>.
- (110) Weilbeer, C.; Selent, D.; Dyballa, K. M.; Franke, R.; Spannenberg, A.; Börner, A. Evaluation of Organoselenium Based Compounds as Co-Catalysts in Rhodium-Catalyzed Hydroformylation. *ChemistrySelect* **2016**, *1* (17), 5421–5429. <https://doi.org/https://doi.org/10.1002/slct.201601215>.
- (111) Rezaei, R.; Mohammadi, M. K.; Rastin, N. Microwave Assisted, Solvent Free One Pot Synthesis of Nitriles from Aryl Aldehydes on Melamin Formaldehyde as Solid Support. *Chinese J. Chem.* **2010**, *28* (6), 993–996.

<https://doi.org/10.1002/cjoc.201090184>.

Chapter 4: Development of Photoactive Hydroxamate-Based Coordination Cages



4.1 Declaration

The following people have contributed to this work over the past four years:

Emmanouil Broumidis: Synthesis and characterisation of naphthalene- and terephthalate-based hydroxamic acid (HA) ligands, and their corresponding supramolecular complexes, experiment design, data analysis and author of current chapter.

Lisa Harkins: Synthesis and characterisation of terephthalate and succinyl-based HA ligands and their corresponding supramolecular complexes.

Hayley G. Green: Synthesis and characterisation of isophthalate based HA ligands and their corresponding supramolecular complexes.

Gareth O. Lloyd and Filipe Vilela: Overall project supervision, experiment design, manuscript review.

4.2 Background and Aims

This project builds upon previous work carried out by Dr G. O Lloyd and his group on the chemistry of metallosupramolecular cages bearing hydroxamate linkers.¹⁻³ More specifically, it was established that small dihydroxamic acid compounds, based on the isophthaloyl motif, are able to coordinate with Fe^{3+} , Ga^{3+} , Al^{3+} and In^{3+} ions to form clusters which possess an internal cavity, as depicted in Figure 1.⁴

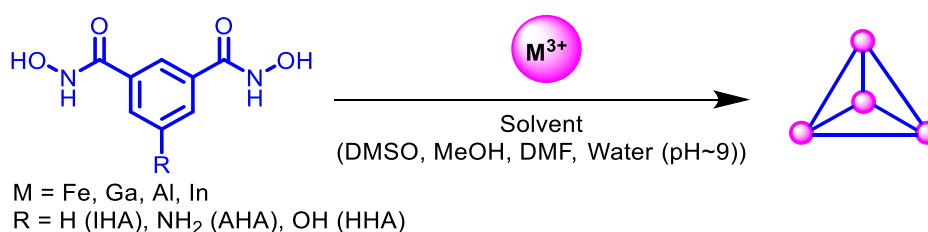


Figure 1. Past work involving isophthalic dihydroxamic acid (diHA) linkers and their resulting tetrahedral clusters.

To determine the geometry of the clusters, several analytical techniques were used, including ^1H NMR titrations, DOSY NMR, Variable-Temperature NMR, molecular dynamics simulations and MS. Although these methods can offer crucial information that can be used to provide evidence for a certain geometry, the most reliable way to determine their geometry is by growing single crystals of the respective clusters and then elucidating their structure using SC-XRD. Fortunately, in the case of the aforementioned complexes, it was possible to grow SC-XRD quality crystals, which showed that in the solid-state the coordinated linkers form M_4L_6 (M=Metal, L=Ligand) type tetrahedral clusters. These type of clusters have been studied extensively over the past 20 years, as their internal cavity can be utilised for a multitude of applications, including catalysis,⁵ sensing,⁶ smart materials,⁷ medicine,⁸ and photochemistry.⁹ Despite the substantial maturity of this field, the utilisation of HAs as ligands has remained relatively unexplored, as most of the known examples are made using catecholate,¹⁰ or pyridyl¹¹ containing ligands. The reason behind this probably relates to the ease of synthetic access for each functional group, and as will be discussed later, it will become clear that accessing HA functionalities poses several challenges. Intrigued by the encouraging results obtained from the isophthaloyl type ligands, we set off to develop a library of larger HA containing ligands, as the pore size of the isophthaloyl cages was not sufficiently large enough to accommodate organic guest compounds. The following work describes our efforts to achieve this goal, and the challenges that we had to face.

4.3 Introduction

4.3.1 Introduction to Supramolecular Cages and Their Applications

Molecular receptors can be defined as molecules that have the ability to ‘communicate’ selectively with ionic or molecular substrates (or both) *via* various intermolecular interactions.¹² In order to achieve this, a wide range of factors must be taken into account during the process of designing a molecule which will act as a receptor.¹³ The desired complementarity depends on a very well-defined three-dimensional architecture that has the appropriate configuration and conformation for the necessary binding motifs.¹⁴ More specifically, the receptor and the substrate will be able to come into contact and bind only if the receptor is able to physically cover a large region of the substrate, to maximise the binding motifs and thus the intermolecular bonding forces and the overall stability. Another important benefit of a large contact area is that the probability of compatibility between the receptor and substrate (size, shape, structure) is increased. This illustrates the reason why the receptor (host) must have molecular cavities which can be tuned to be complimentary to the substrate (guest). In those with concave shaped-hosts, the cavity possesses binding motifs which ‘point’ towards the guest and this is why they are so-called *endo-receptors*.¹⁵ Alternatively, a host can act as an *exo-receptor*, where the guest molecule can bind on its exterior wall. In those cases, physical encapsulation within the host is less likely to occur, as dictated by the geometry of the host (e.g. bowl-shaped,¹⁶ lantern-shaped¹⁷), the shape of the guest,¹⁸ and the various host-guest interactions, such as CT,¹⁹ π - π stacking,²⁰ H-bonding,²¹ ion-dipole interactions,²² among others.

Until today, there have been receptors synthesised and studied with a great structural variety.²³ They are designed with the goal of having an easily controllable geometry, which can be achieved by employing a specific organisation pattern, something which increases with a cyclic orientation (preferred) and also depends partly on various physico-chemical factors, namely structural rigidity, solubility and electronic properties. The desirability for this kind of pre-organisation is that which led the researchers to shift their focus from acyclic to macrocyclic receptors, like crown-ethers²⁴ and macropolycyclic receptors, such as calixarenes,²⁵ which have led to the advent of supramolecular capsule

systems. D. J. Cram was the first to conceptualise these systems in 1983, and coined the term ‘cavitands’ to describe them.²⁶ Later in 1985, his research group reported the first example of such a cavitand,²⁷ and in 1987 he, along with J-M Lehn and C. J. Pedersen won the Nobel prize in Chemistry for their seminal contributions to the field of supramolecular chemistry.²⁸

A cavitand (also known in literature as nanoreactors, molecular flasks, supramolecular coordination cages, or nano-containers; these terms are used interchangeably) can be defined as a molecule (host) which has an internal cavity or opening, large enough to accommodate a smaller molecule inside it (guest) (Figure 2). In order to form a capsule both the host and the guest must fulfil certain criteria: (i) The host must be defined by pre-organisation so that it can resist conformational changes during the encapsulation process; (ii) its functional groups must be complementary to the guest’s functional groups so there can be maximum interaction and minimum repulsion (steric factors) between the two molecules; (iii) besides chemical complementarity, a large number of functional groups must be present, so they can be used to promote the encapsulation process.²⁹ This process is governed mostly by the chelate effect, which describes the high stability of complexes that are formed using polydentate ligands, compared to the corresponding complex that is being formed using monodentate ligands.³⁰ Moreover, depending on the stoichiometry between the host and the guest there are different types of capsules, such as 1:1 and 2:1. For instance, most capsules that contain fullerenes are 2:1 capsules which means that two host molecules are required to trap a single fullerene molecule.³¹

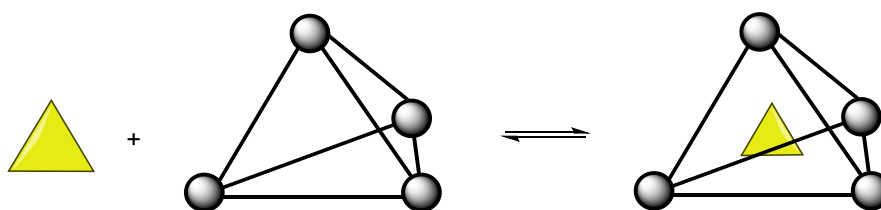


Figure 2. Schematic representation of the mechanism that describes the formation of a molecular capsule.

By exploiting the property of metals that coordinate with organic ligands over different conformations and angles, it is possible to synthesise many complex supramolecular structures. For the formation of a molecular capsule to be viable, the host must have the appropriate conformation, which will allow the incoming guest to be tethered to it. Besides non-covalent interactions such as van der Waals forces,³² π - π stacking,³³ hydrogen bonding,³⁴ and electrostatic interactions,³⁵ molecular capsules can also be

formed with the use of covalent bonds.³⁶ These kinds of capsules have several advantages because they are held together *via* covalent bonds (which are strong in nature), the capsules display enhanced stability and are therefore harder to decompose. On the other hand, both hydrogen bonding and metal coordination containing capsules, can be sensitive under certain conditions (e.g., pH changes,³⁷ high temperatures,³⁸ light irradiation³⁹) and can decompose fairly easily. This ‘stimuli-response’ property of many such cages has been exploited by scientists to construct ‘smart’ supramolecular systems with many practical applications, including gas storage,³⁸ chemical separations,⁴⁰ and anti-counterfeight inks.⁴¹

4.3.2 Hydroxamic Acids and Their Use in Supramolecular Assemblies

4.3.2.1 Properties and Structure of Hydroxamic Acids

Hydroxamic acids (the term ‘HAs’ can be used interchangeably) are a class of molecules, which are known to exhibit interesting and medically important properties, due to their ability to form stable complexes with transition metal ions, particularly gallium and iron.⁴² Many studies have been undertaken to improve our understanding of the coordination interactions between hydroxamic acids and various metals. It has been shown that due to the various binding modes available to hydroxamates they are very effective and versatile ligands, and because of this, their applications in coordination chemistry can be vast. Hydroxamic acids of the form RCONHOH have two potentially labile protons (O–H, N–H). Therefore, for a long time, it remained unclear whether the most predominant form is mono- (m) or di-deprotonated (d) and how the protonation state affects the binding mode. Recent literature⁴³ has shed light on how titanium dioxide (TiO₂), a widely used metal oxide semiconductor found in photoelectrochemical devices,⁴⁴ interacts with hydroxamic acids and has suggested many possible modes for hydroxamate binding. Figure 3 depicts the most likely binding forms.

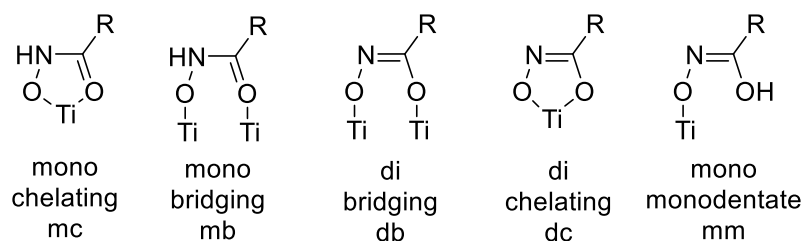
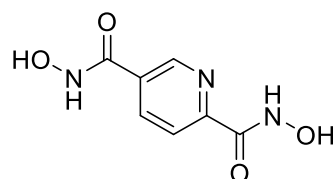


Figure 3. Examples of hydroxamic acid binding forms.⁴³

The binding modes represented in Figure 3 involve binding through the oxygen atoms within the molecule. It is worth noting that it is also possible to coordinate to a metal centre *via* the nitrogen-containing group. A good example comes from work of Buglyó *et al.*,⁴⁵ wherein they successfully synthesised a Pd(II) hydroxamate complex, to prove the effective use of hydroxamic acids in palladium scavenging. The group synthesised and determined the structure of [Pd(en)(2,5-pyha_{-1H})]Cl (where 2,5-pyha_{-1H} = 2,5-pyridinedihydroxamic acid and en = ethylenediamine) by X-ray crystallography (Figure 4).



2,5-Pyridinedihydroxamic acid

Figure 4. Structure of the ligand used by Buglyo *et al.*⁴⁵

Through density functional theory (DFT) it was shown that the structure with the palladium coordinating to both nitrogens in 2,5-pyridinedihydroxamic acid, was 5.7 kcal/mol more stable than the other binding modes wherein the oxygens coordinate to the metal centre. This was also true of the *di*-nuclear species, indicating that the resulting distorted square-planar complex is more favourable than the assumed non-distorted square-planar geometry of the other binding modes, thus, complicating the coordination chemistry of hydroxamic acids, where there is more than one functional group to which a metal centre can bind.

The same team also synthesised several novel dipeptide hydroxamic acids, such as L-Ala-L-AlaN(R)OH and L-Ala-L-SerN(R)OH and studied their binding modes using several metals.⁴⁵ Depending on whether the dipeptide was *N*-protected, the

corresponding binding form would switch between the nitrogen and oxygen atoms (Figure 5).

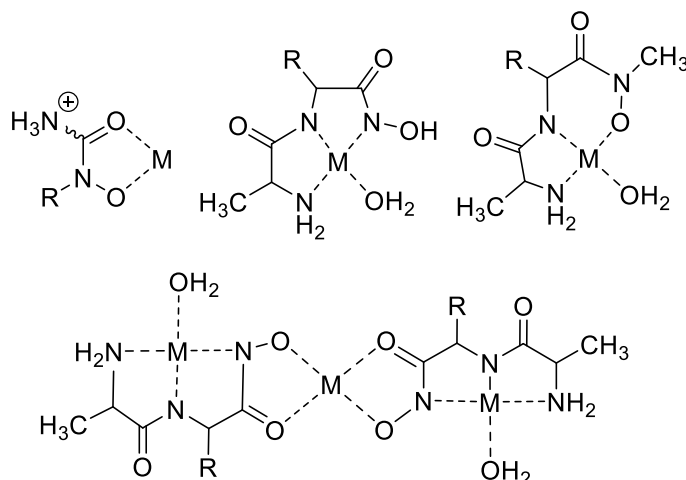


Figure 5. Depiction of different binding modes of hydroxamate species.⁴⁵

Although iron is one of the most abundant elements on the planet, its pivotal role in biology is dependent on the development of effective methods for its assimilation.⁴⁶ Ionic forms of iron, especially iron (III) (the most common oxidation state^{47,48}), are very insoluble under physiological conditions.⁴⁹ To circumvent the solubility problem, many microbial, plant, and even higher organisms (e.g., mammals), synthesise and utilise very specific low molecular weight iron chelators called siderophores.⁵⁰ Hydroxamic acids can occur in siderophore natural products that bind iron, and they have several applications in medicinal chemistry as inhibitors of metalloenzymes.⁴² As a result, there are many commercially available drugs containing the hydroxamate moiety (Figure 6).

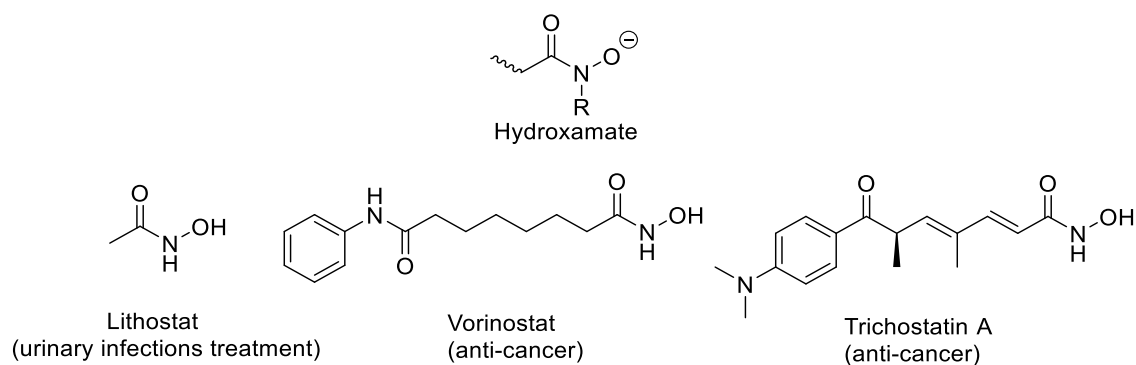


Figure 6. The hydroxamate moiety and three examples of HA containing drugs.

4.3.2.2 Supramolecular Cages based on Hydroxamic Acid Ligands

Being such good chelators, hydroxamate ligands are an excellent choice for binding units in supramolecular complexes, especially due to the high stability of these chelates with 3+ ions with octahedral coordination environments,^{51,52} and as a result they tend to form neutral $M(\text{hydroxamate})_3$ units.⁵³ When two HA moieties are present within a compound, then assemblies with various topologies can form, the simplest being M_2L_3 . Surprisingly, the first M_2L_3 complex was reported in 1978 by Raymond *et. al.*,⁵⁴ when rhodotorulic acid, a naturally occurring secondary hydroxamic acid, produced by the yeast *Rhodotorula mucilaginosa*,⁵⁵ was used as a ligand to coordinate with Fe^{3+} , Al^{3+} and Cr^{3+} ions (Figure 7). The resulting $M_2(\text{rhodotorulic acid})_3$ complexes appeared to possess helical geometries, and they were aptly named triple helicates.

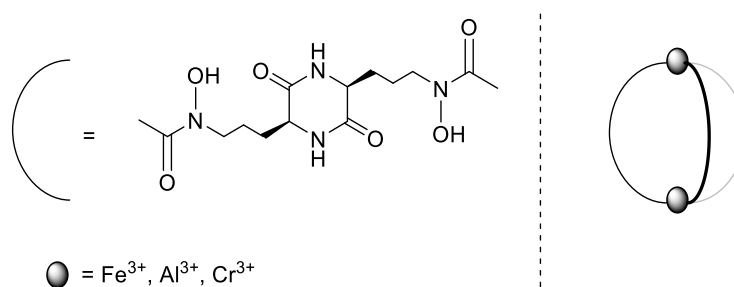


Figure 7. Structure of rhodotorulic acid (left) and a triple stranded helicate complex (right).

An interesting property of these helicates is that they are optically active; the metal vertex of the helicate consists of six metal-oxygen bonds and is a distorted octahedron. The O-N bond of the hydroxamate is always located on one face of the octahedron and consequently provides the vertex with its *fac* (facial) isomerism. In addition to their geometries the vertices are also chiral and can display lambda (Λ) or delta (Δ) chirality. This type of chirality is also known as axial chirality⁵⁶ or helicity since the axis of the structure has a helical, propeller, or screw-shaped geometry. *P* (plus) or Δ is a right-handed helix, whereas *M* (minus) or Λ is a left-handed helix. The *P/M* or Δ/Λ terminology is used particularly for molecules that actually resemble a helix, such as hexahelicene⁵⁷ (Figure 8). It can also be applied to other structures having axial chirality by considering the helical orientation of the "front" vs "back" Cahn-Ingold-Prelog rankings.⁵⁸

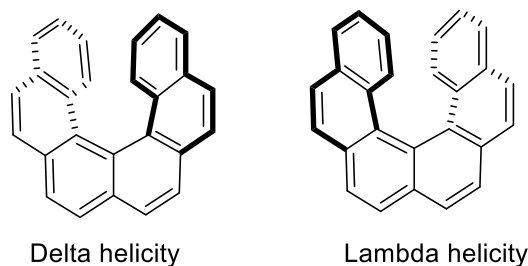


Figure 8. The two axial conformations of hexahelicene (Δ/Λ).

As such, these M_2L_3 type compounds can exist as three optical isomers, namely as ($\Delta\Delta$), ($\Lambda\Lambda$) and ($\Delta\Lambda$). In the last case, as each metal vertex has opposite helicity the complex is optically inactive. This class of isomers are known as meso-helicates, or mesocates.⁵⁹

Similarly, when it comes to tetrahedral M_4L_6 topologies, since each metal vertex can have two distinct chiralities (Δ or Λ), and there are four metal centres in total, then five potential cage isomers are possible overall. There are two T-type symmetry cages ($\Lambda\Lambda\Lambda\Lambda$ or $\Delta\Delta\Delta\Delta$) two C_3 cages ($\Delta\Lambda\Lambda\Lambda$ or $\Lambda\Delta\Delta\Delta$), and one S_4 cage ($\Lambda\Lambda\Delta\Delta$). These names are derived from their point group symmetries and are solely related to the chiralities of the vertices. In contrast to kinetically inert materials whose structures are fixed at the time of synthesis, the supramolecular structures found in nature are dynamic and typically on the nanometer scale. For those types of cages, Raymond *et al.*⁶⁰ have used VT 1H NMR to elucidate the different isomers that are present in those systems. They have found that when at room temperature, a M_4L_6 cage ($M=Ga$, $L=$ isophthaldi-*N*-(4-methylphenyl)hydroxamate), the activation barrier for the inversion of configuration is 58 KJ/mol (at room temperature). The different isomers are visible as distinct 1H NMR peaks, however, this becomes apparent only at lower temperatures, as at 300 K, they interconvert at speeds that are comparable with the NMR time-scale.

Trischelate or tritopic ligands such as these hydroxamate clusters mentioned above are well-known examples of metal complexes, which can exist as separate enantiomers, belonging (if appropriately substituted) to the chiral D_3 or C_3 point groups. Two proposed mechanisms exist by which a trischelate cluster like the one discussed can racemize without any M–L bonds breaking. The first one is known as the Bailar twist,⁶¹ where the opposite triangular faces of the octahedron, which lie normal to the C_3 axis of the molecule, twist to give a trigonal prismatic transition state. An alternate process is the Ray–Dutt Twist⁶¹ in which the faces involved in the twist are any opposite pair other than the ones normal to the C_3 axis, (Figure 9). With this in mind, it is postulated that since

four coordination centres are tethered in the M_4L_6 tetrahedron, the Bailar twist is the only mechanically possible rearrangement.⁶⁰

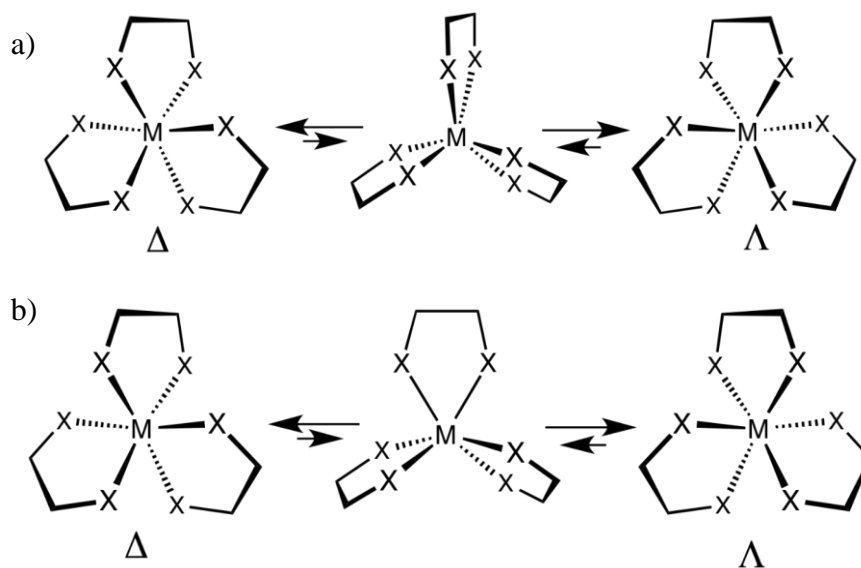


Figure 9 An Illustration of a) the Bailar b) Ray-Dutt racemisation mechanisms.

4.3.2.3 Previous Work on M_4L_6 Tetrahedral Cages

The Lloyd lab⁶² has used hydroxamic acids in the past to form small organic cages, using ligands such as N^1,N^3 -dihydroxyisophthalamide (IHA), 5-amino- N^1,N^3 -dihydroxyisophthalamide (AHA) and $N^1,N^3,5$ -trihydroxyisophthalamide (HHA) (Figure 10) to form M_4L_6 type cages. Hydroxamate cages of this type usually tend to self-assemble in solution, and a range of solvents have been used such as DMF, DMSO,

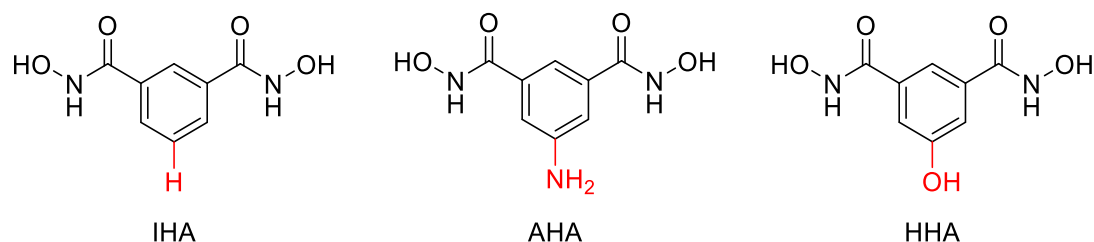


Figure 10. Hydroxamic acid ligands for cage formation.

alkaline water, MeOH and their mixtures. However, it needs to be stressed that predicting the final architecture of a self-assembly process is not a trivial matter, as it is dependent on several factors.¹¹ Solvent of choice is important if we take into account the low solubility of these ligands as they contribute to difficulties in characterising the assembled

cages. Experience gained by working with these cages has shown that MS analysis of these compounds can be cumbersome since subjecting them to standard techniques, such as ESI, can produce ambiguous fragments. Moreover, due to their generally low solubility, the determination of a viable solvent system that is compatible with the analytical instrumentation is challenging. As mentioned in section 4.2, SC-XRD was used to unambiguously characterise the unknown cage. Figure 11 depicts the crystal structure of one of the hydroxamic acid cages made previously in the Lloyd group, using the IHA ligand and $\text{Fe}(\text{NO}_3)_3 \cdot 9\text{H}_2\text{O}$ as the metal source.

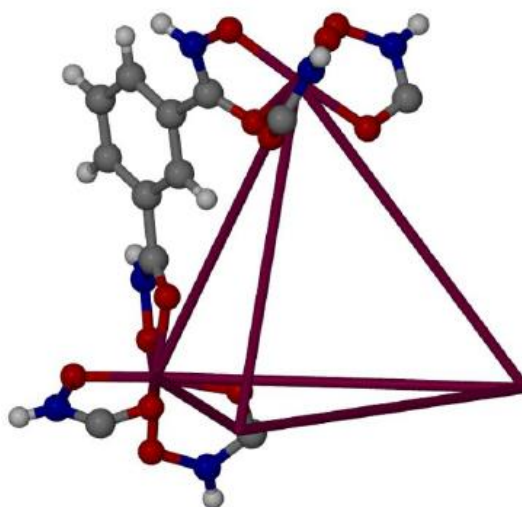


Figure 11. Crystal structure showing the tetrahedral shape of the M_4L_6 cage formed from Fe^{3+} and IHA. The iron vertices are connected by purple lines to illustrate the shape. One ligand is shown, connecting to iron coordination spheres that are shown with a complete coordination sphere of the hydroxamate functionality. Atoms shown in ball-and-stick representation.⁶²

The hydroxyl oxygen is deprotonated and located on the outside of the cage. The NH group, also located on the outside of the cage, remains protonated. The hydroxyl oxygen has a formal negative charge with each metal coordinating with three of these oxygens. It was found that the crystallised cages had T symmetry only. Additionally, since the 3+ charge of the metal is neutralised upon complexation, the cage is overall charge-neutral, which is relatively rare, as most metallocages are usually charged,⁶³ massively increasing their solubility in polar solvents, and their ability to crystallise, making them, therefore, easier to characterise. On the other hand, this presents an opportunity for us to study these elusive systems.

4.4 Results and Discussion

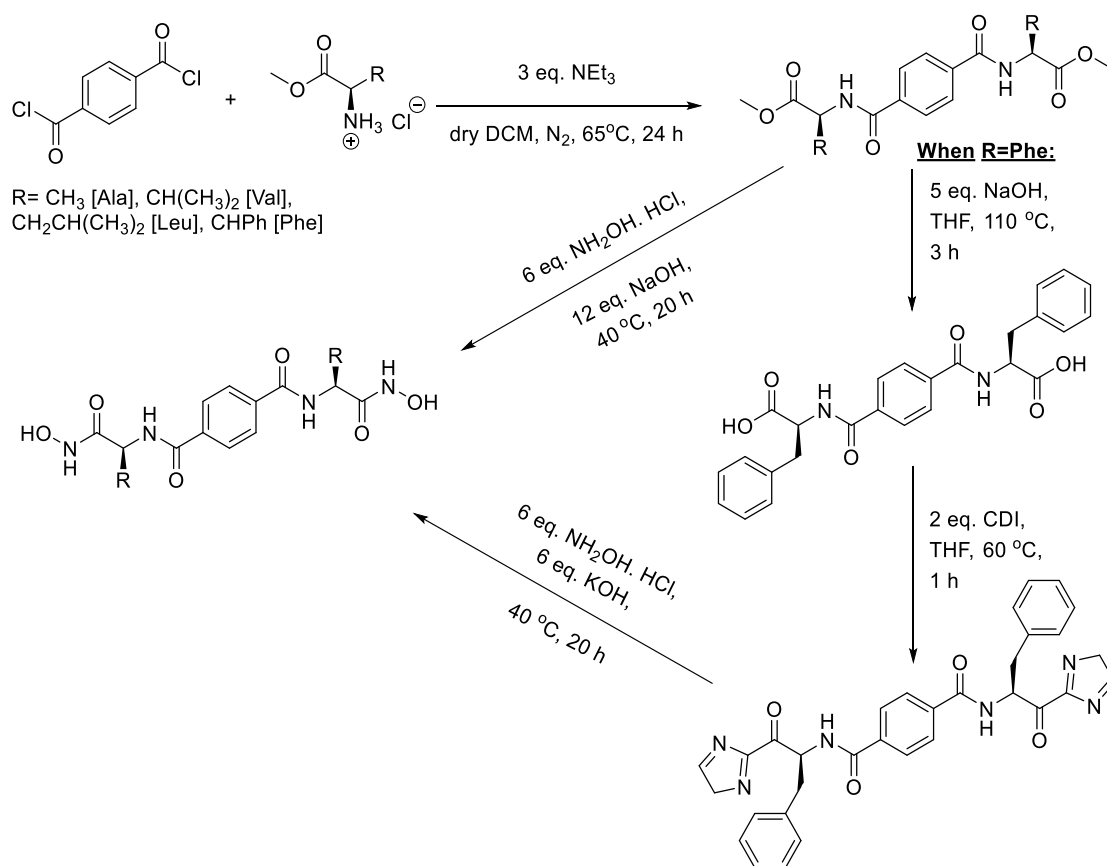
4.4.1 Terephthaloyl Dihydroxamic Acid-Based Complexes⁸

4.4.1.1 Synthesis of Ligands **H₂A**-**H₂D**

In order to increase the length of the ligands and create a larger pore size, we decided to synthesise a series of dihydroxamic acids with a terephthaloyl core that is coupled with various amino acids. The presence of the amino acid motifs serves two purposes, as they increase the overall length of the ligand, and they also contain a stereogenic centre, making them optically active. The introduction of a chiral ligand is generally a strategy to generate discrete metallocsupramolecular architectures, as their chirality tends to be predetermined by the enantiopure ligand.⁶⁴ Consequently, these complexes possess dual chirality, which allows them to act as ‘chiral traps’, by encapsulating guest compounds with high diastereomeric excess.⁶⁵ More specifically, amino acid-containing ligands also promote H-bonding interactions and have been used before to construct interesting architectures and encapsulate unusual guests.⁶⁶⁻⁶⁸

The ligands *N*¹,*N*⁴-bis((*S*)-1-(hydroxyamino)-1-oxopropan-2-yl)terephthalamide (**H₂A**), *N*¹,*N*⁴-bis((*S*)-1-(hydroxyamino)-3-methyl-1-oxobutan-2-yl)terephthalamide (**H₂B**) and *N*¹,*N*⁴-bis((*S*)-1-(hydroxyamino)-4-methyl-1-oxopentan-2-yl)terephthalamide (**H₂C**) were prepared through a simple two-step reaction as shown in Scheme 1. The first step of the reaction was an amide coupling in which the intermediate was prepared through the use of terephthalate chloride with 2 equivalents of the associated L-amino acid methyl ester hydrochloride (**H₂A**= L-alanine methyl ester HCl, **H₂B**= L-valine methyl ester HCl and **H₂C**= L-leucine methyl ester HCl).

Due to the moisture-sensitive nature of terephthalate chloride the reaction was proceeding under nitrogen. The second step was a hydroxamic acid synthesis reaction to produce ligands **H₂A**, **H₂B** and **H₂C**. This involved reaction with the methyl ester intermediate from step 1 with 6 equivalents of hydroxylamine hydrochloride and 12 equivalents of sodium hydroxide. The ¹H NMR spectra of these compounds displayed the characteristic hydroxamic acid OH and NH peaks at approximately 9 and 11 ppm, respectively.⁶⁹ The overall yields were generally modest (**H₂A**= 33%, **H₂B**= 39% and **H₂C**= 43%).



Scheme 1. Synthetic pathway for hydroxamic acid ligands **H₂A**, **H₂B**, **H₂C** and **H₂D**.

Ligand **N¹,N⁴-bis((S)-1-(hydroxyamino)-1-oxo-3-phenylpropan-2-yl)terephthalamide H₂D** was prepared using a four-step synthetic pathway instead, as the same hydroxamic acid synthesis pathway could not be implemented here due to this particular ester intermediate being insoluble in methanol. Step 1 involved amide coupling as carried out previously using terephthaloyl chloride and L-phenylalanine methyl ester hydrochloride. Then, ester hydrolysis of the intermediate was performed to afford a carboxylic acid. Step 3 involved the use of 1,1'-Carbonyldiimidazole (CDI) to convert the carboxylic acid to a carbonylimidazole intermediate,⁷⁰ followed by conversion to the target dihydroxamic acid by using 6 eq. of NH₂OH·HCl and 6 eq. of KOH.

It is noted that, to isolate the diHAs, the solution after the final synthetic step must be carefully acidified to a pH~6, as more alkaline solutions usually contain the hydroxamate anions. If on the other hand, the solution's pH is further reduced, then it is possible that the dihydroxamic acid will decompose *via* Loosen rearrangement,⁷¹ or unreacted dicarboxylic acid intermediate will co-precipitate. The work up procedure is detailed in SI, 4.8.2. The overall yield for the three steps was 12%.

4.4.1.2 Synthesis and Characterisation of Ga³⁺/Fe³⁺ Complexes with ligands H₂A-H₂D

At this point we were ready to initiate the cage synthesis, which is a trivial process, as it was based on previous work using the smaller IHA/AHA/HHA ligands.⁴ To form the cages in solution, the desired ligand is dissolved in DMSO, to which is added a stoichiometric amount of a metal salt, usually the nitrate. When iron was used as the metal centre, a striking colour change occurred as soon as it mixed with the HA, which was expected, since Fe-HA complexes almost always form intense purple solutions.⁷² On the other hand, when gallium was used, no colour change was observed. After the desired complexes (Ga³⁺) were formed, they were subjected to ¹H NMR analysis, and their spectrum was compared to that of the free ligand.

Multiple ¹H NMR spectra were collected in-between sequential additions of the metal salt, and stacked on top of each other, a technique that is known as NMR titration.⁷³ This allowed us to detect minute differences in the chemical shifts after each addition and is a frequently used diagnostic tool when working with supramolecular clusters. In general, as a new complex forms, several of the NMR resonances shift, as the protons that are pointing towards the inside of the cage are ‘shielded’ from the solvent, resulting in a different chemical environment and thus appear downfield.⁶⁵

It is also important to mention, that since Fe³⁺ is paramagnetic, it cannot be used for NMR studies, as paramagnetic metal centres (such as Fe³⁺ or high-spin Fe²⁺, Co²⁺, Ni²⁺ etc.) cause signal broadening along with large shifts due to short relaxation times.⁷⁴ For this reason we used the diamagnetic Ga³⁺ (in the form of Ga(NO₃)₃·H₂O) as the metal source for the NMR studies. Below is described the ¹H NMR titration using ligand **H₂B**, the results of which are representative of all the set. Gratifyingly, the anticipated downfield shift of certain proton resonances was observed, as shown in Figure 12.

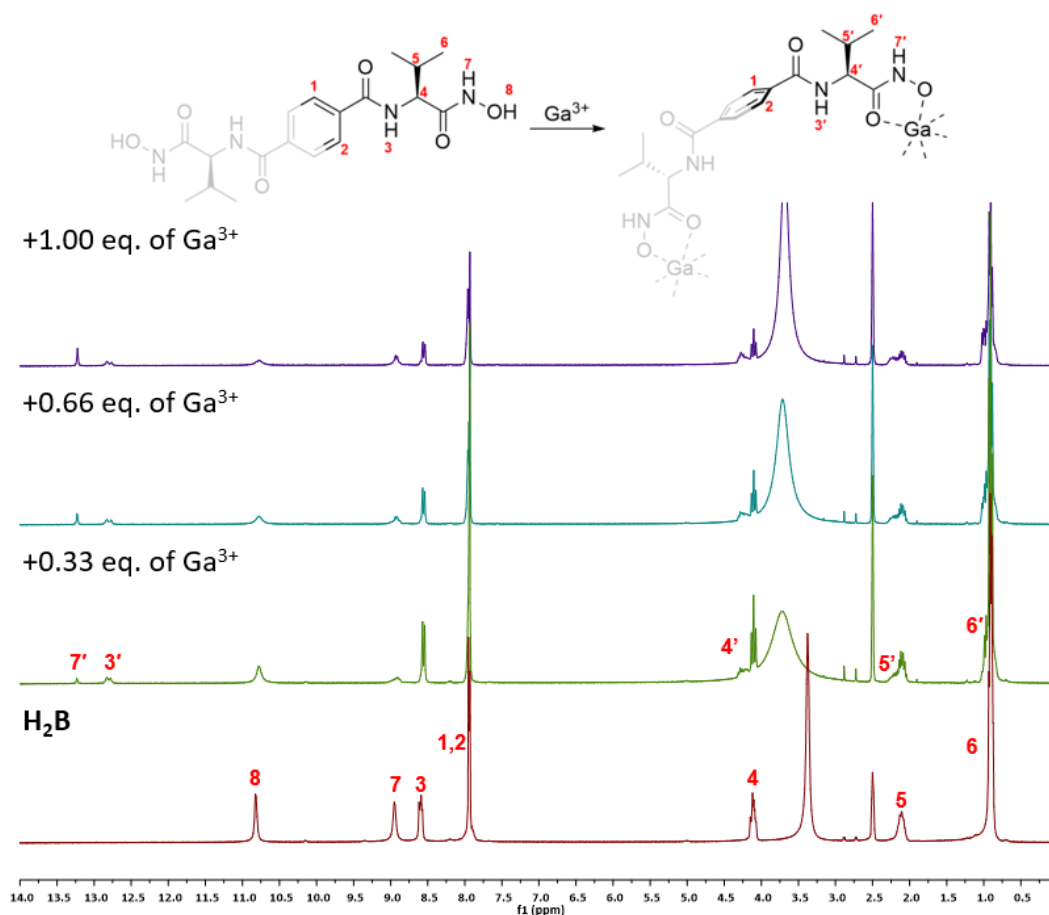


Figure 12. ^1H NMR titration study using the ligand **H₂B**.

Specifically, aromatic protons 1 and 2 did not demonstrate any discernible shift or change in morphology of their peaks even after the addition of 1 eq. of Ga^{3+} , indicating that their microenvironment did not change. However, when looking at peaks 3 and 7 corresponding to the amidic (NH) and hydroxamic acid hydrogens (NH), we see that their intensity is reduced while a new set of peaks, 7' (singlet) and 3' (doublet) appear at ~ 13 and ~ 13.2 ppm, respectively. These are tentatively assigned to the amide (NH) and HA (NH) hydrogens of the newly formed cage. At the same time, peak 8, belonging to the HA (OH), is reduced in intensity, as the -OH group is deprotonated to coordinate with the Ga^{3+} . Similarly, we observe that the alkyl hydrogens (CH) 4, 5 and 6 behave in an analogous manner to that of 3 and 7, albeit their downfield shift is much less pronounced, since they are likely located on the exterior of the cage. It is also worth mentioning that, after adding 1 eq. of Ga^{3+} in the ligand solution, the complexation was not complete, as evidenced by the remaining peak 8, representing the protonated ligand.

To obtain evidence for the topology of the newly formed supramolecular constructs, a series of attempts to grow crystals suitable for SC-XRD were carried out. We employed

several crystallisation techniques, including heating and subsequent cooling, slow evaporation, vapour diffusion, and layering (solvent diffusion), using a range of solvent mixtures with different polarities. Unfortunately, despite numerous attempts over several months, we were unable to obtain the desired crystals which left us with MS as the other reliable method of inferring the topology.

Luckily the cages were able to dissolve in MeOH, which is a suitable solvent for EI techniques and to our surprise, the measured masses matched the M_2L_3 topology (Figure 13). Without the SC-XRD data, however, it is unclear whether the helicate, or mesocate or a mixture of two isomers was formed in each case. Notwithstanding, the fact that only one set of new peaks appeared downfield ($7'$ and $3'$), might imply that only one diastereomer is present ($\Delta\Delta/\Lambda\Lambda$ or $\Delta\Lambda/\Lambda\Delta$), however as we will see in the next section (4.4.2), there are other plausible explanations for the emergence of these peaks.

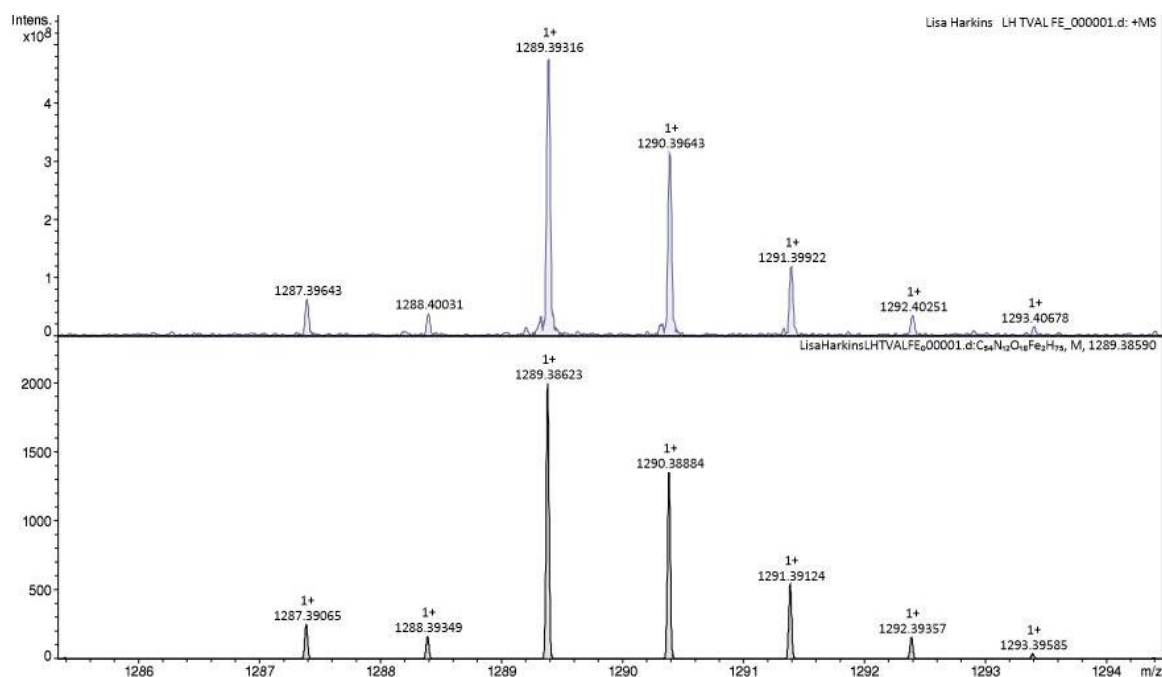


Figure 13. MS spectrum (EI) showing the theoretical (bottom) and measured (top) mass pattern for the complex $Fe_2(H_2B)_3$.

4.4.2 Naphthaloyl Dihydroxamic Acid-Based Complexes

4.4.2.1 Synthesis and Characterisation of Ligands AlaHA, ValHA, LeuHA and PheHA

Since the goal of this project was to expand the internal cavity volume found in the original IHA tetrahedral cage, the triple helicate/mesocate complexes that were obtained meant that they could not be utilised for our intended purposes since the cavity in those architectures with short spacers (in our case terephthaloyl unit) is usually small and inaccessible to most guest compounds.⁷⁵ The main strategy to overcome this challenge is to select a larger spacer, ideally with a relatively rigid structure, as too much flexibility can lead to binding of the two hydroxamate units to the same metal centre.^{76,77} Based on this and inspired by earlier work from Raymond *et al.*,⁷⁸ illustrating a series of tetrahedral M_4L_6 clusters with 1,5-naphthalene-containing, catechol spacers (Figure 14a), we decided to employ the more elongated 2,6-naphthalene regioisomer, to further increase the length of the ligand. Furthermore, we decided to keep the amino acid moieties, since they offer a series of benefits, as mentioned in section 4.4.1.1 and they appeared to behave as intended when used with the terephthaloyl-based ligands (Figure 14b).

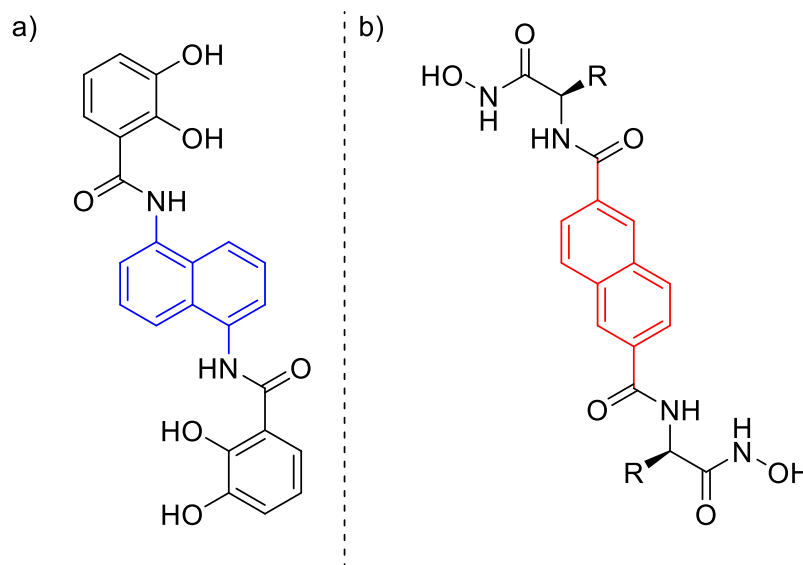
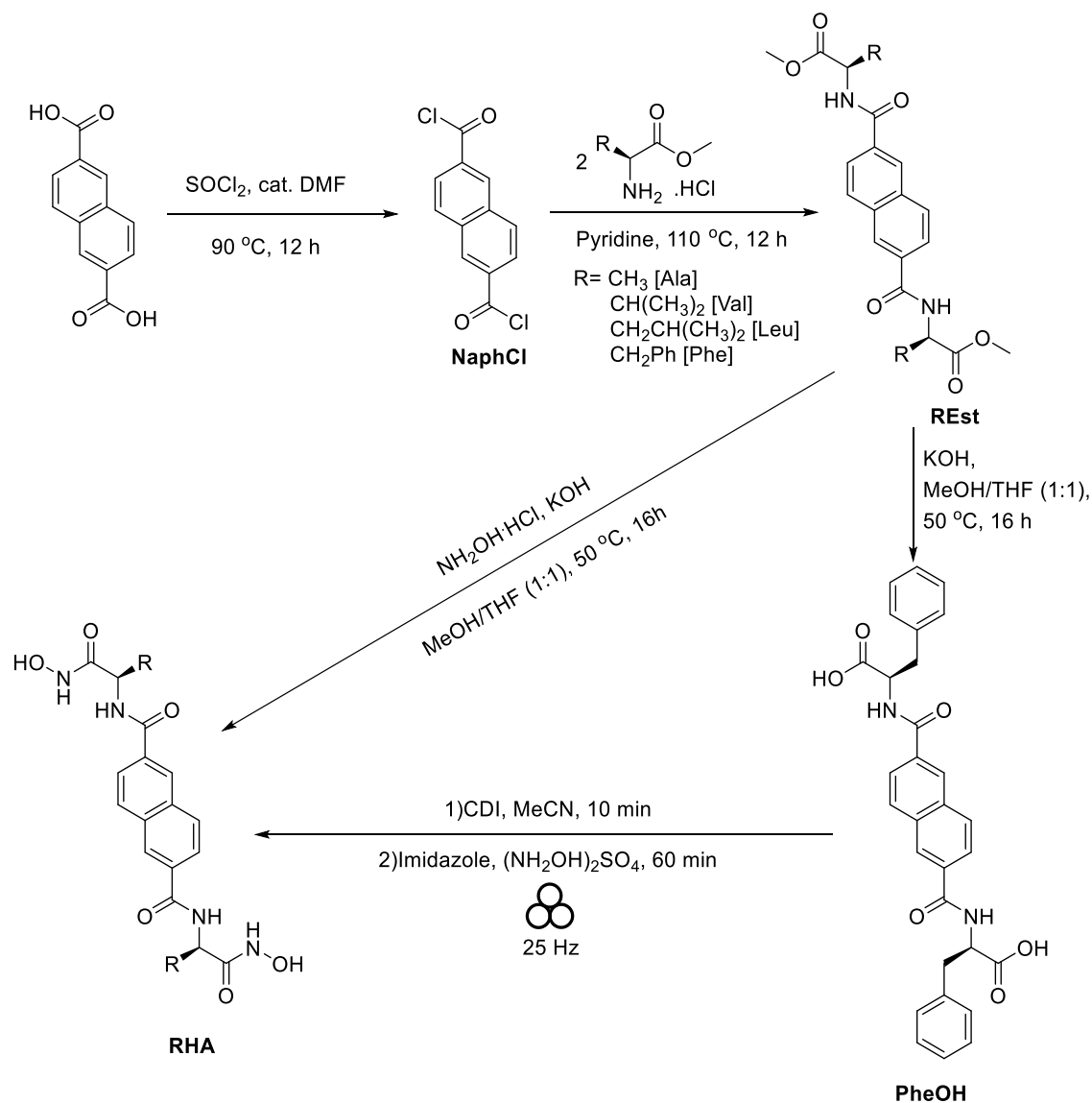


Figure 14. a) Catechol-based ligand featuring the 1,5-naphthalene unit (blue) as a spacer used by Raymond *et al.* b) Our proposed hydroxamic acid-based ligand containing the more elongated 2,6-naphthalene unit (red) as a spacer, along with chiral amino acid extensions.

We started by using the commercially available 2,6-naphthalene dicarboxylic acid, as the main building block for the synthesis of the target compounds (Scheme 2). We proceeded by chlorinating the dicarboxylic acid using thionyl chloride, a commonly used chlorinating reagent,⁷⁹ to obtain 2,6-naphthalene dicarbonyl dichloride (**NaphCl**) which was used as a coupling partner with a series of amino acid methyl ester HCl salts.



Scheme 2. Synthetic steps followed to access the desired dihydroxamic acid ligands.

In total, we used five different amino acids, namely L-alanine, L-valine, L-leucine, L-phenylalanine and L-histidine. However, it was quickly discovered that histidine was an incompatible amino acid for our method, as the coupling step involves the use of pyridine, which may act as a base to deprotonate the histidine moiety, leading to salt formation and side-reactions. As such, we obtained four coupling products, which were then converted

to the target dihydroxamic acids using the same method employed in section 4.4.1.1. In general, this method afforded N^2,N^6 -bis(1-(hydroxyamino)-1-oxopropan-2-yl)naphthalene-2,6-dicarboxamide (**AlaHA**), N^2,N^6 -bis(1-(hydroxyamino)-3-methyl-1-oxobutan-2-yl)naphthalene-2,6-dicarboxamide (**ValHA**), N^2,N^6 -bis(1-(hydroxyamino)-4-methyl-1-oxopentan-2-yl)naphthalene-2,6-dicarboxamide (**LeuHA**) in poor yields (10–20%). In an attempt to improve the yields, we tried to raise the temperature of the last step above 50 °C, however we noticed that the opposite was achieved; in many cases, no product was formed, and a sticky tar was produced instead. The few attempts that did work, gave products with even poorer yields (<10%) than the original ones. It is postulated, that this is due to the tendency of many hydroxamic acids to decompose upon heating and participate in a plethora of side-reactions,^{80–82} the most common one being the Loosen rearrangement,⁷¹ where a hydroxamic acid can convert to an isocyanate intermediate.

Particularly difficult was the case of N^2,N^6 -bis(1-(hydroxyamino)-1-oxo-3-phenylpropan-2-yl)naphthalene-2,6-dicarboxamide (**PheHA**), as it was insoluble in virtually all solvents besides DMF and DMSO, making its use incompatible with the method employed for the other substrates, and afforded **PheHA** at 5% yield, and only after several attempts. For this reason, we decided to employ a mechanochemical, solvent-free method, which should be able to circumvent the solubility problem. We used a modified protocol that was first developed by Porcheddu *et al.*,⁸³ which utilises CDI to install an imidazole moiety adjacent to a carbonyl group. This imidazole then acts as a good leaving group in the presence of a hydroxylamine, to give the corresponding HA. In our lab we have established that using hydroxylamine sulphate $(\text{NH}_3\text{OH})_2\text{SO}_4$ and imidazole as a base in the presence of CH_3NO_2 as a LAG agent, generally works best. To our satisfaction, this method gave compound **PheHA** at a 42% yield, after 110 min of total reaction time (compared to 16 h for the solution method). Furthermore, since the Retsch MM400 mixer mill that was used to grind the sample can hold two jars, the reaction throughput was doubled, which saved us time and resources. In addition, this mechanochemical protocol takes place at room temperature (compared to 50 °C in solution), limiting the decomposition of the dihydroxamic acids. The main downside was that this method requires the use of a carboxylic acid as a starting material, which added an extra step into the synthesis, however obtaining the carboxylic acid 2,2'-((naphthalene-2,6-dicarbonyl)bis(azanediyl))bis(3-phenylpropanoic acid) (**PheOH**) was not a difficult

undertaking, as it simply involved the hydrolysis of a suspension of the ester precursor, dimethyl 2,2'-((naphthalene-2,6-dicarbonyl)bis(azanediy))bis(3-phenylpropanoate) (**PheEst**), in a mixture of THF/Methanol (1:1).

After the dihydroxamic acids were synthesised, we proceeded to characterise them by using key analytical techniques (^1H , ^{13}C , NOESY and DOSY NMR, IR, MS and m.p). Almost immediately, an interesting observation was made regarding their NMR spectra; it appeared as if most of the proton and carbon resonances were doubled. This effect was present in all four compounds, however, in **ValHA** it was the most prominent, as seen in Figure 15.

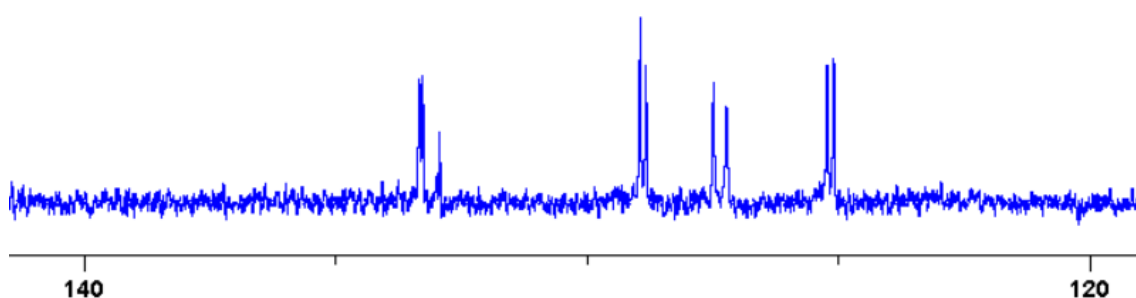


Figure 15. Part of (120-140 ppm) the ^{13}C spectrum of **ValHA**, showing an apparent doubling of the expected resonances.

We felt confident that the compounds were sufficiently free of impurities, and the structure assignments were correct, as evidenced by MS and TLC observations. Potential contamination with carboxylic acid or ester analogues was ruled out, since their corresponding masses were absent from the MS spectra. For reference, we also compared the NMR spectra of **PheHA** and **PheOH**, and the extra peaks in the former did not match those observed in the latter. This led us to consider an alternative hypothesis; the racemisation of the amino acid moieties. It is a well-known fact, that chiral compounds and most specifically enantiopure amino acids can lose their optical purity and racemise, a process which is dependent on many factors, including temperature, pH, presence of catalysts and time,⁸⁴ albeit there are still many unknown parameters that are under investigation.⁸⁵ If that had occurred with our compounds, then in principle we should be left with at least three stereoisomers (Figure 16). Taking **ValHA** as an example, if partial racemisation had occurred during the last step of its synthesis, then we would expect to have a mixture of (**S,S**)-**ValHA** (**SM**), (**R,R**)-**ValHA**, (**S,R**)-**ValHA** and (**R,S**)-**ValHA**. As illustrated in Figure 16, the latter two enantiomers are actually the same compound, since there is an internal plane of symmetry that bisects them, and they have two opposite

stereogenic centres, they fulfil the criteria of a meso compound.⁸⁶ As such, they are achiral and should not respond to polarised light. When we measured the optical rotation of **ValHA** using a polarimeter, it was $[\alpha]_{\text{D}} = +4$ (c 1.00, MeOH, 20.1 °C) compared to $[\alpha]_{\text{D}} = +16$ (c 1.00, MeOH, 21.0 °C) for **ValEst**. This inferred that the compound that we had was optically active, meaning that we had an excess of a certain enantiomer.

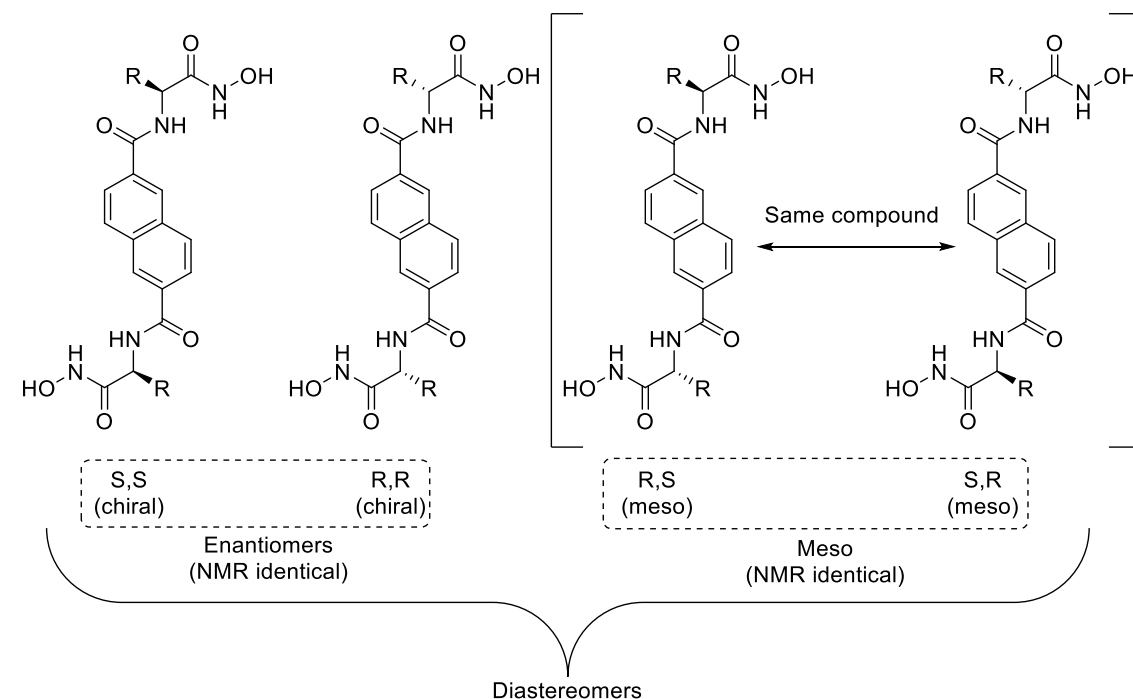


Figure 16. Possible stereoisomers stemmed from the partial racemisation of an enantiopure (S,S) ligand.

It is also worth mentioning, that out of the (S,S)-**ValHA**, (R,R)-**ValHA** and meso-**ValHA** stereoisomers, the first two (enantiomers) are diastereomers with relation to the third, and since ^1H NMR can be used to detect diastereomers, and diastereomeric ratios (d.r.),^{87,88} but not enantiomers, we would expect to have two sets of signals in total, which is in agreement with our observations. When it comes to the ^1H NMR spectra of the precursors, the resonances appeared to be as expected, meaning that the racemisation must have occurred during the last step of the synthesis. Next, we attempted to calculate the d.r. for each of the four compounds (Table 1), by integrating the NMR resonances for each diastereomeric pair. To ensure the reliability of the data, the average of several integrals was calculated for each compound. In cases where there was significant overlap or ambiguity in the ^1H NMR peaks, ^{13}C NMR integrations were used instead, as it has been shown that even proton decoupled ^{13}C NMR with short relaxation times, can provide a quantitative diastereomeric resolution which is comparable to those obtained by ^1H

NMR.⁸⁹ This was confirmed by our study, as the difference between the two methods was less than 3%. Even though we could measure the d.r., assigning a structure to each

Table 1. Diastereomeric analysis for the dihydroxamic acids as determined by NMR spectroscopy.

Compound	mol% major by ¹H NMR	mol% major by ¹³C NMR
AlaHA	90.9	88.5
ValHA	51.7	53.5
LeuHA	82.0	79.3
PheHA	81.8 (solution) 80.8 (mechanochemistry)	83.7 (mechanochemistry)

percentage is not possible. It might be argued, that since we began the synthesis with a single enantiomer (S,S) which resisted racemisation up until the final step of the synthesis, then the major diastereomer would belong to the (S,S) stereoisomer. However, this cannot be proven with the data in hand. It is also not clear why **ValHA** appeared to deviate from the other compounds, by having an almost 50:50 relationship between the diastereomers. Finally, it seems that when it comes to the d.r. of **PheHA**, both batch and mechanochemical methods give rise to the same outcome.

4.4.2.2 Synthesis and Characterisation Ga³⁺ Complexes with Ligands AlaHA, ValHA, LeuHA and PheHA

To obtain the desired complexes in solution was relatively trivial; similarly to the process followed with the terephthaloyl ligands used in section 4.4.1, we formed the complexes by adding Ga(NO₃)₃·H₂O to a DMSO-d₆ solution of each ligand. The process was monitored by ¹H NMR (titrations). Starting with **AlaHA** (Figure 17), it quickly became evident that even 3 eq. of Ga³⁺ was not enough to fully coordinate the hydroxamic acid moieties, and as such, we added an additional 2 eq. of triethylamine (TEA), a bulky organic base which has been used to promote the complexation of hydroxamate ligands with Ga³⁺.⁹⁰ In our case, this seemed to completely deprotonate **AlaHA**, however, the addition also caused moderate broadening of most peaks, something which has been associated with the formation of several oligomeric aggregates.⁹¹ This was further

supported by the apparent gelation of a solution of **AlaHA** in the presence of excess Fe^{3+} (SI, 4.7.3). Despite this, the titration offers us significant clues regarding the fate of the hydroxamate ligand.

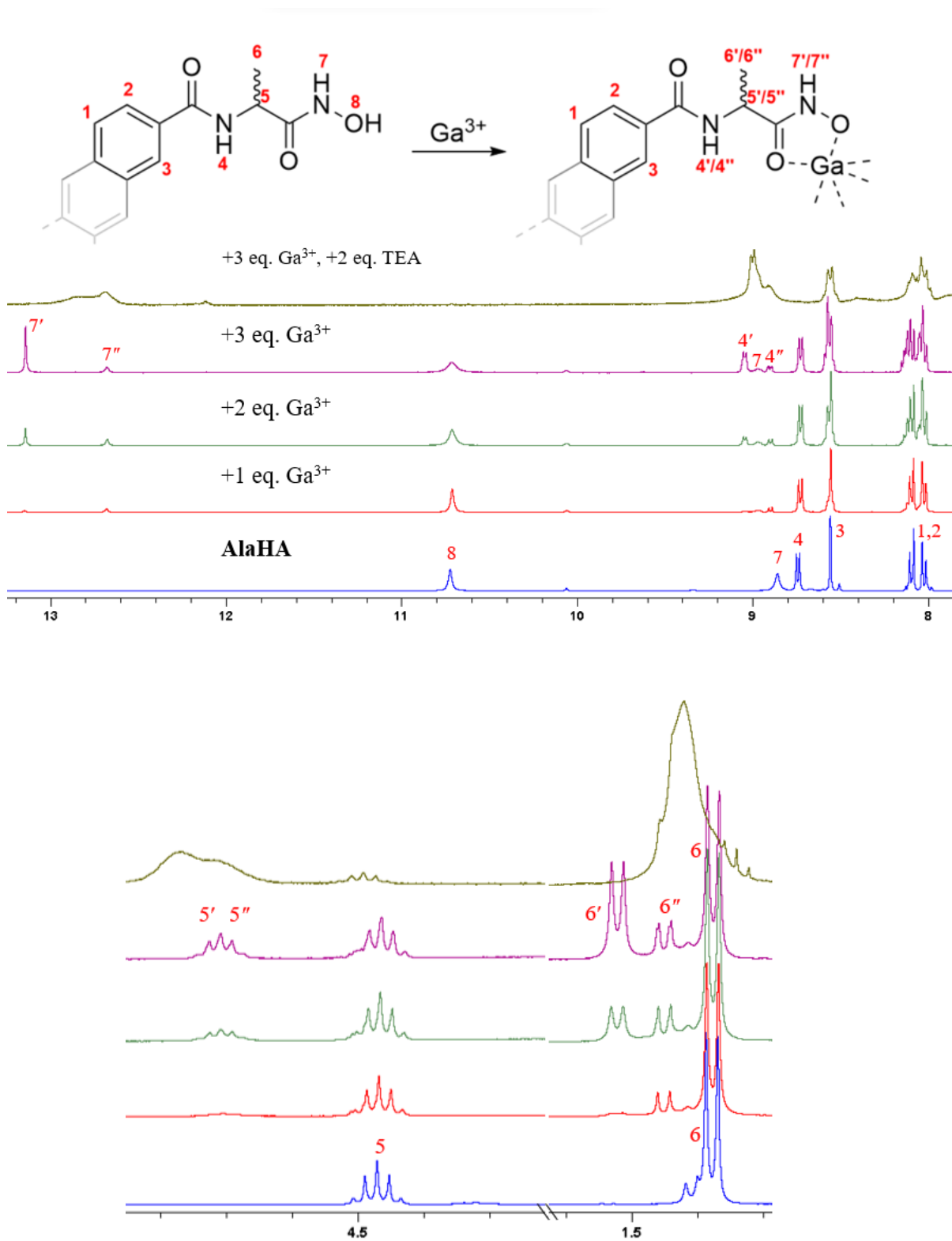


Figure 17. ^1H NMR titration of **AlaHA**.

The most striking difference between **AlaHA** and the addition of 3eq. of Ga^{3+} seems to be the appearance of two new sets of peaks, with the concomitant disappearance of the **AlaHA** peaks. Then, the same titrations experiment was also carried out using **ValHA** and **LeuHA**, however, the resulting spectra were particularly hard to interpret, as there was a lot of peak overlap after the Ga^{3+} addition was completed (SI, 4.7.4, 4.7.5). Fortunately, when **PheHA** was employed, the overlap was reduced (Figure 18).

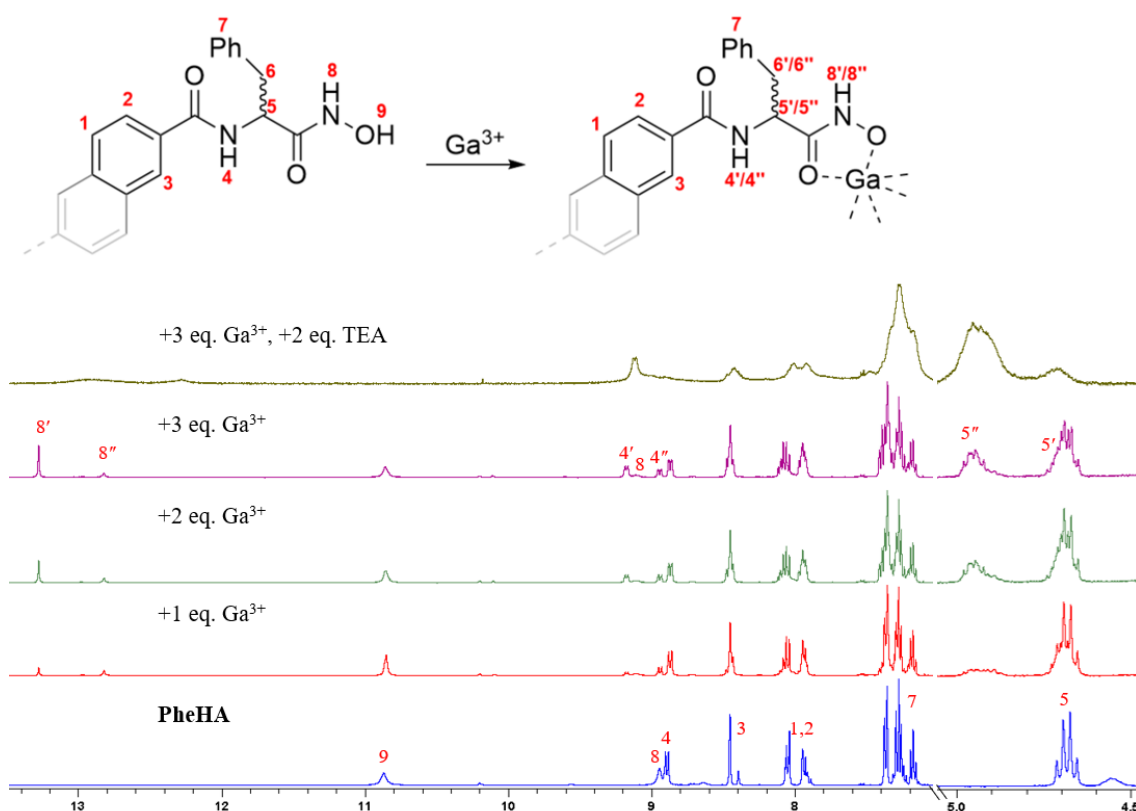


Figure 18. ^1H NMR titration of **PheHA**. Methylene protons 6 were omitted as they overlap with H_2O peak.

In accordance with the behaviour seen with **AlaHA**, it appears that after the metal is added two new distinct peaks appear downfield ($8'$ and $8''$). Their relationship to the hydroxamate proton 8 can be discerned by: i) Their morphology, as they appear as sharp singlets, ii) their simultaneous appearance as peak 8 is reduced in intensity and iii) by the fact that when D_2O drops are added in the solution after the titration, both $8'$ and $8''$ disappear, signifying their labile nature. Furthermore, the final addition of TEA helps us distinguish between peaks 8 and 9, as it is expected that only peak 9 (OH) would disappear upon addition of a base. The same behaviour was seen with the other substituents as well. We then decided to test whether the newly formed supramolecular

architectures were able to act as hosts for small organic compounds, as this would give us information about their geometry and potential cavity space (Figure 19). We decided to use imidazole (**Im**) as the potential guest, as it is small, polar, with neutral charge and a flat geometry, which should make it able to access even relatively small pores.

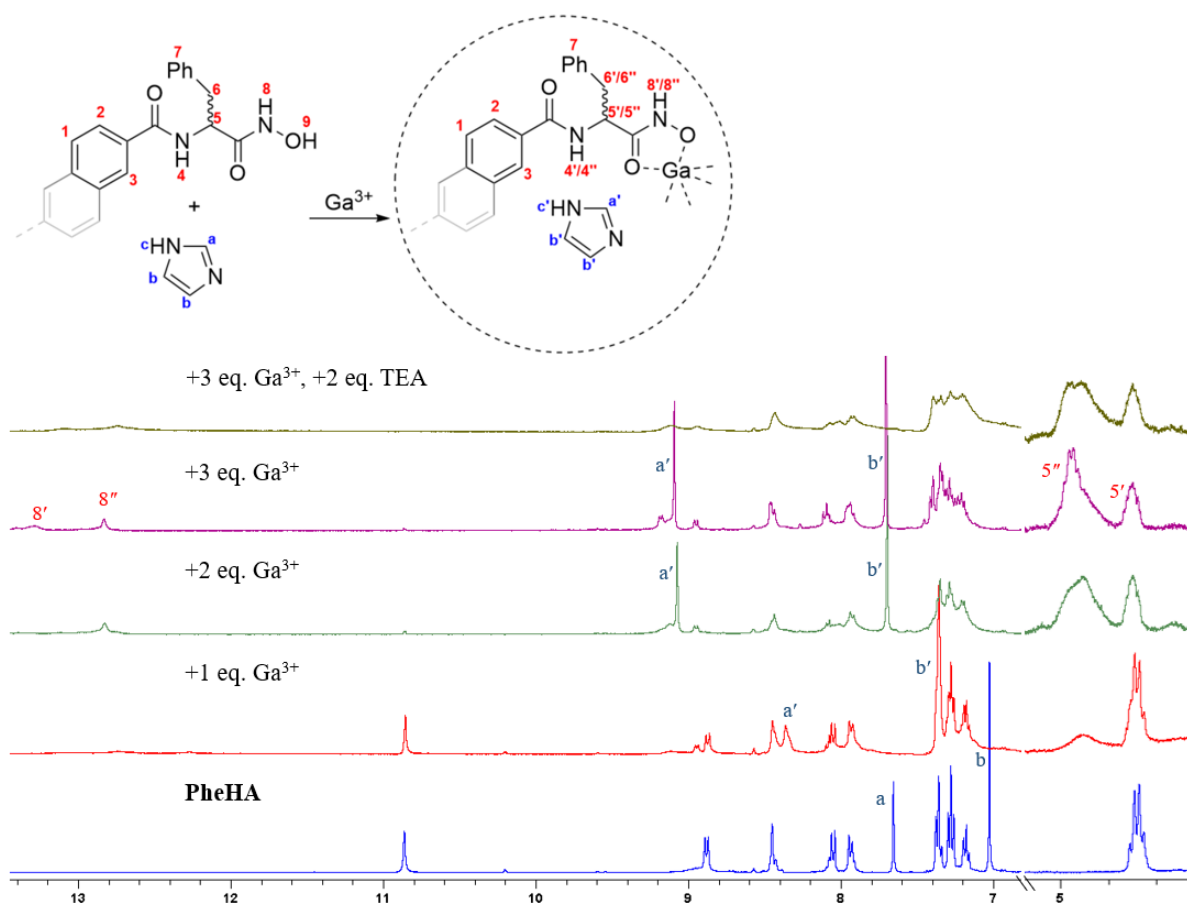


Figure 19. ^1H NMR titration showing an encapsulation attempt of **Im** within the tentative **PheHA-Ga** cage.

Upon adding 1.5 eq. of **Im** to a solution of **PheHA**, we observed a set of peaks (a and b), corresponding to free **Im**, although the amine proton was not observed (based on comparing its resonances when in solution on its own), possibly due to overlapping with **PheHA** protons. To our surprise, upon adding 1 eq. of Ga^{3+} peaks a and b immediately shifted downfield. After 2 eq. were added, the tentative encapsulation was complete, and further addition did not shift the peaks any further. Furthermore, not only was the assembly able to encapsulate 1.5 eq. of **Im**, but its presence altered the relative ratios of peaks 8' and 8''. By comparing Figure 18 and 19, it is evident that initially peak 8' was the major one compared to 8''. We can also see that analogous inversion in peak intensity occurred in peaks 5' and 5'' after **Im** encapsulation. This result is intriguing, as assuming

that the different peaks belong to separate chemical entities, it implies that **Im** acts as a template that promotes the formation one particular architecture. To gain further insights into the peaks involved, we obtained the DOSY spectra before, and after the addition of Ga^{3+} (Table 2).

Table 2. DOSY analysis of tentative host-guest assembly **Im**⊂**PheHA-Ga**

Compound	M _w (predicted)	D (x10 ⁻¹⁰ m ² /s)	Hydrodynamic Radius (Å)	M _w (lowest estimate) ^a
PheHA	540.58	1.28	8.30	904.4
Im	68.08 (Free)	4.90 (free)	3.39 (free)	61.6
		2.35 (Hosted)	5.41 (hosted)	
PheHA-Ga	1755.13 (Helicate)	0.77	12.34	2973.32
	3510.25 (Tetrahedron)	0.55	16.35	6916.47

^a Lowest end of estimate range was used since it was a best match for **Im**'s M_w. Confidence of prediction is 95%.

The estimations for the M_w values were made using a modified Stokes-Einstein equation (SEGWE method) which tends to perform better for smaller compounds.⁹⁰ As DOSY is meant to be used as a qualitative method, the accuracy of the method is not as important as the diffusion coefficient (D) for each compound. For instance, we notice that free **Im**, has a higher D value compared to the restricted environment of a cage, which is what we would expect to see in this situation. Moreover, it appears that there are two sets of signals with discrete D values when **PheHA-Ga** complex is measured. This suggests that at least two different architectures are forming, one of which is about twice as heavy as the other.

By careful observation, we also noticed that it was possible to assign the proton peaks 5' and 5'' to two different diffusion bands, the latter belonging to the heavier architecture (Figure 20). Although further evidence is needed to definitively prove this hypothesis, with the data that we have in hand so far it seems that we have uncovered a relatively rare example of template-induced interconversion of one supramolecular architecture to another. The first example of this effect was described in 1999 by Raymond *et al.*, where they showed how a charged guest (Me_4N^+) can induce the conversion of a triple helicate to a tetrahedral complex.⁹² Interestingly, their ligand was based on a 2,6-anthracene spacer, which is structurally similar to our 2,6-naphthalene spacers. Moving away from

NMR spectroscopy, we were also interested to obtain the MS spectra of these cages, as this would help us determine the topology of the architectures, as demonstrated in section

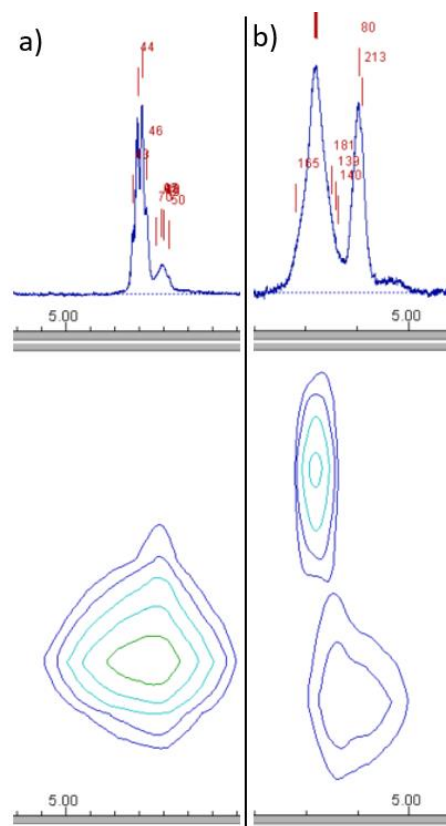


Figure 20. DOSY NMR comparison of a) **PheHA** and b) **PheHA-Ga** CH peaks. Note that the y axis (D) is at a different scale for a) and b).

4.4.1.2. Unfortunately, in this case, we were not able to achieve this goal as we quickly discovered that these complexes can only be dissolved in very polar solvents such as DMSO, DMF, or NMP, however technical limitations with the MS instrumentation that was available to us meant that these solvents could not be used at this time. Finally, the low solubility of our compounds also prevented us from being able to grow SC-XRD quality crystals, even after several months of attempts. This is quite limiting when it comes to characterising these assemblies (architecture and chirality), as the vast majority of groups working on such systems usually rely on crystallography to provide proof for their hypotheses,¹⁰ and as such, the techniques that we were able to use (namely NMR), usually have a complementary role to the evidence.

4.5 Conclusions

We have developed two sets of dihydroxamic acid containing ligands that were used to form a series of metallosupramolecular assemblies. For the smaller, terephthaloyl- containing ligands, we were able to demonstrate that they form M_2L_3 type topologies, instead of the desired tetrahedral (M_4L_6) one. The larger, naphthaloyl-containing ligands were more challenging to work with in many aspects; firstly, their synthesis proved to be relatively demanding, especially for the derivative **PheHA**, which could only be obtained reliably by using a solid-free, mechanochemical protocol. Secondly, these ligands appeared to consist of stereoisomeric mixtures, which made their characterisation problematic. Thirdly, the low solubility of the ligands and corresponding clusters prevented us from obtaining MS data. Finally, due to a combination of low solubility, neutral charge, and poor solid-state packing, we were unable to grow any suitable crystals for SC-XRD analysis. Despite these setbacks, we have shown that assemblies do indeed form with these types of ligands, and we have made substantial progress towards understanding their topologies, and it appears their architecture may be tuneable by host-guest interactions.

4.6 Future Work

4.6.1 Work Involving 2,6-Naphthalene-Based Ligands

As mentioned, it is necessary to obtain MS spectra of the ligands and clusters, to help us determine their topology. For this reason, effort should be made toward finding an analytical technique which is compatible with the solvent systems that we have developed. Moreover, computational modelling of these systems using DFT, and related methods should provide us with very useful insights, especially with regards to predicting the total number and stereoisomeric distribution of our assemblies.⁹³ For example, in an M_2L_3 assembly with two octahedral metal centres and three ligands, each of which contains two stereogenic centres (yielding three stereoisomeric combinations, (R,R), (S,S) and meso- (R,S), we would expect to have a maximum $2^8 = 256$ possible

stereoisomers, although assuming that the two metal centres are homochiral ($\Delta\Delta/\Lambda\Lambda$), which can be favoured,⁹⁴ that number would be 64. Even worse, in the case of a M_4L_6 tetrahedral cage with octahedral geometry we would expect to see $2^{16} = 65,536$ stereoisomers or 8,192 if the metals had adopted the most common⁹⁵ homochiral T symmetry ($\Delta\Delta\Delta\Delta/\Lambda\Lambda\Lambda\Lambda$).

As part of our long-term aim for this project to develop cages with large enough cavities to be used in areas such as photocatalysis, future work should involve measuring their photophysical properties, including UV-Vis. absorption, emission, photoluminescence quantum yield (PLQY) and excited state lifetime. This data can then be used to make informed decisions about the suitability of the assemblies to be used as photocatalysts or participate in photoredox reactions.

Using cages (or nanocontainers) to enhance photochemical processes is an active area of research, and there are many reported examples where their cavity was used to enhance the photocatalytic performance of known chromophores. Examples of this include using the confined environment to extend their excited state,⁹⁶ promoting photocatalytic H_2 generation,⁹⁷ improving the efficacy of (photodynamic therapy) PDT agents,⁹⁸ promoting photo-switching of alkenes,⁹⁹ and protecting light-sensitive compounds from irradiation.¹⁰⁰

This last potential application inspired us to test whether or not our complexes could be used to encapsulate a 1,2,6-thiadiazine compound and prevent it from producing the ring contracted 1,2,5-thiadiazole 1-oxide product by using the internal cavity of the cage to protect it from light and/or coming into contact with O_2 . In a preliminary experiment (Figure 21), we used 3,5-dimethoxy-4H-1,2,6-thiadiazin-4-one, primarily for its small size, to maximise the probability of encapsulation. We used 1 eq. of **PheHA** in a $DMSO-d_6$ solution, along with 3 eq. of Ga^{3+} and 1 eq. of thiadiazine. The encapsulation was tested by how the thiadiazine resonances behaved when the Ga^{3+} was added. If it had occurred, then we would expect to see a noticeable downfield shift, in the same manner we did when **Im** was used. Unfortunately, no such shift was detected, even after addition of 2eq. of TEA, to ensure that all the **PheHA** was coordinated. This might suggest that an even larger spacer might be needed in the future, to further enlarge the pore size of the cavity.

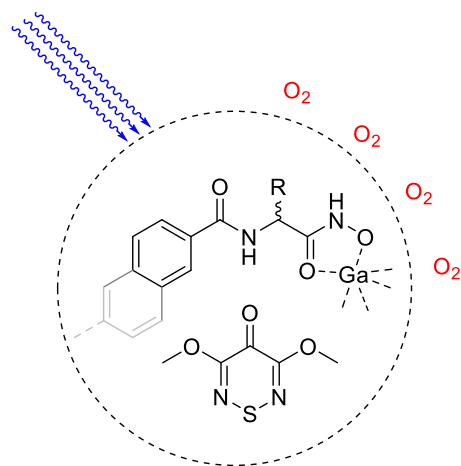


Figure 21. Illustration of how the cavity of our cage could in principle shield a 1,2,6-thiadiazine from external light and O₂.

Another promising application for these cages could be their use as AIEgens. As we have discussed in detail in chapter 2, AIEgens are versatile materials with many applications. Recently, it was demonstrated that self-assembly of metallocages can be used to enable AIE in compounds that would otherwise not be emissive when aggregated.¹⁰¹ It was shown that this works because as the cage forms, the ligand is rigidified, which substantially lowers radiative relaxation pathways and allows them to fluoresce. Theoretical calculations also showed that this was not due to the coordinating metals ability to participate in the excited state of the ligands, thus proving that this is caused by the linkage-induced stabilisation of the ligand.

Inspired by this work, we wanted to assess whether this technique could also be exploited with our assemblies. For this reason, we prepared a series of solutions containing different fractions of water in DMSO (f_w). In one series we added **AlaHA** (10 mg, 0.03 mmol) on its own, and in the second the same amount of **AlaHA**, along with 3 eq. of Ga³⁺. Each series consisted of three f_w (0, 0.5, and 0.9) values. To our surprise, the $f_w=0.9$ fraction containing the **AlaHA-Ga** complex showed strong blue fluorescence, when irradiated with long UV light (Figure 22). Moreover, when the same experiment was conducted by using **PheHA** as the ligand, the $f_w=0.9$ fraction did not fluoresce, even though aggregation had occurred. This may be explained by the presence of the Ph groups in **PheHA-Ga** which might suppress the fluorescence by π - π stacking deactivation. Unfortunately, it was not possible to acquire the relevant absorption and emission spectra of these experiments at the time and the experiments were only conducted on a qualitative basis. Thus, it can be concluded that this phenomenon might be attributable to linkage-

induced enhancement of fluorescence, as described above, however it cannot be used as a proof of metallocage formation. Another mechanism that could explain this behaviour was described by Lei *et al.*, as they developed a selective and sensitive Ga^{3+} ‘turn-on’ fluorescent probe, consisting of a simple naphthalene-L-serine containing Schiff base.¹⁰¹ It was established that when the Ga^{3+} coordinates with the compound, photo-induced electron transfer (PET), and excited-state intramolecular proton transfer (ESIPT)

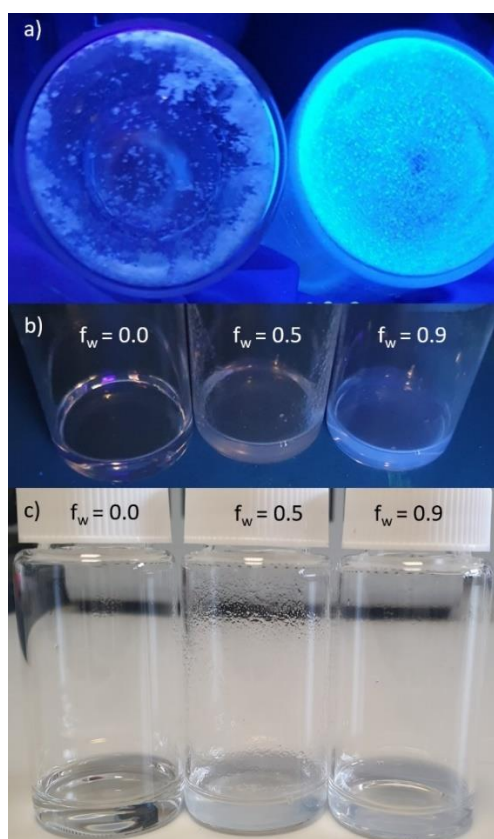
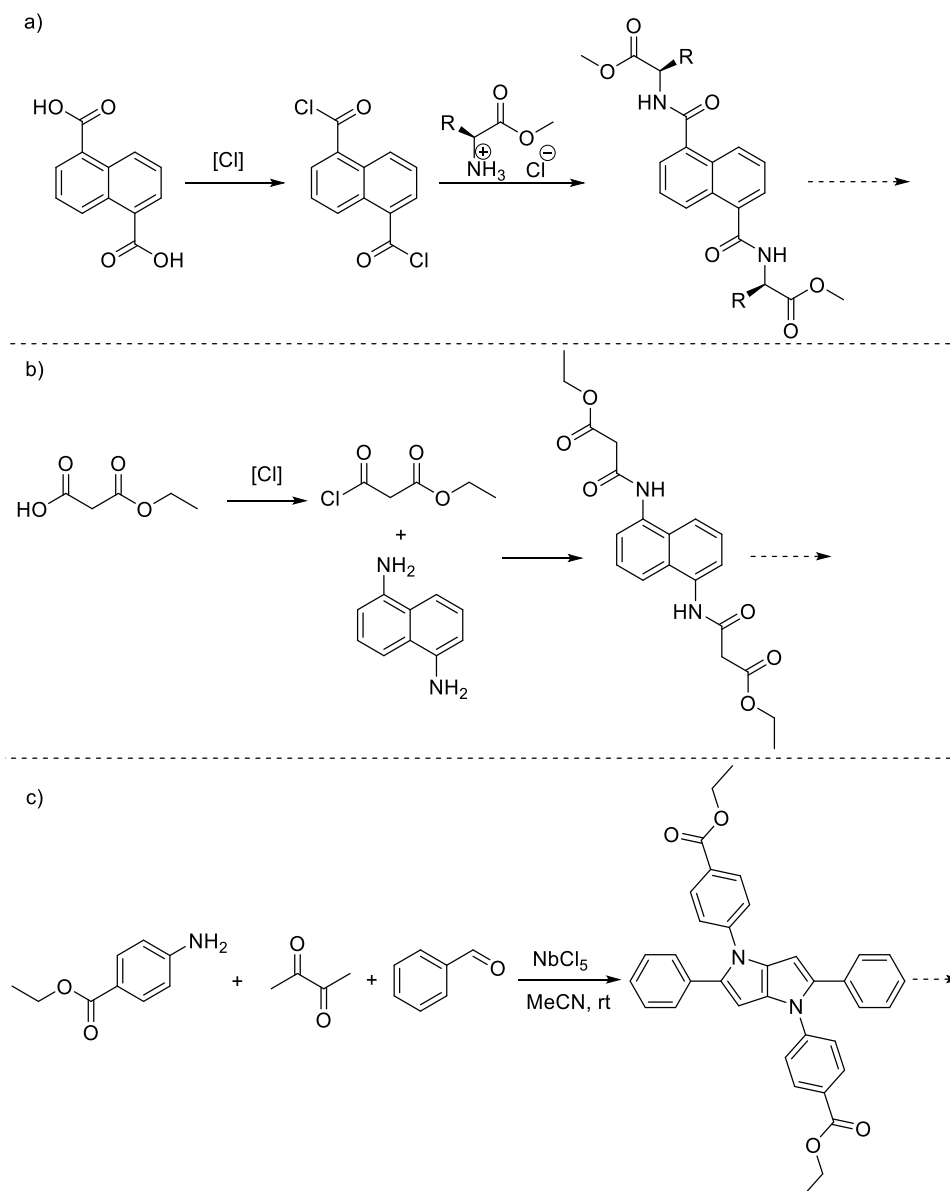


Figure 22. Photographs of a) **AlaHA** (left) and **AlaHA-Ga** (right) in the solid form, b) fractions of **AlaHA-Ga** complex under long UV irradiation, and c) fractions of **AlaHA-Ga** under visible light.

(caused by tautomerism) processes, are suppressed allowing radiative relaxation pathways to emerge. As such, even though these results are promising, additional work is required to acquire qualitative results and understand the mechanism that enables the fluorescence.

4.6.2 Work Involving Ligands with Other Spacer Units

Besides the 2,6-naphthalene backbone, the 1,5- regioisomer could also prove to be a good alternative spacer for dihydroxamic acid linkers (Scheme 3a), as it has been the main backbone adopted by the Raymond research group, and its use helped pioneer this area of metallosupramolecular cages.¹⁰



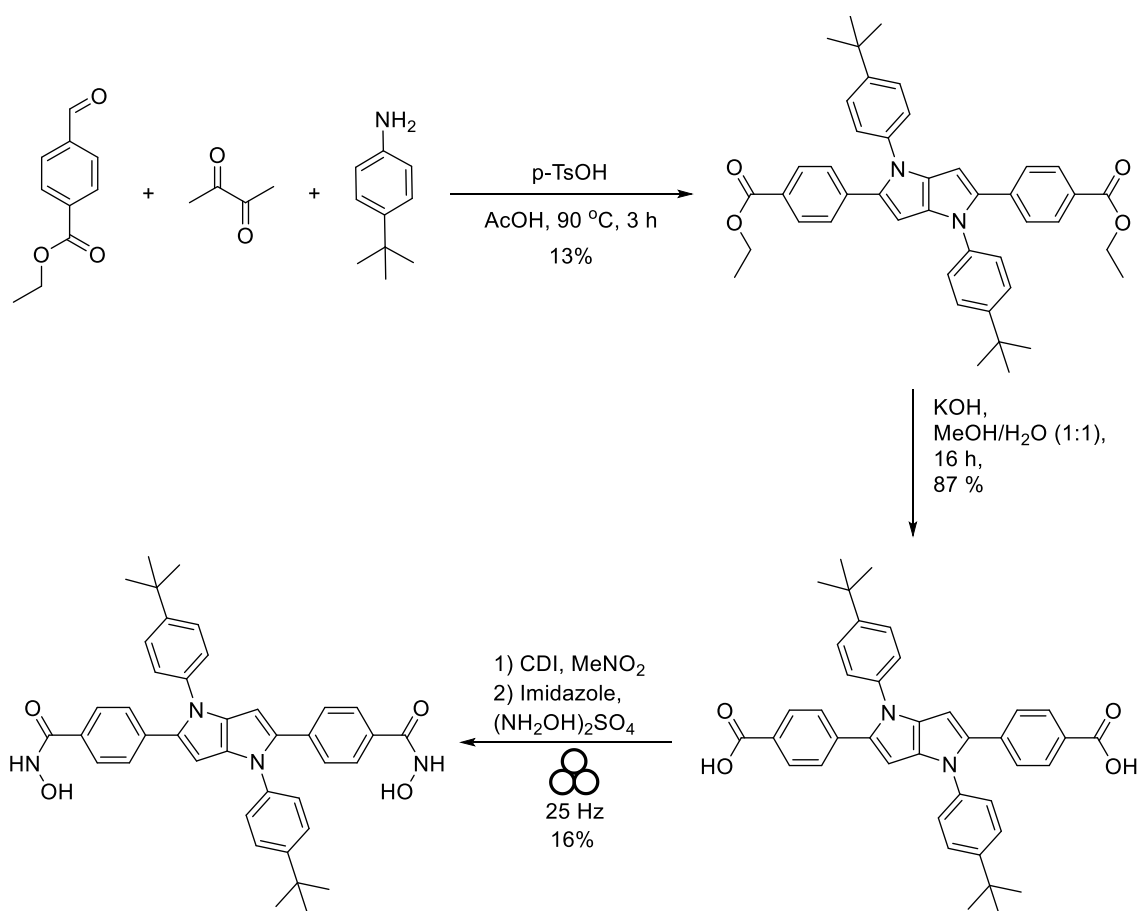
Scheme 3. Alternative synthetic routes for cluster scaffolds that are currently in development.

In addition, instead of amino acids other groups can be installed on these backbones that may be of interest. For instance, we attempted using monomethylmalonic chloride coupled with naphthalene-1,5-diamine to produce an alternative, more flexible ligand

(Scheme 3b), however during the conversion of monomethylmalonic acid SM to the corresponding chloride, the reaction failed to yield a product, and instead, a viscous dark oily tar was formed, that appeared to be a mixture of decomposed products (based on multiple TLC spots). Several chlorinating agents were employed such as oxalyl chloride, thionyl chloride and phosphorus pentachloride, but none of them afforded the desired product. Despite these setbacks, efforts to circumvent this issue are underway. Finally, a third scaffold was also made, which utilises hexaaryl-1,4-dihydropyrrolo[3,2-b]pyrroles as linkers for the cages (Scheme 3c).

Those scaffolds have quite rigid structure, and in principle should be able to form cages with a single topology. Furthermore, due to the X shape of their structure, they tend to adopt propeller-like geometries in the solid-state and have been used as potent AIEgens.^{102,103} In addition, they are known for their interesting optical properties, which give rise to intense colours and fluorescence, leading to their use as fluorescent dyes.¹⁰⁴ Since they have a similar size to the naphthalene scaffolds we have used, we believe that the dihydroxamic acid analogue of these compounds could be a viable way to generate photoactive metallocages, enabling them to act as potent photocatalysts.¹⁰⁵

There are two main methods for synthesising these compounds,^{104,106} and both of them involve use of a three-component, one-pot approach, where an aniline, benzaldehyde and diketone (diacetyl) react in the presence of an acid catalyst to yield the final product, although the exact mechanism of the reaction is still not understood. We started exploring this chemistry by synthesising a diethyl ester intermediate, as seen in Scheme 4. The SMs reacted together in acetic acid at around 90-100 °C with the addition of *p*-toluenesulfonic acid catalyst.



Scheme 4. Synthesis of a hexaaryl-1,4-dihydropyrrolo[3,2-b]pyrrole dihydroxamic acid intermediate.

Subsequently, the ester was hydrolysed to form the dicarboxylic acid, which was insoluble in common organic solvents, making it very hard to convert to the dihydroxamic acid target using conventional batch methods. As such, we decided to utilise the mechanochemical protocol that was described earlier to form compound **PheHA**.

Although this reaction seemed to work, the product was found to be contaminated with iron that tentatively leached from the ball mill cup during the milling process. The presence of iron was confirmed by NMR, since the paramagnetic iron (III) that was bound to the siderophoric dihydroxamic acid moiety reduced the relaxation times and thus, made the peaks appear broader^{74,107} (Figure 23a), however after filtering through celite, most of it was removed, judging by the change in the ¹H NMR spectrum (Figure 23b). Unfortunately, due to the low solubility in DMSO-d₆, a satisfactory ¹³C NMR spectrum could not be acquired.

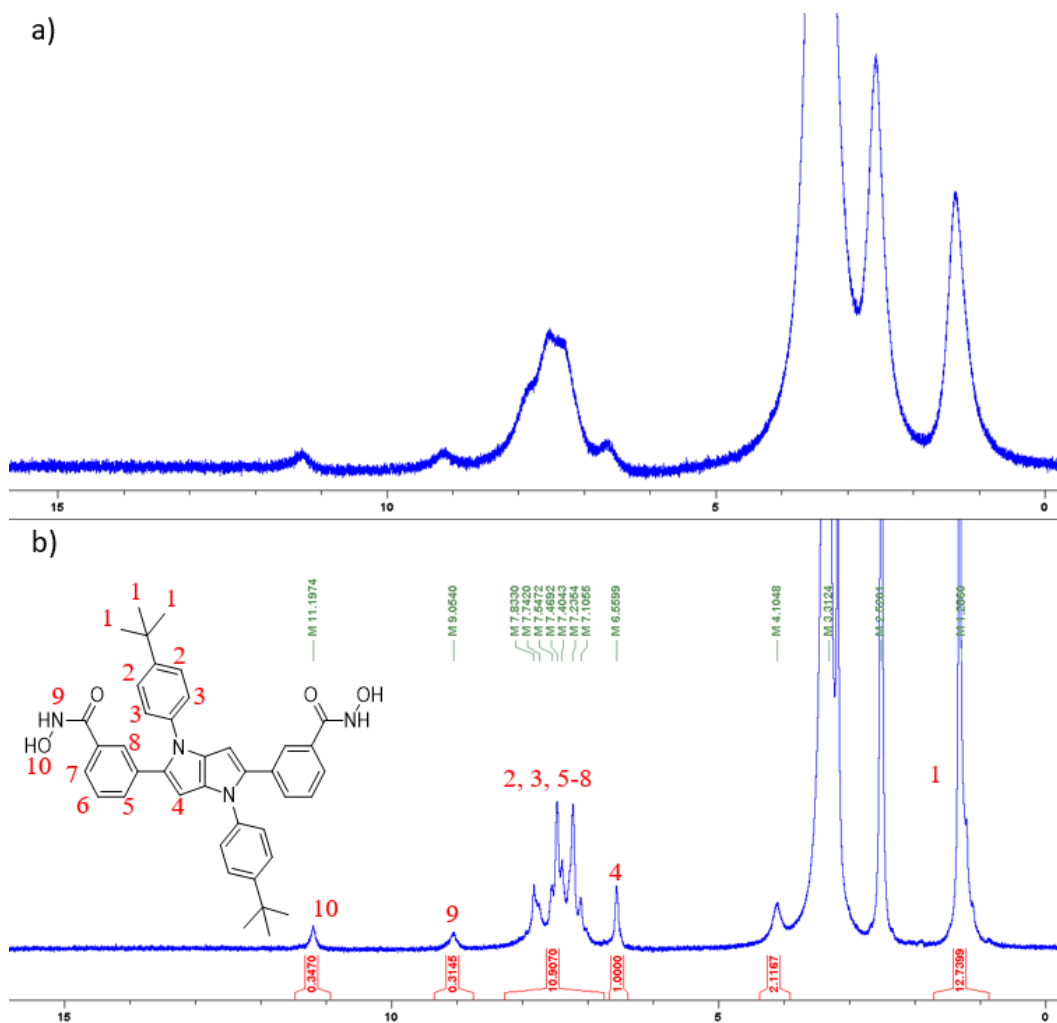
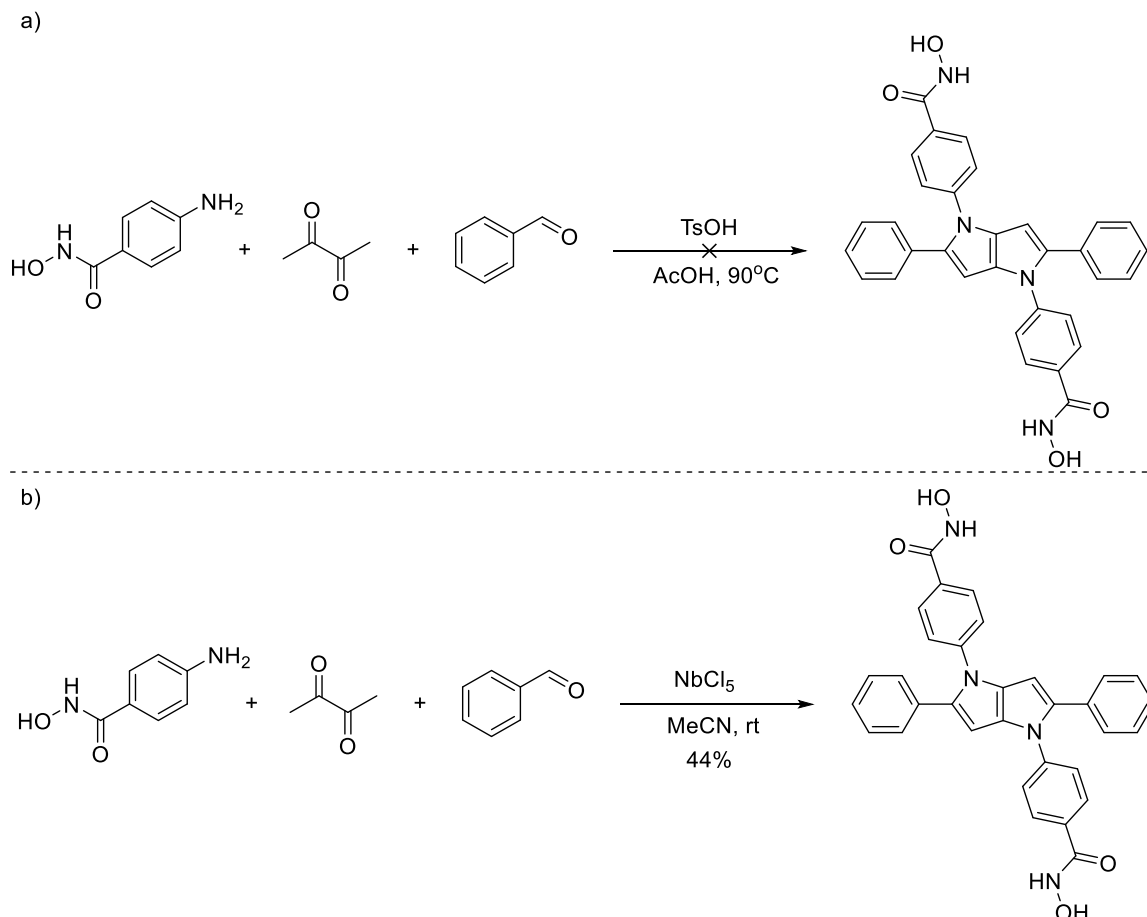


Figure 23. a) Broadening of the NMR peaks due to the presence of paramagnetic iron. b) Filtering with celite removes most of the iron, revealing the target dihydroxamic acid, as evidenced by the characteristic singlet NH and OH peaks at ~9 and 11 ppm respectively.

Finally, we also investigated the use of an aniline SM that bears a hydroxamic acid moiety at the *para* position, to construct the target molecule in one step, allowing us to circumvent the synthesis of the diester and dicarboxylic acid intermediates. However, for this to work, we had to use more benign conditions, as the hydroxamic acid moiety did not survive the conditions used previously (AcOH, 90 °C) (Scheme 5a).

For this reason, we decided to exploit the second synthetic method available,¹⁰⁶ which uses a niobium (V) source, acting as a Lewis acid catalyst that was found to be very effective for this type of transformation. Furthermore, this methodology uses acetonitrile as solvent instead of acetic acid, and the reaction takes place at room temperature. By employing those conditions, we postulated that the hydroxamic acid could survive and successfully produce the target compound (Scheme 5b).



Scheme 5. a) Using the first method led to decomposition of the aniline SM and we could not detect any product. b) By using a set of more benign conditions, the reaction proceeded to afford the target compound.

Interestingly, it appeared that the reaction worked, and we managed to form the product in a modest yield (44%). Unfortunately, its ^1H NMR spectrum revealed that it contains several impurities, and due to its low solubility in most solvents except DMSO and DMF, it has thus far not been possible to purify it (Figure 24).

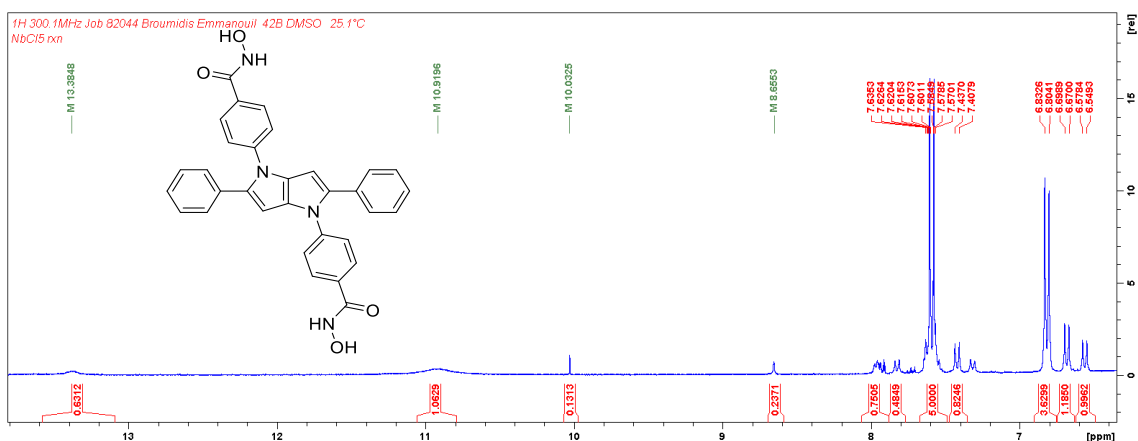


Figure 24. ^1H NMR spectrum of the impure dihydroxamic acid.

The main purification method that was tested was recrystallisation from DMSO, but this did not improve the purity of the compound, as the impurities crashed out along with the desired compound. Currently, we are exploring possible solutions to this issue, which include optimising the original reaction, employing mechanochemical methods, or finding more suitable recrystallisation systems.

In the following and final chapter, we will first attempt to develop a mechanochemical protocol for the *N*-protection of the HA ligands presented here. However, as it will become evident, our efforts eventually led to the development of a novel solvent-free pathway which allowed us to access a series of *N*-arylbenzamides from *O*-protected hydroxamic acids. Furthermore, we will show how 3D printing was utilised for scaling up our reactions.

4.7 Supporting Information

4.7.1 D₂O Effect on AlaHA, ValHA, LeuHA and PheHA ¹H NMR Spectra

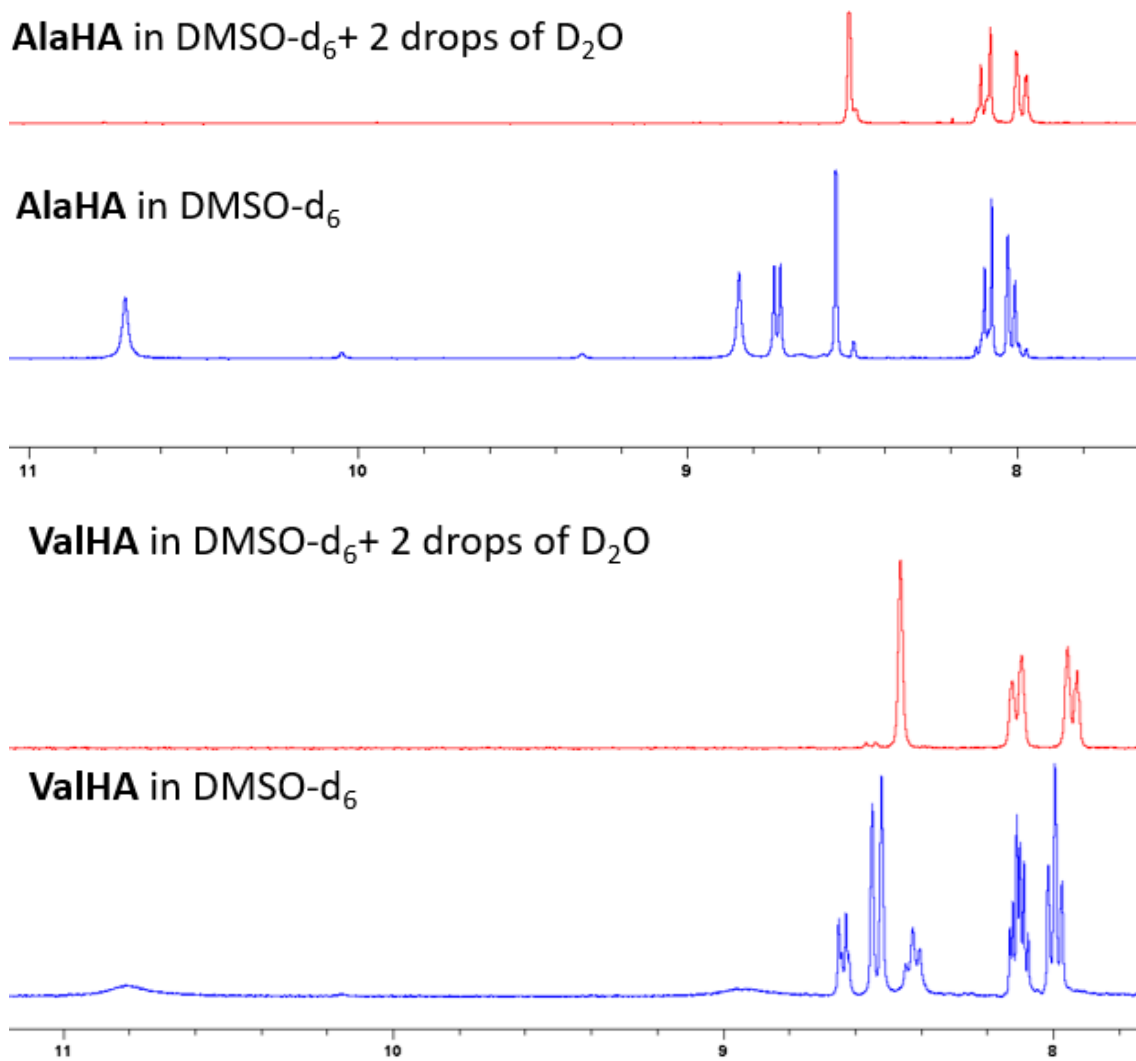


Figure S1. ¹H NMR Spectra of **AlaHA** and **ValHA**, showing vanishing of labile proton signals upon addition of D₂O. Total volume 0.6 mL.

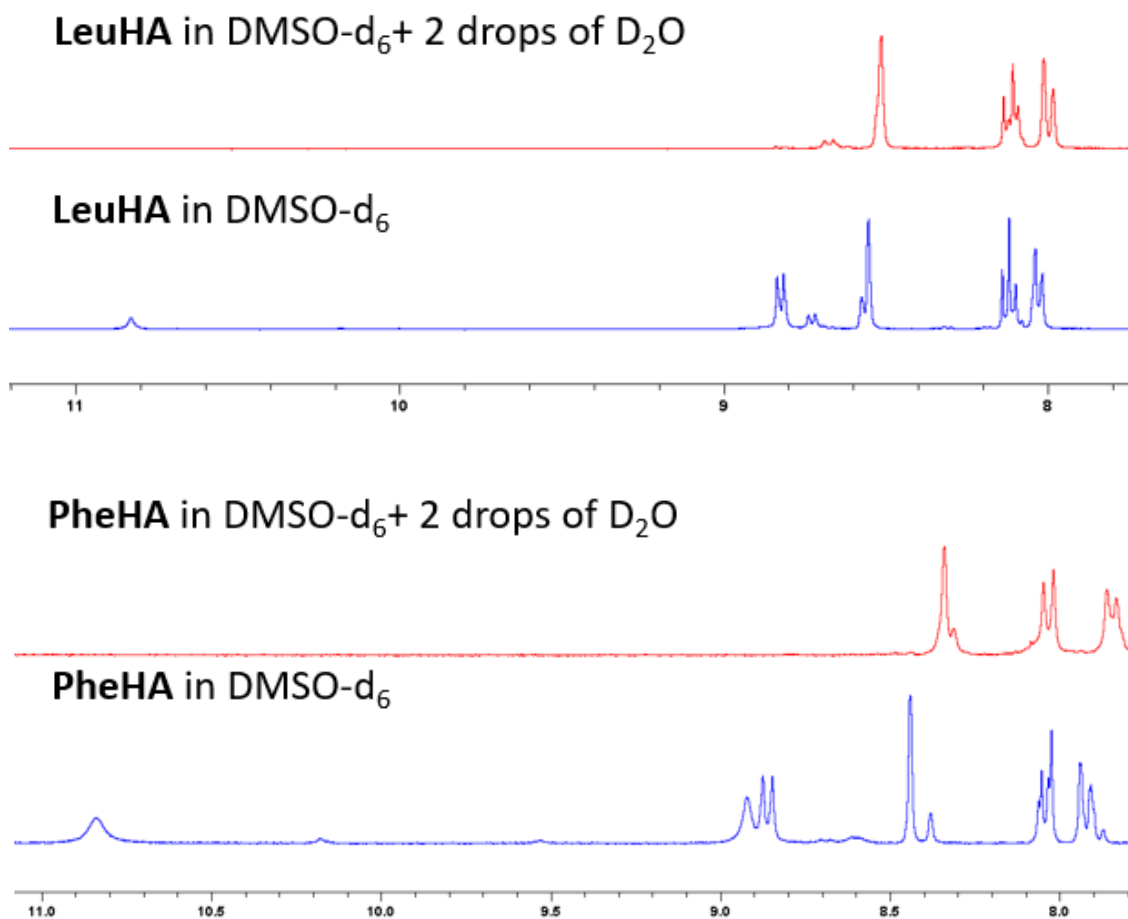


Figure S2. ¹H NMR spectra of **LeuHA** and **PheHA**, showing vanishing of labile proton signals upon addition of D₂O. Total volume 0.6 mL.

4.7.2 D₂O Effect on AlaHA-Ga Complex

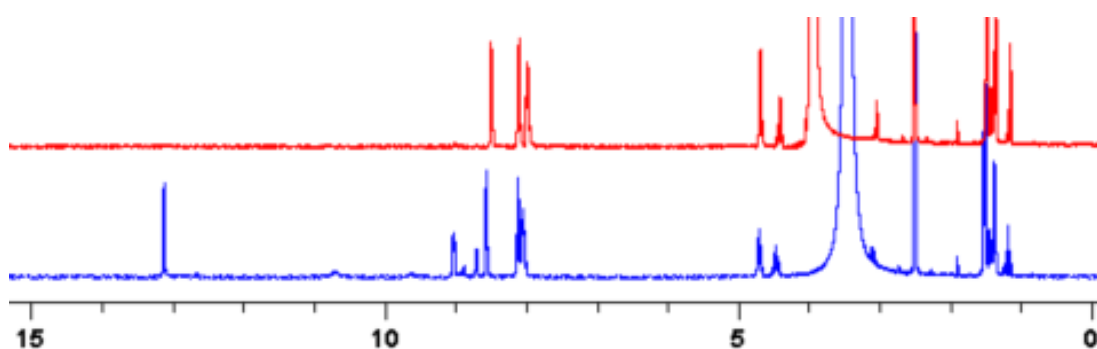


Figure S3. ¹H NMR spectra comparison between **AlaHA-Ga** dissolved in DMSO-d₆ (lower) and the same solution after adding two drops of D₂O (upper). It is clear that the peak at ~13 ppm which appears after **AlaHA** is coordinated to Ga³⁺ belongs to an easily exchangeable proton. Total volume 0.6 mL

4.7.3 Gel Formation After TEA addition to AlaHA-Fe Complex



Figure S4. A gel was formed after 2eq. of TEA were added in a solution containing **AlaHA** and 3eq. of Fe^{3+} dissolved in $\sim 1\text{mL}$ of DMSO. Similar behaviour was observed in Ga^{3+} complexes after TEA addition, forming clear gels. In general, it was observed that gelation was generally more pronounced the more TEA was added.

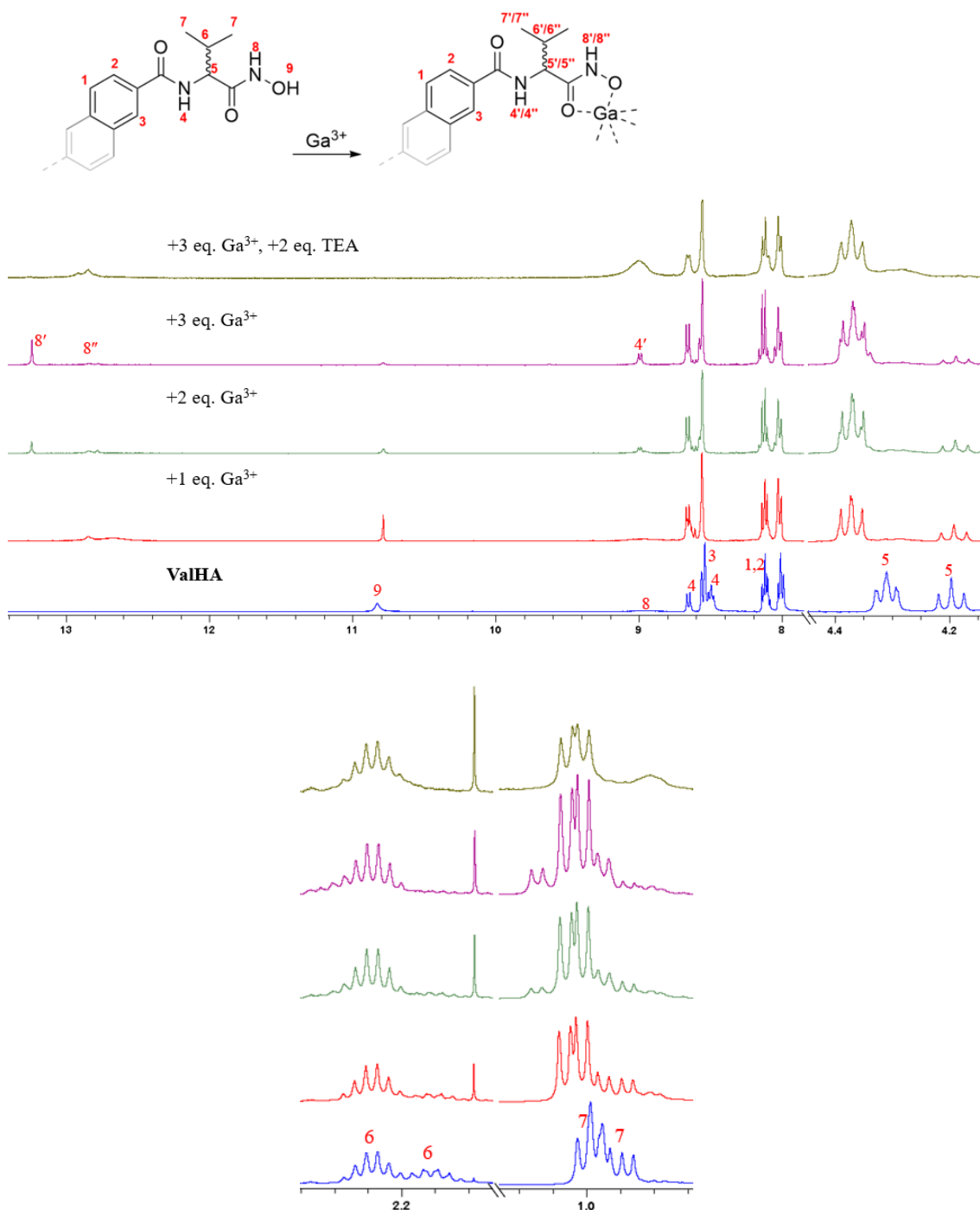
4.7.4 ^1H NMR Titration Experiment Using ValHA

Figure S5. ^1H NMR titration using **ValHA** as ligand. Even after adding 3 eq. of Ga^{3+} it appears that the coordination process was not completed, as evidenced by the presence of peak 9. Only after 2 eq. of TEA were added all of **ValHA** was consumed. Proton assignment on the resulting spectra was challenging, due to overlap of various signals, and ambiguity regarding their origin. The two separate peaks from proton 5 in the **ValHA** spectrum are ascribed to the diastereomeric pair (S,S)/meso-(S,R).

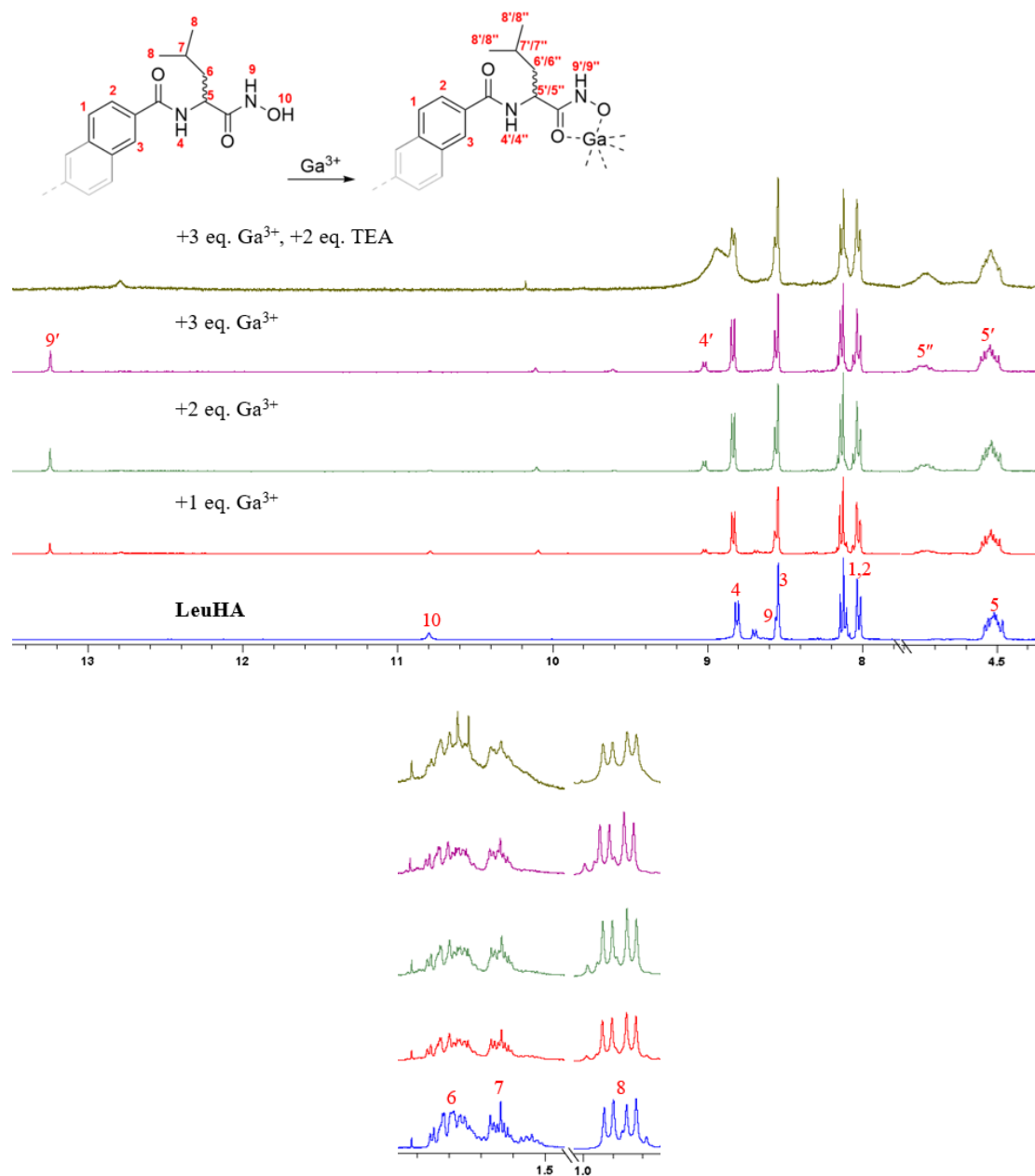
4.7.5 ^1H NMR Titration Experiment Using LeuHA

Figure S6. ^1H NMR titration using **LeuHA** as ligand. As seen previously, after adding 3 eq. of Ga^{3+} it appears that the coordination process was not completed, as evidenced by the presence of peak 10. Only after 2 eq. of TEA were added all of **LeuHA** was consumed. Proton assignment on the resulting spectra was challenging, due to overlap of various signals, and ambiguity regarding their origin. In contrast with the other SMs, it seems that **LeuHA** only forms one supramolecular construct when Ga^{3+} is added, based on the appearance of only one peak past 12 ppm (peak 9'). It is not yet clear why this difference exists, although it has been shown before that different ligand substitution can lead to complexes of different topology.¹⁰⁸

4.7.6 DOSY Spectra of PheHA and PheHA-Ga Complexes

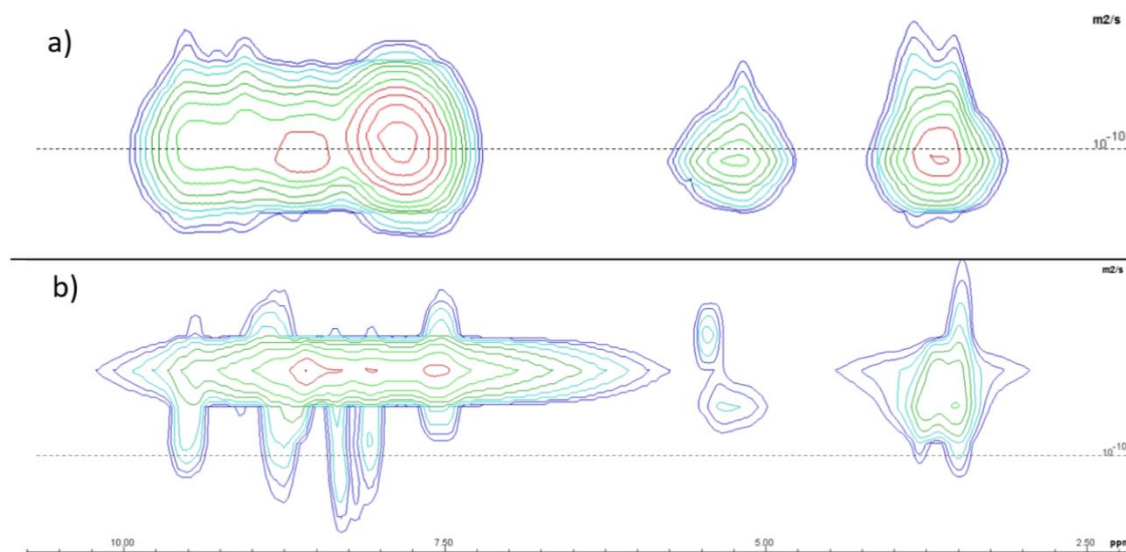


Figure S7. Comparison between a) DOSY spectrum of **PheHA** on its own, and b) DOSY spectrum of **PheHA** after adding 3eq. of Ga^{3+} . Dashed line is centred on $1.00 \times 10^{-10} \text{ m}^2/\text{s}$. The y axis is on a logarithmic scale. The x axis ranges from 2.2 to 10.9 ppm. It is quite evident that when the metal is added, the diffusion coefficient shifts to lower values, signifying the presence of a different molecular species with a larger hydrodynamic radius and molecular weight. It can also be seen that in graph b) there are two bands present, although due to the broadness of the signals it is hard to discern the exact diffusion coefficient for each signal band. In general, the signals are of low quality, and should only be used to make qualitative comparisons.

4.8 Experimental Section

4.8.1 General Methods and Materials

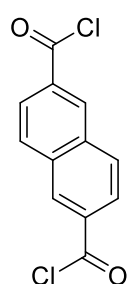
General Methods and Materials

All chemicals were commercially available except those whose synthesis is herein described. Anhydrous MgSO_4 was used for drying organic extracts and all volatiles were removed under reduced pressure. All reaction mixtures and column eluents were monitored by TLC using commercial aluminium backed thin layer chromatography (TLC) plates (Merck Kieselgel 60 F₂₅₄). The plates were observed under UV light at 254 and 365 nm. The technique of flash chromatography was used throughout for all non-TLC scale chromatographic separations using Merck Silica Gel 60 (less than 0.063 mm).

Melting points were determined using a Stuart SMP10 digital melting point apparatus. Small scale (μL) liquid handling measurements were made using variable volume (1.00–100.00 μL) single channel Gilson PIPETMAN precision micropipettes. Solvents used for recrystallisation are indicated after the melting point. IR spectra were recorded on a Thermo Scientific Nicolet iS5 FTIR spectrometer with iD5 ATR accessory and broad, strong, medium and weak peaks are represented by b, s, m and w, respectively. ^1H and ^{13}C NMR spectra were recorded on a Bruker AVANCE III HD machine (at 400 and 100 MHz, respectively). An AVANCE III 300 MHz NMR Spectrometer was also used for reaction monitoring. Chemical shifts (δ) are expressed in ppm and coupling constants J are given in Hz. Data are represented as follows: chemical shift, multiplicity (s = singlet, d = doublet, t = triplet, q = quartet, p = quintet/pentet, sp = septet, oc = octet, m = multiplet and/or multiple resonances, br s = broad singlet). Deuterated solvents were used for homonuclear lock and the signals are referenced to the deuterated solvent peaks. For the acquisition of mass spectra the samples were prepared as detailed below and analysed by positive ion nanoelectrospray (nES) using a Thermo Scientific™ LTQ Orbitrap XL™ ETD Hybrid Ion Trap-Orbitrap Mass Spectrometer. Low resolution mass spectra were acquired using a Shimadzu LC-2040C 3D Plus instrument equipped with an Atmospheric Solids Analysis Probe (ASAP). For the mechanochemical synthesis of HAs, a Retsch MM400 mixer mill was used, along with two stainless steel jars with each having 10 mL of internal volume. Additionally, two steel balls with a diameter of 8 mm were used in each jar.

4.8.2 Preparation of New Compounds

Preparation of naphthalene-2,6-dicarbonyl dichloride (**NaphCl**)

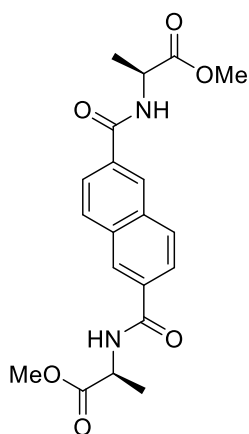


To a stirred solution of thionyl chloride (SOCl_2) (25 mL) was added 2,6-naphthalenedicarboxylic acid (1.73 g, 8 mmol) along with a catalytic amount of DMF (five drops). The reaction mixture was then refluxed at 90 °C for 12 h. The resultant light-green solution was then allowed to cool to room temperature and n-hexane (100 mL) was added, which caused the formation of an off-yellow precipitate. The precipitate was then isolated by simple

filtration, washed with n-hexane (3x20 mL), and dried under reduced pressure, to give

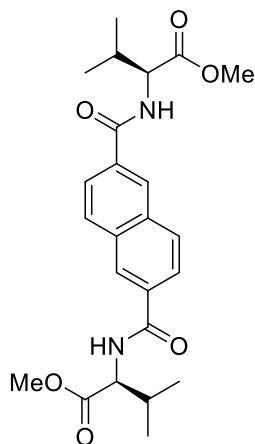
the title compound **NaphCl** as off-yellow plates (1.86g, 92%). mp (hot-stage) 187-190 °C (CHCl₃) [literature value: 188-189 °C (THF/n-hexane)¹⁰⁹]; $\nu_{\max}/\text{cm}^{-1}$ 3089w (aryl C-H), 1739s (C=O), 1596s, 1491w, 1383m, 1336s, 1277m, 1211s, 1162s, 1121s, 975w, 939s, 936s, 798s, 707s; δ_{H} (400 MHz, CDCl₃) 8.79 (2H, d, *J* 2.0, Ar *H*), 8.19 (2H, dd, *J* 8.8, 2.0, Ar *H*), 8.13 (2H, d, *J* 8.8, Ar *H*); δ_{C} (100 MHz, CDCl₃) 168.2, 135.4, 133.8, 133.8, 131.0, 126.9; identical to literature data.¹⁰⁹

Preparation of dimethyl 2,2'-((naphthalene-2,6-dicarbonyl)bis(azanediyl))(2*S*,2'*S*)-dipropionate (**AlaEst**)



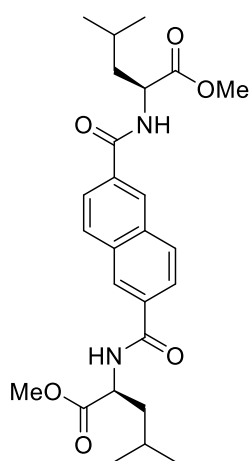
Typical procedure A: To a stirred solution of pyridine (25 mL) naphthalene-2,6-dicarbonyl dichloride (**NaphCl**) (1.86g, 7.34mmol), and L-alanine methyl ester hydrochloride (2.07 g, 14.8 mmol, 2.02 eq.) was added and left to stir at room temperature for 15 hours. Water (30 mL) was then added to the solution and the resulting precipitate was filtered, washed with water (3 x 15 mL) and dried in the oven overnight to afford the title compound **AlaEst** as a white powder (2.04 g, 72%) mp (hot-stage) 216-217 °C; $\nu_{\max}/\text{cm}^{-1}$ 3314br (N-H), 3060w (aryl C-H), 2935w (alkyl C-H), 1742s (C=O), 1631s (C=O), 1599m, 1522s, 1462w, 1447m, 1436w, 1376w, 1369w, 1361w, 1348m, 1313s, 1277w, 1268m, 1211s, 1205m, 1158m, 1146m, 1107m, 1096w, 1068w, 1050w, 981m, 978w, 948w, 934w, 922m, 905m, 890w, 862m, 847m, 832m, 821m, 802s, 769s, 748m, 740w; δ_{H} (400 MHz, DMSO-d₆) 9.03 (2H, d, *J* 7.2, NH), 8.54 (2H, d, *J* 1.2, Ar *H*), 8.13 (2H, d, *J* 8.4, Ar *H*), 8.02 (2H, dd, *J* 8.4, 1.2), 4.55 (2H, p, *J* 7.2, CH), 3.67 (6H, s, OCH₃), 1.46 (6H, d, *J* 7.6, CH₃); δ_{C} (100 MHz, DMSO-d₆) 173.1, 166.2, 133.4, 132.6, 129.0, 127.5, 125.1, 51.9, 48.4, 16.8; *m/z* (ASAP): Calculated for [M+H]⁺ 387.16, found: 387.15.

Preparation of dimethyl 2,2'-((naphthalene-2,6-dicarbonyl)bis(azanediyl))(2*S*,2'*S*)-bis(3-methylbutanoate) (**ValEst**)



Similar treatment (typical procedure A) of L-valine methyl ester hydrochloride (2.48 g, 14.8 mmol) afforded the title compound **ValEst** as a white powder (2.63 g, 81%) mp (hot-stage) 177-178 °C; $\nu_{\max}/\text{cm}^{-1}$ 3311br (N-H), 3051w (aryl C-H), 2966m (alkyl C-H), 2875w (alkyl C-H), 1742s (C=O), 1637s (C=O), 1621w, 1516s, 1466w, 1431m, 1390w, 1372m, 1353w, 1327w, 1308m, 1268w, 1244m, 1197s, 1149s, 1071m, 1042w, 994s, 963w, 947w, 907s, 822m, 815m, 792m, 765s, 764m, 756w, 709w; δ_{H} (400 MHz, DMSO- d_6) 8.84 (2H, d, J 8.0, NH), 8.55 (2H, s, Ar H), 8.13 (2H, d, J 8.4, Ar H), 8.01 (2H, dd, J 8.4, 1.2, Ar H), 4.37 (2H, t, J 7.6, CH), 3.68 (6H, s, OCH₃), 2.19-2.27 (2H, m, CH(CH₃)₂), 1.00 (12H, dd, J 21.6, 6.8, CH₃); δ_{C} (100 MHz, DMSO- d_6) 172.2, 166.9, 133.3, 132.7, 128.9, 127.7, 125.3, 58.8, 51.7, 29.6, 19.2, 19.1; m/z (ASAP): Calculated for [M+H]⁺ 443.22, found: 443.20.

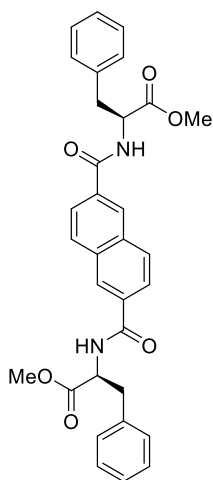
Preparation of dimethyl 2,2'-((naphthalene-2,6-dicarbonyl)bis(azanediyl))(2*S*,2'*S*)-bis(4-methylpentanoate) (**LeuEst**)



Similar treatment (typical procedure A) of L-leucine methyl ester hydrochloride (2.69 g, 14.8 mmol) afforded the title compound **LeuEst** as a white powder (2.59 g, 75%) mp (hot-stage) 227-228 °C; $\nu_{\max}/\text{cm}^{-1}$ 3300br (N-H), 3083w (aryl C-H), 3061w (aryl C-H), 2956m (alkyl C-H), 2871w (alkyl C-H), 1744s (C=O), 1637s (C=O), 1599m, 1545s, 1496m, 1468m, 1436m, 1387w, 1369w, 1340s, 1309m, 1272m, 1241w, 1211m, 1197s, 1156s, 1123w, 1076m, 1019m, 991m, 959w, 938w, 907s, 855w, 827m, 810m, 768s, 745w; δ_{H} (400 MHz, DMSO- d_6) 8.96 (2H, d, J 7.6, NH), 8.55 (2H, s, Ar H), 8.14 (2H, d, J 8.8, Ar H), 8.02 (2H, dd, J 8.4, 1.2, Ar H), 4.58 (2H, ddd, J 10.7, 7.6, 4.7 CH), 3.67 (6H, s, OCH₃), 1.77-1.88 (4H, m, CH₂), 1.59-1.65 (2H, m, CH(CH₃)₂), 0.96 (12H, dd, J 16.4, 6.4, CH₃); δ_{C} (100 MHz, DMSO- d_6) 173.1, 166.5,

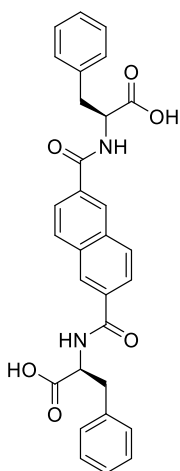
133.4, 132.6, 129.0, 127.5, 125.1, 51.9, 51.1, 24.5, 22.9, 21.2; m/z (ASAP): Calculated for $[M+2H]^+$ 472.26, found: 472.30.

Preparation of dimethyl 2,2'-((naphthalene-2,6-dicarbonyl)bis(azanediyl))(2*S*,2'*S*)-bis(3-phenylpropanoate) (**PheEst**)



Similar treatment (typical procedure A) of L-phenylalanine methyl ester hydrochloride (3.19 g, 14.8 mmol) afforded the title compound **PheEst** as a white powder (2.45 g, 62%) mp (hot-stage) 215-216 °C (dec.); $\nu_{\max}/\text{cm}^{-1}$ 3260br (N-H), 3064w (aryl C-H), 3026w (aryl C-H), 2952m (alkyl C-H), 1745s (C=O), 1637s (C=O), 1600w, 1533s, 1495m, 1455w, 1436s, 1353s, 1319w, 1272m, 1216s, 1196s, 1151m, 1129w, 1089s, 1031m, 991m, 928w, 904s, 879w, 866w, 830w, 811s, 760w, 746s; δ_{H} (400 MHz, DMSO- d_6) 9.09 (2H, d, J 7.6, NH), 8.44 (2H, d, J 1.6, Ar H), 8.09 (2H, d, J 8.4, Ar H), 7.92 (2H, dd, J 8.8, 1.6, Ar H), 7.18-7.35 (10H, m, Ar H), 4.74 (2H, ddd, J 9.9, 7.8, 5.5, CH), 3.66 (6H, s, OCH₃), 3.11-3.24 (4H, m, CH₂); δ_{C} (100 MHz, DMSO- d_6) 172.1, 166.3, 137.6, 133.3, 132.6, 129.1, 128.3, 127.5, 126.5, 125.0, 54.4, 52.0, 36.2; m/z (ASAP): Calculated for $[M-H]^-$ 537.20, found: 537.35.

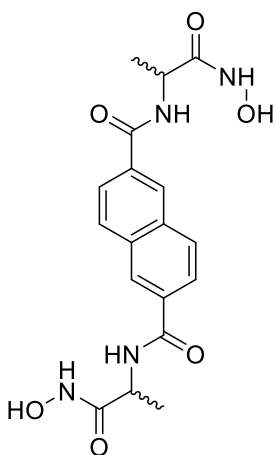
Preparation of (2*S*,2'*S*)-2,2'-((naphthalene-2,6-dicarbonyl)bis(azanediyl))bis(3-phenylpropanoic acid) (**PheOH**)



To a stirred solution of KOH (15.0 g, 267 mmol) in THF (100 mL) was added 2,2'-((naphthalene-2,6-dicarbonyl)bis(azanediyl))(2*S*,2'*S*)-bis(3-phenylpropanoate) (**PheEst**) (3.57 g, 6.63 mmol) as a suspension in 100 mL of MeOH and was left to stir until fully dissolved. The reaction mixture was then heated to 50 °C for 16 h before it was allowed to cool to room temperature. The solution was then acidified to a pH of 1 by portion wise addition of aqueous HCl (1N). When the pH fell below 5, a white precipitate started to appear. When the solution was fully acidified the precipitate, which stopped forming upon further HCl addition, and was filtered, washed with water (3x 20 mL) and dried under reduced pressure, to afford the

title compound **PheOH** as a white powder (3.11 g, 92%). mp (hot-stage) 259-260 °C (dec.); $\nu_{\max}/\text{cm}^{-1}$ 3355br (N-H), 3064w (aryl C-H), 3028w (aryl C-H), 2989br (O-H), 2900w (alkyl C-H), 1734w (C=O), 1690s (C=O), 1601m, 1538s, 1496m, 1478w, 1456w, 1423s, 1340m, 1294s, 1268w, 1227s, 1191s, 1169m, 1080s, 1028w, 961w, 915s, 839w, 823s, 793w, 769s, 740m; δ_{H} (300 MHz, DMSO- d_6) 12.88 (2H, s, OH), 8.93 (2H, d, J 8.1, NH), 8.43 (2H, s, Ar H), 8.08 (2H, d, J 8.7, Ar H), 7.92 (2H, dd, J 8.7, 1.2, Ar H), 7.35 (4H, d, J 6.9, Ar H), 7.25-7.30 (4H, m, Ar H), 7.15-7.21 (2H, m, Ar H), 4.69 (2H, ddd, J 10.4, 8.2, 4.6, CH), 3.07-3.27 (4H, m, CH₂); δ_{C} (75 MHz, DMSO- d_6) 173.1, 166.2, 138.2, 133.3, 132.8, 129.1, 129.0, 128.2, 127.4, 126.4, 125.0, 54.4, 36.4; m/z (ASAP): Calculated for [M+H]⁺ 511.19, found: 511.25.

Preparation of N2,N6-bis(1-(hydroxyamino)-1-oxopropan-2-yl)naphthalene-2,6-dicarboxamide (**AlaHA**) as a mixture of (S,S), (S,R), (R,S), and (R,R) stereoisomers.

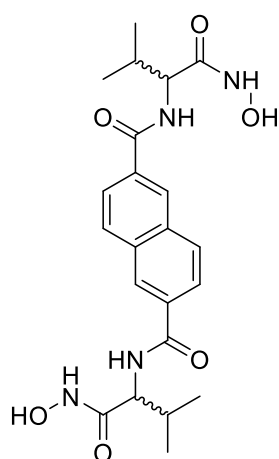


Typical procedure B (solution synthesis of Hydroxamic acids): To a round bottom flask containing a solution of THF (100 mL) was added dimethyl 2,2'-((naphthalene-2,6-dicarbonyl)bis(azanediyl))(2S,2'S)-dipropionate (**AlaEst**) (1.92 g, 4.97 mmol) and was left to stir until fully dissolved. In a separate flask, NH₂OH·HCl (2.1 g, 30.0 mmol) was dissolved in 100 mL of MeOH, followed by the addition of KOH (3.36 g, 60.0 mmol), which caused the solution to turn cloudy, as KCl precipitate formed. The precipitate was filtered off and discarded. The

resulting clear solution was then added to the THF solution of **AlaEst** and the combined mixture was heated to 50 °C and stirred for 16 h. The solution was then allowed to cool to room temperature and the solvent mixture was subsequently removed under reduced pressure, until approximately 10 mL remained in the flask. To the solution it was then added 100 mL of water, and the resulting aqueous mixture was acidified by portion wise addition of aqueous HCl (1N), until the pH reached 6.2, at which point a white precipitate was formed. The precipitate was filtered, washed with water (3x 10 mL) and left to dry in an oven at 40 °C for 16 h, affording the title compound **AlaHA** as a white powder (0.367 g, 19%). mp (hot-stage) 186-187 °C (dec.); $\nu_{\max}/\text{cm}^{-1}$ 3291m (N-H), 3168br (N-H), 3060w (aryl C-H), 2997w (alkyl C-H), 2916br (O-H), 1634s, 1595m, 1533s, 1492m,

1451m, 1392w, 1373m, 1338w, 1309s, 1271m, 1197s, 1156m, 1135w, 1123w, 1093w, 1080m, 1039m, 1019m, 1015w, 975w, 959m, 934m, 917s, 914s, 876w, 838s, 834m, 777s; δ_{H} (400 MHz, DMSO- d_6) 10.70 (2H, s, NHOH), 8.84 (2H, s, NHOH) 8.72 (2H, d, J 7.6, NH), 8.55 (2H, s, Ar H), 8.09 (2H, d, J 8.4, Ar H), 8.02 (2H, dd, J 8.4, 1.2, Ar H), 4.46 (2H, p, J 7.2, CH), 1.37 (6H, d, J 7.2, CH_3); δ_{C} (100 MHz, DMSO- d_6) 169.2, 165.9, 133.2, 132.9, 128.7, 127.5, 125.2, 47.0, 18.1; m/z (ASAP): Calculated for $[\text{M}-\text{H}]^-$ 387.13, found: 387.05.

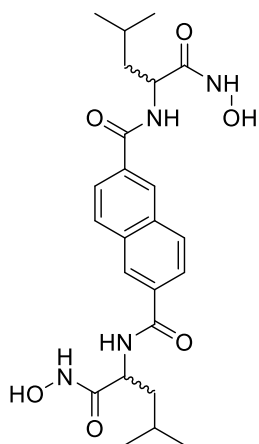
Preparation of N2,N6-bis(1-(hydroxyamino)-3-methyl-1-oxobutan-2-yl)naphthalene-2,6-dicarboxamide (**ValHA**), as a mixture of (S,S), (S,R), (R,S), and (R,R) stereoisomers.



Similar treatment (typical procedure B) of dimethyl 2,2'-((naphthalene-2,6-dicarbonyl)bis(azanediyl))(2S,2'S)-bis(3-methylbutanoate) (**ValEst**) (2.2 g, 4.97 mmol) afforded the title compound **ValHA** as a white powder (0.265 g, 12%). mp (hot-stage) 190-197 °C (dec.); $\nu_{\text{max}}/\text{cm}^{-1}$ 3269br (N-H), 3068w (aryl C-H), 2966m (alkyl C-H), 2953w (alkyl C-H), 2825w (alkyl C-H), 1724w (C=O), 1635s (C=O), 1595m, 1533s, 1495m, 1471w, 1387w, 1341m, 1323m, 1263m, 1218w, 1192s, 1147m, 1065m, 1037m, 997w, 965w, 944w, 928w, 900s, 866w, 847w, 820s,

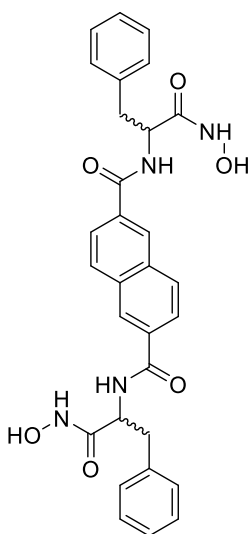
767s, 762m, 699s; δ_{H} (400 MHz, DMSO- d_6) 10.81 (0.69H, s, NHOH), 8.95 (0.53H, s, NHOH), 8.62-8.65 (0.80H, m, NH), 8.55 (1H, s, Ar H), 8.52 (1.08H, s, Ar H), 8.43 (1.01H, dd, J 8.4, 8.4, Ar H), 8.09-8.13 (2.00H, m, Ar H), 7.97-8.08 (2.08H, m, Ar H), 4.25-4.29 (1.10H, m, CH), 4.19 (1.03H, t, J 8.8, CH), 2.12-2.25 (2.08H, m, $\text{CH}(\text{CH}_3)_2$), 0.92-0.99 (12.02H, m, CH_3); δ_{C} (100 MHz, DMSO- d_6) 173.1, 173.0, 167.7, 166.2, 133.32, 133.30, 133.2, 132.9, 128.9, 128.8, 127.5, 127.2, 127.2, 125.2, 125.1, 58.9, 57.1, 30.1, 29.9, 19.5, 19.3, 19.2, 18.7; m/z (ASAP): Calculated for $[\text{M}+\text{NH}_4]^+$ 462.23, found: 462.20.

Preparation of N2,N6-bis(1-(hydroxyamino)-4-methyl-1-oxopentan-2-yl)naphthalene-2,6-dicarboxamide (**LeuHA**), as a mixture of (S,S), (S,R), (R,S), and (R,R) stereoisomers.



Similar treatment (typical procedure B) of dimethyl 2,2'-((naphthalene-2,6-dicarbonyl)bis(azanediyl))(2S,2'S)-bis(3-methylbutanoate) (**LeuEst**) (2.34 g, 4.97 mmol) afforded the title compound **LeuHA** as a white powder (0.446 g, 19%). mp (hot-stage) >110 °C (dec.); $\nu_{\max}/\text{cm}^{-1}$ 3268br (N-H), 3061w (aryl C-H), 2958m (alkyl C-H), 2946w (alkyl C-H), 2869w (alkyl C-H), 1717w (C=O), 1637s (C=O), 1601w, 1532s, 1496w, 1469w, 1436w, 1403w, 1386w, 1368w, 1338w, 1306m, 1270m, 1230w, 1194m, 1158m, 1127w, 1082w, 1044w, 1013s, 951s, 920w, 880w, 862w, 824w, 808w, 768m, 702w; δ_{H} (400 MHz, DMSO- d_6) 10.83 (0.36H, s, NHOH), 8.83 (1.50H, d, J 7.6, NH), 8.72 (0.44H, d, J 8.0, NHOH), 8.57 (0.50H, s, Ar H), 8.55 (1H, s, Ar H), 8.10-8.14 (1.94H, m, Ar H), 8.02-8.04 (2H, m, Ar H), 4.48-4.54 (2.27H, m, CH), 1.74-1.85 (6.39H, m, $\text{CH}(\text{CH}_3)_2$), 0.91-0.96 (12.17H, m, CH_3). NHOH resonance appears to be overlapped by peak at 8.84 ppm; δ_{C} (100 MHz, DMSO- d_6) 174.2, 168.8, 166.3, 166.1, 133.31, 132.93, 132.87, 132.82, 128.9, 128.8, 127.5, 127.4, 125.3, 125.1, 51.1, 49.8, 24.6, 24.4, 23.0, 22.9, 21.6, 21.2; m/z (ASAP): Calculated for $[\text{M-H}]^-$ 471.22, found: 471.15

Preparation of N2,N6-bis(1-(hydroxyamino)-1-oxo-3-phenylpropan-2-yl)naphthalene-2,6-dicarboxamide (**PheHA**), as a mixture of (S,S), (S,R), (R,S), and (R,R) stereoisomers.



Solution procedure: Similar treatment (typical procedure B) of dimethyl 2,2'-((naphthalene-2,6-dicarbonyl)bis(azanediyl))(2S,2'S)-bis(3-phenylpropanoate) (**PheEst**) (2.68 g, 4.97 mmol) afforded the title compound **PheHA** as a white powder (0.150 g, 5%).

Mechanochemical procedure (adapted from Mocci *et. al*):⁸³ To a 10 mL stainless steel jar which contained two 8 mm stainless steel balls, was added (2S,2'S)-2,2'-((naphthalene-2,6-dicarbonyl)bis(azanediyl))bis(3-phenylpropanoic acid) **PheOH** (200 mg, 0.391 mmol), along with 1,1'-Carbonyldiimidazole (CDI) (162.2 mg, 1.00 mmol) and CH_3NO_2 (40 μL). The jar was then sealed, and

milled at 25 Hz for 10 min, after which it was reopened and imidazole (68.1 mg, 1.00 mmol) along with $(\text{NH}_3\text{OH})_2\text{SO}_4$ (164.1 mg, 1.00 mmol) was added to the mixture. The jar was then resealed, and the contents milled at 25 Hz for 1 h. The contents of the jar were then transferred to a 50 mL beaker containing 20 mL of water, and acidified to a pH of 6.2, by portion wise addition of an aqueous solution of HCl (1N). The resulting precipitate was then filtered, washed with water (3x 10 mL) and left to dry in an oven at 40 °C for 16 h, affording the title compound **PheHA** as a white powder (0.089 g, 42%).

mp (hot-stage) 154-155 °C (dec.); $\nu_{\text{max}}/\text{cm}^{-1}$ 3255br/s, 3063w (aryl C-H), 3029w (aryl C-H), 2926w (alkyl C-H), 2857w (alkyl C-H), 1632s (C=O), 1596m, 1521s, 1493s, 1456m, 1377m, 1339w, 1328m, 1308s, 1271w, 1257w, 1191m, 1163w, 1144w, 1093m, 1065s, 1023m, 970w, 935w, 922m, 900s, 823s, 787w, 748s; δ_{H} (300 MHz, DMSO- d_6) 10.84 (1.38H, s, NHOH), 8.92 (1.14H, s, NHOH), 8.86 (1.63H, d, J 8.4, NH), 8.44 (1.60H, s, Ar H), 8.38 (0.39H, s, Ar H), 8.02-8.06 (2.00H, m, Ar H), 7.90-7.94 (2.01H, m, Ar H), 7.24-7.37 (8.05H, m, Ar H), 7.14-7.21 (2.11H, m, Ar H), 4.54-4.71 (1.89H, m, CH); δ_{C} (75 MHz, DMSO- d_6) 167.9, 166.0, 138.2, 133.2, 132.8, 129.2, 129.1, 128.7, 128.1, 128.0, 127.4, 126.3, 125.0, 52.9, 37.4 ; m/z (ASAP): Calculated for $[\text{M-H}]^-$ 539.19, found: 539.30.

4.9 References

- (1) Bai, Y.; Guo, D.; Duan, C.; Dang, D.; Pang, K.; Meng, Q. A Three Dimensional Porous Metal–Organic Framework $[\text{Fe}_4\text{L}_6 \cdot (\text{DMF})_3 \cdot (\text{H}_2\text{O})_{10}]$ Constructed from Neutral Discrete Fe_4L_6 Pyramids $[\text{H}_2\text{L} = 1,3\text{-Benzodihydroxamic Acid}]$. *Chem. Commun.* **2004**, No. 2, 186–187. <https://doi.org/10.1039/B306264C>.
- (2) Beissel, T.; Powers, R. E.; Raymond, K. N. Symmetry-Based Metal Complex Cluster Formation. *Angew. Chem. Int. Ed.* **1996**, 35 (10), 1084–1086. <https://doi.org/10.1002/anie.199610841>.
- (3) Lerma-Berlanga, B.; Castells-Gil, J.; Ganivet, C. R.; Almora-Barrios, N.; González-Platas, J.; Fabelo, O.; Padial, N. M.; Martí-Gastaldo, C. Permanent Porosity in Hydroxamate Titanium–Organic Polyhedra. *J. Am. Chem. Soc.* **2021**, 143 (50), 21195–21199. <https://doi.org/10.1021/jacs.1c09278>.
- (4) Green, H. R. *Hydroxamic Acids and Their Porous Materials*, Heriot-Watt University, 2018.
- (5) Pluth, M. D.; Bergman, R. G.; Raymond, K. N. Acceleration of Amide Bond Rotation by Encapsulation in the Hydrophobic Interior of a Water-Soluble Supramolecular Assembly. *J. Org. Chem.* **2008**, 73 (18), 7132–7136. <https://doi.org/10.1021/jo800991g>.
- (6) Yao, Y.; Zhou, Y.; Zhu, T.; Gao, T.; Li, H.; Yan, P. Eu(III) Tetrahedron Cage as a Luminescent Chemosensor for Rapidly Reversible and Turn-On Detection of Volatile Amine/ NH_3 . *ACS Appl. Mater. Interfaces* **2020**, 12 (13), 15338–15347. <https://doi.org/10.1021/acsami.9b21425>.
- (7) Prasenjit, M.; Boris, B.; Kari, R.; R., N. J. White Phosphorus Is Air-Stable Within a Self-Assembled Tetrahedral Capsule. *Science* **2009**, 324 (5935), 1697–1699. <https://doi.org/10.1126/science.1175313>.
- (8) Zhu, J.; Yan, Z.; Bošković, F.; Haynes, C. J. E.; Kieffer, M.; Greenfield, J. L.; Wang, J.; Nitschke, J. R.; Keyser, U. F. $\text{Fe}^{\text{II}}_4\text{L}_4$ Tetrahedron Binds and Aggregates DNA G-Quadruplexes. *Chem. Sci.* **2021**, 12 (43), 14564–14569. <https://doi.org/10.1039/D1SC04430C>.

- (9) Zhou, Y.; Li, H.; Zhu, T.; Gao, T.; Yan, P. A Highly Luminescent Chiral Tetrahedral $\text{Eu}_4\text{L}_4(\text{L}')_4$ Cage: Chirality Induction, Chirality Memory, and Circularly Polarized Luminescence. *J. Am. Chem. Soc.* **2019**, *141* (50), 19634–19643. <https://doi.org/10.1021/jacs.9b07178>.
- (10) Hong, C. M.; Bergman, R. G.; Raymond, K. N.; Toste, F. D. Self-Assembled Tetrahedral Hosts as Supramolecular Catalysts. *Acc. Chem. Res.* **2018**, *51* (10), 2447–2455. <https://doi.org/10.1021/acs.accounts.8b00328>.
- (11) McConnell, A. J. Metallosupramolecular Cages: From Design Principles and Characterisation Techniques to Applications. *Chem. Soc. Rev.* **2022**, *51* (8), 2957–2971. <https://doi.org/10.1039/D1CS01143J>.
- (12) Jean-Marie, L. Supramolecular Chemistry: Receptors, Catalysts, and Carriers. *Science* **1985**, *227* (4689), 849–856. <https://doi.org/10.1126/science.227.4689.849>.
- (13) Bao, S.-J.; Xu, Z.-M.; Yu, T.-C.; Song, Y.-L.; Wang, H.; Niu, Z.; Li, X.; Abrahams, B. F.; Braunstein, P.; Lang, J.-P. Flexible Vertex Engineers the Controlled Assembly of Distorted Supramolecular Tetrahedral and Octahedral Cages. *Research* **2022**, 9819343. <https://doi.org/10.34133/2022/9819343>.
- (14) J.-M. Lehn. International Edition in English. *Angew. Chem. Int. Ed.* **1985**, *24* (10), 799–810.
- (15) Hilmey, D. G.; Paquette, L. A. Exo- and Endo-Receptors in One. A Novel Class of Supramolecular Structures Housing Transition-Metal-Binding Bi- and Terpyridine Units alongside Lithium Ion-Selective Trispirotetrahydrofuranyl Components. *J. Org. Chem.* **2004**, *69* (10), 3262–3270. <https://doi.org/10.1021/jo030373t>.
- (16) He, C.; Chen, X.; Sun, C.-Z.; Zhang, L.-Y.; Xu, W.; Zhang, S.; Wang, Z.; Dai, F.-R. Decahexanuclear Zinc(II) Coordination Container Featuring a Flexible Tetracarboxylate Ligand: A Self-Assembly Supermolecule for Highly Efficient Drug Delivery of Anti-Inflammatory Agents. *ACS Appl. Mater. Interfaces* **2021**, *13* (29), 33812–33820. <https://doi.org/10.1021/acsami.1c06311>.
- (17) Zhang, Y.; Zhou, Q.-F.; Huo, G.-F.; Yin, G.-Q.; Zhao, X.-L.; Jiang, B.; Tan, H.;

- Li, X.; Yang, H.-B. Hierarchical Self-Assembly of an Alkynylplatinum(II) Bzimpy-Functionalized Metallocage via Pt···Pt and π - π Interactions. *Inorg. Chem.* **2018**, *57* (7), 3516–3520. <https://doi.org/10.1021/acs.inorgchem.7b02777>.
- (18) Zhang, G.; Mastalerz, M. Organic Cage Compounds--from Shape-Persistency to Function. *Chem. Soc. Rev.* **2014**, *43* 6, 1934–1947.
- (19) Han, X.-N.; Han, Y.; Chen, C.-F. Supramolecular Tessellations by the Exo-Wall Interactions of Pagoda[4]Arene. *Nat. Commun.* **2021**, *12* (1), 6378. <https://doi.org/10.1038/s41467-021-26729-3>.
- (20) Janiak, A.; Gajewy, J.; Szymkowiak, J.; Gierczyk, B.; Kwit, M. Specific Noncovalent Association of Truncated Exo-Functionalized Triangular Homochiral Isotrianglimines through Head-to-Head, Tail-to-Tail, and Honeycomb Supramolecular Motifs. *J. Org. Chem.* **2022**, *87* (5), 2356–2366. <https://doi.org/10.1021/acs.joc.1c02238>.
- (21) Lewis, J. E. M.; Crowley, J. D. Exo- and Endo-Hedral Interactions of Counteranions with Tetracationic Pd₂L₄ Metallosupramolecular Architectures. *Supramol. Chem.* **2014**, *26* (3–4), 173–181. <https://doi.org/10.1080/10610278.2013.842644>.
- (22) Qu, Y.-X.; Lin, R.-L.; Zhang, Y.-Q.; Zhou, K.-Z.; Zhou, Q.-D.; Zhu, Q.-J.; Tao, Z.; Ma, P.-H.; Liu, J.-X.; Wei, G. Endo/Exo Binding of Alkyl and Aryl Diammonium Ions by Cyclopentanocucurbit[6]Urils. *Org. Chem. Front.* **2017**, *4* (9), 1799–1805. <https://doi.org/10.1039/C7QO00376E>.
- (23) J.-M. Lehn, J. Simon, J. W. No Title. *Angew. Chem. Int. Ed.* **1973**, *12*, 578.
- (24) J., P. C. The Discovery of Crown Ethers. *Science* **1988**, *241* (4865), 536–540. <https://doi.org/10.1126/science.241.4865.536>.
- (25) Gutsche, C. D. Calixarenes. *Acc. Chem. Res.* **1983**, *16* (5), 161–170. <https://doi.org/10.1021/ar00089a003>.
- (26) J., C. D. Cavitands: Organic Hosts with Enforced Cavities. *Science* **1983**, *219* (4589), 1177–1183. <https://doi.org/10.1126/science.219.4589.1177>.
- (27) Cram, D. J.; Karbach, S.; Kim, Y. H.; Baczynskyj, L.; Kallemeyn, G. W. Shell Closure of Two Cavitands Forms Carcerand Complexes with Components of the

- Medium as Permanent Guests. *J. Am. Chem. Soc.* **1985**, *107* (8), 2575–2576. <https://doi.org/10.1021/ja00294a076>.
- (28) Cram, D. J. The Design of Molecular Hosts, Guests, and Their Complexes (Nobel Lecture). *Angew. Chem. Int. Ed.* **1988**, *27* (8), 1009–1020. <https://doi.org/10.1002/anie.198810093>.
- (29) Lehn, J. M. Towards Complex Matter: Supramolecular Chemistry and Self-Organization. *Eur. Rev.* **2009**, *17* (2), 263–280. <https://doi.org/10.1017/S1062798709000805>.
- (30) Frausto da Silva, J. J. R. The Chelate Effect Redefined. *J. Chem. Educ.* **2009**, *60* (5), 390. <https://doi.org/10.1021/ed060p390>.
- (31) Han, W.-K.; Zhang, H.-X.; Wang, Y.; Liu, W.; Yan, X.; Li, T.; Gu, Z.-G. Tetrahedral Metal–Organic Cages with Cube-like Cavities for Selective Encapsulation of Fullerene Guests and Their Spin-Crossover Properties. *Chem. Commun.* **2018**, *54* (89), 12646–12649. <https://doi.org/10.1039/C8CC06652C>.
- (32) Tahara, K.; Lei, S.; Adisojoso, J.; De Feyter, S.; Tobe, Y. Supramolecular Surface-Confined Architectures Created by Self-Assembly of Triangular Phenylene–Ethyne Macrocycles via van Der Waals Interaction. *Chem. Commun.* **2010**, *46* (45), 8507–8525. <https://doi.org/10.1039/C0CC02780D>.
- (33) Shen, Z.; Wang, T.; Liu, M. H-Bond and π – π Stacking Directed Self-Assembly of Two-Component Supramolecular Nanotubes: Tuning Length, Diameter and Wall Thickness. *Chem. Commun.* **2014**, *50* (17), 2096–2099. <https://doi.org/10.1039/C3CC48350A>.
- (34) Sava, D. F.; Kravtsov, V. C.; Eckert, J.; Eubank, J. F.; Nouar, F.; Eddaoudi, M. Exceptional Stability and High Hydrogen Uptake in Hydrogen-Bonded Metal–Organic Cubes Possessing ACO and AST Zeolite-like Topologies. *J. Am. Chem. Soc.* **2009**, *131* (30), 10394–10396. <https://doi.org/10.1021/ja903287v>.
- (35) Liu, G.; Liu, T.; Mal, S. S.; Kortz, U. Wheel-Shaped Polyoxotungstate $[\text{Cu}_{20}\text{Cl}(\text{OH})_{24}(\text{H}_2\text{O})_{12}(\text{P}_8\text{W}_{48}\text{O}_{184})]^{25-}$ Macroanions Form Supramolecular “Blackberry” Structure in Aqueous Solution. *J. Am. Chem. Soc.* **2006**, *128* (31), 10103–10110. <https://doi.org/10.1021/ja0610840>.

- (36) Nam, D.; Huh, J.; Lee, J.; Kwak, J. H.; Jeong, H. Y.; Choi, K.; Choe, W. Cross-Linking Zr-Based Metal–Organic Polyhedra via Postsynthetic Polymerization. *Chem. Sci.* **2017**, *8* (11), 7765–7771. <https://doi.org/10.1039/C7SC03847J>.
- (37) Mal, P.; Schultz, D.; Beyeh, K.; Rissanen, K.; Nitschke, J. R. An Unlockable–Relockable Iron Cage by Subcomponent Self-Assembly. *Angew. Chem. Int. Ed.* **2008**, *47* (43), 8297–8301. <https://doi.org/10.1002/anie.200803066>.
- (38) Juul, S.; Iacovelli, F.; Falconi, M.; Kragh, S. L.; Christensen, B.; Frøhlich, R.; Franch, O.; Kristoffersen, E. L.; Stougaard, M.; Leong, K. W.; et al. Temperature-Controlled Encapsulation and Release of an Active Enzyme in the Cavity of a Self-Assembled DNA Nanocage. *ACS Nano* **2013**, *7* (11), 9724–9734. <https://doi.org/10.1021/nn4030543>.
- (39) Jansze, S. M.; Cecot, G.; Severin, K. Reversible Disassembly of Metallasupramolecular Structures Mediated by a Metastable-State Photoacid. *Chem. Sci.* **2018**, *9* (18), 4253–4257. <https://doi.org/10.1039/C8SC01108G>.
- (40) Zhang, D.; Ronson, T. K.; Zou, Y.-Q.; Nitschke, J. R. Metal–Organic Cages for Molecular Separations. *Nat. Rev. Chem.* **2021**, *5* (3), 168–182. <https://doi.org/10.1038/s41570-020-00246-1>.
- (41) Liu, W.; Liu, G.; Zhu, X.; Han, X.; Lu, A.; Lu, S.; Shi, L.; Hao, X.-Q.; Song, M.-P. Tailored Metal–Organic Tetrahedral Nanocages with Aggregation-Induced Emission for an Anti-Counterfeiting Ink and Stimulus-Responsive Luminescence. *New J. Chem.* **2022**, *46* (17), 8062–8068. <https://doi.org/10.1039/D2NJ00382A>.
- (42) Codd, R. Traversing the Coordination Chemistry and Chemical Biology of Hydroxamic Acids. *Coord. Chem. Rev.* **2008**, *252* (12–14), 1387–1408. <https://doi.org/10.1016/j.ccr.2007.08.001>.
- (43) Brennan, B. J.; Chen, J.; Rudshiteyn, B.; Chaudhuri, S.; Mercado, B. Q.; Batista, V. S.; Crabtree, R. H.; Brudvig, G. W. Molecular Titanium-Hydroxamate Complexes as Models for TiO₂ surface Binding. *Chem. Commun.* **2016**, *52* (14), 2972–2975. <https://doi.org/10.1039/c5cc09857b>.
- (44) Kang, X.; Liu, S.; Dai, Z.; He, Y.; Song, X.; Tan, Z. Titanium Dioxide: From Engineering to Applications. *Catalysts* . **2019**, *9* (2), 191.

<https://doi.org/10.3390/catal9020191>.

- (45) Buglyó, P.; Nagy, E. M.; Sóvágó, I.; Ozsváth, A.; Sanna, D.; Farkas, E. Metal Ion Binding Capability of Secondary (*N*-Methyl) versus Primary (*N*-H) Dipeptide Hydroxamic Acids. *Polyhedron* **2016**, *110*, 172–181. <https://doi.org/10.1016/j.poly.2016.02.031>.
- (46) Sahoo, S. K.; Sharma, D.; Bera, R. K.; Crisponi, G.; Callan, J. F. Iron(III) Selective Molecular and Supramolecular Fluorescent Probes. *Chem. Soc. Rev.* **2012**, *41* (21), 7195–7227. <https://doi.org/10.1039/C2CS35152H>.
- (47) Yariv, S.; Mendelovici, E. The Effect of Degree of Crystallinity on the Infrared Spectrum of Hematite. *Appl. Spectrosc.* **1979**, *33* (4), 410–411.
- (48) Aisen, P.; Enns, C.; Wessling-Resnick, M. Chemistry and Biology of Eukaryotic Iron Metabolism. *Int. J. Biochem. Cell Biol.* **2001**, *33* (10), 940–959. [https://doi.org/10.1016/S1357-2725\(01\)00063-2](https://doi.org/10.1016/S1357-2725(01)00063-2).
- (49) Butler, A.; Theisen, R. M. Iron(III)–Siderophore Coordination Chemistry: Reactivity of Marine Siderophores. *Coord. Chem. Rev.* **2010**, *254* (3), 288–296. <https://doi.org/10.1016/j.ccr.2009.09.010>.
- (50) Miller, M. J. Syntheses and Therapeutic Potential of Hydroxamic Acid Based Siderophores and Analogues. *Chem. Rev.* **1989**, *89* (7), 1563–1579. <https://doi.org/10.1021/cr00097a011>.
- (51) Agrawal, Y. K. Hydroxamic Acids and Their Metal Complexes. *Russ. Chem. Rev.* **1979**, *48* (10), 948–963. <https://doi.org/10.1070/rc1979v048n10abeh002422>.
- (52) Bhatt, K.; Agrawal, Y. K. Hydroxamic Acids and Their Metal Complexes: Preparation, Properties, and Infrared Spectra. *Synth. React. Inorg. Met. Chem.* **1972**, *2* (3), 175–179. <https://doi.org/10.1080/00945717208069598>.
- (53) Li, Z.; Yamamoto, H. Hydroxamic Acids in Asymmetric Synthesis. *Acc. Chem. Res.* **2013**, *46* (2), 506–518. <https://doi.org/10.1021/ar300216r>.
- (54) Carrano, C. J.; Raymond, K. N. Coordination Chemistry of Microbial Iron Transport Compounds. 10. Characterization of the Complexes of Rhodotorulic Acid, a Dihydroxamate Siderophore. *J. Am. Chem. Soc.* **1978**, *100* (17), 5371–5374. <https://doi.org/10.1021/ja00485a019>.

- (55) Atkin, C. L.; Neilands, J. B. Rhodotorulic Acid, a Diketopiperazine Dihydroxamic Acid with Growth-Factor Activity. I. Isolation and Characterization. *Biochemistry* **1968**, 7 (10), 3734–3739. <https://doi.org/10.1021/bi00850a054>.
- (56) Enamullah, M.; Uddin, A. K. M. R.; Pescitelli, G.; Berardozi, R.; Makhloufi, G.; Vasylyeva, V.; Chamayou, A.-C.; Janiak, C. Induced Chirality-at-Metal and Diastereoselectivity at Δ/Λ -Configured Distorted Square-Planar Copper Complexes by Enantiopure Schiff Base Ligands: Combined Circular Dichroism, DFT and X-Ray Structural Studies. *Dalt. Trans.* **2014**, 43 (8), 3313–3329. <https://doi.org/10.1039/C3DT52871E>.
- (57) Hentschel, M.; Schäferling, M.; Duan, X.; Giessen, H.; Liu, N. Chiral Plasmonics. *Sci. Adv.* **2017**, 3 (5), 1–13. <https://doi.org/10.1126/sciadv.1602735>.
- (58) Favre, H. A.; Powell, W. H. *Nomenclature of Organic Chemistry*; The Royal Society of Chemistry, 2014. <https://doi.org/10.1039/9781849733069>.
- (59) Albrecht, M. Catecholate-Based Helicates. *Eur. J. Inorg. Chem.* **2020**, 2020 (23), 2227–2237. <https://doi.org/10.1002/ejic.202000255>.
- (60) Beissel, T.; Powers, R. E.; Parac, T. N.; Raymond, K. N. Dynamic Isomerization of a Supramolecular Tetrahedral M_4L_6 Cluster. *J. Am. Chem. Soc.* **1999**, 121 (17), 4200–4206. <https://doi.org/10.1021/ja984046s>.
- (61) Rzepa, H. S.; Cass, M. E. In Search of the Bailar and Ray–Dutt Twist Mechanisms That Racemize Chiral Trischelates : A Computational Study of Sc^{III} , Ti^{IV} , Co^{III} , Zn^{II} , Ga^{III} , and Ge^{IV} Complexes of a Ligand Analogue. *Inorg. Chem.* **2007**, 46 (19), 451–457.
- (62) Hayley R. Green and Gareth O. Lloyd. Porous Metal Organic Polygons and Polyhedra – Intrinsic vs. Extrinsic Porosity in *Functional Supramolecular Materials: From Surfaces to MOFs*; pp 297-324, Royal Society of Chemistry, 2017.
- (63) Percástegui, E. G.; Ronson, T. K.; Nitschke, J. R. Design and Applications of Water-Soluble Coordination Cages. *Chem. Rev.* **2020**, 120 (24), 13480–13544. <https://doi.org/10.1021/acs.chemrev.0c00672>.
- (64) Chen, L.-J.; Yang, H.-B.; Shionoya, M. Chiral Metallosupramolecular

- Architectures. *Chem. Soc. Rev.* **2017**, *46* (9), 2555–2576. <https://doi.org/10.1039/C7CS00173H>.
- (65) Fiedler, D.; Leung, D. H.; Bergman, R. G.; Raymond, K. N. Enantioselective Guest Binding and Dynamic Resolution of Cationic Ruthenium Complexes by a Chiral Metal–Ligand Assembly. *J. Am. Chem. Soc.* **2004**, *126* (12), 3674–3675. <https://doi.org/10.1021/ja039225a>.
- (66) Sreenivasulu, B.; Vittal, J. J. Helix inside a Helix: Encapsulation of Hydrogen-Bonded Water Molecules in a Staircase Coordination Polymer. *Angew. Chem. Int. Ed.* **2004**, *43* (43), 5769–5772. <https://doi.org/10.1002/anie.200460516>.
- (67) Lou, B.; Jiang, F.; Yuan, D.; Wu, B.; Hong, M. Synthesis and Characterization of a 3D H-Bonded Supramolecular Complex with Chiral Channels Encapsulating 1D Left-Handed Helical Water Chains. *Eur. J. Inorg. Chem.* **2005**, (16), 3214–3216. <https://doi.org/10.1002/ejic.200500324>.
- (68) Xu, J.; Wang, R.; Li, Y.; Gao, Z.; Yao, R.; Wang, S.; Wu, B. Chiral Supramolecular Frameworks Based on Chiral Metalloacycles: Crystal Structures and Photophysical Properties. *Eur. J. Inorg. Chem.* **2012**, (20), 3349–3360. <https://doi.org/10.1002/ejic.201200100>.
- (69) Rudolf Seidl, P.; Fernandes Dias, J. NMR Spectra of Hydroxylamines, Oximes and Hydroxamic Acids. *PATAI'S Chemistry of Functional Groups*. Wiley, 2010. <https://doi.org/10.1002/9780470682531.pat0456>.
- (70) Métro, T. X.; Martinez, J.; Lamaty, F. 1,1'-Carbonyldiimidazole and Mechanochemistry: A Shining Green Combination. *ACS Sustain. Chem. Eng.* **2017**, *5* (11), 9599–9602. <https://doi.org/10.1021/acssuschemeng.7b03260>.
- (71) Thomas, M.; Alsarraf, J.; Araji, N.; Tranoy-Opalinski, I.; Renoux, B.; Papot, S. The Lossen Rearrangement from Free Hydroxamic Acids. *Org. Biomol. Chem.* **2019**, *17* (22), 5420–5427. <https://doi.org/10.1039/C9OB00789J>.
- (72) Johann, T.; Keth, J.; Bros, M.; Frey, H. A General Concept for the Introduction of Hydroxamic Acids into Polymers. *Chem. Sci.* **2019**, *10* (29), 7009–7022. <https://doi.org/10.1039/c9sc02557j>.
- (73) Macomber, R. S. An Introduction to NMR Titration for Studying Rapid Reversible

- Complexation. *J. Chem. Educ.* **1992**, *69* (5), 375. <https://doi.org/10.1021/ed069p375>.
- (74) Lehr, M.; Paschelke, T.; Trumpf, E.; Vogt, A.-M.; Näther, C.; Sönnichsen, F. D.; McConnell, A. J. A Paramagnetic NMR Spectroscopy Toolbox for the Characterisation of Paramagnetic/Spin-Crossover Coordination Complexes and Metal–Organic Cages. *Angew. Chem. Int. Ed.* **2020**, *59* (43), 19344–19351. <https://doi.org/10.1002/anie.202008439>.
- (75) Markus, A.; Oliver, B.; Roland, F. “Size-Selectivity” in the Template-Directed Assembly of Dinuclear Triple-Stranded Helicates. *Proc. Natl. Acad. Sci.* **2002**, *99* (8), 4867–4872. <https://doi.org/10.1073/pnas.062600799>.
- (76) Piguet, C.; Bernardinelli, G.; Hopfgartner, G. Helicates as Versatile Supramolecular Complexes. *Chem. Rev.* **1997**, *97* (6), 2005–2062. <https://doi.org/10.1021/cr960053s>.
- (77) Caulder, D. L.; Raymond, K. N. The Rational Design of High Symmetry Coordination Clusters. *J. Chem. Soc., Dalton Trans.* **1999**, No. 8, 1185–1200. <https://doi.org/10.1039/a808370c>.
- (78) Andersen, U. N.; Seeber, G.; Fiedler, D.; Raymond, K. N.; Lin, D.; Harris, D. Characterization of Self-Assembled Supramolecular [Ga₄L₆] Host-Guest Complexes by Electrospray Ionization Mass Spectrometry. *J. Am. Soc. Mass Spectrom.* **2006**, *17* (3), 292–296. <https://doi.org/10.1016/j.jasms.2005.10.011>.
- (79) Pradhan, S.; John, R. P. A Discrete Self-Assembled Palladium Nano-Cage Catalyses Suzuki-Miyaura Coupling Heterogeneously and Heck-Mizoroki Coupling Homogeneously. *New J. Chem.* **2015**, *39* (7), 5759–5766. <https://doi.org/10.1039/c5nj01032b>.
- (80) Naumov, A. A.; Goletskii, N. D.; Zilberman, B. Y.; Murzin, A. A. Specific Features of Decomposition of Hydroxamic Acids in Two-Phase Nitric Acid Systems with Alcohols and TBP, as Applied to ⁹⁹Mo Stripping. *Radiochemistry* **2017**, *59* (6), 596–606. <https://doi.org/10.1134/S1066362217060078>.
- (81) Christie, R. M.; Moss, S. Cyclisation of Schiff Bases Containing Amide or Hydroxamic Acid Groups to 1,2-Dihydroquinazolin-4-Ones; Thermal

- Decomposition Reactions of the 1,2-Dihydroquinazolin-4-Ones. *J. Chem. Soc. Perkin Trans. 1* **1985**, No. 0, 2779–2783. <https://doi.org/10.1039/P19850002779>.
- (82) Berndt, D. C.; Fuller, R. L. The Kinetics and Mechanism of the Hydrolysis of Benzohydroxamic Acid. *J. Org. Chem.* **1966**, *31* (10), 3312–3314. <https://doi.org/10.1021/jo01348a048>.
- (83) Mocci, R.; De Luca, L.; Delogu, F.; Porcheddu, A. An Environmentally Sustainable Mechanochemical Route to Hydroxamic Acid Derivatives. *Adv. Synth. Catal.* **2016**, *358* (19), 3135–3144. <https://doi.org/10.1002/adsc.201600350>.
- (84) McCudden, C. R.; Kraus, V. B. Biochemistry of Amino Acid Racemization and Clinical Application to Musculoskeletal Disease. *Clin. Biochem.* **2006**, *39* (12), 1112–1130. <https://doi.org/10.1016/j.clinbiochem.2006.07.009>.
- (85) Ballard, A.; Narduolo, S.; Ahmed, H. O.; Keymer, N. I.; Asaad, N.; Cosgrove, D. A.; Buurma, N. J.; Leach, A. G. Racemisation in Chemistry and Biology. *Chem. Eur. J.* **2020**, *26* (17), 3661–3687. <https://doi.org/10.1002/chem.201903917>.
- (86) Hoffmann, R. W. Meso Compounds: Stepchildren or Favored Children of Stereoselective Synthesis? *Angew. Chem. Int. Ed.* **2003**, *42* (10), 1096–1109. <https://doi.org/10.1002/anie.200390291>.
- (87) Nagaraj, R.; Balaram, P. Racemization at Proline Residues during Peptide Bond Formation: A Study of Diastereomeric Mixtures of Synthetic Alamethicin Fragments by 270 MHz ¹H NMR. *Tetrahedron* **1981**, *37* (10), 2001–2005. [https://doi.org/10.1016/S0040-4020\(01\)97953-0](https://doi.org/10.1016/S0040-4020(01)97953-0).
- (88) Adams, R. W.; Byrne, L.; Király, P.; Foroozandeh, M.; Paudel, L.; Nilsson, M.; Clayden, J.; Morris, G. A. Diastereomeric Ratio Determination by High Sensitivity Band-Selective Pure Shift NMR Spectroscopy. *Chem. Commun.* **2014**, *50* (19), 2512–2514. <https://doi.org/10.1039/C3CC49659G>.
- (89) Otte, D. A. L.; Borchmann, D. E.; Lin, C.; Weck, M.; Woerpel, K. A. ¹³C NMR Spectroscopy for the Quantitative Determination of Compound Ratios and Polymer End Groups. *Org. Lett.* **2014**, *16* (6), 1566–1569. <https://doi.org/10.1021/ol403776k>.
- (90) Beissel, T.; Powers, R. E.; Parac, T. N.; Raymond, K. N. Dynamic Isomerization

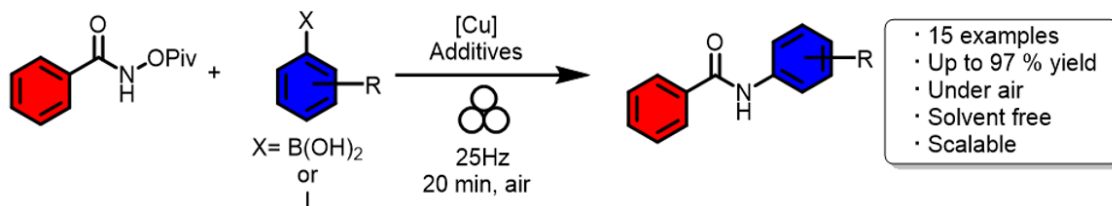
- of a Supramolecular Tetrahedral M_4L_6 Cluster. *J. Am. Chem. Soc.* **1999**, *121* (17), 4200–4206. <https://doi.org/10.1021/ja984046s>.
- (91) Holloway, L. R.; McGarraugh, H. H.; Young, M. C.; Sontising, W.; Beran, G. J. O.; Hooley, R. J. Structural Switching in Self-Assembled Metal–Ligand Helicate Complexes via Ligand-Centered Reactions. *Chem. Sci.* **2016**, *7* (7), 4423–4427. <https://doi.org/10.1039/C6SC01038E>.
- (92) Scherer, M.; Caulder, D. L.; Johnson, D. W.; Raymond, K. N. Triple Helicate—Tetrahedral Cluster Interconversion Controlled by Host–Guest Interactions. *Angew. Chem. Int. Ed.* **1999**, *38* (11), 1587–1592. [https://doi.org/10.1002/\(SICI\)1521-3773\(19990601\)38:11<1587::AID-ANIE1587>3.0.CO;2-R](https://doi.org/10.1002/(SICI)1521-3773(19990601)38:11<1587::AID-ANIE1587>3.0.CO;2-R).
- (93) Piskorz, T. K.; Martí-Centelles, V.; Young, T. A.; Lusby, P. J.; Duarte, F. Computational Modeling of Supramolecular Metallo–Organic Cages—Challenges and Opportunities. *ACS Catal.* **2022**, *12* (10), 5806–5826. <https://doi.org/10.1021/acscatal.2c00837>.
- (94) Glasson, C. R. K.; Meehan, G. V.; Motti, C. A.; Clegg, J. K.; Turner, P.; Jensen, P.; Lindoy, L. F. New Nickel(II) and Iron(II) Helicates and Tetrahedra Derived from Expanded Quaterpyridines. *Dalt. Trans.* **2011**, *40* (40), 10481–10490. <https://doi.org/10.1039/C1DT10667H>.
- (95) Wenjing, M.; K., R. T.; R., N. J. Symmetry Breaking in Self-Assembled M_4L_6 Cage Complexes. *Proc. Natl. Acad. Sci.* **2013**, *110* (26), 10531–10535. <https://doi.org/10.1073/pnas.1302683110>.
- (96) Ramamurthy, V. Photochemistry in a Capsule: Controlling Excited State Dynamics via Confinement. *Chem. Commun.* **2022**, *58* (46), 6571–6585. <https://doi.org/10.1039/D2CC01758J>.
- (97) Chen, S.; Li, K.; Zhao, F.; Zhang, L.; Pan, M.; Fan, Y.-Z.; Guo, J.; Shi, J.; Su, C.-Y. A Metal–Organic Cage Incorporating Multiple Light Harvesting and Catalytic Centres for Photochemical Hydrogen Production. *Nat. Commun.* **2016**, *7* (1), 13169. <https://doi.org/10.1038/ncomms13169>.
- (98) Casellas, N. M.; Dai, G.; Xue, E. Y.; Fonseca, A.; Ng, D. K. P.; García-Iglesias,

- M.; Torres, T. A Self-Assembled Subphthalocyanine-Based Nanophotosensitizer for Photodynamic Therapy. *Chem. Commun.* **2022**, 58 (5), 669–672. <https://doi.org/10.1039/D1CC05977G>.
- (99) Sunohara, H.; Koyamada, K.; Takezawa, H.; Fujita, M. An Ir₃L₂ Complex with Anion Binding Pockets: Photocatalytic E–Z Isomerization *via* Molecular Recognition. *Chem. Commun.* **2021**, 57 (73), 9300–9302. <https://doi.org/10.1039/D1CC03620C>.
- (100) Nakamura, M.; Tsukamoto, Y.; Ueta, T.; Sei, Y.; Fukushima, T.; Yoza, K.; Kobayashi, K. Cavitand-Based Pd-Pyridyl Coordination Capsules: Guest-Induced Homo- or Heterocapsule Selection and Applications of Homocapsules to the Protection of a Photosensitive Guest and Chiral Capsule Formation. *Chem. Asian J.* **2020**, 15 (14), 2218–2230. <https://doi.org/10.1002/asia.202000603>.
- (101) Purba, P. C.; Bhattacharyya, S.; Maity, M.; Mukhopadhyay, S.; Howlader, P.; Mukherjee, P. S. Linkage Induced Enhancement of Fluorescence in Metal–Carbene Bond Directed Metallacycles and Metallacages. *Chem. Commun.* **2019**, 55 (57), 8309–8312. <https://doi.org/10.1039/C9CC04444B>.
- (102) Ma, Y.; Zhang, Y.; Kong, L.; Yang, J. Mechanoresponsive Material of AIE-Active 1,4-Dihydropyrrolo[3,2-b]Pyrrole Luminophores Bearing Tetraphenylethylene Group with Rewritable Data Storage. *Molecules* **2018**, 23 (12), 1–10. <https://doi.org/10.3390/molecules23123255>.
- (103) Hou, H.; Liu, Y.; Feng, Q.; Tang, B. Z.; Li, K.; Li, Y. 2,5-Bis(4-Alkoxy-carbonylphenyl)-1,4-Diaryl-1,4-Dihydropyrrolo[3,2-b]Pyrrole (AAPP) AIEgens: Tunable RIR and TICT Characteristics and Their Multifunctional Applications. *Chem. Sci.* **2017**, 8 (10), 7258–7267. <https://doi.org/10.1039/c7sc03076b>.
- (104) Krzeszewski, M.; Thorsted, B.; Brewer, J.; Gryko, D. T. Tetraaryl-, Pentaaryl-, and Hexaaryl-1,4-Dihydropyrrolo[3,2-b]Pyrroles: Synthesis and Optical Properties. *J. Org. Chem.* **2014**, 79 (7), 3119–3128. <https://doi.org/10.1021/jo5002643>.
- (105) Fang, Y.; Xiao, Z.; Kirchon, A.; Li, J.; Jin, F.; Togo, T.; Zhang, L.; Zhu, C.; Zhou, H. Bimolecular Proximity of Ruthenium Complex and Methylene Blue within an Anionic Porous Coordination Cage for Enhancing Photocatalytic Activity. *Chem.*

Sci. **2019**. <https://doi.org/2019/SC/C8SC05315D>.

- (106) Martins, L. M.; de Faria Vieira, S.; Baldacim, G. B.; Bregadiolli, B. A.; Caraschi, J. C.; Batagin-Neto, A.; da Silva-Filho, L. C. Improved Synthesis of Tetraaryl-1,4-Dihydropyrrolo[3,2-b]Pyrroles a Promising Dye for Organic Electronic Devices: An Experimental and Theoretical Approach. *Dye. Pigment.* **2018**, *148*, 81–90. <https://doi.org/10.1016/j.dyepig.2017.08.056>.
- (107) Corsi, D. M.; Platas-Iglesias, C.; Van Bekkum, H.; Peters, J. A. Determination of Paramagnetic Lanthanide(III) Concentrations from Bulk Magnetic Susceptibility Shifts in NMR Spectra. *Magn. Reson. Chem.* **2001**, *39* (11), 723–726. <https://doi.org/10.1002/mrc.922>.
- (108) Siddique, R. G.; Arachchige, K. S. A.; AL-Fayaad, H. A.; Thoburn, J. D.; McMurtrie, J. C.; Clegg, J. K. Controlling the Complexity and Interconversion Mechanisms in Self-Assembled $[\text{Fe}_2\text{L}_3]^{4+}$ Helicates and $[\text{Fe}_4\text{L}_6]^{8+}$ Cages. *Angew. Chem. Int. Ed.* **2022**, *61* (7). <https://doi.org/10.1002/anie.202115555>.
- (109) Xie, D.; Slebodnick, C.; Gibson, H. W. Synthesis and Characterization of 24-Membered Cyclobis(Ethylene 2,6-Naphthalate). *J. Polym. Sci.* **2020**, *58* (7), 932–936. <https://doi.org/10.1002/pol.20190251>.

Chapter 5: Mechanochemically Mediated Synthesis of *N*-Aryl Benzamides from *O*-protected Hydroxamic Acids



5.1 Declaration

This chapter contains sections of work that have been published:

E. Broumidis, M. C. Jones, F. Vilela, G. O. Lloyd, *ChemPlusChem* **2020**, *85*, 1754.

As the primary author of this publication, I can confirm that most of the work is my own. The contributions of each collaborator are outlined below:

Emmanouil Broumidis: Discovery of the transformation, reaction optimisations, reaction scope, mechanistic experiments, data analysis, CAD design of milling jars, 3D printing, writing of the published manuscript (main text and supporting information).

Mary C. Jones: Batch photosensitisation experiment, collection of UV-Vis absorption spectrum of compound **2l**, manuscript revision.

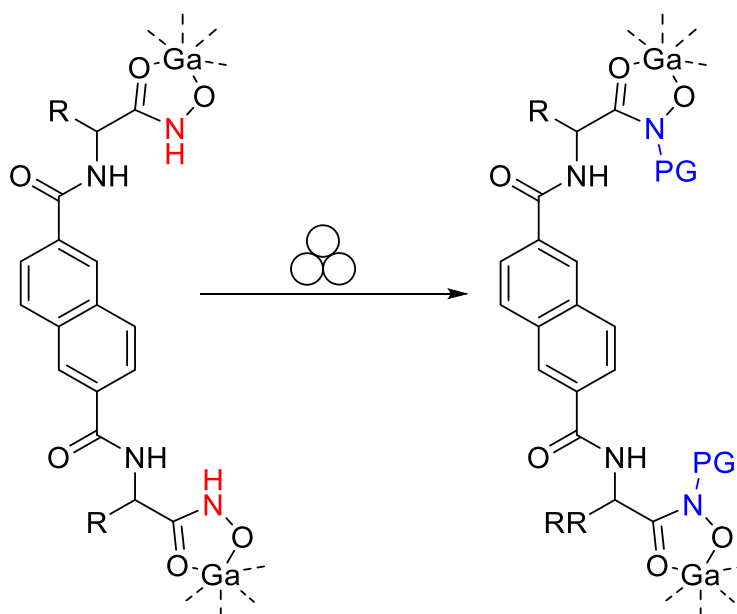
Adilet Zhakeyev: Preparation of photoactive resin, 3D printing of photoactive balls and jars (unpublished results).

Gareth O. Lloyd and Filipe Vilela: Overall project supervision, experiment design, manuscript review.

5.2 Background and Aims

This project started when a need for post-synthetic modification of the metal-organic assemblies that were described in Chapter 4 was identified as being potentially useful. In recent years, many such modification strategies have been reported, whereby the structure of a supramolecular cage is altered to change its properties.^{1,2} The main

modification on the hydroxamate linkers that we aimed to perform, was the substitution of the -NH part of the hydroxamate moiety, as this would in principle significantly alter key properties of the assemblies (Scheme 1). By varying the nature of the substituents we could engineer them to increase their solubility³ or tune the way in which they pack in the solid state,⁴ and therefore their crystallinity. Since both the HA linkers and their assemblies were particularly insoluble in most solvents, such modification could be carried out in a mechanochemical reactor.



Scheme 1. Proposed mechanochemical post-synthetic modification of the assemblies made in chapter 4. PG= protecting group.

A common choice of protecting groups to enhance the overall solubility of insoluble cages are alkyl chains.^{5,6} On the other hand, their presence would also increase the flexibility of the resulting cages, and their capacity to act as AIE agents could diminish, as it was discussed in Chapter 2. Thus, to minimise non-radiative relaxation processes, it was hypothesised that *N*-Aryl substitutions would be a suitable choice. Predicting the effect of these changes on the ability of the assemblies to crystallise is a more challenging undertaking, and many research groups are working towards the development of computational methods to help make such predictions.⁷

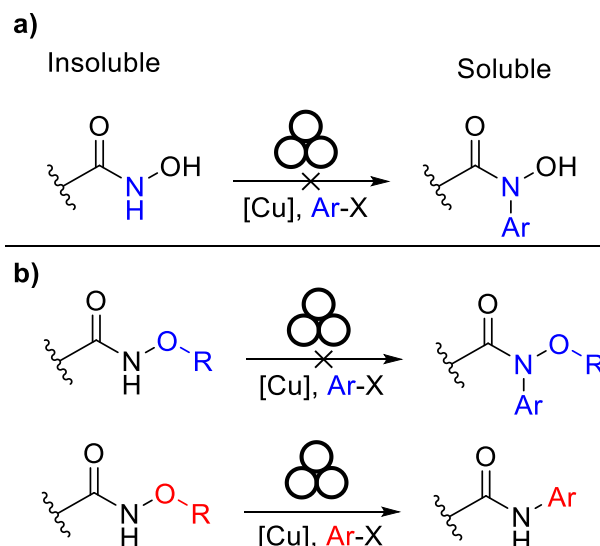
The most usual avenues for making these substitutions would be by reacting the corresponding HA ester,⁸ chloride,⁹ or acid¹⁰ precursors with an *N*-Aryl hydroxylamine salt. The downside of this methodology is the poor chemical stability¹¹ and the high cost of *N*-substituted hydroxylamines and their salts,¹² and thus, this renders the process of

making large quantities (gram-scale) of substituted linkers cost and time prohibitive. Another method includes the partial reduction of a nitro compound to the corresponding hydroxylamine. This method usually suffers from over reduction issues, often leading to reaction mixtures containing both the desired hydroxylamine and the corresponding amine compound.¹³ The reducing reagent varies depending on the substrate but zinc metal and Ag loaded TiO₂ nanoparticles have been successfully employed.¹⁴

However, all of these reactions need to occur in solution in order to succeed, and the *N*-hydroxylamine usually needs to be used immediately upon formation, since the freebase form is usually unstable.¹⁵ Moreover, while the aforementioned methodologies may be applied to the linker synthesis, they cannot be used on HA motifs, making them unsuitable for post-synthetic cage modification. Various methods for *N*-substitution of HAs are known, but usually they target specific HA-containing compounds and require the use of a solvent. To our knowledge at the time, a broadly applicable, solvent-free protocol for the *N*-substitution of HAs had not yet been reported, and as such we wanted to explore this further.

We wanted to develop a mechanosynthetic route that worked by directly reacting an aryl halide (inexpensive) with a hydroxamic acid to form the desired product. Essentially, the goal was to develop and optimise a well-known batch C-N coupling protocol such as the Ullmann coupling that utilises Cu (I) catalysts¹⁶ for mechanochemical use, and thus avoiding the use of solvents. While there are some examples of other type of couplings done in the ball mill (C-C couplings, Suzuki-Miyaura, oxidative couplings)¹⁷ there was still no example of a C-N Ullmann-type coupling in the literature.

It was soon realised that the *O*-unprotected HAs are not reactive towards those conditions, and thus *O*-protected starting materials were used (-OBz and -OMe mainly). Interestingly, the only reaction observed with those conditions, yielded the corresponding amide, as the -OBz group was exchanged for the Ar group, in low to moderate yields (Scheme 2). This result was something that Zhang *et al.* has reported, by reacting *O*-acetyl hydroxamic acids with boronic acids, in the presence of copper (I) and copper (II) catalysts.¹⁸



Scheme 2. a) Initial plan involved the conversion of an unprotected HA to a *N*-substituted HA under mechanochemical conditions; however, the desired product could not be obtained. b) An *O*-protected HA was tested as an alternative, but the corresponding amide was obtained instead.

Despite failing to develop a solvent free method for the synthesis of *N*-protected HAs, the preliminary results of this work showed us that it was possible to convert *O*-protected HAs into amides under mechanochemical conditions. Since at the time there were no other known solid-state Ullmann coupling methodologies, and our group was interested in promoting the use and versatility of new synthetic technologies, we felt developing this reaction further was a worthy endeavour. The following sections describe the process of optimising and exploring the scope of this reaction.

5.3 Abstract

Two robust and efficient mechanochemical protocols for the synthesis of an array of *N*-arylamides have been developed. This was achieved by a C-N cross-coupling between *O*-pivaloyl hydroxamic acids and aryl iodides or aryl boronic acids, in the presence of a stoichiometric amount of a copper mediator. The effectiveness of this method is highlighted by the high-yielding, scalable, and rapid synthesis of *N*-aryl amides, using a variety of deactivated and sterically encumbered substrates, whilst employing mild conditions in the absence of solvents. In addition, it was determined that whilst the *O*-pivaloyl hydroxamic acid precursors can be successfully synthesised mechanochemically, iron contamination originating from the steel milling jars was found

to occur which can hinder the efficacy of this process. Thus, and since steel milling jars are commonly used for mechanosynthesis, this iron leaching should be considered as a source of potential interference with the reaction. Furthermore, 3D printing was used to produce inexpensive, durable, and customisable milling jars which were used to successfully accommodate a scaled-up version of the two protocols.

5.4 Introduction

The amide functionality has proven to be extremely important in most areas of organic chemistry and is present in a vast number of contemporary pharmaceuticals, agrochemicals, polymers, as well as natural products and biological molecules.^{19,20} Since there is an intrinsic need for large scale production of amide-bearing compounds, it is imperative that improved and sustainable methods are developed to provide high atom efficiency, low energy consumption, and minimal waste, whilst maintaining acceptable yields.²¹ It is noted that within the pharmaceutical industry alone, amides constitute by far the most abundant functionality (16% of all reactions within the sector), and subsequently, synthetic routes that provide access to this moiety are the most commonly used in the sector.²² Aryl amides can be problematic to synthesise due to the reduced reactivity/nucleophilicity of the amine. Furthermore, it has been reported that around 85% of the chemicals that are being used are solvents,²¹ of which a large percentage are never recycled, ending up in the environment as pollutants. Large database searches have revealed that the most prevalent solvents employed in amide couplings are dichloromethane (DCM) and *N,N*-dimethylformamide (DMF), used in 36% and 47% of the reactions respectively.²³ It is widely accepted that both of these solvents pose issues,²⁴ both in handling them and discarding them to the environment.^{25,26} Thus, it is now becoming increasingly important for chemists to seriously consider implementing alternative and greener methods for synthesising compounds and mechanochemistry is a great means to achieve this. Traditionally, mechanochemistry was considered as a technique of less versatility and scope for chemists, and as a result, it has not been widely accepted by the synthetic community as a plausible method of inducing chemical reactions. However, this is now rapidly changing, as researchers are starting to recognise the versatility and potential mechanochemistry has to offer, mainly due to the advent of

green chemistry and the need to find more environmentally friendly and sustainable methods of producing chemicals, both in research laboratories^{17,27,28} and on an industrial scale.²⁹ These realisations have led to rapid developments in key areas of synthetic organic chemistry spanning from catalysis and coupling reactions³⁰ to more niche topics such as fullerene chemistry,³¹ photocatalysis,³² and supramolecular chemistry.³³ Through this apparent era of 'mechanochemical enlightenment', it has become clear that an optimised mechanochemical protocol can not only provide improved performance compared to equivalent batch reactions but it can also unlock new mechanistic pathways which lead to products previously unattainable through batch techniques.^{34,35} Amides have understandably been a target for mechanochemical synthesis with activated carboxylic acids (carbodiimides, for example), peptides, and materials being common themes. Herein we describe two mechanochemical protocols for the high yielding *N*-amidation of aryl iodides (protocol **A**) and aryl boronic acids (protocol **B**) by *O*-protected hydroxamic acids, mediated by the stoichiometric presence of a Cu(I/II) species.

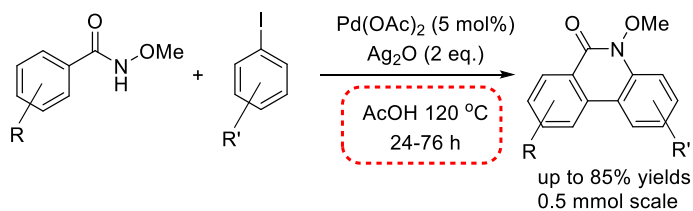
5.5 Results and Discussion

5.5.1 Mechanochemical SM Synthesis and Iron Leaching Problem

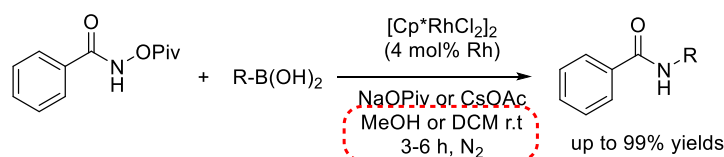
There are several examples within the literature^{18,36,37} (see Figure 1 for comparison of literature methods and work presented here) describing protected hydroxamic acids that can be converted into amides, and it is clear that high temperatures, inert atmospheres, harsh solvents and moderate to long reaction times are in most cases indispensable to achieve the desired outcome. Additionally, only one of the reports³⁶ employs aryl halides, where the starting reagent *N*-methoxybenzamide undergoes a double oxidative C-C and C-N bond formation to afford a cyclic phenanthridinone, circumventing the formation of a secondary amide. The most common coupling partners used in those reactions are boronic acids. Our main goal for this study was to find a set of more benign and sustainable reaction conditions that could be implemented with mechanochemistry. Initially, the possibility of using ball milling to gain access to the *O*-pivaloyl protected hydroxamic acids starting materials was examined (Scheme 3). It was found, that, although it was possible to achieve comparable yields with reduced reaction

times by applying the mainstream solution-based conditions^{18,38} to the ball mill, in the absence of a solvent, iron leaching from the steel jars occurred during the milling process.

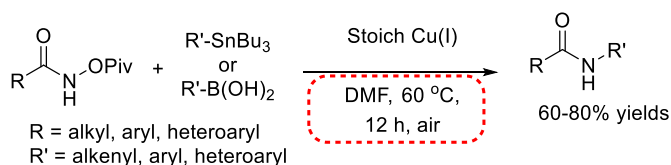
1. Wang *et al.*, *Angew. Chem. Int. Ed.* **2011**, 50, 1380–1383



2. Yasuhisa *et al.*, *Chem. Lett.* **2017**, 46, 463–465



3. Zhang *et al.*, *Org. Lett.* **2008**, 10, 3005–3008



4. This work

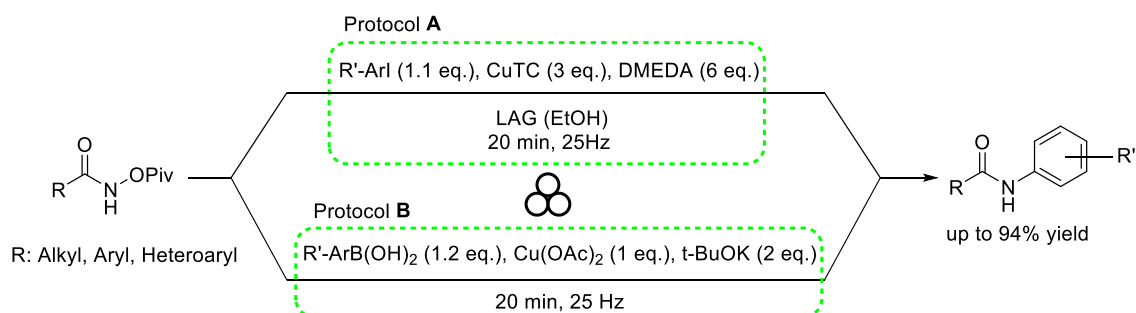
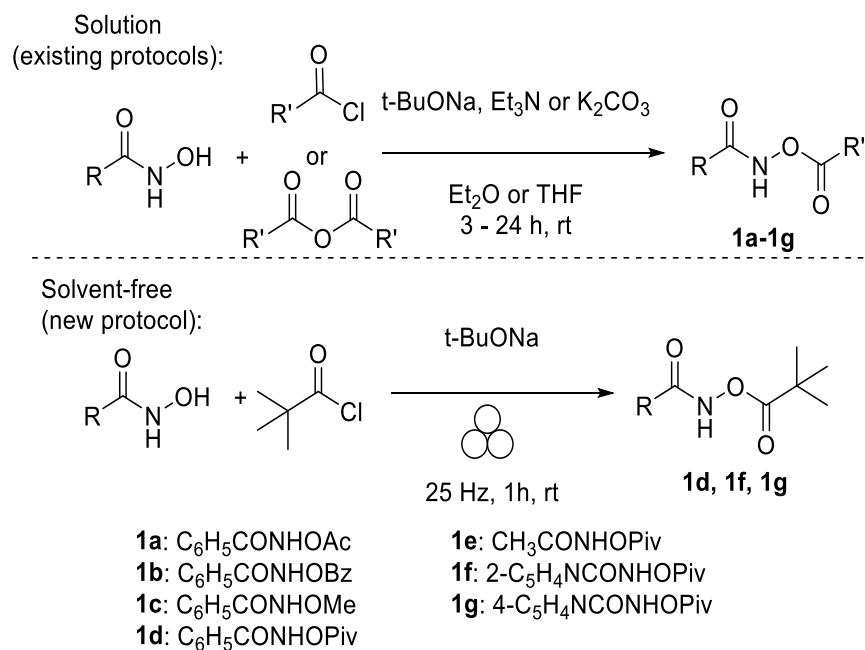


Figure 1. Comparison between previous *N*-benzamide synthetic contributions using *O*-protected hydroxamic acids and current work.



Scheme 3. Most common syntheses conditions of various *O*-protected hydroxamic acids involve the use of solvents such as diethyl ether (Et₂O) or tetrahydrofuran (THF).

It has also been shown that iron particles which become dislodged during the milling process can then be oxidised to form Fe(II) and Fe(III) species.³⁹ We found that when this occurs, the Fe-hydroxamate complex becomes unreactive and due to the paramagnetic nature of Fe(III), during NMR analysis we observed reduced relaxation times, which causes an extreme broadening of the NMR peaks (Figure 2 and SI, 5.8.3). Furthermore, energy dispersive x-ray spectroscopy (EDX) analysis with a scanning electron microscope (SEM) of pristine and milled benzohydroxamic acid samples confirmed the presence of iron and chromium in the latter samples, both of which are contained within the steel jars that were used.

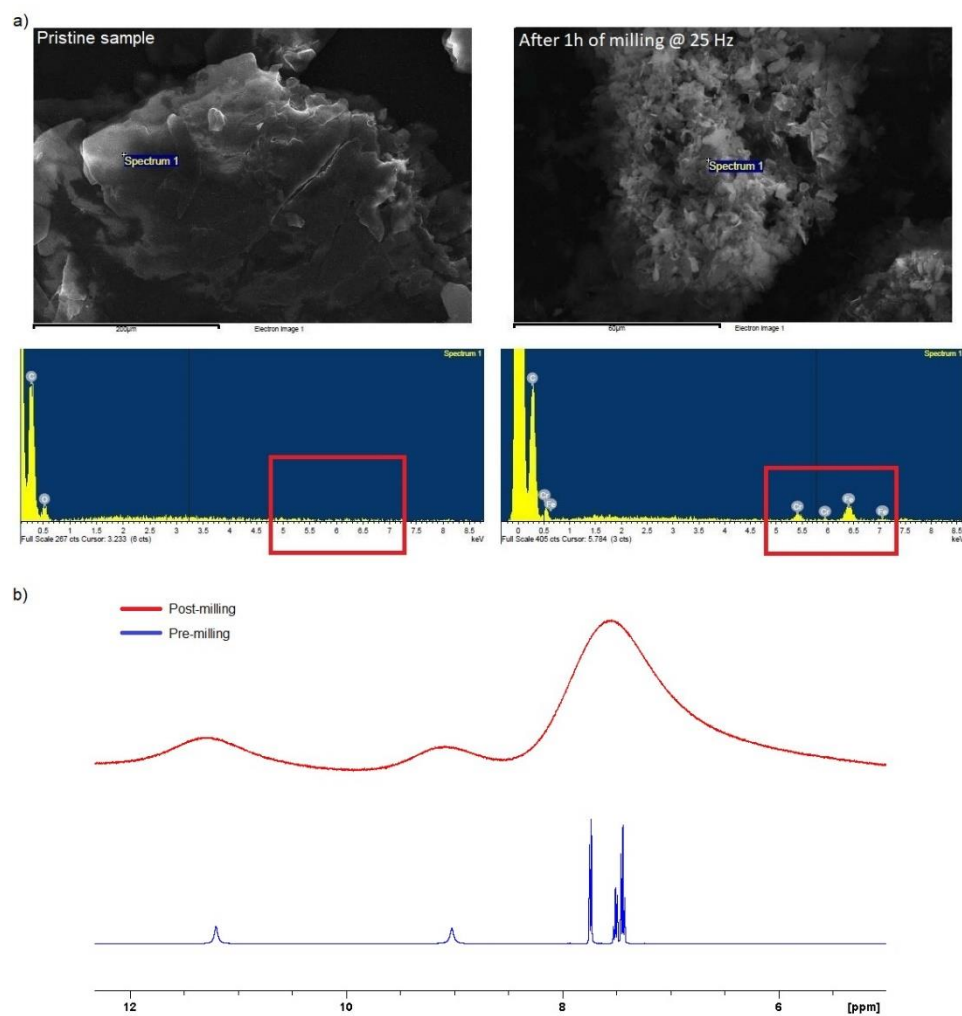


Figure 2. a) SEM/EDX analysis of pristine (left) and milled (right) benzohydroxamic acid clearly shows that iron and chromium leaches from the steel jars to the sample. b) Pre-milled and post-milled H-NMR spectra of benzohydroxamic acid illustrating peak broadening due to the presence of paramagnetic Fe(III).

It is interesting to note that Mocci *et al.*¹⁰ do not mention the leaching of iron during their hydroxamic acid mechanochemical synthesis. We can only speculate that ageing of the steel-constructed jars may be the cause of our observation of leaching and we advise when using mechanochemistry to be aware of this issue with steel grinding jars, as leaching of iron or chromium may not only interfere with the reactants but also catalyse reactions^{40,41} both of which may lead to inaccurate results.

Unsurprisingly, this leaching occasionally caused interference with the reaction leading to inconsistent results, as hydroxamic acids and their derivatives are well-known siderophores and iron sequestrers.^{42,43} As such, in order to reliably obtain the desired *O*-protected hydroxamic acids we opted to use traditional batch procedures, although we believe that future research endeavours focusing on addressing this issue are required to

allow iron-sensitive chemistries to work reliably under mechanochemical conditions using steel grinding jars. Use of jars made from different materials such as Teflon (PTFE) and agate may be a way to circumvent this issue, however, the aforementioned reaction did not work when we tried using PTFE instead of steel jars, perhaps due to their softness compared to steel.⁴⁴

5.5.2 Reaction Optimisation

For the optimisation of the Ullmann coupling (protocol **A**, Figure 1), we were interested in determining the optimal conditions for the preparation of *N*-phenylbenzamide (**2a**). Although synthesis of this compound is trivial,⁴⁵ the starting materials are relatively cheap, easily available, and allow for ease of testing and optimisation of the initial reaction conditions. These include the determination of an appropriate catalyst/promoter, base (if required), ligand, and protecting group for the HA. It was found that by using 3 equivalents (eq.) of copper (I) thiophene-2-carboxylate (CuTC), *N,N'*-dimethylethylenediamine (DMEDA) (6 eq.), *O*-pivaloyl protected benzohydroxamic acid and iodobenzene the Ullmann-type transformation (protocol **A**) proceeded to give the best results under liquid-assisted grinding (LAG, EtOH, $\eta = 0.16 \mu\text{L}/\text{mg}$)⁴⁶ mechanochemical transformations. No other additives were deemed necessary. All mechanochemical reactions were carried out using a 10 mL steel jar with 2 steel balls (8 mm in diameter), and the optimised reaction was complete in under 20 minutes, which is significantly less than comparable batch reactions.

With these optimal conditions in hand, we proceeded to investigate whether the use of LAG is necessary (Table 1). A range of solvents was tested spanning a wide spectrum of polarities. It immediately became obvious that using small amounts of EtOH has a profound effect on the efficiency of the reaction (entry 3). When the reaction was performed without any solvent, (entry 1) the yield dropped significantly, highlighting the importance of LAG in this mechanochemical synthesis.⁴⁷ The use of water as a LAG additive (entry 2) further reduced the overall yield, while DMF (entry 4) offers a substantial conversion but lower than EtOH. Non-polar LAGs did not affect the yield.

Table 1. Investigation of LAG effects on the yield of **2a**^[a].

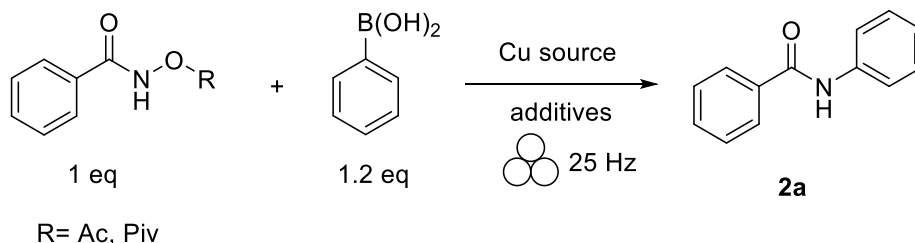
Entry	LAG ^[b]	Yield (%) ^[c]
1	Neat	65
2	Water	46
3	Ethanol (EtOH)	94
4	Dimethylformamide (DMF)	88
5	3-Hexyne	66
6	Toluene	65

[a] 10 mL stainless-steel jar with two 8 mm diameter stainless-steel balls were used for the ball-milling reactions. An average of two runs is reported for the ball-milling reactions. [b] $\eta = 0.16 \mu\text{L}/\text{mg}$, based on adding 100 μL of solvent in 618 mg of reactants. [c] Isolated yield

Olefins and alkynes are known to act as π -Lewis base ligands that can coordinate with various copper species and enhance the yields of Ullmann oxidative couplings.⁴⁸ Moreover, it was recently found^{28,49} that olefins can be used as effective molecular dispersants for solid-state Pd promoted cross-coupling reactions. For those reasons 3-hexyne was used to test whether any enhancement could be observed. The overall yield of the reaction (Table 1, entry 5) was no different than the LAG-free benchmark. We also noticed that the two best LAG additives (EtOH and DMF) were found to dissolve all components of the mixture well, albeit when we tried applying the same reaction protocol in solution the reactivity was reduced significantly (SI, 5.8.6). After establishing that EtOH is the most efficient LAG additive, we wanted to examine the respective reactivity of bromo- and chloro-benzene as coupling partners. It was found that, under the aforementioned optimal reaction conditions, bromobenzene only afforded **2a** at a yield of 16% while chlorobenzene was completely unreactive (SI, 5.8.2). This was not unexpected, as aryl iodides are known to be the most reactive aryl halides towards Ullmann couplings.⁵⁰ Commercial grinding jars are available in a range of materials therefore further optimisation may be achieved by changing the jars used. The reaction was repeated for jars and 8 mm balls made out of Teflon (PTFE) and poly(methyl methacrylate) (PMMA). It was found that stainless steel and Teflon had comparable performances, and the acrylic jars and balls did not perform as well (SI, 5.8.5).

In order to extend the utility of the *O*-protected hydroxamic acid starting materials, and inspired by previously reported⁵¹ solution-based *N*-amidations, we developed a separate,

mechanochemical Chan-Lam type coupling procedure (protocol **B**), which uses arylboronic acids as the coupling partner together with a stoichiometric amount of $\text{Cu}(\text{OAc})_2$ as a mediator.⁵² We initiated our optimisation (Scheme 4), by adopting the conditions that were developed for solution-based chemistry by Zhang *et al.*⁵¹



Scheme 4. The Chan-Lam reaction parameters that were explored for optimisation under mechanochemical conditions (protocol **B**).

We found that both acetyl (**1a**) and pivaloyl (**1d**) *O*-protected hydroxamic acids were effective coupling partners affording **2a** in a 90% and 92% yield, respectively. The presence of a base was deemed necessary for the reaction to proceed to completion and after a base screening, 2 equivalents of potassium *tert*-butoxide (*t*-BuOK) were found to be the best choice (SI, 5.8.1). In contrast with the Ullmann protocol **A**, the addition of a LAG solvent did not improve the reaction efficacy with a reduction in the overall yield when EtOH was used as a LAG component (SI, 5.8.1). The minimum amount of time for the reaction to go to completion was determined to be 20 minutes, which is comparable with the corresponding time for protocol **A**. It was observed that when the $\text{Cu}(\text{OAc})_2$ equivalents were less than one, the reaction did not proceed to completion. This result is in line with most Chan-Lam coupling procedures in the literature,⁵³ where a stoichiometric amount of copper is required. Overall, the optimised conditions were determined to be 1 eq. of **1d**, 1 eq. of $\text{Cu}(\text{OAc})_2$ and 2 eq. of *t*-BuOK which afforded product **2a** in high yield (92%) after 20 minutes of milling. For comparison, when applying these conditions to a solution-based set-up using various solvents and heating the reaction mixture we found that even after 16 hours the reaction was not complete and thin-layer chromatography (TLC) analysis revealed many side-products and unreacted starting material (SI, 5.8.6).

5.5.3 Reaction Scope

The optimised protocols (**A** and **B**) were applied to a range of different aryl iodides and aryl boronic acids to explore their effectiveness and versatility (Figure 3). Overall, both protocols **A** and **B** proved to be highly efficient and provided access to moderate to high yielding *N*-arylamides.

Compounds bearing electron-deficient functional groups (**2d**, **2f**, **2g**, **2i**, **2j**, **2l**, **2m**) and sterically encumbering functional groups (**2e**, **2h**, **2i**, **2o**) were accessed, although **2m** and **2o** only in trace amounts. Furthermore, protocol **A** also works when varying the starting *O*-protected hydroxamic acid, as demonstrated by the use of *N*-(pivaloyloxy)acetamide **1e** and *N*-(pivaloyloxy)picolinamide **1f** to give the commercial pharmaceutical paracetamol, **2k**, in moderate yield and traces of **2m**. Interestingly, when diiodo aryl starting materials were used only the monosubstituted compounds were formed (**2i**, **2l**, **2m**, **2l**), even when the CuTC and DMEDA equivalents were doubled. Similar results were observed under solution control conditions.

Heteroaryl **1f** was used to afford compound **2m**, but only a trace amount (< 5 % yield) was isolated and when *N*-(pivaloyloxy)isonicotinamide (**1g**) was used the reaction failed. Similarly, when these heteroaryl starting materials were used in conjunction with protocol **B** conditions, the reaction also did not work. We postulate that this unreactivity stems from the pyridyl moiety binding to the copper mediator.⁵⁴ Interestingly, when 1,4-diodobenzene was used under protocol **A** conditions, compound **2n** was isolated (27% yield) and no traces of diamide were detected in the reaction mixture. Even when we used 2 eq. of **1d** only the monoamide **2n** formed, despite having a second iodine available for further cross-coupling. This apparent inertness of **2n** towards protocol **A**'s Ullmann-like conditions was further established when we used a pure sample of **2n** as the halide source and it did not react with **1d**.

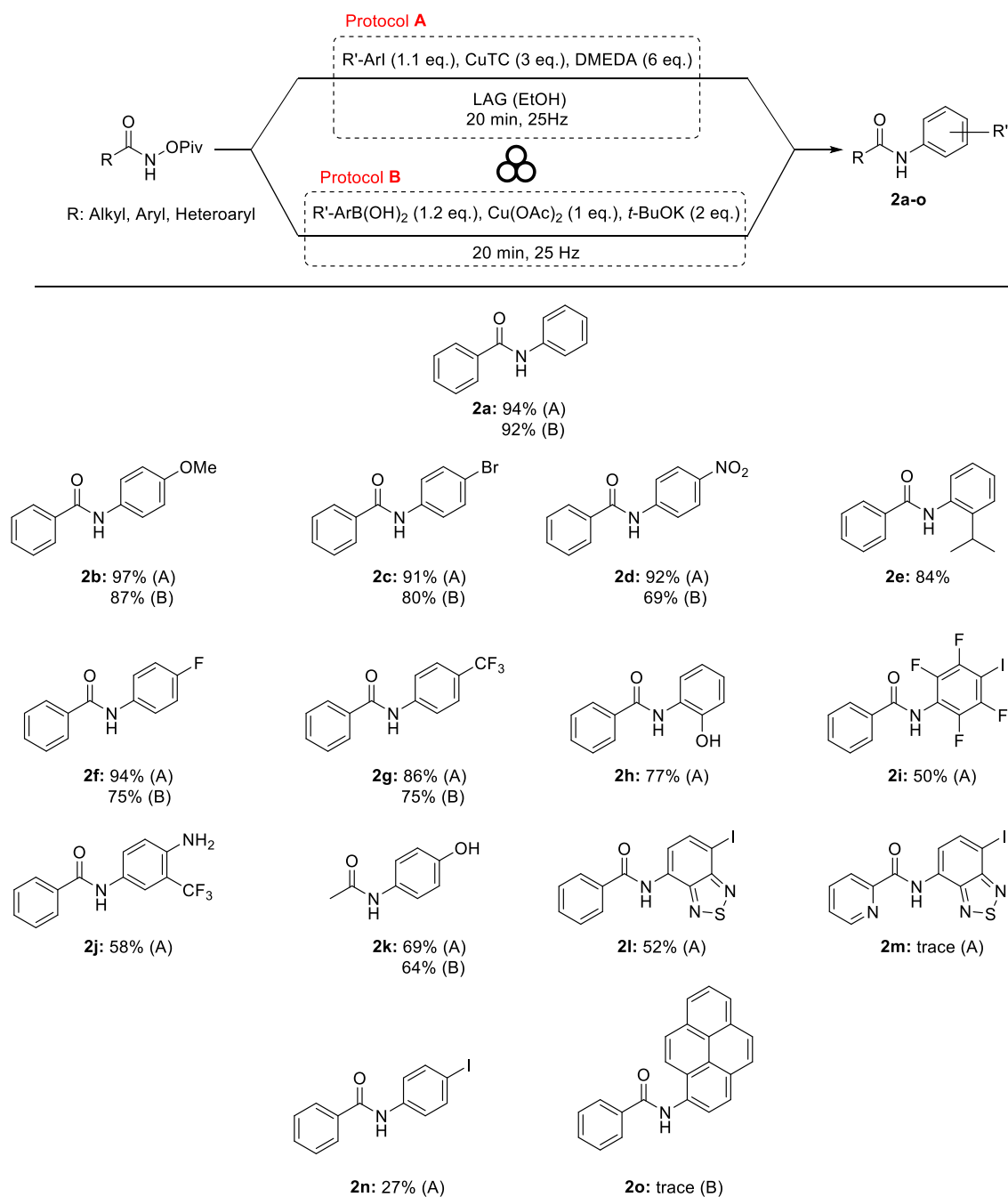


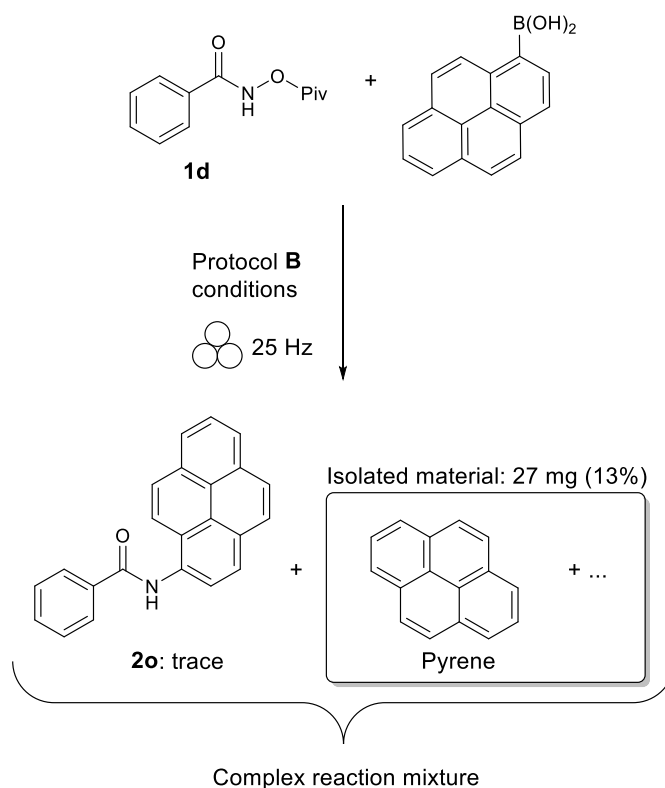
Figure 3. Reaction scope using the optimised protocols **A** and **B**.

Similar results were observed when 1,4-dibromobenzene and 4,7-diiodobenzo[*c*][1,2,5]thiadiazole were used for the formation of **2c** and **2l**, respectively. Overall, this selective reactivity towards aryl dihalides expands the scope of the method and makes it possible to synthesise halogen-bearing *N*-benzamides which can be then used for further synthetic modifications.

We postulated that the electron donor-acceptor (D-A) type compound, **2l**, could be used for photochemical applications. This was demonstrated by using it as a photosensitiser

for the mechanochemically-assisted solid-state photocatalytic (MASSPC)⁵⁵ conversion of anthracene to anthracene-endoperoxide (SI, 5.8.8 and 5.8.9) which was subsequently catalytically decomposed to anthraquinone.⁵⁶

Since polycyclic aromatic hydrocarbons (PAHs) are known for their low solubility in most organic solvents, due to strong intermolecular π - π interactions which stem from their extended planar structures,⁵⁷ we decided to use pyrene-1-boronic acid as a coupling partner to **1d** to gain access the corresponding *N*-benzamide **2o** via protocol **B**. Unexpectedly, after 20 minutes of milling, TLC analysis of the reaction mixture showed a multitude of trailing spots, indicating a deviation from the expected outcome. Upon subjecting the reaction mixture to mass spectrometry (MS) analysis, it was revealed that the target amide **2o** was present amongst other side-products. Purification of the crude reaction mixture *via* preparative thin layer chromatography afforded 27 mg of a yellow solid (13% yield), however, we were not able to isolate amide **2o**. Interestingly, upon analysis, the isolated yellow solid was found to be primarily pyrene and although it was contaminated with other by-products it was reasonably pure (based on the number of MS peaks) (Scheme 5).

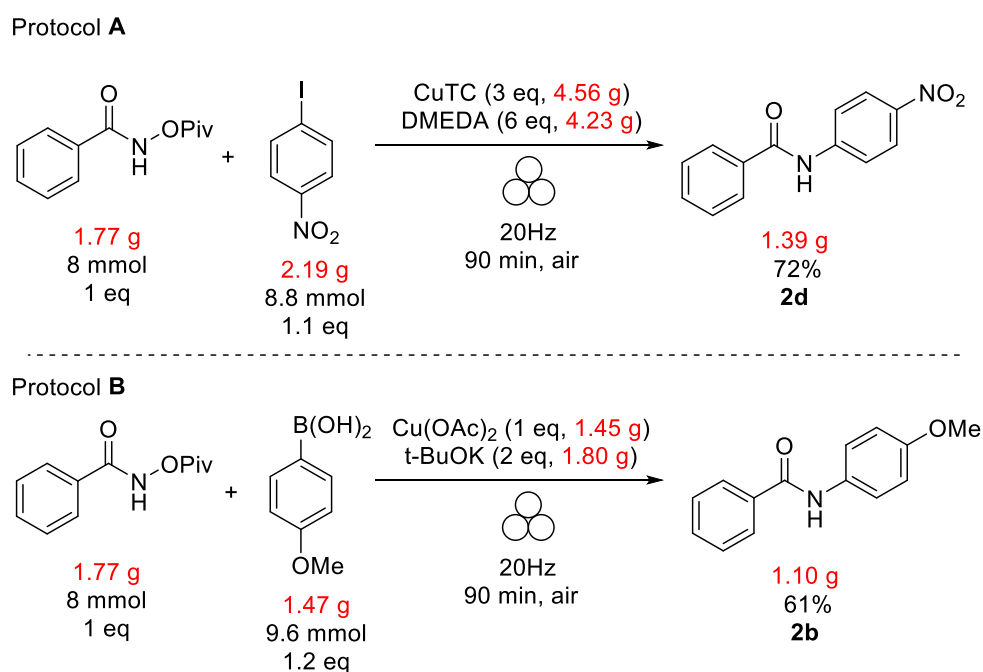


Scheme 5. The mechanochemical reaction between **1d** and pyrene-1-boronic acid under protocol **B** conditions leads to the formation of pyrene as the major isolatable product.

We postulate that the formation of pyrene can be the result of a protodeboronation side-reaction which may have been catalysed by the presence of $\text{Cu}(\text{OAc})_2$. A solution-based copper catalysed protodeboronation procedure under basic conditions was reported in 2014,⁵⁸ however, to the best of our knowledge, this is the first example of a mechanochemical protodeboronation reaction. Although historically protodeboronations have been considered of lesser importance by organic chemists, recently this reaction has found a variety of applications in synthetic procedures^{59,60} and thus the aforementioned example may form a stepping stone for further development of such solventless protodeboronations. In general, protocol **B** gave slightly lower yields than protocol **A**, which can be rationalised since we know that side-reactions such as protodeboronations may occur, under protocol's **B** conditions.

5.5.4 Custom 3D Printed Jars for Reaction Scale-Up

We found that both protocols are scalable up to the gram scale with only slight modifications (Scheme 6). Machining⁶¹ and 3D printing of custom milling jars⁶² are examples of customisation techniques mechanochemists have used in the past to adjust the milling jars to their needs.



Scheme 6. Gram-scale synthesis using protocols **A** and **B**.

To accommodate the large quantity of reactants, custom milling jars were made using a commercial 3D printer that uses methacrylate photopolymers to produce the desired object *via* a stereolithographic (SLA) printing technique.⁶³ The 3D printed jar that was used was printed using a commercial Form 2 SLA printer along with tough v5 resin, both supplied by Formlabs.⁶⁴ The jars had an internal volume of 70 mL, a wall thickness of 10 mm and could easily accommodate the reactants, which combined had a mass of 12.75 g and 6.49 g for protocols **A** and **B**, respectively. The milling frequency was reduced to 20 Hz to ensure that the printed jars could withstand the prolonged milling forces, as it was found that at 25 Hz and above, cracks would form on the inner surface of the jars after about 30 – 45 minutes of milling. As a result of the lower milling frequency, the reaction time to completion increased to about 90 minutes, for both protocols.

Initially, 25 x 8 mm Teflon balls with a total mass of 6 g were used (protocol **A**), but the mixture remained unreactive. However, when 6 ZrO₂ balls of variable diameter (6 – 15 mm) were used with a total mass of 16.11 g, the reaction gave product **2d** at 72% yield. This agrees with the studies made by Fischer *et al.*,⁶⁵ which showed that the total energy input of each collision during the milling process has a higher impact on the reactivity than the number of collisions during the milling process. Similarly, by using the mixed ZrO₂ balls, protocol **B** was successfully used at gram scale and afforded **2b** at 61%.

5.6 Conclusions

We report here the synthesis of amides using two mechanochemical protocols. As a comparison to previously reported methodologies, we believe that these methods add to the current knowledge base. As early as 2008, Gao and Wang⁶⁶ used potassium peroxymonosulfate, also known as Oxone, as an environmentally friendly non-toxic oxidant⁶⁷ to synthesise a range of aromatic benzamides by oxidative amidation of aldehydes with anilines under mechanochemical, solvent-free conditions. Other notable amide synthesis examples include mechanochemically activating carboxylic acids using *N*-ethyl-*N'*-(3-dimethylaminopropyl)carbodiimide hydrochloride (EDC·HCl) for the chemoselective and high yielding synthesis of aromatic amides and dipeptides, developed by Štrukil *et al.*⁶⁸ A similarly enticing report emerged in 2013 by Bonnamour *et al.*⁶⁹ demonstrating a method that uses EtOAc LAG mechanochemistry to access a variety of

peptides in high yields after 20 minutes of milling, compared to traditional solution syntheses which primarily use harsh solvents such as DMF. Finally, a more recent example from 2020 by Dayaker *et al.*,²⁷ introduced a copper-catalysed milling synthesis affording a plethora of carbamoyl-amides in high yields, whilst analogous batch experiments required high temperatures to work, while producing unwanted by-products not seen under mechanochemical conditions. These examples are a small part of an ongoing effort for utilising mechanochemical techniques to form amide and peptide bonds and they all operate under the same principles as our study, offering high yielding amide syntheses, minimal ecological impact, chemoselectivity, minimisation of unwanted by-products, and synthesis of difficult-to-access amides (e.g., aryl amides).

In summary, we developed two high yielding and scalable mechanochemical protocols that provide access to various secondary *N*-arylamides from readily available *O*-protected hydroxamic acids, iodoaryls and arylboronic acids. As the industrial community recognises the need for the development of new and sustainable amidation methodologies, this work acts as a proof-of-concept that may encourage other researchers to delve into solvent-free syntheses of amides and utilise the many benefits mechanochemistry has to offer compared to the traditional batch-based chemistries. Protocol **B** produced lower yields than protocol **A**, most likely due to protodeboronation acting as a side-reaction.

In addition, we identified and highlighted the fact that iron leaching originating from the steel milling jars should be considered when using reactants with high affinity for iron such as hydroxamic acids or when iron contamination may alter the reaction outcome. Moreover, we utilised SLA 3D printing to produce jars that were suitable for scaling up the new synthetic protocols. Finally, to expand the scope of the methodology that was developed, further work is currently underway that aims to synthesise efficient BTZ-containing *N*-Arylamides for MASSPC ¹O₂ generation.

5.7 Future Work

The successful implementation of a MASSPC reaction during this project, paired with our group's interest for the development of bespoke 3D printed continuous flow photoreactors^{70,71} inspired us to utilise the same technology for the fabrication of a photoactive milling jar and balls, to be used for heterogeneous, solvent-free ROS generation. Heterogeneous photocatalysts are typically inferior to homogeneous systems as it is difficult for photons to penetrate through a materials surface and their characterisation can be challenging.⁷² Additionally, the photocatalysis events are localised to the materials surface, hence efficient mass transport of the adsorbing reactants, and desorbing products at the surface is critical to productivity.⁷³ To overcome these obstacles, we used a 2,1,3-benzothiadiazole (BTZ) enriched photopolymerisable resin for SLA 3D printing, which enables us to confine a photocatalyst material within a custom milling jar and balls. These are semi-transparent and have high surface to volume ratio, providing efficient irradiation of the material (Figure 4). The pressure generated from individual impacts during milling greatly enhances the mass transfer at the photocatalyst surface, and should provide systems, which can be competitive with homogeneous photocatalysts in terms of kinetics, but with far greater productivity and reduced purification requirements.



Figure 4. a) Example of photoactive 3D printed milling jar (right half), b) balls, and c) their fluorescence under long UV irradiation.

To test the efficacy of the aforementioned reactionware, we used two BTZ-enriched (0.1% loading by mass) balls (8 mm diameter) as photosensitisers for singlet oxygen ($^1\text{O}_2$)

production. Due to the unavailability of a sufficient quantity of photoactive resin at the time, only one-half of a jar that was printed contained BTZ, and thus we opted to test the balls only.

α -terpinene was ball-milled for 1 hour at 30 Hz under blue (420 nm) light irradiation (28 W light output, 3.5 W/cm² light intensity, OSA opto lights) using a 10 mL optically transparent poly(methyl methacrylate) (PMMA) jar (purchased from Form-tech Scientific). After the milling was complete, NMR analysis revealed the presence of ascaridole, which is an endoperoxide that forms when α -terpinene reacts with ¹O₂ (Figure 5). Although the conversion was low (3%), this was obtained without using the photoactive jars and can be optimised further.

We anticipate that future work will involve optimisation of the jar geometry, its internal volume, and the number of milling balls. Moreover, varying the photocatalyst loading in the resin, as well as using different types of resin materials should also be explored.

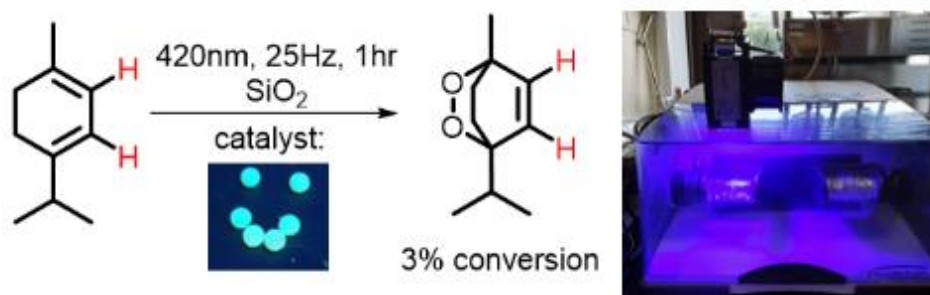


Figure 5. Demonstration of ¹O₂ generation using photoactive milling balls.

Time and progress dependent, this project has further avenues of development, such as: (i) Making a ‘library’ of photoactive jars/balls using different sensitizers; (ii) using photoactive jars/balls for the development of various solid-state photoredox transformations such as alkylations (Minisci) or trifluoromethylations;⁷⁴ (iii) using *in situ* X-ray diffraction to monitor and understand the mechanism of solid-state photochemistry.^{61,75}

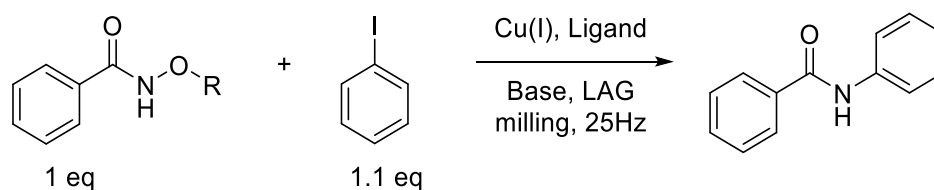
5.8 Supporting Information

5.8.1 Optimisation of protocols A and B

Based on literature information,⁷⁶ we wanted to investigate the potential of various copper (I) salts as possible catalysts for the Ullmann-type coupling reaction, mainly for the relative ease of access, low cost and low environmental impact compared to other coupling agents.⁷⁷ The main copper sources were, CuI and copper (I) thiophene-2-carboxylate (CuTC), since they are known to be very effective C-N coupling agents and their use has been widespread in many procedures.^{76,78} We investigated the use of tetramethylethylenediamine (TMEDA), *N,N'*-dimethylethylenediamine (DMEDA) and *trans-N,N'*-dimethylcyclohexane-1,2-diamine (DMCDA) as bidentate ligands as well as Na₂CO₃ and potassium *tert*-butoxide (*t-BuOK*) as bases, since those are one of the most common and effective Ullmann C-N coupling reagents reported in the literature.⁷⁹

Another consideration was the mechanochemical conditions that we were going to use, and we adopted the initial parameters of milling at 25 Hz, for 1-3 hours using two steel balls of 8 mm in diameter, paired with a 10 mL stainless-steel grinding jar. A liquid assisted grinding (LAG) approach was adopted using EtOH ($\eta = 0.16 \mu\text{L}/\text{mg}$)⁴⁶ based on other solid-state coupling protocols reported in the literature.^{17,80}

Regarding aryl halides we began by using iodobenzene, since its known that the iodo-substrates are usually the most reactive.⁸¹ As such, we applied these parameters, which resulted in the discovery of the optimal reaction conditions (Table S1).

Table S1. Optimisation conditions for protocol A^a.

Entry	R	Catalyst	Catalyst/Ligand (eq.)	Base (2eq)	Yield ^b (%)	Time (h)
1	Bz	CuI/DMCDA	1/2	K ₂ CO ₃	24	3
2	Bz	CuI/DMCDA	1/2	<i>t</i> -BuOK	46	3
3	Ac	CuI/DMCDA	1/2	K ₂ CO ₃	26	1
4	Ac	CuI/DMCDA	1/2	<i>t</i> -BuOK	44	1
5	Ac	CuI/TMEDA	1/2	K ₂ CO ₃	NR ^c	3
6	Ac	CuI/TMEDA	1/2	<i>t</i> -BuOK	NR ^c	3
7	Ac	CuI/DMEDA	1/2	K ₂ CO ₃	3	3
8	Ac	CuI/DMEDA	1/2	<i>t</i> -BuOK	12	3
9	Me	CuI/DMCDA	1/2	K ₂ CO ₃	NR ^c	3
10	Me	CuI/DMCDA	1/2	<i>t</i> -BuOK	NR ^c	3
11	Me	CuI/DMEDA	1/2	K ₂ CO ₃	IR ^d , 2	3
12	Me	CuI/DMEDA	1/2	<i>t</i> -BuOK	NR ^c	3
13	Bz	CuI/DMEDA	1/2	K ₂ CO ₃	30	2
14	Bz	CuI/DMEDA	1/2	<i>t</i> -BuOK	28	2
15	Piv	CuI/DMCDA	1/2	K ₂ CO ₃	IR ^d , 7	1
16	Piv	CuI/DMCDA	1/2	<i>t</i> -BuOK	52	1
17	Piv	CuI/TMEDA	1/2	K ₂ CO ₃	NR ^c	3
18	Piv	CuI/TMEDA	1/2	<i>t</i> -BuOK	NR ^c	3
19	Piv	CuI/DMEDA	1/2	K ₂ CO ₃	IR ^d , 9	1
20	Piv	CuI/DMEDA	1/2	<i>t</i> -BuOK	53	1
21	Piv	CuI/DMEDA	2/4	<i>t</i> -BuOK	78	1
22	Piv	CuI/DMEDA	3/6	<i>t</i> -BuOK	89	1
23	Piv	CuI/DMEDA	2/2	<i>t</i> -BuOK	21	2
24	Piv	CuI/DMEDA	3/6	K ₂ CO ₃	IR ^d , 75	1
25	Piv	CuI/DMCDA	3/6	<i>t</i> -BuOK	89	1

Entry	R	Catalyst	Catalyst/Ligand (eq.)	Base (2 eq.)	Yield ^b (%)	Time (h)
26	Ac	CuI/DMEDA	3/6	<i>t</i> -BuOK	37	1
27	Piv	CuTC/-	2/-	<i>t</i> -BuOK	NR ^c	3
28	Piv	CuTC/-	3/-	<i>t</i> -BuOK	IR ^d , trace	3
29	Piv	CuTC/DMEDA	3/6	<i>t</i> -BuOK	99	1
30	Piv	CuTC/DMEDA	3/6	K ₂ CO ₃	95	1
31	Piv	CuTC/DMEDA	3/6	<i>t</i> -BuOK	99	0.33
32	Piv	CuTC/DMEDA	3/6	-	93	1
33	Piv	CuTC/DMEDA	3/6	-	94	0.33
33	Piv	CuTC/DMEDA	1/2	<i>t</i> -BuOK	55	1

^a10 mL stainless-steel jars with two 8 mm diameter stainless-steel balls for the ball-milling reactions. The average of two runs is reported for the ball-milling reactions. LAG was EtOH, $\eta = 0.16 \mu\text{L}/\text{mg}$ ^bIsolated product, ^cNR: No reaction, ^dIR: Incomplete reaction (TLC).

Initially, we investigated the reaction using four different protecting groups, acetyl (Ac), benzoyl (Bz), methoxy (Me), and pivaloyl (Piv), to compare between their respective reactivities. It soon became apparent that all but the *O*-methoxy hydroxamic acids (**1c**) are relatively reactive towards iodobenzene, as even after 3 hours of milling no product was formed. Overall **1d** was deemed to be the most reactive of the protected hydroxamic acids (entry 20).

Additionally, it was revealed that the use of TMEDA was ineffective, and in all cases, no reactivity was observed, while both DMEDA and DMEDA performed equally well. For that reason, DMEDA was chosen as the best ligand since it is considerably more affordable than DMEDA. We then turned our attention to the amount of copper required, as it seemed that even after the addition of 1 equivalent (eq.) the yield would not exceed 53% (entry 20). The use of stoichiometric amounts of copper is widespread in Cu mediated Ullmann-type couplings, although the exact mechanism of the reaction is still under debate.⁸² Nevertheless, by increasing the total amount of Cu to 2 eq. (entry 21), the yield improved significantly and when 3 eq. were used (entry 22), 89% of product 2 was isolated, while *t*-BuOK consistently outperformed K₂CO₃ as a base.

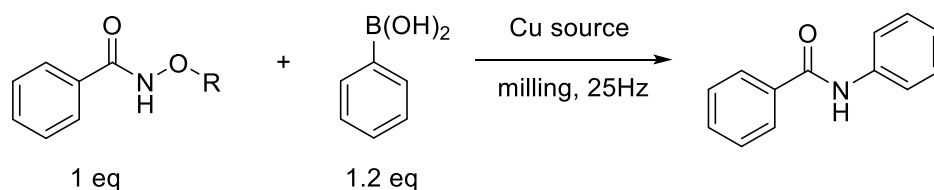
We then proceeded to test the efficacy of CuTC as a copper source and it proved to be able to surpass CuI in terms of performance, leading the reaction to completion in under 1 hour (entry 29). The ratio between copper and ligand was also probed, and we

concluded that 2 eq. of ligand are required for every eq. of copper. Absence of the ligand leads to the inhibition of the reaction, even after 3 hours, although a trace of **2a** was observed by TLC after using 3 eq. of CuTC (entries 27, 28). Using the best conditions, (entry 29) the actual reaction time was probed using TLC over 5-minute time intervals, and after 20 minutes the reaction had progressed to completion (entry 31). At this point, we also questioned whether the presence of a base was required. Although the base unquestionably played a role when the Cu/L ratio was at or below 2/4 (entry 21) when it was increased to 3/6 its use was no longer needed, as demonstrated by the high yield of 94% and low reaction time of 20 min (confirmed by TLC) (entry 33).

For the Chan-Lam based coupling (protocol **B**), we began the optimisation by using a similar, solution-based protocol first introduced by Zhang *et al.*,⁵¹ which uses acetyl *O*-protected hydroxamic acids and boronic acids as the coupling partners, along with a source of stoichiometric Cu(II). In Table S2 below we present the results of this optimisation.

It was found that both acetyl (**1a**) and pivaloyl (**1d**) *O*-protected hydroxamic acids were effective coupling partners. Furthermore, the presence of a base was deemed necessary for the reaction to proceed to completion. In contrast with the Ullmann (protocol **A**), the addition of a LAG solvent did not improve the reaction efficacy and it appeared that there is a reduction in the overall yield when EtOH was used as a LAG component (Table S2, entry 8). The minimum amount of time for the reaction to go to completion was determined to be 20 minutes, which is comparable with the corresponding time for protocol **A**.

Interestingly when the copper equivalents were less than 1, the reaction did not proceed to completion. This result is in line with most Chan-Lam coupling procedures in the literature, where a stoichiometric amount of copper is required. Overall, the optimised conditions were determined to be when **1d** was used with 1 eq. of Cu(OAc)₂ and 2 eq. of *t*-BuOK and the reaction afforded product **2a** in high yield (Table S2, entry 9).

Table S2. Optimisation conditions (protocol **B**)^a

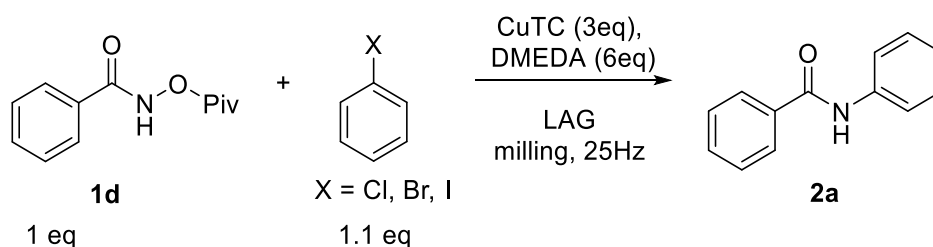
Entry	R	Catalyst (eq)	LAG	Base (2eq)	Yield ^b (%)	Time (h)
1	Ac	Cu(OAc) ₂ (0.1)	-	<i>t</i> -BuOK	IR ^d	3
2	Ac	Cu(OAc) ₂ (0.1)	EtOH	<i>t</i> -BuOK	IR ^d	3
3	Ac	Cu(OAc) ₂ (0.5)	-	<i>t</i> -BuOK	IR ^d	3
4	Ac	Cu(OAc) ₂ (1)	-	<i>t</i> -BuOK	90	1
5	Ac	Cu(OAc) ₂ (1)	-	<i>t</i> -BuOK	87	0.5
6	Ac	Cu(OAc) ₂ (1)	-	<i>t</i> -BuOK	88	0.33
7	Ac	Cu(OAc) ₂ (1)	-	<i>t</i> -BuOK	IR ^d	0.2
8	Ac	Cu(OAc) ₂ (1)	EtOH	<i>t</i> -BuOK	85	0.33
9	Piv	Cu(OAc) ₂ (1)	-	<i>t</i> -BuOK	92	0.33
10	Piv	Cu(OAc) ₂ (1)	-	-	NR ^c	3
11	Piv	Cu(OAc) ₂ (1)	-	K ₂ CO ₃	55	2
12	Piv	CuTC (1)	-	<i>t</i> -BuOK	NR ^c	3
13	Piv	CuTC (1)	-	-	NR ^c	3

^a10 mL stainless-steel jar with two 8 mm diameter stainless-steel balls for the ball-milling reactions. The average of two runs is reported for the ball-milling reactions. LAG was EtOH, $\eta = 0.16 \mu\text{L}/\text{mg}$ ^bIsolated product, ^cNR: No reaction, ^dIR: incomplete reaction (TLC).

5.8.2 Aryl Halide Scope

We wanted to examine the use of chloro- and bromobenzene to compare their reactivity with iodobenzene. We found that under the optimised milling conditions (Table S1, entry 33), bromobenzene only afforded **2a** at a yield of 16% (Table S3, entry 2) after 1 hour of milling, while chlorobenzene was completely unreactive towards compound **1d**. As such, because of the poor performance of chloro- and bromobenzene, aryl iodides were used throughout the additional experiments.

Table S3. Aryl halide scope



Entry	Ph-X	Base (2eq)	Yield (%)	Time (h)
1	Br	K ₂ CO ₃	14	1
2	Br	<i>t</i> -BuOK	16	1
3	Br	-	16	1
4	Cl	K ₂ CO ₃	NR ^a	1
5	Cl	<i>t</i> -BuOK	NR ^a	1

^a N.R : No reaction

5.8.3 Iron Leaching During Milling

In order to demonstrate the leaching of iron during the milling process, we utilised the strong iron affinity of most hydroxamic acids, which coincides with a purple colour.⁴² As such, we milled benzohydroxamic acid (54.9 mg, 0.4 mmol) in a 10 mL stainless-steel jar for 1 hour at 25 Hz. After the milling was complete, the jar was opened, and the striking colour difference (from white to dark red) confirmed that iron was bound with the hydroxamic acid (Figure S1). Further evidence for iron complexation came from the comparison between the ¹H NMR spectra of the compound pre- and post-milling (Figure 2b).

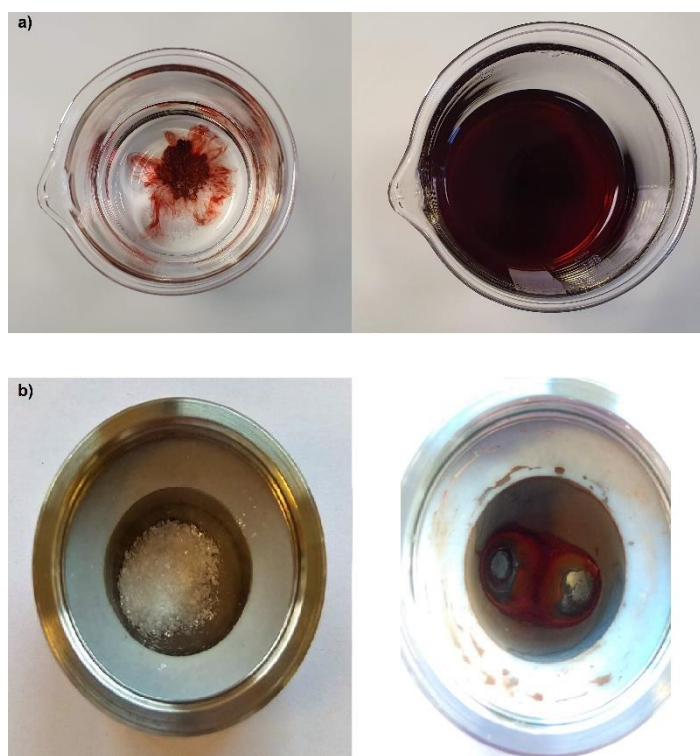


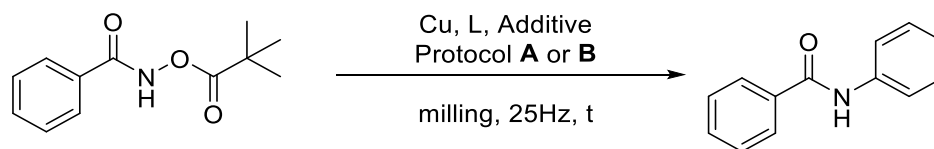
Figure S1. a) Deep purple/red colour generated by the addition of a small amount of $\text{Fe}(\text{NO}_3)_3$ to a solution of benzenhydroxamic acid in EtOH. b) Pristine sample of benzenhydroxamic acid prior to milling (left) and same sample after milling (right).

5.8.4 Effect of Various Catalysts and Additives

Besides CuI, CuTC and $\text{Cu}(\text{OAc})_2$, we also tried using other copper species, as well as iron(III) nitrate and iron(II) chloride, in order to test if they have any effect on the

reaction outcome. It is known that milling using steel grinding jars results in iron leaching into the reaction mixture and as a result of the grinding motion the iron particles can oxidise to form Fe(II) and Fe(III)³⁹ species, which could subsequently affect the outcome of the reaction (Table S4).

Table S4. Testing of different catalysts and additives



Entry	Protocol	Additive (3 eq.)	Catalyst/Ligand	Cat/L (eq.)	Yield ^a	Time (h)
1	A	TEMPO	CuTC/DMEDA	3/6	98	1
2	A	Fe(NO ₃) ₃	CuTC/DMEDA	3/6	99	1
3	A	FeCl ₂	CuTC/DMEDA	3/6	98	1
4	A	-	Cu(OAc) ₂ /-	3/-	NR ^b	3
5	A	-	Cu(OAc) ₂ /DMEDA	3/6	NR ^b	3
6	A	-	Fe(NO ₃) ₃ /-	3/-	NR ^b	3
7	B	Fe(NO ₃) ₃	Cu(OAc) ₂	1	92	1
8	B	FeCl ₂	Cu(OAc) ₂	1	87	1
9	B	TEMPO	Cu(OAc) ₂	1	88	1

^a Isolated yield. ^b No reaction

We used 2,2,6,6-tetramethylpiperidin-1-yl)oxyl (TEMPO) as a radical trap (Table S4, entry 1, 9) to test whether a tempo intermediate could form, something that would indicate a radical-mediated process,⁸³ however, this never occurred and the reaction proceeded as normal. The introduction of iron in the reaction mixture had no effect (entries 2, 3, 6, 7, 8), which leads to the conclusion that the use of stainless-steel jars is suitable for this reaction. Finally, the use of Cu(OAc)₂ as the copper source did not produce any product under the standard reaction conditions (entries 4,5).

5.8.5 Comparison of Jar Materials (Protocol A)

Presented below are the different jar materials that were tested on the optimised reaction (Table S1, entry 33), after 1 hour of milling (Figure S3). The yields are the average of two reaction tests for each material.

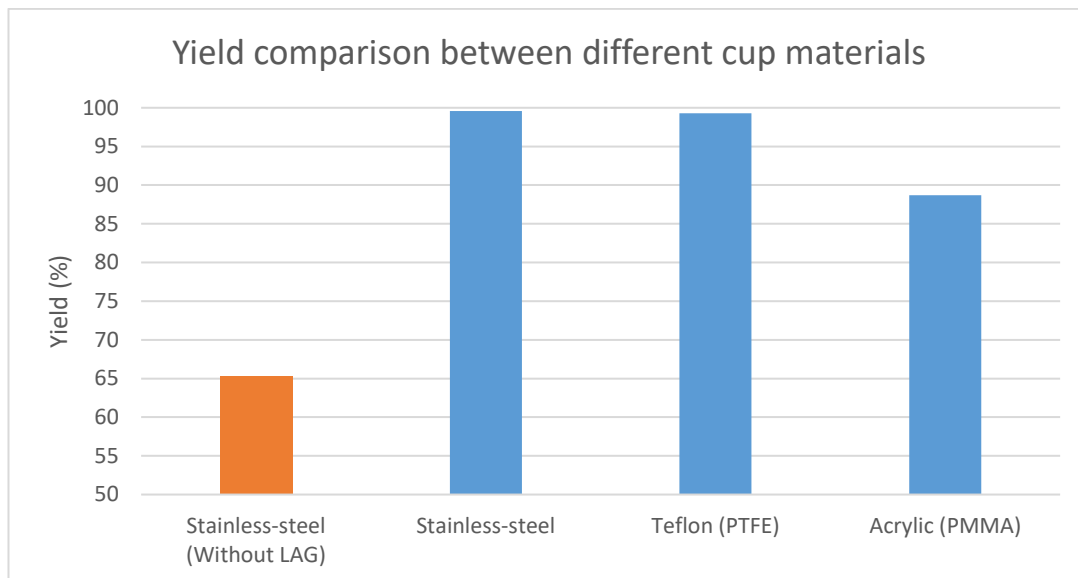
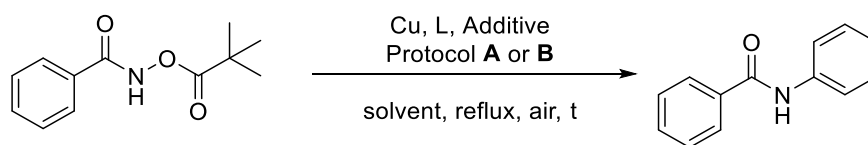


Figure S3. Yield comparison between different jar materials.

Surprisingly, even though acrylic is usually harder than teflon, the latter gave significantly higher yields, that are comparable with those of stainless-steel. A possible explanation may stem from the fact that acrylic is prone to EtOH sorption, hence, it may have removed the LAG element from the milling process, resulting in the lower yield.⁸⁴

5.8.6 Efficacy of Solution Chemistry Versus Mechanochemistry (Protocols A and B)

To establish whether or not the mechanochemical protocol that was developed offers any benefits in the yield and time of completion compared to a solution-based approach, we applied the optimised conditions (Table S1, entry 33 and Table S2, entry 9) in solution using various solvents at reflux temperatures (Table S5).

Table S5. Reaction protocol under wet-chemistry conditionsProtocol **A**Protocol **B**

Best results:

Mechanochemistry: 94%, 0.33 h
Solution (Ethanol): 75%, 1.5 h

Mechanochemistry: 92%, 0.33 h
Solution (THF): IR, 16 h

Entry	Protocol	Solvent	Yield ^a (%)	Time (h)
1	A	EtOH	75	1.5
2	A	THF	70	1.5
3	A	Toluene	54	1
4	B	DMF	IR ^b	16
5	B	THF	IR ^b	16
6^c	B	DMF	IR ^b	16
7^c	B	THF	IR ^b	16

^a Isolated yields, ^b IR = incomplete reaction, ^c Reactions were carried out under N₂ atmosphere.

Protocol A:

It quickly became apparent that the solution approach is significantly inferior to the solid-state one, highlighted by the overall lower reaction yields time to completion and the unnecessary use of solvent. Using EtOH as a solvent seems to work better compared with THF and toluene, although the latter went to completion faster (TLC), something that may be attributed to the higher reflux temperature of toluene (~ 110 °C) compared to that of EtOH (~78 °C). However, we need to note that the reaction above was optimised using mechanochemical conditions, and a solution-based optimisation may also be possible, but it is not part of the scope of this work.

Protocol B:

For the Chan-Lam type coupling protocol **B**, the optimised conditions (Table S2, entry 9) were not effective in producing product **2a**, as even after 16 hours under reflux conditions,

the TLC analysis of the reaction mixture revealed a multitude of spots (5 or more), indicating the presence of a plethora of compounds, which were not isolated due to the overlapping R_f values of the spots. Interestingly, by removing the base (*t*-BuOK), the reaction produces at least two products (**2a** and the *N*-substituted *O*-protected hydroxamic acid), as it was shown by Zhang *et al.*,⁵¹ but as mentioned before, the removal of the base in the ball mill (protocol **B**) eliminates the reactivity and doesn't produce any products.

5.8.7 3D Printing of Large Volume Milling Jars

Machining⁶¹ and 3D printing of custom milling jars⁶² are examples of customisation techniques mechanochemists have used in the past to adjust the milling jars to their needs. To demonstrate the scalability of the developed protocol, we had to use milling jars with a larger internal volume than the standard 10 mL jars that were used for the preparative (0.4 mmol) scale reactions. As such, jars of an internal volume of 20, 40 and 70 mL (Figure S4) were made using the stereolithographic (SLA) 3D printing technique that many commercial 3D printers use. For this case, we used a Formlabs Form 2 SLA 3D printer, along with the tough V5/durable V2 photopolymerisable resin. The resulting jars were made to a maximum length of 6.5 cm, ensuring that they could easily fit inside the Retch MM400 mixer mill.

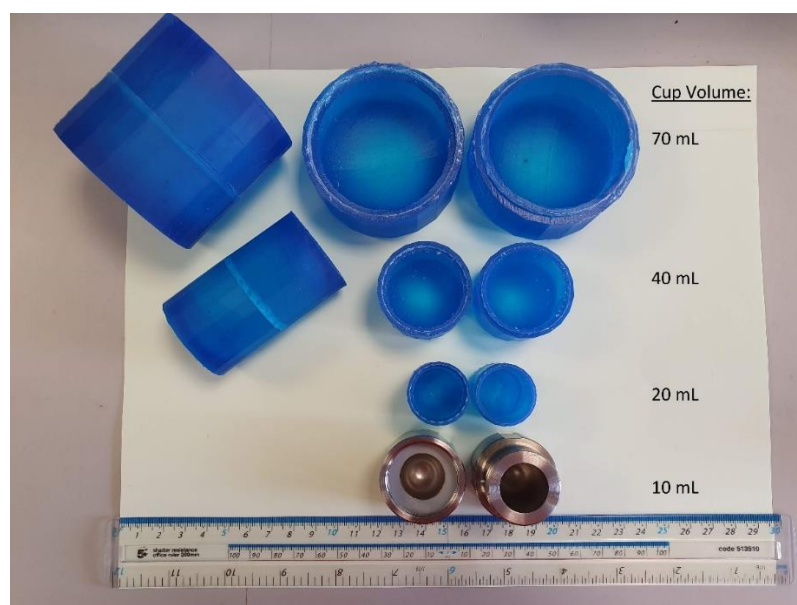


Figure S4. Collection of commercial (bottom, 10 mL) and SLA 3D printed jars.

The durability of the 3D printed jars was tested before they were used as reactionware, by milling blank samples of SiO₂ (5 g) using 15 g ZrO₂ balls (4 balls of variable diameters) at 20 Hz for 1 h. All jars were left undamaged by the durability tests and thus they were then used for large-scale reactions. It was found that the 70 mL jar was best suited for the gram-scale preparation of *N*-benzamides. To demonstrate the inexpensiveness of the 3D printed jars we present the approximate cost of printing the custom jars (Table S6).

Table S6. Materials and cost analysis for a pair of grinding jars printed using SLA with commercial resins

Material (resin)	Ball mill type	Internal volume (mL)	Price per pair	Date of quote
Acrylonitrile butadiene styrene analogue (Tough resin V5)	Mixer mill	70	~£49 (327 mL of resin)	29/11/2019
Acrylonitrile butadiene styrene analogue (Tough resin V5)	Mixer mill	40	~£11 (78 mL of resin)	29/11/2019
High-density polyethylene analogue (Durable resin V2)	Planetary mill	60	~£21 (142 mL of resin)	29/11/2019

The estimated cost for the 3D printed parts was calculated based on the amount of resin (mL) that was used for the parts (pair of jars + structure supports) divided by the cost of the resin that was used (£150/L as of 29/11/2019). In all cases, the print resolution was 50 microns per layer.

5.8.8 Generation of $^1\text{O}_2$ Under Batch Conditions⁸

Photocatalyst **2I** (1.3 mg, 0.0034 mmol) and α -terpinene (53 μL , 0.33 mmol) were dissolved in CDCl_3 (1 mL) in a glass vial. The vial was irradiated by a blue LED (28 W light output, 3.5 W/cm^2 light intensity, OSA opto lights, olm-018 series), situated 7 cm from the centre of the vial, for 1 hour and the final conversion was determined by ^1H -NMR spectroscopy (Figure S5). UV/vis spectroscopy shows maximum absorption at 394 nm (Figure S6) and the experimental set-up is shown in Figure S7.

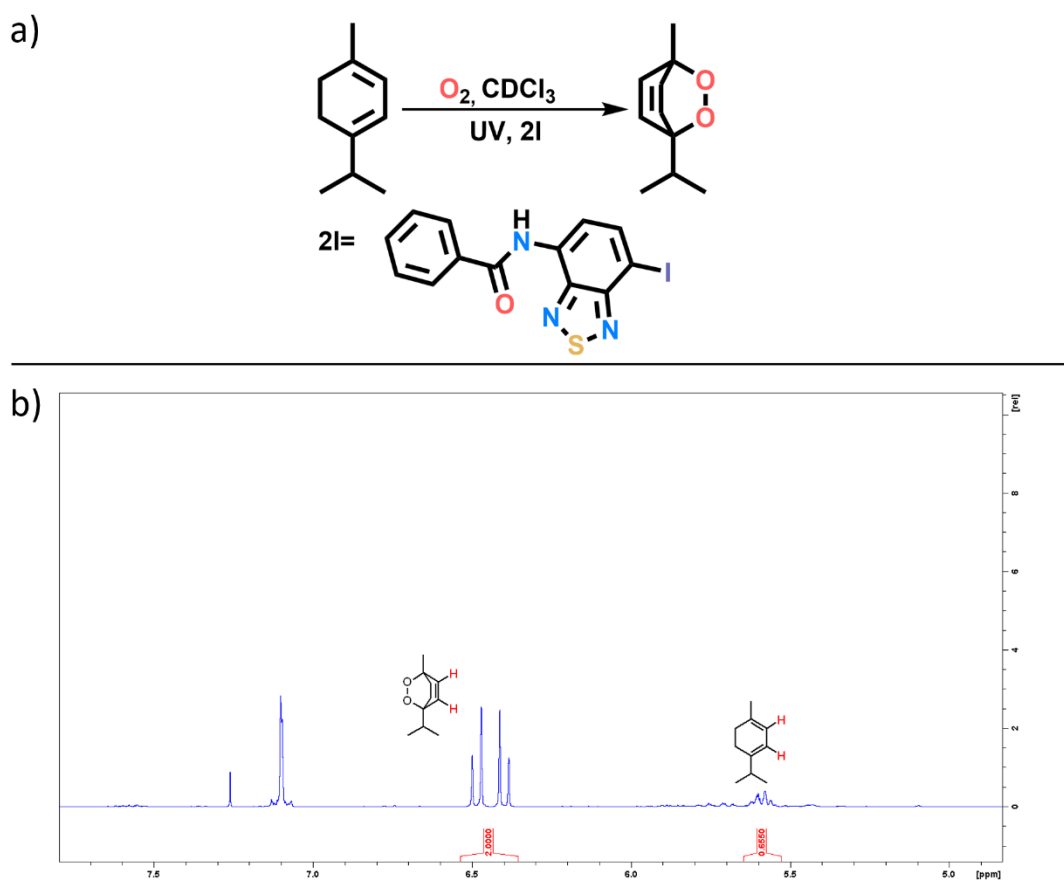


Figure S5. a) Conversion of α -terpinene to ascaridole using **2I** as a photosensitizer. b) ^1H -NMR showing the conversion of α -terpinene to ascaridole.

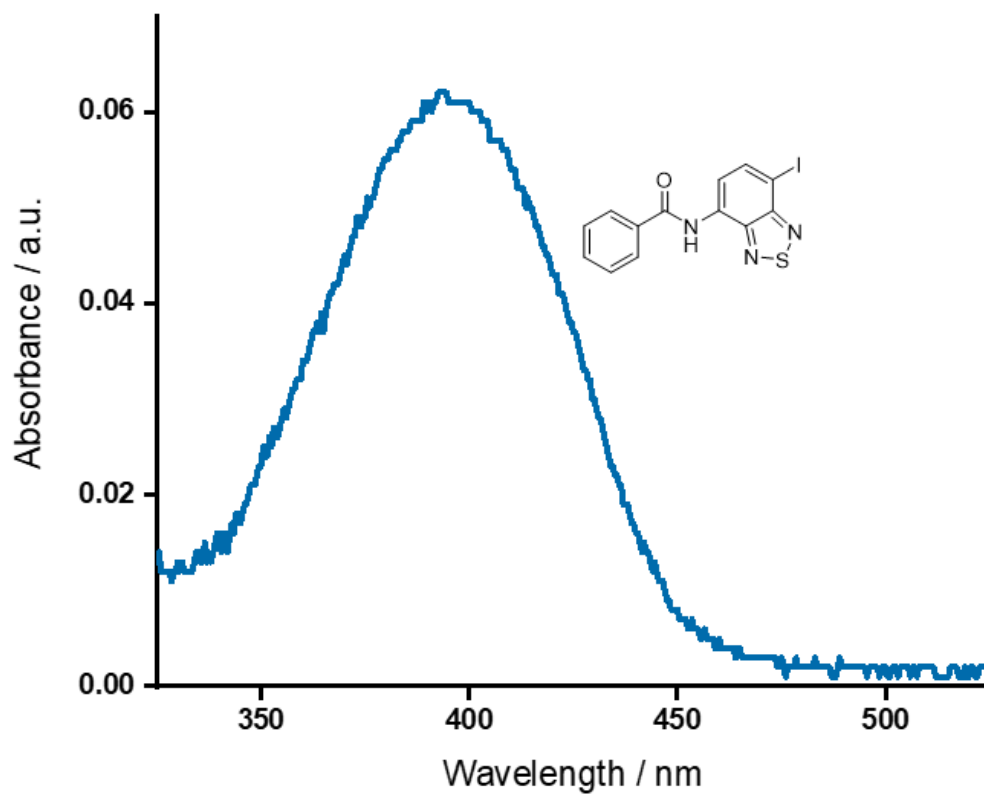


Figure S6. UV-Vis spectrum of **2l** showing a maximum absorption at 398 nm.

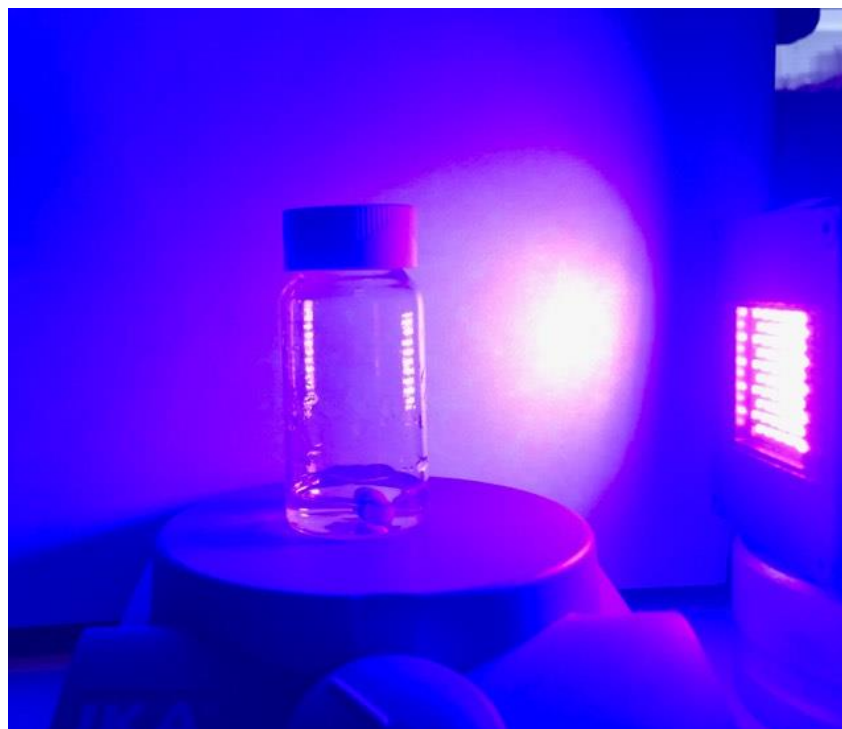


Figure S7. Experimental set-up for the generation of $^1\text{O}_2$ in batch conditions.

5.8.9 Generation of $^1\text{O}_2$ Under Mechanochemically-Assisted Solid-State Photocatalysed (MASSPC) Conditions

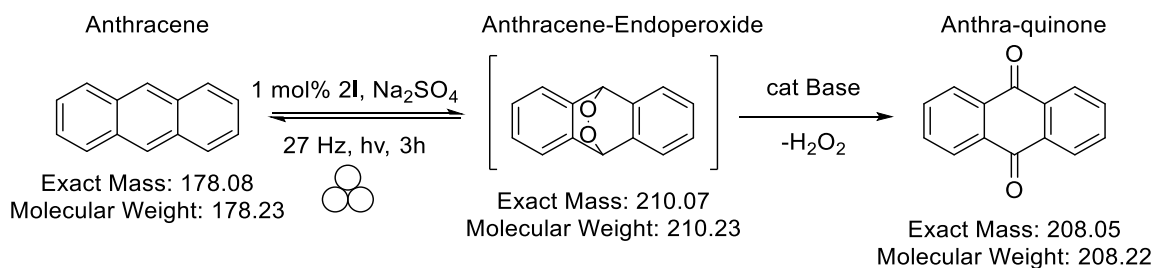


Figure S8. $^1\text{O}_2$ mediated conversion of anthracene to the corresponding endoperoxide and subsequent base-catalysed decomposition to anthraquinone.

The procedure for the mechanochemically-assisted solid-state photocatalysed conversion of anthracene was adapted from Strukil and Sajko⁵⁵ and was carried out as follows (Figure S8): A mixture of catalyst **2I** (0.4 mg,) anthracene (17.8 mg, 0.1 mmol) and anhydrous sodium sulfate (750 mg) was ball milled for 3 hours at 27 Hz under blue light irradiation (28 W light output, 3.5 W/cm² light intensity, OSA opto lights, olm-018 series) using a 10 mL optically transparent poly(methyl methacrylate) (PMMA) jar (purchased from Form-tech Scientific) and a 8 mm PMMA ball. TLC analysis of the reaction mixture in chloroform:hexane (4:1) revealed the presence of unreacted anthracene and a new product (Figure S9).

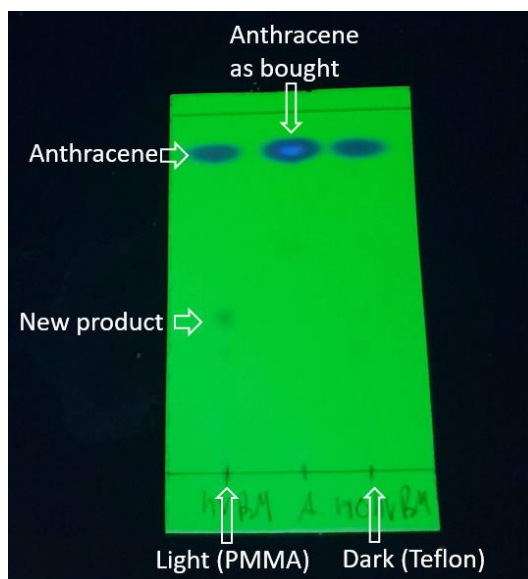


Figure S9. TLC plate of MASSPC conversion of anthracene. A new spot has formed on the reaction mixture that was illuminated with light, whereas the reference reaction (Dark) on the right does not show any new spots.

The same reaction mixture was prepared and milled under the same conditions in a opaque 10 mL Teflon jar using a 8 mm Teflon ball. The jar was covered in aluminium foil prior to milling to eliminate any light passing through. This mixture was used as a reference.

The ^1H NMR spectrum of the reaction mixture (Figure S10) shows the appearance of a new set of peaks corresponding to the anthraquinone product. The ratio between anthracene and anthraquinone is 1.00:0.05 or 4.8% conversion. This reaction was completed primarily as proof of concept. Possible optimisation of the reaction parameters to increase the overall conversion include the increase of the mol % of the photosensitiser, conducting the reaction under an oxygen atmosphere to increase the amount of $^3\text{O}_2$ available, changing the light source, increasing the milling frequency, and changing the milling materials.

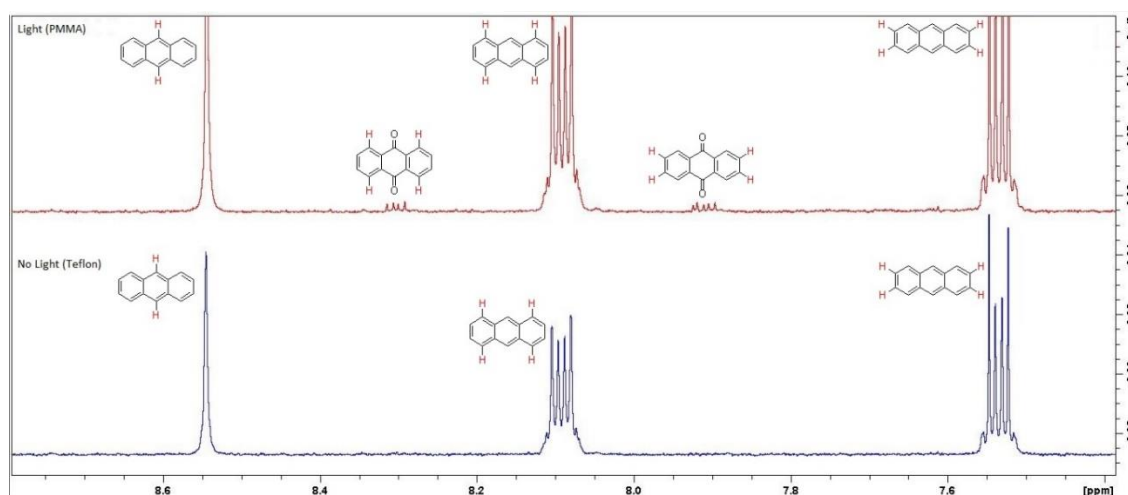


Figure S10. ^1H NMR spectra of the MASSPC reaction mixture. The reaction that occurred in the presence of light (PMMA jar) produced a spectrum that shows the presence of anthraquinone (upper). In the absence of light, there is only the starting material present (lower).

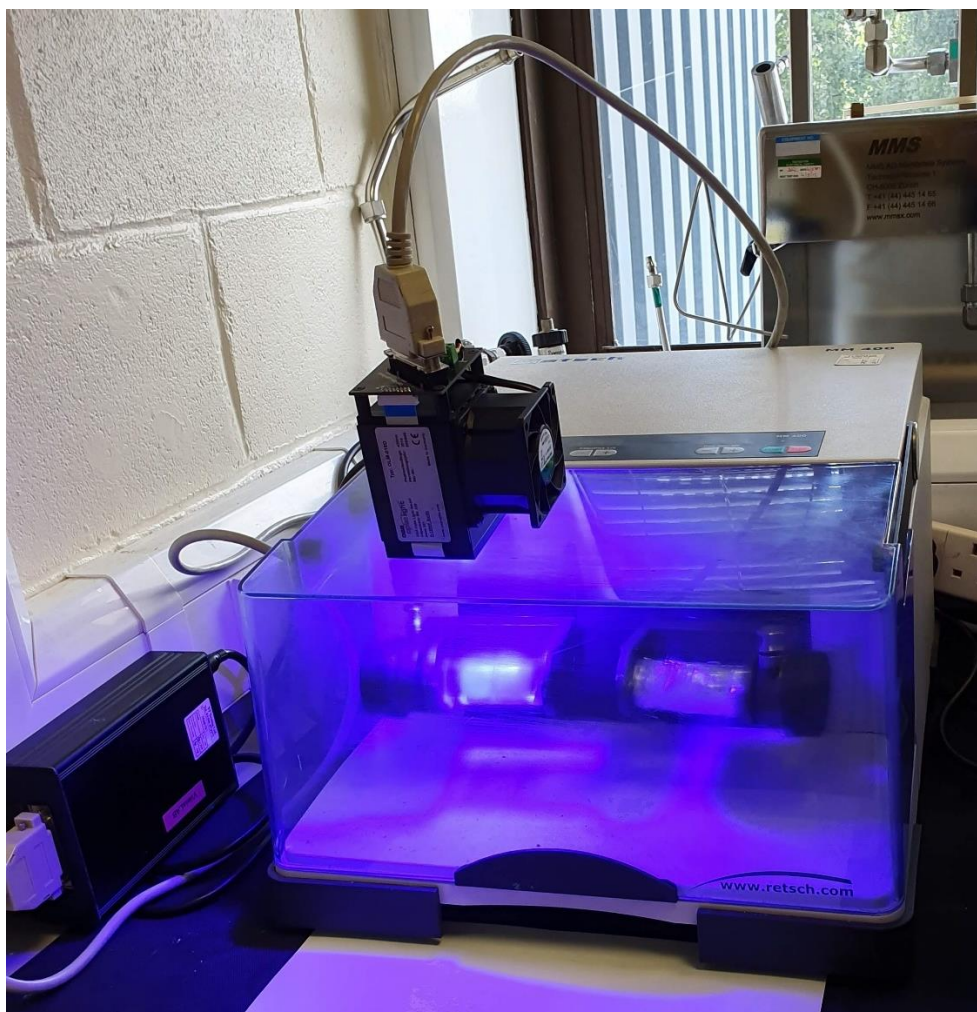


Figure S11: Experimental set-up for the MASSPC reaction.

The air-cooled light source was secured on top of the mixer's protective screen using double sided adhesive tape. No modifications were required to take place on the mixer apparatus and once the reaction was complete, the light source could easily be removed. During the experiments, the light source was located approximately 4 cm above the transparent PMMA jar (left), and the Teflon jar (right) was used as a reference and was wrapped in aluminium foil to exclude all light (Figure S11).

The mass spectrum (Figure S12) of the reaction mixture revealed the presence of anthraquinone in the mixture along with a small peak corresponding to the mass of anthracene-endoperoxide as well as the photocatalyst **21**, indicating the base catalysed decomposition of the anthracene-endoperoxide.

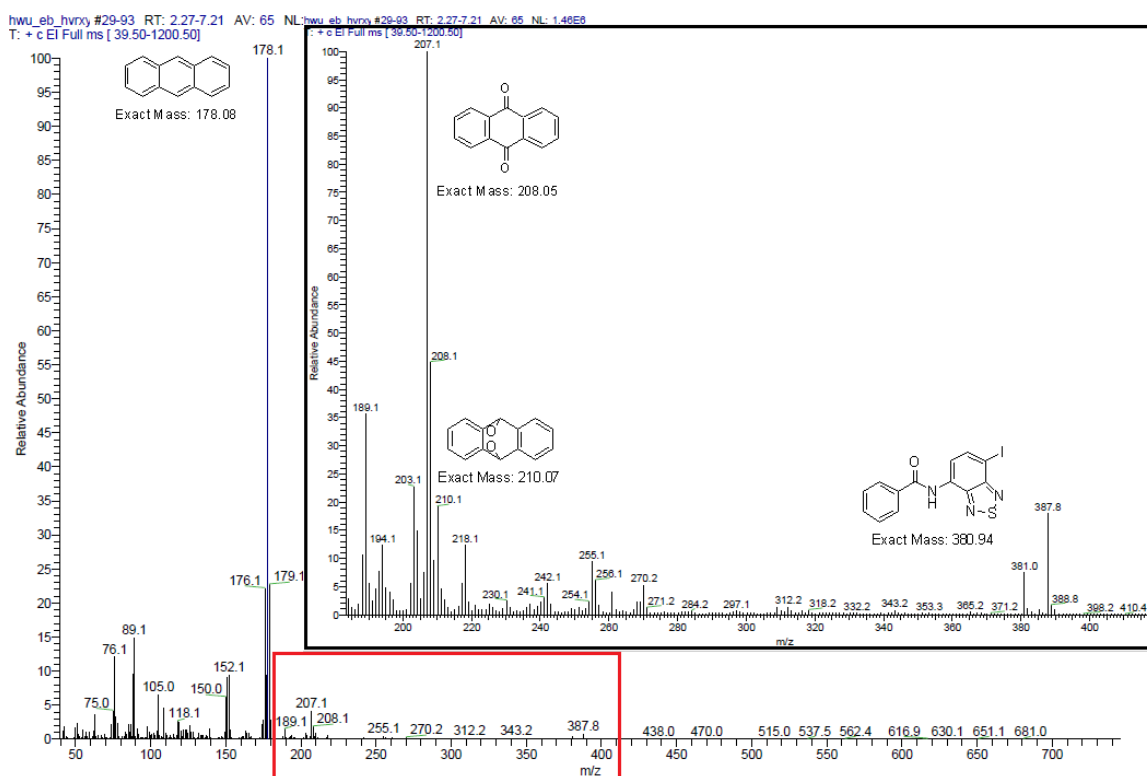


Figure S12. Mass spectrum of illuminated milled sample confirming presence of anthraquinone. Electron ionization (EI) in positive mode was used for acquiring the spectrum. As a result, the peaks of interest are representing charged adducts ($[M]^+$).

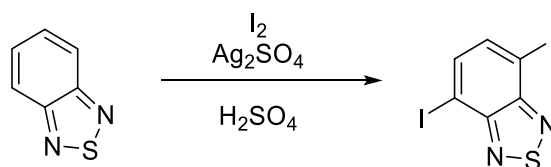
5.9 Experimental Section

5.9.1 General Methods and Materials

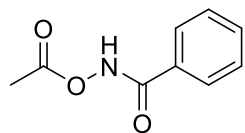
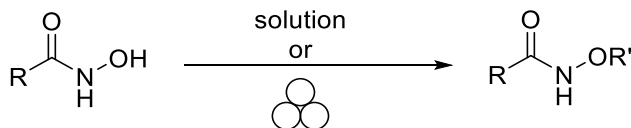
All chemicals were commercially available except those whose syntheses are described. Anhydrous $MgSO_4$ was used for drying organic extracts and all volatiles were removed under reduced pressure. All reaction mixtures and column eluents were monitored by TLC using commercial aluminium-backed thin layer chromatography (TLC) plates (Merck Kieselgel 60 F₂₅₄). The plates were observed under UV light at 254 and 365 nm. The technique of dry flash chromatography was used throughout for all non-TLC scale chromatographic separations using Merck Silica Gel 60 (less than 0.063 mm). Melting points were determined using a Stuart SMP10 digital melting point apparatus. Small scale (μL) liquid handling measurements were made using variable volume (1.00–5000.00 μL) single-channel Gilson PIPETMAN precision micropipettes. Solvents used

for recrystallization are indicated after the melting point. IR spectra were recorded on a Thermo Scientific Nicolet iS5 FTIR spectrometer with iD5 ATR accessory and broad, strong, medium, and weak peaks are represented by b, s, m and w, respectively. ^1H - and ^{13}C -NMR spectra were recorded on a Bruker AVANCE III HD machine (at 400 and 100 MHz, respectively). Chemical shifts (δ) are expressed in ppm and coupling constants J are given in Hz. Data are represented as follows: chemical shift, multiplicity (s=singlet, d=doublet, t=triplet, q=quartet, m=multiplet and/or multiple resonances, br s=broad singlet). Deuterated solvents were used for homonuclear lock, and the signals are referenced to the deuterated solvent peaks. The ball mill used was a Retsch MM 400 mixer mill. Milling balls were 8mm in diameter. Unless otherwise stated, mechanochemical reactions were performed in 10 mL stainless steel jars made by Retsch with two stainless steel balls of mass 1.3 g each. The mass of each acrylic (PMMA) and Teflon (PTFE) ball is 0.29 g and 0.24 g, respectively. Unless otherwise stated, all reactions were performed at room temperature. The 3D printer that was used to print the custom-made milling jars was a Formlabs Form 2 SLA 3D printer.

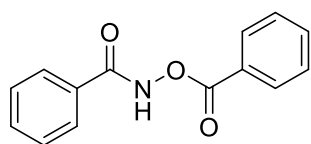
5.9.2 Preparation of 4,7-Diiodobenzo[c][1,2,5]thiadiazole⁸⁵



4,7-Diiodobenzo[c][1,2,5]thiadiazole was prepared from the commercially available benzo[c][1,2,5]thiadiazole according to the modified method based on the literature.⁸⁵ Under an argon atmosphere, benzo[c][1,2,5]thiadiazole (2.72 g, 20.0 mmol), iodine (12.7 g, 50.0 mmol), silver(I) sulfate (6.24 g, 20 mmol) were added to a 100 mL round bottom flask containing concentrated sulfuric acid (30 mL). The reaction mixture was then stirred at 120 °C for 23 hours. After cooling to ambient temperature, the reaction mixture was quenched with water at 0 °C, and the precipitate was collected by filtration. The compounds were extracted with CH₂Cl₂ from the precipitate three times. The organic solution was washed with saturated aqueous NaHCO₃ and brine, and dried over Na₂SO₄. After evaporation of dichloromethane, the residue was recrystallized with ethyl acetate to give 4,7-diiodobenzo[c][1,2,5]thiadiazole (2.92 g, 7.54 mmol) in 38% yield.

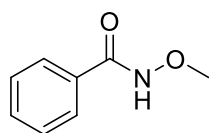
5.9.3 Preparation of *O*-Protected Hydroxamic Acids^{38,86}

***N*-Acetoxybenzamide (1a).** Benzohydroxamic acid (1.23 g, 9 mmol, 1 eq.), CH₂Cl₂ (30 mL) and NaOH 2M (30 mL) were charged in a round bottom flask. Ac₂O (936 μL, 9.9 mmol, 1.1 eq.) was added via syringe. After stirring at room temperature for 3 h, the organic layer was separated, and the aqueous layer was extracted with CH₂Cl₂. The combined organic fractions were washed with brine, dried with MgSO₄, filtered, and evaporated under reduced pressure to afford the desired product as a white solid (1.46 g, 91%). Mp, IR, ¹H- and ¹³C- NMR were in agreement with the literature.^{38,86} Mp 90-92 °C (EtOH); $\nu_{\max}/\text{cm}^{-1}$ 3141m (Amide N-H), 2958m (Aryl C-H), 2815m (Aryl C-H), 1790s (AcO, C=O), 1654s (Amide, C=O), 1616w, 1600w, 1579m, 1528m, 1490w, 1447w, 1364m, 1312m, 1290w, 1171s, 1077m, 1033m, 1018s, 977w, 931m, 895m, 855m, 849m, 798m, 732w, 694s; δ_{H} (400 MHz, DMSO-d₆) 12.31 (1H, s, NH), 7.81 (2H, d, J = 7.2 Hz, ArH), 7.61 (1H, t, J = 7.2, ArH), 7.52 (2H, t, J = 7.2, ArH), 2.23 (3H, s, CH₃); δ_{C} (100 MHz, DMSO-d₆) 168.7, 164.6, 132.3, 131.0, 128.6, 127.4, 18.1.

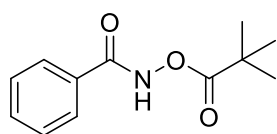


***N*-(Benzoyloxy)benzamide (1b).** Benzohydroxamic acid (1.00 g, 7.29 mmol, 1 eq.) and sodium *tert*-butoxide (701 mg, 7.29 mmol, 1 eq.) were stirred together at room temperature in diethyl ether (30 mL) for 30 min. Benzoyl chloride (850 μL, 7.29 mmol, 1 eq.) was then added dropwise and the reaction mixture was allowed to stir at room temperature for 16 hours. It was then diluted with EtOAc and washed with water and brine. The organic fraction containing the product in the solid form was diluted with acetone to dissolve it almost completely. The organic phase was dried over MgSO₄, filtered, and evaporated under reduced pressure to afford the desired product as a white solid (1.12 g, 63%) without needing any further purification. Mp, IR, ¹H- and ¹³C-NMR were in agreement with the literature.^{38,86} Mp 161-163 °C (EtOH); $\nu_{\max}/\text{cm}^{-1}$ 3168m (Amide N-H), 2978m (Aryl C-H), 1764s (BzO, C=O), 1654s (Amide, C=O), 1652w, 1641m, 1601w, 1578m,

1514m, 1484m, 1451m, 1447m, 1309m, 1260w, 1235s, 1179w, 1154m, 1078m, 1041m, 1022s, 1001m, 988w, 941w, 935w, 900m, 847m, 796m, 698s, 692m; δ_{H} (400 MHz, DMSO-*d*₆) 12.67 (1H, s, NH), 8.09-8.12 (2H, m, ArH), 7.87-7.93 (2H, m, ArH), 7.77 (1H, t, *J* = 8.0 Hz, ArH), 7.60-7.66 (3H, m, ArH), 7.56 (2H, t, *J* = 8.0, ArH); δ_{C} (100 MHz, DMSO-*d*₆) 164.9, 164.4, 134.4, 133.0, 131.0, 129.5, 129.2, 128.7, 127.5, 126.9.

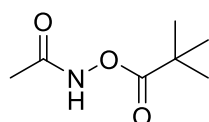


***N*-Methoxybenzamide (1c).** To a solution of 20 mL EtOAc and 10 mL H₂O containing Na₂CO₃ (2 eq.) *O*-methylhydroxamine hydrochloride (835 mg, 10 mmol, 1 eq.) was added. The mixture was cooled to 0°C and benzoyl chloride (1.4 g, 1.15 mL, 10 mmol, 1 eq.) was added dropwise to the mixture. It was then allowed to stir at 0°C for 2 hours. The reaction was then quenched with brine and more EtOAc was added. The organic layer was washed twice with brine. It was then dried over MgSO₄, filtered, and evaporated under reduced pressure. The purification was made by flash column chromatography using 20% EtOAc in pet. ether as eluent. The product obtained was a white solid (1.1 g, 73 %). Mp, IR, ¹H- and ¹³C-NMR agreed with literature data.^{38,86} Mp 58-59°C (n-Hexane); $\nu_{\text{max}}/\text{cm}^{-1}$ 3193m (Amide N-H), 2978w (Aryl C-H), 2936w (Aryl C-H), 1645s (Amide, C=O), 1579m, 1516m, 1481m, 1439w, 1308m, 1291w, 1190w, 1152m, 1075w, 1043m, 1025m, 942m, 879m, 798m, 691m, 668w; δ_{H} (400 MHz, DMSO-*d*₆) 11.74 (1H, s, NH), 7.74-7.76 (2H, m, ArH), 7.61 (1H, t, *J* = 7.6, ArH), 7.46 (2H, t, *J* = 7.6, ArH), 3.71 (3H, s, (CH₃)); δ_{C} (100 MHz, DMSO-*d*₆) 164.1, 132.3, 131.6, 128.5, 127.0, 63.2.

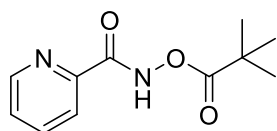


***N*-(Pivaloyloxy)benzamide (1d).** Benzohydroxamic acid (6.93 g, 50 mmol, 1 eq.) and sodium *tert*-butoxide (4.08 g, 50 mmol, 1 eq.) were stirred together at room temperature in diethyl ether (100 mL) for 30 min. Pivaloyl chloride (6.12 mL, 50 mmol, 1 eq.) was then added dropwise and the reaction mixture was allowed to stir at room temperature overnight. It was then diluted with 100 mL of EtOAc and washed with water and brine. The organic fraction containing the product in the solid form was diluted with acetone to dissolve it almost completely. The organic phase was dried over MgSO₄, filtered, and evaporated under reduced pressure to afford the desired product as a white solid (7.23 g, 65%) without needing any further purification. Mp, IR, ¹H- and ¹³C-NMR were in agreement with the

literature.^{38,86} Mp 170-172 °C (CHCl₃); $\nu_{\max}/\text{cm}^{-1}$ 3230m (Amide N-H), 2975m (Aryl C-H), 1780m (PivO, C=O), 1651s (Amide, C=O), 1601w, 1579w, 1575w, 1562s, 1557m, 1538m, 1516m, 1482m, 1451m, 1436w, 1400w, 1369w, 1309w, 1290m, 1267w, 1240w, 1163m, 1146m, 1064m, 1042w, 1022s, 1001w, 935w, 900m, 868m, 811m, 800m, 755w, 708s, 688m; δ_{H} (400 MHz, DMSO-d₆) 12.27 (1H, s, NH), 7.81 (2H, dd, J = 7.2, 1.6 Hz, ArH), 7.61 (1H, tt, J = 6.8, 1.6, ArH), 7.52 (1H, t, J = 7.6, ArH), 1.29 (9H, s, (CH₃)₃); δ_{C} (100 MHz, DMSO-d₆) 175.7, 164.6, 132.2, 131.1, 128.6, 127.3, 37.8, 26.8.

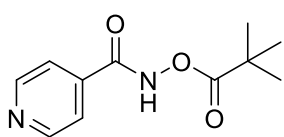


***N*-(Pivaloyloxy)acetamide (1e).** Acetohydroxamic acid (750.7 mg, 10 mmol, 1 eq.) and sodium *tert*-butoxide (816 mg, 10 mmol, 1 eq.) were stirred together at room temperature in diethyl ether (50 mL) for 30 min. Pivaloyl chloride (1.22 mL, 10 mmol, 1 eq.) was then added dropwise and the reaction mixture was allowed to stir at room temperature overnight. It was then diluted with 50 mL of EtOAc and washed with water and brine. The organic fraction containing the product in the solid form was diluted with acetone to dissolve it almost completely. The organic phase was dried over MgSO₄, filtered, and evaporated under reduced pressure. The residue was then subjected to flash chromatography (CHCl₃/EtOAc, 80/20) to afford the desired product as a viscous colourless oil (1.23 g, 77%). IR, ¹H- and ¹³C-NMR were in agreement with the literature.^{38,86} $\nu_{\max}/\text{cm}^{-1}$ 3193bm (Amide N-H), 2975s (Aryl C-H), 1780m (PivO, C=O), 1677s (Amide, C=O), 1481m, 1456m, 1398w, 1368m, 1269m, 1092s, 1022m, 990m, 941w, 874m, 757m; δ_{H} (400 MHz, DMSO-d₆) 11.47 (1H, s, NH), 1.85 (3H, s, CH₃), 1.22 (9H, s, (CH₃)₃); δ_{C} (100 MHz, DMSO-d₆) 175.6, 166.9, 26.8, 19.3.



***N*-(Pivaloyloxy)picolinamide (1f).** *N*-Hydroxypicolinamide (1.38 g, 10 mmol, 1 eq.) and sodium *tert*-butoxide (816 mg, 10 mmol, 1 eq.) were stirred together at room temperature in diethyl ether (50 mL) for 30 min. Pivaloyl chloride (1.22 mL, 10 mmol, 1 eq.) was then added dropwise and the reaction mixture was allowed to stir at room temperature overnight. It was then diluted with 50 mL of EtOAc and washed with water and brine. The organic fraction containing the product in the solid form was diluted with acetone to dissolve it almost completely. The organic phase was dried over MgSO₄, filtered, and evaporated under reduced pressure to afford the desired product as a white solid (1.42 g, 63.8%)

without needing any further purification. Mp 102-103 °C (CHCl₃); IR, ¹H- and ¹³C-NMR were in agreement with the literature.^{38,86} $\nu_{\max}/\text{cm}^{-1}$ 3086bm (Amide N-H), 2974m, 2906wm, 1772m (PivO, C=O), 1689s (Amide, C=O), 1591m, 1567w, 1504w, 1469w, 1437m, 1396w, 1363w, 1307m, 1287m, 1268m, 1246w, 1149w, 1075s, 1045m, 1027m, 1003m, 904m, 877w, 819m, 754m, 701m, 626m, 576w; δ_{H} (400 MHz, DMSO-d₆) 12.49 (1H, s, NH), 8.67 (1H, dd, J = 4.7 Hz, 0.9, ArH), 7.97-8.02 (2H, m, ArH), 7.47-7.73 (1H, m, ArH) 1.27 (9H, s, (CH₃)₃); δ_{C} (100 MHz, DMSO-d₆) 175.3, 161.7, 148.8, 148.7, 137.9, 127.2, 122.4, 37.7, 26.8.

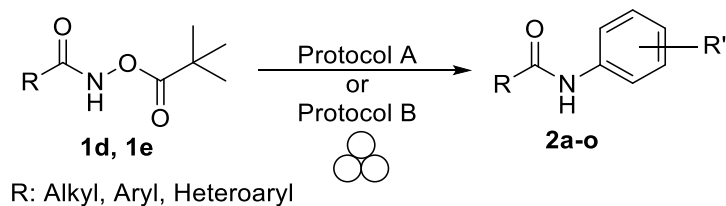


***N*-(Pivaloyloxy)isonicotinamide (1g).**

N-

Hydroxyisonicotinamide (1.38 g, 10 mmol, 1 eq.) and sodium *tert*-butoxide (816 mg, 10 mmol, 1 eq.) were stirred together at room temperature in diethyl ether (50 mL) for 30 min. Pivaloyl chloride (1.22 mL, 10 mmol, 1 eq.) was then added dropwise and the reaction mixture was allowed to stir at room temperature overnight. It was then diluted with 50 mL of EtOAc and washed with water and brine. The organic fraction containing the product in the solid form was diluted with acetone to dissolve it almost completely. The organic phase was dried over MgSO₄, filtered, and evaporated under reduced pressure to afford the desired product as a white solid (1.12 g, 50.3%) without needing any further purification. Mp 118-119 °C (CHCl₃); $\nu_{\max}/\text{cm}^{-1}$ 3091bm (Amide N-H), 2984m, 2873m, 2755bm, 1772m (PivO, C=O), 1691s (Amide, C=O), 1605w, 1538m, 1461m, 1413m, 1397w, 1371w, 1330w, 1296m, 1268w, 1219m, 1160m, 1074s, 1062m, 1028m, 1003m, 938m, 913w, 871w, 850w, 754m, 685s, 577w; δ_{H} (400 MHz, DMSO-d₆) 12.66 (1H, s, NH), 8.78 (2H, dd, J = 4.5 Hz, 1.5, ArH), 7.71. (2H, dd, J = 4.5 Hz, 1.4, ArH), 1.29 (9H, s, (CH₃)₃); δ_{C} (100 MHz, DMSO-d₆) 175.6, 162.7, 150.6, 138.2, 121.2, 37.9, 26.8.

5.9.4 Preparation of *N*-Aryl Benzamides (Protocols A and B)



Mechanochemical preparation:

Protocol A:

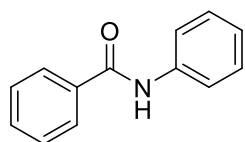
To a stainless-steel ball mill jar (10 mL internal volume) *N*-(pivaloyloxy)benzamide (88.5 mg, 0.4 mmol, 1 eq.) was added, followed by the corresponding phenyl iodide (0.44 mmol, 1.1 eq.), copper (I) thiophene-2-carboxylate (228.2 mg, 1.2 mmol, 3 eq.) and *N,N'*-dimethylethylenediamine (211.6 mg, 2.4 mmol, 6 eq.). In addition to these reagents, EtOH ($\eta = 0.16 \mu\text{L}/\text{mg}$) was added to the jar, along with two steel balls (8 mm in diameter). The jar was sealed and milled for 20 minutes at 25 Hz. After the completion of the reaction which was confirmed by TLC ($\text{CHCl}_3:\text{EtOAc}$, 90:10), the jar was opened and the reaction mixture was passed through a short silica plug (eluted with $\text{CHCl}_3:\text{EtOAc}$, 80:20). The resulting solution was evaporated under reduced pressure, and the residue was recrystallised to afford the title compound (**2a-n**).

Protocol B:

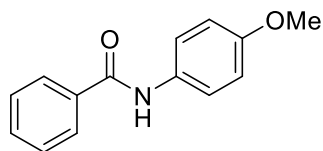
To a stainless-steel ball mill jar (10 mL internal volume) *N*-(pivaloyloxy)benzamide (88.5 mg, 0.4 mmol, 1 eq.) was added, followed by the corresponding phenyl boronic acid (0.48 mmol, 1.2 eq.), copper(II) acetate (72.7 mg, 0.4 mmol, 1 eq.) and potassium *tert*-butoxide (89.77 mg, 0.8 mmol, 2 eq.). In addition to these reagents, two steel balls were added to the jar (8 mm in diameter). The jar was then sealed and milled for 20 minutes at 25 Hz. After the completion of the reaction which was confirmed by TLC ($\text{CHCl}_3:\text{EtOAc}$, 90:10), the jar was opened and the reaction mixture was passed through a short silica plug (eluted with $\text{CHCl}_3:\text{EtOAc}$, 80:20). The resulting solution was evaporated under reduced pressure, and the residue was recrystallised to afford the title compound (**2a-n**).

Solution preparation (protocol **A** and **B**):

The aforementioned mechanochemical procedures were tested in solution by using the same quantity of reagents as described above, which were added in a sealable glass vial along with a stir bar. In addition to these reagents, 5 mL of the preferred solvent was added. The vial was sealed, and the reaction was stirred under air at reflux temperature. After the completion of the reaction which was confirmed by TLC (CHCl₃:EtOAc, 90:10), the vial was opened, and the reaction mixture was evaporated under reduced pressure. When DMF was used, an aqueous work-up was required, in which water (50 mL) was added to the reaction mixture and subsequently extracted by EtOAc (2 x 5mL). The combined organic layers were washed twice with brine and the crude mixture was then subjected to column chromatography (eluted with CHCl₃:EtOAc, 80:20) to afford the desired *N*-aryl benzamide.

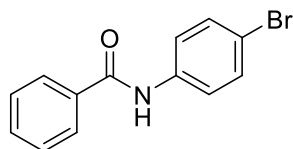


***N*-Phenylbenzamide (2a)**. Colourless plates (78.9 mg, 99%). Mp, IR, ¹H- and ¹³C-NMR were in agreement with the literature.⁸⁷ Mp 162-163 °C (CHCl₃); $\nu_{\max}/\text{cm}^{-1}$ 3345m (Amide N-H), 3051w (Aryl C-H), 2951w (Aryl C-H), 1724m and 1654s (C=O), 1599m, 1579s, 1526m, 1489m, 1448s, 1436m, 1320m, 1257m, 1178s, 1165s, 1147m, 1114m, 1074w, 1027m, 1001m, 979m, 927w, 885w, 791w, 748s, 714s; δ_{H} (400 MHz, DMSO-d₆) 10.25 (1H, s, NH), 7.79 (2H, d, J = 7.2 Hz, ArH), 7.79 (2H, d, J = 8.0, ArH), 7.51-7.61 (3H, m, ArH), 7.35 (2H, t, J = 7.4, ArH), 7.10 (1H, t, J = 7.2, ArH); δ_{C} (100 MHz, DMSO-d₆) 165.5, 139.2, 135.0, 131.5, 128.6, 128.4, 127.6, 123.6, 120.3.

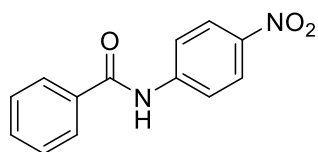


***N*-(4-Methoxyphenyl)benzamide (2b)**. Colourless plates (88.2 mg, 97%). Mp, IR, ¹H- and ¹³C- NMR were in agreement with the literature.^{87,88} Mp 155-157 °C (CHCl₃); $\nu_{\max}/\text{cm}^{-1}$ 3345m (Amide N-H), 2965w (Aryl C-H), 2838w (Aryl C-H), 1646m (C=O), 1615m, 1603w, 1512s, 1492m, 1459m, 1409m, 1326w, 1305m, 1268m, 1246m, 1186m, 1175w, 1118m, 1107m, 1074w, 1031m, 1002w, 977w, 933w, 928w, 899w, 813s, 792m, 761m, 715m, 691s; δ_{H} (400 MHz, DMSO-d₆) 10.12 (1H, s, NH), 7.94 (2H, d, J = 7.6 Hz, ArH), 7.68 (2H, d, J = 9.6, ArH), 7.58 (1H, t, J = 6.8 ArH), 7.52 (2H, t, J = 6.8, ArH),

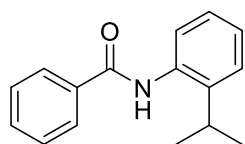
6.93 (2H, d, $J = 8.8$, ArH), 3.75 (3H, s, OCH₃); δ_C (100 MHz, DMSO-d₆) 165.1, 155.5, 135.0, 132.2, 131.4, 128.3, 127.5, 122.0, 113.7, 55.2.



***N*-(4-Bromophenyl)benzamide (2c)**. Colourless plates (100.5 mg, 91%). Mp, IR, ¹H- and ¹³C-NMR were in agreement with the literature.⁸⁹ Mp 200-202 °C (CHCl₃); $\nu_{\max}/\text{cm}^{-1}$ 3329m (Amide N-H), 1645m (C=O), 1590m, 1579w, 1511s, 1485m, 1449w, 1436w, 1392m, 1356w, 1302m, 1288m, 1240m, 1179m, 1159w, 1100w, 1073m, 1026m, 1009m, 939w, 929w, 900w, 795m, 716s, 691s; δ_H (400 MHz, DMSO-d₆) 10.37 (1H, s, NH), 7.95 (2H, dd, $J = 7.2, 1.2$ Hz, ArH), 7.78 (2H, dt, $J = 10.0, 2.4$ ArH), 7.6 (1H, t, $J = 7.2$ ArH), 7.52-7.55 (4H, m, ArH); δ_C (100 MHz, DMSO-d₆) 165.7, 138.6, 134.7, 131.7, 131.4, 128.4, 127.7, 122.2, 115.3.

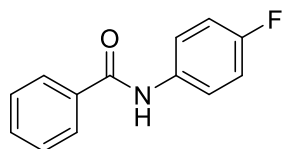


***N*-(4-Nitrophenyl)benzamide (2d)**. Yellow needles (89.1 mg, 92%). Mp, IR, ¹H- and ¹³C-NMR were in agreement with the literature.⁹⁰ Mp 198-199 °C (CHCl₃); $\nu_{\max}/\text{cm}^{-1}$ 3328m (Amide N-H), 1656m (C=O), 1613m, 1594m, 1580w, 1530w, 1498s, 1486m, 1446w, 1436w, 1406m, 1334s, 1303m, 1248m, 1178m, 1110m, 1074w, 1031m, 1001m, 960w, 931w, 901w, 847s, 820m, 795m, 748m, 737m, 718m, 689s; δ_H (400 MHz, DMSO-d₆) 10.80 (1H, s, NH), 8.27 (2H, dt, $J = 10, 2.6$ Hz, ArH), 7.78 (2H, dt, $J = 10.4, 2.4$ ArH), 7.98 (2H, dd, $J = 7.4, 1.4$ ArH), 7.64 (1H, t, $J = 7.6$, ArH), 7.56 (2H, t, $J = 7.6$, ArH); δ_C (100 MHz, DMSO-d₆) 166.3, 145.5, 142.5, 134.2, 132.2, 128.5, 127.9, 124.8, 119.8.

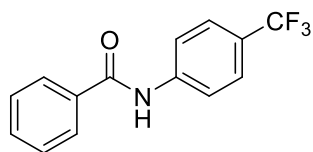


***N*-(2-Isopropylphenyl)benzamide (2e)**. Colourless plates (80.4 mg, 84%). Mp, IR, ¹H- and ¹³C-NMR were in agreement with the literature.⁹¹ Mp 149-150 °C (CHCl₃); $\nu_{\max}/\text{cm}^{-1}$ 3207m (Amide N-H), 2957m (Aryl C-H), 2866w (Aryl C-H), 1637s (C=O), 1600w, 1579w, 1527s, 1493m, 1446m, 1436w, 1418w, 1384w, 1363w, 1310s, 1296m, 1076m, 1027m, 932w, 912m, 838m, 801m, 756w, 694s; δ_H (400 MHz, DMSO-d₆) 9.91 (1H, s, NH), 8.27 (2H, d, $J = 7.98$ Hz, ArH), 7.59 (1H, d, $J = 7.6$, ArH), 7.53 (2H, t, $J = 7.6$, ArH), 7.37 (1H, d, $J = 7.6$, ArH), 7.26 – 7.30 (1H, m, ArH), 7.23 (2H, m, ArH), 3.22 (1H, sep, $J = 7.2$, CH(CH₃)₂),

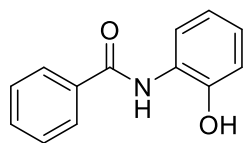
1.16 (6H, d, $J = 7.2$, $\text{CH}(\text{CH}_3)_2$); δ_{C} (100 MHz, DMSO- d_6) 165.9, 144.9, 135.1, 134.5, 131.5, 128.4, 128.2, 127.6, 127.0, 125.9, 125.6, 27.6, 23.2.



***N*-(4-Fluorophenyl)benzamide (2f)**. Colourless needles (80.9 mg, 94%). Mp, IR, ^1H - and ^{13}C -NMR were in agreement with the literature.^{88,92} Mp 183-184 °C ($\text{CHCl}_3/\text{EtOAc}$, 90/10); $\nu_{\text{max}}/\text{cm}^{-1}$ 3346m (Amide N-H), 1652m (C=O), 1614m, 1580w, 1522s, 1508s, 1490m, 1456w, 1446w, 1436m, 1406s, 1331m, 1312m, 1259w, 1209s, 1158m, 1112w, 1095m, 1073w, 1029m, 1014m, 1001m, 984m, 959m, 929m, 900m, 826s, 795s, 773m, 701s, 690s; δ_{H} (400 MHz, DMSO- d_6) 10.30 (1H, s, NH), 7.95 (2H, dd, $J = 7.2$, 1.6 Hz, ArH), 7.78-7.82 (2H, m, ArH), 7.59 (1H, t, $J = 7.6$, ArH), 7.53 (2H, t, $J = 7.6$, ArH), 7.19 (2H, t, $J = 8.0$, ArH); δ_{C} (100 MHz, DMSO- d_6) 165.5, 158.3 (d, $^1J_{\text{CF}}$ 240.5 Hz), 135.5 (d, $^4J_{\text{CF}}$ 2.7), 134.8, 131.6, 128.4, 127.6, 122.2 (d, $^3J_{\text{CF}}$ 7.7), 115.2 (d, $^2J_{\text{CF}}$ 21.8).

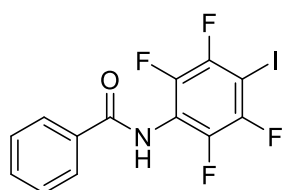


***N*-(4-(Trifluoromethyl)phenyl)benzamide (2g)**. Colourless needles (91.2 mg, 86%). Mp, IR, ^1H - and ^{13}C -NMR were in agreement with the literature.⁸⁸ Mp 204-205 °C (CHCl_3); $\nu_{\text{max}}/\text{cm}^{-1}$ 3328m (Amide N-H), 1652m (C=O), 1616m, 1599m, 1581w, 1527m, 1513m, 1487w, 1407m, 1302m, 1251m, 1182w, 1169w, 1155w, 1070m, 1027w, 1015m, 1000w, 950w, 929w, 902w, 834s, 795m, 762w, 733s, 716m, 690m; δ_{H} (400 MHz, DMSO- d_6) 10.58 (1H, s, NH), 8.03 (2H, d, $J = 8.8$ Hz, ArH), 7.98 (2H, dd, $J = 7.0$, 1.6 ArH), 7.72 (2H, d, $J = 8.4$, ArH), 7.62 (1H, t, $J = 7.2$, ArH), 7.55 (2H, t, $J = 8.0$, ArH); δ_{C} (100 MHz, DMSO- d_6) 166.1, 142.8, 134.5, 131.9, 128.5, 127.8, 125.9 (q, $^3J_{\text{CF}}$ 3.6 Hz), 124.4 (q, $^1J_{\text{CF}}$ 271.3), 123.6 (q, $^2J_{\text{CF}}$ 32.6), 120.36. Note: The first peak of the $^1J_{\text{CF}}$ quartet is hidden under the peak at 128.5 ppm. The quartet resonances are located at 128.4, 125.8, 123.1 and 120.4 ppm.



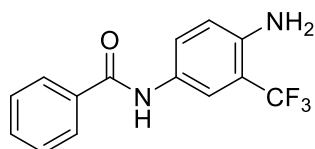
***N*-(2-Hydroxyphenyl)benzamide (2h)**. Colourless needles (65.4 mg, 77%). Mp, IR, ^1H - and ^{13}C -NMR were in agreement with the literature⁹³, mp 169-170 °C (CHCl_3); $\nu_{\text{max}}/\text{cm}^{-1}$ 3234br,m (Hydroxyl O-H), 2917m (Amide N-H), 1646m (C=O), 1598m, 1577w, 1523s, 1496m, 1453s,

1328m, 1282w, 1240m, 1200w, 1158w, 1120w, 1093w, 1074m, 1025m, 1001m, 930w, 898w, 852w, 748s, 705s, 690m, 635w, 608w, 591w, 559w; δ_{H} (400 MHz, DMSO-*d*₆) 9.74 (1H, s, OH), 9.51 (1H, s, NH), 8.01 – 7.93 (2H, m, ArH), 7.71 – 7.63 (1H, m, ArH), 7.63 – 7.57 (1H, m, ArH), 7.56 – 7.49 (2H, m), 7.04 (1H, td, *J* = 7.7, 1.4 Hz, ArH), 6.92 (1H, dd, *J* = 8.1, 1.4, Ar), 6.84 (1H, td, *J* = 7.7, 1.4, ArH). δ_{C} (100 MHz, DMSO-*d*₆) 165.25, 149.36, 134.38, 131.67, 128.52, 127.50, 125.86, 125.70, 124.15, 119.04, 115.99.



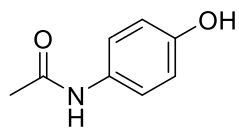
***N*-(2,3,5,6-Tetrafluoro-4-iodophenyl)benzamide (2i).**

Colourless needles (39 mg, 50%). Mp 195-196 °C (CHCl₃); $\nu_{\text{max}}/\text{cm}^{-1}$ 3259m (Amide N-H), 1679m (C=O), 1637w, 1609w, 1511s, 1487m, 1459s, 1445m, 1370w, 1304w, 1283m, 1252m, 1186w, 1172w, 1138m, 1079w, 1058w, 1027w, 1001w, 978s, 931m, 890s, 809m, 795m, 710s, 689m, 647m, 618m, 601w, 560w; δ_{H} (400 MHz, DMSO-*d*₆) 10.58 (1H, s, NH), 8.00 (2H, d, *J* = 7.2 Hz, ArH), 7.66 (1H, t, *J* = 7.4, ArH), 7.57 (1H, t, *J* = 7.5, ArH); δ_{C} (100 MHz, DMSO-*d*₆) 165.3, 132.6, 132.4, 128.7, 128.0, 117.8, 72.9. two CF resonances missing; δ_{F} (282.4 MHz, DMSO-*d*₆) -122.6 - -122.7 (2F, m, C-F(adjacent to I)), -143.2 - -143.3 (2F, m, C-F(adjacent to C=O)); *m/z* (ESI +): calculated for [M+H]⁺ 395.9508, found: 395.9504; calculated for [M+NH₄]⁺ 412.9774, found: 412.9771; calculated for [M+Na]⁺ 417.9328, found: 417.9311.



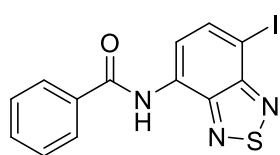
***N*-(4-Amino-3-(trifluoromethyl)phenyl)benzamide (2j).**

Pale purple needles (39 mg, 50%). Mp 115-116 °C (CHCl₃); $\nu_{\text{max}}/\text{cm}^{-1}$ 3412m (Amide N-H), 3277m (Ar NH₂), 1643m (C=O), 1579w, 1530m, 1505m, 1446w, 1431m, 1338w, 1310m, 1293m, 1267m, 1225m, 1174m, 1149m, 1108s, 1052m, 1026w, 999w, 946w, 927w, 901w, 877w, 827m, 799m, 756w, 737w, 695m, 674s, 668s, 619m, 570w; δ_{H} (400 MHz, CDCl₃) δ 8.10 (1H, s, NH), 7.82 (2H, d, *J* = 7.5 Hz, ArH), 7.62 (1H, s, ArH), 7.52 (2H, dd, *J* = 19.8, 8.0, ArH), 7.41 (2H, t, *J* = 7.4, ArH), 6.67 (1H, d, *J* = 8.6 Hz, ArH), 4.13 (2H, s, NH₂); δ_{C} (100 MHz, CDCl₃) 166.08, 141.72, 134.70, 131.93, 128.82, 128.51, 127.13, 126.53, 124.7 (q, ¹J_{CF} 270.0), 119.6 (q, ³J_{CF} 4.0), 117.85, 113.9 (q, ²J_{CF} 30.0); *m/z* (ESI +): calculated for [M+H]⁺ 281.0902, found: 281.0900; calculated for [M+Na]⁺ 303.0716, found: 303.0713.



***N*-(4-Hydroxyphenyl)acetamide (2k).** Colourless needles (41.7 mg, 69%). Mp, IR, ¹H- and ¹³C-NMR were in agreement with the literature.⁹⁴ Mp 169-170 °C (CHCl₃ /EtOH, 90/10); $\nu_{\max}/\text{cm}^{-1}$

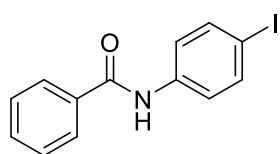
3097m (Amide N-H), 2961bw (Alcohol, O-H), 1662s (C=O), 1575w, 1528s, 1486w, 1429m, 1404m, 1353m, 1279s, 1231s, 1170w, 1107m, 1077w, 1043m, 1006w, 931w, 909m, 866w, 857m, 822m, 760w, 748w, 735s, 722s; δ_{H} (400 MHz, DMSO-d₆) 9.63 (1H, s, OH), 9.12 (1H, s, NH), 7.33 (2H, d, *J* = 9.2, ArH), 6.67 (2H, d, *J* = 8.4, ArH), 1.97 (3H, s, CH₃); δ_{C} (100 MHz, DMSO-d₆) 167.5, 153.1, 131.1, 120.8, 115.0, 23.7.



***N*-(7-Iodobenzo[*c*][1,2,5]thiadiazol-4-yl)benzamide (2l).**

Yellow needles (79.3 mg, 52%). Mp 164-165 °C (CHCl₃); $\nu_{\max}/\text{cm}^{-1}$ 3427m (Amide N-H), 2965m, 1682m (C=O), 1537m,

1505m, 1475m, 1434w, 1483m, 1310w, 1273w, 1247m, 1183w, 1139w, 1098w, 1084m, 1069m, 1020w, 1000w, 921m, 875m, 837s, 791m, 782w, 719w, 682m, 649m, 614m, 585m; δ_{H} (400 MHz, CDCl₃) δ 10.46 (1H, s, NH), 8.26 (1H, d, *J* = 8.0 Hz, ArH), 8.01-8.06 (3H, m, ArH), 7.65 (1H, tt, *J* = 7.2, 1.2, ArH), 7.56-7.60 (2H, m, ArH); δ_{C} (100 MHz, CDCl₃) 165.7, 155.4, 147.5, 139.5, 133.9, 132.2, 130.7, 128.6, 127.8, 121.0, 81.4.; *m/z* (ESI +): calculated for [M+H]⁺ 381.9511, found: 381.9509; calculated for [M+Na]⁺ 403.9330, found: 403.9288.

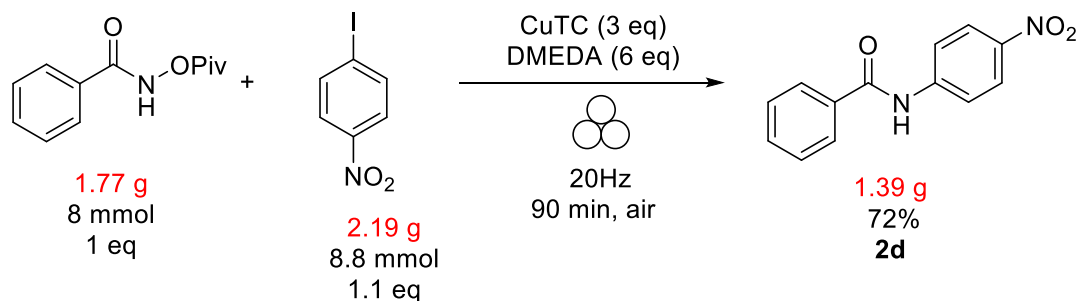


***N*-(4-Iodophenyl)benzamide (2n).** White needles (35.0 mg, 27%). Mp, IR, ¹H- and ¹³C-NMR were in agreement with the literature.⁹⁵ Mp 217-218 °C (CHCl₃); $\nu_{\max}/\text{cm}^{-1}$ 3327m (Amide

N-H), 2920m, 1643s (C=O), 1589m, 1578m, 1514m, 1485m, 1449w, 1422w, 1389m, 1310m, 1287w, 1241m, 1183w, 1100w, 1076w, 1062w, 1026w, 1004m, 982w, 930w, 900w, 816s, 794m, 710s, 692s, 655s, 613w, 585w, 576m, 562w; δ_{H} (400 MHz, Acetone-d₆) δ 9.61 (1H, s, NH), 7.97-8.00 (2H, m, ArH), 7.71 (4H, s, ArH), 7.49-7.58 (3H, m, ArH); δ_{C} (100 MHz, Acetone-d₆) 166.4, 140.5, 140.4, 136.1, 132.6, 129.3, 128.4, 123.1, 123.0, 87.0; *m/z* (ESI +): calculated for [M]⁺ 322.98, found: 323.0; calculated for [M+H]⁺ 323.99, found: 324.0.

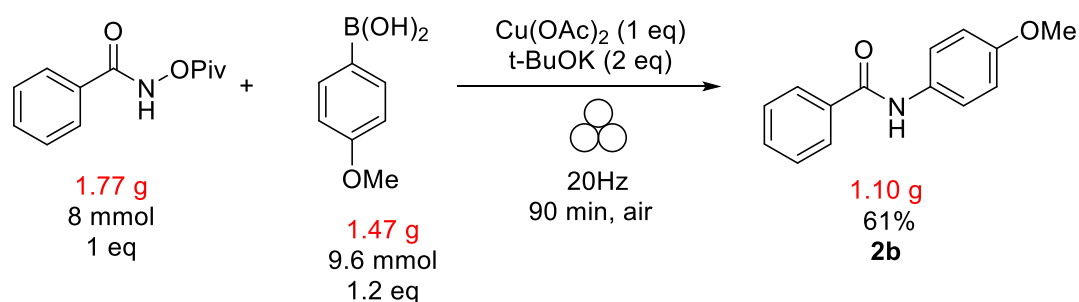
5.9.5 Gram-Scale Mechanochemical Preparations (Protocol A and B)

Protocol A:



To an SLA 3D printed milling jar (70 mL internal volume) *N*-(pivaloyloxy)benzamide (1.77 g, 8 mmol, 1 eq) was added, followed by 1-iodo-4-nitrobenzene (2.19 g, 8.8 mmol, 1.1 eq.), copper (I) thiophene-2-carboxylate (4.56 g, 24 mmol, 3 eq.) and *N,N'*-dimethylethylenediamine (4.23 g, 48 mmol, 6 eq.), along with 4 ZrO₂ balls of variable diameter (6 - 15 mm) with a total mass of 16.11 g. The jar was sealed and milled for 90 minutes at 20 Hz. After the completion of the reaction which was confirmed by TLC (CHCl₃:EtOAc, 90:10), the jar was opened and the reaction mixture was passed through a short silica plug (eluted with CHCl₃:EtOAc, 80:20). The resulting solution was evaporated under reduced pressure, and the residue was recrystallised to afford the title compound as a yellow powder (1.39 g, 72%).

Protocol B:



To an SLA 3D printed milling jar (70 mL internal volume) *N*-(pivaloyloxy)benzamide (1.77 g, 8 mmol, 1 eq.) was added, followed by 4-methoxyphenylboronic acid (1.47 g, 9.6 mmol, 1.2 eq.), copper(II) acetate (1.45 g, 8 mmol, 1 eq.) and potassium *tert*-butoxide (1.80 g, 16 mmol, 2 eq.). In addition to these reagents, 4 ZrO₂ balls of variable diameter (6 - 15 mm) with a total mass of 16.11 g were added. The jar was sealed and milled for 90 minutes at 20 Hz. After the completion of the reaction which was confirmed by TLC

(CHCl₃:EtOAc, 90:10), the jar was opened and the reaction mixture was passed through a short silica plug (eluted with CHCl₃:EtOAc, 80:20). The resulting solution was evaporated under reduced pressure, and the residue was recrystallised to afford the title compound as a white powder (1.10 g, 61%).

5.10 References

- (1) Liu, J.; Wang, Z.; Cheng, P.; Zaworotko, M. J.; Chen, Y.; Zhang, Z. Post-Synthetic Modifications of Metal–Organic Cages. *Nat. Rev. Chem.* **2022**, *6* (5), 339–356. <https://doi.org/10.1038/s41570-022-00380-y>.
- (2) Wang, H.; Jin, Y.; Sun, N.; Zhang, W.; Jiang, J. Post-Synthetic Modification of Porous Organic Cages. *Chem. Soc. Rev.* **2021**, *50* (16), 8874–8886. <https://doi.org/10.1039/D0CS01142H>.
- (3) Carné-Sánchez, A.; Albalad, J.; Grancha, T.; Imaz, I.; Juanhuix, J.; Larpent, P.; Furukawa, S.; MasPOCH, D. Postsynthetic Covalent and Coordination Functionalization of Rhodium(II)-Based Metal–Organic Polyhedra. *J. Am. Chem. Soc.* **2019**, *141* (9), 4094–4102. <https://doi.org/10.1021/jacs.8b13593>.
- (4) Antonio, A. M.; Korman, K. J.; Yap, G. P. A.; Bloch, E. D. Porous Metal–Organic Alloys Based on Soluble Coordination Cages. *Chem. Sci.* **2020**, *11* (46), 12540–12546. <https://doi.org/10.1039/D0SC04941G>.
- (5) Cheng, F.; Zhu, J.; Adronov, A. Supramolecular Functionalization of Single-Walled Carbon Nanotubes with Triply Fused Porphyrin Dimers: A Study of Structure–Property Relationships. *Chem. Mater.* **2011**, *23* (13), 3188–3194. <https://doi.org/10.1021/cm2004648>.
- (6) Ravikumar, V.; Fin, A.; Sakai, N.; Matile, S. Solubilising Groups: A Conceptual Equivalent of Protecting Groups in Organic Synthesis. *Supramol. Chem.* **2011**, *23* (1–2), 69–73. <https://doi.org/10.1080/10610278.2010.510193>.
- (7) Tarzia, A.; Jelfs, K. E. Unlocking the Computational Design of Metal–Organic Cages. *Chem. Commun.* **2022**, *58* (23), 3717–3730. <https://doi.org/10.1039/D2CC00532H>.

- (8) Green, H. R. *Hydroxamic Acids and Their Porous Materials*, Heriot-Watt University, 2018.
- (9) Chuang, H.-Y.; Schupp, M.; Meyrelles, R.; Maryasin, B.; Maulide, N. Redox-Neutral Selenium-Catalysed Isomerisation of Para-Hydroxamic Acids into Para-Aminophenols. *Angew. Chem. Int. Ed.* **2021**, *60* (25), 13778–13782. <https://doi.org/10.1002/anie.202100801>.
- (10) Mocci, R.; De Luca, L.; Delogu, F.; Porcheddu, A. An Environmentally Sustainable Mechanochemical Route to Hydroxamic Acid Derivatives. *Adv. Synth. Catal.* **2016**, *358* (19), 3135–3144. <https://doi.org/10.1002/adsc.201600350>.
- (11) Jones, K. L. *New Chemistry of Hydroxylamines*, Cardiff University, 2011.
- (12) Wang, Q.; Wei, C.; Pérez, L. M.; Rogers, W. J.; Hall, M. B.; Mannan, M. S. Thermal Decomposition Pathways of Hydroxylamine: Theoretical Investigation on the Initial Steps. *J. Phys. Chem. A* **2010**, *114* (34), 9262–9269. <https://doi.org/10.1021/jp104144x>.
- (13) Takenaka, Y.; Kiyosu, T.; Choi, J.-C.; Sakakura, T.; Yasuda, H. Selective Synthesis of N-Aryl Hydroxylamines by the Hydrogenation of Nitroaromatics Using Supported Platinum Catalysts. *Green Chem.* **2009**, *11* (9), 1385–1390. <https://doi.org/10.1039/B904672K>.
- (14) Andreou, D.; Iordanidou, D.; Tamiolakis, I.; Armatas, G.; Lykakis, I. Reduction of Nitroarenes into Aryl Amines and N-Aryl Hydroxylamines *via* Activation of NaBH₄ and Ammonia-Borane Complexes by Ag/TiO₂ Catalyst. *Nanomaterials* **2016**, *6* (3), 54. <https://doi.org/10.3390/nano6030054>.
- (15) Izato, Y.; Koshi, M.; Miyake, A. Initial Decomposition Pathways of Aqueous Hydroxylamine Solutions. *J. Phys. Chem. B* **2017**, *121* (17), 4502–4511. <https://doi.org/10.1021/acs.jpcc.6b10546>.
- (16) Monnier, F.; Taillefer, M. Catalytic C-C, C-N, and C-O Ullmann-Type Coupling Reactions. *Angew. Chem. Int. Ed.* **2009**, *48* (38), 6954–6971. <https://doi.org/10.1002/anie.200804497>.
- (17) Cao, Q.; Nicholson, W. I.; Jones, A. C.; Browne, D. L. Robust Buchwald–Hartwig Amination Enabled by Ball-Milling. *Org. Biomol. Chem.* **2018**.

<https://doi.org/10.1039/C8OB01781F>.

- (18) Zhang, Z.; Yu, Y.; Liebeskind, L. S. N-Amidation by Copper-Mediated Cross-Coupling of Organostannanes or Boronic Acids with *O*-Acetyl Hydroxamic Acids. *Org. Lett.* **2008**, *10* (14), 3005–3008. <https://doi.org/10.1021/ol8009682>.
- (19) Li, G.; Szostak, M. Highly Selective Transition-Metal-Free Transamidation of Amides and Amidation of Esters at Room Temperature. *Nat. Commun.* **2018**, *9* (1), 1–8. <https://doi.org/10.1038/s41467-018-06623-1>.
- (20) Bradshaw, P. R.; Wilson, I. D.; Gill, R. U.; Butler, P. J.; Dilworth, C.; Athersuch, T. J. Metabolic Hydrolysis of Aromatic Amides in Selected Rat, Minipig, and Human in Vitro Systems. *Sci. Rep.* **2018**, *8* (1), 1–8. <https://doi.org/10.1038/s41598-018-20464-4>.
- (21) Sabatini, M. T.; Boulton, L. T.; Sneddon, H. F.; Sheppard, T. D. A Green Chemistry Perspective on Catalytic Amide Bond Formation. *Nat. Catal.* **2019**, *2* (1), 10–17. <https://doi.org/10.1038/s41929-018-0211-5>.
- (22) Dunetz, J. R.; Magano, J.; Weisenburger, G. A. Large-Scale Applications of Amide Coupling Reagents for the Synthesis of Pharmaceuticals. *Org. Process Res. Dev.* **2016**, *20* (2), 140–177. <https://doi.org/10.1021/op500305s>.
- (23) Sneddon, H. F.; Murray, J.; MacMillan, D. S.; Watson, A. J. B.; Jamieson, C. Evaluation of Alternative Solvents in Common Amide Coupling Reactions: Replacement of Dichloromethane and *N,N*-Dimethylformamide. *Green Chem.* **2012**, *15* (3), 596. <https://doi.org/10.1039/c2gc36900a>.
- (24) Gonzalez, C.; Ponder, C. S.; Broxterman, Q. B.; Manley, J. B. Using the Right Green Yardstick: Why Process Mass Intensity Is Used in the Pharmaceutical Industry To Drive More Sustainable Processes. *Org. Process Res. Dev.* **2011**, *15*, 4, 912–917. <https://doi.org/10.1021/op200097d>.
- (25) Rioux, J. P.; Myers, R. A. M. Methylene Chloride Poisoning: A Paradigmatic Review. *J. Emerg. Med.* **1988**, *6* (3), 227–238. [https://doi.org/10.1016/0736-4679\(88\)90330-7](https://doi.org/10.1016/0736-4679(88)90330-7).
- (26) Redlich, A. C.; Beckett, W.; Sparer, J.; Barwick, W. K.; Riely, A. C.; Miller, H.; Sigal, L. Liver Disease Associated with Occupational Exposure to the Solvent

- Dimethylformamide. *Ann. Intern. Med.* **1988**, 108, 680-686. doi:10.7326/0003-4819-108-5-680.
- (27) Dayaker, G.; Tan, D.; Biggins, N.; Shelam, A.; Do, J.-L.; Katsenis, A. D.; Friscic, T. Catalytic Room-Temperature C-N Coupling of Amides and Isocyanates Using Mechanochemistry. *ChemSusChem* **2020**, 13 (11), 2966-2972. <https://doi.org/10.1002/cssc.201902576>.
- (28) Kubota, K.; Seo, T.; Koide, K.; Hasegawa, Y.; Ito, H. Olefin-Accelerated Solid-State C–N Cross-Coupling Reactions Using Mechanochemistry. *Nat. Commun.* **2019**, 10 (1), 1–11. <https://doi.org/10.1038/s41467-018-08017-9>.
- (29) James, S. L.; Adams, C. J.; Bolm, C.; Braga, D.; Collier, P.; Friščic, T.; Grepioni, F.; Harris, K. D. M.; Hyett, G.; Jones, W.; et al. Playing with Organic Radicals as Building Blocks for Functional Molecular Materials. *Chem. Soc. Rev.* **2012**, 41 (1), 413–447. <https://doi.org/10.1039/c1cs15171a>.
- (30) Wang, G. W. Mechanochemical Organic Synthesis. *Chem. Soc. Rev.* **2013**, 42 (18), 7668–7700. <https://doi.org/10.1039/c3cs35526h>.
- (31) Zhu, S. E.; Li, F.; Wang, G. W. Mechanochemistry of Fullerenes and Related Materials. *Chem. Soc. Rev.* **2013**, 42 (18), 7535–7570. <https://doi.org/10.1039/c3cs35494f>.
- (32) Obst, M.; König, B. Solvent-Free, Visible-Light Photocatalytic Alcohol Oxidations Applying an Organic Photocatalyst. *Beilstein J. Org. Chem.* **2016**, 12, 2358–2363. <https://doi.org/10.3762/bjoc.12.229>.
- (33) Friščić, T.; Mottillo, C.; Titi, H. M. Mechanochemistry for Synthesis. *Angew. Chem. Int. Ed.* **2020**, 59 (3), 1018–1029. <https://doi.org/10.1002/anie.201906755>.
- (34) Zory Vlad Todres. *Organic Mechanochemistry and Its Practical Applications*, 1st ed.; CRC Press, 2006.
- (35) Diesendruck, C. E. Mechanophores for Chemical Function. In *Mechanochemistry in Materials*; The Royal Society of Chemistry, 2018; pp 36–52. <https://doi.org/10.1039/9781782623885-00036>.
- (36) Wang, G.; Yuan, T.; Li, D. One-Pot Formation of C-C and C-N Bonds through Palladium-Catalyzed Dual C-H Activation: Synthesis of Phenanthridinones.

- Angew. Chem. Int. Ed.* **2011**, 50 (6), 1380-1383.
<https://doi.org/10.1002/anie.201005874>
- (37) Yasuhisa, T.; Hirano, K.; Miura, M.; Yasuhisa, T.; Hirano, K.; Miura, M. Rhodium-Catalyzed Electrophilic Amination of Arylboronic Acids with Secondary Hydroxylamines. *Chem. Lett.* **2017**, 10-13.
<https://doi.org/10.1246/cl.161158>.
- (38) Guimond, N.; Gorelsky, S. I.; Fagnou, K. Rhodium(III)-Catalyzed Heterocycle Synthesis Using an Internal Oxidant: Improved Reactivity and Mechanistic Studies. *J. Am. Chem. Soc.* **2011**, 133 (16), 6449-6457.
<https://doi.org/10.1021/ja201143v>.
- (39) Štefanić, G.; Krehula, S.; Štefanić, I. The High Impact of a Milling Atmosphere on Steel Contamination. *Chem. Commun.* **2013**, 49 (81), 9245-9247.
<https://doi.org/10.1039/c3cc44803g>.
- (40) Mako, T. L.; Byers, J. A. Recent Advances in Iron-Catalysed Cross Coupling Reactions and Their Mechanistic Underpinning. *Inorg. Chem. Front.* **2016**, 3 (6), 766-790. <https://doi.org/10.1039/c5qi00295h>.
- (41) Muzart, J. Chromium-Catalyzed Oxidations in Organic Synthesis. *Chem. Rev.* **1992**, 92 (1), 113-140. <https://doi.org/10.1021/cr00009a005>.
- (42) Codd, R. Traversing the Coordination Chemistry and Chemical Biology of Hydroxamic Acids. *Coord. Chem. Rev.* **2008**, 252 (12-14), 1387-1408.
<https://doi.org/10.1016/j.ccr.2007.08.001>.
- (43) Brennan, B. J.; Chen, J.; Rudshiteyn, B.; Chaudhuri, S.; Mercado, B. Q.; Batista, V. S.; Crabtree, R. H.; Brudvig, G. W. Molecular Titanium-Hydroxamate Complexes as Models for TiO₂ surface Binding. *Chem. Commun.* **2016**, 52 (14), 2972-2975. <https://doi.org/10.1039/c5cc09857b>.
- (44) Shen, M.; Li, B.; Zhang, Z.; Zhao, L.; Xiong, G. Abrasive Wear Behavior of PTFE for Seal Applications under Abrasive-Atmosphere Sliding Condition. *Friction* **2020**, 8 (4), 755-767. <https://doi.org/10.1007/s40544-019-0301-7>.
- (45) Swamy, T.; Raviteja, P.; Subba-Reddy, B. V.; Ravinder, V. Efficient Method for the Synthesis of Benzamides from Benzoic Acids and Aryl Isothiocyanates Using

- K_2HPO_4 . *ChemistrySelect* **2017**, *2* (25), 7612–7614. <https://doi.org/10.1002/slct.201701580>.
- (46) Friščić, T.; Childs, L. S.; Rizvi, A. A. S.; Jones, W. The Role of Solvent in Mechanochemical and Sonochemical Cocrystal Formation: A Solubility-Based Approach for Predicting Cocrystallisation Outcome. *CrystEngComm* **2009**, *11* (3), 388–403. <https://doi.org/10.1039/B815174A>.
- (47) Friščić, T.; Reid, D. G.; Halasz, I.; Stein, R. S.; Dinnebier, R. E.; Duer, M. J. Ion- and Liquid-Assisted Grinding: Improved Mechanochemical Synthesis of Metal-Organic Frameworks Reveals Salt Inclusion and Anion Templating. *Angew. Chem. Int. Ed.* **2010**, *49* (4), 712–715. <https://doi.org/10.1002/anie.200906583>.
- (48) Winternheimer, D.; Merlic, C. Alkoxydienes *via* Copper-Promoted Couplings. *Org. Lett.* **2010**, *12* (11), 2508–2510. <https://doi.org/10.1055/s-0030-1257904>.
- (49) Seo, T.; Ishiyama, T.; Kubota, K.; Ito, H. Solid-State Suzuki–Miyaura Cross-Coupling Reactions: Olefin-Accelerated C–C Coupling Using Mechanochemistry. *Chem. Sci.* **2019**. <https://doi.org/10.1039/c9sc02185j>.
- (50) Rao, H.; Fu, H.; Jiang, Y.; Zhao, Y. Copper-Catalyzed Arylation of Amines Using Diphenyl Pyrrolidine-2- Phosphonate as the New Ligand. *J. Org. Chem.* **2005**, *70* (20), 8107–8109. <https://doi.org/10.1021/jo051221w>.
- (51) Zhang, Z.; Yu, Y.; Liebeskind, L. S. *N*-Amidation by Copper-Mediated Cross-Coupling of Organostannanes or Boronic Acids with *O*-Acetyl Hydroxamic Acids. *Org. Lett.* **2008**, *10* (14), 3005–3008. <https://doi.org/10.1021/ol8009682>.
- (52) Chen, J.-Q.; Li, J.-H.; Dong, Z.-B. A Review on the Latest Progress of Chan-Lam Coupling Reaction. *Adv. Synth. Catal.* **2020**, *362* (16), 3311–3331. <https://doi.org/10.1002/adsc.202000495>.
- (53) Munir, I.; Zahoor, A. F.; Rasool, N.; Naqvi, S. A. R.; Zia, K. M.; Ahmad, R. Synthetic Applications and Methodology Development of Chan–Lam Coupling: A Review. *Mol. Divers.* **2019**, *23* (1), 215–259. <https://doi.org/10.1007/s11030-018-9870-z>.
- (54) Leussing, D. L.; Hansen, R. C. The Copper(II)-Pyridine Complexes and Their Reaction with Hydroxide Ions. *J. Am. Chem. Soc.* **1957**, *79* (16), 4270–4273.

<https://doi.org/10.1021/ja01573a008>.

- (55) Štrukil, V.; Sajko, I. Mechanochemically-Assisted Solid-State Photocatalysis (MASSPC). *Chem. Commun.* **2017**, 53 (65), 9101–9104. <https://doi.org/10.1039/c7cc03510a>.
- (56) Klaper, M.; Wessig, P.; Linker, T. Base Catalysed Decomposition of Anthracene Endoperoxide. *Chem. Commun.* **2016**, 52 (6), 1210–1213. <https://doi.org/10.1039/c5cc08606j>.
- (57) Shixiang, G.; Liansheng, W.; Qingguo, H.; Sukui, H. Solubilization of Polycyclic Aromatic Hydrocarbons by β -Cyclodextrin and Carboxymethyl- β -Cyclodextrin. *Chemosphere* **1998**, 37 (7), 1299–1305. [https://doi.org/10.1016/S0045-6535\(98\)00127-1](https://doi.org/10.1016/S0045-6535(98)00127-1).
- (58) Liu, C.; Li, X.; Wu, Y.; Qiu, J. Copper-Catalyzed Protodeboronation of Arylboronic Acids in Aqueous Media. *RSC Adv.* **2014**, 4 (97), 54307–54311. <https://doi.org/10.1039/c4ra11659c>.
- (59) Lee, C. Y.; Ahn, S. J.; Cheon, C. H. Protodeboronation of *Ortho*- and *Para*-Phenol Boronic Acids and Application to *Ortho* and *Meta* Functionalization of Phenols Using Boronic Acids as Blocking and Directing Groups. *J. Org. Chem.* **2013**, 78 (23), 12154–12160. <https://doi.org/10.1021/jo402174v>.
- (60) Veguillas, M.; Ribagorda, M.; Carreño, M. C. Regioselective Alkylation of Heteroaromatic Compounds with 3-Methyl-2-Quinonyl Boronic Acids. *Org. Lett.* **2011**, 13 (4), 656–659. <https://doi.org/10.1021/ol1028964>.
- (61) Halasz, I.; Kimber, S. A. J.; Beldon, P. J.; Belenguer, A. M.; Adams, F.; Honkimäki, V.; Nightingale, R. C.; Dinnebier, R. E.; Friščić, T. *In Situ* and Real-Time Monitoring of Mechanochemical Milling Reactions Using Synchrotron X-Ray Diffraction. *Nat. Protoc.* **2013**, 8 (9), 1718–1729. <https://doi.org/10.1038/nprot.2013.100>.
- (62) Tumanov, N.; Ban, V.; Poulain, A.; Filinchuk, Y. 3D-Printed Jars for Ball-Milling Experiments Monitored *in situ* by X-Ray Powder Diffraction. *J. Appl. Cryst.* **2017**, 50, 994–999. <https://doi.org/10.1107/S1600576717006744>.
- (63) <https://formlabs.com/materials/> (accessed Sep 13, 2019).

- (64) <https://formlabs.com/eu/blog/introducing-the-form-2/> (accessed Sep 13, 2019).
- (65) Fischer, F.; Fendel, N.; Greiser, S.; Rademann, K.; Emmerling, F. Impact Is Important - Systematic Investigation of the Influence of Milling Balls in Mechanochemical Reactions. *Org. Process Res. Dev.* **2017**, *21* (4), 655–659. <https://doi.org/10.1021/acs.oprd.6b00435>.
- (66) Gao, J.; Wang, G. W. Direct Oxidative Amidation of Aldehydes with Anilines under Mechanical Milling Conditions. *J. Org. Chem.* **2008**, *73* (7), 2955–2958. <https://doi.org/10.1021/jo800075t>.
- (67) Hussain, H.; Green, I. R.; Ahmed, I. Journey Describing Applications of Oxone in Synthetic Chemistry. *Chem. Rev.* **2013**, *113* (5), 3329–3371. <https://doi.org/10.1021/cr3004373>.
- (68) Štrukil, V.; Bartolec, B.; Portada, T.; Đilović, I.; Halasz, I.; Margetić, D. One-Pot Mechanochemical Synthesis of Aromatic Amides and Dipeptides from Carboxylic Acids and Amines. *Chem. Commun.* **2012**, *48* (99), 12100–12102. <https://doi.org/10.1039/c2cc36613d>.
- (69) Bonnamour, J.; Métro, T. X.; Martinez, J.; Lamaty, F. Environmentally Benign Peptide Synthesis Using Liquid-Assisted Ball-Milling: Application to the Synthesis of Leu-Enkephalin. *Green Chem.* **2013**, *15* (5), 1116–1120. <https://doi.org/10.1039/c3gc40302e>.
- (70) Zhakeyev, A.; Tobin, J.; Wang, H.; Vilela, F.; Xuan, J. Additive Manufacturing of Photoactive Polymers for Visible Light Harvesting. *Energy Procedia* **2019**, *158*, 5608–5614. <https://doi.org/10.1016/j.egypro.2019.01.579>.
- (71) Zhakeyev, A.; Jones, M. C.; Thomson, C. G.; Tobin, J. M.; Wang, H.; Vilela, F.; Xuan, J. Additive Manufacturing of Intricate and Inherently Photocatalytic Flow Reactor Components. *Addit. Manuf.* **2021**, *38*, 101828. <https://doi.org/10.1016/j.addma.2020.101828>.
- (72) Tan, H. L.; Abdi, F. F.; Ng, Y. H. Heterogeneous Photocatalysts: An Overview of Classic and Modern Approaches for Optical, Electronic, and Charge Dynamics Evaluation. *Chem. Soc. Rev.* **2019**, *48* (5), 1255–1271. <https://doi.org/10.1039/C8CS00882E>.

- (73) Thomson, C. G.; Lee, A.-L.; Vilela, F. Heterogeneous Photocatalysis in Flow Chemical Reactors. *Beilstein J. Org. Chem.* **2020**, *16*, 1495–1549.
- (74) Romero, N. A.; Nicewicz, D. A. Organic Photoredox Catalysis. *Chem. Rev.* **2016**, *116* (17), 10075–10166. <https://doi.org/10.1021/acs.chemrev.6b00057>.
- (75) Friščić, T.; Halasz, I.; Beldon, P. J.; Belenguer, A. M.; Adams, F.; Kimber, S. A. J.; Honkimäki, V.; Dinnebier, R. E. Real-Time and *in situ* Monitoring of Mechanochemical Milling Reactions. *Nat. Chem.* **2013**, *5* (1), 66–73. <https://doi.org/10.1038/nchem.1505>.
- (76) Hassan, J; Sévignon, M; Gozzi, C; Schulz, E; Lemaire, M. *Chemical Reviews* **2002**, *102* (5), 1359-1470. <https://doi.org/10.1021/cr000664r>.
- (77) Ruiz-castillo, P.; Buchwald, S. L. Applications of Palladium-Catalyzed C-N Cross-Coupling Reactions. *Chem. Rev.* **2016**, *116* (19), 12564–12649 <https://doi.org/10.1021/acs.chemrev.6b00512>.
- (78) Innitzer, A. Copper(I) Thiophene-2-Carboxylate (CuTC). *Synlett* **2005**, *15*, 2405–2406. <https://doi.org/10.1055/s-2005-872681>.
- (79) Beletskaya, I. P.; Cheprakov, A. V. Copper in Cross-Coupling Reactions: The Post-Ullmann Chemistry. *Coord. Chem. Rev.* **2004**, *248* (21–24), 2337–2364. <https://doi.org/10.1016/j.ccr.2004.09.014>.
- (80) Lou, S. J.; Mao, Y. J.; Xu, D. Q.; He, J. Q.; Chen, Q.; Xu, Z. Y. Fast and Selective Dehydrogenative C-H/C-H Arylation Using Mechanochemistry. *ACS Catal.* **2016**, *6* (6), 3890–3894. <https://doi.org/10.1021/acscatal.6b00861>.
- (81) Liori, A. A.; Stamatopoulos, I. K.; Papastavrou, A. T.; Pinaka, A.; Vougioukalakis, G. C. A Sustainable, User-Friendly Protocol for the Pd-Free Sonogashira Coupling Reaction. *Eur. J. Org. Chem.* **2018**, (44), 6134–6139. <https://doi.org/10.1002/ejoc.201800827>.
- (82) Sperotto, E.; van Klink, G. P. M.; van Koten, G.; de Vries, J. G. The Mechanism of the Modified Ullmann Reaction. *Dalt. Trans.* **2010**, *39* (43), 10352–10361. <https://doi.org/10.1039/C0DT00674B>.
- (83) Lee, P. Y.; Liang, P.; Yu, W. Y. Pd(II)-Catalyzed Direct *Ortho*- C-H Acylation of Aromatic Ketones by Oxidative Decarboxylation of α -Oxocarboxylic Acids. *Org.*

- Lett.* **2017**, *19* (8), 2082–2085. <https://doi.org/10.1021/acs.orglett.7b00677>.
- (84) Hoogenboom, R.; Becer, C. R.; Guerrero-Sanchez, C.; Hoepfener, S.; Schubert, U. S. Solubility and Thermoresponsiveness of PMMA in Alcohol-Water Solvent Mixtures. *Aust. J. Chem.* **2010**, *63* (8), 1173–1178. <https://doi.org/10.1071/CH10083>.
- (85) Shimada, M.; Tsuchiya, M.; Sakamoto, R.; Yamanoi, Y.; Nishibori, E.; Sugimoto, K.; Nishihara, H. Bright Solid-State Emission of Disilane-Bridged Donor-Acceptor-Donor and Acceptor-Donor-Acceptor Chromophores. *Angew. Chem. Int. Ed.* **2016**, *55* (9), 3022–3026. <https://doi.org/10.1002/anie.201509380>.
- (86) Beletskaya, I. P.; Cheprakov, A. V. The Complementary Competitors: Palladium and Copper in C–N Cross-Coupling Reactions. *Organometallics* **2012**, *31* (22), 7753–7808. <https://doi.org/10.1021/om300683c>.
- (87) Katritzky, A. R.; Cai, C.; Singh, S. K. Efficient Microwave Access to Polysubstituted Amidines from Imidoylbenzotriazoles. *J. Org. Chem.* **2006**, *71* (9), 3375–3380. <https://doi.org/10.1021/jo052443x>.
- (88) Racine, E.; Monnier, F.; Vors, J. P.; Taillefer, M. A Simple Copper-Catalyzed Synthesis of Tertiary Acyclic Amides. *Org. Lett.* **2011**, *13* (11), 2818–2821. <https://doi.org/10.1021/ol200750p>.
- (89) Weisblat, D. I.; Magerlein, B. J.; Myers, D. R. The Cleavage of Sulfonamides. *J. Am. Chem. Soc.* **1953**, *75* (15), 3630–3632. <https://doi.org/10.1021/ja01111a007>.
- (90) Suresh Babu, V. V.; Vasanthakumar, G. R.; Tantry, S. J. N-Silylation of Amines and Amino Acid Esters under Neutral Conditions Employing TMS-Cl in the Presence of Zinc Dust. *Tetrahedron Lett.* **2005**, *46* (23), 4099–4102. <https://doi.org/10.1016/j.tetlet.2005.04.007>.
- (91) Karthik, S.; Muthuvel, K.; Gandhi, T. Base-Promoted Amidation and Esterification of Imidazolium Salts via Acyl C–C Bond Cleavage: Access to Aromatic Amides and Esters. *J. Org. Chem.* **2019**, *84* (2), 738–751. <https://doi.org/10.1021/acs.joc.8b02567>.
- (92) Ueda, S.; Nagasawa, H. Copper-Catalyzed Synthesis of Benzoxazoles via a Regioselective C–H Functionalization/C–O Bond Formation under an Air

- Atmosphere. *J. Org. Chem.* **2009**, *74* (11), 4272–4277.
<https://doi.org/10.1021/jo900513z>.
- (93) Faler, C. A.; Joullié, M. M. Aminolysis of Allyl Esters with Bislithium Aryl Amides. *Tetrahedron Lett.* **2006**, *47* (40), 7229–7231.
<https://doi.org/10.1016/j.tetlet.2006.07.136>.
- (94) Kukut, M.; Kiskan, B.; Yagci, Y. Self-Curable Benzoxazine Functional Polybutadienes Synthesized by Click Chemistry. *Des. Monomers Polym.* **2009**, *12* (2), 167–176. <https://doi.org/10.1163/156855509X412108>.
- (95) Zhu, Y. Y.; Yi, H. P.; Li, C.; Jiang, X. K.; Li, Z. T. The N-H···X (X = Cl, Br, and I) Hydrogen-Bonding Pattern in Aromatic Amides: A Crystallographic and ¹H NMR Study. *Cryst. Growth Des.* **2008**, *8* (4), 1294–1300.
<https://doi.org/10.1021/cg7010293>.